



Contents lists available at ScienceDirect

Progress in Materials Science

journal homepage: www.elsevier.com/locate/pmatsci



Progress in material selection for solid oxide fuel cell technology: A review



Neelima Mahato ^{a,b}, Amitava Banerjee ^a, Alka Gupta ^a, Shobit Omar ^c,
Kantesh Balani ^{a,*}

^a High Temperature Fuel Cell Laboratory, Department of Materials Science and Engineering, Indian Institute of Technology Kanpur, Kanpur 208016, India

^b Department of Chemical Engineering, Yeungnam University, Gyeongsan, Republic of Korea

^c Electroceramics Laboratory, Department of Materials Science and Engineering, Indian Institute of Technology Kanpur, Kanpur 208016, India

ARTICLE INFO

Article history:

Received 28 May 2013

Received in revised form 4 January 2015

Accepted 7 January 2015

Available online 13 February 2015

Keywords:

Solid oxide fuel cells (SOFC)

Anode

Yttria stabilized zirconia (YSZ)

Solid electrolyte

Cathode

Interconnects

Sealant

Structure

Material degradation

ABSTRACT

Solid oxide fuel cells (SOFC) have emerged as energy conversion devices in achieving high efficiency of over 70% with regeneration. The critical components of SOFC include anode, electrolyte, and cathode. However, for a stack of individual SOFCs, the evaluation of sealants and interconnects are also essential. In this review article, material selection, fundamentals of operation and underlying mechanisms, processing, microstructural and phase characterization, and the functionality and performance of individual SOFC components are presented in detail. The major challenges and complexity in functional section of SOFC include: (i) poisoning via sulfur and coke deposition, surface diffusion of adsorbate, and charge transfer at triple-phase boundary (TPB) in anode, (ii) hindered O²⁻ migration that converts chemical energy into electrical energy in the solid electrolyte (thus, the creation of ion transfer channels, ease of O²⁻ migration, dissociation of vacancy around dopants, straining of lattice, and other factors such as control of phase and its distribution, grain and grain boundary conductivity, become critical in designing the electrolytes for SOFCs), (iii) multiple rate determining factors such as geometry of active surfaces, and existence of overpotential, in cathode (thereby, comprehensive electrochemical impedance spectroscopy is required for the analysis of solid cathodes in SOFC), (iv) chemical incompatibility and instability in both oxidizing and reducing environments while

* Corresponding author. Tel.: +91 5122596194.

E-mail address: kbalani@iitk.ac.in (K. Balani).

matching the coefficient of thermal expansion (CTE) in the *interconnects* in order to sustain large number of thermal cycling during the operation of SOFC, and (v) isolation of the fuel and oxidizing gases while matching the CTE of the anode, cathode and interconnects, using *sealant*. Moreover, the glass-transition of sealant dictates the maximum allowable working temperature of SOFC. Thus, the necessitated temporal progress in material selection along with a detailed insight into the conceptual role of thermodynamics and kinetics of surface/cell reactions, effect of phases and microstructure on conductivity, fuel flexibility and deterioration in performance of individual fuel cell components, and evolution of new materials are coherently presented. This article provides a comprehensive review with respect to the structure, chemistry, design and selection of materials, underlying mechanisms, and performance of each SOFC component, and it opens up the future directions towards pursuing SOFC research.

© 2015 Elsevier Ltd. All rights reserved.

Contents

1. Introduction	143
1.1. Historical background	144
1.2. Electrochemistry, kinetics and thermodynamics of fuel-cell reactions	150
2. Anode	152
2.1. Nickel metal anodes	155
2.2. Nickel/YSZ cermet	164
2.3. Sulfur poisoning and carbon deposition	182
2.4. Copper and other noble metal cermets	190
2.5. Ceria and other compounds	191
2.6. Perovskite and double-perovskite structure based anodes	194
2.7. Pyrochlores	197
3. Electrolyte	210
3.1. Fluorite structure oxides	211
3.1.1. Ionic conductivity	213
3.1.2. Effect of defect association	214
3.1.3. Dependence on oxygen partial pressure	215
3.1.4. Effect of dopant cations	216
3.1.5. Effect of microstructure: grain boundaries and grain size	221
3.2. δ - Bi_2O_3 - and $\text{Bi}_4\text{V}_2\text{O}_{11}$ -based ceramics	225
3.3. Pyrochlores based electrolytes	226
3.4. Hetero-structured bi-, tri- and multiple-layered composite electrolytes	229
3.5. Perovskite and related intergrowth structures (LaGaO_3 , Brownmillerites, La-MOX and Apatites)	235
3.5.1. Perovskite-based electrolytes	235
3.5.2. Perovskites based on LnBO_3 (B = Al, In, Sc, Y)	237
3.5.3. Brownmillerite-like phases	238
3.5.4. $\text{La}_2\text{Mo}_2\text{O}_9$ (LAMOX) based electrolyte materials	240
3.5.5. Apatite structure	242
3.6. Other structure compounds	244
4. Cathode	245
4.1. Requirements of cathode material	246
4.1.1. Focus of cathode research and development	246
4.2. Material selection for cathode	246
4.3. Perovskite materials	251
4.4. Mechanism of cathode reactions	255

4.4.1. At atomic scale	255
4.4.2. At bulk scale	256
4.5. Strategies of materials selection for intermediate (or low) temperature cathodes	264
4.6. Degradation problems	266
4.6.1. Reaction with other cell components	271
5. Interconnects	274
5.1. Ceramic interconnect materials	275
5.2. Metallic alloys as interconnect materials	281
5.3. Material degradation and protection	286
6. Sealants	288
6.1. Compressive seals	289
6.2. Rigid seals	295
6.3. Methods of using sealing glass	300
7. Conclusions	304
Acknowledgements	305
References	305

1. Introduction

Solid oxide fuel cell (SOFC) is an electrochemical energy-conversion device, which offers tremendous promise for delivering high electrical efficiency and significant environmental benefits in terms of fuel flexibility (hydrocarbons, and municipal waste), as well as clean and efficient (>70% with fuel regeneration) electric power generation [1,2]. A SOFC produces useful electricity by the reaction of fuel with an oxidant via diffusion of oxide ions (or protons) through an ion-conducting solid-electrolyte layer [3].

SOFC is composed of a dense electrolyte layer that is sandwiched between two porous electrodes (i.e., cathode and anode) as shown in Fig. 1. The SOFC can use either an oxide ion (Fig. 1a) and/or proton conduction through the electrolyte (Fig. 1b). The electrons generated through the oxidation of fuel at anode are accepted for oxygen reduction at cathode, which completes the external circuit. The electricity is, thus, produced by the flow of electrons in the external circuit (viz., from the anode to the cathode). Since current is obtained via diffusion of oxide ions (or protons) through a solid electrolyte,

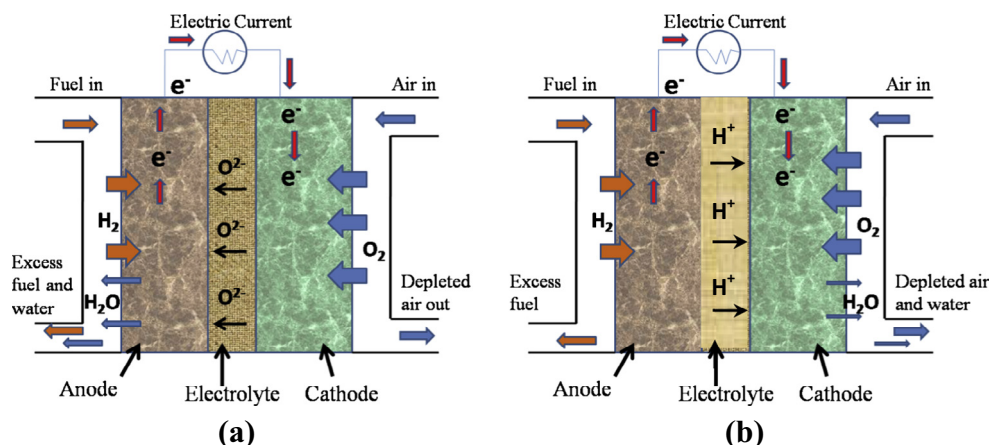


Fig. 1. Schematic diagram of solid oxide fuel cell (SOFC) showing: (a) oxide-ion conducting electrolyte, and (b) proton conducting electrolyte during its operation. A key advantage of SOFCs is the fuel flexibility (i.e., they also allow hydrocarbons to be used as a fuel source). Adapted from: http://www.fuelcellmarkets.com/fuel_cell_markets/solid_oxide_fuel_cells_sofc/4.1.1.2503.html.

it becomes imperative to use high operating temperatures ($\sim 800\text{--}1000\text{ }^{\circ}\text{C}$) for achieving high ionic conductivity (of $\sim 0.1\text{ S/cm}$) [1–7].

However, the practical implications (domestic and industrial) of SOFCs have not been realized as it has high material cost (of electrode, electrolyte, and catalyst), complex cell and stack fabrication, high operational temperature, issues of safety, and concerns with regard to handling of gases and routine maintenance. In addition, high operating temperatures ($\sim 800\text{--}1000\text{ }^{\circ}\text{C}$) of SOFCs can lead to multiple materials problems which include electrode sintering, catalyst poisoning, interfacial diffusion between electrolyte and electrode materials, thermal instability, and mechanical (or thermal) stresses due to different coefficients of thermal expansion (CTE) of the cell components. Such problems have limited the development and use of SOFCs to a greater extent. However, experiments to overcome such limitations and device material selection are the focus of ongoing technology developments. Further, reduction of the operating temperature can allow selection among a wider choice of interconnect materials (including metals/alloys). The approaches to minimize resistive losses across the electrolyte have included replacing yttrium stabilized zirconia (YSZ) by alternative electrolyte materials (such as scandia doped zirconia, samarium doped ceria to name a few) with much higher ionic conductivity, and/or making a thin solid oxide electrolyte sandwich. Electrolyte is considered as the heart, and its properties play a key role in dictating the performance of SOFCs. At present, YSZ is the most commonly used electrolyte as it possess an adequate oxide-ion conductivity ($\sim 0.13\text{ S/cm}$ at $1000\text{ }^{\circ}\text{C}$), and also shows a desirable phase stability in both oxidizing and reducing atmospheres.

The present review discusses the issues associated with such high operational temperature, and presents significant solutions regarding material selection, synthesis, and processing. This article also highlights the techniques used for cell fabrication by systematically investigating the available literature on modeling, and developing an understanding of thermodynamic mechanisms associated with ionic conductivity enhancement. The lowering of the operational temperature of SOFCs (down to $300\text{--}400\text{ }^{\circ}\text{C}$), while retaining phase/thermal-stability and achieving required level of conductivity ($\sim 0.1\text{ S/cm}$), are the main goals in current SOFCs research [8,9]. In order to improve the overall performance of SOFCs, the major challenge is the choice of material based on material properties, i.e., low electronic resistance of electrodes, catalysts, sealants and interconnects, and low ionic resistance of electrolytes. Furthermore, low polarization losses are expected with high electrochemical activity (rapid kinetics) at lower temperatures. The processing of the fuel cell materials also influences the performance of SOFCs due to associated phase evolution, grain size, and distribution of phases (even purity and residual stresses). Thus, the optimization of various synthesis processes for such materials used as electrodes, electrolytes and interconnects are of primary concern in taking SOFC science to real-life applications [10].

High operating temperature requirements exert many constraints on the selection of materials for electrodes, electrolytes, interconnect and sealant materials. This, as a result, limits the commercial application of SOFCs. Summarizing the solution to these issues, this review illuminates the effect of material selection on material's stability, microstructural changes that occur during operation, thermo-mechanical mismatch, and reduction in the operating temperature down to intermediate range ($\sim 300\text{--}400\text{ }^{\circ}\text{C}$). Starting with the state-of-the-art materials used for various components of SOFCs, discussion will be followed based on the criteria for enhancing ionic conductivity in the intermediate range of temperatures.

In the past few decades, numerous researchers have worked on developing the SOFC materials (electrolyte, cathode, anode, and interconnects) and stack designs [10,11]. This step wise progress is presented in the following section. This article elucidates some of the most important properties of ceramic oxide materials, and its possible role in enhancing the ionic conductivity of electrolyte. The strategies of improving the performance of SOFCs are also discussed herewith in this review article.

1.1. Historical background

A brief history of the development of fuel cells (since 1838) is presented in Fig. 2, and the record of publications since the last seventeen decades on various aspects of SOFC is presented in Fig. 3. The first fuel cell was invented in 1838 by an English scientist, William Grove. He named it "wet cell battery" or "Grove cell", which operates by reversing the electrolysis phenomena of water [12]. The fuel cell,

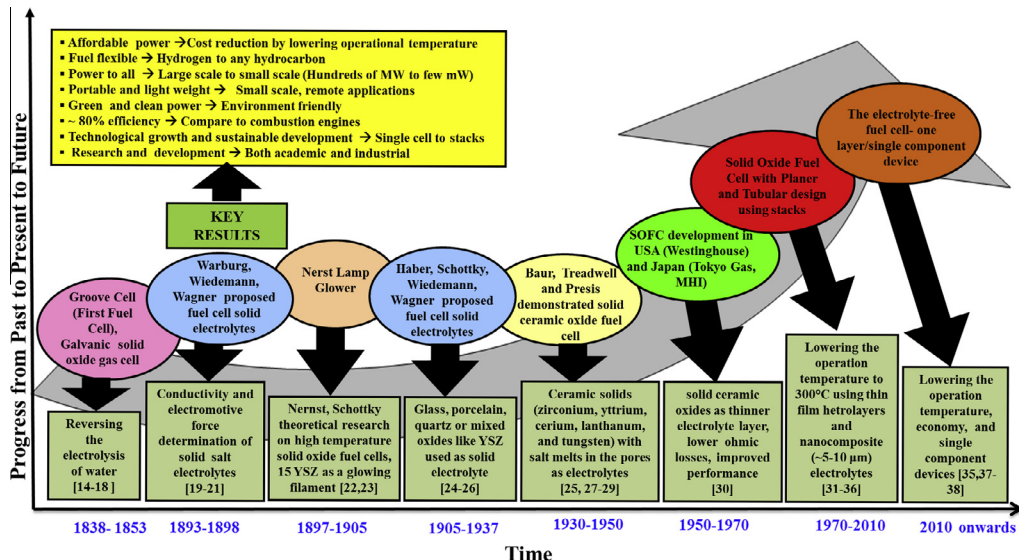


Fig. 2. Time line graph representing progress of SOFC over the last seventeen decades.

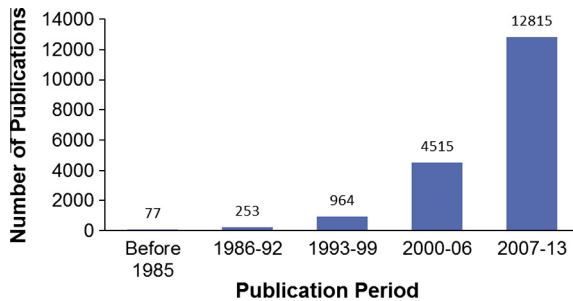


Fig. 3. Number of publications in solid oxide fuel cells since 1838. Source: Scopus.

invented in 1839 by Grove [12], is an electrochemical device that converts the chemical energy of fuels directly into electricity and heat by electrochemically combining the H₂, CO/H₂ or reformed hydrocarbons in fuel and an oxidant gas transported via an ion-conducting electrolyte. The direct combustion of fuels is eliminated here, which renders fuel cells much higher conversion efficiencies compared to other conventional thermomechanical methods. Moreover, with fuel-cells, power generation is virtually noise-free and per unit of power output can produce 0.9 times lower emissions of NO_x and SO_x compared to that of conventional technologies [13]. Additionally, it is possible to use fuel cells for combined heat and power (CHP or cogeneration).

Gaugain and Becquerel have published experimental details on the thermoelectricity mechanism involved in the fuel cell using glass and porcelain by putting metal contacts on them [14-18]. Again, Buff related this thermoelectric force with the voltage associated with galvanic cells and batteries using mercury, zinc amalgam, and various solid metals as electrodes, and glass as the moist conductor [16].

SOFCs came into existence after the discovery of solid electrolyte by Gaugain in 1853 [19,20]. At the end of the 19th century, the word "solid electrolyte" was used more frequently as reported by Wiedemann in 1893/99 [21]. Nernst in 1899 showed that apart from other mixture of metal oxides, 15 mol.% Y₂O₃ doped ZrO₂ (15YSZ) exhibits high conductivity at elevated temperature and suggested

that 15YSZ can be used in lamps as a glowing filament [22,23]. In later years (1905), Haber patented fuel cells using glass and porcelain as solid electrolyte, and platinum and gold as electrodes [19,24,25]. In 1935, Schottky proposed that 15YSZ could be a potential candidate for solid electrolyte [26]. In 1943, Wagner showed that oxide solid-solutions permit ionic conduction where oxide ion hop through oxygen vacancies created by acceptor doping in host lattice [22,27,28]. Baur and Presis in the subsequent years proved this by demonstrating solid ceramic oxide fuel cell working with YSZ at 1000 °C [29–31]. A number of patents were filed during 1960s and 1970s, related to the use of thin layer of solid ceramic oxides as electrolyte material and designs of single SOFCs using various planar and tubular designs to improve its performance. All these worldwide developments of SOFC technology were very well summarized and reported by Blum et.al. [32]. From 1970s to 2010, SOFC technology moved towards lowering down the operation temperature down to 300°C using thin film heterolayers and nanocomposite (~5–10 μm) electrolytes [33–38].

The development of high-performance SOFC involves materials selection and operational-related issues (of anode, cathode, electrolyte, sealant, and interconnects), Fig. 4. These challenges open up myriad research opportunities for researchers in the field of SOFC. A list of various materials used in SOFC is presented in Fig. 5. From 2010 to the present, the electrolyte-free fuel cell with one layer/single component devices were proposed to fulfill low temperature operation requirement [39]. Two-phase nanocomposite functional materials for low temperature (LT: 300–600 °C) SOFCs were successfully developed and demonstrated. Since 2010, many researchers from all over the world (see Table 1) have worked on ceria-carbonate composites for low temperature SOFCs following Zhu et.al.'s introduction to nanocomposite electrolyte [39]. In two-phase nanocomposite materials, the desired superionic conduction occurs at the interfaces of the electrolyte at low temperature (300–600 °C) [37]. Zhu [39] has also worked on single component/layer fuel cell devices by integrating both ionic and semiconducting material in a single layer. This single-component alone can perform the function of energy conversion; so this is a very new approach to fuel cell research and development, and would serve as a great breakthrough in the arena of hydrogen production and fuel cell development [39,40].

In spite of the consistent progress by researchers regarding the understanding of the material requirement and their electrochemical behavior, the commercialization of SOFC is still inadequate because of significantly high cost of SOFC-based power systems, which is a key issue to pervasive

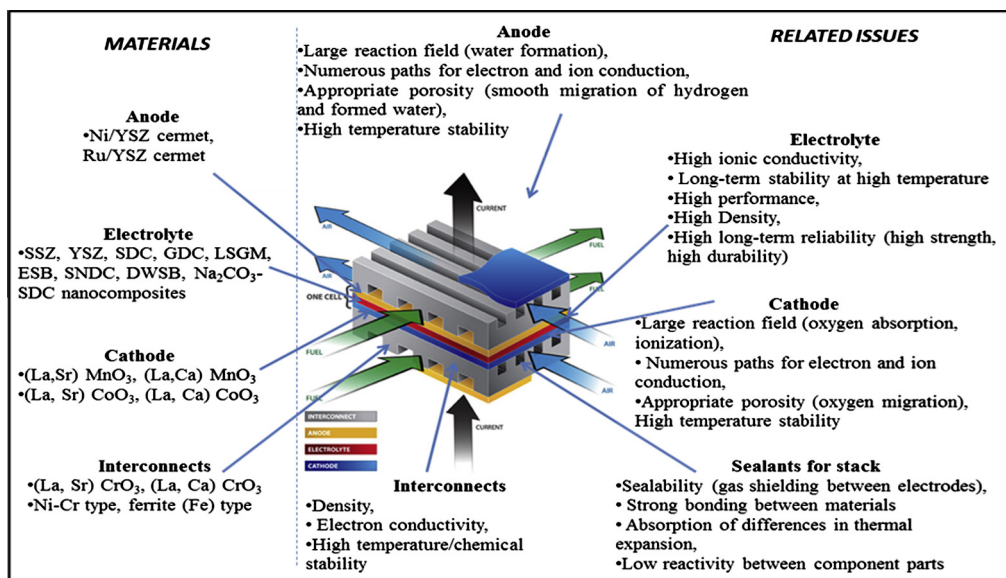


Fig. 4. Materials and related issues for SOFC. (Adapted from Ref. [41] and http://nino.mse.ufl.edu/Nino_Research_Group_research_electronics.htm).

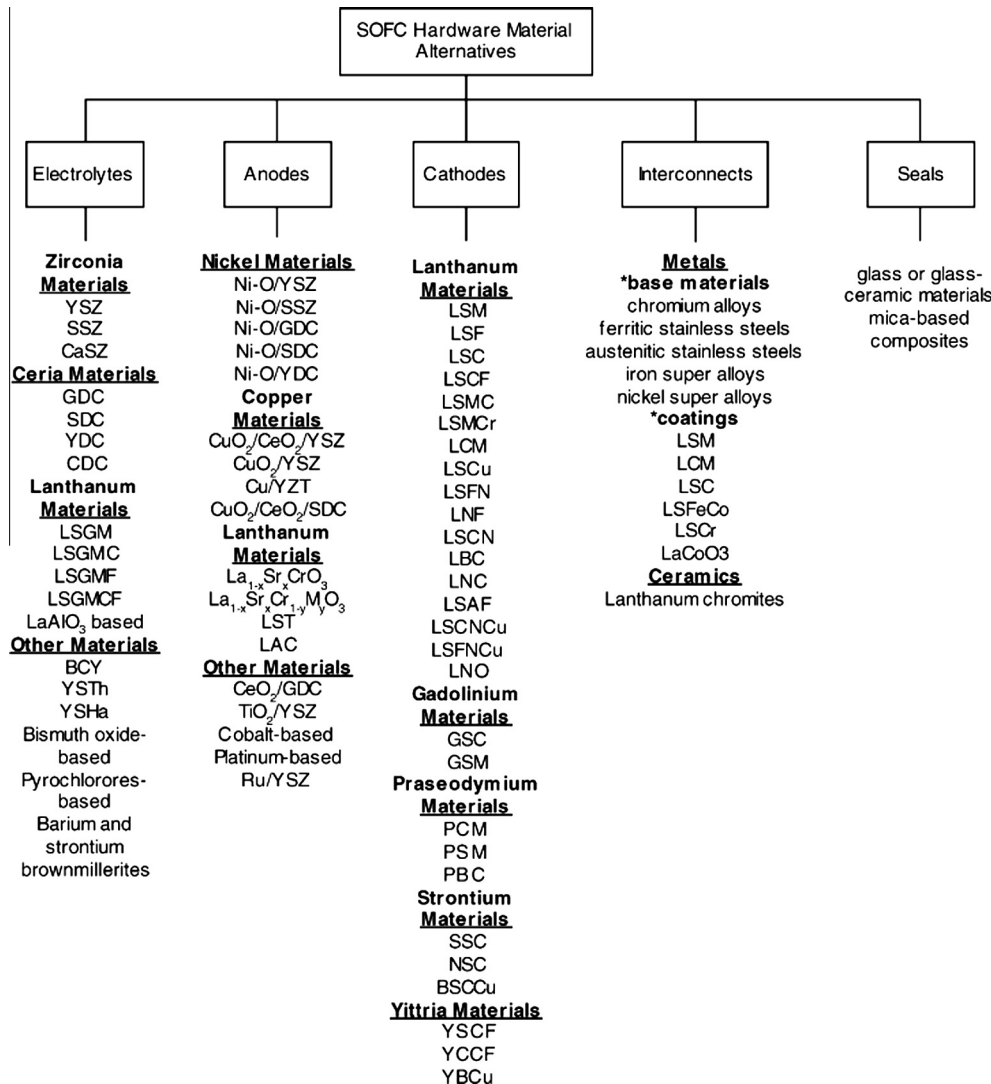


Fig. 5. Comprehensive list of various materials used in SOFC. Reprinted with permission from Ref. [42], copyright Elsevier, 2005.

commercialization of SOFCs. To make SOFC systems more economically viable, and thus, reduce system costs, the incorporation of lower cost stainless steel into the stack design is one of the solutions. However, these steel parts need coatings against protection of air-facing surfaces from high temperature oxidation. In addition, it is also necessary to minimize volatilization of chromium from the alloy, as chromium vapors poison the cathode and degrade the cell's overall SOFC performance.

Lowering the operation temperature of SOFC and using a less expensive metallic interconnects is one of the solutions for reducing the maintenance cost. But, this occurs with high ohmic losses of the electrolyte (i.e., reduced ionic conductivity) and lower catalytic activity of the electrodes, which deteriorate the cell performance. In order to improve the cell performance at lower temperatures, the proposed alternates are use of very thin electrolyte (~ few micrometers) and nanoscale materials for the electrodes and electrolytes [39]. Apart from cost, thermal-mechanical stability is one of the key issues for SOFC fabrication. Residual compressive or tensile stresses generating from CTE mismatch

Table 1

Details of SOFC processing and design by some noteworthy industries. Adapted and minorly modified from Ref. [42,43].

Component	Material	Thickness	Processing	Company/country
Electrolyte	3YSZ, 8YSZ	100 µm	Tape casting	Ceramic Fuel Cells Limited, Australia (electrolyte-supported planar cell design)
Cathode	(La, Sr)MnO ₃	50–60 µm	Screen printing	
Anode	Ni/YSZ	50 µm	Screen printing	
Anode substrate	Ni/YSZ	500–700 µm	Tape casting	
Electrolyte	YSZ	10–30 µm	Lamination and sintering	
Electrolyte	YSZ	<16 µm	Reactive magnetron	
Cathode	(La, Sr) MnO ₃		Sputtering	
			Screen printing	
Electrolyte	3YSZ	50–100 µm	Tape casting	Tokyo Gas; Japan (electrolyte-supported planar cell design)
Cathode	(La, Sr)MnO ₃	150 µm	Screen printing	
Anode	Ni/(Ce, Y)SZ	30 µm	Screen printing	
Electrolyte	8YSZ	300 µm	Tape casting	Mitsui Engineering & Shipbuilding Corporation Limited; Japan (electrolyte-supported planar cell design)
Cathode	Ni/YSZ	150 µm	Painting	
Anode	(La, Sr)(Mn, Cr)O ₃	150 µm	Painting	
Anode substrate	Ni/YSZ	500–800 µm	Tape casting	Energy Research Centre/Innovation Dutch Electro ceramics; Netherlands (anode-supported planar cell design)
Anode	Ni/YSZ	3–7 µm	Screen printing	
Electrolyte	YSZ	7–10 µm	Screen printing	
Cathode				
Anode substrate	Ni/YSZ	200–500 µm	Tape casting	Forschungszentrum Jülich; Germany (anode-supported planar cell design)
Anode substrate	Ni/YSZ	1500 µm	Warm pressing	

Anode	Ni/YSZ	5–15 µm	Vacuum slip casting	
Electrolyte	YSZ	5–30 µm	Vacuum slip casting	
Electrolyte	YSZ	2–10 µm	React. Magnetron Sput.	
Cathode	(La, Sr)MnO ₃ + YSZ	50 µm	Wet powder spraying	
Anode substrate	Ni/YSZ	200–300 µm	Tape casting	Risø National Laboratory; Denmark (anode-supported planar cell design)
Electrolyte	YSZ	10–25 µm	Wet powder spraying	
Cathode	(La, Sr)MnO ₃ + YSZ	50 µm	Screen printing	
Anode substrate	Ni/YSZ	1000 µm	Tape casting	Global Thermoelectric; Canada (anode-supported planar cell design)
Electrolyte	YSZ	10 µm	Vacuum slip casting	
Cathode	(La, Sr)MnO ₃	40 µm	Screen printing	
Cathode tube	Doped LaMnO ₃	2200 µm	Extrusion and sintering	Space Weather Prediction Center; USA
Electrolyte	YSZ	40 µm	Electrochemical vapor Deposition (EVD)	
Anode	Ni/YSZ	100 µm	Slurry coating or EVD	Tubular cell design
Interconnect	Doped LaCrO ₃	85 µm	Plasma spraying	
Substrate tube	Ca-SZ	(out) 21 mm	Extrusion	Mitsubishi Heavy Industries & Electric Power
Cathode	LaCoO ₃	150–200 µm	Atm. Plasma Spraying	Development Company; Japan (Tubular cell design)
Electrolyte	new: (La, Sr)MnO ₃	100–150 µm	new: slurry coating	
	YSZ		Low pr. plasma spraying	
Anode	Ni/YSZ	80–100 µm	new: slurry coating	
Interconnect	NiAl/Al ₂ O ₃	80–100 µm	Atm. Plasma Spraying	
	new: (Ln, AE)TiO ₃		a new: slurry coating	

with the substrate, may result in buckling and failure of the each component layer of SOFC. It was reported by Baertsch [44] that deposition technique can also affect the extent at which residual stress is generated in the electrolyte films.

The main challenges of the operation of SOFCs at high operating temperatures (800–1000 °C) include:

1. Extended startup times: Herein, a period of fuel burning is required in order to reach the operating temperatures. Hence, start-up times for SOFC operation are prolonged.
2. Exert sealing problems and requires expensive interconnect and integration of materials for SOFC stacks. The relative CTE of adjoining materials mandates good sealing that does not react with joining parts. In addition, tapping of useful power requires the connection of SOFC units with interconnects, and thus, the balance of the stack also requires a good integration of these sections.
3. It can induce thermal stresses at electrolyte–electrode interfaces, as well as cause interdiffusion between cell components. High temperature thermal cycles not only induce a substantial thermal stress on the materials, but it also increases the diffusion kinetics which can change the chemistry of the adjoining components. Hence, these aspects must also be kept under consideration during SOFC operation.

Therefore, most of these problems will be solved if the operating temperature can be lowered down to around 500 °C. An added bonus of lowered operating temperatures is the possibility of direct (and cleaner) oxidation of methane without any carbon deposition, which would eliminate the need of reforming fuel. For these reasons, recent research focus has been towards lowering the operating temperature of SOFC. However, the barriers to low operating temperatures are significantly many. To gain a better insight into lowering the operating temperature of SOFC, one must first understand the construction of SOFC, the various reactions and losses that occurs in the different components of SOFC, as well as explore some of the progress already made by researchers. In order to appreciate the importance of various reactions which have resulted to the conversion of fuel into electrical energy, it is imperative that the electrochemistry and thermodynamics of the reactions should be assessed. The same is discussed in the following section.

1.2. Electrochemistry, kinetics and thermodynamics of fuel-cell reactions

Oxygen molecules consume electrons at cathode and get reduced to oxide ions, which diffuse through electrolyte and results in the generation of ionic current. At cathode, the reaction can be represented as:



Eq. (1) can be presented in Kröger–Vink notation as:



where V_0^{\cdot} is a vacant oxygen site while O_0^{\times} is an oxide ion sitting at its allocated oxygen site in the oxide sublattice. As apparent from the above equations, the oxygen reduction process in utilizing oxide ion has three basic requirements, viz., (i) presence of oxygen, (ii) presence of electrons, and (iii) diffusion of oxide ions (from reaction site (cathode) to the electrolyte). As a result, the electrode material must possess high electronic conductivity, whereas solid electrolyte material must exhibit high ionic conductivity for the completion of the circuit (and maintain charge neutrality). In addition, electrode material should be porous (with interconnected porosity) to facilitate gas permeation to and from the reaction sites. Thus, the reaction proceeds at a triple phase boundary (TPB) at the adjoining portions of electrode, electrolyte materials, and where oxidant gas is present. Oxide ions move through the electrolyte and at the same time, oxygen vacancies (point defects in an oxide sublattice where a normally occupied oxygen site is left vacant) migrate from the anode side to the

cathode side via an ion conducting electrolyte. After migrating through the electrolyte, the oxide ions emerge at the anode and react with fuel (H_2 or CO) as follows:



The electrons produced during the reactions are carried by the current collector in the anode to an external load via externally connected electrical circuit. As apparent from Fig. 1, to get maximum output, the electrolyte must conduct ions but block electrons. The gradient in the oxide ions concentration or oxygen partial pressure (P_{O_2}) or oxygen chemical potential across the electrolyte provides the driving force for all the above described electrochemical processes. Thus, SOFCs can also be termed as oxygen concentration cells. The theoretical reversible voltage (*emf*, electromotive force) ' E_{th} ' of the SOFCs can be given by Nernst equation:

$$E_{th} = \frac{RT}{4F} \ln \left(\frac{P_{O_2, \text{cathode}}}{P_{O_2, \text{anode}}} \right) \quad (5)$$

where 'R' is the universal gas constant, 'T' is an absolute temperature, and 'F' is the Faraday's constant (96,500 C/mol). The coefficient '4' in the denominator represents the number of electrons transferred per mole of oxygen molecule reacted in the cell. Since, air is fed as an oxidant through the cathode side of the SOFC, the P_{O_2} at the cathode is 0.21 atm. Whereas, in laboratory experiments related to SOFCs, the commonly used hydrogen gas is generally fed into the anode, and the overall cell reaction can be expressed as:



and, K_{eq} (mass action expression) is

$$K_{eq} = \frac{P_{H_2O}}{(P_{H_2})(P_{O_2})^{1/2}} \quad (7)$$

where K_{eq} is the equilibrium constant for the fuel gas reaction. Therefore, at the anode side, the Gibbs free energy change and oxygen partial pressure can be predicted using equations given by Eqs. (7) and (8), respectively, assuming no water condensation occurs in the gas delivery system between the water bubbler and the SOFC anode.

$$\Delta G_T = \Delta H_T - T\Delta S_T = -RT \ln(K_{eq}) \quad (8)$$

Here, ΔH_T is heat change, ΔS_T is entropy change, and

$$P_{O_2} = \left(\frac{P_{H_2O}}{P_{H_2}} \right)^2 \exp \left[\frac{2(T\Delta S_T - \Delta H_T)}{RT} \right] \quad (9)$$

This expression for P_{O_2} can be substituted for P_{O_2} (anode) in Eq. (5) to estimate the theoretical Nernst potential at any SOFC operation temperature. In order to augment the cell voltage and power output, multiple individual cells are combined in series to form a stack and the adjoining anodes and cathodes are separated by interconnect materials.

The actual cell voltage that can be obtained during operation is always lower than the theoretical Nernst value because of some electrochemical or polarization losses. The cell polarization or overpotential ' η ' is the difference between the theoretical and the operating voltages, and it includes: (i) resistance (ohmic), (ii) charge transfer (activation) polarization, and (iii) diffusion (concentration) polarization. Ohmic loss arises due to resistance offered to the flow of ions in ionic conductors or electrons in electronic conductors. It also arises due to the contact resistances between cell components, i.e., electrodes and electrolyte. However, the main contribution to the ohmic polarization is due to the electrolyte material [45], the magnitude of which (ohmic polarization) is directly proportional to the amount of current passing through the cell. Activation polarization arises whenever reacting chemical species are participating. Thus, for a reaction to proceed, the activation energy barrier of the rate

determining step of the reaction taking place in multiple steps has to be overcome. This requires an extra potential energy and is governed via Butler–Volmer relation.

$$i = i_0 \left\{ \exp \left(\frac{\alpha nF\eta_{act}}{RT} \right) - \exp \left(\frac{-(1-\alpha)nF\eta_{act}}{RT} \right) \right\} \quad (10)$$

where ' i_0 ' is the exchange current density, ' α ' is the transfer coefficient, ' n ' is the number of electrons participating in the reaction at electrode, and ' η_{act} ' is the activation overpotential. This equation relates to the rate of charge transfer of the reaction occurring at the electrocatalyst (electrode)/electrolyte interface, i.e., ' i ' or current density to the activation overpotential ' η_{act} '. The activation polarization arises during transfer of charges between the electronic and ionic conductors, and therefore, it is also termed as charge transfer polarization. Nevertheless, when current densities are considerably low, Eq. (10) reduces to:

$$\eta_{act} \approx \left(\frac{RT}{nF} \right) i = R_{ct} i \quad (11)$$

Here, $\frac{RT}{nF} i_0$ or R_{ct} is intrinsic charge transfer resistance limited to specific electrode/electrolyte interface area [45]. Activation polarization is typically an issue occurring in cathodes. This is attributed to the slow oxygen reduction reaction kinetics, which involves the breaking of high strength bonds present in oxygen molecules [46–52]. Thus, the reaction rate using oxygen gas as an oxidizer (at cathode) becomes slower by several orders of magnitude compared with fuel oxidation reactions at the anode [46–52].

Concentration polarization occurs when the reacting molecules are consumed at a faster rate, or when products are not removed quickly enough from the reaction sites. This lowers the concentration of reactant species, i.e., low oxygen partial pressures (P_{O_2}) at the cathode or low partial pressure of fuel (P_{H_2}) at the anode compared with that of bulk supply. However, such a behavior leads to a reduction in the voltage output, and creates a significant disadvantage when high current is drawn from the SOFC. In extreme cases, the concentrations of reacting molecules (gases) reduces to zero at the reaction site, current drops to a limiting unsustainable value, and the fuel cell ceases to run. These losses cannot be eliminated, but it is possible to minimize these losses by incorporating proper choice of materials, organized microstructural engineering, and optimized fabrication/or design of each cell component.

In order to delineate the significance of SOFC components, the sequence of processes supported at each component of SOFC must be isolated. Hence, it becomes essential to assess the reactions occurring at each of the electrode (i.e., anode and cathode), the oxide diffusion through electrolyte, passage of electronic current through interconnects, and the separation of fuel and oxidizer through sealants. Thus, each cell component (anode, electrolyte, cathode, sealant, and interconnect) of solid oxide fuel cell is presented through their functionality, material and microstructural aspects, and their associated problems in the following sections.

2. Anode

At anode, electrochemical oxidation of fuels takes place preferentially at certain surface sites called triple-phase boundaries (TPBs), which are essentially an interface between electrolyte, electrode, and gas. The electrochemical oxidation of H_2 occurring at the most commonly used Ni/YSZ cermet anode can be written in terms of Kröger–Vink notation as:



where O_{YSZ}^{2-} and $V_{O,YSZ}^-$ are the oxide ion and the vacant oxygen site, respectively, inside the $Y_2O_3-ZrO_2$ (YSZ) electrolyte lattice. The anode polarization is largely influenced by the microstructure of anode material, morphology of anode, exposed/active area, porosity content, size and distribution of porosity for efficient gas transportation in high-temperature reducing environment, and promotion of catalytic activities (toward fuel oxidation and reforming) on the intrinsic surface of the fabricated material. Anode materials should possess high electronic conductivity and sufficient electrocatalytic activity in order to minimize the polarization losses of the H_2 oxidation reaction and achieve complete fuel

oxidation. Besides these requirements, it must also possess good chemical and thermal stability along with minimal CTE mismatch with other adjacent cell components, and sufficient mechanical strength to withstand physical weight and mechanical stresses. Moreover, it is desired that the anode material should be able to handle fuel flexibility (and not react) with commonly used fuel gases, e.g., hydrogen, CO, natural gas, and other hydrocarbons while tolerating carbon deposition, sulfur poisoning and reoxidation [53,54]. The critical challenge of all time, regarding the development of SOFC anode material is to understand and be able to engineer both: the charge- and mass-transfer through the bulk, along the surfaces and across interfaces via the development of convenient, efficient and economic processing methods, and fabrication technologies.

Conventionally, metals (or carbon) were both used as anode and cathode, which include graphite, platinum, iron, cobalt, and nickel. Due to low cost, good chemical stability and excellent catalytic activity towards hydrogen oxidation and reforming of hydrocarbon fuels, Ni had been used as an anode for several years. However, pure Ni has a considerable CTE mismatch with commonly used electrolyte material, such as, YSZ, which leads to weakening of its interface with the electrolyte material. While optimizing metal electrodes, cermets (i.e., ceramic–metallic composite e.g., Ni–YSZ) and metal oxides were introduced. The latter has an added advantage of extended lengths of triple phase boundaries (TPB; discussed in detail in cathode section). The development of Ni–YSZ cermet anodes by Spacil [55] was a major breakthrough because most of the basic requirements for SOFC anodes were satisfied. In addition, Ni–YSZ enhances the overall efficiency of SOFC as it possesses high electronic conductivity, reasonable ionic conductivity, and good catalytic activity for hydrogen oxidation.

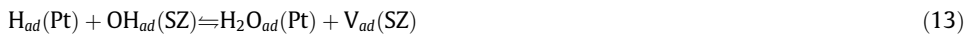
A potential SOFC anode material must exhibit an electrical conductivity of ~ 100 S/cm or higher at operational temperature [56]. The electrical conductivity of Ni is 2×10^5 S/cm, whereas that of porous Ni–YSZ ranges between 10^2 and 10^4 S/cm at 1000 °C. In a porous Ni–YSZ cermet, the metal phase (Ni) provides the required catalytic activity and electronic conductivity for the oxidation of hydrogen fuel. The polycrystalline ceramic phase of YSZ lowers the CTE of the anode material to match with that of the electrolyte material, prevents Ni phase from coarsening, and most importantly, offers a conduction path for oxide ions, which as a result, extend the active zones for anode reactions [57]. The cermet materials as anode, however face several issues, i.e., variation in the performance upon altering the fuel environment, and change in the material compatibility with adjoining cell components. Moreover, when hydrocarbons are used as fuels, Ni/YSZ cermet exhibits redox instability which occurs due to the expansion during anodic re-oxidation from Ni to NiO [58], causing stresses at the anode–electrolyte interface [59,60]. Besides this, Ni–YSZ also shows susceptibility to carbon deposition or coking [61], sulfur poisoning [62], (because of impurities in the fuel stream, particularly sulfur) and nickel coarsening/agglomeration upon prolonged usage at high operational temperatures (600–1000 °C) [63]. The problem of redox instability can be marginally alleviated by controlling the microstructural distribution of Ni and YSZ phases in the cermet matrix [64,65]. Coking and sulfur poisoning was found to be marginally reduced by substituting transition metal in the place of Ni [62,63]. However, it can also lead to significant reduction in the efficiency of anode [66,67]. Development of potential anode materials has also led to significant research and development of various types of materials, such as, anodes based on a perovskite structure [53,68–72], ceramic composites [73], titanates and donor-doped titanate-based anodes [74–76], spinels [77], pyrochlores [78,79], tungsten bronzes [80], and fluorites [81–84]. It appears that the key driver for the development of better anode materials is to prevent the poisoning of the electrode. In this direction, attempts have been made to evaluate Cu based cermets [85–88] as anode material. Other motivations, so as to enhance cell performance include: (i) minimization of electrode resistances, (ii) improvement in the durability of anode materials (mainly Ni in YSZ and CGO at high operating temperature), and (iii) development of novel anodes for intermediate temperature fuel cells (600–800 °C).

Early reports of oxygen reduction kinetics at metal-anode surface in compound gas mixtures such as H₂–H₂O, and CH₄–H₂O or CO–CO₂, are attributed to electrode overpotential on the interface of electrolyte and metal electrode, a concept similar to that present in aqueous electrolyte systems. Mizusaki et al. [89,90] carried out an extensive investigation to study the electrode reaction mechanism at the interface of porous Pt and stabilized ZrO₂ in Ar–O₂, H₂–H₂O, and CO–CO₂ atmospheres. In Ar–O₂ and CO–CO₂ atmospheres, it was proposed that the rate determining step is essentially due to the chemical reaction of adsorbed species on the Pt surface or Pt-stabilized zirconia surfaces, rather than the charge

transfer reaction [91]. The reaction process consists of two major steps, i.e., step 1: oxygen exchange between gas phase and TPB, and step 2: chemical reaction at the Pt particles/stabilized zirconia interface as shown in Fig. 6a. It was also proposed that in Ar–O₂ atmosphere, the oxygen atoms are supplied to the TPB from the Pt surface. Furthermore, the rate of anodic reaction can be determined by the rate of surface diffusion of adsorbed oxygen atoms on Pt surface (at $T \geq ca. 600^\circ C$) or the rate of dissociative adsorption of O₂ molecules on Pt-surface near the TPB (at $T \leq ca. 500^\circ C$) as shown in Fig. 6b [92]. In the case of CO–CO₂ atmosphere, the rate of reaction is given by the rate of oxygen exchange between adsorbed CO and/or CO₂ molecules on Pt electrode surface and adsorbed oxygen atoms on stabilized ZrO₂ surface at TPB sites (as shown in Fig. 6c) [91].

In H₂–H₂O atmospheres, the rate determining steps was identified to be the exchange of adsorbed OH[–] radicals between the Pt and the stabilized ZrO₂-surface at TPB of gas/Pt/stabilized ZrO₂ (Fig. 6d). The two significant observations on TPB sites of stabilized ZrO₂ surface at different oxygen activity (a_o) vs. O₂ gas of 1.01×10^5 Pa were:

(i) At $a_o > 10^{-10}$



The expression for current 'I' (steady state polarization current as a function of H₂ partial pressure and H₂O partial pressure) was given as:

$$I = k_1 \theta_{H,Pt}^{1/2} \theta_{OH,SZ}^{1/2} - k'_1 \theta_{H_2O,Pt}^{1/2} \theta_{V,SZ}^{1/2} \quad (14)$$

Therefore, such a behavior suggests that the rate determining step has dependence on the square root of exchange reaction of adsorbed species across the boundary of two surfaces (i.e., at TPB).

(ii) At $a_o < 10^{-12}$



and the expression for current was given as:

$$I = k_2 \theta_{H,Pt}^{1/2} \theta_{H_2O,SZ}^{1/2} - k'_2 \theta_{H_2O,Pt}^{1/2} \theta_{H,SZ}^{1/2} \quad (16)$$

where k_1, k_2, k'_1 , and k'_2 are the rate constants, and θ denotes the coverage of adsorbed species. At 700–800 °C, the rate of electrode reactions in various atmospheres were found in the order of O₂ > H₂–H₂O > CO–CO₂. Furthermore, the rate of electrode reaction in O₂ atmosphere was higher than H₂–H₂O atmosphere by 1–2 orders of magnitude.

A variety of possibilities exist in the selection of anode, since the major role of anode is to conduct electrons, it should also show a reasonable ionic conductivity towards achieving extended TPBs. Details of various types of anodes, and their development are presented in the following section.

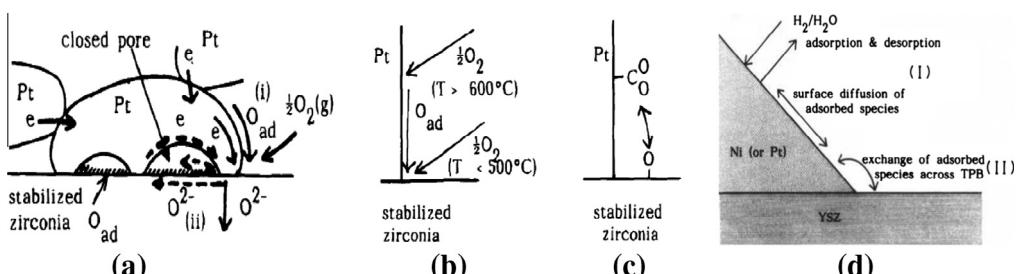


Fig. 6. Schematic showing anode reaction model at the porous Pt/stabilized zirconia interface. (a) Reaction process around the TPB, (i) between the TPB and gas phase, (ii) Charge transfer at Pt particles/stabilized zirconia interface. Rate determining process (b) in Ar–O₂ atmosphere, (c) in CO–CO₂ atmospheres, (d) in H₂–H₂O atmosphere ((a–c) reprinted with permission from Ref. [90], and (d) from Ref. [89], respectively, copyright Journal of The Electrochemical Society, 1994).

2.1. Nickel metal anodes

Although Pt electrode behaves similar to Ni electrode in many respects, on comparing the shape of the semicircular arcs in the Nyquist plot (Fig. 7), the value of polarization resistance for Pt electrode has always been found to be higher than that of Ni-patterned electrode. It is an important experimental observation which shows that Pt is electrochemically less active than Ni. Thus, Ni electrodes have attracted extensive research activities and are investigated as potential SOFC anode materials.

In order to understand the reaction mechanism at the electrodes of SOFC, it is essential that the electrodes must possess controlled microstructure. This will assist in accurately determining the site of reaction as well as the reaction rate corresponding to the unit area of the reaction site on the electrode. On the contrary, it is rather difficult to determine the reaction paths and deduce the accurate rate-determining step for Ni anode, which is prepared as porous Ni-YSZ cermet with complicated/heterogeneous microstructure [94,95]. Yamamura et al. [96] and Norby et al. [97] have reported patterned Ni anode and Ni mesh as a model anode respectively to study the reaction kinetics of the anode. Mizusaki et al. [89,98] investigated the anode kinetics of the electrochemical oxidation reaction of H₂ on patterned Ni anodes with YSZ electrolytes. A total of 20 different types of nickel stripe patterns (line widths of 5, 10, 25, and 50 μm) were patterned on 8YSZ single crystal surface (to create gas/nickel/YSZ TPBs) using ionized cluster beam method and photolithography (shown in Fig. 8a). The obtained real and imaginary impedance data are shown in Fig. 8b.

On varying P_{H₂} and P_{H₂O} in the anode feeds, Mizusaki et al. [99] observed that the electrode interface conductivity is proportional to the length of TPB, and the rate of the electrode reaction is essentially determined by the reaction process on the Ni surface close to TPB.

Furthermore, the electrode interfacial conductivity σ_E was found to be essentially independent of P_{H₂} (it increases only slightly with increasing P_{H₂} at very low P_{H₂O}). However, σ_E was found to be proportional to P_{H₂O} at high P_{H₂O} values. On decreasing P_{H₂O}, σ_E decreases and approaches a certain constant value (as shown in Fig. 8c and d). Assuming that the rate determining step is a chemical reaction (adsorption and radical exchange) between gas phase and Ni surface or surface diffusion process in series followed by charge transfer process, the electromotive force E is related to the oxygen activity a_o, in YSZ at TPB by the following expression.

$$E = \left(\frac{RT}{2F} \right) \ln a_o \quad (17)$$

While analyzing polarization curves (Fig. 8e and f), the anodic current was found to be essentially proportional to a_o, while the cathodic current was observed to be proportional to a_o^{-1/2}. Furthermore, on plotting anodic and cathodic current as a function of P_{H₂} at constant P_{H₂O} and electrode potential, the anodic current was found to be proportional to P_{H₂}, while cathodic current was found to be

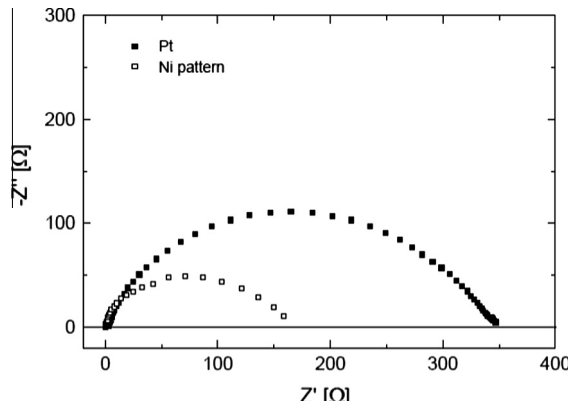


Fig. 7. Impedance data for Pt and Ni patterned electrode at open circuit potential. Courtesy from thesis Ref. [93].

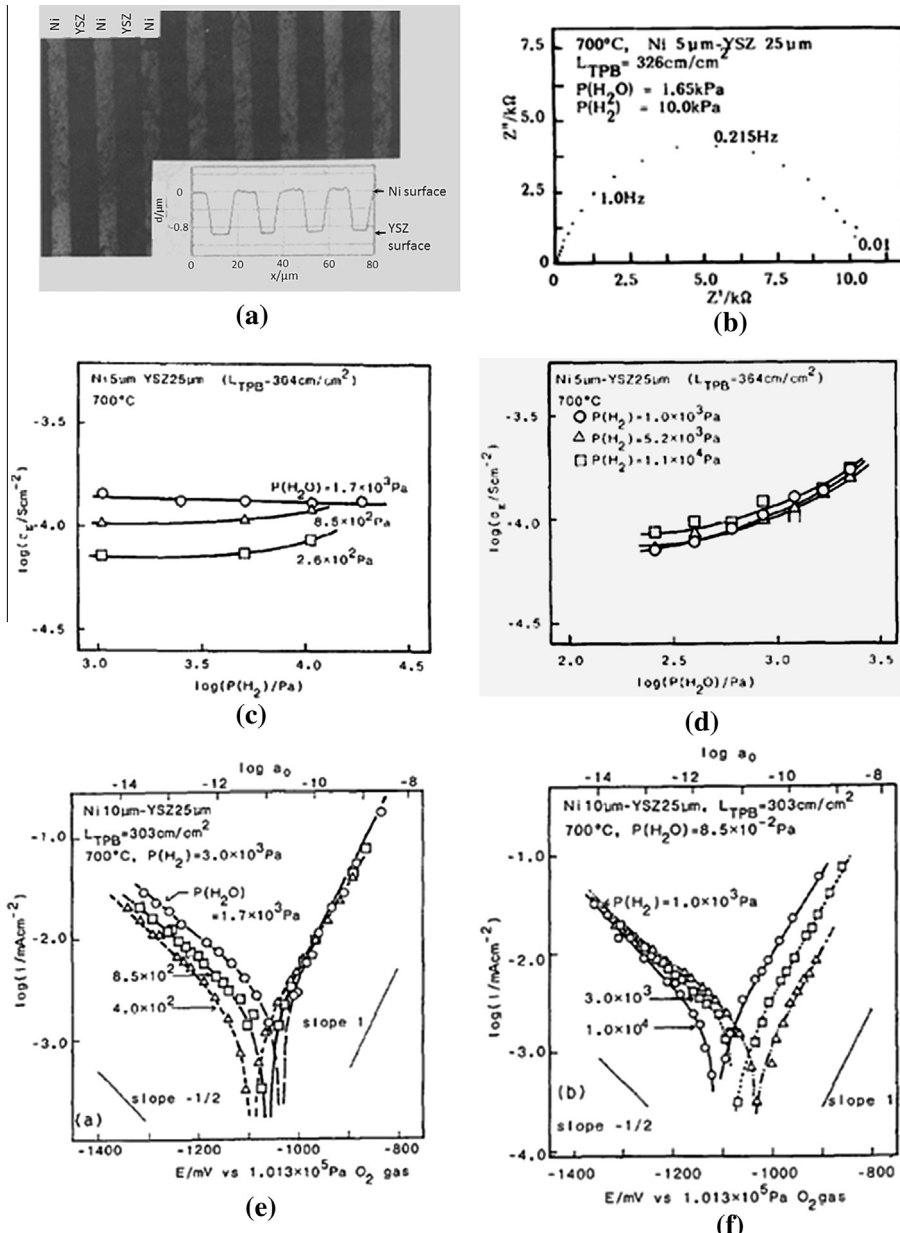


Fig. 8. (a) Optical micrograph and surface profile data of nickel pattern (Nickel lines $\sim 10 \mu\text{m}$; YSZ lines $\sim 10 \mu\text{m}$) on single crystal $\langle 110 \rangle$ 8YSZ surface, and its corresponding. (b) Impedance spectra ((a) and (b) Reprinted with permission from Ref. [89], copyright Journal of The Electrochemical Society, 1994). (c) Variation of σ_E measured at 700°C as a function of P_{H_2} and (d) $P_{\text{H}_2\text{O}}$. σ_E is calculated from the equation $\{\sigma_E = 1/AR_E\}$; where, A is the area of the working electrode (Ni layer prepared by ICP), and R_E is obtained from the complex impedance plot of the electrode impedance which consists of only one semicircle. Steady-state polarization curves at 700°C : (e) at $P_{\text{H}_2} = 3.0 \times 10^3 \text{ Pa}$ with varying $P_{\text{H}_2\text{O}}$; (f) at $P_{\text{H}_2\text{O}} = 8.5 \times 10^{-2} \text{ Pa}$ with varying P_{H_2} ((c–f) Reprinted with permission from Ref. [98], copyright Elsevier, 1994).

independent of P_{H_2} . However, on plotting anodic and cathodic current as a function of P_{H_2O} at constant P_{H_2} and electrode potential, cathodic current was found to be proportional to $P_{H_2O}^{1/2}$, while anodic current was found to be independent of P_{H_2O} . Based on the polarization results, an empirical rate equation was deduced as follows [98]:

$$i = kP_{H_2}a_0 - k'P_{H_2O}^{1/2}a_0^{-1/2} \quad (18)$$

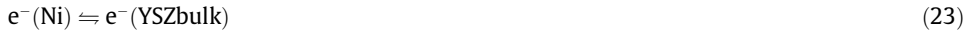
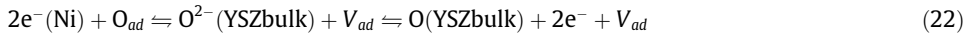
where k and k' are rate constants. Therefore, combining Eqs. (17) and (18) gives an equation similar to Butler–Volmer-like equation (Eq. (19)) which is also consistent with the results reported by Kawada et al. [94,95].

$$i = kP_{H_2} \exp\{2FE/RT\} - k'P_{H_2O}^{1/2} \exp\{-FE/RT\} \quad (19)$$

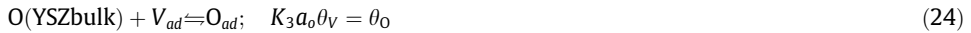
The above equation indicates that more than one elementary reaction processes exist, as orders of anodic and cathodic reactions are different. Mizusaki et al. proposed the stepwise mechanism for H_2 oxidation taking place on Ni surface based on the results obtained from the polarization curves and impedance measurements [98]. It was assumed that O_{ad} , OH_{ad} , H_{ad} , and H_2O_{ad} were adsorbed on the Ni surface. The following equilibria that are likely to exist at or close to TPB were deduced [98].



The local electronic equilibrium existing between Ni and YSZ at Ni/YSZ interface can be expressed as [98]:



On combining Eqs. (22) and (23), the following equation was obtained.



Since the rate limiting step takes place on the Ni surface, the equilibrium between the gas phase and the Ni surface cannot be assumed. However, in order to estimate the concentration of adsorbed hydrogen species, it was approximated that either of the following equilibria exists between the gas phase and the Ni surface.

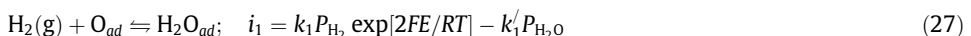


where K_1, K_2, K_3, K_4 , and K_5 are the equilibrium constants; V_{ad} is a vacant adsorption site on nickel surface and θ is the coverage of adsorbed species. On assuming that the equilibrium given by Eq. (25) exists between the gas and Ni surface is satisfied, the concentrations of adsorbed species i.e., $\theta_H, \theta_{OH}, \theta_O$, and θ_{H_2O} were determined. It was observed that the concentration of θ_H is proportional to the term $P_{H_2O}^{1/2}a_0^{-1/2}$ of the cathodic reaction (mentioned in Eq. (18)), while the concentration of θ_O is proportional to a_0 .

On the other hand, if it is assumed that the equilibrium given by Eq. (26) exists between the gas phase and Ni surface, then no adsorbed species exhibited $P_{H_2O}^{1/2}$ or $a_0^{-1/2}$ dependence which is expected for the cathodic reaction. Such a finding indicates that the equilibrium given by Eq. (26) does not exist at or near the TPB.

Thus, depending upon the extent of anodic and cathodic polarizations under virtual equilibrium condition, three possible rate determining steps are possible:

(i) Direct attack of $H_2(g)$ on O_{ad} :



where k and k' are the rate constants and the process is supposed to dominate under anodic polarization.

(ii) Surface diffusion of H_{ad} on the nickel surface towards reaction sites near TPB

$$H_{ad} \rightleftharpoons H_{ad}^{\text{TPB}}; \quad i_2 = k_2 P_{H_2}^{1/2} - k'_2 P_{H_2O}^{1/2} \exp[-FE/RT] \quad (28)$$

This step is expected to dominate under low cathodic polarization.

(iii) Dissociative adsorption of $H_2(g)$ near the TPB.

$$H_2(g) + 2V_{ad} \rightleftharpoons 2H_{ad}; \quad i_3 = k_3 P_{H_2} - k'_3 P_{H_2O} \exp[-2FE/RT] \quad (29)$$

This route is expected to dominate under high cathodic polarization.

All the three rate determining reaction steps are supposed to occur in parallel and the dominating process is governed by the magnitude of the rate constants and oxygen activity at the Ni/YSZ interface. In summary, the rate of the anodic reaction is essentially determined by the reaction of $H_2(g)$ and the adsorbed oxygen on the nickel surface i.e., $H_2(g) + O_{ad} \rightleftharpoons H_2O_{ad}$; and the rate of cathodic reaction is

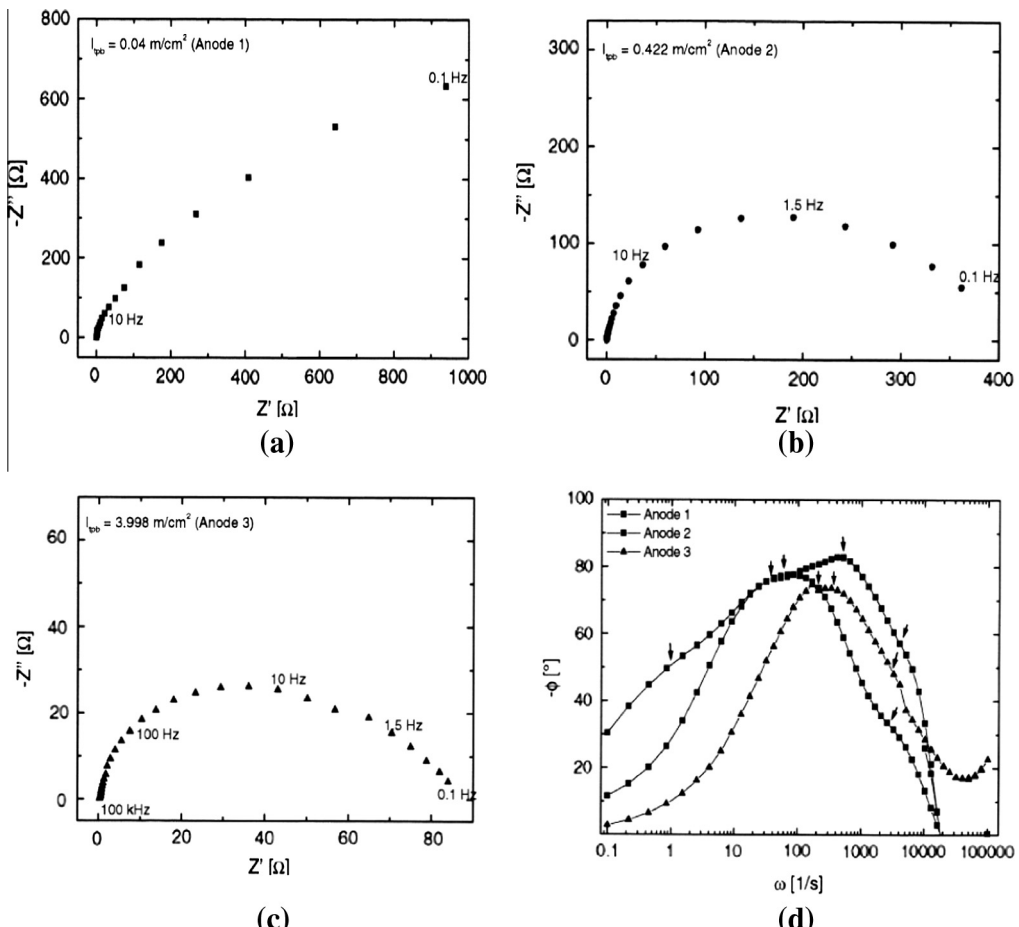


Fig. 9. Nyquist plot of (a) Ni square electrode. Nickel patterned electrode of line width (b) 200 μm , (c) 20 μm , and (d) Bode plots of (a–c). Spectra were measured at 700 $^\circ\text{C}$ between 100 mHz to 100 kHz, at zero overpotential with an excitation amplitude of 10 mV in a single gas-chamber measurement setup in $\text{H}_2/\text{N}_2 = 1:3$ and a total gas flow of 40 ml/min ((a–d) reprinted with permission from Ref. [100], copyright Elsevier, 2000).

determined by the surface diffusion process of adsorbed hydrogen H_{ad} as formed during the reactions given by Eqs. (20) and (21).

In order to elucidate the reaction kinetics at Ni electrodes, several research groups have fabricated different geometries of Ni on 8YSZ electrolyte with a well defined length of TPB. Bieberle and Gauckler [100] fabricated Ni anodes of three different designs, viz., square (TPB length = 0.04 m/cm²) and line patterned anodes of line width of 200 μm (TPB length = 0.422 m/cm²) and 20 μm (TPB length = 3.998 m/cm²), respectively with TPB length varying by two orders of magnitude. The impedance results shown in Fig. 9a–c, suggest that the polarization resistance is an inverse function of the TPB length. It was highest for the square anode and lowest for line patterned anodes of line width of 20 μm. In addition, at least three single processes were identified in a measured frequency range (marked by arrows in the Bode plot (as shown in Fig. 9d). Bieberle and Gauckler [100,101] fabricated Ni anodes of various designs (Fig. 10), viz., Ni patterned anode with line width of Ni and of YSZ = 20 μm; $l_{TPB} = 3.648$ m/cm² (Fig. 10a), Ni gauze (Fig. 10c), and Ni paste (Fig. 10e). The Nyquist plot obtained at various conditions for Ni patterned anodes shown in Fig. 10b, exhibits a single impedance arc in a measured frequency range. As no 45° tangent to the arc in the high frequency region (representative of Warburg element) is observed, it can be concluded that the anode is not limited by diffusion.

There is a strong effect of applied overpotential (between anode and reference anode) on the resistance offered by Ni patterned anodes. Polarization resistance decreases rapidly with the rise in overpotential. However, at very high overpotential ($\eta = 400$ mV) and at lower frequency, a second arc appears which increases the total anode impedance. In the second design, i.e., Ni gauge, the Nyquist plot shown in Fig. 10d exhibits sensitivity to the applied overpotential η only in the low-frequency region, whereas the high frequency features remain same for all overpotentials. The value for electrolyte resistance was also observed to be high (i.e., 14 Ω, characterized by the intercept of the real axis with the impedance arc in the high frequency region). Authors attributed this observation to the comparatively poor contact of the Ni-anode to the YSZ electrolyte (the Ni-gauge was fixed on the electrolyte at the four corners). Although not well defined, the Nyquist plot shows two semicircles, which suggest two characteristic relaxation processes in the electrochemical response of the Ni gauge anode. A 45° tangent (Warburg element) indicates that the anode processes of Ni-gauge structure is limited by diffusion.

In the case of Ni–YSZ paste electrode (shown in Fig. 10e), the porous microstructure consists of particles of YSZ surrounding the larger Ni particles. As a result, polarization resistance of Ni–YSZ is comparatively lower than all metal Ni-anode designs. The Nyquist plot for Ni–YSZ paste shown in Fig. 10f exhibits a large inductive behavior in the low frequency region when no overpotential is applied. The inductive behavior decreases sharply (on applying η) and overlaps with the second semicircle that is separated at an overpotential of $\eta = 200$ mV. Increasing overpotential has correlated well with increasing size of second semicircle in the low frequency region. Diffusion limited anode process is elicited in the high frequency region characterization of Ni-paste.

Boer et al. [102] fabricated porous Ni electrodes using e-beam evaporation process (Fig. 10g), and tailored the microstructure and thickness of the Ni layer by varying the annealing time (2–4 h), and the temperature between the sequential evaporation steps and the total number of evaporation steps. In a parallel study, Ni-electrode surface was also modified by the deposition of fine YSZ particles. Fig. 10h shows the Tafel plots for both the types of electrodes. As no linear region was observed in these plots, determination of the cathodic and anodic transfer coefficients becomes rather difficult. Nevertheless, the anodic transfer coefficient values for porous and modified porous Ni-electrodes were estimated to be 1.4 and 1.2, respectively, whereas cathodic transfer coefficient value for both the types of electrodes was reported to be 0.8. The comparable values for porous and modified Ni-electrodes suggest no evident change in the reaction mechanism upon Ni modification. This is perhaps one of the most important observation which assists in understanding the better efficiency of Ni-cermet anodes compared to other metallic counterparts.

The impedance results of bare porous and modified porous Ni electrode anode are shown in Fig. 10i and j, respectively. Both the impedance spectra data were fitted using an analog electric circuit of $L_wR_e(R_1Q_1)(R_2Q_2)$, where L_w is an inductor, R represents a resistor, and Q represents a constant phase element. It was observed that the modification of the porous Ni electrode surface leads to a decrease in electrode polarization resistance (R_1 and R_2). Authors attributed this to the increase in the number of

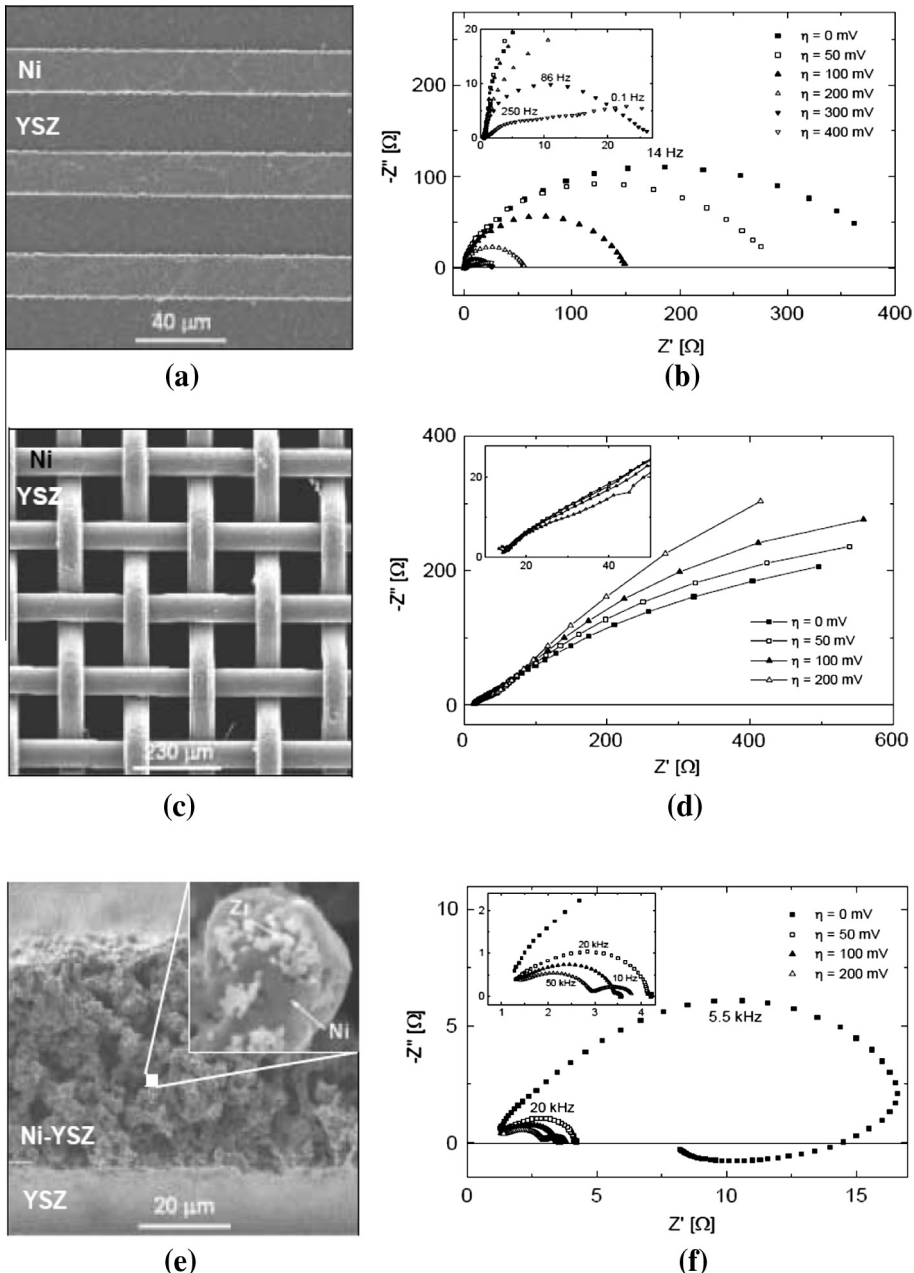


Fig. 10. (a) SEM image of Ni pattern anode (top view) with line width of Ni and of YSZ = 20 μm ; $l_{\text{TPB}} = 3.648 \text{ m}/\text{cm}^2$ and (b) comparison of Nyquist plots at various overpotentials η , (c) Woven structure of the Ni-gauze anode (top view) and (d) comparison of Nyquist plots at various overpotentials, (e) a cross-sectional image of the Ni/YSZ paste of thickness 40–60 μm showing porous microstructure. The paste anode mainly contains Ni and some YSZ particles which sit on large Ni particles (inset). (f) The impedance plot ((a–f) reprinted with courtesy from thesis Ref. [93]), (g) porous Ni electrode, (h) Tafel's plot for bare and modified porous Ni electrodes, (i) impedance results for bare porous Ni and (j) modified porous Ni electrode ((g–j) reprinted with permission from Ref. [102], copyright Elsevier, 2000).

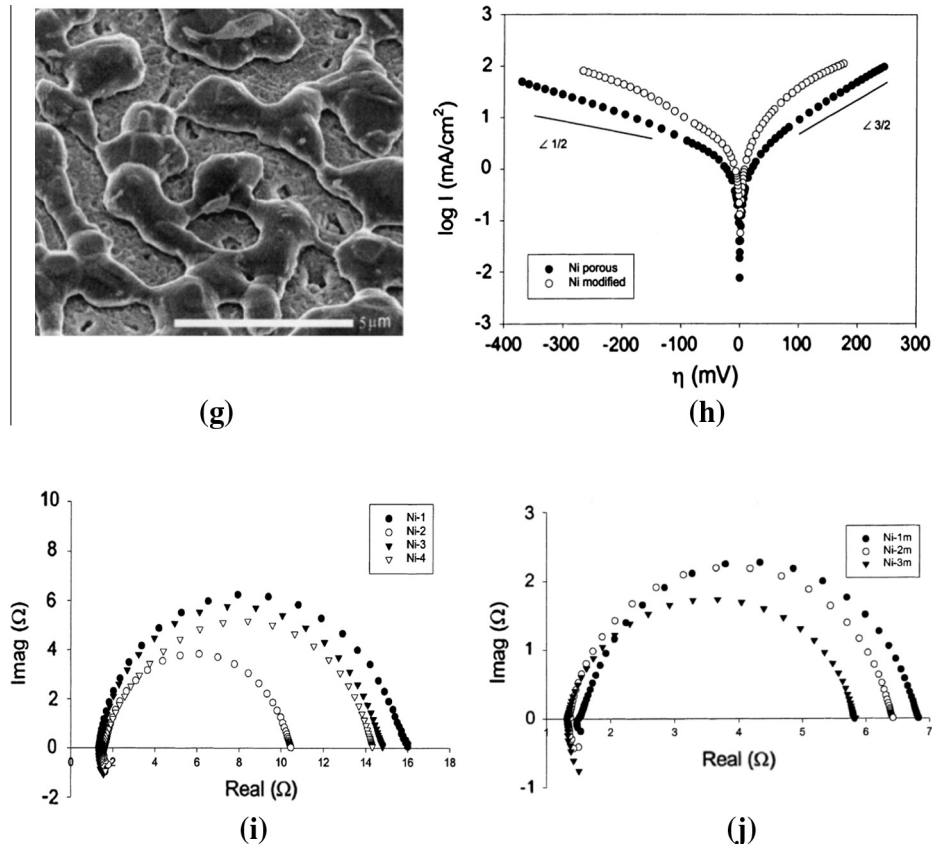


Fig. 10 (continued)

active sites [102]. However, no effect was observed on the constant phase element value. Therefore, this suggests that the surface modification of Ni with fine YSZ particles leads to no change in reaction mechanism.

Aaberg et al. have investigated Ni–YSZ point electrode (Fig. 11a) using long-term potential step measurements and impedance spectroscopy [103]. The point electrode was prepared from Ni wires of diameter 0.5–1 mm, bent into U shape and held at the surface of polycrystalline YSZ electrolyte with alumina support (Fig. 11a). It was reported that on applying anodic overpotentials, redistribution of materials takes place in the reaction zone (Ni and YSZ interface), which is attributed to the migration of Ni particles around the electrode–electrolyte interface (Fig. 11b). This was suggested to increase the length of TPB, which in turn enhances the electrode activity. Due to this induced self-catalytic effect, a significant rise in the anodic current (more than double) occurs in Ni–YSZ anodes. According to Pizzini et al. [104], new catalytic sites are generated by such treatment, which as a result enhances the anode activity. On applying cathodic overpotentials, transfer of Ni particles did not occur and rather agglomeration of the dispersed metallic particles was observed, which tends to reduce the TPB length and reduce the cathodic current [103]. Apart from morphological modifications, authors also reported cubic to tetragonal phase transformation of YSZ under prolonged working hours of ~135 days. Also, this was attributed to the dopant segregation at the grain boundary interfaces and not to the passage of current.

In the open circuit condition, a depressed semicircle was observed in the impedance spectra (shown in Fig. 11c). On applying high anodic overpotential, a low-frequency tail of the impedance curve appears to bend back into the capacitive quadrant of the spectrum (shown in Fig. 11e). The

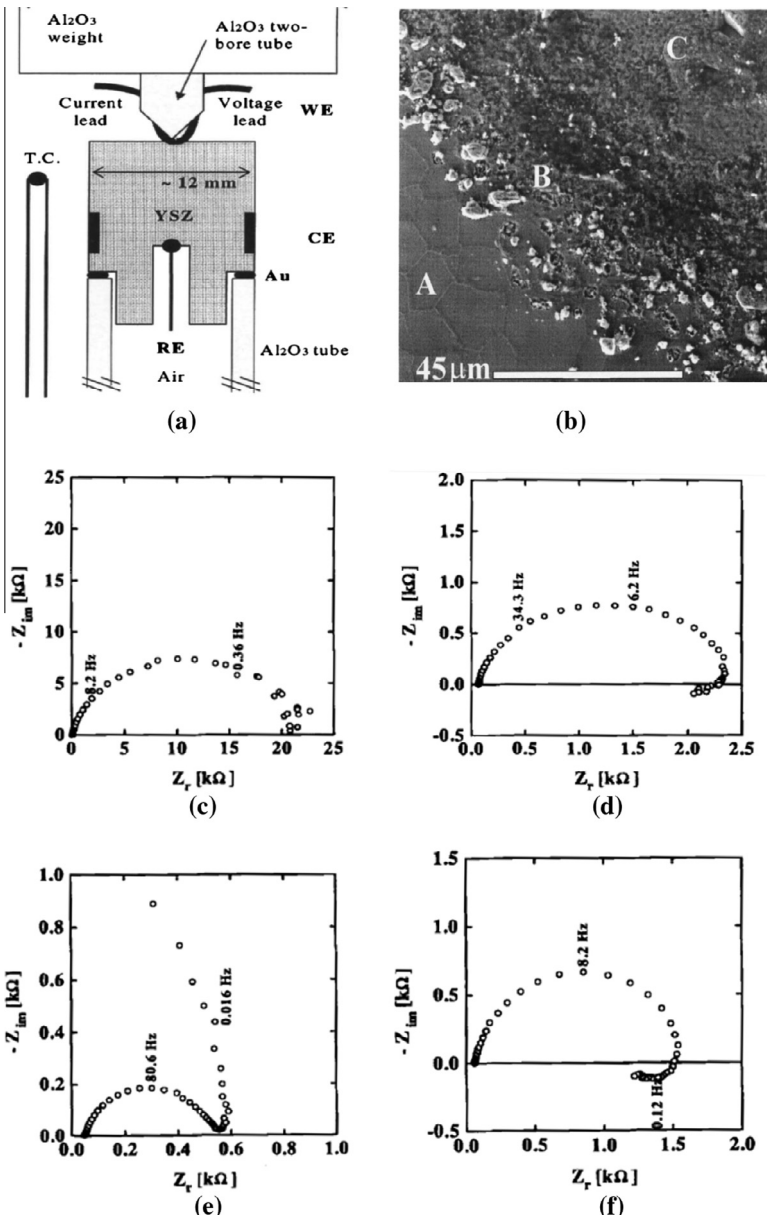


Fig. 11. (a) The point electrode set-up for electrical property measurement, (b) scanning electron micrographs of the YSZ surface at the contact point of Ni-point anode. The three regions, viz., free YSZ surface 'A', border region with adhering Ni-particles 'B', and the actual contact area of the Ni electrode 'C'. Impedance spectra in various gas mixtures and at different anodic and cathodic overpotentials for 135 days, viz., (c) –980 mV (vs. air in 21% H₂/3%H₂O; open circuit), (d) 755 mV (vs. air in 50% H₂/50% H₂O; η = 121 mV), (e) –770 mV (vs. air in 21% H₂/3%H₂O; η = 213 mV), and (f) –1149 mV (vs. air in 50% H₂/50% H₂O; η = –147 mV) ((a–f) reprinted with permission from Ref. [103], copyright Journal of The Electrochemical Society, 1998).

shape of the curve changed slowly to its new steady state appearance. On polarizing the electrode with a moderate anodic or cathodic overpotentials, a low-frequency inductive loop was observed (Fig. 11d and f) probably due to the presence of two or more adsorbed species [103]. According to Schouler and Kleitz [105], the low-frequency inductive loop is related to the onset of electronic

conductivity in the subsurface of the electrolyte material under suitable partial pressure of oxygen and electrode polarization. The increase in electronic carrier concentration not only leads to significant decrease in overpotential, but also results in spreading the reaction zone near TPB. However, the above reasoning cannot account for the negative inductance on increasing anodic overpotentials as observed in Aaberg's experiments (shown in Fig. 11c and d). It should be noted that electrodes are not susceptible to oxidation in a reducing atmosphere (H_2-H_2O) or at lower absolute potential. Thus, the negative inductive loop was thought to be arising due to Faradaic processes as described by the theoretical impedance models [106]. According to Bay and Jacobsen [107], during polarization, the contact area between YSZ and Pt electrode is dynamic in nature. Using atomic force microscopy technique, the surface reorganization such as transport of YSZ material was reported on the passage of current. The resulting morphological changes were suggested to give rise to variations in the reaction zone extension and account for the inductive relaxation times of order 2.5–26 h [103].

Guindet et al. [108] investigated the polarization curves for oxidation reaction on a nickel ball pressed onto YSZ disc at 960 °C, where maximum current density was observed for an anodic polarization close to –850 mV (vs. air). The formation of NiO was suggested at anodic potentials between –850 and –650 mV (vs. air). At lower anodic potentials (–1000 to –850 mV vs. air), the $\log i$ vs. η curve obeys Tafel's behavior. With an increase of anodic potential from –850 to –650 mV (vs. air), formation of NiO gradually occurred until the surface of Ni metal got completely covered with a passive NiO film. The oxidation of H_2 still occurs, but now also on the passivated NiO layer. This caused an increase in the electrode resistance and a large capacitive loop was observed on the impedance plot. Authors attributed this finding to the passivation of the Ni electrode at high anodic potential, which was completely different from the explanation given by Aaberg et al. [103]. At lower anodic overpotential (<–650 mV), H_2 oxidation takes place only on NiO and an inductive loop appears at low frequency side in the Nyquist plot. In addition, Guindet and his coworkers have also investigated the effect of P_{H_2} and P_{H_2O} on interfacial electrode conductivity [108,109]. It was found that the electrode conductivity at low P_{H_2} was proportional to $P_{H_2}^{-1/2}$, and $P_{H_2}^{1/2}$ for high P_{H_2} . Furthermore, when P_{H_2} is fixed, the conductivity was found to be dependent on $P_{H_2O}^{1/2}$. On analyzing the anodic-polarization curves measured as a function of $P_{H_2O}^{1/2}$ using Butler–Volmer-type equations, the apparent anodic transfer coefficient was found to be varying between 1.4 and 1.7. Based on the polarization curves results, it was concluded that the charge transfer process was not the rate determining step in the anodic reaction. In another investigation, Osberg and Norby [110] used two different types of electrode, Ni wire wrapped around an alumina rod and an electroplated Ni layer (2 μm thick) with circular holes made by microlithography. This was done in order to elucidate the role of TPB length on the Ni electrode performance. For the Ni wire electrode, the Nyquist plot showed only one semicircle. The resistance associated with the semicircle was attributed to the charge transfer process occurring during oxidation, while the constant phase element was associated with the double layer capacitance arising from TPB (Fig. 12).

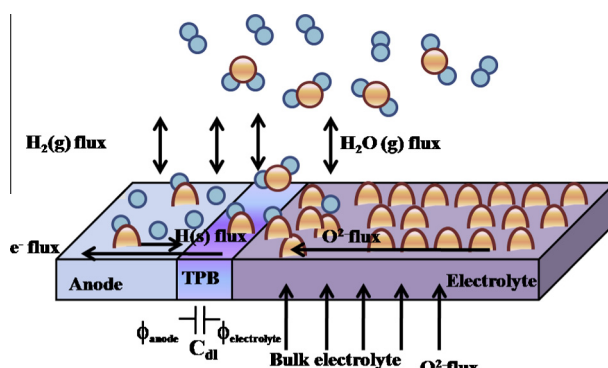


Fig. 12. Schematic showing electrochemical oxidation of H_2 at an SOFC TPB and elements of an electrical equivalent circuit for explaining impedance results (adapted from Ref. [112]).

In the case of porous nickel layer, two semicircles were observed in the Nyquist plot [111]. The semicircle appearing at the low frequency side (dominated part of the spectrum) was attributed to a reaction resistance and was related to the surface coverage of adsorbed intermediates. The resistance was reported to increase on decreasing $P_{\text{H}_2\text{O}}$ and increasing P_{H_2} . At low P_{H_2} values, the charge transfer resistance was found to be proportional to $P_{\text{H}_2\text{O}}^{-1/2}$, while at moderate P_{H_2} , it exhibits an inverse linear relationship with TPB length. From the above results, it was concluded that for electrodes with a small TPB length and a large Ni and YSZ area available per unit TPB length, the rate is limited by charge transfer reaction, owing to the restricted TPB length. However, in the case of electrodes with large TPB length and limited Ni–YSZ interface, the rate becomes limited by reaction resistance.

Recent studies carried out by Bessler et al. [113] reveal that the O^{2-} charge transfer step proposed by Mizusaki et al. was not properly confined to the P_{H_2} and $P_{\text{H}_2\text{O}}$ dependence. Instead, H^+ spillover from the Ni surface onto YSZ occurs in a two-step charge transfer process which can explain the P_{H_2} and $P_{\text{H}_2\text{O}}$ dependence observed by Mizusaki et al. [89,98]. Later, Boer [111] and Bieberle [93] in separate studies, explored and proposed alternative reaction steps to understand the measured impedances and current–voltage curves. Bieberle proposed a single charge transfer reaction step involving H_2 -spillover onto YSZ followed by reactions with 2OH^- to form an O^{2-} ion and an H_2O molecule (which desorbs from the YSZ surface). Bessler [114] applied a transient numerical simulations to analyze Bieberle's reaction mechanism when a periodic modulation of overpotential was imposed on the system, and found a good agreement with their impedance results.

The charge transfer step during hydrogen oxidation reaction in porous Ni electrodes (on YSZ) whose surface is modified with finely dispersed YSZ phase was investigated by Boer [102]. A significant reduction was also observed in the overall electrode resistance of the modified electrodes and the authors attributed the phenomenon to an increased number of active sites, which is an important aspect of cermet structure of Ni–YSZ that later became the most popular material as SOFC anode.

Besides these, Ni-point [103,106,115,116] and Ni-paste [117] were also investigated. However, these electrodes suffered from the problems of non-reproducibility, and contact and sealing issues. Mizusaki et al. [98], Boer [111], and Bieberle et al. [101] studied anodic reaction mechanism on model anodes possessing well defined structures of metallic Ni thin films fabricated by photolithography and wet-chemical etching. The structures determined by Bieberle et al. [101] with $20 \mu\text{m}$ equidistant lines and total TPB length of 3.7 m/cm^2 on a unit area (1 cm^2) sample were found stable up to 700°C . At higher temperatures, Ni was found vulnerable to grain growth and coarsening [98]. The electrochemical performance of the anodes obtained by Bieberle et al. [101] was similar to that of Boer [111], but it differs from that reported by Mizusaki et al. [98] due to lower electrode conductivity. It is important to note that the TPB length was directly correlated (linear relationship, and also as rate limiting step) with electrode conductivity [118].

There is a considerable disagreement among the researchers regarding the identification of a rate determining step. Boer [111] suggested that charge transfer process is the rate determining step in the anode kinetics instead of dissociative adsorption of reactants or surface diffusion of adsorbed species on Ni anode, as suggested by Mizusaki et al. [98]. Bieberle et al. [101] suggested that the dominant arc in the Nyquist plot arises due to adsorption–desorption of hydrogen or by the removal of O^{2-} (from electrolyte). Thus, not only charge transfer, but catalytic activity also affects the anode kinetics upon increasing $P_{\text{H}_2\text{O}}$. Furthermore, Ehn and Høgh [119] and Sukeshini et al. [120] reported similar electrochemical reaction rates on Ni-patterned anodes with wet and dry fuels (H_2 , CO, CH_4). Thus, they found that adsorption–desorption kinetics may play a critical role in the oxidation of fuel (both CH_4 and CO). The electrode reactions were also found to be influenced by impurities at the TPB.

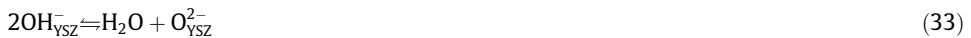
2.2. Nickel/YSZ cermet

Introduction of cermet anodes brought a number of advantages, such as improved adhesion and anchorage between anode and electrolyte materials, stability, and increased area of reaction sites in the form of TPB on the electrode. However, establishing a quantitative description of the complex microstructure of cermet anodes (e.g., Ni/YSZ), and explaining the complex impedance spectra still remains a challenge. Boer [111] has summarized the attempt of Mogensen and Lindegaard [121] to

put forth the mechanism for the oxidation of hydrogen on a Ni/YSZ cermet electrode. The impedance spectra consist of two separate semicircles. The resistance of the high frequency semicircle was attributed to both: ion transfer across the TPB and the internal resistance of anode material. Instead of an ideal capacitor, a constant phase element (CPE) with $n = 0.67$ was used to fit the impedance data due to variation in grain sizes and orientations which results in distribution in relaxation times. The associated capacitance was attributed to the accumulation of charge between the Ni and YSZ interface. The low-frequency semicircle in the impedance spectra arises due to reaction resistance associated with the water formation on the YSZ surface, which is dependent on the surface coverage of Ni by protons and H_2O . Based on the interpretations from impedance spectroscopy results, Mogensen and Lindegaard proposed the following mechanism [121]:



Diffusion of $\text{H}_{ad,\text{Ni}}^+$ to the Ni–YSZ boundary



This mechanism was reformulated again with the incorporation of protons into the bulk of Ni and YSZ as well on the surface



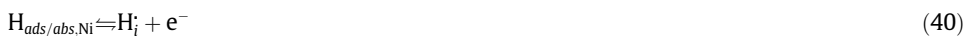
where the subscript i denotes the interstitial site



Eqs. (30) and (31) were assumed to be the rate determining steps, which can explain the two arcs obtained by authors [121] in the Nyquist plots. In the later studies performed by Mogensen et al. [122] on Ni/YSZ cermet electrode, it was reported that most of the structures were well-defined by three, more or less overlapping arcs. This implies that at least three (physical or chemical) processes limit the overall reaction. The high-frequency semicircle (1–50 kHz) was found to be dependent on the particle size of cermet structure. However, compared to low (0.1–10 Hz) and medium (10 Hz–1 kHz) frequency arcs, the high-frequency impedance arc was reported to be insensitive to fuel composition and overvoltage. It was suggested that the associated CPE of high frequency arc was associated with the double layer capacitance at the Ni/YSZ interface. The capacitance of the low frequency semicircle was found to be ideal, and dependent on $P_{\text{H}_2\text{O}}$ with the value in the range of 0.5–2.5 F/cm². From the magnitude of capacitance, it was reported that the low-frequency arc was associated with the changes occurring in the bulk composition of gas phase away from the electrode (rather than the adsorption of charged species on the electrode surface). Aaberg et al. [123] came up with a more or less similar reaction scheme in agreement with those earlier reported by Skaarup et al. [124], where it was suggested that the adsorption and mobility of hydrogen on Ni surface is a fast process. Thus, the hydrogen adsorbed atoms can be assumed to be present in abundance at the Ni/YSZ boundary, even when the electrode is moderately polarized to anodic potentials.



or, alternately



Thus, this illustrates that protons are being absorbed in the electrolyte, and



However, when the combination of proton and oxygen ions is slow (shown in Eq. (41)), the interstitial protons (H_i) accumulate in the electrolyte and exhibit a large capacitance. However, it does not contribute much to the overall rate unless sub-surface diffusion of the protons extends towards the reaction site. The large capacitance experimentally observed in the low frequency region was suggested to be associated with the involvement of interstitial protons, provided that the diffusion coefficient for protons in ZrO_2 is high. It was proposed that the solubility of hydrogen in zirconia contributes towards the extension of the reaction zone. However, the mechanism of actual proton conduction (either as protons across TPB or as dissolved hydrogen across metal-zirconia interface) remains unclear.

Aaberg et al. assumed that the electrochemical transfer of protons from the metal to the electrolyte (Eq. (34)) is a potential dependent step and was close to equilibrium. Therefore, the combination of protons and oxide ions on the electrolyte surface was probably a rate determining multi-step processes. Based on these assumptions, Aaberg expressed the anodic current as:

$$i = 2Fk' P_{H_2} \exp\left(\frac{2FE}{RT}\right) \quad (42)$$

where k' is the rate constant. The above relationship is identical to the one proposed by Mizusaki et al. [98,125] The anodic charge transfer coefficient was found to vary between 1 and 2 depending upon the microstructure.

There are several electrode kinetics models in the literature involving $H_2/H_2O/Ni/SZ$, schematic of which are shown in Fig. 13. The main mechanism supported by several researchers, is charge transfer via proton migration (Fig. 13a) originating from the interaction between Ni and H_2 . However, this mechanism lacks clear electrochemical evidence [122,124]. The oxide ion migration shown in Fig. 13b, is based on the data from patterned electrode reported by Mizusaki et al. [98]. Reaction between H_2 and O^{2-} directly on the stabilized zirconia (SZ) electrolyte followed by electron migration via SZ to the Ni is also mentioned (Fig. 13c), but it lacks experimental evidence [126,127].

Wagner et al. [129] reported the solubility of hydrogen in ZrO_2 , which is proposed to play a role in extension of the reaction zone. However, it is not completely understood whether the protons are transferred across the TPB via adsorbed state only, or additionally, across the metal/zirconia (Ni/YSZ) interface via hydrogen absorption in the metal (Ni). Although impedance analysis is a widely used tool for kinetic studies on electrodes, impedance spectrum can be fitted to a number of RQ-arcs for which physical meaning cannot be assigned in a simplified manner. In the case of cermet electrodes which contain both electronic and ionic conducting phases, the use of a chain ladder network (also known as transmission line model) to analyze impedance data has been found beneficial, as this type of network also visualizes the bulk activity of cermet.

Apart from Ni-patterned, gauge and paste anodes, Bieberle and Gauckler [130] also fabricated Ni-YSZ anodes using screen printing, sputtering and electrostatic spraying techniques (Fig. 14). For the

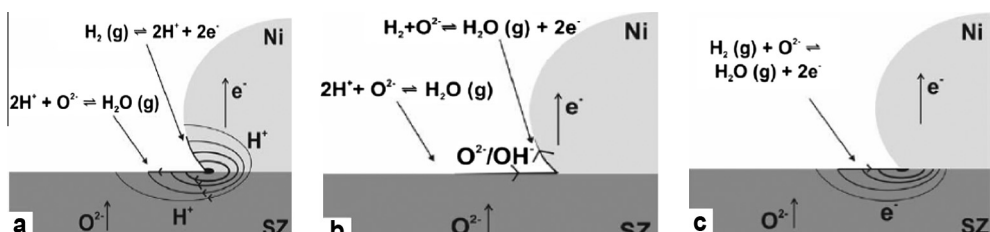


Fig. 13. Schematic representations of the probable mechanisms of anode processes proposed by various research groups: (a) H_2 adsorption on the Ni and formation of H^+ ions. The latter migrate to the site for water formation either along the surfaces or through bulk Ni and bulk stabilized ZrO_2 . (b) Migration of O^{2-} or OH^- from the stabilized ZrO_2 to the Ni along the respective surfaces resulting in the formation of water at Ni sites. (c) Water formation occurs at stabilized zirconia surface and electron transport to the Ni along the surface or via the stabilized ZrO_2 ((a-c) reprinted with permission from Ref. [128], ECS Transactions, 2007).

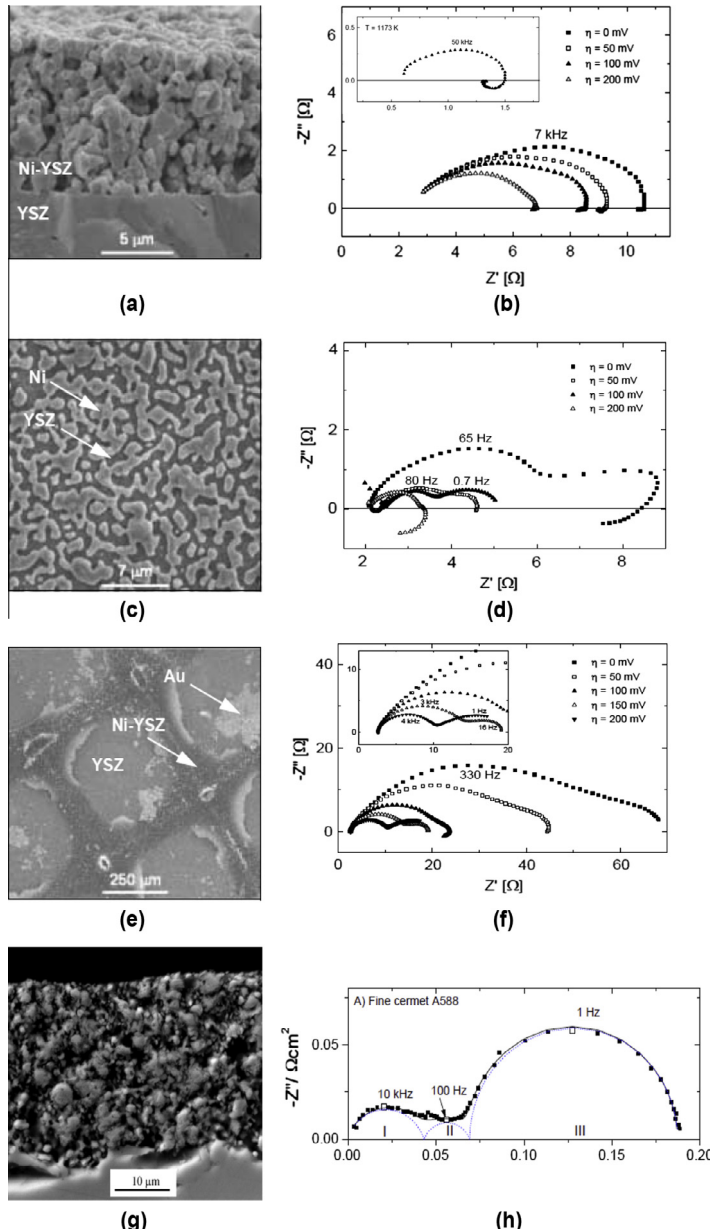


Fig. 14. (a) SEM images of screen-printed Ni–YSZ anode (cross section); of average thickness 10–30 μm , (b) electrochemical impedance data as a function of the overpotential η , (c) top view of sputtered Ni–YSZ anode after electrochemical measurement. Image exhibits islands of Ni in YSZ, (d) impedance data show high obscurity, (e) top view of electrostatically sprayed Ni–YSZ anode after electrochemical measurement and (f) the impedance data, (g) fine cermet Ni/YSZ anode prepared by spray-painting with Ni/YSZ volume ratio 40/60, and (h) the impedance data. (i) Coarse cermet anodes prepared by screen-printing and (j) impedance data, (k) Ni-paste anode prepared by applying a Ni paste without sintering before testing and (l) the impedance data. (m) Ni-felt anode and (n) impedance data. Impedance spectra is obtained at open circuit potential (OCP) at 1000 $^\circ\text{C}$ in $\text{H}_2 + 3\%$ H_2O . Bold dots represent measured spectrum, and solid lines represent total fit ((a–f) reprinted with courtesy: Bieberle, A., Eidgenössische Technische Hochschule Zürich (ETH Zürich). 2000, Swiss Federal Institute of Technology: Zurich [93]), ((g–n) reprinted with permission from Ref. [131], copyright Journal of The Electrochemical Society, 2000. (o): Schematic showing an overall picture on how cermet structure offers extended TPB length (Courtesy: Ref. [132]).

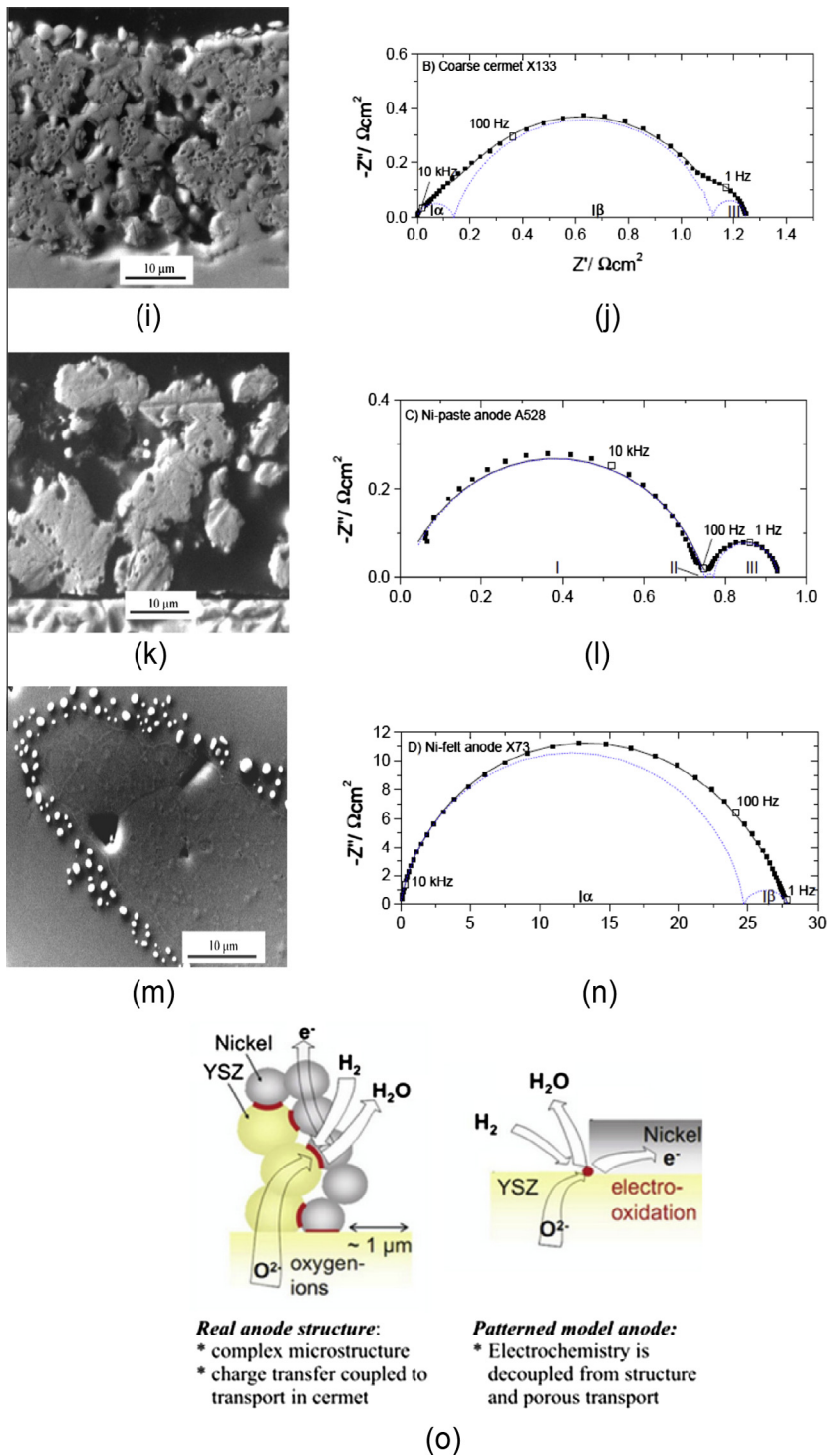


Fig. 14 (continued)

screen-printed Ni–YSZ anode, the Nyquist plot exhibited single dominant arc at 700 °C and the shape of the curve was not found to change significantly with varying applied overpotential. Since the arc tangent is slightly higher than 45°, diffusion limitations for such anodes cannot be ruled out. In the low frequency region, a small inductive loop was also observed. The total anode impedance is around 10 Ω and is same as that of Ni paste anode. Hence, Ni–YSZ can potentially replace Ni-paste effectively as anode for SOFC.

On lowering the temperature, a considerable change in the shape of impedance spectra is observed. The total impedance of the anode increases with the decrease in temperature. At 500 °C, it becomes possible to identify at least two relaxation processes from the impedance spectra. The anodic reaction processes appear to be limited by diffusion. At higher temperatures ($T > 500$ °C), the diffusion effect disappears along with the high frequency region arc. Instead, low-frequency inductive loop appears at higher temperatures (inset Fig. 14b).

SEM image of the sputtered Ni–YSZ anode is shown in Fig. 14c. Impedance data of the sputtered Ni–YSZ anode was found to be most complicated compared to the other anode designs (Fig. 14d). At equilibrium ($\eta = 0$ mV), the Nyquist plot shows a clearly separated low-frequency arc, which go on decreasing with an increase in the overpotential and become invisible at an overpotential of $\eta = 200$ mV (Courtesy: Bieberle, Zurich [93]). The size of arc in the low frequency region again increases at $\eta = 100$ mV. According to Bieberle, the absence of consistent trend observed in the obtained data is associated with the microstructural changes occurring in the sputtered Ni–YSZ during the impedance measurements. Nevertheless, the relaxation frequency of high-frequency process increases with an increase in applied overpotential, whereas the relaxation frequency of low-frequency process exhibits no dependency over the applied overpotential.

For electrostatically sprayed Ni–YSZ cermet anode, the total electrode impedance was found to be rather high (~70 Ω, Fig. 14f), whereas the other Ni–YSZ cermet anode designs exhibited anode impedance of around 10 Ω or lower (Fig. 14b and d). The shape of Nyquist plot shows a considerable dependence on the applied overpotential η . At $\eta = 0$ mV, single dominant semicircular arc exists in the high frequency region and a second smaller arc (which is sensitive to high overpotential) in the low frequency region.

Brown et al. [131] fabricated four types of Ni–YSZ anodes on YSZ three-electrode pellets, viz., a fine 0.5–1 μm particle size cermet (Fig. 14g), a coarse 2–3 μm particle size cermet (Fig. 14i), a porous Ni-paste anode (Fig. 14k), and a Ni felt anode (Fig. 14m), which elucidated the relation between morphology and electrochemical performance via impedance spectroscopy at open circuit potential (OCP). Fig. 14h, j, l and n shows area specific impedance spectra obtained at OCP at 1000 °C in H₂ + 3% H₂O atmosphere after correction for a series resistance of 1–3 V. The characteristic frequencies were marked as I, II and III. Arc I corresponds to the structure dependent part of the impedance spectrum in the Nyquist plots, described by one arc in Fig. 14h and l, but by two arcs I α and I β in Fig. 14j and n.

Arc II corresponds to the diffusion impedance relating to the gas over the anode. It was distinctly resolvable in Fig. 14h and slightly in Fig. 14l as an arc of about 0.025 Ω cm² at an intermediate characteristic frequency of 10–100 Hz [133]. In Fig. 14j, the diffusion impedance cannot be resolved from the impedance spectra. Due to the high relative magnitude of electrode impedance in Fig. 14n, it was rather difficult to deconvolute either of the two concentration polarization processes. Arc III corresponds to gas conversion (between 0.12 and 0.15 Ω) at a characteristic frequency of 1 Hz [134].

Consequently, the polarization resistance R_p , and the electrode's relevant part of the spectra, exhibits activation energy in the range of 0.8–1.8 eV. It is important to note that the fine cermets and Ni anode covering higher percentage of electrolyte shows lower activation energy values, while coarse cermets and Ni anode covering lower area of electrolyte shows higher activation energy values. R_p was found to exhibit no significant dependence on P_{H_2} (0.01–0.97 atm) at 1000 °C; however, it was reported to be proportional to $P_{H_2}^{1/2}$. According to authors, *n*-type conductivity in the electrolyte is the limiting process with the high activation energy at 1000 °C.

Fig. 15 shows the Arrhenius plots for Ni-Stabilized ZrO₂ from different sources [128]. It is quite apparent that the model electrodes are not easily reproducible, and the results span over 3–4 decades at a given temperature. For both cermet and model Ni electrodes on stabilized zirconia, the variation in activation energy values is large, i.e., between 0.6 eV and 1.7 eV. Furthermore, at a given set of

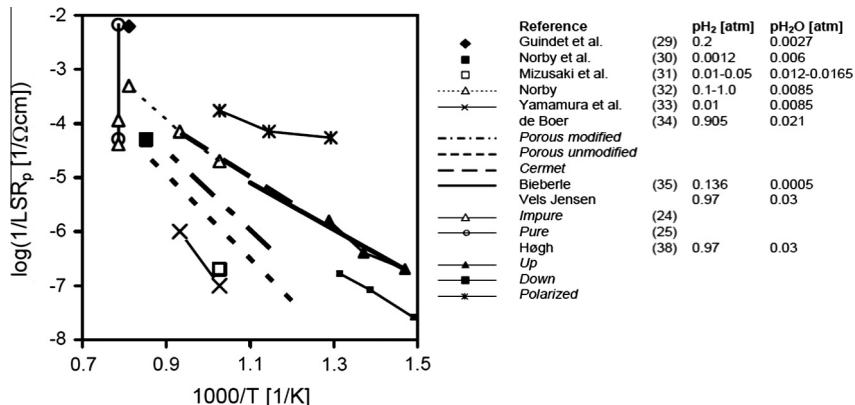


Fig. 15. Arrhenius plots from polarization and impedance results for Ni-stabilized zirconia electrodes. LSR_p stands for length specific polarization. (Reprinted with permission from Ref. [128], copyright ECS Transactions, 2007).

conditions, a large variation in polarization resistance R_p values was observed (shown in Fig. 16). For cermet electrodes, this depends largely on the microstructure of the Ni-SZ composite, viz., porosity, particle size and its distribution, properties of the starting or raw materials, fabrication method employed, and processing parameters. Most of the results were obtained in the range 800–1000 °C, but the values of electrode polarization resistance, R_p , show a wide variation when extrapolated to low temperature region [53]. The R_p of Ni/YSZ based anodes was found to be in the range of 1–30 $\Omega \text{ cm}^2$ and 7–200 $\Omega \text{ cm}^2$ at 700 and 600 °C, respectively, which is still too high for H_2 oxidation at $T < 700$ °C. However, modified Ni/YSZ cermet anodes (with YDC layer) exhibited electrode polarization resistance as low as 0.26 $\Omega \text{ cm}^2$ at 600 °C in wet H_2 [135].

At higher sintering temperature, the microstructure of the processed material (e.g., some non-sintered Ni wire electrodes) becomes coarser, and consequently, the apparent activation energy value was also observed to be higher. The R_p values were found to be dependent on the partial pressure of water P_{H_2O} and hydrogen P_{H_2} , and varied noticeably from one type of electrode to the other. Hence, it is difficult to compare and reproduce cermet electrode data.

The polarization resistance values were found to vary by a factor of 10–10² (Fig. 15), whereas the activation energy increased by over two times for anodes prepared by various processing routes. Researchers attribute this effect arising due to the reduction of all or some of the impurities at TPB

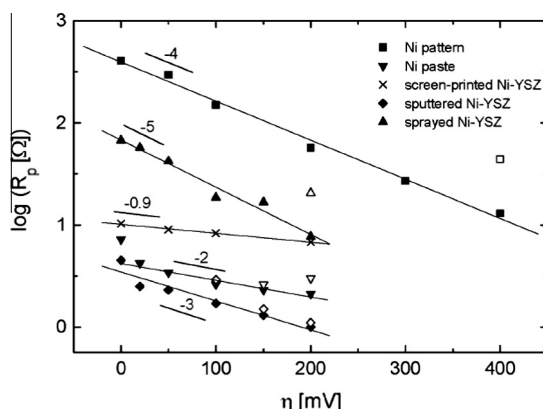


Fig. 16. R_p as a function of applied overpotential η for different types of Ni-YSZ anodes; Closed and open symbols correspond to high frequency impedance arc and total anode impedance, respectively [93]. (Courtesy: Bieberle, A., Eidgenössische Technische Hochschule Zürich. 2000, Swiss Federal Institute of Technology: Zurich).

Table 2

Results of electrochemical measurements on different types of nickel electrodes reported by various researchers. Superscripts represents: 'T' – TPB length; 'a' – for electrode with TPB length of 3.3 mm; 'b' – resistance corresponding to first arc in impedance spectra, representing the charge transfer resistance; 'c' – value given at 700 °C for an electrode with TPB length of 3.26 m/cm²; 'd1, d2 and d3' – Effect of the sintering temperature of the electrode (**d1**) sintering Temperature = 1500 °C, (**d2**) = 1400 °C and (**d3**) = 1200 °C. Adapted from [111].

Type of electrode	Gas phase conditions (10 ⁵ Pa) pH ₂ /pH ₂ O	Temp (°C)	Impedance (No. of arcs)/electrode resistance (Ω)	Current expression	Gas phase dependence of electrode conductivity (1/R)	Ref.
Ni ball (9.4 mm) ^T	(0.2–0.58)/0.027	960	2/850	$i = i_0 \exp(2F\eta/RT)$	–	[108]
Ni ball –	¹ 0.75/0.053 ² 0.7/(0.048–0.2) ³ (0.037–0.9)/0.055	975	¹ 1/1970	² $i = i_0 \exp(\beta_a F\eta/RT)$ with ($\beta_a = 1.4$ –1.7)	² 1.697 pH ₂ O ^{1/2} ³ 0.016 pH ₂ ^{-1/2} + 0.396pH ₂ ^{1/2}	[109]
Ni wire (3.3–15.7 mm) ^T	0.0012/0.0063	900	1/65 k ^a	–	pH ₂ O ^{1/2} (at low pH ₂)	[110,136]
Porous Ni layer (121 mm) ^T	0.0012/0.0063	900	2/1.6 ^b	–	pH ₂ O ^{1/2} (at low pH ₂)	[110,136]
Porous Ni layer	0.98/0.02	1000	1/2.1(Ω cm ²)	–	pH ₂ ⁰ pH ₂ O ^{1/2}	[89,98,99]
Ni stripe (0–6 m cm ²) ^T	¹ 0.1/0.017 ^{0.01} /(0.004–0.16)	500–850	¹ 1 ^c /10.5 k ^c –	(3 parallel reactions) $i_i = k_i pH_2 \exp(2FE/RT) - k'_i pH_2 O$ $i_2 = k_2 (pH_2)^{1/2} - k'_2 (pH_2 O)^{1/2} \exp(-FE/RT)$	pH ₂ O ¹ (at high pH ₂)	[98,99,125,137]
Ni stripe	(0.01–0.19)/0.009	–	–	$i_3 = k_3 pH_2 - k'_3 pH_2 O \exp(-2FE/RT)$	pH ₂ O ⁰ (at low pH ₂ and <750 °C) pH ₂ ⁰ (700–800 °C) pH ₂ ^{-1/2} (850 °C)	[96,138]
NiO-YSZ cermet (55 wt.% NiO)	¹ 0.97/0.03 ² 0.03	1000	¹ 1/0.2(Ω) ² 2/0.2(Ω)	–	pH₂ order dependence ¹ pH ₂ ⁰ ² pH ₂ ^{1–2} (in the pH ₂ range of 0.97×10^5 Pa – 0.015×10^5 Pa and at pO ₂ = 4.5×10^{-18}) pH₂O order dependence ¹ pH ₂ O ⁰ (in the pH ₂ O range of 0.03×10^5 Pa – 0.0022×10^5 Pa (at pH ₂ : 1)) ² pH ₂ O ¹ and (in the pH ₂ O range of 0.25×10^5 Pa – 0.03×10^5 Pa (at pH ₂ : 0.5))	[121,122,139]

(continued on next page)

Table 2 (continued)

Type of electrode	Gas phase conditions (10^5 Pa) pH_2/pH_2O	Temp (°C)	Impedance (No. of arcs)/electrode resistance (Ω)	Current expression	Gas phase dependence of electrode conductivity ($1/R$)	Ref.
Ni-YSZ cermet (40 vol.% Ni)	0.5/0.02	1000	1/0.24 2/0.04 3/0.05		pH₂order dependence pH_2^0 in the pH ₂ range of 0.1×10^5 Pa – 1×10^5 Pa (at pH _{2O} : 0.02)	[123,140]
Ni-YSZ cermet (a) 33 vol.% Ni (b) 50 vol.% Ni	0.3/0.02	1000	2/0.04	$i_i = i_o \exp(\beta F\eta/RT)$	–	
Ni-YSZ cermet (40 vol.% Ni)	0.97/0.03	1000	1/0.3 ^{d1} 1/2.6 ^{d2} 3/10.5(tot) ^{d3}	$i_i = i_o \exp(2F\eta/RT) - \exp(-F\eta/RT)$	–	[95]
				Electrode characteristics depend on sintering temperature (only valid for well prepared electrodes)		

sites [128]. According to Bieberle [93], the polarization resistances decreases on increasing applied overpotential and they are all exponentially dependent on the overpotential with slope between -0.9 and -5 . In the Nyquist plots, usually two distinct semicircles are displayed by anodes in the high and low frequency regions at higher values of applied overpotential. Authors attributed the exponential decrease of the R_p values to the impedance arc in the high frequency region [93]. A survey on some of the noteworthy results from the measurements of various nickel electrodes by different researchers have been summarized in Table 2 [111].

Holtappels et al. studied the reaction of hydrogen/water mixture on Ni-zirconia cermet electrodes at three different partial pressures of H_2 and water between the temperature range of $725\text{ }^\circ\text{C}$ to $950\text{ }^\circ\text{C}$ [141,142]. It was shown by authors that the hydrogen oxidation reaction occurring at anode was actually a multistep electrochemical reaction mechanism involving atomically adsorbed hydrogen species in the charge-transfer reaction. At temperatures less than $845\text{ }^\circ\text{C}$, charge transfer step determines the rate of the anodic reaction. At temperatures above $845\text{ }^\circ\text{C}$, the results for hydrogen oxidation reaction and hydrogen evolution reaction were found inconsistent with the charge transfer controlled electrode reaction. Instead, adsorption and chemical reaction between adsorbed species dominated over the anodic processes and hydrogen evolution reaction in the temperatures higher than $845\text{ }^\circ\text{C}$ [141,142].

The polarization curves of Ni-YSZ cermet electrodes for $P_{H_2} = 0.48$ bar and $P_{H_2O} = 0.05$ bar in the temperature range from $725\text{ }^\circ\text{C}$ to $950\text{ }^\circ\text{C}$ show that the cathodic and anodic branches of polarization curves were not symmetrical. This suggest a different reaction kinetics for the hydrogen oxidation reaction compared to water reduction reaction [141]. The hydrogen oxidation reaction shows an apparent Tafel behavior (linear region) beginning at overpotentials of about $+95\text{ mV}$ at $725\text{ }^\circ\text{C}$ and $+130\text{ mV}$ at $950\text{ }^\circ\text{C}$. The shift in the starting point of Tafel region was attributed to the change in RT/F values ($72\text{ mV}/725\text{ }^\circ\text{C}$ and $105\text{ mV}/950\text{ }^\circ\text{C}$). The water reduction reaction shows apparent Tafel behavior only in low temperatures at overpotentials $>100\text{ mV}$.

In the investigated partial pressure regime, Holtappels reported that at $950\text{ }^\circ\text{C}$ [141], hydrogen evolution reaction is independent of P_{H_2} . However, the hydrogen oxidation reaction was found to be dependent on P_{H_2} at low overpotentials, and becomes independent at high overpotentials [141]. Fig. 17a shows the dependence of current density j on the applied overpotential η for various anodes [93]. Anode materials with longer TPB lengths ($\geq 10\text{ m/cm}^2$, e.g., screen printed, sputtered and sprayed Ni-YSZ) and larger surface area exhibit enhanced performance [93] in terms of current density when compared with the anode materials with ($\sim 3.7\text{--}10\text{ m/cm}^2$, e.g., Ni-pattern, Ni-gauge and Ni-Paste). The curves appear to be very similar in shape, but the variation in current densities and R_p values differ by up to three orders in magnitude. According to de Boer, the total electrode resistance in Ni-YSZ

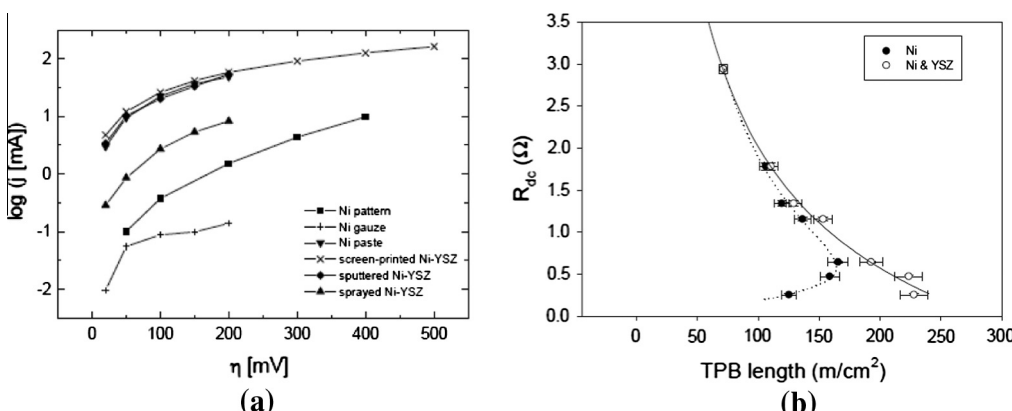


Fig. 17. (a) Current density j as a function of the applied overpotential η for different anodes [93] (Courtesy: Bieberle, A., Eidgenössische Technische Hochschule Zürich. 2000, Swiss Federal Institute of Technology: Zurich). (b) Total anode resistance as a function of TPB length based on Ni-YSZ (cermet) surface (Nickel particle size ranging from 2.2 to $1.0\text{ }\mu\text{m}$ and porosity $63\text{--}50\%$) and Ni-surface coverage ($17\text{--}53\%$) at interface for cermet microstructures with different fractions of fine YSZ (ranging from 0 to 100) [111]. (Courtesy: de Boer, B., 1998, University of Twente: Netherlands).

cermets may decrease by more than 50% (from 1.8 to 0.7 value) with an increasing surface coverage (TPB length from 110 to 180 m/cm²), i.e., length of the TPB at the interface (Fig. 17b) [111].

Polarization curves for H₂/H₂O/Ni-YSZ-anodes, reported by Mogensen et al. [128] exhibited a small linear region of approximately ±25 mV existing around open circuit potential. For the next 50–150 mV in the anodic direction, the current density was found to increase more than linearly. On further polarization, current density became linear again. This is perhaps one of the most beneficial advantages of Ni-stabilized zirconia cermets, over Ni metal electrodes, where current stabilizes almost immediately upon potential changes during operation. However, Ni point electrodes takes considerable time to respond and most often, the current is rather unstable at anodic polarizations.

Impedance measurements performed at OCP by Holtappels et al. on annular-shaped Ni-YSZ anodes, prepared by screen printing method as a function of temperature for different partial pressures of H₂ and H₂O [142]. Bode plots shown in Fig. 18a describe the effect of temperature on the impedance at OCP at P_{H₂} = 0.48 bar and P_{H₂O} = 0.05 bar. In the temperature range of 725–890 °C, the imaginary impedance exhibits three maxima, indicated by f₁, f₂ and f₃ at all the temperatures. The maxima f₁, f₂ and f₃ correspond to three apparent relaxation frequencies. The relaxation frequency f₂ (mid maximum) was found to increase continuously from 10 to 500 Hz on increasing temperature, whereas f₁ increases during temperature rise from 725 to 845 °C, but was found to decrease at higher temperatures (i.e., >890 °C). The relaxation frequency f₃ was difficult to distinguish but it may possess the same order of magnitude as f₂ at 950 °C.

The processes associated with different relaxation frequencies were further analyzed by Holtappels et al. in the admittance plane by plotting the imaginary part of admittance vs. real part (1/Z_{*}). It is important to note that in the admittance plane, the parallel processes appear sequentially. At frequencies above 10 kHz, the charging of double layer capacitance C_{DL} across the charge transfer resistance in the area of Ni/YSZ interface (R_W) dominated the spectrum. At medium frequencies of ~10 Hz, the series of R_W and Z_W (Warburg impedance) in parallel to R_{CT} or charge transfer resistance determine the

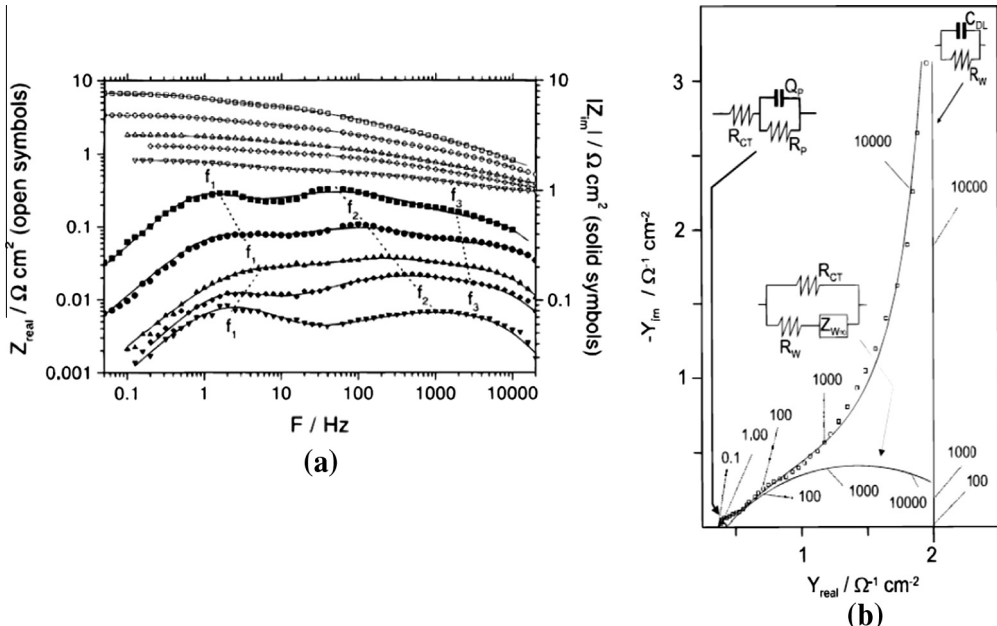


Fig. 18. (a) Bode plots of the impedance spectra measured at open circuit potential as a function of temperature. P_{H₂} = 0.48 bar and P_{H₂O} = 0.05 bar. Z_{Real} is shown by open symbols and Z_{Imaginary} is shown by solid symbols. (□) 725 °C, (○) 780 °C, (△) 845 °C (▽), 950 °C, (—) simulated data. (b) Admittance plot of the impedance spectra at open circuit potential and temperature of 780 °C. (□) represent measured data and (—) represent simulated data ((a and b) reprinted with permission from Ref. [142], copyright Journal of The Electrochemical Society, 1999).

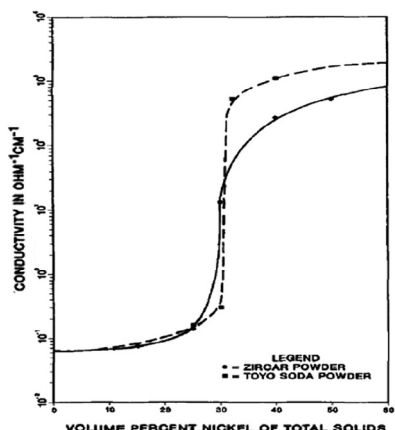
frequency distribution. Below the frequency of 1 Hz, R_{CT} in series with the parameters R_p and Q_p , which essentially describe the time constant for changing the degree of coverage of at least one adsorbed specie on the electrode surface, determine the admittance. The data were analyzed using an analog electrical equivalent circuit representing two parallel reaction pathways, viz., (i) a charge transfer resistance dominating the real part of the impedance, which is attributed to the charge transfer reaction and adsorption occurring at TPB region, and (ii) a diffusion branch described by a resistor in series with a Warburg impedance. An in-depth analysis revealed that the impedance of the H_2/H_2O reaction occurring at Ni–YSZ cermet anodes at OCP involves three different processes with different dependencies on temperature and partial pressures of the reacting gases [142]. Below 845 °C, the real part of the impedance response was found to be charge transfer controlled as the activation enthalpy of the charge transfer resistance R_{CT} matches closely to that for steady-state hydrogen oxidation reaction at OCP. Above 890 °C, the overall reaction rate is determined by two reaction steps, viz., charge transfer and adsorption due to a high fractional surface coverage of the reactant molecules. Furthermore, Holtappels et al. attributed the complexities of the impedance spectra to the changing of electrochemical double layer and a parallel reaction limited by diffusion [142].

The performance of the Ni–YSZ cermet anodes depends upon large number of factors, few of which are presented in Fig. 19. In summary, nickel metal electrodes have been used as SOFC anode materials by the virtue of their less complicated microstructure compared to that of Ni/YSZ cermet electrodes. With pure metal electrodes, it is possible to tailor its fabrication, avoid structural limitations, measure purely chemical parameters, and relate them with the microstructure. Several noteworthy attempts undertaken by various researchers relate the polarization resistance to the length of the TPBs with simple anode geometries of nickel metal, such as wires and porous nickel layers, stripes and a nickel ball pressed on to YSZ disc acting as electrolyte. For charge transfer, the two adjoining phases must have a voltage difference between them and this is thought to be established by a double layer of charge at the solid interface between them. Since gaseous products are formed during the electrochemical oxidation of fuel in a SOFC, the charge transfer processes are most likely to occur at the TPB where there is an access to gas phase for the evolved products. The electrochemical oxidation process involving those steps that may impact electrochemical reaction rates at the anode are summarized below:

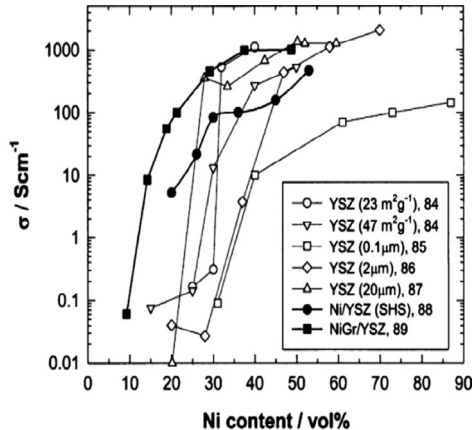
- (1) *On the anode electrocatalyst surface:* The first step is the mass transport of gaseous fuel to the electrochemically active region of porous anode material followed by adsorption of fuel species onto electrocatalyst surface. The surface diffusion of active adsorbate species to the TPB region occurs, which is followed by desorption of any electrocatalyst-adsorbed oxidation products from anode electrocatalyst surface.
- (2) *On the electrolyte surface at the vicinity of the anode:* The O^{2-} ions migrate from the bulk of electrolyte up to the electrolyte surface, ensued with surface diffusion of ionic species to the TPB region and desorption (if necessary) of any electrolyte-adsorbed oxidation products from electrolyte surface.
- (3) *At the three-phase boundaries:* Release of electrons formed during charge transfer reaction into the electrocatalyst bulk [98,111,143,144].

Fig. 19 shows several factors other than charge transfer reaction which may affect the current generation via reactions occurring at Ni/YSZ triple phase boundary. It has been found that increasing the length of TPB per unit volume (l_{TPB}) (ranging between 3.7 and 20 m/cm² in cases of patterned, gauge, paste, mesh, wire Ni-anodes and screen printed, sputtered and sprayed Ni–YSZ anodes, greater than 45–60 m/cm² in case of porous Ni-anodes [93,111]) increases both the charge transfer reaction rate as well the current generation. In order to increase the l_{TPB} in porous electrodes, ceramic based electrolyte material is mixed with the catalyst material (Ni or other noble metal) and fabricated into a porous electrode structure to enhance the diffusion of oxide ions into or out of the electrode.

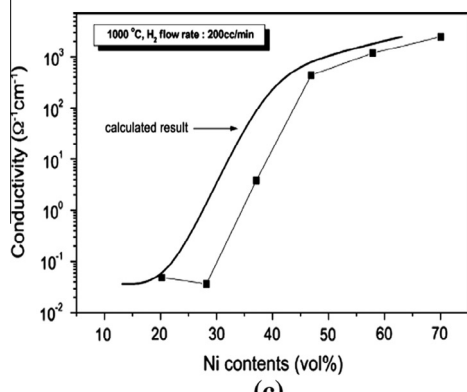
The cermet anodes not only offer enough pores for diffusion of the fuel gases, but also allow adequate O^{2-} ion transport through the electrochemically active region of the anode material, which has been estimated to be around 10–20 μm thick [154,155] in a dense electrolyte/porous anode interface. The development of porous anodes has also made it convenient to implement direct utilization of



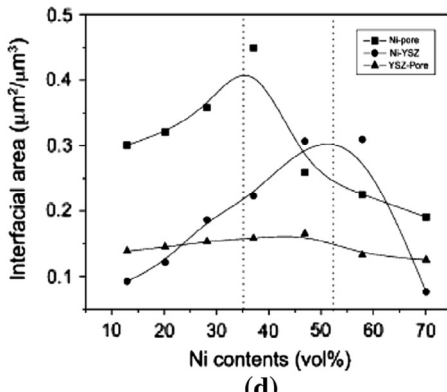
(a)



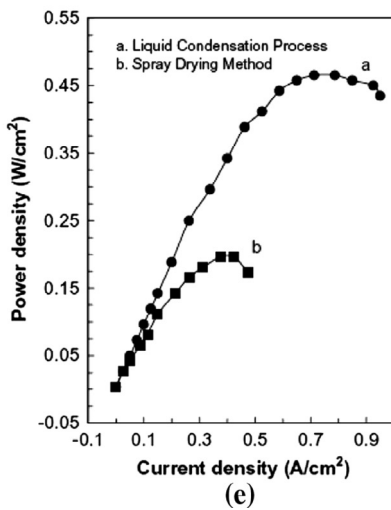
(b)



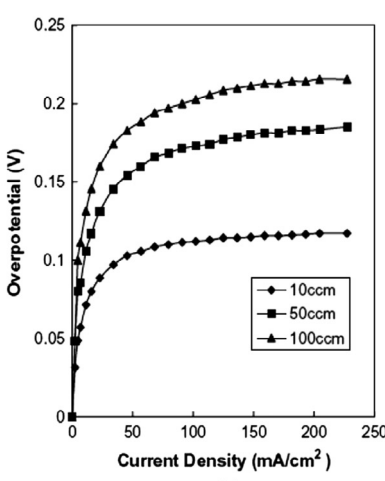
(c)



(d)



(e)



(f)

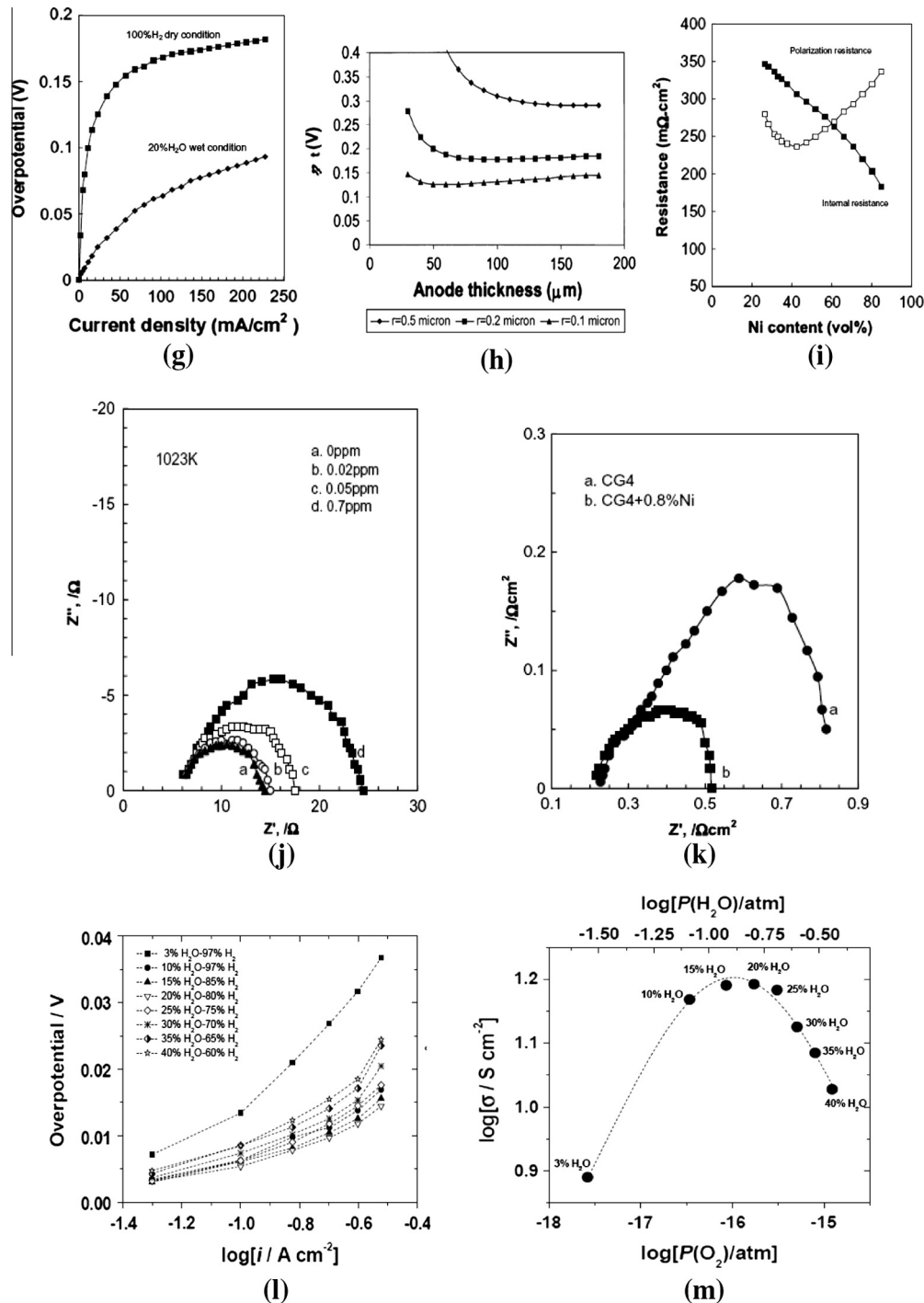


Fig. 19 (continued)

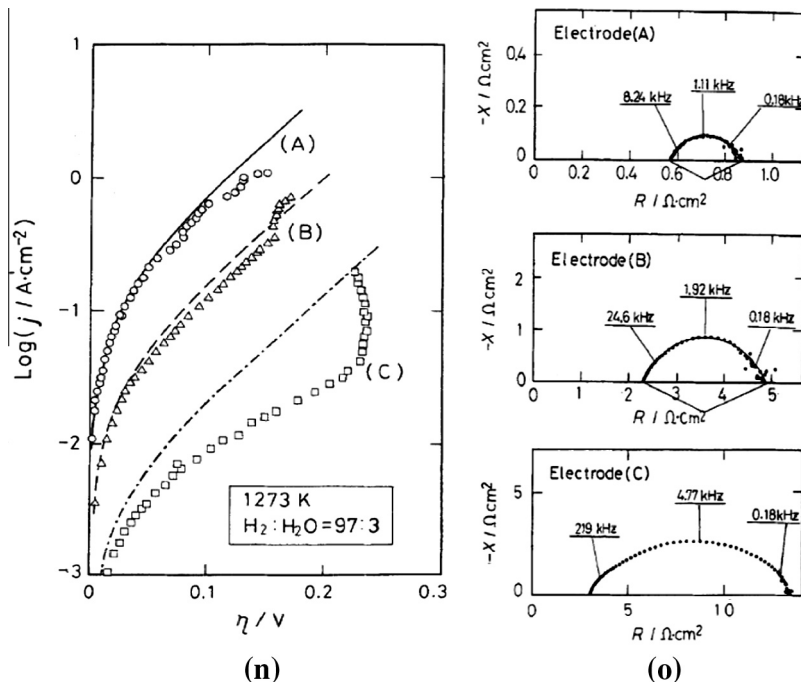


Fig. 19 (continued)

hydrocarbons in SOFCs [156]. However, with Ni/YSZ anodes, the amount of carbon atoms present in the fuel can significantly reduce the voltage output and the overall conversion efficiency of the

Fig. 19. (a) Conductivity of Ni-YSZ cermets vs. the volume percent of Ni fabricated with zirconia powders from two different sources, viz., Toya soda and Zircar (Reprinted with permission from Ref. [145], copyright Journal of The Electrochemical Society, 1987), (b) conductivity of Ni-YSZ cermet anodes as a function of Ni content measured at 1000 °C in humidified H₂ (reprinted with permission from Ref. [146], copyright John Wiley and Sons, 2004), (c) variation of electrical content as a function of Ni content (Reprinted with permission from Ref. [147], copyright Elsevier, 2002), (d) variation of interfacial area of Ni-pore, Ni-YSZ and YSZ pore (reprinted with permission from Ref. [147], copyright Elsevier, 2002), (e) comparison of the power density output of the unit cell fabricated using two different approaches (reprinted with permission from Ref. [148], copyright Elsevier, 2003), (f) dependence of overpotential on the current density of Ni-YSZ cermet anode with 40 vol% of Ni measured at various gas flow rates (reprinted with permission from Ref. [149], copyright Journal of The Electrochemical Society, 2000), (g) dependence of overpotential on the current density of Ni-YSZ cermet anode with 40 vol% of Ni measured in dry and wet conditions at 850 °C (reprinted with permission from Ref. [149], copyright Journal of The Electrochemical Society, 2000), (h) Influence of particle size and anode thickness on the polarization behavior for H₂ oxidation (hydrogen humidified at 50 °C, or H₂:H₂O = 87.6:12.4) (reprinted with permission from Ref. [150], copyright Journal of The Electrochemical Society, 2001), (i) effect of Ni content on the polarization and internal resistance of Ni-YSZ anode tested in 200 ml/min of H₂ as anode gas and 1000 ml min⁻¹ of oxygen as cathode gas (reprinted with permission from Ref. [148], copyright Elsevier, 2000), (j) AC impedance spectra of SOFC with Ni-YSZ cermet anode measured after equilibration in humidified H₂ mixed with several concentrations of H₂S (reprinted with permission from Ref. [151], copyright Elsevier, 2000), (k) AC impedance spectra of CG4 electrode fed with humidified H₂ showing dramatic suppression of the semicircle in the low frequency region as a result of minor Ni addition (reprinted with permission from Ref. [152], copyright Elsevier, 2002), (l) the overpotential of Ni-YSZ cermet (50:50 vol%) anode as a function of current density at 1000 °C (reprinted with permission from Ref. [153], copyright Journal of The Electrochemical Society, 2010), (m) Interfacial conductivity of Ni-YSZ cermet (50:50 vol%) anode as a function of oxygen partial pressure measured at 1000 °C under OCP; Anode gas used: x%H₂O-(100-x)%H₂ (Reprinted with permission from Ref. [153], copyright Journal of The Electrochemical Society, 2010), (n) polarization behavior of Ni-YSZ anode prepared with constant nickel content (40 vol%), at a constant pre-calcination temperature (1400 °C) and at various baking temperatures, (A) 1500 °C, (B) 1400 °C, (C) 1200 °C, and (o) impedance behavior of Ni-YSZ cermet anodes prepared at a constant pre-calcination temperature (1400 °C) and at various baking temperatures, (A) 1500 °C, (B) 1400 °C, (C) 1200 °C ((n-o) reprinted with permission from Ref. [95], copyright Journal of The Electrochemical Society, 1990).

Table 3

A list of studies that have reported sulfur poisoning in long-term operation of SOFC.

Cell structure/sample details	Temperature/duration	Fuel composition	Performance/ current density	Remarks/observations	Ref.
7-Cell stack (Ni-YSZ anode)	1000 °C/800 h	5%H ₂ /10% CO/85% CO ₂ with 50 ppm H ₂ S	150 mA/cm ²	H ₂ S addition to the fuel caused immediate loss of ~5% in operating cell voltage, whereas removing of H ₂ S showed recovery of cell voltage to the original level	[189]
22 cathode supported tubular cell stacks (10 kW SOFC module)	900 °C/170 h	1 ppm H ₂ S in fuel stream	200 mA/cm ²	Gradual drop up to 4.3% in cell voltage. Almost complete recovery (to 98.5%) of the original value in 240 h	[190]
40-cell stack	900 °C	10 ppm H ₂ S in fuel stream	150 mA/cm ²	The ~3% drop in cell voltage. However, degradation fully reversible when H ₂ S concentration < 10 ppm	[191]
5-cell stack	930 °C/400 h	100 ppm H ₂ S in fuel stream	130 mW/cm ²	Stable power output for more than 400 h	[192]
Ni-YSZ cermet anode/electrolyte/cathode symmetrical cell	1000 °C	97% H ₂ -3% H ₂ O with 105 ppm H ₂ S	NA	First to observe the sulfur poisoning. After introducing 100 ppm H ₂ S into the fuel, the total anode interfacial polarization resistance was increased from 0.27 Ω cm ² to 0.45 Ω cm ² (~67% increase). However, there was no change in the bulk resistance (R _b)	[193]
Porous Ni anode, Ni-YSZ cermet anode on YSZ pellets in a three-electrode setup	850, 1000 °C	35 ppm H ₂ S in fuel stream		A 60% increase in anode polarization resistance invariant to anode structure, passage of current, and temperature. The addition of small amount of Mn results in the reduction of polarization resistance by the factor of 2 at 850 °C and 1000 °C. Ni-YSZ cermet anode also displayed poisoning behavior similar to Ni anode, i.e., adsorbed H ₂ S blocks Ni adsorption sites, which participate in the H ₂ /H ₂ O reaction process	[194]
Ni-YSZ cermet anode (84 vol.% Ni-16 vol.% YSZ) and YSZ electrolyte	¹ 750 °C/ 3.33 h ² 900 °C/2.5 h ³ 1000 °C/ 1.1–1.3 h	¹ 0.05–0.7 ppm H ₂ S in fuel stream ² 1–8 ppm H ₂ S ³ 2–15 ppm H ₂ S	0.3 A/cm ² in the fuel without H ₂ S for 5 h	First in adopting impedance spectroscopy for quantifying H ₂ S poisoning effect on Ni-YSZ anode ¹ Degradation in terms of the relative increase in anode interfacial resistance up to 30–115% over 3.33 h of operation, and the time required for recovery ~100 h ² Degradation up to 60–116%; the time for recovery ≥25 h ³ Degradation up to 15–45%; the time for recovery ~1.1 h	[151,195]
¹ Ni-YSZ cermet anode and YSZ electrolyte	¹ 1000 °C	¹ 1, 3 and 5 ppm H ₂ S	² 200 mA/cm ²	¹ Degradation up to 6.3%, 15.2% and 22.8% when H ₂ S concentration was 1 ppm, 3 ppm and 5 ppm, respectively; degradation triggered by 5 ppm H ₂ S was 20%, 27% and 81% at 1000, 900 and 850 °C, respectively	[196]

(continued on next page)

Table 3 (continued)

Cell structure/sample details	Temperature/duration	Fuel composition	Performance/current density	Remarks/observations	Ref.
² Ni-YSZ, Ni-SSZ cermet anode and YSZ electrolyte	² 800 °C	² pH ₂ S/pH ₂ (ppm) = 5–100		² Degradation of cermet anode was reversible above ~900 °C when the exposure time ~1 h. However, at lower temperatures, fatal irreversible degradation occurs. Ni particles were found to oxidize to form NiO for cells that suffered irreversible voltage drop. Sulfur tolerance was found to improve on using Ni-SSZ instead of Ni-YSZ as anode	² [161]
Ni-YSZ cermet anode/electrolyte-supported cells	800 °C/2–16 h	10 ppm H ₂ S	100–400 mA/cm ²	For the first 2 h, the cell's anode polarization resistance under OCP remained almost unchanged and then increased from 1.6 to 8.2 Ω cm ² (400%) in the next 16 h. Degradation was partial recoverable due to surface adsorption of sulfur, which could be displaced upon discontinuation of H ₂ S. The irrecoverable degradation was thought to result because of Ni-S compound formation (e.g., Ni ₃ S ₂)	[197]
¹ Ni-GDC cermet anode/3YSZ electrolyte; Electrolyte-supported cell	¹ 850 °C/450 h	¹ 24.8% H ₂ /35.7% N ₂ /40% CO/200–240 ppm H ₂ S	¹ 200 mA/cm ²	¹ On exposure to 200–240 ppm of H ₂ S, the cell voltage begin to decrease from ~0.74 until a final value of 0.64 V is reached after 650 h. An approximately 10–12.5% loss in cell voltage was observed which suggest that cells based on Ni-GDC performed reasonably well when H ₂ S was present in syngas. Mechanism for degraded cell performance might be due to formation of NiS	¹ [198]
² Ni-YSZ and Ni-GDC	² 800 °C	² 5–700 ppm H ₂ S		² The degradation in the performance for the hydrogen oxidation in H ₂ S containing H ₂ fuel was found to be significantly smaller in Ni-GDC (0.78–0.72 V) when compared with Ni-YSZ based anode (0.61–0.34 V). The better performance of NiGDC anode was associated with the mixed ionic electronic conducting nature of GDC. Further, a significant change in the morphology of Ni and CGO was observed. This was attributed to their reaction with H ₂ S to form NiS and Ce ₂ O ₂ S, respectively. However, the morphology of YSZ remains unchanged after the exposure	² [199]
¹ Ni-YSZ anode-supported button cell	¹ 750 °C/200 h	pH ₂ S/pH ₂ (ppm) = ¹ 0.1, 1, 10	¹ 1100 mA/cm ² ² 1000 mA/cm ²	¹ The 2nd stage of slow sulfur poisoning starts after 200 h	¹ [200,201]
	² 850 °C/500 h	² 2, 10 and 20 ppm H ₂ S		² The cells based on Ni/YSZ anode exhibits significant performance degradation on exposure even to 2 ppm of H ₂ S containing fuel. This was attributed to the loss of percolation of Ni particles in the layers close to electrolyte. The cells with Ni/ScYSZ exhibits a considerably improve performance even at higher H ₂ S levels over a few hundred hours	² [171]

² Ni/YSZ and Ni/ScYSZ anode supported cells with YSZ as an electrolyte and LSM as cathode				A small amount of H ₂ S causes an instantaneous drop in cell voltage. The 2nd stage of the sulfur poisoning with slower degradation lasts for days or even longer. For a given concentration of H ₂ S, the poisoning effect increased with decreasing cell operating temperature range (700–900 °C). Further, the higher cell voltage leads to greater cell voltage drop due to sulfur poisoning. In addition, the degradation was fully or partially recoverable depending on the temperature and duration of H ₂ S exposure
Single (Ni–YSZ anode) electrolyte-supported button cell	800 °C/24–120 h	50 ppm H ₂ S/50% H ₂ /1.5% H ₂ O/48.5%N ₂		
¹ Ni (56%)–YSZ anode-supported SOFC (YSZ electrolyte, LSM/YSZ composite cathode)	¹ 750–850 °C ² 750 °C	¹ 0.2% H ₂ S ² 100–1500 ppm H ₂ S	250 mA/cm ² 250 mA/cm ²	¹ The cell voltage drop decreases with increasing water content (from 0% to 10%). After poisoning, nickel sulfides (Ni ₃ , Ni ₄ S ₃) agglomerates with diameter 3 μm were detected ¹ [202,203] ² [204]
² Electrolyte supported cells with 3YSZ as an electrolyte, LSM20 as a cathode and Ni–YSZ ^a , Ni–GDC ^b , and Ni–GDC–YSZ ^c as anode materials ³ Ni (40 vol.%)–YSZ (60 vol.%)	³ 500–800 °C/2–48 h	³ 100 ppm H ₂ S		³ The migration of nickel from anode was observed on exposure of anode to H ₂ S containing fuel (in the 200–500 ppm range). The depletion of Ni from anode was also confirmed from the quantitative XPS analysis. The cell voltage drop significantly due to the absence of electronic conductive pathways in anode ³ The in situ Raman spectroscopy suggests that the sulfur poisoning of Ni–YSZ does not occur due to the formation of nickel sulfide. NiS was not formed in bulk at ~500 °C and above. The bulk sulfides (e.g., Ni ₃ S ₂) started forming on slow cooling of Ni–YSZ in H ₂ S containing environment. This is accompanied with the morphological changes at temperatures below

SOFC cell. Therefore, most SOFCs developers have preferred to use hydrocarbons in conjunction with an external reformer (with partial oxidation and/or steam reforming) for long-term operations [157,158]. This is because of the lack of durability of most fuel catalysts under conditions where carbon build-up can occur. Numerous studies on electrodes using Ni, as well as Au or Pt, have shown that with CO (and in some cases, CH₄), the electrochemical reaction rates are much slower than with H₂ as a fuel [85,159,160].

2.3. Sulfur poisoning and carbon deposition

SOFCs are intended to be used with a variety of fuels, viz., natural gas, biogas, alcohol, gasoline, etc., besides hydrogen. These fuel gases are either directly utilized or given simple pre-reforming treatment prior to utilization. Since, fuel gases are inflammable, therefore, in order to detect leakages, sulfur based compounds (though as impurity) are artificially mixed with it as odorants. However, addition of sulfur as odorant also causes degradation of cell performance and affects system durability. A detailed summary of long-term sulfur poisoning effects on SOFC performance is provided in Table 3. The general observation while investigating the effect of sulfur poisoning on the single SOFC performance is a considerable drop in cell voltage upon introduction/continuous exposure to H₂S (up to 40 ppm) in fuel [161–163]. Nevertheless, the cell voltage can be completely or partially recovered when H₂S flow is stopped depending on the operating conditions and duration of H₂S also Table 4).

Fig. 20a and b shows *ex situ* optical and SEM images, respectively, of Ni–YSZ composite tested in fuel mixture with a nominal composition of 50 ppm H₂S/50% H₂/1.5% H₂O/48.5% N₂ for 48 h followed by gradual cooling while in exposure to the same fuel atmosphere. On exposure to sulfur containing fuel, the color of Ni surface was observed to change from metallic white to brown (Fig. 20a) or yellow (Fig. 20b). In some regions, the edge of the Ni particles rises above the center and the surrounding YSZ (Fig. 20a and c), whereas in other regions, the Ni surface was covered by micro-scale sphere like structures (Fig. 20b, d, and e). The surface of the spheres and the regions in between them seem to be composed of submicron-scale irregular shape particles.

Fig. 20f shows the low magnification SEM image and EDX elemental mapping of the Ni–YSZ composite after exposure to H₂S-containing fuel (50 ppm H₂S/50% H₂/1.5% H₂O/48.5% N₂) at 800 °C for 48 h [164]. The elemental maps of Zr and S clearly suggest that sulfur selectively attacks Ni in the Ni–YSZ composite which confirms sulfur poisoning at Ni sites.

Rasmussen and Hagen [163] tested the single anode-supported planar SOFCs in the presence of H₂S under 1 A/cm² current load at 850 °C. The development of impedance spectra was found to be similar for all the imposed H₂S concentrations (2–42 ppm) as shown in Fig. 21a. The impedance spectra for 7 ppm H₂S addition is shown in Fig. 21b. The Nyquist plots show an increase in the total internal resistor of the cell upon H₂S addition till saturation occurs in the in-plane voltage. The total internal resistance returns to its initial value when H₂S flow was stopped at the fuel supply; in other words, the cell voltage can be regenerated once H₂S is removed from the system. The equivalent electrical circuit used to fit the impedance spectra consists of an inductor L, a series resistance R_s, and three R-CPE elements (R₁Q₁, R₂Q₂ and R₃Q₃). The fitted spectrum for the case of 2 ppm H₂S at T = 850 °C is shown in the inset of Fig. 21a. The low frequency R₃ was found to be stable upon H₂S addition. On the other hand, the high frequency counterparts R₁ and R₂, which represent the internal resistance of the cell, increase upon H₂S addition. Therefore, authors concluded that the poisoning effect of S is primarily

Table 4

Cell performance at 800 °C using Sr₂MM/O_{6- δ} anodes. (Figs. (a) and (b) Reprinted with permission from Ref. [300], copyright Science, 2006).

	Mg	Mg _{0.80} Mn _{0.20}	Mg _{0.50} Mn _{0.50}	Mn	Mg _{0.90} Cr _{0.10}	LSCM
P _{max,1} (mW/cm ²), H ₂	838	700	650	650	791	577
Power loss over 50 cycles (%), H ₂	3.5	1.3	1.4	6.3	7.5	14.1
P _{max,1} (mW/cm ²), H ₂ /H ₂ S	829	659	595	568	607	395
Power loss over 50 cycles (%), H ₂ /H ₂ S	2.5	0.7	9.2	4.8	1.7	16.1
Fade in P _{max} by H ₂ S (%)	1.1	5.8	8.5	12.6	23.3	31.5

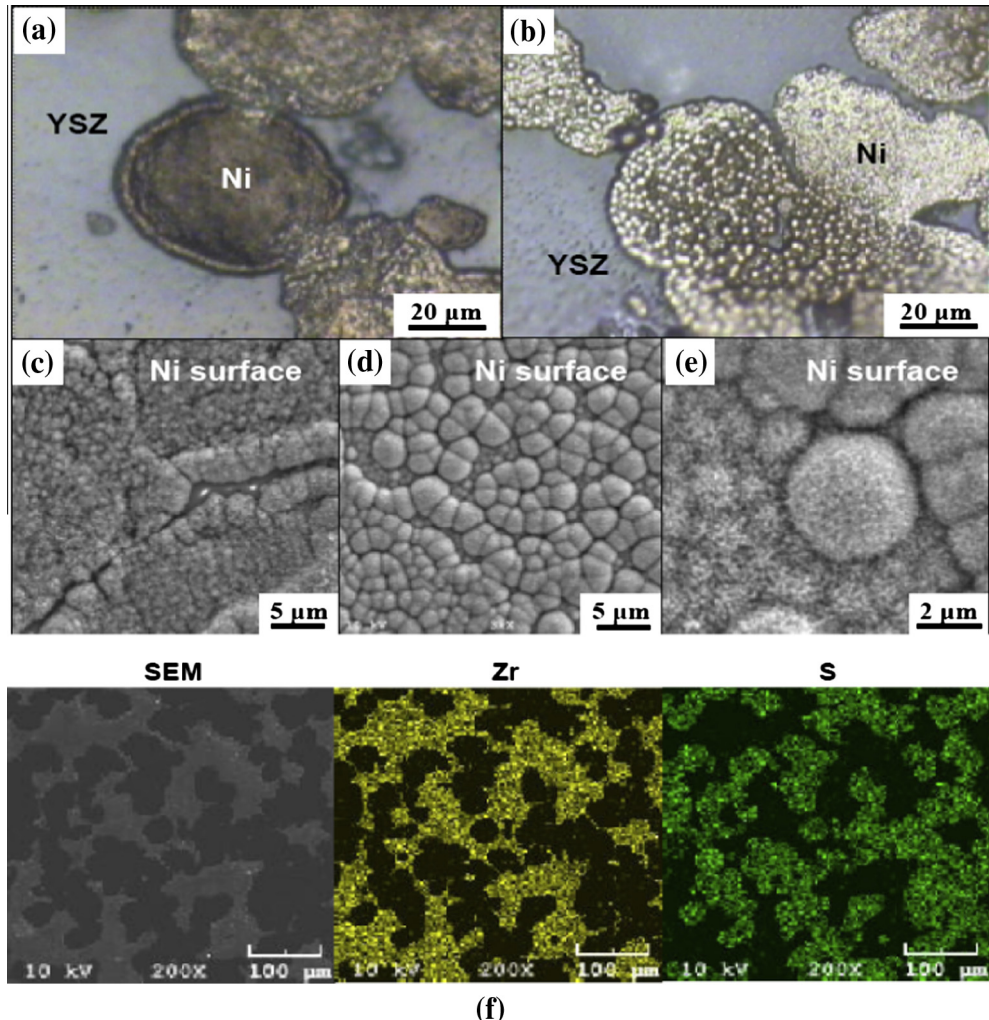


Fig. 20. (a and b) Optical and (c–e) SEM images of Ni–YSZ surface recovered after operation in H_2S containing fuel for 48 h, (f) EDX elemental map of the Ni–YSZ surface showing sulfur depositions primarily occurring at Ni sites rather than YSZ sites ((a–f) reprinted with permission from Ref. [164], copyright Elsevier, 2007).

due to chemisorption which blocks the active sites on Ni surface. Furthermore, addition of H_2S does not lead to any considerable microstructural changes and the formation of an insulating phase.

Zha et al. [162] attributed the first voltage drop to both restricted hydrogen adsorption and oxidation, when sulfur adsorption occurs on the active Ni surface. According to Bartholomew [165], sulfur adsorption at the anode surface is mostly selective (depending on the S/Ni surface ratios), i.e., it takes place initially at the sites of lowest coordination number (most open structure binds sulfur as the strongest). In the Ni–YSZ cermet anode structures, the reactive Ni particle allowed rapid restructuring of surface, which gave rise to a large number of low coordination sites. Rapid chemisorption of sulfur on the anode surface, and consequent blocking of Ni active sites leads to limited H_2 conversion, and show initial voltage drop, whose magnitude is proportional to the number of blocked sites, i.e., equilibrium coverage at a given H_2S concentration.

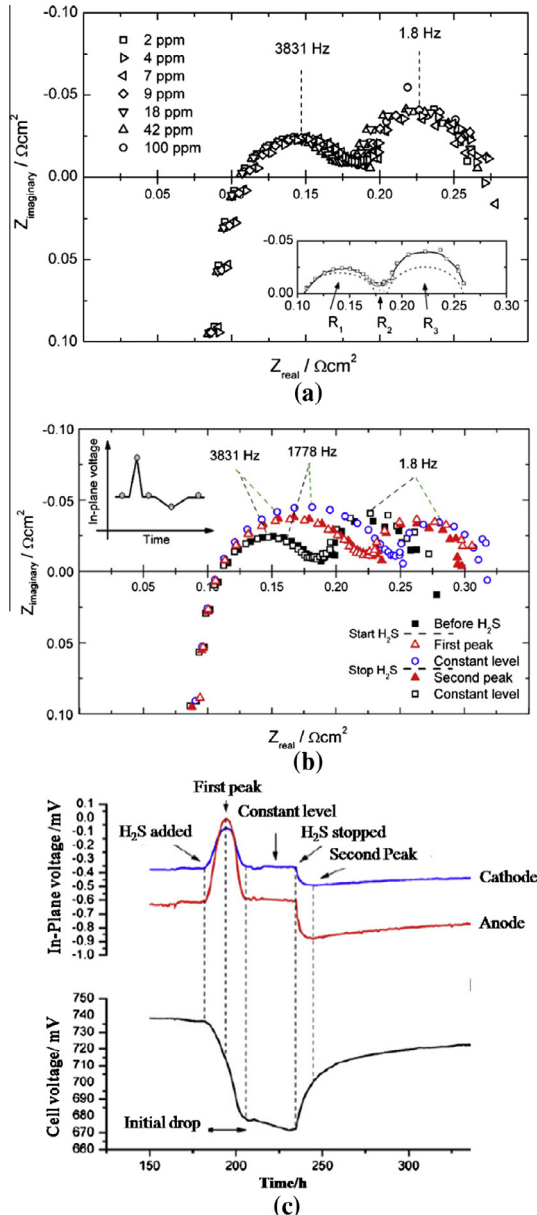


Fig. 21. (a) Impedance spectra measured before each addition step of H₂S. The measurements at 3831 Hz, 1778 Hz and 1.8 Hz are marked in order to show the development of the individual impedance arcs range of the resistances R_1 , R_2 , R_3 , and the fitted spectrum are indicated for the case of 2 ppm H₂S at $T = 850^\circ\text{C}$, current load = 1 A/cm². (b) Impedance spectra taken during the addition of 7 ppm H₂S to the fuel. The inserted figure shows when the impedance spectra were measured during the in-plane voltage development. The measurements at 3831 Hz, 1778 Hz and 1.8 Hz are marked, in order to show the development of the individual impedance arcs. $T = 850^\circ\text{C}$, current load = 1 A/cm². (c) The in-plane voltage development when 2 ppm H₂S was added to the fuel at $T = 850^\circ\text{C}$, current load = 1 A/cm². ((a–c) reprinted with permission from Ref. [163], copyright Elsevier, 2009) (d) Effect of sulfur on the performance of single SOFC with more tolerant anodes, such as, GDC (i and ii) Ni sites are blocked by adsorbed sulfur (YSZ remain inactive), and hence, stopping the electrochemical reaction, (iii and iv) Ni sites are blocked by adsorbed sulfur stopping electrochemical reaction, but the extension of the reaction zone (TPB) due to electronic conductivity of GDC continues the electrochemical reaction, and thus not restricting adsorption and desorption of hydrogen even in H₂S containing fuel. [93] (courtesy: from Ref. [168]).

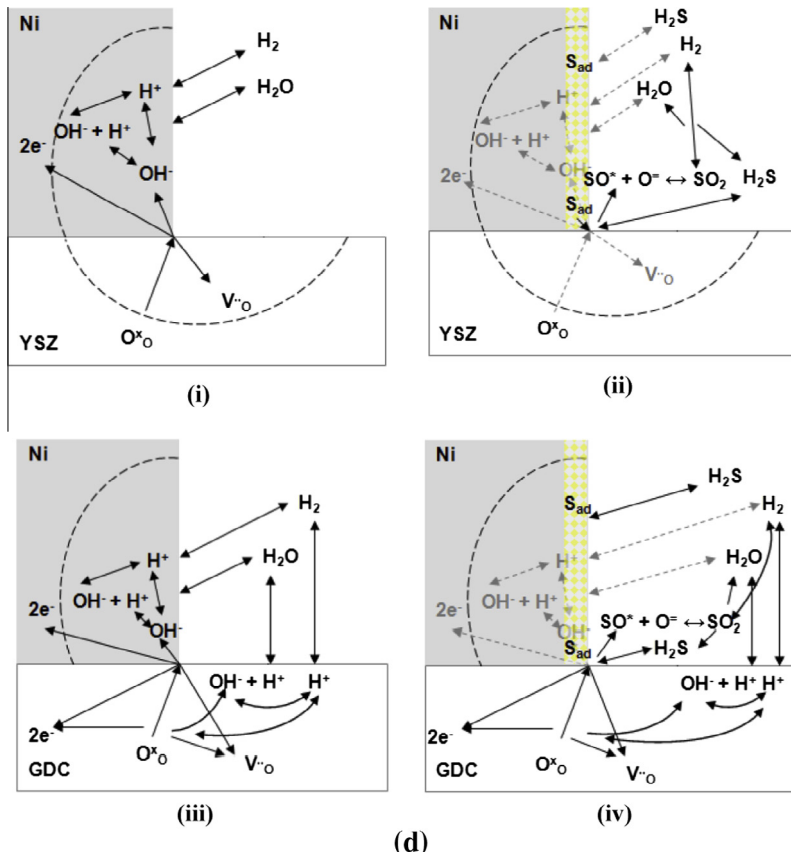


Fig. 21 (continued)

On stopping the H_2S supply to the fuel entering anode material, almost a complete recovery of the cell voltage can be achieved within 50–250 h, which is attributed to sulfur desorption from the anode surface. Adsorbed sulfur species are believed to either react with the H_2 from the fuel or O^{2-} ions from the cathode-electrolyte which facilitates its removal/desorption [162,166,167].



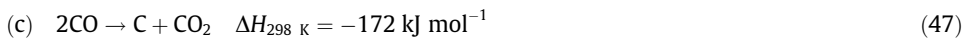
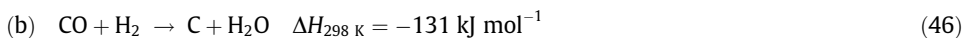
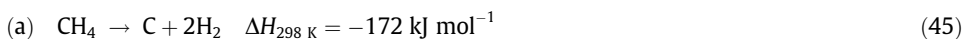
Wang and Liu [169] used ab initio atomistic thermodynamic calculations to study the de-sulfurization process of the sulfur poisoned Ni surface using H_2O and O_2 . It was suggested that while both H_2O and O_2 can be used in the regeneration process, H_2O appears to be a better de-sulfurization agent due to its wide pressure range for removing sulfur without over-oxidizing the Ni particles. H_2S molecules on coming in contact with anode dissociatively adsorb on Ni particles (at inlet portion). The exposed anode surface gets partially covered with sulfur, which lead to variation in current distribution over anode surface. At this situation, the in-plane voltage reaches a maximum value, as shown in Fig. 21c [170]. When the equilibrium between adsorption–desorption is established, the in-plane voltage again drops and attains a constant value suggesting that a homogeneous layer of sulfur species has covered the anode. Then after, a constant current value is observed over the anode surface. The extent of coverage of sulfur species in equilibrium depends on H_2S concentration in the fuel, concentration of desorption agent and operating parameters, viz., temperature, current load, fuel

utilization, cell polarization, etc. When H_2S supply to the fuel is stopped, sulfur on the Ni particles is observed to desorb after reacting with H_2 (probably with O^{2-} ions and H_2O). Desorption starts at the inlet, leading to the variation in current distribution over the anode surface which leads to change in the in-plane voltage as observed in Fig. 21c.

The desorption process is rather slower than adsorption process, i.e., the active site binds sulfur at a higher rate than its release. Thus, there exist two philosophies, viz., (i) either to remove sulfur completely from the fuel or (ii) develop sulfur tolerant materials. The first direction led to costlier fuel processing, whereas the latter attracted researchers to develop novel materials, by either using ScSZ or GDC (Gd-doped ceria) in place of YSZ in Ni-YSZ cermets or using metals/alloys other than Ni [169,171]. GDC exhibits higher electronic conductivity ($\sigma_{e,\text{GDC}} = 1 \times 10^{-5} \text{ S/cm}$; $\sigma_{e,\text{ScSZ}} = 2 \text{ S/cm}$ at 850 °C in an atmosphere of 97% H_2 and 3% H_2O [152]) and the surface catalytic activity of ceria is remarkably high [172]. Fig. 21 summarizes the possible working mechanism of Ni-YSZ and Ni-GDC anodes with and without H_2S in the fuel supply. The dotted lines represent triple phase boundary region. At Ni-YSZ anode, H_2 adsorption (via dissociative adsorption) takes place only at Ni surfaces at TPB; whereas YSZ remains either inactive or shows limited H_2 adsorption; the latter may be active for chemisorption of water [93,173].

Upon introduction of H_2S in the fuel, sulfur gets adsorbed on the active sites, blocking the electrochemical reactions. The reasons for better performance of Ni-GDC anodes are attributed to their mixed ionic- and electronic-conductivity and H_2 adsorption on GDC. Thus, even though when Ni surface is blocked by the adsorption of S, GDC can continue to allow these required electrochemical reactions. However, with other fuels, viz., hydrocarbons, CO, etc., the poisoning mechanisms are different and still under investigation in research community. Observations by various researchers on sulfur poisoning have been summarized in Table 3.

Carbon deposition on the Ni-YSZ cermet anode materials mainly takes place via the following chemical reactions [174]: (i) Methane cracking occurs at high temperature and under low steam to carbon (S/C) ratio in thermodynamic equilibrium, (ii) reduction of carbon monoxide, and (iii) disproportionation of CO (Boudouard reaction) occurs at low temperatures because of high CO concentration in reformatte gas.



The morphology of carbon depends on the operation temperature [174,175], fuel composition (reactant), and anode material (catalytic surface sites) [176,177]. No degradation of anode material and current collection was observed at high S/C ratio (~2), but at S/C = 0.5 (despite stable operation), the Ni mesh current collector was found to be partly disintegrated because of metal dusting [178]. The situation becomes more complicated because of the presence of water which is generally present in the reformatte gas, syngas, biogas, etc., and causes water gas shift reaction. The electrochemical oxidation occurring at anode produces electrons, which imparts additional electronic conductivity and also enhances the efficiency of the SOFC due to electrochemical oxidation (removal) of deposited carbon on the anode surface. McIntosh et al. investigated the performance of cells using Cu (20 wt.%)–Ceria (10 wt.%)–YSZ as anodes at 700 °C with n-butane as fuel [179]. The maximum power densities were found to be ~70 mW cm⁻² in pure H_2 , 120 mW/cm² in pure n- butane, and ~200 mW/cm² after switching back to H_2 fuel as shown in Fig. 22a. Chun et al. [180] investigated the mechanism of carbon induced corrosion of Ni anode. It was proposed that at high temperatures (<900 °C) initially, the carbon is transferred from the carbon supersaturated gaseous fuel environment to the metal surface. This is followed by the precipitation of graphite on Ni surface via catalytic graphitization mechanism. At several regions on Ni surface, the basal planes of graphite are found to be perpendicularly oriented to the metal surface. The formation of channeled structure between the graphitic planes is schematically shown in Fig. 22b [181]. The Ni metal cations intercalate into these graphitic channels, and subsequently coalesce at the outer surface of the graphite to form Ni particles. These Ni particles at

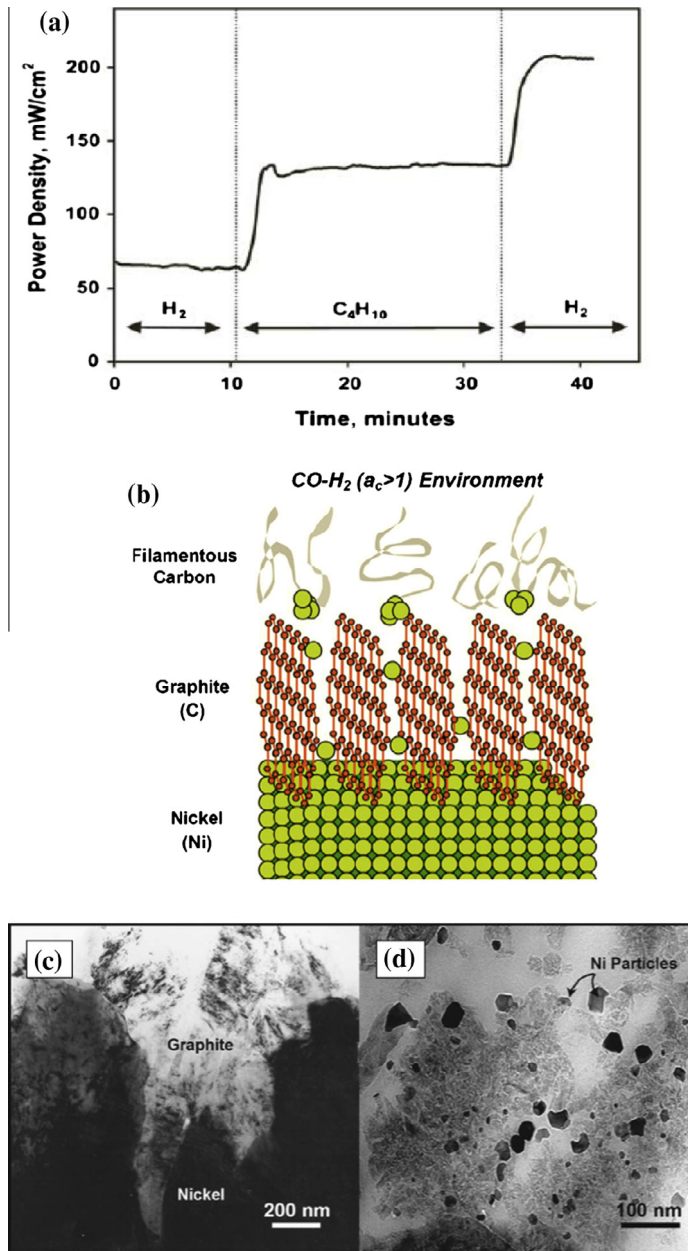


Fig. 22. (a) Exposure of Cu-ceria-YSZ anodes to n-butane. Power densities measured at a cell potential of 0.5 V as a function of fuel exposure at 700 °C. The anode contained 10 wt.% CeO₂ and 20 wt.% Cu (Reprinted with permission from Ref. [179], copyright Elsevier, 2004). (b) formation of filamentous carbon by the fine metal particles Ref. [180], (c) cross section BF TEM images showing deposits at the interface between nickel and graphite and (d) filamentous carbon at the outer region of carbon deposit after reaction at 550 °C for 7 h at CO/H₂ = 25 ((b-d) reprinted with permission from Ref. [181], copyright Journal of The Electrochemical Society, 2007).

the outer surface catalyze the formation of filamentous carbon which transports the metal particles away and lead to the corrosion of Ni (Fig. 22c and d) [180].

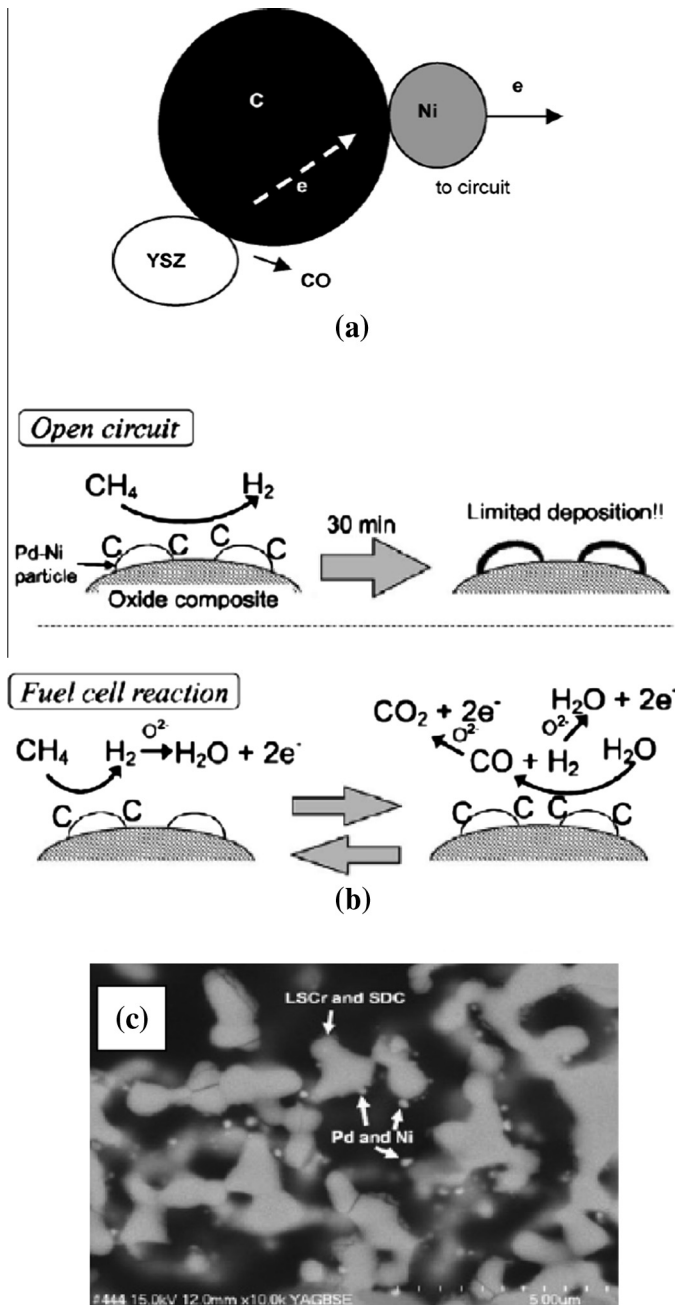


Fig. 23. (a) Schematic showing direct carbon electrochemical oxidization (reprinted with permission from Ref. [182], copyright Elsevier, 2008), (b) schematic for the direct oxidation of CH_4 over the surface of Pd-Ni/composite anode. Precious metals like Pt, Pd and Ru are very effective in carbon oxidation reactions, but are very expensive, and (c) dispersion of the catalyst and concentration around anode electrolyte interface ((b-c) reprinted with permission from Ref. [183], copyright Journal of The Electrochemical Society, 2006).

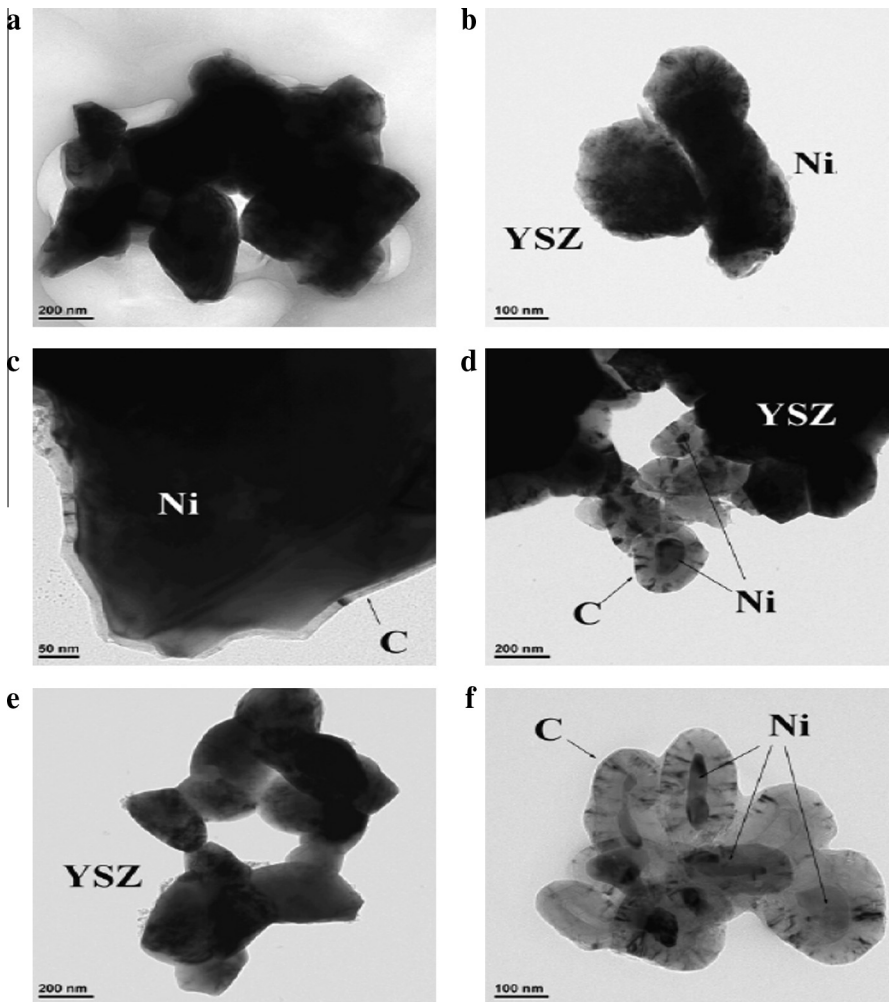


Fig. 24. Transmission electron micrographs showing the anode (a and b) operated with hydrogen fuel, (c) operated with syngas (23.64% CH₄, 7.6% CO, 14.27% CO₂, 49.48% H₂ and 5% H₂O) for 15 min; thin C deposit around Ni particles, (d-f) operated under same gas mixture for 2 h; Ni particles covered with thick carbon deposit ((a-f) reprinted with permission from Ref. [176], copyright Elsevier, 2011).

Chun et al. [180] further studied the influence of operation temperature on the corrosion rate of Ni in CO/H₂ mixture at ratio of 25. In the temperature range from 350 °C to 750 °C, the corrosion rate was found to increase with the increase in temperature. The nature of carbon deposit in this temperature regime was mostly amorphous with a small amount of graphite. The graphitic carbon was found to be randomly oriented within an amorphous carbon matrix. Furthermore, the amount of graphitic carbon increases with the rise in temperature. Above 750 °C, the corrosion rate becomes independent of temperature with substantial amount of graphitic carbon present on the Ni surface. The channels between the basal planes of graphite provide an easy pathway for Ni atoms to move towards the outer surface which leads to unrestricted diffusion of Ni atoms through graphite. The corrosion of Ni results in a decrease in conductivity and deterioration of the overall cell performance at an operational temperature of ~750 °C.

At lower temperatures such as 650 °C, the degradation behavior is largely due to carbon deposition on the anode that retards the diffusion of fuel to the triple phase boundary, and thus limits the

electrochemical reaction on the anode side. Researchers have attempted to improve the anode performance and durability by adopting several measures to suppress carbon deposition in SOFC, such as, (i) lowering working temperature (to <700 °C) and increasing the current density in order to facilitate oxidation of carbon (Fig. 23a). However, the preference of carbon atoms to reside over Ni surface restricts achieving the same, (ii) high S/C ratio to avoid carbon deposition during internal steam reforming, but may lead to dilution of fuel and consequent reduction of electrical efficiency and Ni-growth, and (iii) use of alloys with small amounts of precious metals, such as, Pt, Pd and Ru as catalysts, as shown in Fig. 23b and c [182,183]. Fig. 24 shows the thermal degradation of Ni–YSZ due to carbon deposition [176]. Ceria upon loading of precious metals like Pt, Pd and Rh serves as one of the best catalysts for total oxidation of hydrocarbons compared with that of ceria alone or any other oxide. Carbon deposited at triple phase boundary in vicinity of YSZ gets oxidized to CO and CO₂, leaving behind a free anode catalytic surface. In Ni-GDC, oxygen get adsorbed into the anode material due to the release of electrons to Ni particles, and about 8-times higher power density can be drawn out of cell when compared to that of Ni–YSZ [182].

Nabae et al. [183] investigated the electrocatalysis of Pd–Ni/composite anode which consists of Pd–Ni as catalysts in porous layers of Ce_{0.8}Sm_{0.2}O_{1.9} (SDC, as first layer) and 1:1 wt.% of SDC and La_{0.8}Sr_{0.2}CrO₃ (as second layer) in SOFCs for the direct oxidation of dry CH₄ at 800–900 °C. La_{0.83}Sr_{0.17}Ga_{0.8}Mg_{0.2}O₃ was used as an electrolyte, while La_{0.8}Sr_{0.2}CoO₃ was used as a cathode material. The maximum power densities of 150 mW/cm² and 420 mW/cm² were achieved at 800 °C and 900 °C, respectively, with negligible amount of carbon deposition at both open and closed circuit conditions. A stable power generation was observed under the closed-circuit condition in dry CH₄ atmosphere without any significant physical damage to the cell.

2.4. Copper and other noble metal cermets

Cu has been found inactive to carbon deposition [85] during the reformation of hydrocarbon fuels, such as CH₄ and syngas. However, Cu has a lower melting point (1083 °C) compared to that of Ni (1453 °C), and therefore, sintering at high temperatures is impractical. Instead, a new fabrication method, i.e., wet impregnation method was adopted to fabricate Cu based anodes [76,184,185]. Lu et al. [88] investigated impedance and current–voltage characteristics of SOFCs prepared with samaria doped ceria (SDC) as an electrolyte and anode based on either Cu-SDC or Au-SDC. The SOFCs were tested in H₂ and n-butane fuels at 650 °C. Similar performances were observed for both the cells based on Au-SDC and Cu-SDC, which suggest that both Au and Cu are acting solely as electronic conductors in the anode. Thus, it was concluded that Cu does not render any catalytic activity for the breaking of hydrocarbons in anode. Cu was found to be a poor catalyst for C–H and C–C bond-breaking, which makes Cu stable in the environment of hydrocarbon fuels. This also leads to increase in activation polarization of the cell. One possible solution is to combine Cu with other materials exhibiting higher catalytic activity, such as ceria, to achieve enhanced activity and stability.

Ceria acts as an excellent oxidation catalyst, while Cu provides electronic conductivity to the anode. Kim et al. [186] fabricated and tested Cu–Ni alloys (with 0%, 10%, 20%, 50% and 100% Ni) as anode at 800 °C in dry CH₄. It was demonstrated that carbon deposit was greatly suppressed on the Cu–Ni alloys compared to that on pure Ni. The impedance spectra performed on the cells suggest that a small carbon deposits were formed in anode. Nevertheless, a significant increase in power density of cells based on Cu–Ni alloys was observed over time. This was attributed to an enhanced electronic conductivity of anode. Finally, authors suggested that the direct oxidation fuel cells based on Cu–Ni alloy cermet are feasible at 800 °C for CH₄. Tsipis et al. [79] investigated current density and overpotential characteristic for both Cu-CGO (50:50 mol.%) and Ni-CGO (50:50 mol.%) cermets using three-electrode technique from 600 °C to 800 °C in flowing wet 10% H₂–90% N₂ gas mixture. The Ni-CGO anode was found to exhibit lower overpotentials compared to Cu-CGO anode. This behavior was associated with the poor catalytic activity and high sinterability of Cu when compared with that of Ni. Costa-Nunes et al. [85] compared the performance of SOFCs with composite anode of Cu–CeO₂-YSZ to the SOFCs based on Ni–YSZ anodes operating under H₂, CO and syngas as fuel environments. The SOFCs based on Cu–CeO₂-YSZ were found to exhibit marked improvement in the anode performance compared to SOFCs with Ni–YSZ anode. On one hand, Ni–YSZ anode yielded maximum power densities of

136, 120 and 73 mW/cm² in H₂, syngas and CO fuel atmospheres, respectively, while on the other hand, Cu–CeO₂–YSZ based anodes exhibited similar maximum power density under H₂ and CO (305 mW/cm²) at 700 °C. Authors also explored the role of cobalt (Co) addition in Cu–CeO₂–YSZ cermet [85]. A significant enhancement in catalytic activity of Co–Cu–CeO₂–YSZ cermet was found in CO fuel compared with that in H₂ at 700 °C. SOFCs based on Co–Cu–CeO₂–YSZ cermet anode yielded maximum power densities up to 310 mW/cm² with H₂ and 370 mW/cm² with CO fuel. Extensive research on Cu-based anodes can be found in the literature [6,85,185,187,188].

2.5. Ceria and other compounds

CeO₂ is a mixed ionic-electronic conductor in reducing atmospheres, which helps in expanding the reaction zones beyond triple phase boundaries. It possesses electronic conductivity sufficiently higher than that of YSZ, standing at 1 S/cm at 900 °C (and $P_{O_2} \sim 10^{-18}$ atm). Further, its ionic conductivity can be controlled by adding acceptor dopant oxides such as CaO, Y₂O₃, GdO₃, and Sm₂O₃ [135,207–212]. In addition, it acts as a catalyst for direct oxidation of hydrocarbon containing fuels, such as, methane, ethane, 1-butene, n-butane, and toluene. Moreover, it also exhibits good compatibility with adjoining cell component materials. Park et al. [6] demonstrated the direct electrochemical oxidation of various hydrocarbons using Cu–CeO₂ composite anode (fabricated by wet impregnation technique) in SOFCs at 700 °C and 1000 °C. The final products of oxidation were H₂O and CO₂. It was shown that a reasonably good maximum power density values can be achieved using these SOFCs (0.31 W/cm² for H₂ and 0.18 W/cm² for n-butane at 800 °C). Steele et al. [213] explored electrochemical oxidation of CH₄ at high temperature (~990 °C) using CeO_{2–δ} as the anode material. Direct oxidation of CH₄ without carbon deposition was successfully demonstrated by Murray et al. (Fig. 25) by applying a 0.5 μm thick porous YDC ((Y₂O₃)_{1.5} doped (CeO₂)_{0.85}) layer, via DC reactive magnetron sputtering, on both sides of 8YSZ electrolyte (8 μm thickness) with Ni–YSZ (2 μm thickness) as anode and La_{0.8}Sr_{0.2}MnO₃ (1 mm thickness) as cathode [134].

The maximum power density of 0.37 W/cm² was achieved at 650 °C in wet CH₄, which is comparable to that of using H₂ fuel cell [135,214]. Authors attributed this finding to the ceria –zirconia interfaces facilitating enhanced oxygen storage which result in an increase methane oxidation rate. The higher ionic conductivity of YDC also improves the transport of oxygen from the electrolyte to the anode. In addition, the mixed ionic-electronic conductive nature of ceria expands the reaction zone beyond the triple phase boundaries. The YDC interlayer was also considered to lower the interfacial resistance (by the factor of 6) measured in 97% H₂ + 3% H₂O [135]. There was no carbon deposition observed at <700 °C (therefore, there was no methane pyrolysis i.e., CH₄ → C + 2H₂ and carbon monoxide disproportionation i.e., 2CO → C + CO₂). Upon increasing the temperature above 700 °C, some carbon deposition was evidenced, but was less when compared to that observed in Ni–YSZ.

Doping CeO₂ with Sm₂O₃ (SDC) is however reported to slightly reduce the cell performance as well as catalytic activity (in spite of increasing conductivity) for direct electrochemical oxidation of butane [215]. Adding ScSZ (scandia stabilized zirconia) and GDC (gadolinia doped ceria) in place of YSZ in Ni–YSZ, i.e., Ni–ScSZ [161], and Ni–GDC [198,199,216,217], result in the enhancement in power outputs relative to Ni–YSZ with the benefits observed in terms of sulfur tolerance. Zhang et al. [199] performed the comparative study of H₂S poisoning on electrode behavior of Ni/YSZ and Ni/GDC anodes of SOFCs. Using polarization and impedance measurements at 800 °C on SOFCs in pure H₂ and H₂S-containing H₂ fuel with H₂S increasing from 5 ppm to 700 ppm, it was reported that the cell voltage of Ni/YSZ anode based SOFCs decreases from 0.61 V to 0.34 V at 200 A/cm² current density. Under the similar test conditions, the cell voltage of SOFCs with Ni/GDC anode decreases from 0.78 V to 0.72 V. It was shown that the degradation in performance for the hydrogen oxidation in H₂S containing H₂ fuel, is significantly smaller on Ni/GDC compared with that on Ni/YSZ [199]. Ouweltjes et al. [217] tested the performance of SOFCs with Ni/GDC as anode and biosyngas as fuel at 850 °C and 920 °C. A stable electrochemical performance has been reported with 80% fuel utilization and the power densities of 2600 W/m² and 3000 W/m² at 850 °C and 920 °C, respectively.

Cu based anodes have also exhibited no sulfur poisoning or carbon deposition when CH₄ is used as a fuel [184]. According to He et al. [218], in H₂ fuel containing 450 ppm H₂S, Cu–CeO₂–YSZ anodes have

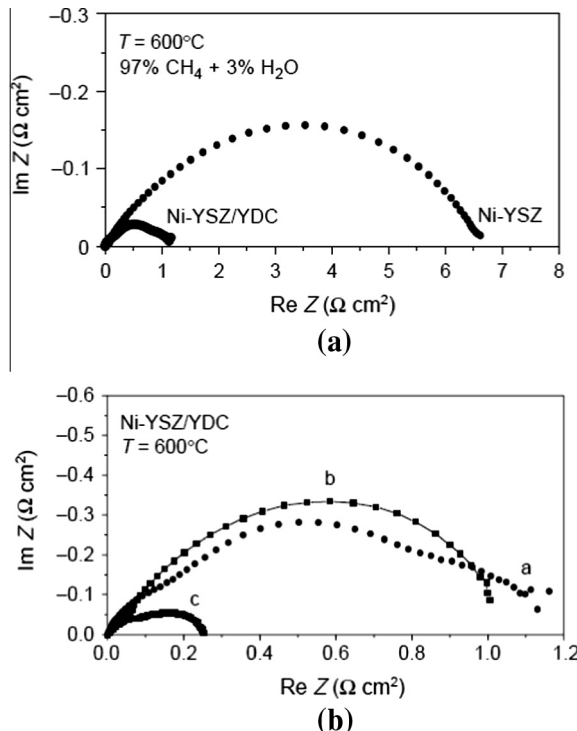


Fig. 25. (a) Impedance spectra for Ni-YSZ and Ni-YSZ/YDC anodes operated in 97% $\text{CH}_4 + 3\% \text{H}_2\text{O}$ at 600°C . The interfacial resistance gives rise to the difference between the real-axis intercepts. (b) Comparison of electrode impedances for Ni-YSZ/YDC anodes. Experiments were carried out at 600°C in 97% $\text{CH}_4 + 3\% \text{H}_2\text{O}$ (trace a), 3% $\text{H}_2 + 3\% \text{H}_2\text{O} + 94\%$ Ar (trace b) and 97% $\text{H}_2 + 3\% \text{H}_2\text{O}$ (trace c) ((a-b) reprinted with permission from Ref. [135], copyright Nature Publishing Group, 1999).

shown no sulfur poisoning at 800°C . However, when concentration of H_2S was raised (>450 ppm), sulfur poisoning due to the formation of $\text{Ce}_2\text{O}_2\text{S}$ was observed. Stable performance of Cu– CeO_2 –YSZ anode in H_2 fuel with high sulfur content (5000 ppm) was also reported by Kim et al. [185]. Sasaki et al. [196] investigated the reduction of sulfur poisoning via surface modification using impregnation of various additives, such as, CeO_2 , Y_2O_3 and MgO into Ni-YSZ and using Sc_2O_3 -doped ZrO_2 instead of YSZ.

Liu et al. [219] investigated composite metal sulfides, such as, M–Mo–S (M = Fe, Co or Ni) and MoS_2 and reported that Co–Mo–S mixed with 10% Ag powder exhibit reasonable performance in H_2S containing fuel. Yates and Winnick [220] reported a high power density (of 412 mW/cm^2 at 770°C) in cells having LiCoS_2 as anode, 8YSZ as electrolyte, and Pt as cathode in 25% H_2S containing fuel. Furthermore, LiCoS_2 as anode material was shown to be stable in H_2S environment over an extended period of time. Smith and McEvoy [221] fabricated Mo salt impregnated Ni-YSZ anode and reported the improved stability in sulfur containing fuels. In this regard, titanium based anodes have also shown enhanced sulfur tolerance. While studying $\text{La}_{1-x}\text{Sr}_x\text{MO}_3$ /YSZ (M = Cr, Mn and Ti) anodes, Mukundan et al. [222] did not find any degradation in $\text{La}_{1-x}\text{Sr}_x\text{TiO}_3$ anode tested under H_2 fuel containing up to 5000 ppm H_2S . $\text{La}_{0.75}\text{Sr}_{0.25}\text{Cr}_{0.5}\text{Mn}_{0.5}\text{O}_3$ developed by Tao and Irvine [223] showed anode polarization of $0.2 \Omega \text{ cm}^2$ at 900°C in 97% H_2 –3% H_2O (comparable to Ni-YSZ). However, the sulfur resistance of such materials (in 10% of H_2S) were not in par with the requirements for practical applications [224]. Aguilar et al. [225] studied a new class of materials based on $\text{La}_{1-x}\text{Sr}_x\text{VO}_3$ (LSV) as anode in H_2S containing fuel. From the open circuit voltage and impedance spectroscopy, it was suggested that LSV based anodes are preferentially more active toward the electrochemical oxidation of H_2S compared to H_2 . At 1000°C , the cell with configuration of $\text{La}_{0.7}\text{Sr}_{0.3}\text{VO}_3$ /8YSZ/ $\text{La}_{0.15}\text{Sr}_{0.85}\text{MnO}_3$ -8YSZ exhibits maximum power density of 90 mW/cm^2 at current density of 220 mA/cm^2 in 5% H_2S –95%

N_2 fuel environment. Similar cell configuration exhibits maximum power density of 90 mW/cm^2 at current density of 280 mA/cm^2 in 5% H_2S –95% H_2 fuel environment. The cell performance was found to be stable with no significant degradation over a period of 48 h. In an interesting experiment performed by the same group [226], SOFCs with the configuration of $\text{La}_{0.7}\text{Sr}_{0.3}\text{VO}_3/8\text{YSZ}/\text{La}_{0.15}\text{Sr}_{0.85}\text{MnO}_3/8\text{YSZ}$ were tested in 5% H_2S –95% CH_4 as fuel and air as oxidant at 950°C . The maximum power density of 280 mW/cm^2 was achieved at 950°C . From the analysis of effluent gas, it was observed that H_2S not only oxidize to S and SO_2 , but it also form carbon disulfide (CS_2) which is known to be used as solvent for heavy hydrocarbons deposits. From the observations, author suggested that SOFC with LSV based anodes has an advantage of processing sour natural gas (containing CH_4 , H_2S , etc.) to produce not only electricity but also high value chemicals.

In the recent years, infiltration of various materials, such as, Cu-ceria infiltration into a YSZ scaffold, has been introduced for developing anode materials [227]. The main reason to use Cu in place of Ni is the possibility of direct electrochemical oxidation of hydrocarbons. Cu solely provides electronic conductivity, while ceria acts as a mixed conductor as well as catalyst for electrochemical oxidation of the fuel. Infiltration with ceria nanoparticles in Ni-YSZ based anodes have been reported to exhibit appreciable sulfur tolerance when operated in humidified H_2 fuel containing 40 ppm H_2S [228]. Infiltration of Gd-doped ceria (CGO) in $\text{La}_{0.75}\text{Sr}_{0.25}\text{Mn}_{0.5}\text{Cr}_{0.5}\text{O}_3$ and nanosize CGO particles in Nb-doped SrTiO_3 have shown improved performance compared with Ni-YSZ [229–231]. Singhal et al. reported infiltration of Ni-YSZ with various oxides such as doped ceria, B-site doped strontium titanate ($\text{SrTi}_{1-x}\text{M}_x\text{O}_3$) and high surface area Ni and Co precursors [232]. Later Sasaki et al. [161] investigated electrochemical behavior of modified porous Ni-YSZ anodes (in H_2S fuel) in which several additives such as CeO_2 , Y_2O_3 , La_2O_3 , MgO , Nb_2O_3 , Sc_2O_3 , ZrO_2 , TiO_2 , CaO , Al_2O_3 , Ru, and Co, were impregnated. It was found that some of the additives were effective in reducing the cell-voltage drop due to H_2S presence in the fuel, while others have no influence on the cell voltage drop. From the results, Sasaki et al. suggested that by modifying Ni-YSZ anode via impregnation method, sulfur poisoning and tolerance can be controlled. Infiltration of CeO_2 and Sm_2O_3 doped CeO_2 in Ni-YSZ [233,234], ammonium metatungstate in pre-reduced Ni-YSZ [235], and Sn and Sb incorporation into Ni-YSZ via in situ vapor phase deposition [236] are some of the noteworthy endeavors in literature. Although, most of the anodes based Ni-YSZ impregnated with foreign oxides/elements show better sulfur tolerance compared to conventional Ni-YSZ, the rapid initial decay of cell voltage still exist with these anodes. An insufficient sulfur tolerance was attributed to the complications in achieving uniform and homogenous impregnation of deposits on the entire surface of porous anodes. Moreover, impregnation of foreign material tends to form a continuous dense layer which may block electron pathways in a modified Ni-YSZ anode.

Xie et al. [237] investigated the cell performance with the cermet, which consist of trimetal alloys of $\text{Fe}_x\text{Co}_{0.5-x}\text{Ni}_{0.5}$ and $\text{Sm}_{0.2}\text{Ce}_{0.8}\text{O}_{1.9}$, as anode, $\text{Ce}_{0.9}\text{Gd}_{0.1}\text{O}_{1.95}$ as electrolyte, and $\text{Sm}_{0.5}\text{Sr}_{0.5}\text{CoO}_3/\text{Sm}_{0.2}\text{Ce}_{0.8}\text{O}_{1.9}$ as cathode. At 600°C , the lowest interfacial resistance of $0.11 \Omega \text{ cm}^2$ and the highest power density of 750 mW/cm^2 was reported for the anode based on $\text{Fe}_{0.25}\text{Co}_{0.25}\text{Ni}_{0.5}$, when humidified H_2 (3% H_2O) was used as fuel and air was used as oxidant. Other cermets, such as, $\text{Ni}/\text{Sm}_{0.15}\text{Ce}_{0.85}\text{O}_{2-\delta}$ [238], $\text{Ir}/\text{Ce}_{0.9}\text{Gd}_{0.1}\text{O}_{(2-x)}$ [239], $\text{Fe}_x\text{Co}_{0.5-x}\text{Ni}_{0.5}/\text{Sm}_{0.2}\text{Ce}_{0.8}\text{O}_{1.9}$ [237], $\text{Ni}/\text{Ca}(\text{Fe})\text{TiO}_3$ [240], $\text{Cu}-\text{CeO}_2-\text{ScSZ}$ [241], $\text{Cu}-\text{CeO}_2-\text{YSZ}$ and Ru/YSZ [240] have been observed to exhibit good electrochemical performance at intermediate temperature range (600 – 800°C).

Mixed conducting ceramics, e.g., $\text{ZrO}_2/\text{TiO}_2/\text{Y}_2\text{O}_3$ [242–245], doped LaCrO_3 [246–248], $\text{La}_{0.6}\text{Sr}_{0.4}\text{Co}_{0.2}\text{Fe}_{0.8}\text{O}_3$ (LSCF) [249], $\text{La}_{0.8}\text{Sr}_{0.2}\text{Cr}_{0.97}\text{V}_{0.03}\text{O}_3$ (LSCV) [250] and La, Fe and Y doped SrTiO_3 [250,251] exhibit both oxide ion and electronic conductivity. A stable anode can be attained by enabling the charge transfer reaction over the entire electrode/gas interface. Although, these materials exhibit good stability toward sulfur poisoning/carbon deposition, they possess certain limitations, e.g., catalytic activity of $\text{La}_{1-x}\text{Sr}_x\text{Cr}_{1-y}\text{Ni}_y\text{O}_{3-\delta}$ is lower than that of Ni composites in $\text{CH}_4/\text{H}_2\text{O}$ fuel [246,247].

Instability of LSCF under reducing conditions and weight-loss at high temperature [253] favors use of LSCV, which is stable over long duration of operation (~ 100 h) at 800°C without any performance deterioration due to carbon deposition [250]. In addition, it does exhibit catalytic activity toward CH_4 -steam reforming at 800°C . Skarmoutsos et al. [254] investigated addition of Ti to YSZ, and synthesized $\text{Ni}-\text{Y}_{0.25}\text{Zr}_{0.60}\text{Ti}_{0.15}\text{O}_{2-x}$ (Ni-YZT) with different Ni contents. The cermets were annealed at 1000°C for up to 1000 h in a flowing 4% H_2 -Ar gas mixture. The Ni-YZT cermets exhibit better long

term stability in terms of electronic conductivity and microstructure when compared to that of Ni-8YSZ. Authors attributed this to a different bonding strength between Ni and ceramic interface due to the presence of Ti. However, lower electrochemical performance was observed for Ni-YZT when compared to Ni-8YSZ which was associated with an order lower ionic conductivity of YZT than that of 8YSZ [254]. Kikuchi et al. [240] investigated novel anode material based on cermet Ni/Fe-doped CaTiO₃. The current-voltage characteristics of cells based on Ni/Fe-doped CaTiO₃ anode (sintered at 1300 °C) were reported to be similar compared to the cells based on Ni/YSZ anode. However, the cells based on Ni/Fe-doped CaTiO₃ anode exhibited a stable terminal voltage (>20 h operation at 1000 °C) when a gas mixture of CH₄, N₂ and H₂O is supplied as fuel, whereas the cells based on Ni/YSZ anode showed degradation. The results suggest low carbon deposition rate in Ni/Fe-doped CaTiO₃ when compared with Ni/YSZ.

Tsai and Barnett [255] observed the reduction of interfacial resistance between Ni-YSZ anode and 8YSZ electrolyte by inserting thin interfacial layers of TiO₂-doped YSZ (YZT) and Yttria doped CeO₂. The lowest interfacial resistance value was observed to be 0.13 Ω cm² at 600 °C for 0.5 μm thick YDC interfacial layer in 97% H₂–3% H₂O. Authors attributed this finding to the enhancement in charge transfer due to the mixed conductivity or enhanced redox reaction rate of the interfacial layer. In another study, Wu et al. [256] fabricated flake shaped NiO-YSZ particles with nanocrystalline YSZ grains (via sucrose concentrated H₂SO₄ dehydration reaction) and observed improved catalytic performance in the reforming of CH₄ with both steam and CO₂. On a Ni-based anode, hydrogen oxidation process can be explained by: (i) transfer of fuel gas to the anode region, (ii) diffusion of gas in porous surface of the anode material, (iii) surface adsorption over the nickel surface, (iv) surface diffusion of the H species to the triple phase boundary, and (v) charge transfer involved oxidation reaction. The steps of charge transfer and H-H bond breaking of hydrogen over Ni-surface are not the major contributor to the anode resistance measurement; therefore, the major part of the anode polarization resistance arises from limited surface diffusion rate and restricted material conductivity [52,131,134]. An anode made from flake-shaped powder possesses much higher electrical conductivity compared with that of mixed commercial powder [257], which is reflected in a lower polarization resistance compared with conventional Ni/YSZ cermet at the temperatures lower than 800 °C [256]. Thus, microstructure can play a critical part in optimizing the surface diffusion and resulting polarization. A detailed review of nanostructured and other noteworthy materials investigated for SOFC anode along with the advantages and drawbacks can be found in the literature [75,258].

2.6. Perovskite and double-perovskite structure based anodes

In a quest to develop sulfur tolerant anode materials, other than Ni-based structures, nickel free conductive metal oxide based perovskites were invented [259–261], e.g., Sr_{1-x}La_xTiO₃ (LST; x = 0.3–0.4) [72,222,262,263], Y-doped SrTiO₃ [264], La_{1-x}Sr_xVO₃ (LSV; x = 0.5) [225,226,265–268], Ce_{0.9}Sr_{0.1}VO_x (x = 3,4) and its doped variations [269,270], La_{1-x}Sr_xCr_{1-y}Mn_yO₃ (LSCM; x = 0.25, y = 0.5) [271], and double perovskite structured materials such as Sr₂Mg_{2-x}Mo_xO₆ (SMMO; x = 1) [272,273], Sr₂Fe_{4/3}Mo_{2/3}O₆ [274], and pyrochlore structured Gd₂Ti_{2-x}Mo_xO₇ (x = 0.6) [275,276]. Except for Sr₂Mg_{2-x}Mo_xO₆ stated above (where LSGM, i.e., La_{1-x}Sr_xGa_{1-y}Mg_yO_{3-δ}; x = 0.2, y = 0.17, δ = 0.185 was used as electrolyte material), all the investigations were carried out using YSZ as an electrolyte material. Conductive oxides show improved sulfur tolerance, but exhibit: (i) lower electrical conductivity than Ni-cermet counterparts which leads to inferior anode performance [277], (ii) poor fuel oxidation, (iii) reduced catalytic activity, and (iv) incompatibility with the adjoining cell components during service at high temperatures. Metal sulfides formed during the test/operation have been found to reduce the oxide composition (to metal) when the relative concentration of H₂S is reduced. At 1000 °C, P_{H₂S}/P_{H₂} <~ 3 × 10³ ppm (0.3%), Ni₃S₂ and MoS₂ were reported to have decomposed [278]. Gd₂Ti_{1.4}Mo_{0.6}O₇ (GTMO) display higher power output in 10% H₂S–90% H₂ at 950 °C when compared to that in pure H₂fuel, and no bulk sulfide phase was detected after 5 days. Peaks corresponding to MoS₂ were observed in Raman spectra indicating phase change from oxide to sulfide, which apparently might be one of the reasons for enhanced electrochemical performance of GTMO [279].

Conductivity of SrTiO_3 was found to increase up to 100 S/cm (at 800 °C) when lanthanides and yttrium replace strontium [280,281]. Doping with Nb at Ti sites has also been reported to increase conductivity up to 120 S/cm [231]. However, the titanates, exhibit good chemical stability, but show poor electrocatalytic activity toward H_2 oxidation [262]. Doping with Nb or Mn and Ga at Ti sites has been reported to improve conductivity [231]. Under reducing condition, Mn^{3+} and Ti^{4+} reduce to Mn^{2+} and Ti^{3+} , respectively (in single phase $\text{La}_4\text{Sr}_8\text{Ti}_{11}\text{Mn}_{0.5}\text{Ga}_{0.5}\text{O}_{37.5}$), resulting in an enhanced electronic conductivity [282]. The oxygen vacancies created in the perovskite material replenish the O^{2-} ions on the oxide anode surface which leads to increase in ionic conductivity. This composition was reported to be efficient for methane oxidation and was found to exhibit good performance in wet hydrogen fuel [283]. Nb-doped SrTiO_3 anodes or donor (n)-doped ABO_3 perovskite with various A/B ratios $\text{Sr}_{0.99}\text{Ti}_{1-x}\text{Nb}_x\text{O}_3$, $\text{Sr}_{(1-x/2)}\text{Ti}_{(1-x)}\text{Nb}_x\text{O}_3$, and $\text{Sr}_{(1-x)}\text{Ti}_{(1-x)}\text{Nb}_x\text{O}_3$ ($x = 0, 0.01, 0.02, 0.05$, and 0.10) exhibited electrical conductivity of >120 S/cm at 1000 °C and P_{O_2} of 10^{-18} atm [284]. A detailed XANES (X-ray absorption near edge spectroscopy) study shows that Ti^{4+} reduces to Ti^{3+} , whereas Nb remains in +5 oxidation state and hence, does not play a direct role in affecting the electrical conductivity. However, increase in the amount of Nb in the lattice facilitates the overlapping (or mixing) of p-d atomic orbitals between adjacent Ti while enhancing the formation of Ti^{3+} ions. The overall improvement in the electronic conductivity of Nb-doped SrTiO_3 titanates were also reported to be tolerant to the fuels with high sulfur (with up to 1% H_2O) content and found stable even after exposure for 5 days at 950 °C [285,286]. La-based strontium titanate (LaSrTiO_3) and doped ceria exhibited appreciable conductivity [287] and promising electrocatalytic behavior toward hydrogen oxidation [75,288–290]. Moreover, the doped strontium titanate composite anodes were also found tolerant to fuel atmospheres containing oxygen, carbon, and sulfur [251,252,291,292]. Ruiz-Morales et al. [283] reported that titanate based anodes were remarkably active for the CH_4 oxidation at high temperature in the absence of excess steam. $\text{La}_x\text{Sr}_{1-x}\text{TiO}_3$ ($x = 0.1–0.4$) anodes fabricated by Marina et al. [262] showed electrical conductivity in the order of 0.01–500 S/cm at 800–1000 °C, and CTE of $11–12 \times 10^{-6}/\text{K}$, which is very similar to that of YSZ (CTE of undoped SrTiO_3 : $10.8 \times 10^{-6}/\text{K}$; CTE of YSZ: $10^{-2}–10.5 \times 10^{-6}/\text{K}$). When utilized in a cell, redox tolerance was exhibited at $x = 0.35$ in fuel with low hydrogen content. However, at low operating temperatures, inferior cell performance was found due to large anode overpotentials. La-doped SrTiO_3 with small additions of Mn and Ga at Ti site and high level Mn-doping to lanthanum strontium chromite were found to exhibit good electrochemical behavior [222,281,293,294]. However, single component materials do not show very high conductivity in fuel conditions, and therefore, researchers have moved towards the development of composite or cermet materials for practical SOFC application. First row transition metal perovskite materials employed as SOFC anodes show limited success owing to their limited redox stability. The relative stability of such perovskite materials are in the order $\text{Cr}^{3+} > \text{Fe}^{3+} > \text{Mn}^{3+} > \text{Co}^{3+}$, which was found to be largely dependent on the tendency of B-site cation against reduction. In addition, the perovskite should also exhibit good conductivity of oxide ions. However, an increasing stability of perovskites shows an opposite trend to oxide ion conductivity and oxygen permeability [295–298].

$\text{Sr}_2\text{MgMoO}_{6-\delta}$, double perovskite yielded a maximum power density of 0.84 W/cm² at 800 °C (see Table 4) when operated in H_2 fuel, and improved sulfur tolerance (see Table 4) compared to Ni-YSZ anodes [301,302]. These exhibit mixed ionic electronic conductivity, excellent sulfur tolerance that gives direct electrochemical oxidation in dry methane at 800 °C [299,300]. La-doped $\text{Sr}_2\text{MgMoO}_6$ perform somewhat better in natural gas [303]. In $\text{Sr}_2\text{MgMoO}_6$, Mg ions show unchanged +2 charge valence, whereas valence of Mo ions changes from +6 to +5 with the introduction of oxygen vacancies in the double perovskite structure. Introduction of dopants like Co and Ni, which exhibit multivalence, create much complicated cation valance and oxygen vacancy concentration in $\text{Sr}_2\text{CoMoO}_6$ and $\text{Sr}_2\text{NiMoO}_6$ compared with that of $\text{Sr}_2\text{MgMoO}_6$. In other words, substituting A or B site cations in an ordered double perovskites of $\text{A}_2\text{BB}'\text{O}_6$, which has alternating $\text{BO}_{6/2}$ and $\text{B}'\text{O}_{6/2}$ corner shared octahedral, can alter cation valance and oxygen vacancy concentration, and the latter plays a crucial role in dictating the physical and electrochemical properties [302–305]. Sr_2MMoO_6 (with M = Co and Ni) have a highly ordered structure due to a large difference in the ionic radii and charge valance between Co^{2+} (0.65 Å low spin; 0.745 Å high spin) and Mo^{6+} (0.59 Å) and Ni^{2+} (0.67 Å) and Mo^{6+} (0.59 Å). Tetragonal crystal structure of $\text{Sr}_2\text{CoMoO}_6$ and $\text{Sr}_2\text{NiMoO}_6$ with space group I4/m contains a limited concentration

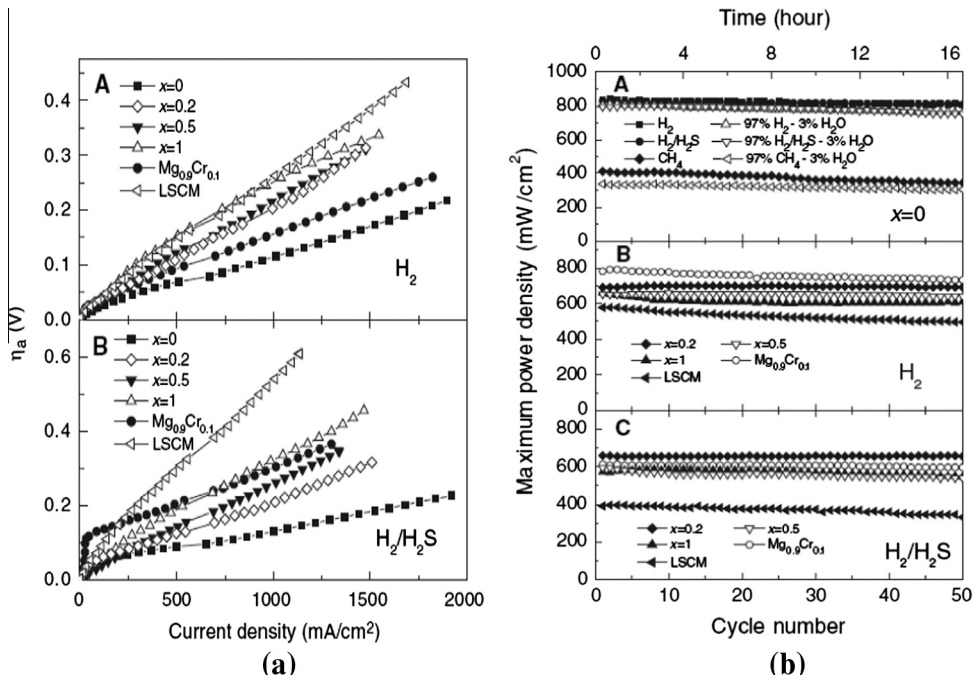


Fig. 26. (a) Overpotential of various $Sr_2MM' O_{6-\delta}$ anodes as a function of current density for the single fuel cells operating at (A) 800 °C in dry H_2 and (B) H_2/H_2S . (b) The maximum power density at 800 °C vs. cycle number and testing time for single fuel cells with various $Sr_2Mg_{1-x}Mn_xMoO_{6-\delta}$ anodes; (A) $Sr_2MgMoO_{6-\delta}$ ($x = 0$) obtained in dry and wet H_2 , H_2/H_2S and CH_4 , (B) anodes in dry H_2 (C) anodes in dry H_2/H_2S . ((a and b) reprinted with permission from Ref. [300], copyright Science, 2006).

of oxygen vacancies in reducing atmosphere at anode [299,300]. Bernuy-Lopez and Marrero-Lopez et al. in their independent endeavors observed that reduction of $SrMgMoO_6$ can give rise to a limited number of oxygen vacancies and oxygen states of less +6 in Mo [306,307]. Huang et al. estimated the percentages of Co^{3+}/Co and Ni^{3+}/Ni in as-prepared Sr_2CoMoO_6 and Sr_2NiMoO_6 samples sintered in air (via iodometric titration method) [297,300] to be 6.7% and 4.2%, respectively. In such Mo-based double perovskites, Mo is present at the B-site and Mo^{6+} or Mo^{5+} is also paired with 2+ or 3+ valence ions, respectively. Since perovskite structure does not allow interstitial oxygen, therefore the presence of M^{3+} species in the air-sintered samples would mandate formation of some cation vacancy. Under the reducing environment (typical of anode), oxygen leaves the crystal ensuing formation of oxygen vacancies and release of electrons. A fraction of Mo^{6+} ions accept the electrons to form Mo^{5+} . Both +6 and +2 cations offer coordination flexibility towards the release of oxygen from the crystal lattice. Huang et al. [300] attributed the improved electrochemical performance of the double perovskite anodes to mixed ionic and electronic conductivity. The existence of Co^{2+}/Mo^{6+} and Ni^{2+}/Mo^{6+} was established by authors [273,300] in the double perovskite materials via magnetic, structural, and XAS studies. Since Mo^{6+}/Mo^{5+} reduction potential is low, it accepts electrons from H_2 and CH_4 . Thus, dissociative chemisorption of the fuel occurs on the perovskite surface. Graves et al. investigated a number of Mo-based ceramics and observed high electrochemical performance (and mixed ionic-electronic conductivity) for H_2O/CO_2 reduction and H_2/CO oxidation [308]. Reduction of Sr_2NiMoO_6 and Sr_2CoMoO_6 and decomposition to form Ni and Ni-Mo precipitate nanoparticles on the surface and grain boundaries were also observed by these investigators. This unique nanostructured surface was believed to enhance the electron conductive phases and has resulted in desirable electrocatalytic activity. Effect of Mn and Cr incorporation in a double perovskite structure, investigated by Huang et al. [300], is shown in Fig. 26. It was observed that the overpotential of the anode linearly increased with the increase in current density (Fig. 26a), and power density was more or less constant with operating cycles (Fig. 26b), e.g., 600–800 mW/cm² in dry H_2 and 400–600 mW/cm² in dry H_2/H_2S . Cells

with $\text{Sr}_2\text{CoMoO}_6$ as anode, $\text{La}_{0.8}\text{Sr}_{0.2}\text{Ga}_{0.83}\text{Mg}_{0.17}\text{O}_{2.815}$ as electrolyte, and $\text{SrFe}_{0.2}\text{Co}_{0.8}\text{O}_{3-\delta}$ as cathode were tested at 800 °C. The maximum power densities were observed to be 735 mW/cm² and 527 mW/cm² in H₂ and wet CH₄, respectively [300]. On one hand, $\text{Sr}_2\text{NiMoO}_6$ exhibited notable power density (~273 mW/cm²) only in dry CH₄ because of stronger octahedral site preference of Ni²⁺ (favouring direct methane oxidation), whereas on the other hand, high power density (~527 mW/cm²) of $\text{Sr}_2\text{CoMoO}_6$ in wet CH₄ was attributed to the good catalytic effect due to available preferential steam reforming pathway of methane on $\text{Sr}_2\text{CoMoO}_6$ anode [309].

(LaSr)(FeCr)O_{3-δ} based anode materials, such as, $\text{La}_{0.75}\text{Sr}_{0.25}\text{Cr}_{0.5}\text{Fe}_{0.5}\text{O}_{3-\delta}$ are proved to be appropriate methane oxidation catalyst at high temperatures [289]. However, H₂S containing fuel deteriorate the performance of anode [310–312]. $\text{La}_{0.7}\text{Sr}_{0.3}\text{Cr}_{1-x}\text{Fe}_x\text{O}_{3-\delta}$ perovskite series with $x = 0.2, 0.3, 0.4$ and 0.5 have exhibited appreciable sulfur tolerance (up to 50 ppm H₂S) [313]. Under humidified H₂ fuel, $\text{La}_{1/3}\text{Sr}_{2/3}\text{Fe}_{2/3}\text{Cr}_{1/3}\text{O}_{3-\delta}/\text{Gd}_{0.1}\text{Ce}_{0.9}\text{O}_{2-\delta}$ (GDC) composite anode investigated by Haag et al. [295] exhibited polarization resistance of ~0.25 Ω cm² at 800 °C. The system was also found active toward CO oxidation [314]. A synergistic combination of conductive oxide with impregnated Pd metal catalyst [315] and buffer layers or interlayers, e.g., $\text{La}_{0.4}\text{Ce}_{0.6}\text{O}_{2-\delta}$ and $\text{Ce}_{0.8}\text{Gd}_{0.2}\text{O}_{2-\delta}$ for SMMO [272] and LSCM [316] have also exhibited considerable improvement in sulfur tolerance. The critical $P_{\text{H}_2\text{S}}/P_{\text{H}_2}$ ratio is significantly higher than usual when compared to that of Ni-YSZ anodes, but mixed results have been reported against their electrochemical performance (as discussed herewith). For example, $\text{La}_{0.35}\text{Sr}_{0.65}\text{TiO}_{3-\delta}/\text{Ce}_{1-y}\text{La}_y\text{O}_{2-\delta}$ composite anode tested in 7.8 ppm $P_{\text{H}_2\text{S}}/P_{\text{H}_2}$ ratio at 750 °C, exhibited no increase in anode polarization resistance [317] compared to that of Ni-YSZ tested in 0.02 ppm H₂S [318]. At 1000 °C and 10 ppm H₂S atmosphere, $\text{La}_{0.8}\text{Sr}_{0.2}\text{Cr}_{0.8}\text{Mn}_{0.2}\text{O}_3$ (LSCM) anode did not exhibit sulfur poisoning [319]. When sulfur content was increased up to 280 ppm H₂S, (La) SrTiO_{3-δ}/Ce(La)O_{2-δ} (Ti/Ce = 4) and tested at 850 °C (current density of ~0.66 A/cm² at 0.3 V), a sudden drop was observed in the current density (down to ~0.45 A/cm² at 0.3 V), which showed complete recovery after H₂S was shut down. Even when $\text{La}_{0.35}\text{Sr}_{0.65}\text{TiO}_{3-\delta}\text{Ce}_{0.7}\text{La}_{0.3}\text{O}_2$ was tested (initial power density of 0.252 W/cm²) at 1000 ppm of H₂S, performance drop of 40% was observed, and self-recovery of anode occurred (with power density of 0.224 W/cm²) after shutting down H₂S (and sulfur removal did not require air purging) [263,317,320]. Kim et al. [321] performed microstructural characterization and investigated the electrochemical properties of liquid phase impregnated $\text{La}_{0.4}\text{Sr}_{0.6}\text{Ti}_{0.8}\text{Mn}_{0.2}\text{O}_{3-\delta}$ (LSTM), wherein electrical conductivity for 10 wt.% CeO₂–50 wt.% LSTM-8YSZ composite anode (150 mW/cm²) was observed to be 1.5 times higher than that of 50 wt.% LSTM-8YSZ composite anode (<100 mW/cm²) at 700–900 °C. Furthermore, the addition of 1 wt.% Pd as catalyst increased the power density up to 201 mW/cm² at 800–850 °C.

2.7. Pyrochlores

Pyrochlores are A₂B₂O₇ type oxides usually with A^{III}/B^{IV} and A^{II}/B^V, which displays diverse electrical, magnetic, dielectric, and catalytic properties [322–324]. The crystal structure of these oxides can accommodate high oxygen content and allow flexible cation combinations on both A and B sites. The latter enables one to make changes in the combination of A and B type cations, and it tailors the structural stability and electrical properties, particularly high temperature stability to meet the practical requirements of SOFC. Pyrochlores of type $(\text{Ln}_{0.9}\text{Ca}_{0.1})_2\text{Ti}_2\text{O}_7$ (Ln = Gd, Y and Yb) are reported to exhibit good oxide ion conductivity at high temperatures [325–328]. Under reducing conditions, $\text{Gd}_2(\text{Ti}_{1-x}\text{Mo}_x)_2\text{O}_7$ ($0.1 \leq x \leq 0.7$) with Mo in +IV state exhibits high electronic conductivity (>10 S/cm), however, narrow stability range was observed in low partial pressures of oxygen ($P_{\text{O}_2} \sim 10^{-12.9} - 10^{-14.9}$) at 1000 °C [329,330]. For example, $\text{Gd}_2(\text{Ti}_{0.3}\text{Mo}_{0.7})_2\text{O}_7$ was found to be stable in the P_{O_2} range $10^{-12.9}-10^{-14.9}$ at 1000 °C. At higher P_{O_2} ($>10^{-12.9}$), decomposition of pyrochlore phase occurs due to the oxidation of Mo⁴⁺ ions to either Mo⁵⁺ or Mo⁶⁺, which leads to sharp decrease in electronic conductivity. At lower P_{O_2} ($< 10^{-14.9}$), conductivity continues to decrease with decrease in P_{O_2} . According to authors, different phases are formed at low P_{O_2} which possess similar level of conductivity values [329,330].

Deng et al. [322] investigated the electrical properties and chemical stability of novel oxide material with pyrochlore structure i.e., $\text{Yb}_{0.96}\text{Ca}_{1.04}\text{TiNbO}_{6.98}$. According to authors, the strategy was to

introduce certain elements which are stable in air inside the pyrochlore structure. However, on exposure to low P_{O_2} conditions at high temperatures, these elements can easily reduce to render electronic conductivity in pyrochlore materials. Although this leads to high conductivity, the slow kinetic relating to oxygen loss at lower temperatures does now allow these materials to achieve such high conductivity values below 1000 °C. The oxidized and reduced samples of $Yb_{1.96}Ca_{0.04}Ti_2O_{6.98}$ in air and in 5% H_2-N_2 at 1450 °C/15 h, respectively, and of $Yb_{0.96}Ca_{1.04}TiNbO_{6.98}$ at 1350 °C/15 h were measured for conductivity at 800 °C under same atmosphere as that used in their synthesis. The conductivity of $Yb_{0.96}Ca_{1.04}TiNbO_{6.98}$ measured for oxidized and reduced samples were 1.94×10^{-5} and 9.01 S/cm, respectively, and that for $Yb_{1.96}Ca_{0.04}Ti_2O_{6.98}$ were 6.85×10^{-3} and 1.20×10^{-2} S/cm, respectively. $Yb_{0.96}Ca_{1.04}TiNbO_{6.98}$ exhibited good chemical stability and offer high temperature compatibility with YSZ (up to 1300 °C). However, due to sluggish redox kinetics, these materials can achieve high electrical conductivity only after the reduction in extreme reducing conditions, which limit their potential application as anode in SOFCs. Similar limitations have been observed in $La_{1-x}Sr_xTiO_3$ [72], perovskite titanates [262], and $Sr_{1-1.5x}Y_xTiO_3$ [281]. Redox activity of pyrochlore materials can be enhanced by compositional tuning [322]. For example, Y or Gd can be substituted in place of Yb and Mn or Mg/Mo in place of Ti, i.e., $Ln_{0.96}Ca_{1.04}TiNbO_{6.98}$ ($Ln = Y$ and Gd), $(Yb_{1.9} Ca_{0.1})[Ti(Nb_{0.5}M_{0.5})]O_{6.95}$ ($M = Mn$ and Cr) and $(Yb_{1.9}Ca_{0.1})(Ti(Mo_{0.5}Mg_{0.5}))O_{6.95}$. The B-site substitutions were observed to be more effective than the A-site substitutions regarding improvement in electrical properties. $Ln_{0.96}Ca_{1.04}TiNbO_{6.98}$ ($Ln = Y$ and Gd) after reduction and $Yb_{0.96}Ca_{1.04}TiNbO_{6.98}$ were observed to exhibit similar redox kinetics and comparable conductivities, whereas incorporating Mn or Cr in the B-site (M), i.e., $(Yb_{1.9}Ca_{0.1})(Ti(Nb_{0.5}M_{0.5}))O_{6.95}$ exhibit conductivities of 0.14 and 0.03 S/cm at 850 °C in air respectively which were higher than that observed for $Yb_{0.96}Ca_{1.04}TiNbO_{6.98}$ (i.e., 5.2×10^{-5} S/cm) under similar test conditions. Introduction of Mo (e.g., $Yb_{1.9}Ca_{0.1})(TiMo_{0.5}Mg_{0.5})O_{6.95}$ have shown an increase in conductivity from 7.0×10^{-4} S/cm (in air) to 0.3 S/cm after reduction in 5% H_2-N_2 for 24 h at 850 °C with no change in structure. Authors attributed the increase in conductivity to the Mo(VI) formation in air-synthesized materials, which is consistent with the increased conductivity under reducing conditions [322]. On the other hand, $Yb_{0.96}Ca_{1.04}TiNbO_{6.98}$ synthesized in 5% H_2-N_2 exhibits conductivity of 9.0 and 11.8 S/cm at 800 °C and 900 °C, respectively [322].

The conductivity in $Yb_{0.96}Ca_{1.04}TiNbO_{6.98}$ and $Yb_{1.96}Ca_{0.04}Ti_2O_{6.98}$ was observed to increase with decreasing P_{O_2} which indicates that n-type charge carriers were present in these pyrochlores (shown in Eq. (48)).



where B denotes Ti or Nb. The equilibrium constant can be given as: $K = ([V_O^{\cdot}])n^2P_{O_2}^{1/2}$. Assuming mobility μ of electron to be approximately constant [293] and on applying the simplified electroneutrality condition $2[V_O^{\cdot}] = [B'_B]$, the dependence of electronic conductivity on P_{O_2} is given as $P_{O_2}^{-1/6}$. Similar dependence on P_{O_2} was observed for air synthesized $Yb_{0.96}Ca_{1.04}TiNbO_{6.98}$, in which n-type conduction occurs via oxygen loss under reducing operative conditions [322].

In summary, tailoring the triple phase boundary (TPB) lengths and increasing the area of active reaction sites had always been the main focus of the researchers. Increase in the TPB lengths, i.e., ranging from ~1.0 to 10 m/cm² in the cases of Ni-point, ball, wire, pattern, gauge, paste, etc., to 45–60 m/cm² in the cases of screen printed, sputtered, spray coated or porous Ni-anodes were reported in literature. Even greater than 100 m/cm²TBP length can be achieved in cermet anodes that is commensurate with the increase of the current densities ($\leq 10^{-2}$ to $\geq 10^2$ mA) and drop in polarization resistance (≥ 3.5 – ≤ 0.5 Ω). Advantages of cermet anodes extend to providing larger TPB lengths, and also rendering enough porosity for diffusion and direct utilization of the fuel gases. However, the problem arises when CO and H₂S present in the fuel gases tends to poison the active surface via carbon and sulfur deposition and lower the cell voltage. Thus, it necessitates reforming of the fuel as a mandatory step prior to their use in SOFCs which as a result, increase the operational cost. Later, copper cermets, such as, Cu-SDC, Cu-CGO, CuCeO₂ and other noble metal cermets, such as: Au-, Co-, Ru-, Ti-, Ir-, Pt-, and Pd-cermets, were developed to counter this problem. However, some of these materials are either too expensive or possess low m.p. (e.g., m.p. of Au as 1064 °C compared to that of Ni,

Table 5

Summary of properties and performance of some important anode materials.

Composition	Processing technique	Electrolyte/cathode/ current collector	Fuel/test condition	Anode performance	Cell performance/ maximum power density (mW/cm ²)	Remarks	Ref.
<i>Ni/NiO(/metal)-fluorite cermets</i>							
¹ Ni–YSZ cermet (50 vol.% Ni, 50 vol.% YSZ) ² Ni–YSZ	¹ Tape casting, firing in air, compacted and fired at 950 °C ² Co-pressed at 250 MPa and co- fired at 1400 °C in air for 4 h	² 8YSZ/LSM–8YSZ	¹ H ₂ /H ₂ O, 1000 °C ² 3% H ₂ O–NH ₃ ; 3% H ₂ O–H ₂ ; 850 °C	¹ $\sigma_e \sim 10^2$ – 10^3 S/cm (2×10^4 S/cm for pure Ni)	¹ 1900 (800 °C) ² 526; 530	¹ Porosity ~20–40%	¹ [145,332– 335] ² [336]
¹ Ni–SDC (40–70% Ni)	^{1,8,9} Uniaxially pressed and sintered at 1200 °C for 5 h in air	² YSZ/LSM–YSZ	¹ 40% H ₂ –N ₂ 800 °C	¹ $\sigma_e \sim 1260$ – 4000 S/cm	² 980	^{1,8,9} Porosity ~5–10%	¹ [337,338]
² Ni–Sm _{0.2} Ce _{0.8} O _{1.9}		³ SDC/SSC–SDC		⁷ $\sigma_e \sim 837$ ^{8,9} σ_e	³ 550 ⁴ 545 ⁵ 412 ⁶ 492	⁴ 545	² [339] ³ [340] ⁴ [341]
³ Ni–Sm ₂ O ₃	² Pressed and presintered at 1000 °C for 3 h. LSM–YSZ were screen-printed and then sintered at 1200 °C for 3 h		² H ₂ O saturated H ₂ ; 800 °C	~ 1480 ~ 1320	⁷ 1100 (650 °C)	^{2,3} Porosity ~3 %	
⁴ Ni–CeO ₂		⁴ GDC/SSC				⁷ Porosity ~37%	⁷ [343] ^{8,9} [344]
⁵ Ni–GDC (98 µm electrolyte)		⁵ GDC/LSCF–GDC	^{3–7} 3% H ₂ O–H ₂ ^{3,4} 600 °C, ⁵ 700 °C, ^{6,7} 650 °C	¹¹ $\sigma_e \sim 5.03$	¹⁰ 520 (800 °C) ¹¹ 530 (700 °C)		¹⁰ [345] ¹¹ [346]
⁶ Ni–GDC (19 µm electrolyte)		^{8,9} 8YSZ/LSM					[347]
	³ Dry pressing and then sintered at 1250 °C for 5 h.						
		¹⁰ LSGM/LSC					
			^{8,9} 4% H ₂ –Ar; 800 °C				
⁷ Ni–Sc _{0.1} Ce _{0.01} Zr _{0.89} O _{1.95}		¹¹ LSCM/YSZ					
	⁴ Co-pressed and sintered at 1150 °C for 5 h						

(continued on next page)

Table 5 (continued)

Composition	Processing technique	Electrolyte/cathode/ current collector	Fuel/test condition	Anode performance	Cell performance/ maximum power density (mW/cm ²)	Remarks	Ref.
⁸ Ni-Y _{0.1} Ce _{0.8} Tl _{0.1} O _{1.95}			¹⁰ dry H ₂ /O ₂ – He; dry CH ₄ / O ₂ –He; 800 °C				
⁹ Ni-Y _{0.2} Ce _{0.8} O _{1.9} ^{8,9} (40 vol.% Ni)	⁵ Dry pressing and spin coating			¹¹ Humidified H ₂ ; 800 °C			
¹⁰ Ni/La _{0.8} Sr _{0.2} CrO _{3-δ} – Ce _{0.8} Sm _{0.2} O _{1.9}	⁷ Co-sintering at 1400 °C						
¹¹ Ni–CeO ₂ – La _{0.7} Sr _{0.3} Cr _{1-x} Ni _x O _{3-δ}	¹⁰ Screen printing						
¹ NiO-Gd _{0.1} Ce _{0.9} O _{1.95}	¹¹ Tape casting followed by firing to 1500 °C	¹ GDC/LSCF-GDC	¹ 3% H ₂ O–H ₂ ; 650 °C	¹ 909		² Porosity ~28%	¹ [348]
² NiO-YSZ		² 8YSZ/LSM–8YSZ	² 3% H ₂ O–H ₂ ; 800 °C	² 500			² [349] ³ [350]
³ NiO-La _{0.4} Ce _{0.6} O _{2-δ}	² Planar anodes are fabricated using both dry pressing and roll compaction. Electrolyte layer is spray coated onto the green slip cast. After co-sintering, porous cathode functional layer is applied onto the electrolyte using brush coating	³ LSGM/LSCF	³ H ₂ ; 700 °C	³ 780			
¹ Ag–Ce _{0.8} Gd _{0.2} O _{1.9} (Ag > 45 wt.%)	^{1,2} Uniaxially pressed and then sintered in air at 1500 °C for 5 h	² SDC/LSCF-SDC	^{1,2} CO; ¹ 650 °C; ¹ σ _e ~ 1260 ² 700 °C	² 439 1254		¹ Porosity ~7% ² Test period of 100 h [347] and porosity ~48%	¹ [351], ² [352]

² Ag–Ce _{0.8} Sm _{0.2} O _{1.9} (Ag–45 wt.%)							
¹ Fe _{0.1} Ni _{0.9} /YSZ	¹ Pressed into pellets under a pressure of 300 MPa and pre-sintered at 970 °C for 4 h. Electrolyte coated by using colloidal spray coating technique	¹ YSZ/LSM–YSZ	¹ 3% H ₂ O–H ₂ ; 800 °C	¹⁰ σ _e 417–633	¹ ~960	Sulfur resistance ~450 ppm	^{1,2,3} [353]
^{2,3} 7 wt.% SDC-Ru/NiO-SDC					² 850		³ [354]
⁴ Cu–CeO ₂			² 3% H ₂ O–H ₂ /O ₂ 650 °C	¹¹ 633	³ 462	^{2,3} Mesoporous structure with narrow pore-size distribution	⁴ [355]
^{5,6} Cu–CeO ₂ -YSZ/Ni–ScSZ				¹³ 417			⁵ [261] ^{6,7} [356], ⁷ [357]
⁷ 10% Cu–90% Ce _{0.8} Zr _{0.2} O ₂ /Ni–CeO ₂ /Ni–YSZ	^{2,3} Dual dry pressing process. Screen painting method, followed by dried at 250 °C for 3 h and <i>in situ</i> calcined at 650 °C under H ₂		³ 3%H ₂ O–CH ₄ /O ₂				⁸ [358] ⁹ [357]
⁸ 10% Cu–90% CeO ₂ /Ni–YSZ				⁴ H ₂ /H ₂ O (800 °C) and H ₂ (950 °C)			¹⁰ [359]
⁹ 25% Cu–75% CeO ₂ /Ni–YSZ	⁴ Tape casting at 1550 °C and then heated in air to 1250 °C	^{2,3} SDC/BSCF			⁵ 604, ⁶ 438		^{11,13} [360]
¹⁰ CuO-SDC-CeO ₂					⁷ 601; 519	⁴ Test period 250 h	¹² [361] ¹⁴ [362]
¹¹ Ni _{0.95} Cu _{0.05} /SDC	^{5,6} Tape casting and wet impregnation method.		^{5–9} H ₂ /O ₂ 50% H ₂ O–C ₂ H ₅ OH/O ₂ 800 °C	⁸ ~520; ~410		^{14,15} Test period 80 h	¹⁵ [362] ¹⁶ [345]
					⁹ ~450; ~380		
					¹⁰ 350; 220		
			¹⁰ H ₂ –C ₃ H ₇ OH; 800 °C		¹¹ 338		
		⁴ Au current collector				¹² 320	

(continued on next page)

Table 5 (continued)

Composition	Processing technique	Electrolyte/cathode/ current collector	Fuel/test condition	Anode performance	Cell performance/ maximum power density (mW/cm ²)	Remarks	Ref.
¹² Cu _{0.5} Ni _{0.5} -GDC		5–9ScSZ/PCM	^{11,13} Dry CH ₄ ; 600 °C				
¹³ CuNi/SDC (Ni _{0.95} Cu _{0.05} /SDC)	^{7,9} Different layers are Fabricated by tape casting and co-sintering screen printed and sintered at 1200 °C and 1100 °C				¹⁴ 870; 345		
¹⁴ 1 wt.% Pd–5 wt.% CeO ₂ – La _{0.4} Ce _{0.6} O _{2–δ}			¹² Dry CH ₄ ; 800 °C		¹⁵ ~610; 66		
¹⁵ 1 wt.% Cu–5 wt.% CeO ₂ – La _{0.4} Ce _{0.6} O _{2–δ}			^{14,15} Dry H ₂ /O ₂ ; dry CH ₄ /O ₂ ; 800 °C ¹⁶ dry H ₂ / O ₂ –He; dry CH ₄ /O ₂ –He; 800 °C		¹⁶ 480; 150		
¹⁶ Ni _{0.5} –Pd _{0.5} /La _{0.8} Sr _{0.2} CrO _{3–δ} – Ce _{0.8} Sm _{0.2} O _{1.9}	⁸ Electrophoretic Deposition and fired at 900 °C for 1 h, Uniaxially pressed at 75 MPa followed by sintering at 1490 °C for 6 h Deposition and fired at 900 °C for 1 h, Uniaxially pressed at 75 MPa followed by sintering at 1490 °C for 6 h ¹⁰ Screen printing and fired at 900 °C for 4 h.						
		¹¹ SDC/SSC-SDC					
		¹² GDC/LSCF					
	^{11,13} Pressed at 200 MPa subsequently fired at 1350 °C for 4 h and reduced in flowing H ₂ at 600 °C for 4 h.						
			^{14,15} LSGM/SCF				
	^{14,15} Uniaxial copressing at 40 MPa then fired for 4 h at 1450 °C in air						

¹⁶ LSGM/LSC						
¹⁶ Anode and cathode were sintered at 1300 °C and 1100 °C and reduced with H ₂ at 700 °C						
<i>Modified Ni-YSZ</i>						
¹ Ni-YSZ cermet infiltrated by Mo or W precursors	² Infiltrated with ceria and preheated to 650 °C for 30 min in air	No Pt current collector	¹ H ₂ ; 750 °C	¹ ~300	¹ Still poisoned by sulfur (C ₄ H ₄ S) but to a lesser extent and showed gradual recovery	¹ [221]
³ Copressing and cosintering in 4% H ₂ with Ar at 1400 °C for 3 h			² H ₂ ; 750 °C	² ~300		² [228] ³ [363]
² Ni-YSZ infiltrated with ceria nanoparticles			³ H ₂ ; 700 °C	³ 50		
³ Ni-YSZ sputtered with Nb ₂ O ₅					² Still poisoned by 40 ppm H ₂ S but to a lesser extent ³ Not poisoned by 50 ppm H ₂ S	
<i>Perovskites</i>						
<i>SrTiO₃ based materials</i>						
¹ La _{0.4} Sr _{0.6} TiO _{3-δ} (LST)	³⁻⁶ Uniaxially pressed, and then heated at 1500 °C for 10 h in 5% H ₂ /Ar	¹ Pt as current collector	^{1,2} H ₂ ; ¹ 1000 °C, ³ σ _e ~ 220 ² 850 °C	¹ ~200	¹ Performance not influenced by up to	¹ [364]
² La _{0.35} Sr _{0.65} TiO _{3-δ} (LST)-Ce _{1-x} La _x O _{2-δ} composite		² Pt or Au current collector	⁴ σ _e ~ 145 ^{3-6,12-} ¹⁴ H ₂ (<5.8%)/N ₂ ; 800 °C	² ~400 ⁷ 1066, 577		² [264,365]
³ La _{0.3} Sr _{0.7} TiO _{3-δ}	⁷ Uniaxially pressed with 103 MPa, and then sintered at 1400 °C for 14.4 ks in air	⁷ LSGM/SSC ⁸ YSZ/LSF-YSZ	⁵ σ _e ~ 49 ⁵ σ _i ~ 0.01	⁸ 780 ⁹ 570	1000 ppm H ₂ S and enhanced by 5000 ppm H ₂ S	³ [366]
⁴ (La _{0.3} Sr _{0.7}) _{0.93} TiO _{3-δ}		⁷ Dry H ₂ ; 850 °C, 800 °C ^{9,16} YSZ/LSCF-YSZ	⁶ σ _e ~ 45			⁴ [367]
					² Poisoned by 26–1000 ppm H ₂ S	⁵ [368] ⁶ [366] ⁷ [369] ⁸ [370]

(continued on next page)

Table 5 (continued)

Composition	Processing technique	Electrolyte/cathode/ current collector	Fuel/test condition	Anode performance	Cell performance/ maximum power density (mW/cm ²)	Remarks	Ref.
⁵ La _{0.3} Sr _{0.7} Sc _{0.1} Ti _{0.9} O _{3-δ}				⁶ σ _i ~ 0.011			⁹ [355]
⁶ La _{0.3} Sr _{0.7} Ti _{0.93} Co _{0.07} O _{3-δ}		^{17,18} YSZ/LSM–YSZ	⁸⁻ ^{10,16} Humidified H ₂ ; 800 °C, ¹⁰ 600 °C, ¹⁷ 750 °C	¹⁰ σ _e ~ 200			¹⁰ [371] ¹¹ [372]
⁷ 1.5 wt.% Pd–Sr _{0.88} Y _{0.08} TiO ₃ – La _{0.4} Ce _{0.6} O _{1.8}	⁹ Tape casting and co-sintering pellet was reduced at 1050 °C in 5% H ₂ /Ar and fired at 650 °C for 2 h			¹¹ σ _e ~ 80 ¹¹ σ _i ~ 0.014			
⁸ 5% CeO ₂ –0.5% Pd–45% La _{0.3} Sr _{0.7} TiO _{3-δ} –65% Y _{0.08} Zr _{0.92} O _{2-δ}				¹² σ _e ~ 73.7	¹⁶ 640		
⁹ 1 wt.% Pd–10 wt.% CeO ₂ –75% La _{0.3} Sr _{0.7} TiO _{3-δ} –25% Y _{0.08} Zr _{0.92} O _{2-δ}	¹⁰ Pressed and sintered at 1500 °C for 5 h and treated in H ₂ at 1400 °C for 10 h		¹¹ 5%H ₂ /Ar; 800 °C	¹³ σ _e ~ 35	¹⁷ 550 ¹⁸ 510; 470		¹² [373]
¹⁰ Y _{0.08} Sr _{0.92} Ti _{0.92} Nb _{0.08} O _{3-δ}			¹⁵ 50% H ₂ /N ₂ ; 800 °C	¹⁴ σ _e ~ 20 ¹⁴ σ _i ~ 0.0007			¹³ [374] ¹⁴ [375]
¹¹ (Y _{0.08} Sr _{0.92}) _{0.95} TiO _{3-δ}	^{11–13} Uniaxial pressing at 115 MPa and sintered in Ar/ H ₂ (5%) at 1500°C for 10 h. (cooling rate of 3–5 °C min ⁻¹)		Humidified H ₂ ; Humidified H ₂ with 10 ppm H ₂ S; 800 °C	¹⁵ σ _e ~ 23			¹⁵ [376] ¹⁶ [377] ¹⁷ [378] ¹⁸ [379]
¹² Y _{0.09} Sr _{0.91} TiO _{3-δ} ¹³ Y _{0.08} Sr _{0.92} Ti _{0.97} O _{3-δ} ¹⁴ Y _{0.08} Sr _{0.92} Ti _{0.96} Co _{0.04} O _{3-δ} ¹⁵ Sr _{0.86} Y _{0.08} TiO _{3-δ}	¹⁴ Uniaxially pressed and then heated to 1500 °C for 10 h in forming gas						

¹⁶1 wt.% Pd–3 wt.% CeO₂–60% SrTi_{0.99}Nb_{0.01}O_{3-δ}–40% Y_{0.08}Zr_{0.92}O_{2-δ}

¹⁵Manual uniaxial hydraulic pressed at 180 MPa and sintered at 1400 °C for 6 h in 10% CO + 90% N₂

¹⁷Cu–Gd_{0.2}Ce_{0.8}O_{2-δ}–La_{0.2}Sr_{0.7}TiO_{3-δ}
¹⁸Ru–CeO₂–50% Sr_{0.88}Y_{0.08}TiO_{3-δ}–50% Y_{0.08}Zr_{0.92}O_{2-δ}

¹⁶Pressed at 100 MPa, sintered at 1200 °C for 3 h in air. Electrode was sintered at 1350 °C for 5 h. Cathode was screen printed, sintered at 1000 °C for 3 h
¹⁷Tape casting and then fired to 1500 °C

La_{0.75}Sr_{0.25}Cr_{0.5}Mn_{0.5}O_{3-δ}(LSCM) based materials

¹ La _{0.75} Sr _{0.25} Cr _{0.5} Mn _{0.5} O _{3-δ} (LSCM)	¹ Dry pressed and sintered at 1500 °C for 5 h	¹ Pt as current collector	¹ 10% H ₂ S–90% H ₂ ; 950 °C ² σ _e ~ 2.4 ³ σ _e ~ 0.4	¹ ~340 ⁵ 1302; 769	¹ Cell poisoned in the presence of 10% H ₂ S ² [381] ³ [382] ⁴ [383]	¹ [380]
² La _{0.75} Sr _{0.25} Cr _{0.5} Mn _{0.44} Ni _{0.66} O _{3-δ}	² Prepared by auto ignition process and co-fired at 1150 °C for 2 h in air		² 5% H ₂ /Ar; 800 °C ⁴ σ _e ~ 0.14	⁶ 1151; 704	¹ Density ~95%	^{5,10} [384]
³ La _{0.65} Ce _{0.1} Sr _{0.25} Cr _{0.5} Mn _{0.5} O _{3-δ}	³ Tape casting and firing at 1000 °C and 1300 °C		³ Humidified H ₂ ; 700 °C	⁷ 960; 744; 406	⁶ Test period 6 h	⁶ [385] ⁷ [386]
⁴ Pr _{0.75} Sr _{0.25} Cr _{0.5} Mn _{0.5} O _{3-δ}			⁴ 5% H ₂ –Ar; 900 °C	⁸ 948; 197 ⁹ 890; 600	⁸ 7 h ¹¹ 20; 120 h	^{8,9,11} [387] ^{9,11} [388]
⁵ 2 wt.% Ag–6 wt.% Ni–32 wt.% La _{0.75} Sr _{0.25} Cr _{0.5} Mn _{0.5} O _{3-δ} –60 wt.%	⁴ Screen printing and fired at 1400 °C for 18 h					

(continued on next page)

Table 5 (continued)

Composition	Processing technique	Electrolyte/cathode/ current collector	Fuel/test condition	Anode performance	Cell performance/ maximum power density (mW/cm ²)	Remarks	Ref.
			5, ⁶ Dry H ₂ ; Dry CH ₄ ; ^{5,9,10} 850 °C, ^{6,8} 800 °C		¹⁰ 567; 561	¹⁵ 24 h	¹² [389]
Y _{0.08} Zr _{0.92} O _{2-δ}	^{5,10} Spin coating and sintered at 1400 °C for 4 h				¹¹ 534; 384		¹³ [346]
⁶ 37 wt.% (NiO– La _{0.75} Sr _{0.25} Cr _{0.5} Mn _{0.5} O _{3-δ})– 63 wt.% Y _{0.08} Zr _{0.92} O ₂			⁷ Dry H ₂ ; Dry CH ₄		¹² 530		¹⁴ [390]
⁶ Thermally treated at 900 °C in air for 1 h and then sintered at 1100 °C in air for 2 h			Dry C ₂ H ₅ OH; 800 °C		¹³ 520		¹⁵ [391]
⁷ Ni-Sm _{0.2} Ce _{0.8} O _{2-δ} – La _{0.75} Sr _{0.25} Cr _{0.5} Fe _{0.5} O _{3-δ} – Y _{0.08} Zr _{0.92} O _{2-δ}		^{5,6,8,10} YSZ/LSM		¹¹ 2:1 mixture of H ₂ and CH ₃ CH ₂ OH– H ₂ O; 800 °C			
	⁷ Slurry spincoating followed by co-sintering at 1400°C in air for 4 h		⁷ YSZ/LSM-SDC				
⁸ 8.9 wt.% Ni–5.8%wt. CeO ₂ – La _{0.75} Sr _{0.25} Cr _{0.5} Mn _{0.5} O _{3-δ}	⁸ Sintered at pressure of about 200 MPa at 1400 °C for 4 h	⁹ LDC/LSGM/					
⁹ 20 wt.% Cu–1.5 wt.% Pd– La _{0.75} Sr _{0.25} Cr _{0.5} Mn _{0.5} O _{3-δ}				^{12,13} Humidified H ₂ ; ¹³ 700 °C; ¹⁴ 750 °C ¹² 800 °C			
	^{9,11} Screen printed and sintered at 1470 °C for 10 h	¹¹ Ni–YSZ/Ni–ScSZ/ ScSZ/					

	PCM						
¹⁰ 35 wt.% $\text{La}_{0.75}\text{Sr}_{0.25}\text{Cr}_{0.5}\text{Mn}_{0.5}\text{O}_{3-\delta}$ – 65 wt.% $\text{Y}_{0.08}\text{Zr}_{0.92}\text{O}_{2-\delta}$	¹³ Tape casting followed by firing ¹² LSGM/LSCF-GDC to 1500 °C			¹⁴ 458			
¹¹ Cu– $\text{La}_{0.7}\text{Sr}_{0.3}\text{Cr}_{0.5}\text{Mn}_{0.5}\text{O}_{3-\delta}$ – $\text{Y}_{0.08}\text{Zr}_{0.92}\text{O}_{2-\delta}$	¹⁴ Uniaxial pressing and sintering for 6 h at 1450 °C		¹⁵ Humidified H_2 Humidified CH_4		¹⁵ 419; 158		
¹² 50% $\text{La}_{0.8}\text{Sr}_{0.2}\text{Cr}_{0.82}\text{Ru}_{0.18}\text{O}_{3-\delta}$ – 50% $\text{Gd}_{0.1}\text{Ce}_{0.9}\text{O}_{2-\delta}$	SCF	800 °C					
¹³ 0.5% Pd–5% CeO_2 –45% $\text{La}_{0.75}\text{Sr}_{0.25}\text{Cr}_{0.5}\text{Mn}_{0.5}\text{O}_{3-\delta}$ – $\text{Y}_{0.08}\text{Zr}_{0.92}\text{O}_{2-\delta}$							
¹⁴ 50% $\text{La}_{0.8}\text{Sr}_{0.2}\text{Cr}_{0.82}\text{Ru}_{0.18}\text{O}_{3-\delta}$ – 50% $\text{Gd}_{0.1}\text{Ce}_{0.9}\text{O}_{2-\delta}$							
¹⁵ $\text{La}_{0.75}\text{Sr}_{0.25}\text{Cr}_{0.5}\text{Mn}_{0.5}\text{O}_{3-\delta}$ – $\text{Gd}_{0.2}\text{Ce}_{0.8}\text{O}_{2-\delta}$	¹³ YSZ/LSF–YSZ ¹⁴ LSGM/LSCF-GDC ¹⁵ YSZ/LSM–YSZ						
<i>Other anode materials</i>							
¹ $\text{Gd}_2\text{Ti}_{1.4}\text{Mo}_{0.6}\text{O}_{7-\delta}$ (GTMO)	¹ Screen printed and co-fired at 1300 °C in 4% H_2 , balanced by Ar	^{1,2,8} Pt current collector	^{1–2} H_2 ; ¹ 750 °C; ² 800 °C		¹ ~300	¹ Better performance in fuels with 10%	¹ [392]
² $\text{Sr}_2\text{MgMoO}_{6-\delta}$ and $\text{Sr}_2\text{MnMoO}_{6-\delta}$					² ~800 ⁸ 1017	² [393,394]	
³ $\text{Ca}(\text{V}_{0.5}\text{Mo}_{0.5})\text{O}_{3-\delta}$	² Pressed and annealed at 1100 °C in 5% H_2/Ar at 1100– 1200 °C for 24 h	⁴ LSGM/SKF ¹⁰ LSGM/SFM	³ 10% $\text{H}_2\text{–N}_2$; 800 °C	³ $\sigma_e \sim 525$		³ H_2S than in pure H_2	³ [395] ⁴ [396]
⁴ $\text{Sr}_{1.6}\text{K}_{0.4}\text{FeMoO}_{6-\delta}$				⁴ $\sigma_e \sim 450$	⁴ 766	² Still slightly poisoned by 5– 50 ppm H_2S	⁵ [397]
			^{4,6,8} H_2 ; 800 °C	⁵ ~250	¹² 584; 476		
		¹¹ CGO/LSGM/LSCF					
			^{5,7} 5% $\text{H}_2\text{S}/\text{N}_2$;	⁶ ~50; ~5	¹⁰ ~500		
						Test period 20 h	⁶ [398] ⁷ [399] ⁸ [400]

(continued on next page)

Table 5 (continued)

Composition	Processing technique	Electrolyte/cathode/ current collector	Fuel/test condition	Anode performance	Cell performance/ maximum power density (mW/cm ²)	Remarks	Ref.
⁵ Ce _{0.9} Sr _{0.1} VO _{3-δ}			⁵ 800 °C, ⁷ 900 °C	⁷ 4.34	¹¹ 330		⁹ [331] ¹⁰ [401]
⁶ Sr ₂ NiMoO _{6-δ}	³ Uniaxially pressed (~1 Tm) and calcined at 1180 °C for 4 h in 1% H ₂ /Ar			⁸ ~1		50 cycles (H ₂)	
⁷ Ce _{0.9} Sr _{0.1} Cr _{0.5} V _{0.5} O _{3-δ}			⁹ 5% H ₂ /Ar; 800 °C	⁹ 0.8			¹¹ [402]
⁸ Sr ₂ CoMoO _{6-δ}	⁴ Screen printed and fired at 1100 °C for 1 h		^{10,11} Humidified H ₂ ; 800 °C				
⁹ Sr ₂ MgMoO _{6-δ}							
¹⁰ Sr ₂ Fe _{1.5} Mo _{0.5} O _{6-δ}							
¹¹ Sr ₂ MgMoO _{6-δ}	⁵ Screen printed and presintered in 10% H ₂ /Ar for 2 h at 1000 °C.						
	⁶ Pressed at 200 MPa and sintered at 1450 °C for 10 h						
	⁷ Pressed at 2 Tonnes and sintered for 2 h at 1350 °C –1550 °C						
	⁸ Pressed and sintering in air at 1250 °C for 24 h						
	⁹ Pressed and sintered at 1400 °C for 3 h in air						
	¹⁰ Pressed and sintered in 5% H ₂ /Ar at 1000 °C–1200 °C for 20–24 h						
	¹¹ Pressing at 125 MPa and sintered at 1200 °C in both air and 5% H ₂ /Ar for 4 h–24 h						

$\text{Ln}_{2/3-x}\text{TiO}_{3-3x/2}$ ($\text{Ln} = \text{La}, \text{Pr}$ and Nd) ($0.07 \leq x \leq 0.13$)	Ceramic and sol-gel (Pechini method)	$\text{N}_2, \text{Ar}, \text{H}_2\text{-Ar},$ air and O_2 ; 150°C	¹ Bulk σ 7.35×10^{-5} – 1.30×10^{-4} (for $\text{Ln} = \text{La})$ ² Bulk σ 9.75×10^{-6} – 1.65×10^{-5}	¹ Densification (52– 61%) and Activation energy (0.48–0.42) ² Densification (50– 60%) Activation energy (0.59–0.54)	[69,403]
<i>Sulfur tolerant Anode materials</i>					
$\text{CuCo}_2\text{S}_4, \text{CuFe}_2\text{S}_4, \text{CuNi}_2\text{S}_4,$ $\text{NiFe}_2\text{S}_4, \text{NiCo}_2\text{S}_4, \text{WS}_2$	Heating to 800°C in air for 1 h, and then sintering at 1200°C – 1250°C for 1 h	$\text{H}_2\text{S}, 900^\circ\text{C}$	up to 10 mW/cm^2 for NiFe_2S_4	Anode exchange current density decreases in the sequence of: $\text{NiFe}_2\text{S}_4 >$ $\text{WS}_2 > \text{CuCo}_2\text{S}_4 >$	
$\text{CuFe}_2\text{S}_4 > \text{NiCo}_2\text{S}_4 > \text{CuNi}_2\text{S}_4$	[407,408]				
$\text{Co-Mo-S}, \text{Fe-Mo-S}, \text{Ni-Mo-S},$ and MoS_2 with or without Ag	Screen printed and fired in air at 1050°C for 30 min	Pt as current collector	$\text{H}_2\text{S}, 850^\circ\text{C}$	up to $\sim 220 \text{ mW}/$ cm^2	[404,405]

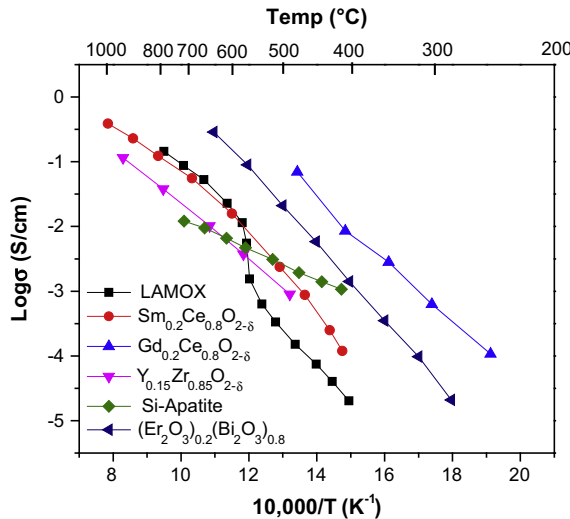


Fig. 27. Inverse temperature dependence of total conductivities of LAMOX, SDC (Samarium doped ceria), GDC (Gadolinia doped ceria), 8YSZ (8 mol.% yttria stabilized zirconia), Si-apatite, and ESB (Erbium stabilized Bismuth oxide) [410–412].

i.e., 1453 °C) which leads to sintering related issues. Other approaches to combat sulfur poisoning were via development of infiltration anodes, i.e., Cu–CeO₂ infiltrated into YSZ backbone, Gd–CeO₂ in Mn-doped lanthanum strontium chromite, nano CGO in Nb-doped SrTiO₃, and other perovskites, double perovskites and pyrochlores-based anodes, such as, lanthanum strontium titanates, and lanthanum strontium vanadates. Although these materials exhibited appreciable sulfur tolerance, their electrical conductivity was found to be somewhat lower than Ni-cermet anodes. Other issues with these materials are formation of reaction intermediates or new phases, which were stable and degraded the electrocatalytic properties of the anode material. However, some noteworthy anode materials, such as, Sr₂MgMoO_{6-δ} and La-doped Sr₂MgMoO_{6-δ} show promising results in terms of power density (up to 0.84 W/cm² at 800 °C in H₂S containing H₂ fuel) [331] and improved carbon and sulfur tolerance (power density degradation of only 1% in 5 ppm H₂S and of 16% in 50 ppm H₂S mixed with H₂, when compared with the output in pure H₂) when compared to Ni-YSZ anodes. However, the summary of progress so far in the anode material development, properties, and performance is presented in Table 5.

3. Electrolyte

An electrolyte is the heart of a SOFC unit, which conducts oxide ions from cathode to anode where it reacts with hydrocarbons to form H₂O and CO₂, and thus completes the overall electrochemical reaction. The oxide ion conduction occurs via oxygen vacancy hopping mechanism, which is a thermally activated process. For achieving a high ionic conductivity in electrolyte materials, their crystal structure must possess large interionic open space that allows high level of point defect disorder, and low migration enthalpy ≤ 1 eV [408]. Typically in such metal oxides, the size of the oxide ion is larger than the metal cation. Thus, it is expected that the smaller sized cations are more likely to possess an appreciable mobility in the lattice. However, metal cations also possess large charge valence which do not allow free movement of cations inside the lattice. On the other hand, this is achieved by creating oxygen vacancy defect inside the lattice and by applying a driving force to facilitate the diffusion of oxide ions inside the lattice. Some noteworthy examples of such oxides are ZrO₂, CeO₂, Bi₂O₃ based oxides with the fluorite structure, LaGaO₃ based perovskites, Bi₄V₂O₁₁ and La₂Mo₂O₉ based derivatives, Ba₂In₂O₅ derived perovskite, and brownmillerite like phases and pyrochlores [409].

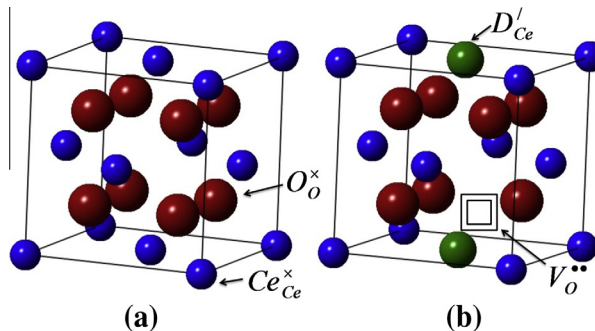


Fig. 28. (a) Cubic fluorite structure of ceria, and (b) oxygen vacancy in acceptor doped ceria system.

Fig. 27 shows the comparison of oxide ion conductivity of some important materials at various temperatures.

The main requirements for an electrolyte to work efficiently are [413]:

- (i) Oxide ion conductivity must be sufficiently high (~0.1 S/cm at operating temperature).
- (ii) Low electronic transference number (<10⁻³).
- (iii) Thermodynamic and chemical stability over wide range of temperatures (from room temperature to 1000 °C) at variable activities of oxygen (1–10⁻²² atm).
- (iv) Negligible volatilization.
- (v) Chemically inertness toward electrode materials both during processing and service.
- (vi) Compatibility of CTE with adjoining cell components.
- (vii) Possessing reliable mechanical properties (such as fracture strength >400 MPa).

3.1. Fluorite structure oxides

Fluorite structure oxides possess face centered cubic arrangement of cations with anions occupying all the tetrahedral sites. CeO_2 , ZrO_2 , HfO_2 , ThO_2 and UO_2 are the few examples of MO_2 oxides which crystallize with fluorite structure. Other oxides such as Bi_2O_3 possess defective fluorite structure in which two of the tetrahedral sites are unoccupied. Among these oxides, only ZrO_2 , CeO_2 and Bi_2O_3 have been of interest to researchers as an electrolyte material in SOFC.

Fig. 28 shows the cubic fluorite structure of CeO_2 , which remains stable from room temperature to its melting point ~2400 °C at ambient 1 atm pressure. The Ce^{4+} and O^{2-} ions are located at 4a (i.e., 0, 0, 0) and 8c (i.e., 1/4, 1/4, 1/4) Wyckoff positions, respectively. The structure possesses 4 large unoccupied octahedral sites which provide a path for rapid oxide ion diffusion. Ionic conduction in these oxides takes place via vacancy diffusion mechanism [414]. However, pure CeO_2 does not possess sufficient amount of oxygen vacancies (Fig. 28a) to exhibit appreciable ionic conductivity. In order to achieve high ionic conductivity, oxygen vacancies are introduced into the structure via substitution of host Ce^{4+} by acceptor cations, such as, Gd^{3+} , Sm^{3+} , or Y^{3+} , (Fig. 28b). This can be represented by defect equation using Kröger Vink notation shown below.



Diffusion of oxygen takes place when oxide ion jumps from its original tetrahedral site to the adjacent oxygen vacant site. This type of migration is termed as discrete hopping (shown in Fig. 29).

Based on Eq. (49), the ionic conductivity should be an increasing function of dopant concentration. However, it is experimentally observed that the ionic conductivity reaches a maximum at dopant concentration of about 10–20 mol.% depending on the type of dopant [415]. This phenomenon is typically associated with the interactions of oxygen vacancies with dopant cation, and forms local defect structures, such as, $(D'_A - V_O^{2-} - D_A)$ and $(D'_A - V_O^{2-})$. This effectively reduces the number of mobile oxide ions and results in a substantial drop in the ionic conductivity of material. This phenomenon

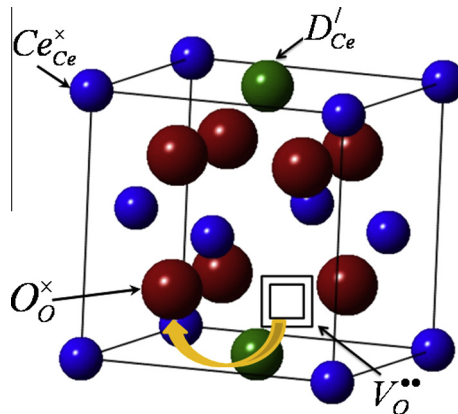


Fig. 29. Schematic showing hopping mechanism in an acceptor doped ceria lattice.

not only occurs in CeO_2 , but also in other oxides such as ZrO_2 and Bi_2O_3 . The conductivity is further influenced by the size of dopant, binding the energy of the oxide ion with the host cation and migration enthalpy of the mobile ions [209]. The theoretical expression of electrical conductivity and affecting factors are briefly described in the later subsection.

Although doped CeO_2 shows phase stability while operating in intermediate temperatures (~ 500 – 700°C), Ce^{4+} have a tendency to reduce and form Ce^{3+} in the fuel environment (typical of an SOFC device). This leads to several disadvantages, such as, high electronic conductivity, chemical expansion (due to larger size of Ce^{3+} when compared to that of Ce^{4+}), and inferior mechanical properties.

Unlike CeO_2 , pure ZrO_2 occurs in three polymorphs, viz., *monoclinic*, stable at room temperature, which transform to *tetragonal* form above 1170°C , and finally to a *cubic* fluorite structure at 2370°C , which remains stable up to its melting point of 2680°C [416]. All these transformations are martensitic in nature and reverse during cooling accompanied by a large volume change. As a result, cracks generate within its structures on cooling, and are responsible for low thermal shock resistance. The high temperature tetragonal or cubic phase of ZrO_2 can be stabilized at room temperature by replacing Zr^{4+} with a small amount of acceptor dopant cations. For example, the addition of 8 mol.% Y_2O_3 can fully stabilize the cubic phase in ZrO_2 . This cubic phase remains stable and does not undergo any phase transformation up to 2500°C .

Y_2O_3 stabilized ZrO_2 (YSZ) materials were first recognized by Nernst in 1890s as a potential electrolyte owing to their high oxide ion conductivity. The mechanism of ionic conduction in YSZ is similar to that of acceptor doped CeO_2 . Thus, the oxygen vacancies, generated by adding acceptor dopant cation, not only stabilizes the cubic phase of ZrO_2 crystal lattice, but also enhances its oxide ion conductivity [54]. Among the various Y_2O_3 – ZrO_2 solid solutions, 8 mol.% Y_2O_3 – ZrO_2 (8YSZ) is reported to exhibit highest ionic conductivity of 0.1 S/cm at 1000°C , which is a minimum ionic conductivity requirement for an electrolyte at working temperatures [414].

Among other doped ZrO_2 systems, Sc_2O_3 doped ZrO_2 (ScSZ) materials have received considerable research interest for the electrolyte application in SOFCs. At 850°C , the ionic conductivity of 11 mol.% Sc_2O_3 doped ZrO_2 is roughly 1.5 times higher than that of 8YSZ [417]. With high ionic transference (and negligible electronic conductivity) over a wide operation temperature range and partial pressures of oxygen, and good thermochemical properties, they offer an advantage of lowering the working temperature of SOFCs to intermediate temperatures. However, a complex phase assembly in ScSZ which includes phase transitions as a function of temperature, conductivity ageing behavior over time at high temperatures, poor accessibility, and the high market price are some of the issues related to ScSZ that needs to be addressed before they can be utilized for commercial applications [418].

The high temperature fluorite structure of bismuth oxide (δ - Bi_2O_3) polymorph exhibits high intrinsic oxygen vacancies concentration (25% of the oxygen sublattice sites) [419], which leads to a

remarkably high ionic conductivity in δ -Bi₂O₃. In fact, the ionic conductivity of δ -Bi₂O₃ is highest among all the studied oxide ion conductors. However, these materials undergoes a phase transformation from cubic (δ) to poorly conducting monoclinic (α) phase on cooling below 600 °C, which results in concomitant drop in the ionic conductivity. Furthermore, bismuth-oxide have structural stability issues in fuel environments (~700 °C), and it possess low bending strength and toughness [419].

3.1.1. Ionic conductivity

The ionic conductivity σ in fluorite oxides depends upon various factors such as temperature, defect dissociation, oxygen partial pressure, dopant concentration, and most importantly, sample preparation. The dependence of ionic conductivity σ on temperature can be represented by Arrhenius relationship:

$$\sigma T = A \exp\left(-\frac{E_a}{kT}\right) \quad (50)$$

where A and E_a are pre-exponential factor, and activation energy for ionic conduction, respectively. For any given material, ionic conductivity can be written in terms of the charge carrier concentration C_i , mobility μ_i , and charge q of the charge carriers. The relationship can be given as,

$$\sigma_i = C_i q_i \mu_i \quad (51)$$

For pure oxide ion conductors, C_i is the concentration of oxide ions, and can be presented by number of oxide ions present in crystal per unit volume N_o , and the site fraction of oxygen vacancies $[V_o^-]$.

$$C_i = (1 - [V_o^-]) N_o \quad (52)$$

However, the ionic mobility can be described via diffusivity (D_i) of the ion as:

$$\mu_i = \frac{q_i D_i}{kT} \quad (53)$$

where diffusivity term can be expanded and written in terms of enthalpy (ΔH_m) and entropy (ΔS_m) of migration, jump distance of an ion (a), appropriate lattice vibration frequency (ν_o), and the concentration of oxygen vacancy per unit volume ($[V_o^-] N_o$).

$$D_i = a^2 \nu_o [V_o^-] N_o \exp\left(\frac{\Delta S_m}{k}\right) \exp\left(-\frac{\Delta H_m}{kT}\right) \quad (54)$$

Inserting Eqs. (52)–(54) in Eq. (51), the detailed expression for the Arrhenius relationship can be obtained.

$$\sigma_i T = A [V_o^-] (1 - [V_o^-]) \exp\left(-\frac{\Delta H_m}{kT}\right) \quad (55)$$

where

$$A = \left(\frac{4e^2}{k}\right) a^2 \nu_o N_o \exp\left(\frac{\Delta S_m}{k}\right) \quad (56)$$

For small values of $[V_o^-]$, Eq. (55) becomes

$$\sigma_i T = A [V_o^-] \exp\left(-\frac{\Delta H_m}{kT}\right) \quad (57)$$

It is, however, inappropriate to express the temperature dependence of ionic conductivity in fluorites in a single exponential function. According to Kilner and Walters [420], the actual temperature dependence of ionic conductivity can be described in three distinctive temperature regions.

- (a) Region I corresponds to high temperatures. The ionic conductivity in this region is dictated by the intrinsic ionic defects (i.e., anion Frenkel) in the host crystal lattice.

- (b) Region II corresponds to intermediate temperatures. In this regime, the ionic conductivity is governed by the concentration of charge carrying defects, which can be estimated by the content of acceptor impurity present in the material.
- (c) Region III corresponds to low temperature and the ionic conductivity in this region, which is largely determined by the equilibrium between the concentration of charge carrying defects and associated pairs.

Thus, the ionic conductivity in regions II and III arises because of presence of mobile oxygen vacancies, which are essentially determined by the amount of acceptor impurity content present in the material.

3.1.2. Effect of defect association

Acceptor cation doping in the host fluorite lattice introduces oxygen vacancies as a compensating defects. However at low temperatures, these oxygen vacancies are not free and are bound to dopant cations that form defect associates, which can be attributed to the columbic interactions between the defects. The binding enthalpy also includes terms due to lattice-relaxation around the defect (depending upon the effective charge), dopant size, and cation polarizability. A detailed description on defect association has been compiled by Kilner and Steele [421]. According to Kilner, the defect association can be divided into three possible cases:

- (a) Case I: A divalent dopant cation in associating with oxygen vacancy, e.g., Ca^{2+} doped in CeO_2 can form only one simple defect associate i.e., $\{\text{Ca}_{\text{Ce}}'' - V_0^{\cdot}\}^{\times}$.



On applying the law of mass action,

$$\frac{[\text{Ca}_{\text{Ce}}''] [\text{V}_0^{\cdot}]}{\left[\{\text{Ca}_{\text{Ce}}'' - V_0^{\cdot}\}^{\times} \right]} = K_{A2} \quad (59)$$

Substituting the charge neutrality condition in Eq. (59),

$$[\text{V}_0^{\cdot}]^2 = [\{\text{Ca}_{\text{Ce}}'' - V_0^{\cdot}\}^{\times}] K_{A2} \quad (60)$$

In the situation when the complete association of defects occurs, the total dopant concentration (C_M) expressed as the fraction of the cation sites per unit volume can be written as:

$$C_M = \left[\{\text{Ca}_{\text{Ce}}'' - V_0^{\cdot}\}^{\times} \right] \gg [\text{V}_0^{\cdot}] \quad (61)$$

Also, the equilibrium constant K_{A2} can be expressed in terms of temperature as:

$$K_{A2} = \left(\frac{1}{W} \right) \exp \left(\frac{\Delta S_{A2}}{k} \right) \exp \left(\frac{-\Delta H_{A2}}{kT} \right) \quad (62)$$

where W is the number of orientations of the associates, while ΔS_{A2} and ΔH_{A2} are the entropy and enthalpy of association, respectively. Inputting Eqs. (61) and (62) in Eq. (60),

$$[\text{V}_0^{\cdot}] = \left(\left[\{\text{Ca}_{\text{Ce}}'' - V_0^{\cdot}\}^{\times} \right] / W \right)^{1/2} \exp (\Delta S_{A2}/2k) \exp (-\Delta H_{A2}/2kT) \quad (63)$$

$$\Rightarrow [\text{V}_0^{\cdot}] = (C_M/W)^{1/2} \exp (\Delta S_{A2}/2k) \exp (-\Delta H_{A2}/2kT) \quad (64)$$

Thus, using Eq. (57), the ionic conductivity can be written as:

$$\sigma_i T = A(C_M/W)^{1/2} \exp (\Delta S_{A2}/2k) \exp \left[- \left(\Delta H_M + \frac{\Delta H_{A2}}{2} \right) / kT \right] \quad (65)$$

- (b) Case II: When the trivalent cation is added as dopant in CeO_2 e.g., Y^{3+} in CeO_2 , the columbic interactions of dopant cation with oxygen vacancy leads to the formation of a positively charged defect associate i.e., $\{\text{Y}'_{\text{M}} - \text{V}_{\text{O}}^{\cdot}\}$:



Similar to Case I, by applying the law of mass-action and charge neutrality condition and taking C_M as the total dopant concentration per unit volume, conductivity dependence over the temperature can be derived. This can be expressed as follows:

$$\sigma T = A(C_M/2W) \exp(\Delta S_{A1}/2k) \exp\left[-\left(\Delta H_M + \frac{\Delta H_{A1}}{2}\right)/kT\right] \quad (67)$$

- (c) Case III: In the case when all the oxygen vacancies are free, ionic conductivity can be expressed as:

$$\sigma T = AC_M \exp(-\Delta H_M/kT) \quad (68)$$

In this case, the electrical conductivity proportionally increases with the increase in dopant concentration (C_M).

3.1.3. Dependence on oxygen partial pressure

The driving force in a working SOFC is the gradient of oxygen partial pressures (P_{O_2}) between the adjoining electrodes (i.e., cathode and anode). Increasing the P_{O_2} gradient across the electrolyte, results in higher power density that can actually be derived from SOFC. Thus, the extreme P_{O_2} condition in the respective electrodes (i.e., highly reducing atmosphere at anode and highly oxidizing atmosphere at cathode side) is required to achieve reasonable power density from the SOFC. Although oxide ceramics possess good phase stability in these extreme conditions, there are certain issues under reducing conditions. In the case of acceptor doped CeO_2 , at high temperatures and under low P_{O_2} environment ($<10^{-15}$ atm), oxygen vacancies are formed with the generation of two electrons as a charge compensating defect (shown in Eq. (69)):



These electrons are typically localized in the periphery of trivalent cerium cations, thus forming small polarons. The presence of polarons enhances electronic conductivity of the electrolyte, which subsequently deteriorates the overall performance of SOFC. Applying the law of mass action, the electron concentration n at equilibrium can be represented as:

$$n = \sqrt{\frac{K}{[V_{\text{O}}^{\cdot}]P_{\text{O}_2}^{1/2}}} \quad (70)$$

where K and $[V_{\text{O}}^{\cdot}]$ are the equilibrium constant and the mole fraction of oxygen vacancies present in the oxygen sublattice, respectively. It can be assumed that the $[V_{\text{O}}^{\cdot}]$ remains nearly the same (even in reducing atmosphere), as the large number of oxygen vacancies are formed by acceptor doping in ceria. In such case, the ionic conductivity is independent of reduction. The ionic transference number is the ratio of ionic conductivity to the total conductivity, and can be represented as:

$$t_{\text{O}_2} = \left[1 + \left(\frac{P_{\text{O}_2}}{P_{\text{O}_2}^*} \right)^{-1/4} \right]^{-1} \quad (71)$$

where $P_{\text{O}_2}^*$ is related with K and for a given temperature, it can be defined as the partial pressure of oxygen at which the value of the transference number is 0.5.

From Table 6, it can be observed that at 850 °C, the value of $P_{\text{O}_2}^*$ for ceria based solid solutions, is higher than 10^{-15} atm, while for calcia stabilized zirconia (CSZ), it is estimated to be as low as 10^{-30} atm [422]. Thus, the zirconia based solid solutions are more useful for high temperature

Table 6

Oxygen partial pressure at which an ionic transference number of ceria and zirconia based solid solutions becomes 0.5. (Adapted from Ref. [426]).

$P_{O_2}^*$ (atm)	500 °C	700 °C	850 °C	1000 °C
Compositions				
Ce _{0.9} Ca _{0.1} O _{1.9})	10 ⁻²⁰	10 ⁻¹³	10 ⁻⁹	—
Ce _{0.905} Y _{0.095} O _{1.95}	10 ⁻²⁶	10 ⁻¹⁷	10 ⁻¹³	10 ⁻¹⁰
Ce _{0.9} Gd _{0.1} O _{1.95}	—	1.2 × 10 ⁻¹⁹	1.7 × 10 ⁻¹⁵	—
Ce _{0.5} Gd _{0.5} O _{1.75}	—	1.5 × 10 ⁻¹⁶	6.5 × 10 ⁻¹⁴	—
Calcia stabilized zirconia (CSZ)	—	10 ⁻³⁴	10 ⁻³⁰	10 ⁻²⁶

SOFCs than the more conductive ceria based solid solutions. Nevertheless, on lowering the temperature, $P_{O_2}^*$ value for ceria based solid solutions decreases, which make them conducive for intermediate temperature SOFCs.

3.1.4. Effect of dopant cations

In order to enhance the oxide ion conductivity, numerous compositions based on ZrO₂ and CeO₂ have been explored. Acceptor dopants such as trivalent lanthanide cations, and divalent alkaline earth cations, were extensively used with varying doping level to understand the correlation between the physical properties of dopant and conductivity. Doping CeO₂ with lanthanide cations exhibit improved performance in the intermediate temperature range. However in the case of ZrO₂, higher activation energy for oxygen diffusion was observed when compared to that of CeO₂. Fig. 30 elicits the effect of dopant ionic size on the total ionic conductivity in ZrO₂ and CeO₂ in air at 1000 °C [423–426]. It can be observed that in the case of ZrO₂, ionic conductivity decreases as the mismatch between the ionic size of host and dopant cations increases. On doping with larger sized dopant stabilizes the cubic fluorite structure of ZrO₂, but will lead to significant increase in the activation energy. Thus, Sc³⁺ exhibits much higher ionic conductivity compared to other dopants, as it possesses ionic radius close to that of Zr⁴⁺. However, a deviation in the above statement is observed in the doped CeO₂ systems. Ionic conductivity in doped ceria increases with the rise in the dopant size (even beyond the ionic radius of Ce⁴⁺), reaches its maximum value at Sm³⁺, and then decreases. The ionic conductivity of the resultant electrolyte material was found to be influenced not only by the ionic radius and charge valence of the dopant cations, but also by the doping level. The oxygen vacancies introduced upon doping, compensate the negative charge of the acceptor dopant cations. As described in the previous section, conduction occurs in these materials via vacancy diffusion mechanism, thus, the ionic conductivity is observed to increase with an increase in oxygen vacancy concentration. In the case of doped ceria electrolytes, high ionic conductivity is essentially due to low activation energy, which in turn, is related to an optimal balance between elastic and electronic columbic defect interactions [426].

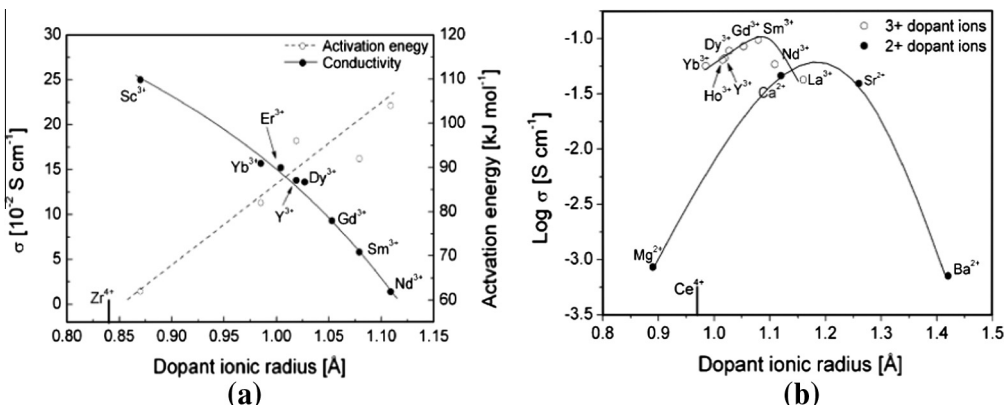


Fig. 30. The dependence of ionic conductivity on the dopant ionic radius in (a) doped ZrO₂ and (b) doped CeO₂ at 1000 °C. (Reprinted with permission from Ref. [427], copyright Elsevier, 2007).

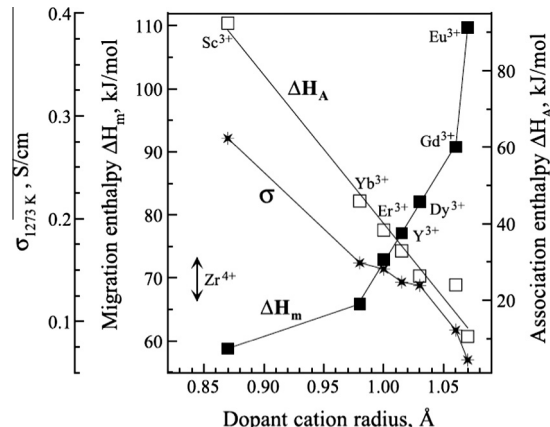


Fig. 31. Maximum conductivity in the $\text{ZrO}_2\text{-Ln}_2\text{O}_3$ binary systems at 1000 °C and the corresponding change in an oxide ion migration and association enthalpies with the radius of Ln^{3+} cations (reprinted with permission from Ref. [431], copyright Elsevier, 2004).

ZrO_2 based systems show that ionic conductivity initially increases with the rise in concentration of acceptor dopant cations. However, conductivity reaches a maxima when the dopant concentration approaches the minimum amount required to completely stabilize the cubic fluorite (high temperature) structure of ZrO_2 at room temperature [414,428]. This minimum amount required to stabilize cubic fluorite phase is also called low stabilization limit. However, both the low stabilization limit and resultant ionic conductivity, depends on thermomechanical history and microstructural features (that includes segregation of dopants, cleanliness of grain boundaries, presence of impurities and metastable phases, and generation of ordered microdomains) [417]. Thus, in the literature, maxima in conductivity in $(\text{Y}_2\text{O}_3)_x\text{-}(\text{ZrO}_2)_{1-x}$ and $(\text{Sc}_2\text{O}_3)_x\text{-}(\text{ZrO}_2)_{1-x}$ systems are reported from 8–11 mol.% to 9–11 mol.%, respectively [417]. However, it is widely accepted that the ionic conductivity in $(\text{Y}_2\text{O}_3)_x\text{-}(\text{ZrO}_2)_{1-x}$ is highest when the Y_2O_3 content is approximately 8 mol.%. In fact, 8 mol.% Y_2O_3 stabilized ZrO_2 is an established electrolyte for SOFCs operating at high temperatures (1000 °C). On further addition of dopant oxide, i.e., beyond 8 mol.% in the case of $(\text{Y}_2\text{O}_3)_x\text{-}(\text{ZrO}_2)_{1-x}$, the defect interactions become the dominating factor which hinder the flow of mobile oxygen vacancy resulting in the decrease in ionic conductivity [429,430].

Fig. 31 shows the maximum conductivity of $\text{ZrO}_2\text{-Ln}_2\text{O}_3$ (where Ln is a rare earth metal cation) systems at 1000 °C, where the association enthalpy decreases and oxide ion migration enthalpy increases with an increase in the radius of trivalent dopant cation [431]. Since the ionic size of Sc^{3+} is close to that of Zr^{4+} , an enhanced ionic conduction is observed when Sc^{3+} is used as dopant. With the increase in the size of the dopant, the tendency to form local defect associates increases, which results a decrease in the ionic conductivity [414,428]. On comparison with other solid oxide electrolytes, stabilized ZrO_2 -systems exhibit an additional advantage of negligible electronic conduction contribution towards the total conductivity.

In CeO_2 , trivalent dopants exhibit much higher conductivity than the divalent dopants due to the lower ionic size mismatch between the trivalent dopants and host Ce^{4+} cation [432]. Similar to doped ZrO_2 based systems, increasing dopant concentration initially enhances the ionic conductivity. However at certain doping level, conductivity reaches its maximum value and then decreases due to low mobility of defect associates. The extent of formation of these associates increases with the increasing ionic-radii mismatch of dopant cations with respect to the host cation [432,433].

Doping has also been used to lower the elastic strain generated in the lattice and reduce the activation energy for oxide ion conduction [408,434]. The dependence of ionic conductivity on the dopant size of trivalent cation doped CeO_2 is shown in Fig. 30. This strong dependence arises due to the formation of local defect complexes between oxygen vacancies and dopant cations. Theoretical calculations by Butler et al. [434] has shown that the phenomenon of relaxation of the dopant cations in CeO_2

towards oxygen vacancy occurs in the case of smaller sized dopant cation, such as, Sc³⁺ ($r_{\text{Sc,VIII}}^{3+} = 0.84 \text{ \AA}$), Y³⁺ ($r_{\text{Yb,VIII}}^{3+} = 1.019 \text{ \AA}$), which, as a result, increases the stability of the complex. On the other hand, in the case of larger sized dopant cations, such as, Gd³⁺ ($r_{\text{Gd,VIII}}^{3+} = 1.053 \text{ \AA}$) and La³⁺ ($r_{\text{La,VIII}}^{3+} = 1.18 \text{ \AA}$), the energy associated with the reduction in elastic strain in the crystal becomes significant when an oxygen vacancy is introduced into a neighboring site. The two opposing effects lead to a minimum value of binding energy (~0.17 eV) corresponding to Gd³⁺. The computed values of the binding energies corresponding to Sc³⁺, Y³⁺, Ce³⁺ and La³⁺ are 0.62, 0.38, 0.25 and 0.26 eV, respectively [434]. Hence, Gd³⁺ is considered to be an ideal dopant for CeO₂.

Kim [435] studied the effect of ionic radius and valence of the dopant cation on the lattice parameter of ceria. Using multiple regression analysis on the experimental data, an empirical model predicting the change in the lattice parameter of doped ceria as a function of ionic radii mismatch, dopant valence and dopant concentration was defined. Further, the concept of critical ionic radius, r_c , was proposed in relation to the ionic conductivity of doped ceria. It was suggested that a dopant with ionic radius equal to r_c will not result any change in the lattice parameter of the fluorite structure (i.e., expansion due to bigger trivalent ionic radius and contraction due to vacancy creation will be nullified). The critical ionic radius r_c of divalent and trivalent dopant cations for CeO₂ were calculated to be 0.1106 and 0.1038 nm, respectively. According to Kilner and Brook [436], maximum ionic conductivity in doped fluorite structured oxide is observed when the lattice elastic strain is minimal. Based on Kilner's conjecture, it can be concluded that the dopants with the ionic radius close to r_c should exhibit minimum association enthalpy, and hence high ionic conductivity. Using a similar argument, Kim suggested that Gd³⁺ exhibits the highest ionic conductivity as the ionic radius of Gd³⁺ ($r_{\text{Gd,VIII}}^{3+} = 1.053 \text{ \AA}$) lies close to r_c [435]. The validity of the argument presented by Kim was tested by Omar et al. [211] using a co-doping approach in CeO₂, where the co-dopant pair, i.e., Lu³⁺ and Nd³⁺, was selected based on their respective ionic radius. Both the co-dopants were added in a proportion that matched r_c , such that the positive elastic strain due to larger dopant cation (i.e., Nd³⁺) can be compensated by the negative elastic strain due to smaller dopant cation (i.e., Lu³⁺). This in turn prevents any distortion in fluorite lattice that is usually present in the singly doped ceria systems. It was observed that even though the lattice elastic strain present in the co-doped compositions is negligible, the ionic conductivity value is less than that of Gd-doped CeO₂ [211]. Furthermore, the ionic conductivity of Y³⁺ doped CeO₂ has been found to be lower compared to Sm³⁺ doped CeO₂ and Gd³⁺ doped CeO₂, even though the ionic radius of Y³⁺ is closer to r_c [210].

Using DFT calculations, Andersson et al. [437] have estimated the interaction energies involved between the dopant cations and oxygen vacancies in doped CeO₂. It was suggested that in the case of Pm³⁺ doped CeO₂, oxygen vacancies have no site preferences and can reside next to both dopant and host cations. This, as a result, facilitates oxygen vacancy diffusion, and enhances the ionic conductivity in this system. Thus, it was predicted that among the rare earth trivalent cations, Pm³⁺ is the best dopant for achieving high ionic conductivity in CeO₂. As Pm³⁺ is a radioactive element and cannot be used for electrolyte applications, a co-doping scheme with Sm³⁺ and Nd³⁺ as co-dopants was suggested for CeO₂. The hypothesis was experimentally tested by keeping the molar ratio 1:1 between the co-dopants such that an average effective ionic radius is near to that of Pm³⁺. The observed grain ionic conductivity of a 10 mol.% co-doped composition samples was found to be 14% higher than that of Gd_{0.10}Ce_{0.90}O_{2- δ} at 550°C [212,438].

Recently, Omar et al. [210] have shown relation of ionic conductivity on lattice elastic strain in 10 mol.% trivalent cations doped CeO₂ at high temperatures in air. It was observed that at a 10 mol.% concentration, the ionic conductivity is an increasing function of the size of the dopant, with Nd³⁺ exhibiting the highest grain ionic conductivity. Furthermore, the r_c values were calculated at intermediate temperatures using the high temperature elastic strain data. It is important to note that the r_c value reported by Kim [435] was determined from the elastic strain data taken at room temperature, while the conductivity was measured at high temperatures. A slight decrease in r_c value was observed with the rise in temperature which indicates that the structure-conductivity relationship based on r_c is not sufficient to explain the ionic conductivity behavior in doped ceria [210].

As doped ceria materials exhibit higher ionic conductivity than YSZ, they can be utilized in the intermediate temperatures. In this category, solid solutions, such as, Ce_{1-x}M_xO_{2- δ} (where, M = Gd or

Table 7

Effect of doping and codoping on the ionic conductivity of various SOFC electrolytes.

Material	Conductivity (S/cm)	Operating temperature (°C)	Thermal expansion coefficient $1 \times 10^{-6}/(K)$	Process/effect	Ref.
<i>Zirconia based electrolytes</i>					
8 mol.% Y_2O_3 –ZrO ₂	0.13	1000	–	Processed via spray drying of nitrate solution	[448]
10.5 mol.% Y_2O_3 –ZrO ₂	0.034	800	–	Thin film synthesized by aerosol-assisted metal–organic chemical vapor deposition	[449]
10 mol.% Y_2O_3 –ZrO ₂	4.52×10^{-6}	400	10.6	300 nm-thick film processed using atomic laser deposition	[450]
9.5 mol.% Y_2O_3 –ZrO ₂	0.057	900	–	15–25 μm-thick film synthesized via magnetic pulse compaction of tapes cast of nanopowders	[451]
6 mol.% Sc_2O_3 –ZrO ₂	0.18	1000	–	The sintered film was synthesized using hot isostatic pressing in order to improve the mechanical strength	[452]
9–11 mol.% Sc_2O_3 –ZrO ₂	0.28–0.34	1000	10.4, 10.9 (8, 10 mol.% Sc_2O_3)	Prepared by sintering of co-precipitated powders	[453–455]
<i>Ceria based electrolytes</i>					
$Ce_{0.85}Gd_{0.15}O_{2-\delta}$	4.07×10^{-2}	700	–	High purity CeO ₂ and Gd ₂ O ₃ powders were used as the starting materials	[456]
$Ce_{0.8}Sm_{0.2}O_{1.9}$	5×10^{-3}	600	–	Solid-solution of $Ce_{0.8}Sm_{0.2}O_{1.9}$ was prepared by sol-gel method	[457]
$^1Ce_{0.9}Gd_{0.1}O_{2-\delta}$			¹ 12.4	Powders were uniaxially pressed to form bulk pellet followed by pressureless sintering	[458,459]
$^2Ce_{0.8}Gd_{0.2}O_{2-\delta}$			¹ 11.8 (27–827 °C) ² 12.5 (50–1000 °C)		
$Ce_{0.75}Gd_{0.25}O_{1.875}$	1.01×10^{-2}	600	–	Solid-solution is synthesized using the flame spray pyrolysis method	[460]
$Ce_{0.8}Sm_{0.2}O_{1.9}$	8.8×10^{-2}	800	–	Powder synthesized via oxalate coprecipitation method	[461]
$Ce_{0.83}Sm_{0.17}O_{1.915}$	5.7×10^{-3}	600	8.6	Synthesized by hydrothermal route	[462]
$Ce_{0.8}Y_{0.2}O_{1.9}$	3.4×10^{-2}	700	–	Synthesized by citric acid–nitrate low-temperature combustion process	[463]
Ca, Na doped CeO ₂	10^{-2} – 10^{-1}	~600	–	The film membrane with thickness 0.1–0.6 μm prepared by sol-gel spin coating	[464]
$Zr_{0.75}Ce_{0.08}Nd_{0.17}O_{1.9}$	3×10^{-4}	~600	–	Solid state sintering	[465]
$Ce_{0.8}) Sm_{0.1}Nd_{0.1}O_{1.9})$	0.012	500	–	Sm ³⁺ and Nd ³⁺ co-doped ceria powder was synthesized via combustion of a citrate/nitrate gel. The bulk sample was prepared via sintering of the powder compact at temperature ~1400 °C	[466]
<i>LaGaO₃- and LaAlO₃-based electrolytes</i>					
$La_{0.9}Sr_{0.1}Ga_{0.8}Mg_{0.2}O_{3-\delta}$	10.2	800	10.4 (27–800 °C)	Powders synthesized using combustion synthesis were pressed and subsequently sintered	[467,468]
$La_{0.9}Sr_{0.1}Ga_{0.8}Mg_{0.2}O_{3-\delta}$ –2 wt.% Al_2O_3	8.8	800	11.9 (27–1200 °C)	Powders synthesized using combustion synthesis were pressed and subsequently sintered	[467]
$La_{0.8}Sr_{0.2}Ga_{0.8}Mg_{0.2}O_{3-\delta}$	0.45–0.025	300–800	12.4 (27–1200 °C)	The compacted powders were isostatically pressed and then sintered in air	[468]

(continued on next page)

Table 7 (continued)

Material	Conductivity (S/cm)	Operating temperature (°C)	Thermal expansion coefficient $1 \times 10^{-6}/(K)$	Process/effect	Ref.
$\text{La}_{0.90}\text{Sr}_{0.10}\text{Ga}_{0.76}\text{Mg}_{0.19}\text{Co}_{0.05}\text{O}_{3-\delta}$	~0.30–0.39	100–1000	12.7 (27–1200 °C)	The compacted powders were isostatically pressed and then sintered in air	[469]
$\text{La}_{0.90}\text{Sr}_{0.10}\text{Ga}_{0.76}\text{Mg}_{0.19}\text{Fe}_{0.05}\text{O}_{3-\delta}$	~0.44–0.39	100–1000	11.6 (27–1200 °C)	The compacted powders were isostatically pressed and then sintered in air	[469]
$\text{La}_{0.90}\text{Sr}_{0.10}\text{Ga}_{0.45}\text{Al}_{0.45}\text{Mg}_{0.10}\text{O}_{3-\delta}$	~0.25	500	10.9 (27–950 °C)	Combustion synthesized powders were pressed and subsequently sintered	[470]
$\text{La}_{0.9}\text{Sr}_{0.1}\text{Al}_{0.9}\text{Mg}_{0.1}\text{O}_{3-\delta}$	0.7	300–1000	11.2 (27–950 °C)	Powders synthesized using solid-state reaction method, and subsequently sintered at 1450–1500 °C for 5 h in air	[470–472]
$\text{La}_{0.9}\text{Sr}_{0.1}\text{Sc}\text{O}_{3-\delta}$	4.6	300–1000	–	Calcined powder was ground and pressed uniaxially at 20 MPa followed by cold isostatic pressing at 150 MPa	[472]
$\text{LaSc}_{0.9}\text{Mg}_{0.1}\text{O}_{3-\delta}$	2	1000	–	Calcined powder was isostatic pressed at 200 MPa and then sintered	[473]
$\text{La}_{0.9}\text{Sr}_{0.1}\text{Sc}_{0.9}\text{Mg}_{0.1}\text{O}_{3-\delta}$	1.9	200–1000	–	Powder prepared via solid state reaction method was calcined and uniaxial pressed	[471]
$\text{La}_{0.9}\text{Sr}_{0.1}\text{InO}_{3-\delta}$	2.3	300–1000	–	Calcined powder was ground and pressed uniaxially at 20 MPa followed by cold isostatic pressing at 150 MPa	[472]
<i>Electrolytes with pyrochlore and apatite structure</i>					
$\text{Gd}_2\text{Ti}_2\text{O}_{7\pm\delta}$	0.44	1000	10.8 (50–1000 °C)	Uniaxially pressed powders were isostatically pressed at a 200 MPa pressure followed by sintering	[474]
$\text{Gd}_{1.86}\text{Ca}_{0.14}\text{Ti}_2\text{O}_{7-\delta}$	10.44	500–820	10.4 (127–1000 °C)	Powders were synthesized by a standard ceramic technique followed by compaction and sintering in air	[475]
$\text{La}_{9.83}\text{Si}_{4.5}\text{AlFe}_{0.5}\text{O}_{26-\delta}$	0.46	1000	8.9 (100–1000 °C)	Ball-milled powders were pressed (120–200 MPa) into bulk ceramic samples followed by sintering at 1600 °C for 10 h in air and annealing at 1000°C for 2–3 h in air	[476]
$\text{La}_7\text{Sr}_3\text{Si}_6\text{O}_{24}$	0.51	1000	9.1 (100–1000°C)	Powders were pressed at ~120–250 MPa and sintered at 1500–1650°C for 10 h in air	[477]
<i>$\text{La}_2\text{Mo}_2\text{O}_9$- and Bi_2O_3-based electrolytes</i>					
$\text{La}_{1.7}\text{Bi}_{0.3}\text{Mo}_2\text{O}_9$	1.4	1000	14.8 (100–350 °C)	Ball milled powders were pressed and then sintered in air using closed alumina container	[478]
$\text{La}_2\text{Mo}_{1.7}\text{W}_{0.3}\text{O}_9$	1.39	1000	16.0 (350–800 °C) 14.4 (100–350 °C)	Ball milled powders were pressed and then sintered in air using closed alumina container	[478]
$\text{Bi}_2\text{V}_{0.9}\text{Cu}_{0.1}\text{O}_{5.5-\delta}$	14.1–10.6	100–750	19.8 (350–800 °C) 15.3 (27–457 °C)	Standard ceramic synthesized powders are pressed and sintered at ~900 °C in air for 15–40 h	[479]
$(\text{Bi}_{0.95}\text{Zr}_{0.05})_{0.85}\text{Y}_{0.15}\text{O}_{1.5+\delta}$	19.2–26.9	250–800	18.0 (457–757 °C) 13.8 (47–437 °C) 16.6 (437–847 °C)	Powders were pressed and sintered in air	[480]

Sm, $x = 0.10\text{--}0.20$) show the highest level of oxide ion transport [409]. For example, $\text{Ce}_{0.9}\text{Gd}_{0.1}\text{O}_{1.95}$ (CGO10) shows grain ionic conductivity of $\sim 0.01 \text{ S/cm}$ at 500°C , while $\text{Ce}_{0.8}\text{Gd}_{0.2}\text{O}_{1.9}$ (CGO20) exhibits lower conductivity (0.0053 S/cm) [209]. The major issue which limits their applications as electrolyte is the tendency of Ce^{4+} to reduce to Ce^{3+} ions in low oxygen partial pressure and high temperature conditions, which typically occurs at the anode side during SOFC operations [433,439,440]. The reaction can be given as follows:



These conditions ensues: (i) generation of n -type electronic conductivity, which lowers the OCP due to short-circuiting, and (ii) incorporation of additional point defects in the lattice which results in the chemical expansion of the material followed by mechanical stress and failure [440]. In order to alleviate these issues, researchers have adopted various approaches (though only partially successful); e.g., either decreasing the operating temperature to lower values or combining doped CeO_2 with stabilized ZrO_2 or doped LaGaO_3 to form bilayered electrolyte [431,433,441]. The latter strategy leads to the formation of interfacial reaction product between the solid electrolyte phases, which lower the overall ionic conductivity. In addition, the layers are prone to microcracks due to the CTE mismatch and resulting thermal stress between the phases [442–444]. Although the reduction of doped CeO_2 is a critical issue, their CTE matches with that of ferritic stainless steel, and suits well for metal supported lower temperature SOFCs. Also, doped CeO_2 is relatively chemically inert towards electrode materials and renders high power density ($\sim 400 \text{ mW/cm}^2$) at intermediate temperatures [445–457].

A large number of articles and reviews are available in literature presenting an elaborated account of doping and codoping materials tested so far. Some of the widely used doping and co-doping materials have been summarized in Table 7.

3.1.5. Effect of microstructure: grain boundaries and grain size

The total ionic conductivity of a polycrystalline electrolyte depends upon the contribution from both grain and grain boundary. The oxide ion conductivity in crystallographically mismatched grain boundaries is dependent on the amount of impurities or secondary phase segregation, extent of lattice mismatch, space charge, microcracks, etc. [481]. Furthermore, the positive potential of grain boundary core renders depletion of oxygen vacancy near the grain boundary region, which makes the grain boundaries highly resistive in the fluorite structured oxides. The separate resistive contributions of both grain interior and the grain boundaries towards the total resistivity can be obtained using ac impedance spectroscopy technique.

Fig. 32a shows the schematic of an impedance plot of an electroded polycrystalline sample (i.e., containing both grains and grain boundaries) of thickness L , and cross-sectional electrode area A . Its

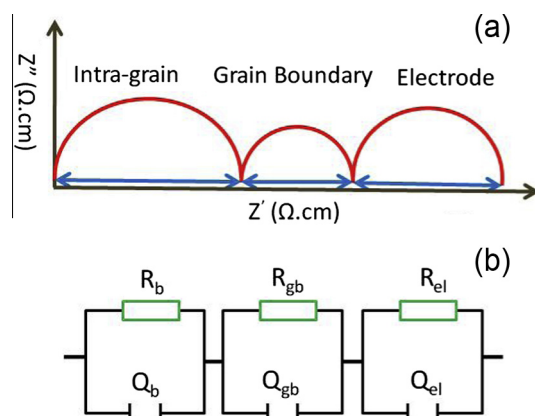


Fig. 32. Schematic of an impedance plot for an electroded polycrystalline sample with an analog equivalent electric circuit.

corresponding analog equivalent electrical circuit is shown in Fig. 32b, where the total electrical conductivity (σ_t) can be obtained from the following expression [482]:

$$\frac{1}{\sigma_t} = \frac{1}{\sigma_g} + \frac{1}{\sigma_{gb}} \quad (73)$$

where σ_g and σ_{gb} are the conductivities of grain interior and grain boundary, respectively. Both σ_g and σ_{gb} can be calculated from $\frac{1}{R} \frac{L}{A}$ using the respective resistance value. Although the grain boundary conductivity derived from the geometrical dimensions of the sample is a parameter of practical importance, a better insight will be gained by characterizing the specific grain boundary conductivity (σ_{gb}^{sp}), which takes into consideration the number and thickness of the grain boundaries present in the polycrystalline material. In order to determine σ_{gb}^{sp} , it is assumed that all the grains are cubic in shape with the edge length equals to d_g such that the magnitude is significantly larger than the grain boundary thickness δ_{gb} . Furthermore, it is assumed that the conduction along the length of grain boundaries is negligible. Then, the specific grain boundary conductivity can be determined as [483]:

$$\sigma_{gb}^{sp} = \frac{\sigma_{gb} \delta_{gb}}{d_g} \quad (74)$$

It has been reported that the grain boundary conductivity is lower than that of grain by 2–3 orders of magnitude [484]. The activation energies calculated for partially stabilized nanocrystalline ZrO_2 with 1.7–2.9 mol.% Y_2O_3 (grain size 25–50 nm) ranges between 1.00–1.04 eV and 0.84–0.81 eV for the grain boundary and grain interior, respectively [483,485]. During the high-temperature sintering process, the dopant cations are prone to diffuse from the grain interiors and segregate near the grain boundaries. The presence of impurity centers and depletion of oxygen vacancy near the grain boundary region enhance the resistance offered by grain boundaries to the oxide ion conduction across the grain boundaries [486]. Much research work has been devoted on limiting the impurities segregation at (and obtaining cleaner) grain boundaries and, thus, enhancing ionic conductivity. It has been shown that by giving specialized heat treatments, such as applying pressure during sintering or by adding certain additives, it is possible to lower the detrimental effect of impurity segregation on the conductivity [483,487–490]. On lowering the sintering temperature (from 1300 °C to 1200 °C) of $Ce_{0.8}Sm_{0.2}O_{1.9}$, Singh et al. [491] observed a drop in the total activation energy in both high and low temperature regimes from 0.827 to 0.691 eV and 1.03 to 0.80 eV, respectively. At 600 °C, the total ionic conductivity of $Ce_{0.8}Sm_{0.2}O_{2-\delta}$ pellet, sintered at 1200 °C, is reported to be 1.0×10^{-2} S/cm. This is attributed to a reduced solute segregation in samples sintered at 1200 °C. Moreover, samples sintered at lower temperatures possess submicrometer sized grains with increased grain boundary interfacial area. This as a result, spreads the segregated impurities over a large area which in turn reduces the thickness of the grain boundary and facilitates the oxide ion conduction. The reduction of sintering temperature up to 900 °C, without compromising with the sample density ($\geq 94\%$ relative theoretical density), can be achieved either by using nano sized starting powders due to their higher surface area or by the addition of sintering additives such as CoO , CuO , Mn_2O_3 , Fe_2O_3 , Bi_2O_3 , Cr_2O_3 , and NiO [492–496]. Fig. 33 shows the scavenging effect of such transition metal oxides in doped CeO_2 .

Ionic conductivity can also be enhanced by trapping the impurity elements and forming small amount of secondary phase at the grain boundaries [498]. However, even if there is no SiO_2 covering at the grain boundaries or the material is highly pure, the grain boundary conductivity still remains lower than that of the grain interior [483]. This is attributed to the space charge layer (or the positive potential of the grain boundary core, which is also considered as the intrinsic property in YSZ and CeO_2) that is further endorsed by acceptor dopant cation segregation in both YSZ and CeO_2 [499,500].

The effect of grain size on ionic conductivity was explained using a brick-layer model [501–503], where a polycrystalline ceramic sample was considered to be composed of grains, which are zones of high conduction, and are separated by poorly conducting and thin grain boundaries. Due to positive space-charge at the grain boundaries, oxygen vacancies and holes (or positive charge carriers) are depleted, while the electrons or acceptor dopants are accumulated near the grain boundary region. From the theoretical calculations, it was determined that the depletion of oxygen vacancies proportionate to the square of comparative enhancement in electrons, which as a result, gives rise to the

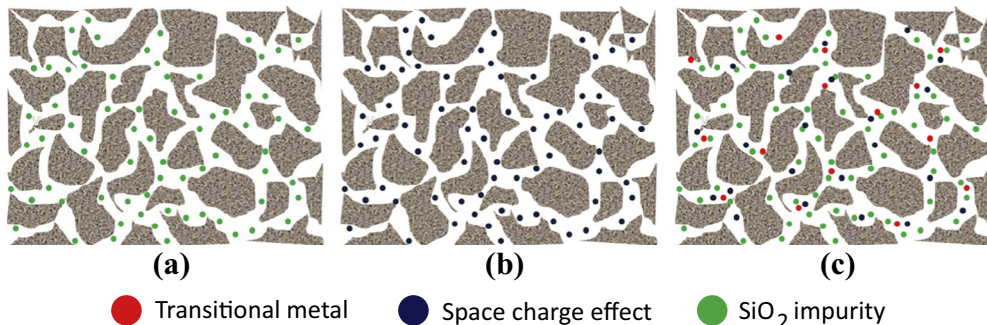


Fig. 33. Grain boundary conductivity can be modified by (a) impurities (siliceous layer) present in the grain boundary region of doped CeO_2 (b) the presence of space charge layer in the grain boundary of highly pure doped CeO_2 (99.99% purity) and (c) the addition of transition metal in doped CeO_2 which scavenges both the space charge and impurities. (Adapted from Ref. [497]).

n-type conductivity in the grain boundaries. Existence of positive space charge potentials in polycrystalline YSZ and CeO_2 is reported to be 0.3 and 0.25 eV, respectively [497]. Based on electrochemical and theoretical results, the presence of a poor conducting layer of thickness ~ 5 nm at the grain boundary interface is observed in the 2–8 mol.% doped microcrystalline ZrO_2 [487]. A comprehensive review article comprising of the grain boundary conduction in ionic conductors (oxides) was published by Guo and Waser [481].

Though increase in temperature can reduce the grain boundary resistance, however, the temperature at which the grain boundary blocking effect (when compared to grain resistance) becomes negligible is dependent on the dopant concentration. Nowick and his co-worker have reported the dopant concentration ≥ 15 mol.%, regardless of the dopant type, in order to achieve negligible grain boundary resistance [504,505]. Hong et al. [506] investigated the contribution of grain boundary towards the total resistivity of doped ceria materials, and reported that the negligible effect of grain boundary is achieved upon doping with 9 mol.% Gd_2O_3 , Sm_2O_3 or La_2O_3 at 725 °C, 775 °C and 650 °C, respectively.

Silica, which is commonly present as an impurity in most of the low grade ceramics, has detrimental effects on the ionic conductivity [507]. According to Badwal and Rajendran, the addition of 0.2 wt.% SiO_2 in YSZ lowers the grain boundary conductivity by a factor of 1.5 [488]. Other reports reveals an 100 times increase in the grain boundary resistivity due to the presence of SiO_2 , which either segregates along the grain boundary region or when present in large amount, forms a secondary phase of poor conductivity [504,505,508–511]. These secondary phases are typically located as isolated grains in the grain boundaries of the dominant $\text{Ce}_{0.8}\text{Gd}_{0.2}\text{O}_{2-\delta}$ phase [512].

Ivanova et al. [512] have investigated the silica scavenging effect in $\text{Ce}_{0.8}\text{Gd}_{0.2}\text{O}_{2-\delta}$ by the addition of La_2O_3 . An improved grain boundary conductivity is reported due to the formation of apatite type $\text{La}_{9.33}(\text{SiO}_4)_6\text{O}_2$ conducting phase in $\text{Ce}_{0.8}\text{Gd}_{0.2}\text{O}_{2-\delta}$ (containing additional lanthanum oxide and silica). The bulk resistivity of pure $\text{Ce}_{0.8}\text{Gd}_{0.2}\text{O}_{2-\delta}$ and apatite (lanthanum silicate) containing $\text{Ce}_{0.8}\text{Gd}_{0.2}\text{O}_{2-\delta}$ samples is almost similar. The decrease in the grain conductivity of silica containing ceramics is attributed to the loss of gadolinium from $\text{Ce}_{0.8}\text{Gd}_{0.2}\text{O}_{2-\delta}$ grains and the formation of low conducting gadolinium based apatite phase. Cho et al. [513] have investigated MgO as a scavenger material that can mitigate the harmful effect of SiO_2 in $\text{Ce}_{0.9}\text{Gd}_{0.1}\text{O}_{2-\delta}$ (10GDC). A significant increase in the grain boundary conductivity (45 times) is reported by the addition of 0.3–10 mol.% MgO in 10GDC containing 500 ppm SiO_2 as impurity. Fig. 34a compares the impedance spectra for the undoped and MgO doped $\text{Ce}_{0.9}\text{Gd}_{0.1}\text{O}_{2-\delta}$ (containing 500 ppm Si) samples at 450 °C. The grain resistivity of GDCSi (10GDC + 500 ppm SiO_2) specimens with 0 to 5 mol.% MgO is observed to be between 0.17 and 0.20 k Ω cm. At 450 °C, the grain boundary resistivity for pure $\text{Ce}_{0.9}\text{Gd}_{0.1}\text{O}_{2-\delta}$ is 0.2 k Ω cm and it rises to 10 k Ω cm for silica containing samples due to the formation of siliceous intergranular phase. The addition of 10 mol.% MgO leads to marginal increase in the grain interior resistivity, which is attributed to the generation of insulating MgO (and secondary phases) dispersed in the electrolyte matrix.

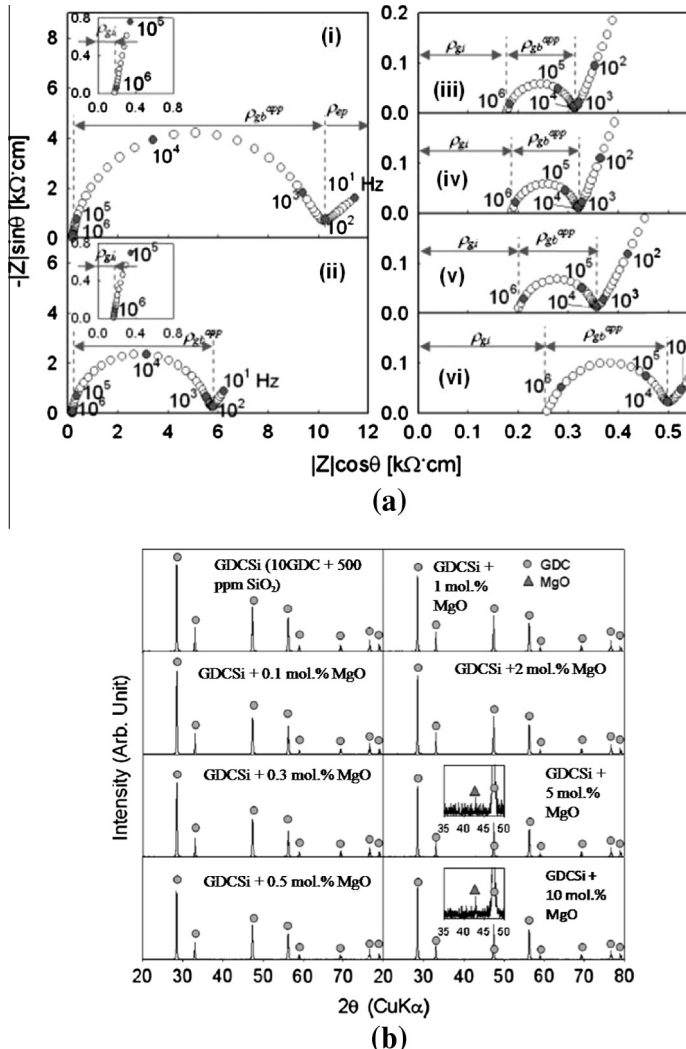


Fig. 34. (a) Complex impedance spectra measured at 450 °C for (i) GDCSi, (ii) GDCSi + 0.05 mol.% MgO, (iii) GDCSi + 0.3 mol.% MgO, (iv) GDCSi + 2 mol.% MgO, (v) GDCSi + 5 mol.% MgO, and (vi) GDCSi + 10 mol.% MgO samples (b) X-ray diffraction pattern collected on the powders heat-treated at 1500 °C for 4 h displaying the formation of secondary phases in the samples containing higher MgO content (>2 mol.%) ((a and b) reprinted with permission from Ref. [513], copyright Elsevier, 2007).

On addition of 0.05 mol.% MgO, the grain boundary resistivity decreases to 5.6 k Ω cm, and it becomes negligible (~0.14 k Ω cm) for samples with 0.3 mol.% MgO. The grain boundary resistivity value ranges between 0.13 and 0.15 k Ω cm for 0.3–0.5 mol.% MgO. However, on further addition of MgO, it can increase to 0.25 k Ω cm. In XRD analyses (shown in Fig. 34b), the presence of any secondary phase has not been detected for GDCSi containing less than 2 mol.% MgO. For 10 mol.% addition, a small MgO peak was observed. The lattice parameters were also found to be approximately similar at 5.418 Å for all the tested MgO containing compositions which indicates very low solubility of MgO in GDC (~0.1 mol.%). Most of the MgO appear as secondary phase at concentration ≥ 0.3 mol.%. Numerous reports are available in which the conductivity of the electrolyte has been improved by engineering the material at the grain boundary level, e.g., addition of Al₂O₃ [508,514–526], Fe₂O₃ [517,518], TiO₂ [519], CoO [520,521], CaO [522] as potential scavenging materials. This is done by

gathering a silica containing phase into a discrete configuration and dewetting of intergranular phase by crystallization [523].

3.2. $\delta\text{-Bi}_2\text{O}_3$ - and $\text{Bi}_4\text{V}_2\text{O}_{11}$ -based Ceramics

In the category of fluorite structure based oxides, $\delta\text{-Bi}_2\text{O}_3$ is perhaps known as the best oxide ion conductor [524,525]. It not only exhibits high ionic conductivity, but also shows good electrocatalytic activity for O_2 and O^{2-} interconversion at low temperatures (300–350 °C). Bi_2O_3 occurs in two stable polymorphs monoclinic α and cubic δ , where the high conductivity is shown by δ -phase. The $\delta\text{-Bi}_2\text{O}_3$ phase is stable from 730 °C to 804 °C (m.p.), and exhibits oxide ion conductivity which is nearly 1–2 orders of magnitude higher than that shown by stabilized ZrO_2 [524]. The high temperature $\delta\text{-Bi}_2\text{O}_3$ can be stabilized to room temperature, but it requires addition of certain dopant cations i.e., Y^{3+} , La^{3+} , Er^{3+} , etc. [526,527]. However, upon cooling below 600 °C, a first order vacancy order-disorder transition takes place, which leads to the drop in conductivity by ~3 orders of magnitude [528].

The basic structure of $\delta\text{-Bi}_2\text{O}_3$ is shown in Fig. 35a which comprises of two partially occupied O sites: 8c (1/4, 1/4, 1/4) and 32f(x, x, x) with $x \approx 0.3$ [529]. The occupancy of the 32f sites has been reported to increase with aging, which, in turn, increases the local vacancy ordering [419,526,530]. To stabilize this structure at room temperature, doping with 15–42 mol.% of rare earth and/or donor dopant cations, such as, W^{6+} or Nb^{5+} have been investigated by various researchers [419,531–537]. According to Verkerk and Burggraaf [537], the room-temperature stabilization of high temperature cubic phase can be achieved by contracting the structure with the aid of doping with smaller sized cations. Large ionic radii mismatch between Bi^{3+} and dopant cation can be compensated by small amount of dopant concentration for stabilizing the cubic phase. Conversely, if the size mismatch is small, then the large concentration of dopant is required. However, doping has been observed to lower the overall conductivity especially at low temperatures when compared with parent compound. At a fixed doping level, the oxide ion conduction increases with the increasing size of Ln^{3+} because of the relatively large size of Bi^{3+} . But, it may be noted that the minimum stabilization limit that is required to retain the fluorite structure also increases with the size of lanthanide cation, which subsequently lowers the maximum oxide ion conductivity [538]. According to Takahashi et al. [527,533], the partial substitution at Bi-sites (e.g., 25–43 mol.% Y_2O_3) stabilizes the δ -phase over a temperature range ~500–700 °C. Various dopant for Bi_2O_3 , including rare earths Gd, Ho, Nd, Sm, Y, Dy, Er and higher valency cations, e.g., W or Nb, have been investigated in this regard [441,480,524,525,533,539]. For example, Er -and Y-doped Bi_2O_3 , namely, $\text{Bi}_{1-x}\text{Er}_x\text{O}_{1.5}$ ($x \sim 0.20$) and $\text{Bi}_{1-x}\text{Y}_x\text{O}_{1.5}$ ($x = 0.23–0.25$) exhibit high ionic conductivity of $\sim 3.7 \times 10^{-1} \text{ S/cm}$ and $\sim 2.3 \times 10^{-2} \text{ S/cm}$ at 700 °C and 500 °C, respectively [540,541].

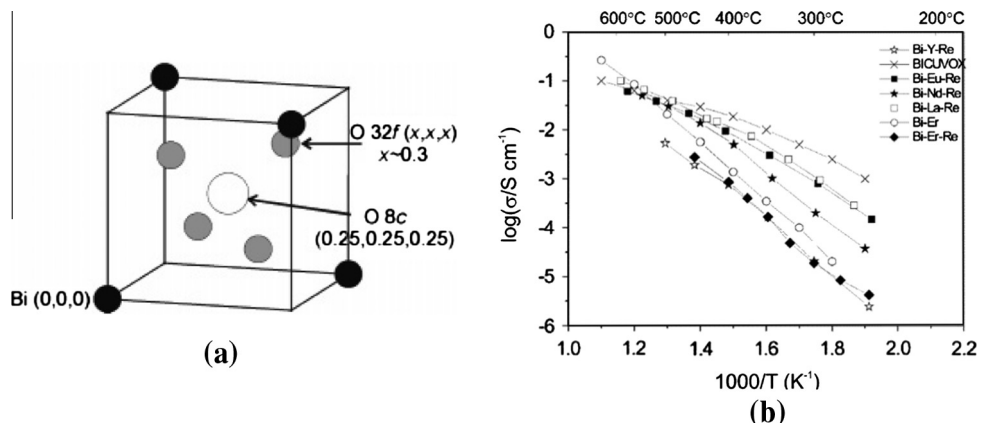


Fig. 35. (a) Part of $\delta\text{-Bi}_2\text{O}_3$ unit cell showing O positions. (b) Variation of conductivities with temperature. The legend indicates the metals in the samples for $\text{Bi}_{12.5}\text{M}_{1.5}\text{ReO}_{24.5}$ (where RE = La, Nd, Eu, Er, and Y); Bi-Er corresponds to $(\text{Bi}_2\text{O}_3)_{0.8}(\text{Er}_2\text{O}_3)_{0.2}$ and BiCUVOX is the layered phase $\text{Bi}_2\text{V}_{0.9}\text{Cu}_{0.1}\text{O}_{3.35}$. ((a and b) Reprinted with permission from Ref. [412].

Table 8

Summary of structural and conductivity data of few rare earth doped $\text{Bi}_{12.5}\text{M}_{1.5}\text{ReO}_{24.5}$ electrolytes, where, M = La, Nd, Er and Y. (a) and (b) Reprinted with permission from Ref. [412]).

	Bi-La-Re	Bi-Nd-Re	Bi-Er-Re	Bi-Y-Re
σ (S/cm; 300 °C)	1.10×10^{-3}	2.04×10^{-4}	1.95×10^{-5}	1.95×10^{-5}
Eact (eV; 250–400 °C)	0.81	0.94	1.08	1.08
Unit cell size (Å; 25 °C)	5.6456(3)	5.6184(4)	5.5689(5)	5.575(1)
32fx	0.356(4)	0.379(3)	0.367(3)	0.367(3)
32f occupancy	0.064(4)	0.047(2)	0.049(3)	0.051(3)

The main challenge associated with stabilized Bi_2O_3 based materials is their tendency to reduce to Bi metal under reducing conditions [537,542,543]. Other disadvantages, such as, volatilization of Bi_2O_3 at moderate temperature, corrosion, and poor mechanical strength restrict their practical applicability. To meet these challenges, a bilayer structure approach was adopted with Bi_2O_3 on the cathode side, and a more stable electrolyte layer (for example doped CeO_2) on the anode side [544].

Punn et al. [412] reported the ionic conductivity of the stabilized δ -cubic phase in $\text{Bi}_{12.5}\text{Ln}_{1.5}\text{ReO}_{24.5}$ (where Re stands for Rhenium and not for rare earth element). It was shown that the δ -phase can be stabilized using the larger sized dopant cations [412]. Furthermore, at 300 °C, the conductivity of $\text{Bi}_{12.5}\text{La}_{1.5}\text{ReO}_{24.5}$ is reported to be an order of magnitude higher than phases stabilized by co-doping Dy/W, which are known to exhibit the highest conductivities in doped Bi_2O_3 category [539]. In addition, the activation energy required for migration of oxide ion for samples containing larger sized lanthanides is lower at low temperatures compared to those of stabilized phases: e.g., the activation energy is 0.81 eV and 1.17 eV, for $\text{Bi}_{12.5}\text{La}_{1.5}\text{ReO}_{24.5}$ and $\text{Bi}_{1.6}\text{Er}_{0.4}\text{O}_3$, respectively, at low temperatures (200–400 °C) [412]. A concise summary of structural and conductivity data of few rare earth doped $\text{Bi}_{12.5}\text{M}_{1.5}\text{ReO}_{24.5}$ electrolytes is listed below in Table 8. Consequently, Fig. 35b shows the comparison of the ionic conductivity reported by Punn et al. for $\text{Bi}_{12.5}\text{M}_{1.5}\text{ReO}_{24.5}$, $(\text{Bi}_2\text{O}_3)_{0.8}(\text{Er}_2\text{O}_3)_{0.2}$, and $\text{Bi}_2\text{V}_{0.9}\text{Cu}_{0.1}\text{O}_{5.35}$ phase [412]. It can be observed that using $\text{Bi}_{12.5}\text{M}_{1.5}\text{ReO}_{24.5}$ electrolytes, high oxide ion conductivity can be achieved at lower temperatures.

Other bismuth oxide based electrolyte materials includes γ - $\text{Bi}_4\text{V}_2\text{O}_{11}$ (parent compound of BIMEVOX materials) which belongs to Aurivillius series. The BIMEVOX (Bi-Bismuth, Me-additive metal, V-Vanadium, Ox-Oxygen) family or doped bismuth vanadates are the new generation of electrolytes based on Bi_2O_3 .

The parent compound or γ - $\text{Bi}_2\text{VO}_{5.5}$ itself exhibits high ionic conductivity. The low temperature stabilization of tetragonal γ - $\text{Bi}_2\text{VO}_{5.5}$ can be obtained by partial substitution of other metals, such as Cu, Ni, Zn, Fe, Co, and Mg, for Vanadium, [524,545–549]. These materials are also reported to self transform into electrode material under polarization which enable them to be used without other electrode materials [549]. The aurivillius series based crystal lattice comprises of alternating layers of $\text{Bi}_2\text{O}_2^{2+}$ and perovskite-like slab of $\text{VO}_{3.5}^{2-}$. Ionic conduction occurs because of oxygen vacancies existing in perovskite layers (as shown in Fig. 36). $\text{Bi}_2\text{V}_{1-x}\text{Me}_x\text{O}_{5.5-\delta}$ (where, Me = Cu, Ni, and $0.07 \leq x \leq 0.12$) type solid solutions have been reported to exhibit highest oxide ion conductivity [545,550,551].

However, highly reactive nature and poor mechanical strength of these materials pose the main challenges in their use [480]. It has been shown that these issues can be minimized by the development of multilayered electrode structure [552]. The multilayered cell consists of a Bi_2O_3 based ionic conducting layer on top of another material which can provide good mechanical support and protection against reduction [553]. Nevertheless, these materials also possess high thermal expansion coefficients which further complicate their usage in practical application.

3.3. Pyrochlores based electrolytes

Materials possessing pyrochlore structure with a general formula of $\text{A}_2^{3+}\text{B}_2^{4+}\text{O}_7$ structure have been actively investigated for ionic conduction since 1960 [474,475,554–562]. Pyrochlore is a superstructure of fluorite structure (AX_2) where A- and B-site cations are ordered and one eighth of the anions are missing (to form vacant sites as shown in Fig. 37a) [563]. The larger-sized A³⁺ resides at 16d site

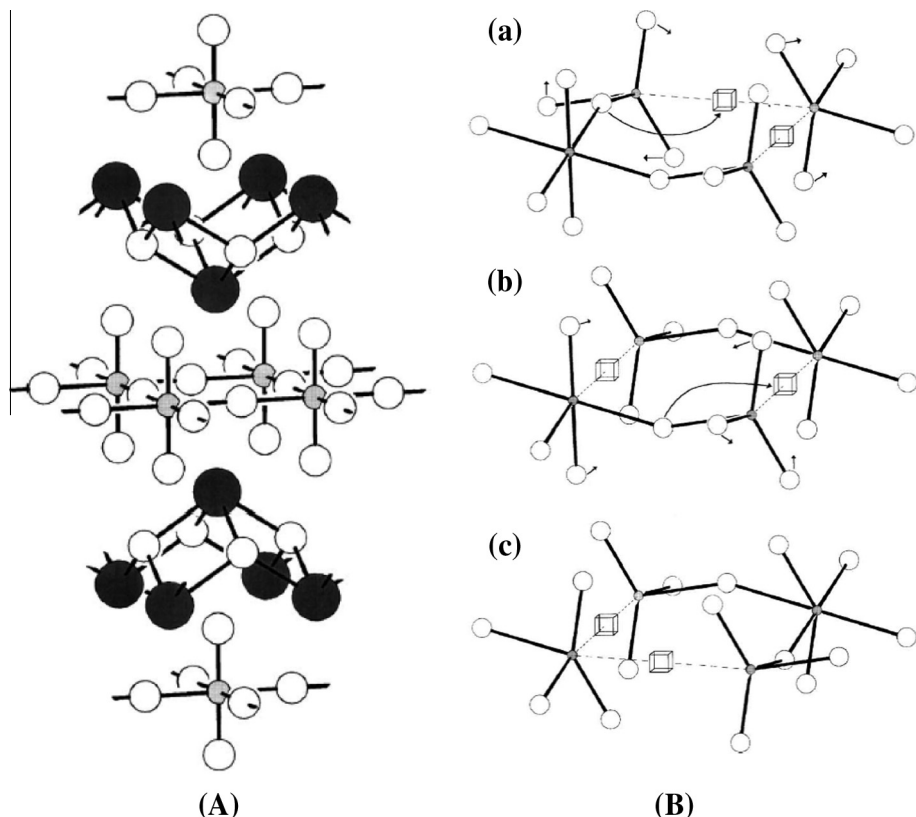


Fig. 36. (A) Idealized structure of $\gamma\text{-Bi}_4\text{V}_2\text{O}_{11-\delta}$. Dark, shaded and open circles represent Bi, V and O atoms, respectively. Vacancies in the vanadate layer are not shown (B) Model for the conduction mechanism in the vanadate layer of divalent substituted $\gamma\text{-BIMEVOX}$. Four vanadium polyhedra are shown, with V and O atoms as shaded and open circles, respectively; vacancies are indicated as open cubes. (a) Initial state showing one octahedron and three tetrahedral, (b) intermediate state with two five co-ordinate polyhedral and two tetrahedral, (c) final state of one octahedron and three tetrahedral ((A and B) reprinted with permission from Ref. [545], copyright Elsevier, 2003).

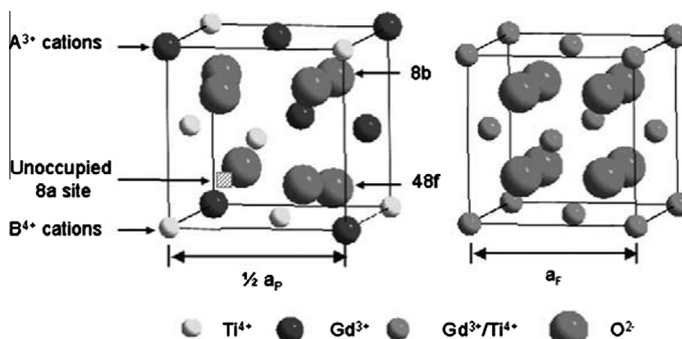


Fig. 37. Structures of pyrochlore and defective fluorite. (a) One eighth of the unit cell of the ordered pyrochlore structure showing specific positions of the cations and anions (B^{4+} cation at the origin). (b) Cation and anion disordering causes the transformation of the ordered pyrochlore to a defective-fluorite structure. The occupancy for each anion site in the defective fluorite structure is 0.875. (Reprinted with permission from Ref. [561], copyright Elsevier, 2003).

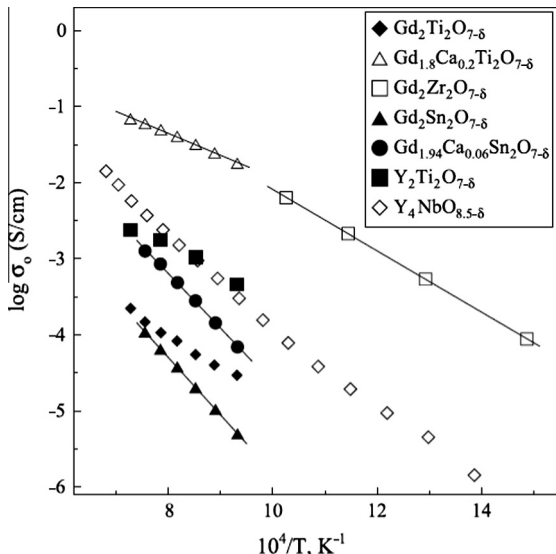


Fig. 38. Oxide ion conductivity of selected pyrochlores as a function of temperature. Total ionic conductivity data of fluorite-type $\text{Y}_4\text{NbO}_{8.5-\delta}$ is also shown for comparison. (Reprinted with permission from Ref. [409], copyright Elsevier, 2004).

and its coordination number is 8, while B^{4+} occupies 16c sites. The coordination number of B^{4+} is 6 and is located at the center of distorted octahedron. The 48f oxide ion is coordinated with two B^{4+} and two A^{3+} cations, whereas 8b oxide ion is in tetrahedral coordination with only A^{3+} cation. The vacant 8a interstitial site is coordinated with four B^{4+} ions (shown in Fig. 37a). It is reported that on reducing the size of A-site cations, pyrochlore to fluorite transition is favored (at elevated temperatures up to 1370–2227 °C) [538]. In general, the degree of cation disordering is related to the ionic radius ratio between A- and B-site cations [564]. This significantly influences the formation of anion Frenkel defect [563]. On reducing the size of the cation, a structural transformation is induced from a fully ordered pyrochlore lattice $\text{A}_2\text{B}_2\text{O}_7$ to a completely disordered anion deficient defective fluorite M_4O_7 (where M can be A or B) [563]. With ionic radius ratio ($r_{\text{A}}/r_{\text{B}}$) of 1.46, the $\text{Gd}_2\text{Zr}_2\text{O}_7$ lies at the boundary between an ordered pyrochlore and the defective fluorite structure. The order-disorder transition is also found to be either thermally driven [565] or brought about via irradiation [563].

The oxide ion conductivity exhibited by pyrochlore based oxides (e.g., $\text{Gd}_2\text{Zr}_2\text{O}_7 \sim 5 \times 10^{-2} \text{ S/cm}$) is comparable to that of YSZ, e.g., at 1000 °C. The ionic conduction in these materials can be tailored either by chemical substitution [555] or thermal treatment [558]; e.g., substituting Zr^{4+} for Ti^{4+} in $\text{Gd}_2(\text{Ti}_{1-x}\text{Zr}_x)_2\text{O}_7$ from $\text{Gd}_2(\text{Zr}_{0.3}\text{Ti}_{0.7})_2\text{O}_7$ to $\text{Gd}_2\text{Zr}_2\text{O}_7$ results in conductivity enhancement by two orders of magnitude [564]. The increase in conductivity is attributed to the disordering occurring in both cation and anion sites in the ordered pyrochlore structure [567–569]. Among various pyrochlore compositions, $\text{Gd}_{2-x}\text{Ca}_x\text{Ti}_2\text{O}_{7-\delta}$ ($x = 0.20$) is reported to exhibits the highest conductivity [555,570]. The comparison of conductivities of various pyrochlore materials is shown in Fig. 38.

Substitution of Gd^{3+} with Ca^{2+} in $\text{Gd}_2\text{Ti}_2\text{O}_{7-\delta}$ increases the p-type conductivity and lowers the n-type electronic conductivity of the material [570]. However, electron transference number of $(\text{Gd}, \text{Ca})_2\text{Ti}_2\text{O}_{7-\delta}$ in air is reported to be on the higher side of acceptable values for solid electrolytes. In addition, few compositions in this category also possess ionic transference number lower than stabilized ZrO_2 . These pyrochlore materials are most likely to find application as protective films on LaGaO_3 - or CeO_2 -based electrolytes. Furthermore, with a moderate CTE ($\sim 10.4\text{--}10.8 \times 10^{-6}/\text{K}$), these materials possess good compatibility with other cell components [409].

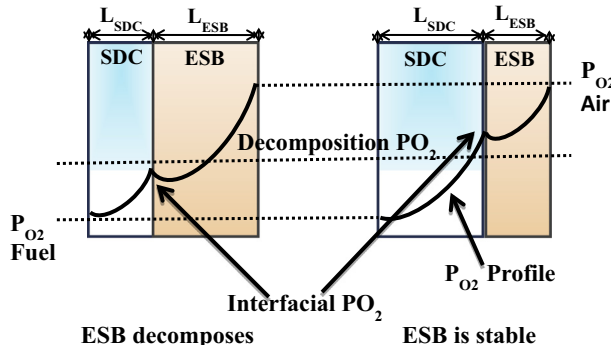


Fig. 39. Schematic representation of an ESB/SDC bilayer electrolyte showing the effect of relative thickness on interfacial P_{O_2} . (Adapted from Ref. [544]).

3.4. Hetero-structured bi-, tri- and multiple-layered composite electrolytes

In order to prevent the decomposition of electrolyte materials, such as Bi_2O_3 , and the reduction of doped CeO_2 in low P_{O_2} , bilayered-structure concept have been explored [553]. In this approach, both types, viz., bilayered structure comprising of a high conductivity oxide layer protected by a relatively low conducting YSZ layer or that comprising of both layers of high conductivity, have been investigated [571]. Bilayered structure of the latter type, e.g., $Sm_{0.2}Ce_{0.8}O_{1.9}$ (SDC)/ $Er_{0.2}Bi_{0.8}O_{1.5}$ (ESB) (fabricated by Park et al. [544]) exhibited total conductivity slightly higher than that of a single layer of SDC in the temperature range of 600–800 °C. Wachsman et al. [553] reported an OCP of 1003 mV at 500 °C and a overall increase from 90 to 160 mV depending on temperature compared to the SDC electrolyte. The OCP was reported to be stable for 1400 h of operation. Furthermore, SOFC button cells based on bilayered structure electrolyte, results in 33% increase in power density when compared to that of the cells based on single electrolyte layer [553,572]. The improvement in efficiency is attributed to:

- (i) high ionic conductivity of SDC as it acts as an efficient electrolyte as well as an anode due to its mixed ionic-electronic nature at low P_{O_2} ,
- (ii) protective barrier to electronic flux provided by ESB,
- (iii) SDC layer prevents decomposition of ESB layer at very low P_{O_2} , provided the relative thickness is well adjusted as shown in Fig. 39.

Suzuki et al. [573] investigated the performance of microtubular SOFCs using the trilayered structure electrolyte of Gd_2O_3 -doped CeO_2 – Sc_2O_3 stabilized ZrO_2 – Gd_2O_3 -doped CeO_2 which was fabricated via multiple dip coating and co-firing technique. At 650°C, the power density obtained from these cells was reported to be 0.35 W/cm² with 0.7 V of OCP [573]. Zhonghe et al. [574] investigated the performance of button cells based on $Gd_{0.1}Ce_{0.9}O_{1.95}/La_{0.45}Ce_{0.55}O_{2-\delta/2}/La_{0.9}Sr_{0.1}Ga_{0.8}Mg_{0.2}O_{2.85}$ trilayered electrolyte, fabricated using citric acid assisted combustion method. The power density value obtained from these cells was reported to be 0.72 W/cm² with an OCP of 0.814 V at 800 °C. However, the performance of these cells was not stable [574].

Extensive research work has been dedicated to reduce the thickness of YSZ electrolyte (~10–50 μm) which has reduced the ohmic resistance of the cells and have achieved low temperature workability [575–577]. However, there are certain limitations to this approach. Electrolytes will not serve the purpose below a certain thickness because the surface exchange reaction at the electrode/electrolyte interface, rather than the diffusion of oxide ion through the electrolyte, becomes the rate determining step. Moreover, fabrication of a ceramic electrolyte layer of thickness less than 1 μm will introduce small pinholes or cracks which open up the possibilities of cross mixing of gases and

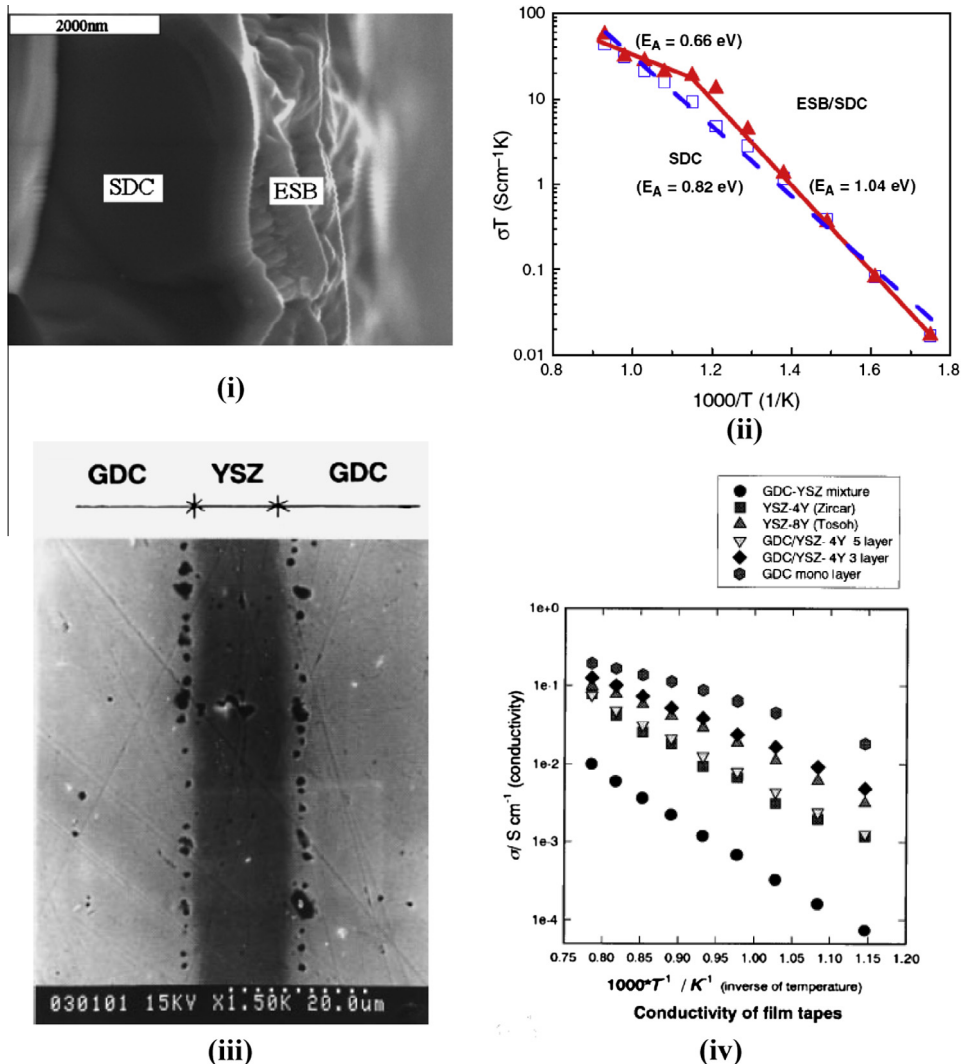
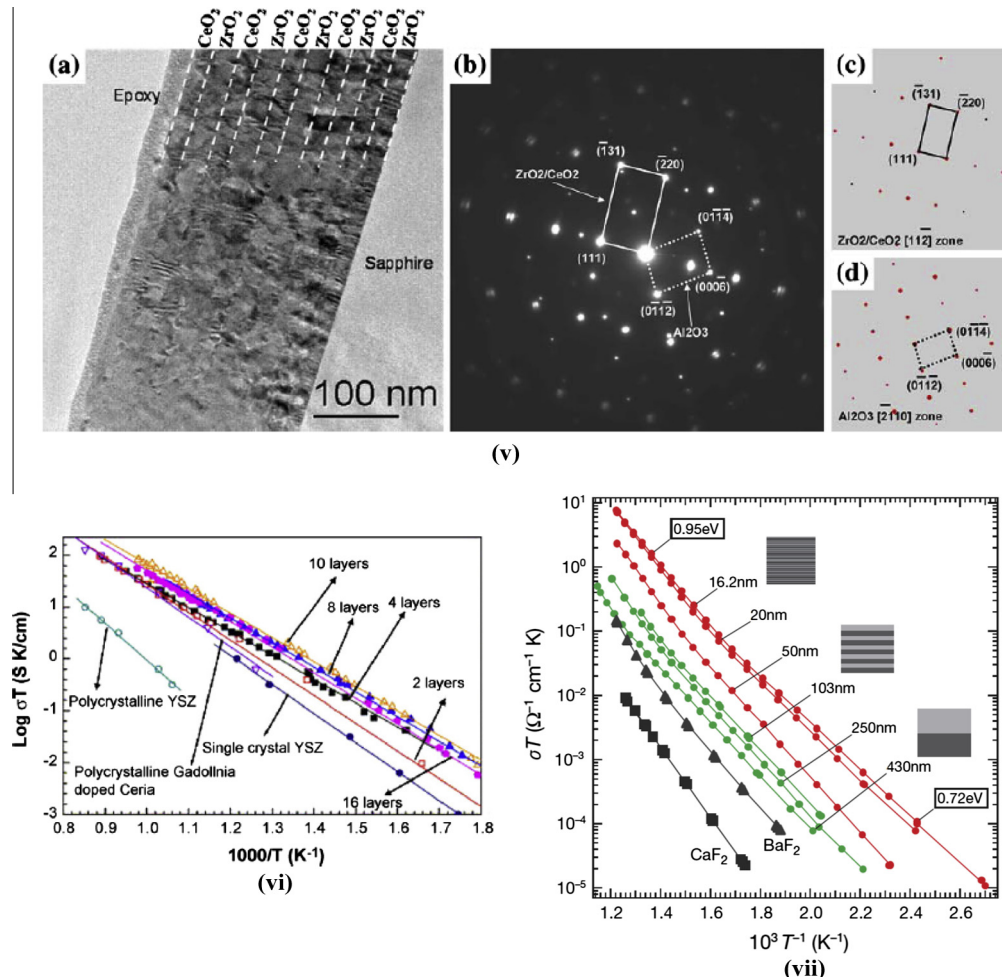


Fig. 40. (i) Scanning electron micrograph showing cross-section of the ESB film on a dense SDC substrate via pulsed laser deposition; (ii) conductivity in air of ESB/SDC bi-layered structure (ESB film thickness: 0.2 μ m) ((i) and (ii) reprinted with permission from Ref. [544], copyright John Wiley and Sons, 2005). (iii) Scanning electron micrograph of the interface of GDC/YSZ/GDC tri-layer composite electrolyte. (iv) Conductivity of composite films as a function of the inverse of temperature, viz., GDC-YSZ mixture film, YSZ-4Y (Zircar), YSZ-8Y (Tosoh), GDC-GDC/YSZ-GDC/GDC/GDC/GDC-4Y 5 layers composite, GDC-GDC/YSZ-GDC-4Y 3 layers composite, GDC mono layer ((iii) and iv) reprinted with permission from Ref. [595], copyright Springer, 1997). (v) (a-d) (a) Cross-sectional TEM images of the 10 layers alternating Gd-doped ZrO_2 and CeO_2 multilayer thin film. (b) Selected area electron diffraction pattern of the film with the basic diffraction vectors indicated for CeO_2/ZrO_2 and α - Al_2O_3 . (c) The schematic of the diffraction pattern of CeO_2/ZrO_2 from (1 1 2) zone axis. (d) The schematic of the diffraction pattern of α - Al_2O_3 from (0 1 1 2) zone axis. (v and vi) Reprinted with permission from Ref. [597], copyright Springer, 2009). (vi) The dependence of the ionic conductivity on the number of layers keeping the constant thickness of the film. Arrhenius plots for the oxide ionic conductivity of 50 layer Gd-doped ZrO_2 and CeO_2 multilayer thin film. The data from the polycrystalline YSZ, polycrystalline Gd-doped ceria, and single crystal YSZ film are also shown for comparison (Reprinted with permission from Ref. [599], copyright AIP Publishing LLC, 2005 that includes that back reference of [600]). (vii) Parallel ionic conductivity in the CaF_2/BaF_2 heterolayers for the various layer thicknesses (the individual layer thicknesses ranging from 16.2 nm to 430 nm with the overall thickness ~500 nm). As the layer thickness decreases from 430 nm to 16.2 nm, the overall parallel conductivity increases by ~2 orders of magnitude in the measured temperature range. (Reprinted with permission from Ref. [598], copyright Nature Publishing Group, 2000).

**Fig. 40 (continued)**

consequently lowering of cell output. Ceria based electrolytes with layer thickness of 5–30 μm are appreciably workable at intermediate (600–800 °C) and low (300–600 °C) temperature and for longer durations (2000 h) [578]. However, thin ceria based electrolyte layers are reported to exhibit mixed ionic-electronic conduction, which further degrades the power density of the cell [579]. Moreover, a very thin electrolyte layer does not possess sufficient mechanical strength to withstand fuel environment. Thus, in order to meet these challenges, a bi-layered structure approach is adopted in which an ionic conducting YSZ is used in combination with mixed ionic-electronic conducting doped ceria as a bi-layer supported by an electrode material [580]. Some of the noteworthy attempts to fabricate bi-layered electrolytes are YSZ/doped CeO_2 [581–585], $\text{Sc}_{0.2}\text{Ce}_{0.01}\text{Zr}_{0.79}\text{O}_{1.9}/\text{Gd}_{0.1}\text{Ce}_{0.9}\text{O}_{1.95}$ [586], $\text{Sm}_{0.2}\text{Ce}_{0.8}\text{O}_{1.9}$ (SDC)/ $\text{Er}_{0.2}\text{Bi}_{0.8}\text{O}_{1.5}$ [544], and $\text{Sm}_{0.2}\text{Ce}_{0.8}\text{O}_{1.9}/8\text{YSZ}$ [587]. Table 9 reports the results for various composites and combinations in bi-layered/multilayered electrolytes, where a significant improvement in the cell performance is accomplished. In this regard, pulse laser deposition (PLD) technique was found to be successful in eliminating the interactions between layer components in the bi-layered electrolyte during fabrication. The cells fabricated using this technique have been reported to exhibit the best performance [544].

Table 9

Summary of fabrication and performance of some hetero-structured bi-, tri-, and multiple-layered composite electrolytes.

System	Purpose	Performance	Remarks	Reference
<i>Composites</i>				
Gd-doped CeO_2 (GDC) manganese/cobalt-doped alumina (nanocomposite)	To reduce the electronic conductivity through incorporation of electron-trapping inclusions	10^{-3} – 10^{-4} S/cm (conductivity)	GDC acts as the oxide conductive phase and Mn/ Co-doped Al_2O_3 as the electron trapping nano-inclusion. Mn- and Co-oxide additions create the necessary electron-trapping sites at the interface	[588]
$(\text{CeO}_2)_{0.8}(\text{SmO}_{1.5})_{0.2}$ – $(\text{ZrO}_2)_{0.92}(\text{Y}_2\text{O}_3)_{0.08}$ (composite)	YSZ matrix is used to block the electronic conduction caused by the reduction of SDC	1.03 V (OCP)	A dual phase electrolyte microstructure with coarse SDC grains (350–840 μm) dispersed in YSZ matrix. This structure prevents the electronic conduction by SDC (arising due to its reduction) because of insulation by immediate YSZ matrix	[589]
$(\text{CeO}_2)_{0.6}(\text{SmO}_{1.5})_{0.2}(\text{GdO}_{1.5})_{0.2}$ [($\text{Ce}_6\text{S}_2\text{G}_2$)] + Al_2O_3 (composite)	To improve sintering behavior and electrical properties by adding Al_2O_3	0.8–1.2 V (OCP) 200 mW/cm ² (power density)	Maximum of sintered density (5.61 g/cm ³), porosity (22.2%) and highest performance (power density = 200 mW/cm ²) was achieved upon doping $\text{Ce}_6\text{S}_2\text{G}_2$ with 10 wt.% Al_2O_3	[590]
Ceria-based composites (CBC)	To achieve co-ionic (oxide ion and proton) conduction	0.1 S/cm at 600 °C (conductivity)	Consists of a doped ceria (Sm doped ceria) host phase, Exhibit oxide on/proton co-ionic conduction	[591]
YSZ/YDC composite	To introduce an electron blocking layer of YSZ in ceria based solid solutions which not only reduces the cell performance, but also causes mechanical instability	Power density of 122 mW/cm ² was achieved at 285 mA/cm ² (800 °C)	YSZ film was coated on a YDC (yttria-doped ceria) substrate via polymeric YSZ sol using a sol-gel spin coating method followed by heat-treatment at 1400 °C for 2 h. The YSZ film acts as an electron blocking layer	[592]
SNDC (Sm ³⁺ and Nd ³⁺ co-doped ceria)-binary carbonates (Li_2CO_3 – Na_2CO_3) composite	To enhance the conductivity at high temperature	0.01 S/cm at 481 °C (with 20 wt.% carbonates in the electrolyte)	Prepared by citric-nitrate combustion synthesis route and co-fired process	[593]

Bi-/trilayered structures

SDC-ESB bilayer (Fig. 40i and ii)	To demonstrate that bilayered structure exhibits higher OCP approaching the theoretical value and exhibits stability against reduction of the electrolyte by H ₂ compared to single layered electrolytes	800–840 mV (500–800 °C) (OCP of SDC) 870–1000 mV (500–800 °C) (OCP of SDC/ESB bilayer)	A 90- to 160-mV increase in OCP of the SDC-ESB bilayer electrolyte was obtained compared to a single layer SDC electrolyte. The OCP was found to be stable for 1400 h of operation. The power density of the button cells based on SDC-ESB bilayer electrolyte was 35% greater than the cell based on single layer SDC SOFCs under identical conditions. No formation of low conducting phase at the interfaces of the bilayer Formation of ZrO ₂ –Sc ₂ O ₃ –CeO ₂ –Gd ₂ O ₃ solid solution takes place at interface which is low conducting phase; a cell bundle of 5 × 5 cell sequence (each tube has 1.6 mm φ, 1 cm length), with the volume of 1 cm ³ is expected to generate 1.9 W at 0.7 V and 700 °C	[544] [586]
GDC/ScSZ bilayer Electrolyte (Microtubular SOFC)	Application of the LSM-GDC activation layer in order to decrease the electrode polarization resistance (~5.3 and 1.2 × cm ² at 600 and 700 °C, respectively)	15 mW/cm ² , 73 mW/cm ² , 230 mW/cm ² , and 378 mW/cm ² at 500 °C, 600 °C, 700 °C, and 750 °C, respectively		
YSZ/SDC bilayer electrolyte	Insertion of doped CeO ₂ between YSZ and LSCF to avoid the interfacial reaction	Power densities > 0.6 W/cm ² at 700 °C were obtained for bilayered electrolyte with 4 μm-thick YSZ and ca. 1 μm-thick SDC films	The bilayered electrolytes were fabricated using electrophoretic deposition of YSZ in ethanol followed by SDC in PE-added ethanol onto the composite substrates. Delamination between YSZ and SDC films was avoidable by reducing the thickness of the SDC films inserted as a barrier layer to ca. 1 μm	[594]
GDC-YSZ-GDC (sandwich structured composite) (Fig. 40iii and iv)	To offer high ionic and low electronic conductivity; a very thin zirconia film to minimize the electronic current of ceria without affecting the ionic conductivity of GDC	~0.1 S/cm (similar to 8YSZ)	GDC-YSZ-GDC sandwich electrolytes were prepared by a wet co-fire process with the optimization of binder content and temperature program; de-lamination between YSZ and GDC films was overcome by the formation of a solid solution phase at the interface of the two films, but the latter degrades the electrical conductivity	[595]
YSB/YSZ/YDC Trilayer	Bi ₂ O ₃ and doped CeO ₂ to reduce interfacial reaction resistances; The YSZ layer provides mechanical strength, prevents electronic conduction across the structure, and protects the Bi ₂ O ₃ layer from reducing fuel gas	110 mW/cm ² in air and water-saturated H ₂ at 750 °C	The three layers were deposited on porous alumina by reactive magnetron co-sputtering method. The cell resistance was reduced by a factor ~3. Consequently, an increase in power density over a YSZ electrolyte by a factor ~3 over a single-layer YSZ electrolyte and by a factor ~6 over previously reported RF- sputter-deposited cells operated at the same temperature	[596]

(continued on next page)

Table 9 (continued)

System	Purpose	Performance	Remarks	Reference
<i>Alternating multilayers and hetero-multilayered electrolytes</i>				
GDC-zirconia multilayered electrolyte (Fig. 40v and vi)	It is indicated that multi-layer thin films of nanometer length scale may lead to an enhancement of oxide ionic conductivity	Activation energy for ionic conductivity (0.83 eV) which is lower than that of single crystalline YSZ (1.04 eV), and Gd-doped ceria (0.97 eV)	Multilayer thin film of Gd-doped ceria and zirconia have been grown by sputter-deposition on $\alpha\text{-Al}_2\text{O}_3$ (0 0 1) substrates; films deposited at a higher temperature normally possess a smooth surface as compared with that deposited at room temperature; The conductivity measured on the multi-layer films are significantly higher than that of either single crystal YSZ thin film or polycrystalline YSZ, or trivalent element doped ceria	[597]
CaF ₂ and BaF ₂ heterolayered Films (Fig. 40vii)	Heterolayers show conductivities higher than that of pure CaF ₂ or BaF ₂ films (and also higher than (Ba, Ca)F ₂)	~1 S/cm (1000 °C)	Heterolayered films composed of CaF ₂ and BaF ₂ by molecular-beam epitaxy method; exhibit ionic conductivity (parallel to the interfaces) increasing proportionally with interface density for interfacial spacing greater than 50 nm. If the spacing is reduced further, the boundary zones overlap and mesoscopic size effect was observed	[598,599]

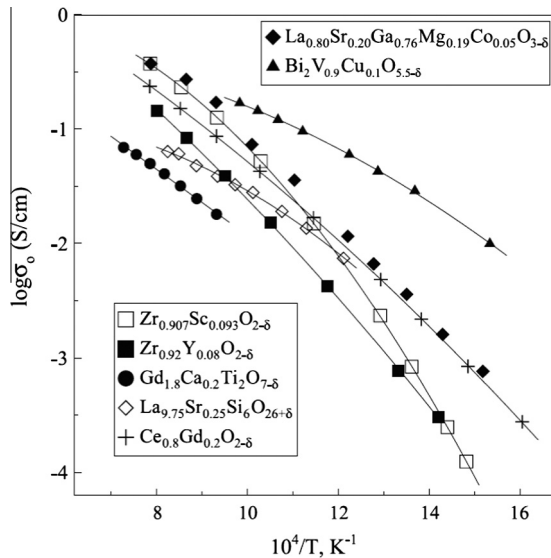


Fig. 41. Oxide ion conductivity of various solid-electrolyte materials. (Reprinted with permission from Ref. [409], copyright Elsevier, 2004).

3.5. Perovskite and related intergrowth structures (LaGaO_3 , Brownmillerites, La-MOX and Apatites)

3.5.1. Perovskite-based electrolytes

Perovskite type oxides with the chemical formula of ABO_3 were investigated as ionic conductors by various groups [601,602]. They exhibit exceptionally high ionic conductivity better than most of the other oxide ion conductors (shown in Fig. 41) [408].

Earlier, it was assumed that the oxide ion diffusion takes place by a rapid transportation of vacancies through a conventional hopping mechanism. However, no experimental evidences were present to support this statement. Cherry et al. [603] carried out the mapping energy profiles based on the calculation of defect energy as the oxide ion migrates along its diffusion path and vacancy relaxation occurs at lattice position. A saddle point configuration was proposed in which the energy barrier (or activation energy) to the oxide ion migration was derived. In this configuration, the migrating ion is expected to migrate through the center of triangle formed by two La^{3+} A-site cations and one Ga^{3+} B-site cation. The repulsive interactions have been shown to be reduced apparently by the outward movement or relaxation of these nearest cations. It was further suggested that the location of ions and the available space in perovskite lattice does not allow interstitial diffusion due to the high energy barrier >1.5 eV. Therefore, the ionic diffusion in perovskite type LaGaO_3 lattices must be occurring via migration of oxide ions jumping into an adjacent vacant site along the (1 1 0) edges of a BO_6 octahedra (as shown in Fig. 42a), which is the lowest energy path [603]. Neutron diffraction analysis and atomistic calculations further confirmed that the oxide ion migration do not adopt a straight route (along the midway of two anions), while the saddle point of curved path stays away from neighboring B-site cation. This has been shown to significantly reduce the energy barrier for oxide ion migration [604–607]. The average displacements of La^{3+} and B^{3+} ions were reported to be 0.08 and 0.07 Å, respectively, away from the mobile oxide ion.

The ionic radii ratio of the A- and B-site cations becomes an important factor, which significantly influences the ionic conductivity in the perovskite material. Theoretical calculations show that the lower migration energy can be obtained by decreasing the size of A-site cation (up to 0.95 Å; below this, the migration energy rises rapidly) and increasing the size of B-site cation (the energy is minimum at ~0.75 Å) [603]. Alternately, or rather simply, the geometrical limits (defined by

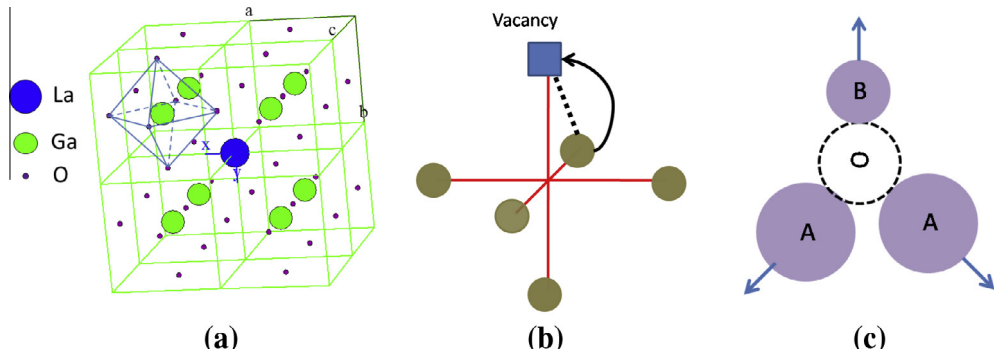


Fig. 42. (a) The cubic ABO_3 perovskite structure, (b) schematic representation of the curved path of oxide ion migration along BO_6 octahedron edge, (c) saddle point configuration for oxide ion migration indicating the cation relaxation.

Goldschmidt) for A and B-site cation in perovskite materials can be described in terms of the tolerance factor (t) which can be given as:

$$t = \frac{(r_A + r_O)}{\sqrt{2}(r_B + r_O)} \quad (75)$$

where r_A , r_B and r_O are the ionic radius of cations (A and B) and oxide ion, respectively, and perovskite structure has been found to be stable for $1.0 > t > 0.75$. Using computer simulation techniques, Cherry et al. [603] have shown that there exists a correlation between the tolerance factor and calculated migration energies with the minimum of migration energy, which occurs at $t = 0.81$. The migration enthalpy increases with an increase in the value of t beyond 0.81. The minimum in the tolerance factor shows a balance between the relaxation of A- and B-cations at the saddle point position, which is an important factor for achieving low activation energies of oxide ion migration. Perovskite based oxides with $t = 0.81$ possess lower migration energies and faster diffusion, i.e., high oxide ion conductivities [603].

Addition of acceptor dopant cation to LaBO_3 oxides, such as, Sr^{2+} , Ca^{2+} , Mg^{2+} or Ba^{2+} at La^{3+} sites have been reported to enhance the catalytic activity and ionic conductivity [54,608–615]. The reduction of effective valence at A-site, creates oxygen vacancies as a compensating defect, which, in turn, increase the ionic conductivity. Doping with Sr^{2+} results in the highest ionic conductivity as the tendency towards the formation of pair cluster is low except for LaCoO_3 [603]. The oxygen vacancies get trapped by host and dopant cations due to electrostatic and elastic interactions between them, which drastically reduces the concentration of mobile vacancies [604,616]. This also results in the increase in activation energy for conduction on lowering the temperature [617,618]. The presence of microdomains with ordered oxygen vacancies have also been detected in the electron diffraction studies which was further supported by atomistic calculations [604,616]. Based on neutron diffraction studies, Slater et al. [619] and Kajitani et al. [620] proposed that the substitution of Sr^{2+} and Mg^{2+} into LaGaO_3 , increases the aperture area of Δ_{AAB} , which, in turn, facilitates the oxide ion conduction in the material. Hayashi et al. [621] related the electrical conductivity of several perovskite based oxides to their respective t . It was reported that the high electrical conductivity is obtained at $t < 1$ with $(\text{La}, \text{Sr})(\text{Ga}, \text{Mg})\text{O}_{3-\delta}$ solid solutions exhibiting the high conductivity with $t = 0.96$. In case of $\text{La}_{1-x}\text{Sr}_x\text{Ga}_{1-y}\text{Mg}_y\text{O}_{3-\delta}$ (LSGM) series, maximum ionic transport have been observed for compositions with x and y lying in the range of 0.10–0.20 and 0.15–0.20, respectively [621]. Fig. 43 gives an overview of the effect of dopant addition to LSGM based electrolyte materials on their ionic conductivity.

Furthermore, it has been reported that replacing Ga^{3+} with Co^{3+} will result in an increase in ionic conductivity. However, this will also slightly increase the electronic conductivity in the material [622–624]. In order to keep electronic conduction low, the amount of Co^{3+} dopant should be limited to below 3–7%. Nevertheless, the following drawbacks restrict adaptation of LaGaO_3 -based ceramic [468,625,626] as potential electrolyte:

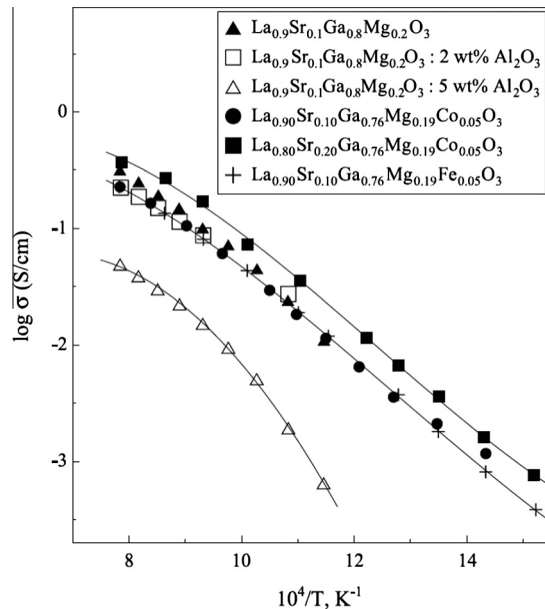


Fig. 43. Ionic conductivities of few selected LaGaO_3 -based ceramic electrolytes with various dopants. Measurements were carried out in air. (Reprinted with permission from Ref. [409], copyright Elsevier, 2004).

- Gallium oxide is prone to reduction, volatilization and reaction with perovskite cathode and metallic or cermet anodes.
- Stable secondary phases are likely to form during processing.

3.5.2. Perovskites based on LnBO_3 ($B = \text{Al}, \text{In}, \text{Sc}, \text{Y}$)

Perovskite aluminates, such as, LaAlO_3 were extensively investigated since 1970s [470–473,621,627–631]. Compared to $\text{LaGaO}_{3-\delta}$ and $\text{CeO}_{2-\delta}$, perovskites based on LnBO_3 ($B = \text{Al}, \text{In}, \text{Sc}$ and Y) exhibit better stability to reduction and volatilization. With moderate CTE values of $10.4\text{--}10.6 \times 10^{-6}/\text{K}$, these materials offer good mechanical compatibility during fabrication. However, they possess relatively low ionic conductivity and high level of *p*-type electronic conduction in oxidizing atmosphere. The main limitation associated with these perovskites is their poor sinterability and relatively high grain boundary resistivity.

Perovskite type aluminates give promising results as protective layers for LaGaO_3 based materials at the anode side. They have been tested successfully as isomorphic additives to composite solid electrolytes [467,470]. Doping with Sr^{2+} at A-site has been shown to provide maximum enhancement in the conductivity and minimum vacancy-association. Among various Sr^{2+} doped LaGaO_3 compositions, the maximum conductivity value has been reported in the case of $\text{La}_{0.9}\text{Sr}_{0.1}\text{AlO}_{3-\delta}$ [471,472,627]. Although, adding Mg^{2+} on B-site increases the oxygen vacancy concentration, however, it has a negative effect on the oxygen vacancy mobility which leads to lower ionic conductivity [631]. Fig. 44 shows the conductivity comparison of $\text{La}_{0.9}\text{Sr}_{0.1}\text{MO}_{3-\delta}$ ($M = \text{In}, \text{Al}$, and Ga) measured in N_2 atmosphere.

In this category, LnBO_3 -based ceramics with In, Sc or Y dopants have also been investigated [471,472,621,632–635]. Nomura and Tanase [472] reported the electrical conductivity of $\text{La}_{0.9}\text{Sr}_{0.1}\text{InO}_{3-\delta}\text{La}_{0.9}\text{Sr}_{0.1}\text{AlO}_{3-\delta}$ and $\text{La}_{0.9}\text{Sr}_{0.1}\text{ScO}_{3-\delta}$ in both air and N_2 atmospheres. It was assumed that the conductivity data measured in N_2 is due to pure ionic conduction. All the composition exhibit 0.1–0.5 orders of lower conductivity in N_2 when compared to that in air, which suggest the presence of relatively large *p*-type conductivity under high oxygen partial pressures. Above 800°C, the ionic conductivity of $\text{La}_{0.9}\text{Sr}_{0.1}\text{InO}_{3-\delta}$ is highest in N_2 atmosphere, while $\text{La}_{0.9}\text{Sr}_{0.1}\text{ScO}_{3-\delta}$ exhibits the highest conductivity below this temperature. According to Lybye et al. [471], Sr-doped LaScO_3 also exhibits

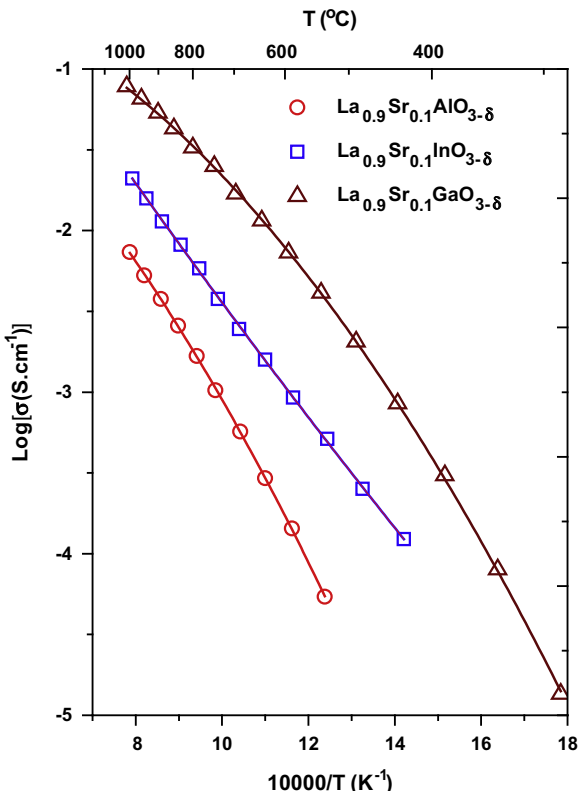


Fig. 44. Comparison of ionic conductivity of $\text{La}_{0.9}\text{Sr}_{0.1}\text{MO}_{3-\delta}$ ($\text{M} = \text{In}, \text{Al}, \text{and Ga}$) in N_2 atmosphere. (Adapted from Ref. [472], copyright Elsevier, 2004).

protonic conductivity, and it is not a pure oxide ion conductor. It was reported that among $\text{La}_{0.9}\text{Sr}_{0.1}\text{Al}_{0.9}\text{Mg}_{0.1}\text{O}_{3-\delta}$, $\text{La}_{0.9}\text{Sr}_{0.1}\text{Sc}_{0.9}\text{Mg}_{0.1}\text{O}_{3-\delta}$ and $\text{La}_{0.9}\text{Sr}_{0.1}\text{In}_{0.9}\text{Mg}_{0.1}\text{O}_{3-\delta}$, scandate composition exhibits the lowest oxide ion conductivity. Similarly, considerable level of protonic as well as *p*-type conduction is reported in some LaYO_3 based electrolytes. Ruiz-Trezo and Kilner [636] investigated the protonic conductivity in $\text{La}_{1-x}\text{Sr}_x\text{YO}_{3-\delta}$ solid solutions. The proton conduction is detected and reported to be dominant in these materials below 550 °C. Furthermore, the oxide ion conductivity is relatively low and contributes very less towards the total conductivity.

3.5.3. Brownmillerite-like phases

Oxides having a brownmillerite structure (with the chemical formula of $\text{A}_2\text{B}_2\text{O}_5$) consists of alternating layers of perovskite sharing corner with BO_6 octahedra and BO_4 tetrahedra [637]. These materials are considered as oxygen deficient perovskites, wherein oxygen vacancies are observed to order along (0 1 0) planes, and more importantly, contribute towards ionic transport. The vacancies form 1-D diffusion pathways, which allow oxide ion migration along tetrahedral layers. The structure contains large number of oxygen vacancies that are present in an ordered fashion. On increasing the temperature (above 900 °C), material undergoes phase transformation from the room temperature orthorhombic phase to the tetragonal phase (at 925–930 °C), and finally to the disordered cubic (at 1040 °C) [638,639]. This disordered cubic phase allows fast oxide ion conduction because of large number of oxygen vacancies present in the structure. However, these materials are sensitive to humid atmospheres. For example, Schober et al. [640] have reported the transformation of $\text{Ba}_2\text{In}_2\text{O}_5$ to a

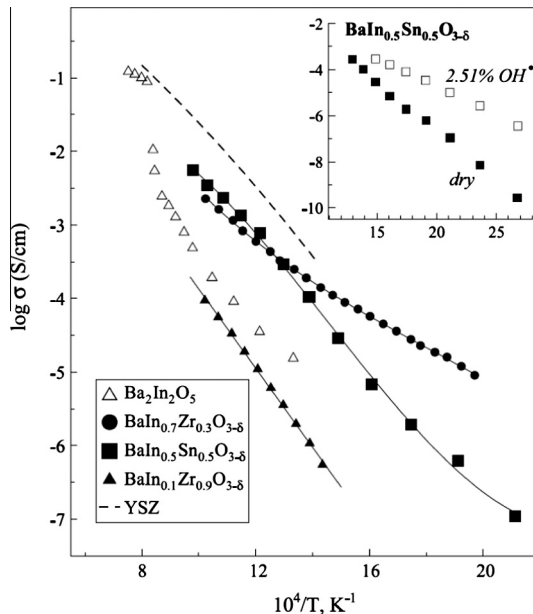


Fig. 45. Total conductivity of a few selected $\text{Ba}_2\text{In}_2\text{O}_5$ -based ceramic electrolytes in comparison to 8 mol.% Y_2O_3 stabilized ZrO_2 . Conductivity of $\text{Ba}_2\text{In}_2\text{O}_5$ is predominantly ionic. (Reprinted with permission from Ref. [409], copyright Elsevier, 2004).

$\text{Ba}_2\text{In}_2\text{O}_5 \cdot 1\text{H}_2\text{O}$ hydrate-like structure when exposed to humidity below 300 °C. In addition, they can also absorb and release H_2O and CO_2 depending on the atmosphere as well as temperature [640–642].

The brownmillerites exhibit different types of electrical conduction, viz., in dry atmosphere and moderate P_{O_2} , it is typically ionic (oxide ion conductivity). Under oxidizing conditions, they exhibit mixed ionic and *p*-type electronic conduction, whereas in H_2O containing gas mixtures, they exhibits protonic conduction.

$\text{Ba}_2\text{In}_2\text{O}_5$ exhibits mixed conductivity with oxide ion conductivity dominating the total conductivity in dry air (ionic transference number ~ 0.93 at 500 °C). The rise in temperature causes a phase transition to a disordered perovskite phase at 930 °C that results in a significant increase in the ionic conduction [643]. The disordered cubic perovskite phase can be stabilized by substituting In-sites with higher-valence cations, e.g., Zr^{4+} , Ce^{4+} , Sn^{4+} or Hf^{4+} that can enhance intermediate temperature ionic conduction [644]. Doping with other cations, such as, Y^{3+} , Yb^{3+} , Ga^{3+} and Sc^{3+} at In-sites, i.e., $\text{Ba}_2\text{In}_{2-x}\text{M}_x\text{O}_5$, where $x = 0.1–0.2$ have also been investigated [634,645,646]. The stabilized perovskite phase of $\text{BaIn}_{0.7}\text{Zr}_{0.3}\text{O}_{3-\delta}$ exhibits a slight *p*-type conductivity (<5%) towards the total conductivity at 500 °C [643]. The total conductivity of a few selected $\text{Ba}_2\text{In}_2\text{O}_5$ -based ceramics have been shown in comparison with 8YSZ electrolyte (Fig. 45) [641,643,647–649].

Despite stabilizing the cubic perovskite phase in $\text{Ba}_2(\text{In}_{1-x}\text{Ga}_x)_2\text{O}_5$ system, Yamamura et al. [650] and Yao et al. [645] reported no significant enhancement in the ionic conductivity. Kuramochi et al. [651] have investigated the correlation between the crystal structure and electrical conductivity in $\text{Ba}_2\text{In}_2\text{O}_5$ system with Pb^{2+} partially substituting the Ba^{2+} cations. It was reported that the low temperature electrical conductivity of partially substituted $\text{Ba}_2\text{In}_2\text{O}_5$ is greater than that of the parent material. Kakinuma et al. [652] have reported the ionic conductivity of $(\text{Ba}_{1-x-y}\text{Sr}_x\text{La}_y)_2\text{In}_2\text{O}_{5+y}$ where Ba^{2+} is partially substituted by La^{3+} and Sr^{2+} . The ionic conductivity in this system is reported to increase with an increase in La^{3+} and Sr^{2+} content. At 800 °C, the maximum conductivity of ~ 0.12 S/cm is reported in $(\text{Ba}_{0.3}\text{Sr}_{0.2}\text{La}_{0.5})_2\text{In}_2\text{O}_{5.5}$ composition, which exceeds that of Y_2O_3 stabilized ZrO_2 .

Besides oxygen vacancy concentration, oxide ion conductivity is also influenced by unit cell free volume [654] (and also, on unit cell volume [472], and saddle point [655,656]), which can be calculated for $(\text{Ba}_{1-x-y}\text{Sr}_x\text{La}_y)_2\text{In}_2\text{O}_{5+y}$ system using the following equation:

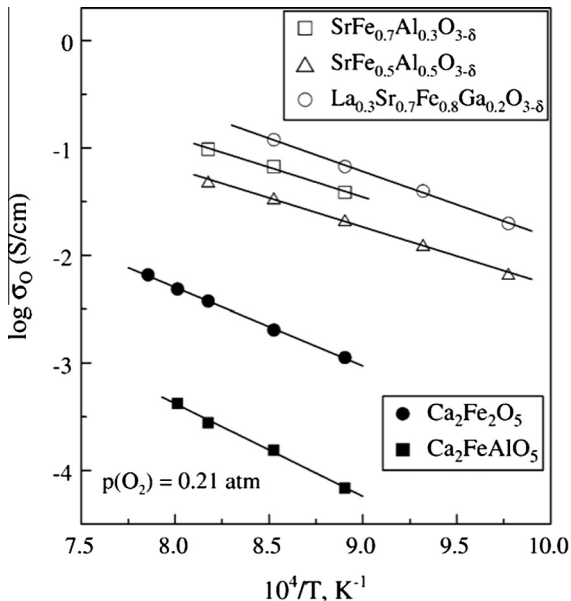


Fig. 46. Role of temperature in affecting oxide ionic conductivity of $\text{Ca}_2\text{Fe}_2\text{O}_5$ and $\text{Ca}_2\text{FeAlO}_5$ brownmillerite ceramics (measured in air). The data is compared to that of oxygen deficient perovskites such as $\text{SrFe}_{1-x}\text{Al}_x\text{O}_{3-\delta}$ and $\text{La}_{0.3}\text{Sr}_{0.7}\text{Fe}_{0.8}\text{Ga}_{0.2}\text{O}_{3-\delta}$. (Reprinted with permission from Ref. [653], copyright Elsevier, 2006).

$$\text{Unit cell free volume} = abc - \sum m_i \frac{4}{3} \pi r_i^3 \quad (76)$$

where a , b and c are the unit cell lattice parameters, m_i is the chemical composition ratio of an ion, and r_i is the ionic radius. Keeping La^{3+} content (y) constant in $(\text{Ba}_{1-x-y}\text{Sr}_x\text{La}_y)_2\text{In}_2\text{O}_{5+y}$, the unit cell free volume and conductivity were shown to increase linearly with an increase in Sr^{2+} content [652]. In this category of electrolytes, some more compositions have been extensively investigated. Shaula et al. [653] have investigated the ionic conductivity of $\text{Ca}_2\text{Fe}_2\text{O}_5$ compound, which is also based on brownmillerite structure. At 900 °C, it possesses ionic conductivity higher than that of $\text{Ca}_2\text{FeAlO}_5$, and it shows lower ionic conductivity when compared with oxygen deficient $\text{SrFeO}_{3-\delta}$ based perovskites (shown in Fig. 46).

3.5.4. $\text{La}_2\text{Mo}_2\text{O}_9$ (LAMOX) based electrolyte materials

Materials based on $\text{La}_2\text{Mo}_2\text{O}_9$ compound or LAMOX, first reported by Lacorre et al. in year 2000, exhibit fast oxide ion conducting property [657–661]. The oxide ion conductivity in LAMOX was found to be $\sim 6 \times 10^{-2} \text{ S/cm}$ which compares well with that of stabilized ZrO_2 at 800 °C. These materials undergo a phase transition from room temperature monoclinic (α -form) to cubic (β -form) at around 580 °C accompanied by a sudden increase in conductivity (by ~ 2 orders of magnitude), which is similar to that observed for Bi_2O_3 and $\text{Ba}_2\text{In}_2\text{O}_5$ oxide ion conducting oxides. The high temperature cubic form of LAMOX possesses the same space group ($P2_13$) and identical cationic positions as that of $\beta\text{-SnWO}_4$. The octahedra represent the coordination environment for lanthanum cations, whereas tetrahedra are relative to the position of molybdenum ions (see Fig. 47). Due to their susceptibility towards phase transition and the tendency of molybdenum to get reduced in fuel environment, researchers have investigated doping at both lanthanum and molybdenum sites. The effect of substitution of lanthanum site with other elements such as Nd, Y and Gd on suppressing the cubic to monoclinic phase transition on cooling have been investigated by Georges et al. [660]. On doping with Nd, phase remains monoclinic in the entire compositional range. However, above a certain dopant level, doping with Gd and Y leads to stabilization of cubic phase at room temperature. Doping with W to

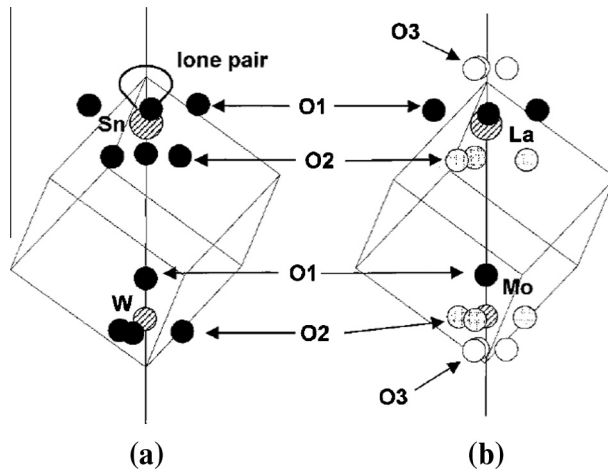


Fig. 47. Cationic environments in (a) β -SnWO₄ and (b) β -La₂Mo₂O₉. For comparison, a limited nearest neighbor environment of La is presented. Gray and open circle oxygen sites are partially occupied. (Reprinted with permission from Ref. [658], copyright JACS, 2000).

form La₂Mo_{2-x}W_xO₉ solid solutions (with $x \leq 1.6$) were reported to exhibit ionic conductivity of $\sim 0.11 \text{ S cm}^{-1}$ ($x = 0$) to 0.05 S cm^{-1} ($x = 1.5$) at 750 °C, which compares well with that of gadolinium doped ceria [662]. The ionic transference number was found to be 0.95 at 700 °C under humidified 5% H₂-Argon atmosphere. Furthermore, these solid solutions exhibit reasonable stability at 600 °C [662].

Ionic transport in these materials has been reported to occur via lone pair substitution mechanism, i.e., lone pairs on cations are capable of stabilizing oxygen vacancies [657]. Structure of β -SnWO₄ provides a suitable model towards understanding the probable mechanism of oxide ion transport in La₂Mo₂O₉. In β -SnWO₄, the lone pairs of Sn²⁺ cation distorts its octahedral environment and occupies a volume similar to that of an O²⁻ ion [663]. Representing a lone pair as 'L', the Sn(II) tungstate can be formulated as SnW⁶⁺O₄L or Sn₂W₂O₈L₂. In La₂Mo₂O₉, La³⁺ is a cation having a similar size as Sn²⁺, but without a lone pair. When substituted at Sn²⁺ sites, two extra vacancies are generated in the structure. One of these vacancies is occupied by extra oxygen atom in order to compensate the cationic valance, i.e., L₂ → □ + O and molybdenum replaces comparable tungsten, so that the formula of the lanthanum molybdate becomes La₂Mo₂O_{9+□}. The extra vacancy is now available for the oxide ion conduction. This is further favored by the presence of Mo⁶⁺ cations in the structure which can adopt a distorted environment with various possible coordinations of 4–6. In Fig. 47, cationic environment of β -La₂Mo₂O₉ has been compared with β -SnWO₄, which shows that the tungsten coordination polyhedron is a tetrahedron, and there is one oxide ion on the 3-fold axis (Fig. 47a) and three other oxide-ions away from it. In Fig. 47b, the structure of La₂Mo₂O₉ is shown, in which Mo coordination seems to be little modified from that of W (as shown in Fig. 47a).

Here, 4a sites are fully occupied (dark circles), whereas 12b site is partially occupied ($\sim 2/3$) and Mo⁶⁺ seems to be somewhat shifted towards the center. Extra oxygen O₃ is located on the other side of the triangular face relative to the fully occupied 4a site, and split at 12b position ($\sim 1/3$ occupied). The Mo–O bond length in this structure ranges between 1.73 and 1.83 Å. At the top side of Fig. 47a, Sn²⁺ resides in a octahedral site, while oxide ions form the distorted octahedron i.e., 3 (three) O²⁻ at 2.21 Å and other 3 (three) O²⁻ at 2.81 Å distance, and form larger triangular face. The lone pair on Sn²⁺ cation, pointing towards the top position, is shown as a curve in the schematic. The corresponding octahedron in β -La₂Mo₂O₉, shown in Fig. 47b, is less distorted compared to β -SnWO₄. The La–O bond length ranges between 2.40 and 2.92 Å [658]. The extra oxide ion O₃ partially occupies the position of the lone pair (refer to the structure of β -SnWO₄). This last feature in this model assists in understanding the origin of oxygen-ion conduction in LAMOX series.

Both ionic and electronic conductivity of $\text{La}_2\text{Mo}_2\text{O}_9$ as a function of temperature was explored by Subasri et al. [664]. It was reported that the phase transition, although present in $\text{La}_2\text{Mo}_2\text{O}_9$, does not have any apparent effect on its conductivity. The total conductivity was observed to be ~3 orders of magnitude lower than that reported by Lacorre et al. [661]. Furthermore, at 900 °C, this material exhibits an ionic conductivity of $\sim 8 \times 10^{-5}$ S/cm which is significantly lower than that of YSZ at the same temperature. Also, there is an onset of high electronic conductivity even at the oxygen partial pressures of the order of 8 Pa. The reported work is in contradiction with the result reported by Lacorre et al. [661]. It was further suggested by Subasri et al. [664] that the high conductivity observed by Lacorre et al. [661] may be due to the presence of impurities in $\text{La}_2\text{Mo}_2\text{O}_9$ samples.

Doping at La-sites with monovalent cation (A^+) results in the creation of additional oxygen vacancies as charge compensation which subsequently increase the ionic conductivity:



Tealdi et al. [665] have investigated alkali metal cation (Na^+ , K^+ and Rb^+) doped $\text{La}_2\text{Mo}_2\text{O}_9$ synthesized by Pechini method. The electrical conductivity was reported to be similar to that of the materials prepared by solid state method. It was reported that K^+ and Rb^+ doping restricts α - β transition exhibited by undoped and Na^+ doped $\text{La}_2\text{Mo}_2\text{O}_9$ materials at ~ 580 °C.

3.5.5. Apatite structure

Apatite based materials have a general formula of $\text{A}_{10}(\text{MO}_4)_6\text{X}_{2\pm\delta}$ (where A is a rare earth or alkaline earth cation or Pb, M is a p-block element, such as, Si, Ge, P or V and X is OH^- , O^{2-} or halides). These materials possess similar structure to that of apatite minerals (especially hydroxyapatite bioceramics). The family of apatite based oxide ion conductors typically consists of $\text{Ln}_{9.33+x}(\text{Si}/\text{GeO}_4)_6\text{O}_{2+3x/2}$. The structure comprises of isolated MO_4 tetrahedra arranged in a way to form distinct anion and La channels running parallel to the c-axis. The oxide ion channels being in central position participate in ionic conductivity [666]. The rare earth cations are located in 7- and 9-coordinated cavity sites, and extra oxide ions occupy positions in channels running through the structure, which is responsible for high ionic conductivity observed in these materials. An alternative description proposed by Baikie et al. [667] proposes a 'microporous' framework ($\text{A}_4(\text{MO}_4)_6$) composed of face sharing AO_6 trigonal prismatic columns that are connected at the corners to the MO_4 tetrahedra. This framework can accommodate the remaining $\text{A}_6\text{O}_{2\pm y}$ units. As O^{2-} residing in the 2a sites does not form a bond with either MO_4 tetrahedron or $\text{La}^{3+}(a \text{ or } b)$, thus the binding force exerted on O^{2-} is not strong. This allows relatively free movement of O^{2-} in the c-axis direction without being constrained to the 2a site. In the case of silicate apatites, the oxide ion conduction is further facilitated by the cooperative displacements of the flexible silicate substructure. On examining and modeling the probable conduction mechanism in apatites silicates, the atomistic simulation results suggest that conduction in $\text{La}_{9.33}(\text{SiO}_4)_6\text{O}_2$ and $\text{La}_8\text{Sr}_2(\text{SiO}_4)_6\text{O}_2$ takes place via interstitial and vacancy mechanism, respectively [668,669]. The predicted pathway

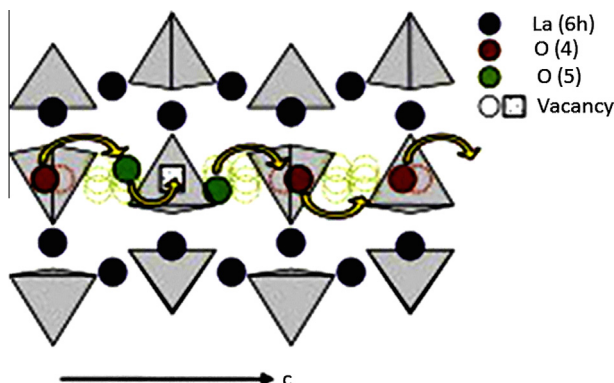


Fig. 48. Structural defect position and possible conduction mechanism along the c axis representation of two adjacent unit-cells. (Reprinted with permission from Ref. [681], copyright Elsevier, 2009).

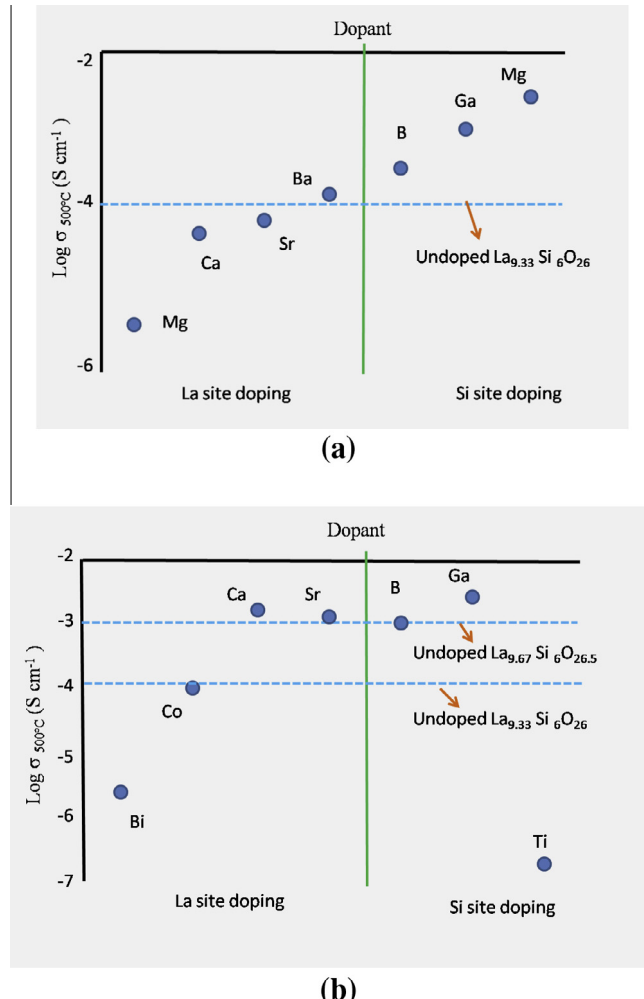


Fig. 49. (a) Comparison of the conductivities (at 500 °C) of oxygen stoichiometric samples at constant cation vacancies, but with various dopants. Compositions = La_{9.67}(SiO₄)₅(MO₄)O₂ (M = B, Ga), La_{9.67}(SiO₄)_{5.5}(MgO₄)_{0.5}O₂, La_{8.67}M(SiO₄)₆O₂ (M = Mg, Ca, Sr, Ba). (b) Comparison of the conductivities (at 500 °C) of samples at constant level of oxygen excess, but with varying dopants. Compositions = La₇BaBi₂(SiO₄)₆O_{2.5}, La_{9.4}Co_{0.4}(SiO₄)₆O_{2.5}, La₉M(SiO₄)₆O_{2.5} (M = Ca, Sr), La₁₀(SiO₄)₅(MO₄)O_{2.5} (M = B, Ga), La₉Ba(SiO₄)₄(TiO₄)₂O_{2.5}. (Adapted from Ref. [666].)

appears to be a complex non linear “sinusoidal like” process for the interstitial oxygen migration along the *c*-axis (as shown in Fig. 48), while a direct linear pathway is predicted for oxygen migration via vacancy mechanism [669]. Furthermore, the most energetically favorable interstitial oxide ion sites identified (via modeling) are at the peripheries of the oxide ion channels neighboring the SiO₄ units. Furthermore, it has been shown that La_{9.33}(SiO₄)₆O₂ exhibits significantly higher ionic conductivity compared to that of La₈Sr₂(SiO₄)₆O₂ [670]. The key difference between the two samples is the presence of lanthanum vacancies in the La_{9.33}Si₆O₂₆ sample, although the oxide ion content is the same and nominally stoichiometric in both samples. Using neutron diffraction investigation in both the compositions, Sansom et al. [670] have shown that channel oxide ion are ordered in La₈Sr₂(SiO₄)₆O₂ composition, while a degree of disorder is present in the case of La_{9.33}(SiO₄)₆O₂, where a significant portion of the channel oxygen is displaced into interstitial sites.

Among several reported rare earth apatites, lanthanum silicates exhibit ionic conductivity higher than their germinate counterparts [477,671–678]. The conductivity obtained is purely ionic as most of the compositions exhibit ionic transference number >0.9, across a wide range of P_{O_2} . Initial investigations carried out by Nakayama et al. [679,680] on an undoped $Ln_{10}(SiO_4)_6O_3$ revealed that the high oxide ion conductivity was observed for larger rare earths cations such as La, Pr, and Nd.

Moreover, oxygen excess compositions ($x > 0$) were reported to exhibit higher conductivity, e.g., at 500 °C, $La_{9.33}(SiO_4)_6O_2$ and $La_{9.67}(SiO_4)_6O_{2.5}$ exhibit ionic conductivity of 1.1×10^{-4} S/cm and 1.3×10^{-3} S/cm, respectively [672]. The results indicate that interstitial oxide ions also significantly contribute in enhancing the oxide ion conductivity in apatite systems. A wide range of compositions have been investigated in this category; however, majority of the work is focused on the La containing system, i.e., $La_{9.33+x}(SiO_4)_6O_{2+3x/2}$ [477,671,672,674,676–680,681–684]. Various types of dopant used for La- and Si-sites are listed below.

La-Site: Mg, Ca, Sr, Ba, Co, Ni, Cu, Mn, Bi

Si-Site: B, Al, Ga, Zn, Mg, Ti, Ge, Fe, Co, Ni, Cu, Mn, P.

In addition, there are certain dopants which can easily occupy both La- and Si-sites (for example Mg^{2+}), and are termed as ‘ambi-site’ dopants. Fig. 49a shows the conductivity data at 500 °C for oxygen stoichiometric samples with various dopants. On doping with smaller sized cation on La-site, a decrease in conductivity is observed. The result is attributed to the change in the coordination environment of the site from 9 (for La^{3+}) to 6 (for Mg^{2+}). The Mg^{2+} doping in La^{3+} leads to the significant displacement of silicates sites towards the oxide ion channels. This has an adverse effect on the oxide ion conduction through these channels [683]. Similar behavior was also reported in the oxygen excess compositions (shown in Fig. 49b). Isovalent dopants, e.g., Ge at Si-sites have been reported to exhibit higher conductivity [675].

Furthermore, in the oxygen excess compositions, Ti^{4+} substitution at Si-sites and Bi^{3+} substitution at La-sites exhibit significant decrease in the conductivity. At 500 °C, conductivity values for $La_9Ba(SiO_4)_4(TiO_4)_2O_{2.5}$ and $La_7BaBi_2(SiO_4)_6O_{2.5}$ were recorded lower than that of $La_9Ba(SiO_4)_6O_{2.5}$ by 4 and 3 orders of magnitude, respectively (as shown in Fig. 49b). Low conductivity in Ti^{4+} doped composition is attributed to the trapping of mobile interstitial oxide ions due to extended coordination sphere of Ti^{4+} [674]. According to Kendrick et al. [666], a significantly low conductivity in Bi^{3+} doped compositions arises due to the influence of lone pairs of Bi^{3+} , which encroaches the oxide ion conduction pathway at lower temperatures (<600 °C).

Compared to silicates, germanate based apatites (or $La_{9.33+x}(GeO_4)_6O_{2+3x/2}$) have shown higher activation energy and hence, lower ionic conductivity at low temperatures. At high temperatures, the triclinic crystal structure of these materials transform to hexagonal cell, which, as a result, lowers the activation energy for oxide ion conductivity [666]. In addition, germanate apatite materials show instability at high temperatures as they tend to volatilize, undergo glass formation, and show poor sinterability. The sinterability is reported to be improved by doping with transition metal cations. Furthermore, these materials have a tendency to incorporate significant amount of water molecules during annealing in wet atmospheres at temperatures below 500 °C, which probably contribute towards protonic conduction [685]. Although their high ionic conductivity at higher temperatures looks promising, the high cost of GeO_2 makes silicate-based apatites of practical interest.

3.6. Other structure compounds

$LaBaGaO_4$ structured compounds constitute another category of oxides containing isolated GaO_4 tetrahedral units which show significantly high ionic conductivity. $La_{1-x}Ba_{1+x}GaO_{4-x/2}$ is one of these phases exhibiting both oxide ion and proton conductivity especially at temperatures <700 °C [683,686]. Stoichiometric compound of $LaBaGaO_4$ possesses β - K_2SO_4 type structure with orthorhombic unit cell in which Ga^{3+} exists in a distorted tetrahedral environment. Both La^{3+} and Ba^{2+} cations form ordered alternating layers, while GaO_4 distorted tetrahedra are isolated from each other. The undoped phase of $LaBaGaO_4$ exhibits significantly lower conductivity than the doped phases. With an increase in the x value in $La_{1-x}Ba_{1+x}GaO_{4-x/2}$, La/Ba concentration ratio decreases, which leads

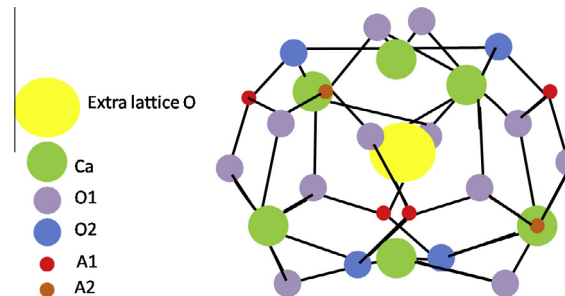


Fig. 50. A mayenite cage containing an extra-lattice oxygen atom. (Adapted from Ref. [689]).

to the formation of oxygen vacancies. However, on increasing $x > 0.2$, impurity phases start to appear. For a single phase solid solutions, the neighboring two GaO_4 units rearrange to form a Ga_2O_7 group, which accommodates the newly formed oxygen vacancy. The rearrangement of GaO_4 units also allows retaining tetrahedral coordination for each Ga^{3+} . The breaking and reformation of Ga_2O_7 units creates low energy pathway for the oxide ion migration between neighboring tetrahedrals, which, in turn, facilitate long-range diffusion. Li et al. [686] have measured the conductivity of $\text{La}_{1-x}\text{Ba}_{1+x}\text{GaO}_{4-x/2}$ in air and in N_2 atmospheres, and observed that the conductivity in N_2 atmosphere is lower than that in air, which suggests the existence of *p*-type conductivity in these materials.

$\text{LaSrGa}_3\text{O}_7$ -based materials adopts melilite crystal structure which comprised of layers of corner sharing GaO_4 units. The Ga^{3+} forms two different types of tetrahedra units. These GaO_4 units link to form distorted pentagons, where both La^{3+} and Sr^{2+} are positioned between two GaO_4 layers, aligned at centers of pentagonal rings [411]. In this category, $\text{LaSrGa}_3\text{O}_7$ is the parent compound which exhibits poor electrical conductivity. However, with an increase in x value in $\text{La}_{1+x}\text{Sr}_{1-x}\text{Ga}_3\text{O}_{7+x/2}$, La/Sr concentration ratio is increased, which results in excess oxygen incorporation into the lattice to maintain the charge balance [687,688]. The extra oxide ion resides in the same Ga^{3+} plane in the tetrahedral layers and is available for ionic conduction. The ease with which Ga^{3+} can change the co-ordination number makes the structural network relatively flexible, which, in turn, facilitates the interstitial oxide ion conduction. However, the large size $\text{La}^{3+}/\text{Sr}^{2+}$ cations occurring in the voids of distorted pentagon rings between GaO_4 layers can cause hindrance to the migration of oxide ion along the c -axis.

Mayenites are $\text{Ca}_{12}\text{Al}_{14}\text{O}_{33}$ based compounds, whose crystal structure comprises of 64 oxide ions within Ca-Al-O framework, and one sixth of the cage-like structure is occupied by two extra-lattice oxygen O1 and O2 as shown in Fig. 50 [689–692]. This structure is capable of accommodating a range of other anions. Oxide ion diffusion takes place via jump-like hopping process that involves exchange between extra-lattice oxide ion and framework oxide ions. The cage wall oxide ions are strongly bonded (though with large relaxations) with nearest neighboring Ca^{2+} ions and other framework ions [689]. Moreover, under reducing atmosphere, limited electronic species concentration has been reported to transform mayenite into an electronic conductor. The defect chemistry of the nanocages is complicated and a complete picture of oxide ion migration is yet to be figured out [691].

4. Cathode

The molecular oxygen (supplied from air) flows and gets adsorbed onto the surface of the porous cathode, and gets reduced to oxide ions by accepting the incoming electrons from the current collector. Depending on the nature of the cathode material, oxygen reduction reaction can occur either on the electrode/gas interface or somewhere in the vicinity of the electrode/electrolyte/gas interface. The fully or partially reduced oxide ions or atomic species are then transported through the bulk or surface pathways to the electrolyte/electrode/gas interface where the complete reduction occurs. The oxide ions are subsequently transported to anode (via diffusion through dense electrolyte), and incur oxidation of fuel.

4.1. Requirements of cathode material

For an efficient operation of SOFC, the cathode should possess the following functionalities [84,693–695]:

- (1) High electronic conductivity (preferably more than 100 S/cm in an oxidizing atmosphere);
- (2) Minimum or no mismatch between the CTE values of the cathode and other components of the cell, such as, electrolyte, and interconnect materials;
- (3) Good chemical compatibility with the electrolyte and interconnect materials;
- (4) Sufficient porosity to allow fast diffusion of O₂ gas from cathode to cathode-electrolyte interface
- (5) High oxide ion conductivity;
- (6) Good stability under an oxidizing atmosphere in the course of fabrication as well as operation;
- (7) High catalytic activity during oxygen reduction reaction (ORR); and
- (8) Cost effective.

4.1.1. Focus of cathode research and development

Most important issues in the field of cathode research are:

- Understanding the oxygen transport mechanisms in different types of cathode materials.
- Designing new compositions and microstructure of cathode materials.
- Exploring structure–property–performance correlations.
- Understanding the influence of various factors such as time, temperature, thermal cycling, polarization, operating conditions, and impurities to the cathode performance.
- Developing advanced processing and characterization techniques that will enable enhanced control and evaluation of cathode microstructure.

4.2. Material selection for cathode

Oxygen reduction using a porous platinum electrode on YSZ was first reported over a 100 years ago [696], and it formed the starting point for understanding the kinetics and mechanism of cathode working. Oxygen reduction reaction is essentially an electrochemical reaction involving charge transfer process, which is believed to occur at TPBs. The process obeys Tafel kinetics (linear dependence of $\ln i$ vs. V) from moderate to high overpotential values. The corresponding steady state i -V characteristics can be measured and analyzed in terms of Tafel parameters i.e., overpotential, anodic and cathodic charge transfer coefficients, exchange current density [697]. These parameters not only assist in distinguishing the non-linear electrode response from the linear electrolyte losses, but also provide a theoretical basis to identify rate determining mechanisms in a given condition. Using current interruption method with the aid of reference electrode, Wang and Nowick studied the Tafel plots for Pt electrodes on CaO doped CeO₂ electrolyte over a broad range of temperatures, and oxygen partial pressures [698,699]. Fig. 51 shows the Tafel plot in steady state condition obtained at 600 °C in pure O₂. A fairly good agreement was observed between the data and the Butler–Volmer expression, except at high cathodic overpotentials where limiting current phenomena occurs. Based on the results, authors concluded that the electrode reaction should be limited by charge transfer mechanism. Furthermore, the study of exchange current density as a function of temperature and oxygen partial pressure indicates that the oxygen molecules are adsorbed on the Pt surface, obeying Langmuir isotherms. In addition, Wang and Nowick [698,699] reported no influence of electrolyte composition on the electrode reaction kinetic, which suggests that rate limiting electrochemical step primarily occurs at Pt-surface.

On the other hand, when electrolyte is a solid ceramic, the electrodes are necessitated to be of gas diffusion type, e.g., porous platinum or other noble metal (Au-YSZ and Fe implanted Au-YSZ) [701]. The operation of gas-diffusion electrodes is entirely different, such that the electrochemical kinetics deviates substantially (from the traditional one used in aqueous electrochemistry) due to the presence of multiple rate determining factors that depend on overpotential and other conditions, e.g., geometry of the active surface. To analyze such electrodes, electrochemical impedance spectroscopy (EIS) or ac impedance is employed. EIS measures complex impedance (Z) by applying a small sinusoidal potential

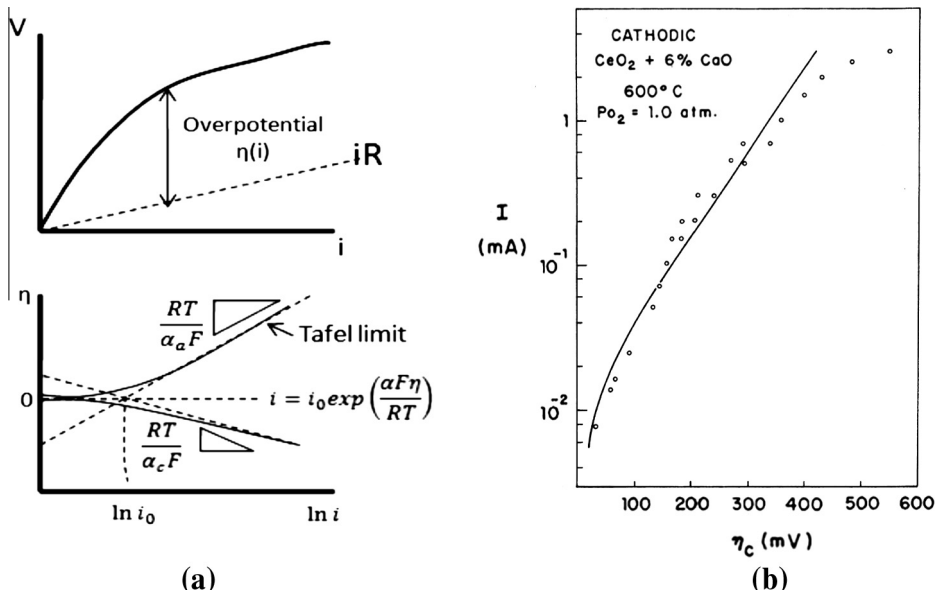


Fig. 51. (a) Plots of electrode overpotential η vs. $\ln i$ representing a system controlled by typical electrochemical kinetics, where the slopes at high over potentials yield anodic charge transfer coefficients (α_a) and cathodic charge transfer coefficient (α_c), and their intercept provides exchange current density (i_0). (Adapted from Ref. [700]), and (b) Steady-state cathodic current-overpotential (cathodic polarization) characteristics of porous Pt electrodes on Ca-doped ceria electrolyte at 600 °C in pure O₂. (Reprinted with permission from Ref. [699], copyright Journal of The Electrochemical Society, 1979).

perturbation at a certain frequency (ω) to an electrochemical cell, and acquiring a current response perturbation through the cell. In this technique, Z is measured as a function of frequency which allows distinguishing between various relaxation phenomena. Thus, the impedance spectra which is typically represented by Nyquist plot ($Z(\omega)$ in complex plane) is successfully used to isolate the electrolyte response from the electrode polarization [702,703]. For each relaxation process with a distinct relaxation frequency occurring in electrolyte (R_e) and electrode (R_1, R_2, C_1, C_2), a depressed semicircle is obtained. In order to determine the individual contribution, impedance spectra is modeled through an analog electrical equivalent circuit constructed using electrical elements e.g., resistors (R_1, R_2, R_e) and constant phase elements (C_1, C_2 , etc.), which define the charge transfer and charge polarization processes, respectively [704].

Thus, the two methods of measurements laid the foundation of two fundamentally different concepts viz., (i) classical electrochemical kinetics focusing electrodes that follows Tafel kinetics (except at lower overpotential), and (ii) impedance investigation of electrodes that elicit electrode performance. Till late 1990s, the opinion that the charge transfer step dominates the electrode kinetics of SOFC electrodes continued to receive support by many researchers [705–707]. In 1969, Bauerle [703] investigated the YSZ electrolyte with porous Pt paste electrode by measuring complex admittance in a wide range of temperatures and oxygen partial pressures. The analysis of the data in complex admittance plane gives a very large electrode capacitance value (550 $\mu\text{F}/\text{cm}^2$), which cannot be explained by a traditional double layer interfacial polarization. In 1973, Kleitz and co-workers [708] have performed EIS study on the electrochemical cells based on porous Pt on YSZ. The electrode response of such cells was reported to be at very low frequency (<1000 Hz) which again cannot be explained through interfacial polarization. The low frequency response of the electrodes was inferred as an outcome of change in the concentration of neutral oxygen in the vicinity of TPBs. It was concluded that the charge transfer itself does not contribute significantly towards the total overpotential. Instead, the electrode kinetics is controlled by adsorption and transport processes.

Later in 1995, Kleitz et al. [709] conducted a series of experiments on Ag point contact microelectrodes that were processed by solidification of small (200–2000 μm) Ag droplets on 10YSZ surface.

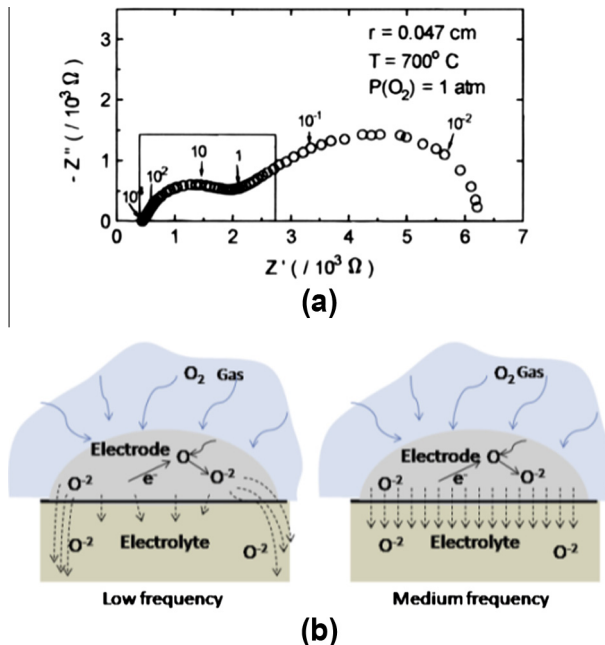


Fig. 52. (a) Impedance at 700 °C in O₂ of a single Ag droplet solidified on YSZ (Reprinted with permission from Ref. [709], copyright Journal of The Electrochemical Society, 1997), and (b) Distribution of oxygen ion diffusion from Ag droplet to electrolyte at low and high frequency conditions. (Adapted from Ref. [709]).

Impedance measurements were conducted on these *in situ* fabricated Ag microelectrodes in the temperature range of 600–800 °C and under 0.01–1 atm of oxygen partial pressures. Fig. 52a shows the Nyquist plot obtained using Ag-droplet electrode under one set of experimental condition. The impedance spectra exhibits two depressed semicircles viz., the large semicircle at low frequency range (0.01–0.1 Hz) and a small semicircle at moderate high or medium frequency (~10 Hz). The capacitance of the low frequency is determined to be in the range of 1–10 F/cm², which must be associated with concentration variations of oxygen dissolved in a certain volume of the Ag droplet above Ag/YSZ interface. Furthermore, the capacitance in medium frequency shows a little dependency over temperature and oxygen partial pressure, suggesting a typical double layer capacitance on YSZ. On the basis of these results, a model was proposed (shown in the Fig. 53b) where oxide ions transport uniformly across the droplet/electrolyte interface at medium frequency, while a higher flux occurs near the triple phase line at low frequency. It is argued that a strong coupling exist between the overpotential and adsorption/migration of atomic oxygen inside the Ag droplet. The cathodic overpotential serves as a driving force for the dissolved atomic oxygen in Ag to be reduced to oxide ions, which are then dragged into the electrolyte at Ag/YSZ interface. The transfer of oxide ions creates a deficiency of oxygen in Ag/YSZ interface, and thereby generates a chemical potential driving force for dissolved oxygen atom to diffuse from the bulk Ag to Ag/YSZ interface. Finally, the depletion of dissolved oxygen atoms in bulk Ag relative to environment leads to dissociative adsorption of oxygen gas in Ag. At steady state, a continuous concentration gradient of oxygen is formed, which dictates the overall reaction-rate. Thus, the high capacitance value obtained for the electrode polarization can be explained on the basis of the proposed mechanism. In addition, the resistance to reduction at Ag/YSZ interface largely depends on how fast O₂ can get to the interface rather than how fast it is reduced at the interface. Kleitz argued that the dissolved oxygen in Ag droplet at equilibrium gets converted into “electroactive species” during reduction, and it contributes to the overall macroscopically observed polarization resistance [709].

Verkerk and Burggraaf [710] modeled the impedance spectra collected on Pt (porous, sputtered and gauge) electrodes on YSZ and GDC using Randles electrical circuit. Randles circuit constitutes of an

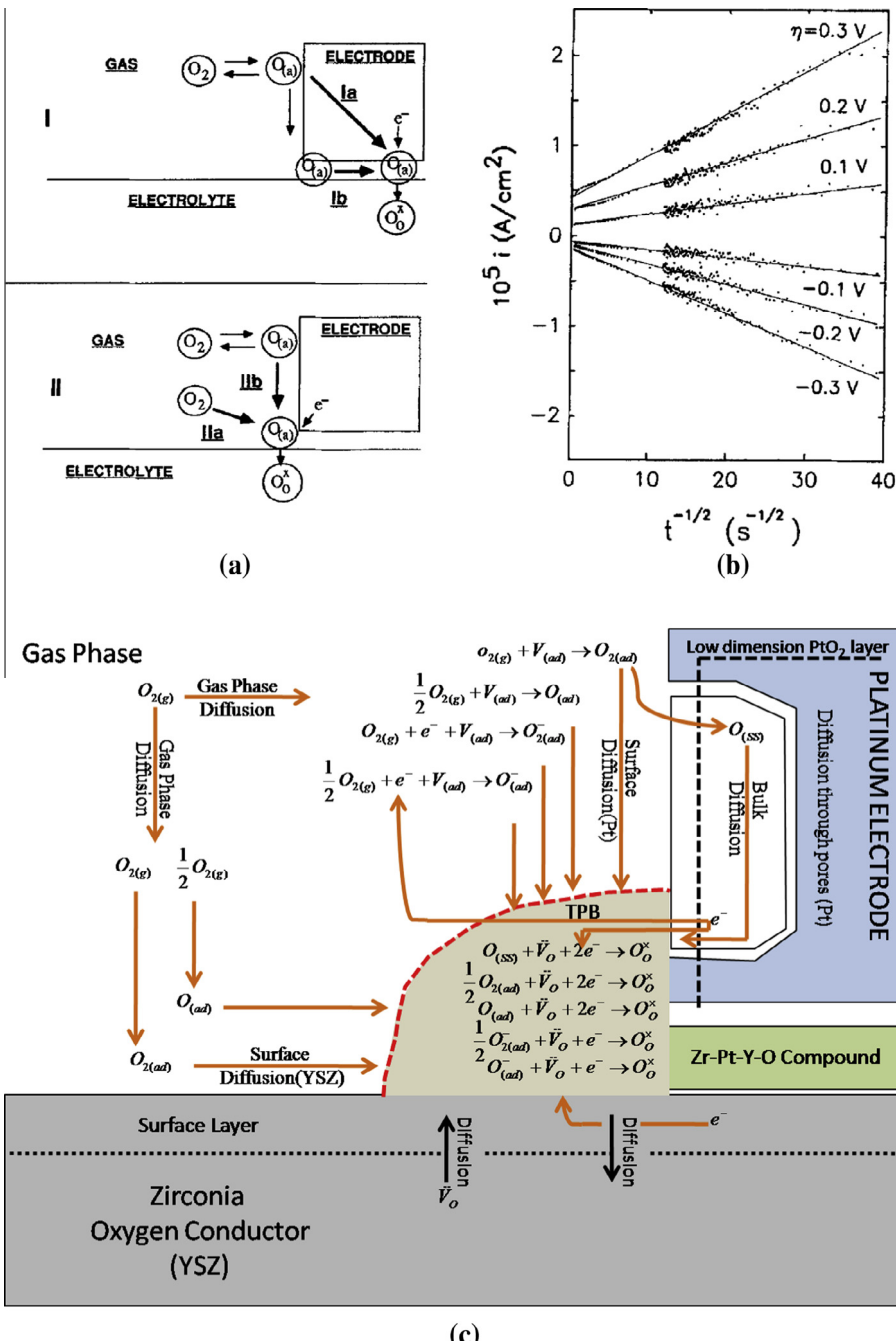


Fig. 53. (a) Models of oxygen surface diffusion on Pt. Model I: Diffusion of surface-adsorbed oxygen (on Pt surface) through the Pt/YSZ interface to an active reduction site. Model II: Diffusion of adsorbed oxygen towards TPB, (b) Cottrell plot of current decay in a porous Pt electrode at 600 °C and P_{O_2} of 10^{-4} atm vs. square root of time at different potential steps. ((a-b) Reprinted with permission from Ref. [714], copyright Journal of The Electrochemical Society, 1990), (c) Reaction pathways taking place at triple phase boundary of Pt-YSZ interface. (Adapted from Ref. [715]).

active electrolyte resistance R_e in series with the parallel combination of the double-layer capacitance C_{dl} at metal-electrolyte interface, and Faradaic impedance, Z_F . The Faradaic impedance is a series combination of charge transfer resistance and concentration impedance, Z_0 . The Randles circuit allows separating and subtracting the contributions of uncompensated iR and double layer capacitance existing at the interface of the metal and electrolyte. In the low frequency range, the Faradaic impedance exhibits a similar real and imaginary impedances in Nyquist plot (constant phase of 45°) indicating that the overall electrode process is rate limited by diffusion of atomic oxygen on the electrode surface [702].

The adsorption and diffusion as rate determining steps for the oxygen exchange on platinum was further confirmed by Mizusaki et al. [711,712]. It was reported that the Faradaic processes occurring at Pt electrode are quite complex; and more than one rate-determining step can rule under different conditions. In the temperature range of $600\text{ }^\circ\text{C} \leq T \leq 750\text{ }^\circ\text{C}$, the rate determining step was shown to be surface diffusion of adsorbed atomic oxygen on Pt (with the activation energy of 41 kcal/mol), while at temperatures below 500 °C, reaction was determined to be limited by the dissociative adsorption of oxygen molecules (with the activation energy of 37 kcal/mol) on the Pt surface near the TPB line. However, in either case, the logarithmic current can be linearly plotted as a function of cathodic overpotential obeying Tafel's behavior. Thus, the chemical steps involved in electrode kinetics can still follow Butler–Volmer relationship.

In the literature, a variety of kinetic models have been proposed, in which the dissociative adsorption of oxygen and diffusion of adsorbed oxygen are the integral steps in reaction mechanism [701,712,713]. The discrepancy occurs at the sites of the electrochemical reaction. In some of the models, electrode/electrolyte interface is the location of electrochemical reaction, while in others, oxygen exchange occurs at the TPBs. The schematic of these two models is shown in Fig. 53a. Robertson and Michaels [714] addressed this issue by measuring the initial current decay in response to potential steps on porous Pt electrode in stabilized ZrO_2 electrochemical cell, with respect to time which is essentially a measure of the rate at which oxygen diffuse on Pt surface. The current decay was shown to be linearly related to $t^{-1/2}$ indicating Cottrell type behavior (shown in Fig. 53b), which is consistent only with the second model as concluded by the author. Thus, it was shown that the mechanism of oxygen exchange reaction occurs at triple phase boundary and not in the two phase boundary of electrode and electrolyte.

Robertson and Michaels [714] further added that the reduction of oxygen on Pt electrodes is probably controlled by both the chemical processes, viz., adsorption and diffusion rather than either of the two in isolation. In this direction, Mitterdorfer and Gauckler [720–722] put forward a noteworthy evidence by measuring impedance of Pt pasted electrodes on YSZ single crystal in the temperature range of 700–800 °C and oxygen partial pressure range of $10^{-4} – 1\text{ atm}$ controlled via ratio of O_2/N_2 mixture. Using the method adopted by Berthier et al. [719], the Faradaic impedance is obtained by subtracting the electrolyte resistance and the impedance due to double- layer capacitance from the overall impedance. A numerical model was constructed in which dissociative adsorption of molecular oxygen on the Pt-surface, diffusion of atomic oxygen, and the charge transfer at TPBs were incorporated in order to study the oxygen reduction at the interfaces between Pt and YSZ. The model allows quantitative estimation of physical parameters governing adsorption, diffusion and charge transfer kinetics. However, when oxygen adsorption kinetic is assumed to follow Langmuir isotherm, a strong dependency of adsorption and diffusion parameters on the surface coverage θ by oxygen molecules was observed. It was concluded that the simple Langmuir kinetic is not sufficient to describe the oxygen interaction with the Pt surface. Thus, a refined adsorption model was used, in which a chemisorbed molecular precursor state O_2^* was introduced when dissociation of molecular oxygen into atoms takes place above ambient temperature. The chemisorbed molecular precursor can either desorb or pass through constrained transition configuration to dissociate and form atoms. The diffusion and adsorption parameters obtained using this alternative precursor mediated adsorption mechanism matches very well with the data measured independently. At temperature greater than 800 °C and at high P_{O_2} , the charge transfer at TPB was observed to compete with adsorption/diffusion contributing half of total impedance. However, at lower temperatures and lower P_{O_2} (or high cathodic overpotential), electrode kinetics is limited mainly by adsorption/diffusion processes (and to certain extent (<10%), by TPB

interface area). This clearly indicates that the system is quite complicated, and the electrode kinetics is governed by multiple factors depending on specific conditions [704].

Janek et al. [720] demonstrated that the gradient in surface coverage by oxygen, which is related to oxygen activity, is the main driving force for the adsorption and transport of adsorbed oxygen. Furthermore, the adsorbed oxygen was reported to be a neutral species. This was further confirmed by Luerßen et al. [721] using XPS investigations. A peak at the binding energy of 530.4 eV appears which clearly indicates that the electronic structure of dissociatively adsorbed oxygen is similar to that of chemisorbed atomic oxygen. In order to study the influence of microstructure on cathodic polarization, Yoon et al. [722] prepared Pt electrodes using different methods, viz., Pt gauze sintered with YSZ, Pt paste applied on YSZ by the tape-casting method, mixture of Pt paste and graphite of 2 μm particle size (pore former) on YSZ and dip coating of Pt electrode with YSZ sol (by sol-gel coating). The characteristics of cathodic polarization were studied using ac impedance spectroscopy in the temperature and P_{O_2} range of 600–1000 °C and 0.01–1 atm, respectively. It was reported that among the electrode reactions, only the gas phase diffusion (occurring via two different ways, i.e., boundary-layer diffusion and pore diffusion) was affected by electrode microstructures.

The complexities of cathodic processes and many of the themes and issues have been found to be a universal feature of all SOFC cathode materials. Adler summarized the working mechanism of Pt cathodes in four important processes [704]:

- A. *Chemical reaction step*: The direct reduction of oxygen molecules to form O^{2-} at the electrode/electrolyte interface does not occur. They should first convert to some “electroactive” intermediate form, i.e., dissociative adsorption of O_2 onto the platinum surface exposed to gas phase followed by surface diffusion and formal reduction by electrochemical processes [699,723,724]. The process is governed by chemical potential gradient which depends on the amount of intermediates present relative to their equilibrium concentration [714,724,725].
- B. *Co-limitation by kinetic and mass transfer*: In the porous electrodes (e.g., Pt paste electrode), the geometric length of active surface is not fixed. Thus, it is difficult to determine the relative significance of diffusion of gases (O_2) and kinetic steps. Hence, both reduction reaction and diffusion possibly takes place simultaneously over an active area. The overall reaction rate is dependent on kinetic and diffusion parameters over a wide range of values. Such type of reaction is termed as co-limited reaction [714,716–718].
- C. *Electrochemical kinetics confined to TPB*: The catalytic reduction of oxygen and the formation of electroactive species occur on Pt surface. These electroactive oxygen species are then transported to Pt/YSZ interface (or TPB) where incorporation of these species into the electrolyte bulk takes place. The process is largely dependent on the active area at and close to TPB [717,721,726,727].
- D. *Non-stationary behavior*: Pt on YSZ shows hysteretic effect so that the passage of current is capable of either altering the reaction kinetics or the dominant reaction pathway [105,728–732].

On the basis of extensive research on Pt electrodes (the only SOFC cathode material used till 1965), it was realized that if the size of active region on the electrode/electrolyte interface is extended, then it is possible to improve the oxygen reduction kinetics at lower temperatures. This led researchers to investigate and invent potential applicability of transition metal oxides (i.e., perovskites) as SOFC cathodes. Besides being a relatively low cost alternative to Pt, perovskites exhibit good catalytic properties for oxygen reduction, chemical and thermal stability, as well as appreciable electronic and ionic conductivity.

4.3. Perovskite materials

For the cathodes of SOFCs, the introduction of perovskite based oxides is of particular importance. In 1966, $La_{1-x}Sr_xCoO_{3-\delta}$ (LSC) was the first perovskite material reported by Button and Archer to be used as cathodes for SOFCs [696,733]. This was followed by synthesis of several perovskite materials which were subsequently tested for their usability. From 1973, $La_{1-x}Sr_xMnO_{3-\delta}$ (LSM) was used

exclusively for cathode application, and till today, it has remained the most investigated cathode material for SOFC.

Perovskites are oxides with general formula ABO_3 (e.g., LaMnO_3 , LaCoO_3 , LaFeO_3) in which A and B cations together possess a net charge of +6. The A sites are occupied by lower valence cations, mainly of rare and alkaline earth metals (alone or mixture), e.g., La, Sr, Ca, Ba, etc., possess larger ionic radius (than B-site cations) and are coordinated to 12 oxide ions. The B-sites are occupied by higher valence reducible transition metal cations (either alone or mixture), e.g., Ti, Cr, Ni, Co, Fe, etc., possess smaller ionic radius and are coordinated to 6 oxide ions [734]. At high temperatures, the octahedral symmetry around the transition metal cations promotes a semiconducting band structure leading to high electronic conductivity. Thus, the B-site cations participate in redox catalytic mechanism.

Most of the undoped perovskite materials are poor oxide ion conductor in air. On partially substituting the A-site cation (or B-site cation) with acceptor cations such as Sr^{2+} , Ca^{2+} , and Ba^{2+} , or the reduction of Mn^{3+} (Co^{3+}) to Mn^{2+} (Co^{2+}) results in the formation of oxygen deficient perovskites such as $\text{La}_{x}\text{Sr}_{1-x}\text{Co}_y\text{Co}_{1-y}\text{O}_{3-\delta}$ [735]. These oxygen vacancy defects form the basis of oxide ion conduction in these perovskites. The conductivity values in some of these materials are as high as observed in typical solid electrolyte material. For example, $\text{Sr}_{0.9}\text{Ce}_{0.1}\text{CoO}_{2-\delta}$ exhibits ionic conductivity of 0.133 S/cm at 800 °C in air.

In the case of LaMnO_3 , Sr^{2+} is the most widely used dopant cation due to small ionic size mismatch between Sr^{2+} and La^{3+} ($r_{\text{Sr,XII}}^{2+} = 1.44 \text{ \AA}$ and $r_{\text{La,XII}}^{3+} = 1.36 \text{ \AA}$) [736]. However, on substituting La^{3+} with Sr^{2+} cations, instead of compensation by the formation of positively charged oxygen vacancy, a common phenomenon in some of the other perovskite materials, an oxidation of manganese cations occurs, which effectively increases the electron-hole concentration and enhances the electrical conductivity [735]. The defect reaction can be given as:



At room temperature, the crystal structure of undoped LaMnO_3 is orthorhombic, which transforms to rhombohedral on doping. The crystallographic transformation from orthorhombic to rhombohedral also occurs at ~600 °C on heating, which is attributed to the partial oxidation of Mn^{3+} to Mn^{4+} ions [737]. This decreases the energy and tends to produce long-range Jahn–Teller ordering. The transition temperature of orthorhombic/rhombohedral is dependent on the Mn^{4+} content and is thus sensitive to

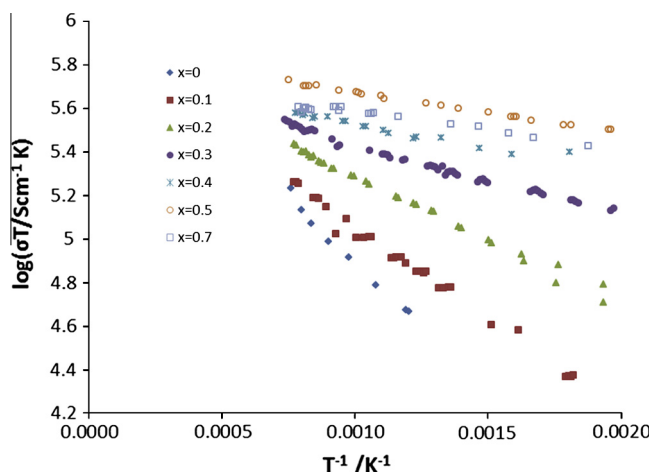


Fig. 54. Variation of electrical conductivity (σ) of $\text{La}_{1-x}\text{Sr}_x\text{MnO}_{3\pm\delta}$ ($0 \leq x \leq 0.7$) at different temperature (at pure oxygen $P_{\text{O}_2} = 1 \text{ bar}$). (Adapted from Ref. [741]).

the stoichiometry of the material. As shown by Eq. (78), the formation of Mn⁴⁺ can be tailored by partially substituting the La³⁺ with lower valence cations such as Sr²⁺ or Ca²⁺ which in turn control the transition temperature.

LaMnO₃ is an intrinsic p-type conductor, and by doping with Sr²⁺ or Ca²⁺ at La³⁺ sites, the electronic conductivity can be enhanced. Divalent alkaline earth dopants are preferred since the resultant perovskites are stable and possess high p-type conductivity in oxidizing atmosphere at the cathode side of SOFC [738,739]. Reports elicit La_{1-x}Sr_xMnO₃ (LSM) with $x = \sim 0.1$ to 0.2 exhibits high conductivity while rendering good mechanical and chemical stability at operational temperatures [738,739]. Mizusaki et al. measured the electronic conductivity of La_{1-x}Sr_xMnO_{3+δ} as a function of temperature (up to 1000 °C) and oxygen partial pressure [741], and a linear increase in electronic conductivity with increasing x was reported. However, conductivity achieved a maxima at $x = 0.5$ [741]. Zhang et al. [742] and Li et al. [743] have also reported an increase of electrical conductivity up to 200–485 S/cm for $x = 0.5$ at 1000 °C. A plot of log σT vs. 1/T for La_{1-x}Sr_xMnO_{3+δ} ($0 \leq x \leq 0.7$) in pure oxygen ($P_{O_2} = 1$ bar) is shown in Fig. 54.

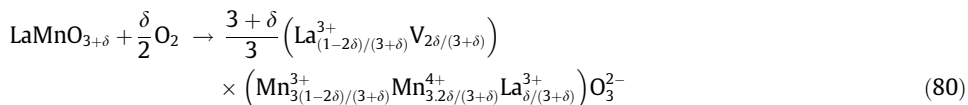
The important issue pertinent to LaMnO₃ based cathodes is their chemical reactivity with YSZ at high temperatures to form poorly conducting La₂Zr₂O₇ at the cathode/electrolyte interface. This chemical reaction can be suppressed by the addition of small amount of Sr²⁺ in LaMnO₃. At higher levels of substitution (>30 mol. %), Sr²⁺ from LSM have a tendency to react with YSZ and form SrZrO₃ at the interface. Thus, 30 mol.% Sr²⁺ added LaMnO₃ is the optimal composition to render good electronic conductivity without the formation of any insulating products.

The linear relationship of electrical conductivity (σ) of undoped LaMnO₃ on plotting ln σT and 1/T indicates conduction occurring due to small polaron hopping mechanism which can be expressed through Arrhenius equation [738,741]:

$$\sigma T = \sigma_0 \exp\left(-\frac{E_a}{kT}\right) \quad (79)$$

where σ_0 and E_a are the pre-exponential factor and activation energy, respectively, for the conduction process. Conductivity is also a function of non-stoichiometry and oxygen partial pressure. It was reported that the σ is constant in the region of excess oxygen (high P_{O_2} , i.e., greater than 10^{-5} bar), and decreases sharply (with $P_{O_2}^{1/4}$) in region of deficient oxygen ($P_{O_2} < 10^{-5}$ – 10^{-10} bar) [744].

Unlike other perovskites, lanthanum manganite exhibits both oxygen excess as well as oxygen deficient non-stoichiometries represented by La_{1-x}A_xMnO_{3±δ} (A is divalent cation, e.g., Sr²⁺ or Ca²⁺; where '+' and '-' indicate excess and deficiency, respectively) [734]. At lower P_{O_2} values, the material becomes oxygen deficient and the positively charge oxygen vacancy defects will then be compensated by the reduction of Mn³⁺ to Mn²⁺. However, in the normal fuel cell operating conditions, the stoichiometry in La_{1-x}A_xMnO_{3±δ} appears to be oxygen excess which indicates the oxidation of Mn³⁺. Numerous defect models have been proposed to describe the defect structure present in oxygen excess LSM. The oxidation of Mn³⁺ in LSM can be either compensated through the formation of oxygen interstitials or cation vacancies. Due to the closed packed structure of the perovskite, it is highly unlikely for the oxide ions to reside in the interstitial sites. Thus, the oxygen excess non-stoichiometry is probably due to the formation of cation vacancies. This has been confirmed by studies performed via neutron diffraction and high resolution transmission electron microscopy [745–747]. Thus, the apparent oxygen excess non-stoichiometry can be considered in terms of Schottky intrinsic disorder, which involves the formation of cation vacancies. In order to explain the upper limit of δ , Van Roosmalen and Cordfunke introduced a parameter ξ which defines the amount of Mn²⁺ and Mn⁴⁺ formed by charge disproportionation of Mn³⁺ [746]. Keeping the constant ratio of La/Mn (or forming equal amounts of La and Mn vacancies), upon addition of excess oxygen, the La-site vacancy model necessitates the occupancy of Mn site by La ions as shown below [746].



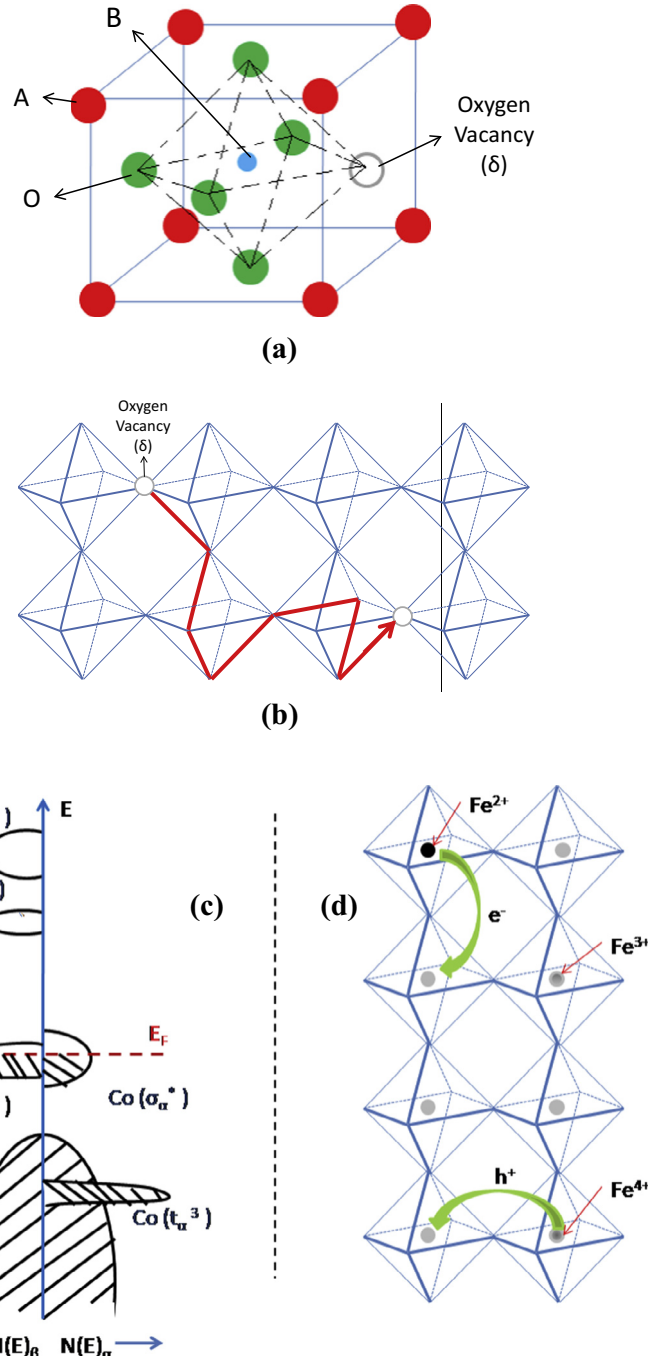


Fig. 55. (a) Crystal lattice structure of $\text{ABO}_{3-\delta}$ with oxygen vacancy, (b) Hopping of oxide ion vacancies governing oxygen migration, (c) Band structure in the metallic $\text{La}_{1-x}\text{Sr}_x\text{CoO}_{3-\delta}$ phase at high-temperature ((a-c) adapted from Ref. [758]), and (d) Electron/hole conduction in semi-metallic $\text{La}_{1-x}\text{Sr}_x\text{FeO}_{3-\delta}$ via hopping mechanism depending on the oxidation states of Fe. (Adapted from Ref. [704]).

Due to dissolution of $3/2\text{O}_2$, 6Mn^{4+} ions and two vacancies (one each at La and Mn sites) are formed:



This model could satisfactorily explain the quantitative dependence between conductivity, non-stoichiometry and oxygen partial pressure [748]. However, the model is applicable only to perovskite system, where charge disproportion reaction occurs. Some other noteworthy works can be found in the published literature [744,749–752].

The electronic conductivity is also dependent on the method of processing the sample, which largely decides the microstructure or crystallinity of the material. The LSM cathodes prepared via solid-state sintering exhibit electronic conductivity between 40 and 485 S/cm at 1000 °C and those by plasma spraying exhibit 50–201 S/cm, i.e., 50% lower than sintered samples [743].

Ionic conduction of LSM arises owing to vacancy of oxygen in the lattice generated due to reduction of Mn^{4+} to Mn^{3+} or of Mn^{3+} to Mn^{2+} [753]. It can be measured either by depolarization with a Hebb Wagner cell or a four-probe technique with electrodes blocking the electron conduction. There lies a significant difference in the measured ionic conductivity values depending upon the method of measurement. For example, the oxygen ion conductivity measured for $\text{La}_{0.9}\text{Sr}_{0.1}\text{MnO}_3$ using Hebb Wagner technique by Endo et al. is 5.9×10^{-8} S/cm at 800 °C [754]. Under similar experimental conditions, Ullmann et al. [755] measured ionic conductivity for $\text{La}_{0.66}\text{Sr}_{0.3}\text{MnO}_{3-\delta}$ to be 1.7×10^{-4} S/cm, which is much higher (by 4 orders of magnitude). Godoi and Souza [756] investigated the electrical conductivity of $\text{La}_{0.7}\text{Sr}_{0.3}\text{MnO}_3$ (LSM)– $\text{Ce}_{0.8}\text{Y}_{0.2}\text{O}_{2-\delta}$ (YDC) composites using dc four-probe technique with Pt electrodes and YSZ as electron blocking electrodes. The use of two types of electrodes allows the measurement of ionic and electronic conductivity of LSM to be 6.3×10^{-5} S/cm and 1.1×10^{-2} S/cm, respectively, at 800 °C.

4.4. Mechanism of cathode reactions

4.4.1. At atomic scale

Fig. 55a shows the perovskite crystal structure ($\text{ABO}_{3-\delta}$) with an oxygen vacancy defect. In this diagram, a reducible transition metal (Mn, Co or Fe alone or mixture) cation sits on B-site and a mix of rare and alkaline earths (La and Sr) cation occupy the A-site. The octahedral symmetry existing around the transition metal cation renders high electronic conduction by promoting a metallic or semiconducting band structure at elevated temperatures. In most of the perovskite oxides, the amount of A and B site cations can be tailored to introduce a high concentration of oxide ion vacancies (δ). At high temperatures, oxide ion vacancies facilitate bulk ionic oxygen transport via discrete hopping on the oxygen sublattice (**Fig. 55b**).

All the materials in the LSCF family (of structure $\text{La}_{1-x}\text{Sr}_x\text{Co}_{1-y}\text{Fe}_y\text{O}_{3-\delta}$) possess the electronic transference number close to ~1. Using crystal field theory, the electronic structure LaCoO_3 can be expressed in terms of partially delocalized $\text{O}_{2\text{p}}\text{-Co}_{3\text{d}}$ band states in the t_{2g} and e_g energy levels [757,758]. The electronic configuration of the Co^{3+} (occupying the octahedral position in LaCoO_3) is $[\text{Ar}] 3\text{d}^6$, where Ar represents the underlying electronic arrangement of the rare gas argon. In an octahedral environment, the crystal field splitting on the energy levels of the 3d orbitals of Co^{3+} gives three equivalent levels of lower energy, t_{2g} levels and two equivalent levels of higher energy, the e_g levels. At low temperatures, Co^{3+} in LaCoO_3 posses low spin configuration. LaCoO_3 has complex electronic properties due to transition of Co^{3+} from low intermediate spin ($t_{2g}^6/t_{2g}^5e_g^1$) to paramagnetic high spin state (t_{2g}^4/e_g^2) at an elevated temperature. At these temperatures, there is an electron transfer from high spin Co^{3+} to low spin ions which generates Co^{4+} , Co^{2+} , etc. Around 930 °C, LaCoO_3 exhibits a transition due to formation of delocalized e_g states. Above this temperature, LaCoO_3 exhibits a metallic behavior. On doping Sr in LaCoO_3 , Co^{4+} holes and d electrons are formed, which lead to high electronic conductivity at relatively lower temperatures (~SOFC operating temperatures). **Fig. 55c** represents the situation of LSC at high temperature. The Fermi energy level falls within a half-filled band by addition of 10 mol.% Sr or higher, containing a mixture of localized t_{2g} and more delocalized $e_g(\sigma^*)$ states [759–766]. LSC shows metallic/semi-metallic conduction, in which conductivity initially increases

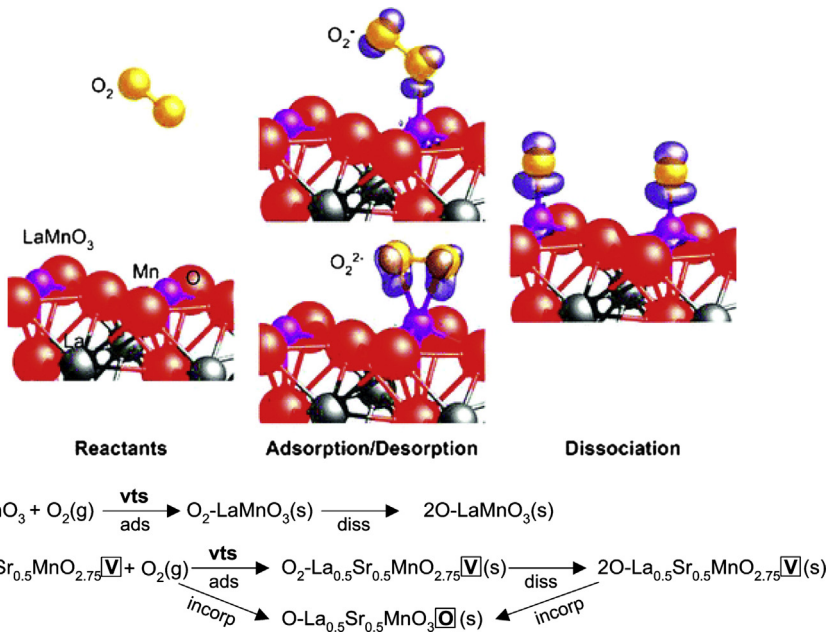


Fig. 56. (a) Elementary reaction steps of interactions between O_2 and LaMnO_3 where isosurfaces in purple represent charge density changes around oxygen species on the surface. O^{2-} and O_2^+ correspond to superoxo and peroxy-like species, respectively, (b) O_2 reduction on LaMnO_3 and Sr-doped $\text{LaMnO}_3(\text{La}_{0.5}\text{Sr}_{0.5}\text{MnO}_{2.75})$ where (g), (s), vts and v denote gas, surface, vibrational transition state and oxygen vacancy, respectively and 'ads', 'diss' and 'incorp' are adsorption, dissociation and incorporation, respectively. (Reprinted with permission from Ref. [774]).

(with temperature) and then decreases beyond 500°C . Also, the Seebeck coefficient approaches to zero at an elevated temperature [765,766].

In contrast, a weak Hubbard or Hubbard-like band gap seems to appear for LSF due to electron-electron repulsion on the iron site [769,770]. Such a repulsion is responsible for spatial and localized charge disproportionation of Fe^{3+} to Fe^{2+} and Fe^{4+} (shown in Fig. 55d). LSF exhibits p-type conductivity at high temperature, and at high P_{O_2} (via hopping from Fe^{4+} to Fe^{3+}) and n-type conductivity at low P_{O_2} (via hopping from Fe^{2+} to Fe^{3+}) [771]. In the case of solid solutions of LSC and LSF where B-site is randomly occupied by iron and cobalt, the electronic structure becomes quite complicated. Nevertheless, the compound exhibits more semiconducting nature when Fe content is high ($y = 0.8$), while more metallic behavior when Co content is high ($y = 0.1$) [772,773].

Choi et al. [774] examined the interactions between molecular oxygen and Sr-doped or undoped LaMnO_3 using DFT calculations and statistical theory methods. Based on the results, it was suggested that the stability of the molecularly adsorbed and dissociated oxygen species depends on the surface orientation and defects present in the cathode materials. They further predicted that the presence of oxygen vacancies on the surface enhances the dissociation rate of adsorbed oxygen species due to lower dissociation barrier on $\text{La}_{0.5}\text{Sr}_{0.5}\text{MnO}_{2.75}$ (0.33 eV) than on LaMnO_3 (0.48 eV). The elementary reaction steps of interactions between O_2 and LaMnO_3 and the mechanism is shown in Fig. 56.

4.4.2. At bulk scale

The oxygen reduction reaction mechanism is more difficult to deduce in porous LSM cathodes due to irregular or poorly defined geometries (electrode morphology). This has a significant effect on the measured kinetic and mechanistic parameters giving an anomalous transfer coefficient value of <0.5 . The rate of oxygen reduction reaction at dense $(\text{La}_{0.8}\text{Sr}_{0.2})_{0.98}\text{MnO}_3$ (LSM) investigated by Co et al. was found to be limited by dissociation of $\text{O}_{2\text{ads}}$ at low currents and by the first electron transfer step reducing $\text{O}_{2\text{ads}}$ to $\text{O}_{2\text{ads}}^-$ at high currents [775]. Understanding the oxygen reduction reaction at bulk scale in

perovskite materials largely depends on the microstructure of the material. As observed in the case of platinum cathode, one or more rates determining steps may be present depending upon the conditions, and a similar feature has been found with perovskite based cathode materials. The ORR mechanism in perovskite at bulk scale has been investigated for both, thin and dense films, as well as in thick and porous cathode samples as discussed in the following sections.

4.4.2.1. Dense thin-film mixed conducting electrodes. In the cathodes based on perovskites, two possible reaction pathways for the oxygen reduction reaction can be given as (i) along the TPBs, and (ii) through the bulk transport of oxide ion. Due to the complicated microstructure of the porous cathode, it is difficult to isolate the contribution from each pathway mechanism. Thus, using cathode with dense thin film structure will allow quantification of TPB and provide better understanding of the reaction through the bulk pathway. In the last two decades, numerous investigations have been performed on dense and thin film mixed ionic electronic conducting electrodes understanding the rate limiting step for cathodic reaction mechanism under different conditions such as temperature, oxygen partial pressure, morphology, and electrode composition, [754,776–790]. In the initial years, researchers did not emphasize much on TPB contact area and the main challenge in their study was to fabricate dense and crack free films. Kawada et al. measured the electrochemical impedance of the dense thin films of $\text{La}_{0.6}\text{Sr}_{0.4}\text{CoO}_{3-\delta}$ deposited on thick plate of $\text{Gd}_{0.1}\text{Ce}_{0.9}\text{O}_{1.95}$ (GDC) using laser ablation [791]. The measurements were performed over a range of temperature (600–800 °C) and P_{O_2} conditions, and also as a function of film thickness in order to understand the factors contributing towards the resistance during oxygen transport process across the mixed electrodes (i.e., transfer of electrons to O_2 , and formation of O_2^-) [777,782]. The Nyquist plot shows a well defined low-frequency semicircle which can be analyzed by fitting an electric circuit of resistor and capacitor in parallel. The chemical capacitance for these films varies significantly with P_{O_2} and dc bias. The obtained results clearly indicate the rate limiting step to be surface oxygen exchange [777]. Isotope exchange ($^{18}\text{O}^{2-}/^{16}\text{O}^{2-}$) measurements performed on dense LSC (~0.5 μm) thin film supported on polycrystalline $\text{Ca}_{0.1}\text{Ce}_{0.9}\text{O}_{1.9}$ (CDC) confirmed that the resistance due to oxide ion transport in the bulk and across the LSC/CDC interface is almost negligible [791]. This was later confirmed by other reports as well on other perovskites exhibiting high ionic conductivity [776,777,786–790]. This study shows that for a dense thin film (up to few μm), bulk will offer a very little resistance and is the dominant pathway for oxide ion diffusion.

Yang et al. [789] performed the impedance studies of oxygen exchange on the dense thin film (0.5 μm) electrodes of $\text{La}_{0.5}\text{Sr}_{0.5}\text{CoO}_{3-\delta}$ supported by single crystal disk of YSZ under various temperature and P_{O_2} conditions. The three distinct arcs were observed in the Nyquist plot: (i) The high frequency arc was assigned to the ionic conduction in YSZ electrolyte response, while (ii) the low frequency arc, which is sensitive to partial pressure of oxygen, was associated with the response of oxygen exchange on the thin film electrode. (iii) The capacitance values from the medium frequency impedance arc were determined to be 0.01–0.04 F/cm² in the temperature range of 500–750 °C, which is close (within an order of magnitude) to the reported interfacial pseudocapacitance at the Pt/YSZ interface. Thus, the authors attributed the observed medium frequency impedance arc to the interfacial resistance arising from oxide ion exchange across the electrode/electrolyte interface. The high interfacial barrier was attributed to the precipitation of $\text{La}_2\text{Zr}_2\text{O}_7$ and SrZrO_3 at the interface formed from the chemical reaction between electrode and electrolyte at elevated temperatures (>1100 °C).

The chemical capacitance (or pseudocapacitance or Faradaic capacitance) is another important parameter, which is widely used to measure the contribution through the bulk toward the oxygen transfer. It is a non-interfacial capacitance which arises from the change in oxygen stoichiometry in the MIEC film. The oxygen reduction reaction in MIEC can be divided into two steps, viz., (i) reduction reaction from O_2 to O^{2-} at the gas-film interface, and (ii) migration of oxide ions through the bulk of film. For a given situation, either of these two steps can be rate determining. The schematic shown in Fig. 57 illustrates the factors contributing to the resistance and capacitance of a dense thin film MIEC. If the step (i) is rate determining, the rapid oxide ion transport through the bulk will provide a uniform supply at the film/electrolyte interface, which will then, serve as a reservoir of oxygen vacancies and

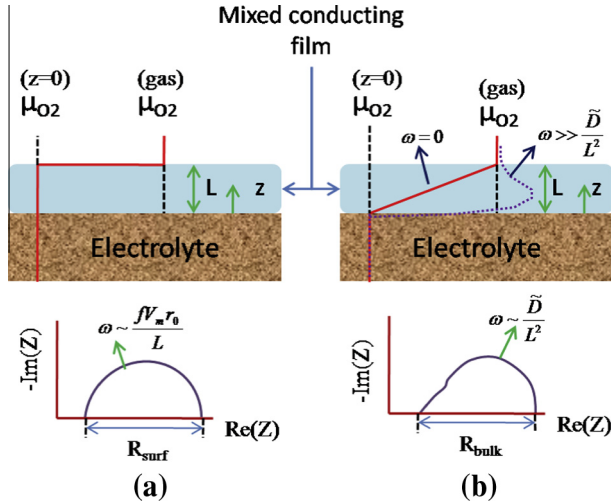


Fig. 57. Model of dense thin-film mixed conducting cathodes showing ‘chemical capacitance’. Here, (a) Limitation of absorption/desorption governs the net reduction/oxidation at cathode surface exposed to gas, and (b) Limitation by ambipolar diffusion of O^{2-} governing the reduction/oxidation through dense and thin mixed-conducting cathode. (Adapted from Ref. [704]).

associated electrons/holes in order to maintain charge neutrality. Assuming both the solid–solid interface and bulk to be in chemical and electrical equilibrium, the impedance (Z) of the film can, then, be expressed as:

$$Z = \frac{R_{surf}}{1 + j\omega R_{surf} C_L} \quad (82)$$

$$R_{surf} = \frac{RT}{4F^2} \frac{1}{2r_0} \quad (83)$$

$$C_L = \frac{4F^2}{RT} \frac{2L}{fV_m} \quad (84)$$

where R_{surf} denotes area of specific resistance related to the oxygen reduction at the gas-film interface; C_L represents the chemical capacitance across the film with thickness L ; r_0 and V_m are the thermodynamic parameter which express the ease with which material changes stoichiometry on changing the P_{O_2} , equilibrium oxygen exchange rate and molar volume of the oxide, respectively [704]. Fig. 57 shows the Nyquist plot for this limiting case, where a semicircular arc can be observed with R_{surf} as a diameter and a characteristic frequency of $1/R_{surf} C_L$.

In the case when step (ii) is rate determining (i.e., limited by transport of oxide ions through the bulk of the film) while the bulk electronic conduction is rapid, Warburg impedance for finite length diffusion is obtained, which can be represented as:

$$Z = R_{bulk} \frac{\tanh(\sqrt{j\omega R_{bulk} C_L})}{\sqrt{j\omega R_{bulk} C_L}} \quad (85)$$

$$R_{bulk} = \frac{RT}{4F^2} \frac{fV_m L}{2\tilde{D}} = \frac{L}{\sigma_i} \quad (86)$$

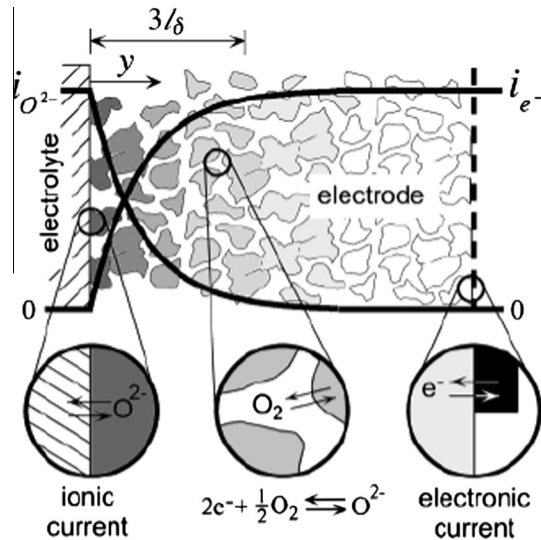


Fig. 58. An impedance response model of a thick porous mixed conducting cathode proposed by Adler. In this model, utilization region is defined by the distance away from the electrode/electrolyte interface l_δ where oxygen reduction takes place. (Reprinted with permission from Ref. [793], copyright Elsevier, 1998).

where R_{bulk} represents area-specific resistance related to the oxide ion conductivity of the film (σ_i); \tilde{D} is the chemical diffusion coefficient for oxide ions. Since the change in oxygen stoichiometry takes place over the entire film thickness, C_L remains the same as in surface limited case [792].

In the thin film electrodes, when these chemical reaction steps are rate limiting, the accumulation of electroactive intermediate species in bulk increases the effective capacitance. The chemical capacitance is proportional to the film thickness and the ease with which it brings change in the bulk stoichiometry. The high capacitance value ($0.1\text{--}1\text{ F/cm}^2$) exists for a very thin cathode film ($1.5\text{ }\mu\text{m}$), which is considerably greater than the pseudocapacitance of Pt cathodes ($\sim 10^{-3}\text{ F/cm}^2$) that results from surface dominated oxygen-adsorption and transport and the interfacial polarization capacitance of Pt/YSZ interface (ranges within $10^{-6}\text{--}10^{-5}\text{ F/cm}^2$). This large difference in the capacitance value indicates the importance of bulk pathway in affecting the reaction kinetics of the cathode film. Alternately, there has been no other satisfactory explanation so far for such a large capacitance rather than bulk reaction pathway.

4.4.2.2. Porous and thick mixed conducting cathodes. In the case of porous cathodes, reaction at gas/solid interface and transport into the bulk are affected by structural parameters, such as, net surface area, content of porosity, and surface tortuosity. The reaction $2e^- + 1/2O_2 \rightarrow O^{2-}$ can be described as an acceptance of electrons by molecular oxygen to produce ionic current over the electrode thickness. The model developed by Adler (shown in Fig. 58) consist of a thick and porous cathode conducting both electrons and ions, while incorporating the effect of gas phase diffusion and charge-transfer resistance at electrolyte-electrode interface with time dependency [793]. The measured impedance is expressed to be the sum of R_e (electrolyte resistance) + $Z_{interface}$ (electrochemical kinetic impedance at electrolyte-electrode interface) + $Z_{chemical}$ (chemical impedance arising from oxygen absorption, and diffusion in solid and gas phase both inside and outside the electrode). In the case of semi-infinite thick porous cathode with no limitations from gas phase diffusion, the chemical impedance is co-limited by absorption and transport of oxygen [793,794]. This can be expressed as follows:

$$Z_{chem} = R_{chem} \sqrt{\frac{1}{1 + j\omega(R_{chem}C_{l_\delta})}} \quad (87)$$

and,

$$R_{chem} = \frac{RT}{4F^2} \sqrt{\frac{fV_m}{\tilde{D}_{eff} ar_0}} = \sqrt{\frac{4R_{surf}}{\sigma_{i,eff} a}} \quad (88)$$

$$C_{l_\delta} = \frac{4F^2}{RT} \frac{(1-\varepsilon)l_\delta}{fV_m} \quad (89)$$

where R_{chem} and C_{l_δ} are the resistance and capacitance, respectively, representing the co-limitation from surface kinetics and ionic/electronic transport of the MIEC. The R_{chem} value depends on surface area (a), porosity (ε), path tortuosity (τ) and the effective chemical diffusion coefficient (\tilde{D}_{eff}) which is corrected for τ and ε , and can be given as $(1-\varepsilon)\tilde{D}/\tau$. As defined earlier in the case of dense thin film, f, r_0 and V_m are the thermodynamic parameter, equilibrium oxygen exchange rate and molar volume of the oxide, respectively. The R_{chem} can also be expressed in terms of surface (R_{surf}) and bulk resistance by inputting Eqs. (83) and (86) in Eq. (88), and using effective ionic conductivity ($\sigma_{i,eff}$) corrected for τ and ε i.e., $\sigma_{i,eff} = (1-\varepsilon)\sigma_i/\tau$.

The capacitance in this case is similar to that of previous (thin film) case; however, the length parameter is a characteristic utilization length (l_δ) instead of a geometric length (L), and is given as [793,794]:

$$l_\delta = \sqrt{\frac{\tilde{D}_{eff}}{fV_m ar_0}} = \sqrt{\frac{\sigma_{i,eff} R_{surf}}{a}} \quad (90)$$

According to Adler's model [793], in the porous electrode at steady state condition, the exponential decay of oxygen vacancy concentration with increasing distance from the electrode/electrolyte interface was predicted. Oxygen conversion primarily occurs within the distance l_δ (expressing the size of active region) from the electrode/electrolyte interface, which underlines the significance of utilization length. The chemical capacitance (shown in Eq. (89)) has been observed to be proportional to l_δ , which is similar to the case of chemical capacitance being proportional to the film thickness in case of dense electrode. However, in the porous electrode case, the capacitance is dependent on diffusion and kinetic parameters instead of the geometrical thickness of the film.

The impedance of thick and porous electrode shown in Eq. (87) [794] is often termed as Gerischer impedance. This impedance is different from the one obtained for Pt electrodes (co-limited by adsorption and surface diffusion), as in this case electrode reaction is co-limited by kinetics and bulk diffusion parameters. Adler et al. [794] measured the impedance of porous and thick $\text{La}_{0.6}\text{Sr}_{0.4}\text{Co}_{0.2}\text{Fe}_{0.8}\text{O}_{3-\delta}$ (LSCF) cathode on SDC. A fairly good fit was obtained when the electrode portion of the impedance spectra was fitted using the impedance model (shown in Eq. (89)) with nonlinear complex least squares method. The obtained R_{chem} and C_{l_δ} values were found to be consistent with those estimated from the known bulk properties of LSCF. However, a large chemical capacitance value was obtained which suggest a considerable oxidation/reduction of the bulk. Furthermore, the large observed chemical capacitance during open circuit condition, suggest that the bulk mediated diffusion process dominates, compared to surface diffusion in the material with good ionic conductivity (and with high oxygen vacancy concentration). In the case of poor ionic conductive materials, such as, LSM, applications of this model underestimate the performance, which suggests that the surface pathway diffusion mechanism is more dominating. Furthermore, when impedance spectra was measured on LSC cathode (with YSZ electrolyte at temperatures higher than 550 °C), no intermediate impedance feature, which typically relate to interfacial impedance, was observed. In the given conditions, only Gerishcher shape impedance was observed, which clearly indicates that the electrode reaction is co-limited by adsorption and transport of oxide ion to the interface. Later, investigations by various research groups on porous mixed conducting electrodes also reinforce the observation that the bulk pathway strongly contribute in governing electrode kinetics [51,795–801]. In a quest to determine the limiting thickness of porous electrode while rendering appreciable performance, Koyama et al. came up with a finding

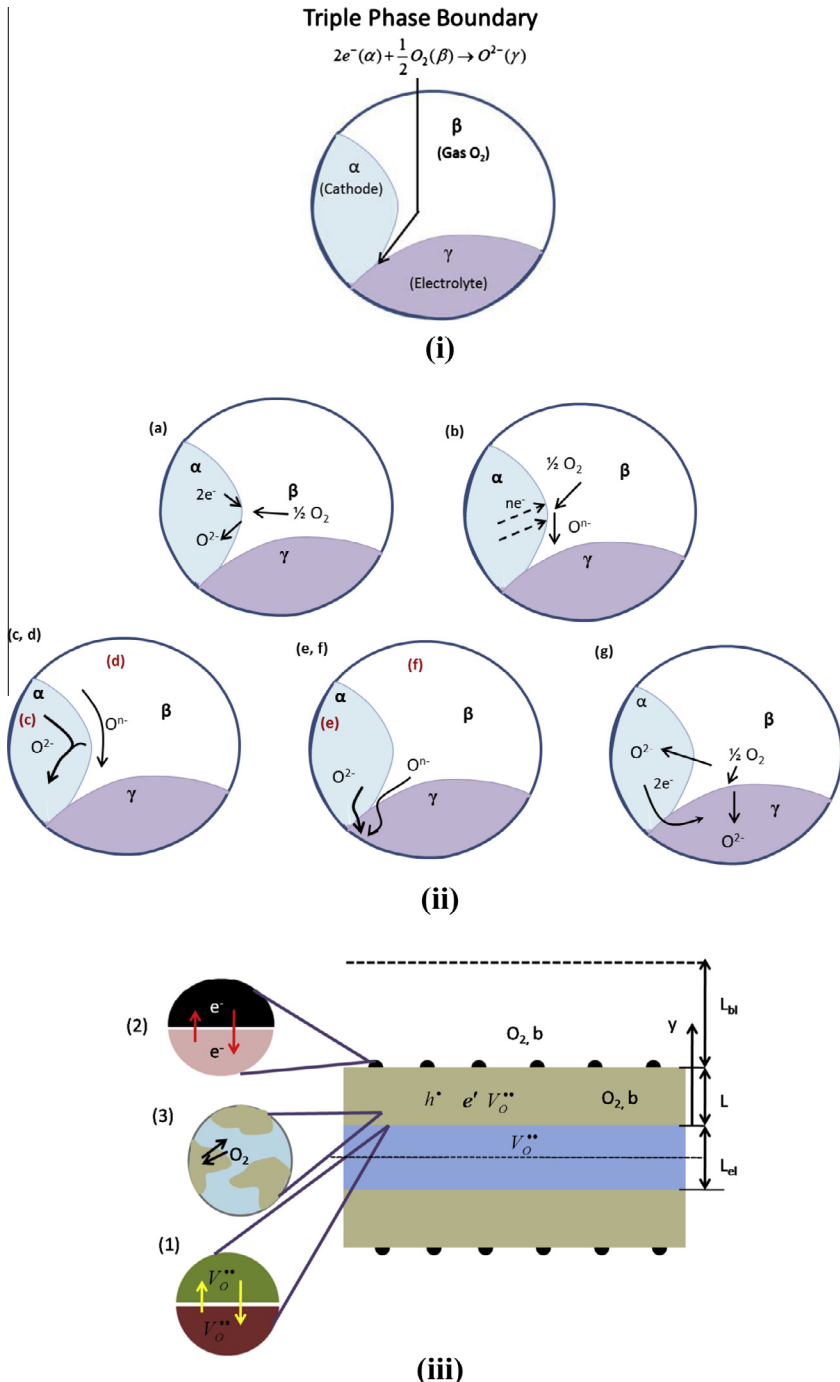


Fig. 59. (i) TPB structure of electronically conducting perovskite electrode material LSM. (Adapted from Ref. [704]). (ii) Sketches of the mechanisms that possibly govern the oxygen reduction reaction at the TPB of porous single-phase mixed ionic-electronic conductor. (Adapted from Ref. [704]) (iii) Schematic of oxygen reduction reaction and cell geometry model proposed by Adler. (Adapted from Ref. [794]).

that the performance of porous $\text{Sm}_{0.5}\text{Sr}_{0.5}\text{CoO}_{3-\delta}$ with SDC electrolyte improves up to 10–15 μm thickness, and beyond which the performance saturates [801].

The performance of Pt-electrode is largely dependent on the length of TPB. Researchers have used similar concept in perovskite cathodes, and examine the relationship between the microstructure and performance of the given material. One of the noteworthy examples is the contribution by Mizusaki and coworkers, stressing on the aspect of adopting appropriate processing technique for correlating the microstructure and morphology of $\text{La}_{1-x}\text{Ca}_x\text{MnO}_3$ electrodes on YSZ with their impedance [802]. The electrode capacitance was observed to increase with the TPB length estimated via electron microscopy, which is anticipated because of interfacial polarization. Furthermore, low polarization studies also elicited an inverse dependence of TPB length with η and resistance. Also, both monolithic and composite electrodes have shown a direct dependence of electrode kinetics on TPB length, which in perovskite cathodes has been discussed in detail.

4.4.2.3. Triple phase boundary. The phenomenon of triple phase boundary was realized in 1920s, while studying the H_2 oxidation on Pt electrodes. The requirement of Pt exposure simultaneously to both solution and gas was described in order to attain a tenable reaction. Alfred Schmid named such a ‘gas-diffusion reaction’ as ‘die Diffusions-Elektrode’ [803]. In SOFCs, the electrochemical reaction of oxygen reduction at the cathode occurs at the intersection between air, electronic conductor (LSM) and oxide-ion conductor (YSZ), which is termed as TPB. Here, the connectivity of gas phase both with the electrode and electrolyte is necessitated, were molecular oxygen diffuses through the open pores of electrode and gets reduced in matrix. This has been advocated as the universal phenomena of all cathodes regardless of the microstructure, example being porous Pt or LSM (see Fig. 59i). The interface of the cathode material (α) (an electronic conductor), and an oxide-ion conducting electrolyte phase (γ) is exposed to molecular oxygen (β). A conduction pathway for electrons to the interface occurs through α phase, which is connected to an electronic current source away from the interface. The oxygen rich gas (β -phase) serves as a reservoir for molecular oxygen. However, the oxide ions formed in the oxygen reduction reaction are incorporated into the electrolyte phase (γ), and are then subsequently diffused towards the anode side under the influence of chemical potential gradient.

Extensive research has been dedicated to evince the role of the geometrical length of these TPBs, where oxygen reduction reaction mainly occurs. This involves the formulation of composites, tailoring the microstructure of the composites in terms of the relative particle size ratio, and selection of appropriate processing and fabrication techniques to obtain highly porous structure with appreciable continuity of the ionic/electronic conduction pathways. LSM/YSZ composite electrodes have been found to perform better due to the additional TPB sites created within the 3-D bulk of the electrode. Since the electrochemical reduction of O_2 occurs within the first few micrometers from the electrolyte interface, the functionally graded electrode materials have also been shown to provide optimal cell performance. In this context, mainly three categories of perovskite materials have been developed, viz.,

- (1) *Electrically conductive single-phase porous oxide*, e.g., $\text{La}_{1-x}\text{Sr}_x\text{MnO}_3$ (LSM).
- (2) *Mixed ionic-electronic conducting (MIEC) single-phase porous oxide*, as it serves as both ionic and electronic conductor, e.g., $\text{La}_{1-x}\text{Sr}_x\text{Co}_y\text{Fe}_{1-y}\text{O}_{3-\delta}$ (LSCF) and renders a significantly extended active region for oxygen reduction reaction. Thus, the surface oxygen can be reduced to O^{2-} at the porous electrode surface, and the transfer of O^{2-} to the electrolyte primarily occurs through bulk ionic transport. This catalyses the oxygen reduction reaction which, in turn, significantly improves the reduction kinetics at lower temperatures (at <800 °C) [705,776,795,804–814]. Thus, a good ion- and electron-conducting electrode serve as a good cathode for SOFCs [704,815–817]. A detailed insight of the reaction mechanism at TPB of MIEC type cathode is illustrated in the sketches shown in Fig. 59ii, where α represents the MIEC phase, β the gaseous phase, and γ the ionic-conducting region. Firstly, the molecular oxygen permeates into the bulk of porous MIEC phase, where molecular oxygen completely (Fig. 59ii(a)) or partially (Fig. 59ii(b)) reduces on the electrode surface. Fig. 59ii(c) and (d) shows the bulk transport of O^{2-} and surface transport of O^{n-} towards α/γ interface. This is followed by charge transfer of O^{2-} (Fig. 59ii(e)) or reduction of O^{n-} (Fig. 59ii(f)) at α/γ interface. In addition,

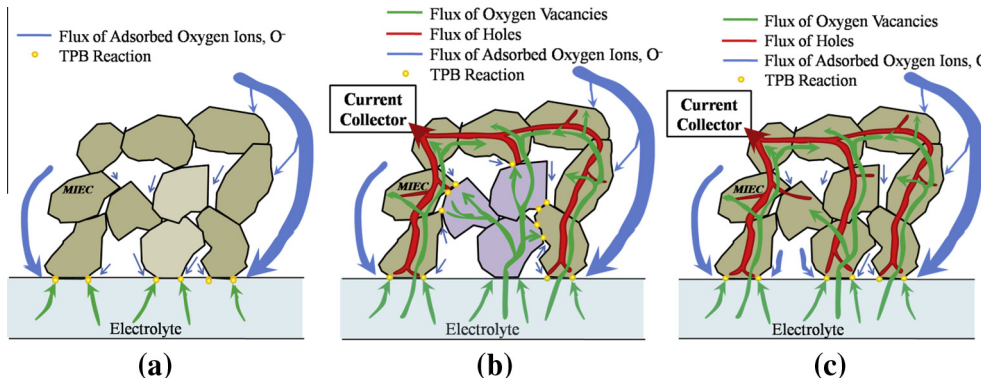


Fig. 60. Schematic diagrams of reaction pathways for SOFC cathodes and processes at TPBs: (a) electronically conducting single-phase porous oxide, (b) mixed conducting single-phase porous oxides, and (c) two-phase porous composites. ((a–c) Adapted from Refs. [704,735,814]).

the generation and/or transport of O^{2-} and/or O^{n-} in electrolyte may be dominated by one or more of these reaction-rates (Fig. 59ii(g)) [704]. Fig. 59iii shows a schematic of the symmetric cell proposed by Adler consisting of an electrolyte pellet with thickness L_{el} with two identical porous electrodes of thickness L [794]. Both electrodes are exposed to the same gas atmosphere and each is separated from the well-mixed gas by a boundary layer of thickness L_{bl} . The overall reaction occurs via three physically separated interfacial reactions: (1) charge-transfer of oxide ion vacancies at MIEC (cathode)/electrolyte interface, (2) charge-transfer of electrons across the current-collector/MIEC interface, and (3) oxygen exchange at the gas/MIEC interface. It is important to note that the interface of gas–MIEC includes the entire internal surface area of the perovskite mixed conductor along with the boundary between porous region and gas phase boundary layer. This layer is considered to be the region where molecular oxygen from gaseous phase, rests (physisorbed) and enters into the pores of the mixed conductor via diffusion.

- (3) *Two-phase porous composite* is the combination of electronically conductive LSM, and an ionically conducting oxide (i.e., electrolyte). In the porous composite, cathodes are processed with the first layer (next to cathode-electrolyte interface) containing 1:1 volume ratio mixture of LSM and YSZ composite to serve as electrocatalytically active layer (due to the large TPB geometric length) and the outer layer(s) consisting mainly of LSM to provide efficient current collection. This approach to develop cathode has an advantage of relatively larger contact area between two conducting phases (electronic and ionic) compared to that of others.

Fig. 59 shows the overall reaction pathways at the TPBs of the three categories of cathodes discussed above [704,814]. Fig. 60 summarizes the three main pathways of oxygen reduction and incorporation reaction that can possibly influence the rate-determining steps. There is always possible modification of these pathways, e.g., adsorption of a molecular rather than an atomic species or diffusion along the cathode/electrolyte interface. Also, a combination of electrode and electrolyte surface pathways, such as cathodic adsorption and electrolytic surface diffusion, are feasible [735,800,814]. The interfacial reactions are directly influenced by the rate of diffusion of molecular oxygen along gas-phase boundary layer, followed by its subsequent diffusion into pores of MIEC material. It also depends on the transport of oxide ions and electrons (or holes) through the bulk of the MIEC. The conceptual models of electrode performance based on TBP have contributed immensely in enabling engineering design and controlling of the microstructure of SOFC cathodes. However, there are certain uncertainties worth noting: (i) under low η values, oxygen reduction pathway operates primarily through surface-mediated mechanism like Pt, but under moderate to high η values, a parallel bulk-mediated transport path is created near TPB. This effect to some extent, explains the complexity

arising from geometry and scaling effect in controlling electrode performance. (ii) There also exist irreversibilities and significant hysteresis in the behavior of LSM, as it is extremely sensitive to processing and operating history [704]. (iii) There also arises some resistance in the region of the solid–solid interface owing to the formation of insulating reaction products (discussed in degradation and failure section) between LSM and electrolyte. Thus, in order to enunciate the underlying mechanisms and electrochemical reactions of processed perovskite materials, an in-depth and refined experimentation is required to evaluate dependency of its performance on specific processes (which actually occur at and near TPB), materials properties, microstructure, etc.

4.5. Strategies of materials selection for intermediate (or low) temperature cathodes

One of the major thrust areas of research relating to SOFC technology is to lower the current operational temperature (~ 1000 °C) of the working cell. Using advanced materials, and better cell designs can result in decreasing the operational temperature range, down to 600–800 °C without compromising with the power output. There are several benefits coming from it, e.g., slower chemical and thermal degradation of cell components or higher long term stability, the possibility of using cheap and easily available materials [818], shorter warm-up time, compatibility with internal fuel reforming and preventing problems relating to cell stack sealing and gas system [819–821]. However, reducing temperature leads to not only high ohmic losses due to electrolyte, but also high electrode polarization losses. The cathodic overpotential of the cathode materials (such as $\text{La}_{0.72}\text{Sr}_{0.18}\text{MnO}_3$ and $\text{La}_{0.6}\text{Sr}_{0.4}\text{Co}_{0.2}\text{Fe}_{0.8}\text{O}_3$) was found to increase significantly on lowering the temperature [799]. In order to reduce the ohmic loss, it is essential to reduce the thickness of electrolyte layer as much as possible. In such SOFCs (with thin film electrolytes), polarization losses at cathode (that occurs due to O_2 reduction) constitutes the major fraction of the overall losses of the cell [820,822,823]. The high cathodic polarization losses are attributed to the high activation energy and slow oxygen reduction reaction. Furthermore, it also depends upon the migration of oxide ions within the porous cathode structure, where the heterogeneous chemical reaction contribution (R_{chem}) can be calculated using ALS model (Adler Lane Steel model) proposed by Adler et al. [794]. This model takes into account the oxygen vacancy transport in the electrode, oxygen exchange at the gas/MIEC cathode interface, gas diffusion in both the electrode and a stagnant gas layer outside the electrode (gas phase boundary layer), and the vacancy concentration of the MIEC. This Gerischer impedance model couples the oxygen exchange at the electrode surface with oxygen ion diffusion, making it possible to adopt a probable strategy for tailoring and optimizing the electrodes composition and structure to gain appreciable performance at intermediate temperatures. By inputting the values of oxygen self-diffusion coefficient (D^* , cm^2/s), oxygen surface exchange coefficient (k , cm/s) and other microstructural parameters, R_{chem} can be calculated using the equation given below:

$$R_{\text{chem}} = \frac{RT}{2F^2} \sqrt{\frac{\tau}{(1-\varepsilon)aC_o^2D^*k}} \quad (91)$$

where τ is the tortuosity, ε is the fractional porosity, a is an internal surface area/unit volume, and C_o is the surface concentration of oxygen.

In practice, the cathode polarization losses can be reduced by two main approaches, viz., either by choosing an appropriate cathode material composition (with optimum TPB match) to improve the oxygen exchange and diffusion kinetics [809], or by modifying the cathode/electrolyte interface microstructure to extend the TPB dimensions. Electrochemical investigations on dense, porous and porous/dense double layered cathode materials based on LSC and LSM (corresponding to $\text{La}_{1-x}\text{Sr}_x\text{CoO}_3$ and $\text{La}_{1-x}\text{Sr}_x\text{MnO}_3$ structures, respectively) revealed that the surface area is also one of the important factors [797].

Thus, the high performance cathodes can be achieved by processing a mixed ionic- and electronic-conducting electrode with a high surface area, such as, porous MIEC cathode. As an alternative method, cathodic biasing or polarization can be utilized to enhance cathode activity [828–830]. This has been reported to notably reduce the oxygen reduction reaction overpotential on porous LSM [827,828] and the phenomenon is termed as ‘activation effect’ [829] or hysteretic behavior of

cathodes [830]. Besides influencing the surface microstructure and composition of the cathode, polarization may also induce morphological changes at the cathode/electrolyte interface. The rate of oxygen reduction reaction is reported to increase due to the formation of oxygen vacancy, adjacent to TPBs during surface and compositional changes [825]. There is always a possibility that manganese dioxide (in LSM) undergoes partial reduction which opens up the pathway for oxygen in the gas to reach directly into the electrolyte material [824]. However, very little is understood till date about the mechanism accountable for electrode activation or for the hysteretic behavior.

The microstructure (which essentially defines the performance of the cathode material) can be tailored by selecting appropriate combination of the constituent materials and optimizing the sintering and processing parameters to generate grains of different sizes. Table 8 reviews the noteworthy investigations by various researchers during the development of perovskite cathode materials. It is compared with the traditionally utilized electrolyte materials for reference. Bebelis et al. [831,832] investigated the electrochemical performances of L58SCF, LS2F and LSM/LSM–8YSZ cathode materials of composition $\text{La}_{0.58}\text{Sr}_{0.4}\text{Cr}_{0.2}\text{Fe}_{0.8}\text{O}_{3-\delta}$, $\text{La}_{0.9}\text{Sr}_{1.1}\text{FeO}_{4-\delta}$, and $\text{La}_{0.65}\text{Sr}_{0.3}\text{MnO}_{3-\delta}$ (LSM)/LSM–8YSZ (50 wt.% LSM–50 wt.% 8YSZ), respectively, interfaced to a bi-layered ($\text{Ce}_{0.8}\text{Gd}_{0.2}\text{O}_{2-\delta}$)/YSZ electrolyte via EIS and current density measurements in the temperature range of 600–850 °C under flow of 21% O_2/He mixture. It was observed that L58SCF exhibits the highest electrocatalytic activity for oxygen reduction reaction followed by LSM/LSM–8YSZ and LS2F [831,832]. Using mechanofusion dry processing method, Simner et al. [833] coated a layer of $(\text{La}_{0.6}\text{Sr}_{0.4})_{0.98}\text{Co}_{0.2}\text{Fe}_{0.8}\text{O}_{3-\delta}$ (of thickness 1 μm) over atomized silver microspheres ($\leq 53 \mu\text{m}$). This material was then tested as a SOFC cathode on an anode-supported YSZ electrolyte. The electrochemical cell when operated at 700 °C generates a power density of $>500 \text{ mW/cm}^2$ at 0.7 V. The cell exhibited quite a stable performance for more than 2000 h of operation with a power degradation of ~3% per 1000 h at 0.7 V [833]. The cells based on $\text{Ba}_{0.5}\text{Sr}_{0.5}\text{Co}_{0.8}\text{Fe}_{0.2}\text{O}_{3-\delta}$ as cathode with doped ceria thin film as electrolyte were found to exhibit high power densities of ~ 1010 and 402 mW/cm^2 at 600 °C and 500 °C, respectively [834].

Thermal internal stress and lattice strain caused by the mismatch in CTE and lattice, respectively, between the electrode and electrolyte may result into material degradation. The crack formation has been a serious problem throughout the development and processing of SOFC cathode materials. In this direction, Yoon et al. fabricated nanostructured LSC and LSCF (of composition $\text{La}_{0.5}\text{Sr}_{0.5}\text{CoO}_3$ and $\text{La}_{0.4}\text{Sr}_{0.6}\text{Co}_{0.8}\text{Fe}_{0.2}\text{O}_3$, respectively) cathode thin films with vertically-aligned nanopores (VANP) deposited on Si, and pressed $\text{Ce}_{0.9}\text{Gd}_{0.1}\text{O}_{1.95}$ discs using pulsed laser deposition technique (PLD) as shown in Fig. 61 [835]. These structures were found to enhance the oxygen diffusivity, as well as contributed fully or partially in relieving the internal stress and lattice strain. These structures extend throughout the film thickness to a depth of 2 μm and demonstrated an appreciably enhanced oxygen conductance in the cathode layer due to vertical alignment, kinetic performance and low polarization resistance values in the low temperature (400–700 °C) regime.

For the intermediate temperature SOFCs, the MIEC materials, such as, BSCF ($\text{Ba}_{1-x}\text{Sr}_x\text{Co}_{1-y}\text{FeO}_{3-\delta}$), Nd-doped BSCF (BSNCF) and LSCF ($\text{La}_{1-x}\text{Sr}_x\text{Co}_{1-y}\text{Fe}_y\text{O}_{3-\delta}$) have shown promise, and have demonstrated faster oxygen diffusion with improved surface exchange kinetics [872–878]. Recently, $\text{LnBaCo}_2\text{O}_{5+\delta}$ ($\text{Ln} = \text{Gd, Pr}$), doped SrFeO_3 [879], $\text{Sr}_{0.5}\text{Sm}_{0.5}\text{CoO}_3$ with cone shape cathode layer [880], $\text{Sr}_{0.7}\text{Y}_{0.3}\text{CoO}_{2.65-\delta}$ [814], and LSCF–LCFN composites (LSCF of composition $\text{La}_{0.8}\text{Sr}_{0.2}\text{Co}_{0.2}\text{Fe}_{0.8}\text{O}_{3-\delta}$ and LCFN of composition $\text{SrCo}_{0.2}\text{Fe}_{0.6}\text{Ni}_{0.2}\text{O}_{3-\delta}$) with varying composition of the latter [819] were investigated as the potential IT-SOFC cathode materials [881]. Considering LSCF based cathodes of combination (La, Sr)(Co, Fe) O_3 , temperature is the predominant factor resulting in the voltage loss during cell operation with time. One of the probable mechanisms responsible for voltage deterioration is the slow decomposition of the LSCF perovskite due to partial de-mixing of strontium [882].

Coating a thin catalytic layer on the cathode surface enhances the activity for oxygen reduction reaction, provides appreciable chemical and thermal stability, and, thus, renders entirely new innovative dimension to cathode material research. Cathodes, consisting LSCF (for their ambipolar conductivity) as backbone and a thin coating of LSM (for their catalytic activity) allow achieving high stability and exploiting the best properties of both the materials [883]. Deposition of nanoparticles of doped ceria (ionic conductor) on LSCF using infiltrations of aqueous nitrate solutions, and porous and dense LSM film on LSCM using non-aqueous solutions were described in the literature [883,884]. The cathode based on $\text{RBa}(\text{Co, M})_4\text{O}_7$ (R = Y, Ca, In and M = Zn, Fe, Al) oxides with a hexagonal structure and

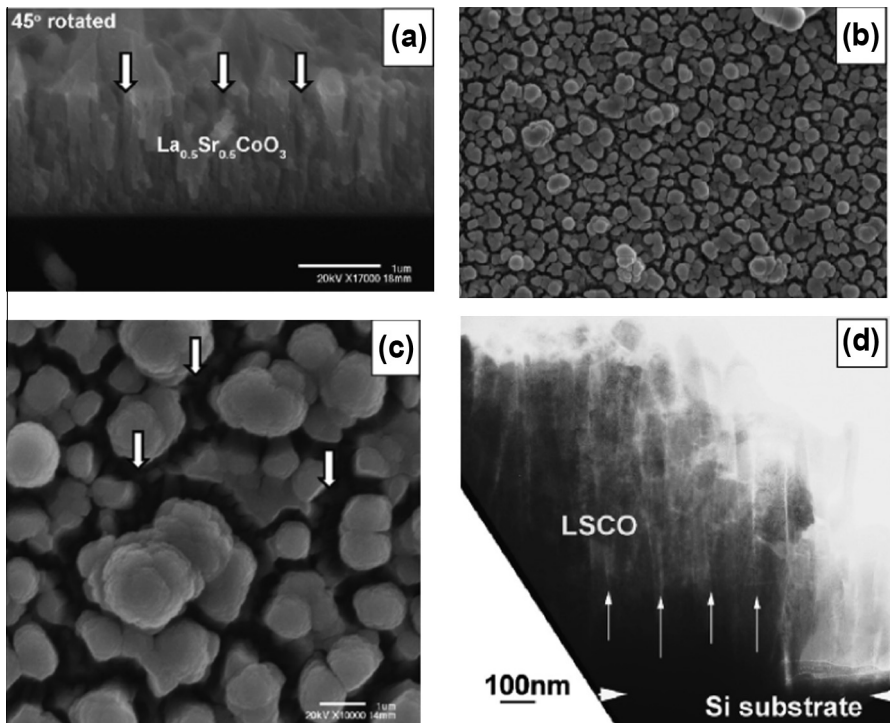


Fig. 61. SEM and HRTEM images of LSC VANP grown on Si substrates, (a) Transverse cross-sectional view (b) low and (c) high magnifications. (d) Low magnification vertical cross- sectional TEM image revealing Si substrate with vertically aligned nanopores (Reprinted with permission from Ref. [835], copyright Elsevier, 2007).

corner-shared tetrahedral $(\text{Co}, \text{M})\text{O}_4$ exhibit a unique combination of high catalytic activity, and a good thermal expansion compatibility with standard electrolyte materials (CTE of $\text{RBa}(\text{Co}, \text{M})_4\text{O}_7$ ranges between 6×10^{-6} – $13 \times 10^{-6}/\text{K}$, while that of electrolyte materials such as YSZ, GDC and LSM range between 10.2×10^{-6} – $10.4 \times 10^{-6}/\text{K}$) [885].

Various strategies to enhance the oxygen reduction catalytic activity of the cathode have been discussed so far in this section. However, most of the reported performances (e.g., those listed in the Table 10) vary tremendously because of several unknown variable factors during the operation/testing. The materials remain far from clear understanding of optimization and calculated predictions of short- and long-term degradation problems. Some of the well-studied reasons for cathode degradation have been discussed in the following section.

4.6. Degradation problems

Degradation of SOFC cathodes is affected by both intrinsic, as well as extrinsic factors. Intrinsic factors arise from the material itself during operation. The major intrinsic factors responsible for cathode degradation are: (a) coarsening of microstructure while undergoing sintering and thermal cycles during operation, (b) decomposition of parent oxide, (c) chemical reaction with other cell components, and (d) spallation of cathode contents from the electrolyte. Extrinsic factors come into picture at the time of testing/operation when the cathode material undergoes poisoning, such as, Cr and SO_2 poisoning from interconnect material, contaminants from sealing materials, and inherent impurities that can be either innocuous or active. A significant number of reports are available in the literature showing that under SOFC operating conditions, LSM based cathodes remain stable [886–888]. For example,

Table 10

Summary of properties and performance of various materials.

Composition	CTE ($\times 10^{-6}/\text{K}$) Temperature range	σ_e (S/cm)	σ_i (S/cm)	D^* (Oxygen diffusion coefficient) (cm^2/s)	k (Oxygen surface exchange coefficient) (cm/s)	Reference
¹ 8YSZ	¹ 10.2–10.5	¹ 0.17 (at 1000 °C)	¹ 0.02–0.0029 (at 700 °C)	² 1.0×10^{-7} (at 900 °C) ³ 8.5×10^{-10} (at 600 °C) ⁴ $1.14\text{--}1.32 \times 10^{-11}$ (at 600 °C)	² 3.0×10^{-6} (at 900 °C) ³ 1.3×10^{-8}	[836–845]
² 9.5YSZ (single crystal)	⁵ 11.5–11.9		⁵ 0.16			
³ 18-YSZ	⁵ 12.5					
⁴ Nano YSZ	⁶ 10.4			(at 1000 °C)	(at 600 °C)	
⁵ GDC				⁶ 0.08 (at 700 °C)	⁵ 1.0×10^{-6} (at 900 °C)	
⁶ LSGM						
⁷ Pt (surface)	–	⁸ $6.6 \pm 0.9 \times 10^{-7}$	Nil	⁷ $4.1 \times 10^{-6}\text{--}1.1 \times 10^{-7}$ (at 702 °C)	⁷ $5 \times 10^{-2}\text{--}1.6$ (at 702 °C)	[718,722,846,847]
⁸ Pt (microporous)		(at TPB, 700 °C)		⁸ 4.65×10^{-8} (at 800 °C)		
⁹ YSZ–40 wt.% LSM	–		⁹ 3×10^{-3} (at 900 °C)	⁹ 1×10^{-9} and 6×10^{-9} (at 800 °C and 900 °C, respectively)	⁹ 7×10^{-7} and 1×10^{-7} (at 800 °C and 900 °C, respectively)	[848]
¹⁰ ABO ₃ A = La, B = Mn,	¹⁰ 11.33–12.4	¹⁰ 40–485 (CS, at 1000 °C)	Poor or negligible	¹⁰ 2.45×10^{-13} (at 1000 °C)	¹⁰ 7.45×10^{-8}	[849–852]
¹¹ A = La, B = Co	¹¹ 20–22			¹¹ 5.31×10^{-9} , 2.41×10^{-11} , 9.20×10^{-13} (at 900, 800 and 700 °C, respectively)	(at 1000 °C)	
¹² A = La, B = Fe		¹¹ 50–201 (PS, at 1000 °C)		¹² 9.84×10^{-13} and 5.28×10^{-12} (at 900 °C and 1000 °C, respectively)	¹¹ 4.57×10^{-9} and 3.47×10^{-7}	
A_{1-x}A'_xBO₃	¹³ 11.84 ($x = 0.2$)	¹³ 90	¹⁴ 1.10×10^{-7} ($x = 0.05$ at 900 °C)	¹⁴ 2.44×10^{-13} ($x = 0.05$, at 900 °C)	¹⁴ $1.78\text{--}9 \times 10^{-8}$	[777,836,839,844,852–856]
¹³ A = La, A' = Ca; B = Mn	¹⁴ 12.4, 12.2		($x = 0.5$, 1000 °C)		($x = 0.05$, at 900 °C)	
¹⁴ A = La, A' = Sr, B = Mn	($x = 0.2$, 0.25, respectively)		¹⁴ $2.09\text{--}5.76 \times 10^{-6}$ ($x = 0.10\text{--}0.20$)	¹⁴ 3×10^{-12} ($x = 0.5$, 900 °C)		
¹⁵ A = La, A' = Sr, B = Co		¹⁴ 200–485		¹⁴ $2.45 \times 10^{-13}\text{--}$ 1.33×10^{-11} ($x = 0.08\text{--}$ 0.20 at 1000 °C)	¹⁴ 7.45×10^{-8} , 10^{-9}	
¹⁶ A = La, A' = Sr, B = Fe	¹⁵ ~20 ($x = 0.4$)	($x = 0.2\text{--}0.5$, at 1000 °C)	¹⁴ $10^{-7}\text{--}10^{-6}$		($x = 0.08$ and 0.2, respectively; at 1000 °C and 700 °C, respectively)	

(continued on next page)

Table 10 (continued)

Composition	CTE ($\times 10^{-6}/\text{K}$) Temperature range	σ_e (S/cm)	σ_i (S/cm)	D^* (Oxygen diffusion coefficient) (cm^2/s)	k (Oxygen surface exchange coefficient) (cm/s)	Reference
¹⁷ A = La, A' = Ba, B = Fe	¹⁹ 7–12		(at 1000 °C)	¹⁵ 1.4×10^{-8} ($x = 0.47$, at 900 °C)		
¹⁸ A = La, A' = Ca, B = Fe	($x = 0.3$ –0.6)	¹⁵ ~2000 ($x = 0.4$, at 850 °C)	¹⁵ 1.20 ($x = 0.4$, 900 °C)			
¹⁹ A = Y, A' = Ca, B = Mn	²¹ 18.3–29.6			¹⁵ 10^{-6} – 10^{-8}		
²⁰ A = Y, A' = Ca, B = Fe	($0 \leq x \leq 0.5$)	³ 1000–2400	¹⁵ 1×10^{-2}	($x = 0.4$, 0.5, at 725 °C)	¹⁵ 4.3×10^{-6} and 2×10^{-5}	
²¹ A = Pr, A' = Sr, B = Co	²² 12.2 ($x = 0.5$)	($x = 0.4$ and 0.5, respectively, at 725 °C)	($x = 0.4$ and 0.5, respectively, at 725 °C)	¹⁶ 2.65×10^{-9}	($x = 0.47$, 900 °C)	
²² A = Pr, A' = Sr, B = Mn	²³ 20–25			($x = 0.1$; at 900 °C)	¹⁵ 4×10^{-4} ($x = 0.4$, at 725 °C)	
²³ SrBa _{1-x} Sr _x Co ₂ O _{5+δ}		¹⁴ 100–200 ($x = 0.2$, at 1000 °C)	¹⁶ 8.3×10^{-4} ($x = 0.2$, at 800 °C) ¹⁷ 3.1×10^{-4} ($x = 0.2$, at 800 °C)		¹⁶ 3.60×10^{-7} and 5×10^{-4} ($x = 0.1$ and 0.4, respectively)	
		¹⁴ 3.5 ($x = 0.3$, 1000 °C)		¹⁷ 3.8×10^{-5}	at 900 °C and 700 °C, respectively)	
		²¹ 1000 ($0 \leq x \leq 0.5$)	($x = 0.2$, at 800 °C)			
		²² 250 ($x = 0.5$, at 600 °C)	²⁰ 3.9×10^{-2}	($x = 0.1$, at 1000 °C)		
		²³ 1280 and 280 (at 50 and 900 °C, respectively)				
AB_{1-y}B_yO₃	²⁴ 11.33 ($y = 0$)	²⁶ 580 ($y = 0.4$; 800 °C)	²⁵ 3.4×10^{-3} ($y = 0.4$, – at 882 °C)		–	[855–863]
²⁴ A = La, B = Mn, B' = nil	²⁵ 11.2 at 97 °C– 377 °C and 15.5 at 377 °C–797 °C ($y = 0.2$)					
²⁵ A = La, B = Ga, B' = Co		²⁸ 1200–1500				
²⁶ A = La, B = Ni, B' = Fe		($y = 0.4$ –0.6, at 1000 °C)				

²⁷ A = La, B = Ni, B' = Co				
²⁸ A = La, B = Co, B' = Ni	²⁵ 17.7 at 27 °C –877 °C) ($y = 0.4$)	²⁹ 300 and 100 ($y = 0.1$; at 400 °C and 650–850 °C, respectively)		
²⁹ A = Sr, B = Co, B' = Sb	²⁵ 18.7 at 157 °C– 407 °C and 22.3 at 407 °C–827 °C ($y = 0.6$)			
	²⁵ 22.2 at 27 °C– 857 °C ($y = 0.8$)			
	²⁶ 11.4 ($y = 0.4$)			
	²⁷ 11.9–14.3 ($y = 0.4$)			
	²⁸ 14–17 ($y = 0.4$ –0.6)			
$\mathbf{A}_{1-x}\mathbf{A}'_x\mathbf{B}_{1-y}\mathbf{B}'_y\mathbf{O}_3$	³⁰ 20.7–15.4	³⁰ 1035	³⁰ 0.18 ($x = 0.4$, $y = 0.2$; at 900 °C)	³⁰ 3×10^{-7} , 1×10^{-7} , 2×10^{-8} ($x = 0.4$, $y = 0.2$; 900, 800, 700 °C, respectively)
LSCF				³⁰ 4×10^{-5} , 2×10^{-5} , 4×10^{-6} [862,864–871]
	($y = 0.2$ –0.8, at 600 °C)	($y = 0.2$, at 600 °C)		($x = 0.4$, $y = 0.2$; at 900 °C, 800 °C, and 700 °C, respectively)
³⁰ A = La, A' = Sr, B = Co, B' = Fe	³⁰ 14.5–15.3	³⁰ 875 ($y = 0.2$, at 1000 °C)	³¹ 3.16 ($x = 0.4$, $y = 0.2$; at 900 °C)	³⁰ 9.6×10^{-10} ($x = 0.2$, $y = 0.8$, at 900 °C)
LSCN	($x = 0.4$, $y = 0.8$, at 600 °C)		³² 2.00 ($x = 0.2$, $y = 0.2$, at 900 °C)	
³¹ A = La, A' = Sr, B = Co, B' = Ni		³⁰ 330–400		³⁰ 3.3×10^{-7} ($x = 0.2$, $y = 0.8$, at 900 °C)
		³⁰ 15.39	($x = 0.4$, $y = 0.8$, at 600 °C)	³³ 1.0×10^{-10} (at 900 °C)
³² A = La, A' = Sr, B = Co, B' = Cu	($x = 0.4$, $y = 0.8$, at 700 °C)			³⁴ 1.0×10^{-11}
			³⁰ 29.2–52.8 ($x = 0.2$, $y = 0.8$; $x = 0.4$, $y = 0.8$)	³⁴ 2.0×10^{-7} ($x = 0.2$, $y = 0.8$; at 900 °C)
³³ LSCM		³¹ 15.6	($x = 0.2$, $y = 0.8$; 900 °C)	³⁷ 7.3×10^{-5} , 1.3×10^{-4} ($x = 0.5$, $y = 0.2$; at 775 °C and 900 °C, respectively)

(continued on next page)

Table 10 (continued)

Composition	CTE ($\times 10^{-6}/\text{K}$) Temperature range	σ_e (S/cm)	σ_i (S/cm)	D^* (Oxygen diffusion coefficient) (cm^2/s)	k (Oxygen surface exchange coefficient) (cm/s)	Reference
³⁴ A = La, A' = Sr, B = Co, B' = Mn	($x = 0.2, y = 0.2$) ³⁵ 12.8	³⁶ 271 ($x = 0.2, y = 0.1$; at 800 °C)			³⁷ 1×10^{-6} ($x = 0.5, y = 0.2$; at 500 °C)	
LSFN	($x = 0.2, y = 0.2$)			³⁸ $4 \times 10^{-10}, 3 \times 10^{-8}$ (at 1000 °C)	³³ 9.7×10^{-9} (at 900 °C)	
³⁵ A = La, A' = Sr, B = Fe, B' = Ni	³⁶ 24 ($x = 0.2$, $y = 0.1$)					
³⁶ A = Gd, A' = Sr, B = Co, B' = Mn						
³⁷ A = Ba, A' = Sr, B = Co, B' = Fe						
³⁸ A = La, A' = Sr, B = Cr, B' = Mn						
$(\text{La}_{0.75}\text{Sr}_{0.25})_{0.95}\text{Cr}_{0.5}\text{Mn}_{0.5}\text{O}_{3-\delta}$						

Singhal investigated the high temperature (1000 °C) long term stability (over 69,000 h) of tubular cell with doped LaMnO₃ cathode. The rate of cell degradation was observed to be less than 0.5% per 1000 h [888].

4.6.1. Reaction with other cell components

At high temperatures, perovskites are highly active and can easily react with other cell component materials. In 1969, Tedmon et al. [889] have tested the performance of cells with porous LaCoO₃ cathode on YSZ electrolyte. Initially, all the cells exhibited fairly good performance (with the power density higher than 500 mW/cm² at 1100 °C). However, with time, the performance of the cells degraded rapidly. After 500 h of operation, the power density was nearly half of the initial value. On examining the cells after operation, it was reported that the LaCoO₃ was chemically reacting to YSZ to form insulating reaction products. Lau et al. have reported the formation of La₂Zr₂O₇ at the interface of LSM and single crystal YSZ at higher temperatures [890]. Furthermore, a significant dissolution of Mn was observed in YSZ. The atomic diffusion and reaction at the boundaries were also observed by Takeda et al. in their investigation on (La, Sr, Ca) MnO₃ and 8YSZ interface [891]. The reactivity between LSM and YSZ electrolyte has been extensively studied both thermodynamically and experimentally. Some of the noteworthy contributions are by Yokokawa et al. [892–895], Waller et al. [896], Mori et al. [897], Mitterdorfer and Gaukler [898], Trickler and Stobbs [899], Jiang et al. [900], etc.

Roosmalen and Cordfunke investigated the reaction between (La, Sr) MnO₃ with 0, 15, 30, and 50 at.% Sr and (Zr, Y) O₂ with 3 and 8 at.% Y as a function of temperature [901]. Through experimentation and thermodynamic consideration, it was reported that at 1027 °C, (La, Sr)MnO₃ reacts with YSZ via La up to about 30 at.% of Sr to form La₂Zr₂O₇. On further increasing, the concentration of Sr above 45 at.% results in the formation of SrZrO₃. Above 1127 °C, (La, Sr)MnO₃ has shown to react with YSZ at all compositions. It was further predicted that the reaction rate between (La, Sr)MnO₃ and (Zr, Y)O₂ can be reduced if the La and Sr contents in (La, Sr) MnO₃ and Zr content in (Zr, Y)O₂ is decreased. However, when A-site deficiency increases above 0.15, or ((La + Sr)/Mn) is less than 0.85, Mn³⁺ ion activity enhances. In such a condition, the dissolution of Mn³⁺ from LSM lattice to electrolyte will be very high [894].

The thermodynamic approach to understand the materials compatibility of LSM and YSZ electrolyte considering the chemical features of interfaces, has been extensively reviewed by Yokokawa [895]. The formation of different phases at the cathode-electrolyte interface largely depends on the stoichiometry of LSM [898,902], La/Sr ratio (at A-site) [903] and the operational conditions, viz., temperature, thermal cycles, and process atmosphere [891,904]. Using the chemical potential diagrams for (La, Sr)MnO₃ and (La, Ca)MnO₃, the formation of La₂Zr₂O₇ and SrZrO₃ (or CaZrO₃) was predicted. However, substitution of Ca²⁺ at La-sites in LaMnO₃ has been found to suppress the Mn migration, and reduce the reactivity with YSZ [738]. Also, it has been found that La-deficient manganite (i.e., La_{1-x}MnO₃ ($x = 0\text{--}0.2$) exhibits less reactivity with YSZ than stoichiometric one [905,906]. However, after some induction period, formation of Ln₂Zr₂O₇ was observed [906]. The formation of Ln₂Zr₂O₇ can also be suppressed by decreasing the size of A-site cation. Thus, Pr_{1-x}Sr_xMnO₃ and Nd_{1-x}Sr_xMnO₃ are more stable from the view point of reactivity with YSZ [907]. Formation of SrZrO₃ phase from Gd_{1-x}Sr_xMnO₃/YSZ system (at 1300 °C for 48 h) was reported by Yoon et al. [908].

Mn exhibits high solubility in YSZ ranging from 5.1% at 1000 °C and 11.4% at 1300 °C. When La_{0.7}Sr_{0.3}Mn_{1.1}O₃ cathode cofired with YSZ electrolyte at 1300 °C for 2 h, Mn penetration depth of up to 20 μm into YSZ was elicited [909]. In YSZ matrix, Mn was observed to be either in divalent (80% of the total content) or trivalent (20%) states. The absence of (+4) state indicates reduction of Mn³⁺ to Mn²⁺ at the YSZ interface. Furthermore, yttria content in ZrO₂ also influences the reaction kinetics at the interface [897]. YSZ having high yttria content (for example 12 mol.%) were observed to be less active with La_{0.9}MnO₃ compared to 8YSZ or 3YSZ [897,901,910] in the creation of pyrochlore phase (Ln₂Zr₂O₇) at their interface. The latter has been observed to be harmful to the electrode performance [904,911]. The electrical conductivity of 2×10^{-4} S/cm was observed in La₂Zr₂O₇ at 1000 °C, whereas other pyrochlores like SrZrO₃, Sr₄Zr₃O₁₀, Sr₃Zr₂O₇ and Sr₂ZrO₄ show the conductivity in the range of $10^{-4}\text{--}10^{-5}$ S/cm at 1000 °C [912]. It must be noticed that conductivity range exhibited by these pyrochlore phases is significantly lower than that of YSZ electrolyte (i.e., 0.185 S/cm).

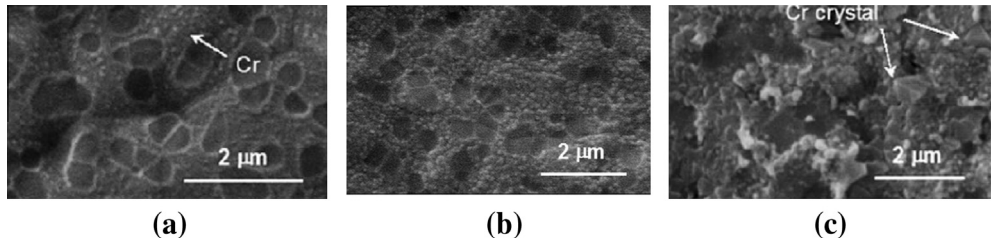
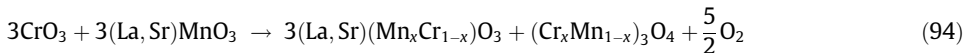
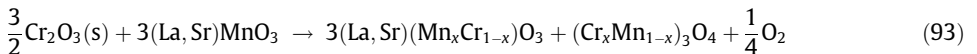
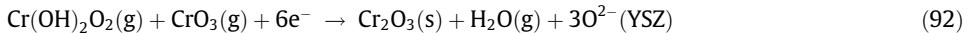


Fig. 62. SEM images of YSZ surface in contact with LSM in presence of a Fe–Cr alloy for different durations (a) 15 min, (b) 4 h, and (c) 20 h. (Reprinted with permission from Ref. [924], copyright Cambridge University Press, 2011).

Moreover, the CTE of $\text{La}_2\text{Zr}_2\text{O}_7$ pyrochlore is also lower ($9.2 \times 10^{-6}/\text{K}$) than 8YSZ ($10.3 \times 10^{-6}/\text{K}$) suggesting thermal expansion mismatch, which may generate thermal stresses during operation [897].

Another important issue with LSM based cathodes materials is their interactions with metallic interconnect, e.g., stainless steels that generate Cr-containing volatile species at operational temperature ($\sim 1000^\circ\text{C}$) and oxidizing atmosphere. According to Taniguchi et al. [913] and Badwal et al. [914], the gaseous Cr-species are electrochemically reduced to solid Cr_2O_3 (in completion with the O_2 reduction reaction) which subsequently deposits on the cathode material, and blocks the TPB active sites [913–918]. It has been observed that $\text{La}_{0.6}\text{Sr}_{0.4}\text{Co}_{0.2}\text{Fe}_{0.8}\text{O}_3$ (LSCF) cathode/SDC electrolyte interface restricts Cr-deposition when compared to that of LSM/YSZ interface [919]. The Cr deposits react with LSM (as shown in Eqs. (92)–(94)), which may lead to the formation of $(\text{Cr}, \text{Mn})_3\text{O}_4$ phases at TPB sites. Thus, the Cr deposition mechanism blocks the active TPB sites, and is believed to impede the reduction of O_2 .



A significant supply of Mn^{2+} ions facilitates the formation of $(\text{C}, \text{Mn})_3\text{O}_4$ -type spinel. However, Jiang et al. [920–924] put forward a different view point which suggest that the kinetics of Cr-deposition is largely influenced by Mn^{2+} species (see Eqs. (95)–(97)) generated either by cathodic polarization or via nucleation and grain growth steps occurring at high temperatures (700 – 900°C) as shown below:

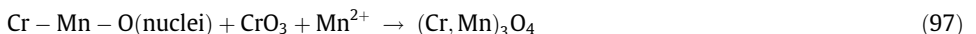
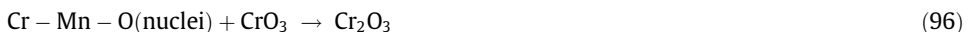


Fig. 62 shows the YSZ surface in contact with LSM after cathodic polarization at 200 mA/cm^2 in the presence of a Fe–Cr alloy at 900°C for different durations [924]. The Cr deposit was observed to increase with time under cathodic polarization. Furthermore, the Cr species are randomly observed on the YSZ surface without exhibiting any preference towards TPBs. This indicates that the Cr deposition reaction is not an electrochemical reduction, and is not competing with O_2 reduction at the TPBs.

The summary of the noteworthy observations by Jiang and his co-workers are: (a) Cr-deposition on YSZ electrolyte can occur under both cathodic and anodic polarization conditions, (b) the initial reversible polarization indicates that the active sites for Cr_2O_3 deposition are not dictated by O_2 reduction at early stage of reaction (c) Cr-deposition does not take place preferentially at TPB sites, and (d) Cr deposition occurs in YSZ surface not in direct contact with LSM electrode. In an another

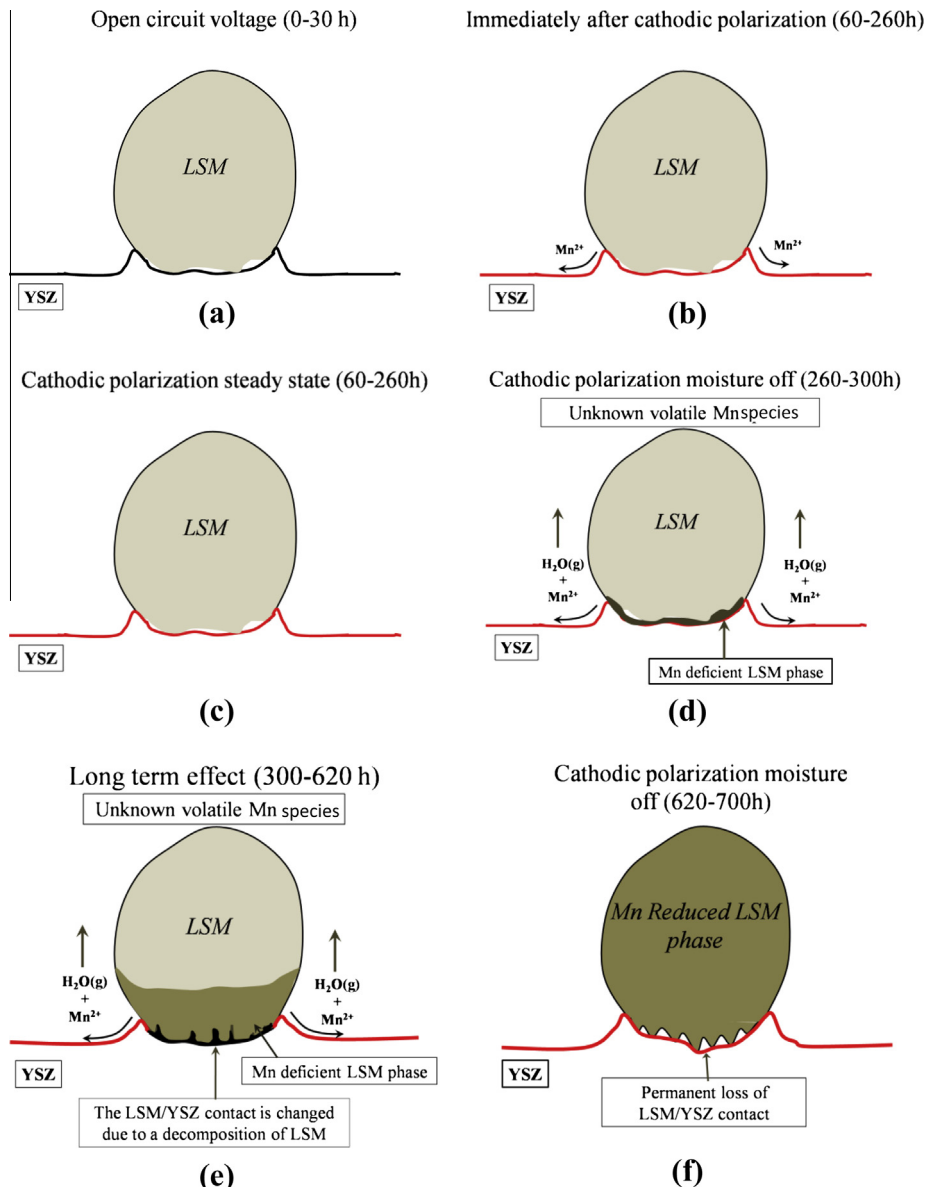


Fig. 63. Schematic exhibiting the effect of moisture on cathode degradation: (a) 0–30 h, (b) Immediately after cathodic polarization 60–260 h, (c) cathodic polarization steady state during 60–260 h, (d) cathodic polarization moisture off during 60–260 h, (e) Long term 300–620 h, and (f) Cathodic polarization moisture off during 620–700 h. (Adapted from Ref. [927]).

study performed by Wang et al. on LSM-YSZ cathodes in SOFCs operated at 800 °C for 500 h under different electrochemical conditions while exposed to a chromia-forming stainless steel [925], the local chemistry and microstructural changes post operation were examined using transmission electron microscopy in order to determine the effect of decomposition [925]. The nature and amount of degradation depends on the electrochemical load, temperature and physical location. Nanoparticles of CrMn₃O₄ and Cr₂O₃ on the surface of YSZ were observed in the TEM images. The results suggest that

the migration of Mn species leads to the formation of stable Cr–Mn–O nuclei on YSZ. In the case of severe degradation, the LSM electrode decomposes completely. Maximum degradation was observed to occur near the region of cathode/electrolyte interface in the vicinity of the interconnect–cathode contact channels, which was attributed to the electrochemical decomposition of $(\text{La}, \text{Sr})\text{MnO}_3$ [925].

The self-explanatory schematic shown in Fig. 63 illustrates the probable mechanism of degradation of cathode material by moisture present in the air supplying oxygen. There occurs the accumulation of Mn^{2+} at the LSM/YSZ interface and TPBs. In the presence of moisture, the Mn^{2+} is believed to spread out on YSZ electrolyte surface and readily remove from the original site. This leads to an accelerated decomposition of LSM at the LSM/YSZ interface. The schematics shown in Fig. 63a–f illustrate the events of degradation at cathode–electrolyte interface during the operation from 0 to 700 h [926].

A single SOFC unit is capable of producing OCP of ~ 1 V. An SOFC array called “stack” is thus utilized to generate a reasonable voltage for real-life applications. Stacking of various SOFCs is possible through ‘interconnects’ joining the cathode of one cell with the anode of an adjoining units. Detailed review on interconnects is presented in the next section.

5. Interconnects

Interconnects provide an electrical connection between cathode of one individual cell to the anode of the adjacent cell in a SOFC stack, and ensure a physical barrier between the reducing atmosphere (at anode) and the oxidizing atmospheres (at cathode). Therefore, the selection criteria of interconnect materials are more important and stringent than other components of the cell. Fig. 64 shows the usage of interconnect in a flat-plate or planar and tubular type of SOFC stacks [928,929]. For proper working

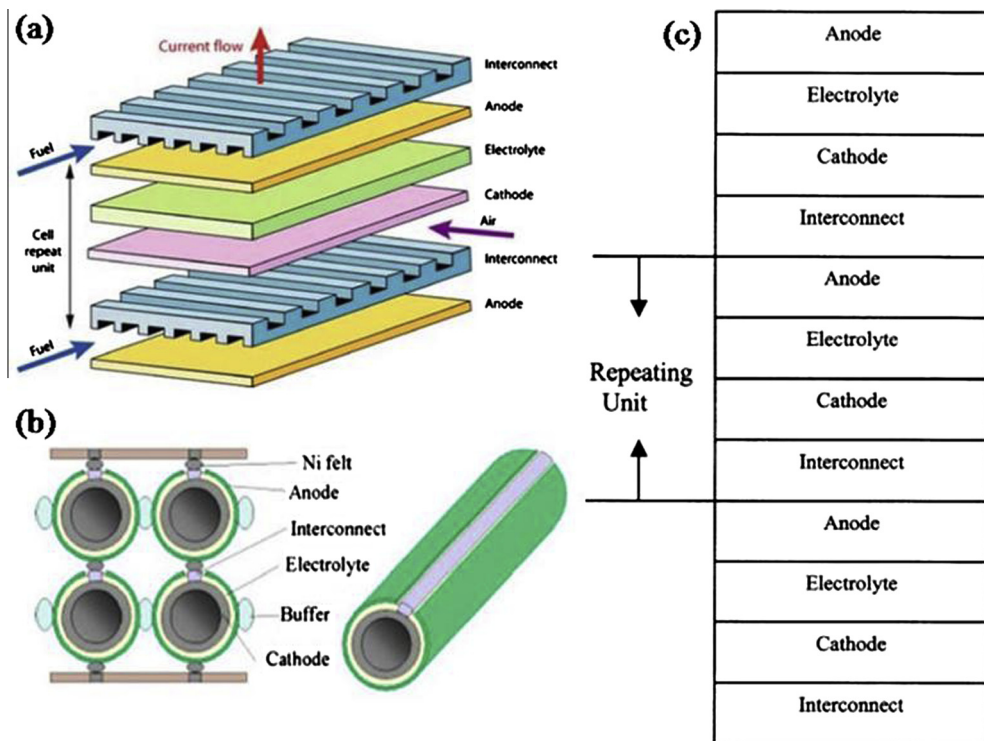


Fig. 64. Schematic of cell components for (a) planar and (b) tubular design, and (c) repeating unit in the planar design of SOFC stack [928,929,931]. (a) Courtesy: <http://www.doitpoms.ac.uk/tplib/fuel-cells/printall.php>, (b) Courtesy: <http://www.aki.che.tohoku.ac.jp/~koyama/html/research/SOFC.html>, and (c) (Reprinted with permission from Ref. [931], copyright Elsevier, 2003).

of SOFC, the interconnect material must possess the following functionalities [930,931]: (i) high electrical conductivity with area-specific resistance (ASR) less than $0.1 \Omega \text{ cm}^2$; (ii) structural-, micro-structural-, chemical- and phase-stability at operating temperature $\sim 800\text{--}1000^\circ\text{C}$ in both oxidizing and reducing atmospheres during its service lifetime i.e., $>40,000 \text{ h}$; (iii) excellent gas tightness or imperviousness for oxygen and hydrogen, in order to provide a barrier for direct combustion between oxidant and fuel during operation; (iv) matching CTE ($\sim 10.5 \times 10^{-6}/\text{K}$) with electrodes and electrolyte materials that assists in minimizing the thermal stresses developed during initiation and close-down of SOFC device; (v) chemical inertness towards adjoining components; (vi) resistance towards oxidation, sulfidation and carbon cementation; (vii) moderate mechanical strength as well as high resistance to creep is required to avoid fracture when stresses are generated during operation since interconnect materials have to bear the load of a stack. Also, (viii) minimal P_{O_2} gradient is required across the interconnects in order to restrict dimensional change and minimize mechanical stress, which might cause cracking of the stack and deteriorates the overall cell functionality. Furthermore, (ix) low cost; and (x) ease of fabrication and shaping are also necessary requirements for developing a commercial interconnect. There are, in general, two classes of interconnect materials for SOFCs, viz. – ceramics and metallic alloys.

5.1. Ceramic interconnect materials

Ceramic interconnects are developed from semiconductor oxides which not only possess fair stability in air, but also retain good compatibility with other SOFC component materials. The conductivity of these oxides is an increasing function of temperature, which makes them suitable for high temperature applications ($>800^\circ\text{C}$). However, the conductivity of ceramics is not appreciable below 600°C . Most commonly used ceramics as interconnects are lanthanum chromite (LaCrO_3) based materials which are among most stable perovskite-type oxides. They possess melting point greater than 2327°C , and are stable even in low $P_{\text{O}_2} \sim 10^{-16} \text{ atm}$ at 1000°C [297]. The trends of research on SOFC interconnect materials (both metallic and ceramic) and lanthanum chromites are summarized in Fig. 65 [932].

LaCrO_3 is a *p*-type semiconductor material under oxidizing conditions [933], and is stable in low P_{O_2} conditions, e.g., 10^{-16} Pa at 1000°C [297]. The *p*-type conductivity decreases on lowering P_{O_2} as LaCrO_3 becomes oxygen deficient, consuming holes to form oxygen vacancy defects. LaCrO_3 exhibits high electrical conductivity ($\sim 1 \text{ S/cm}$ at 1000°C [931]) compared to other ceramics, high melting point (2510°C) [934], a low CTE mismatch with YSZ (CTE _{LaCrO_3} $\sim 9.5 \times 10^{-6}/\text{K}$ and CTE_{YSZ} $\sim 10.5 \times 10^{-6}/\text{K}$) [454] and fairly good compatibility with other cell components, which makes it a

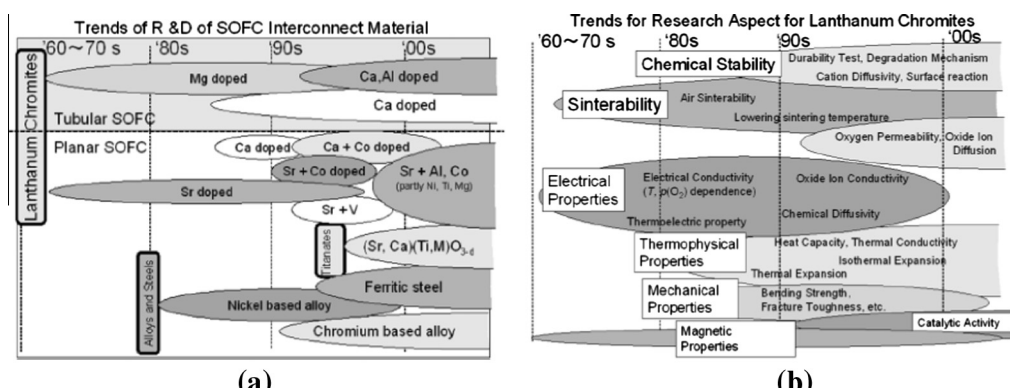


Fig. 65. Trends of research and development on (a) SOFC interconnect materials and (b) for lanthanum chromite based materials. ((a-b) Reprinted with permission from Ref. [932], copyright John Wiley and Sons, 2005)

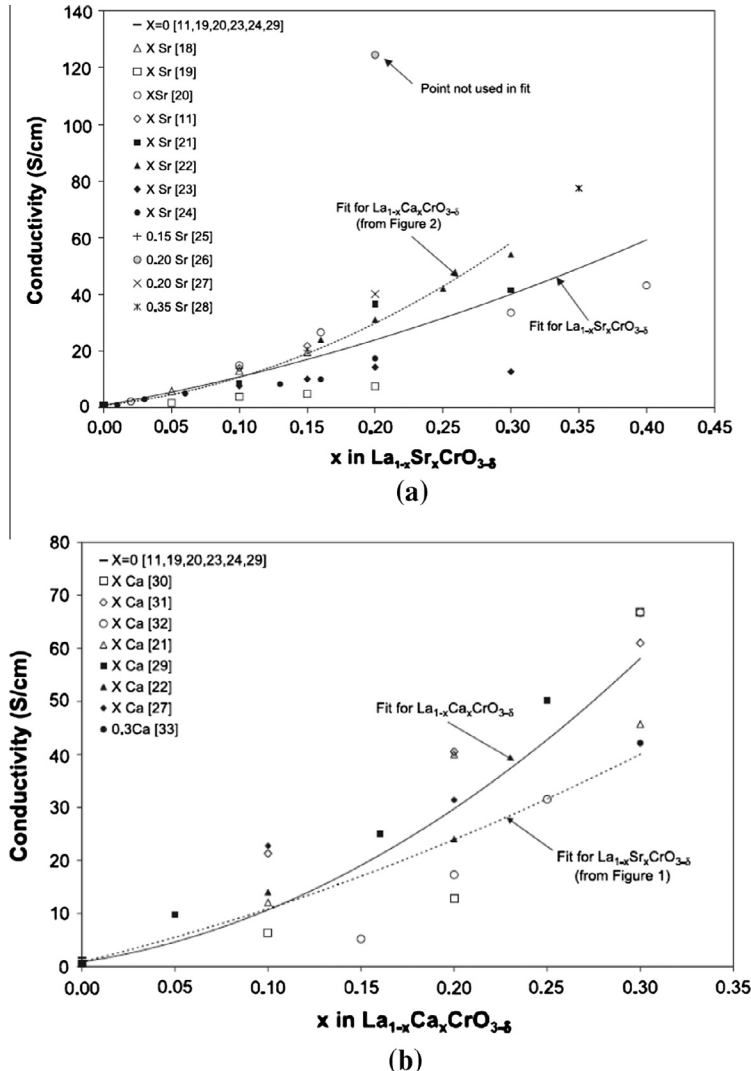


Fig. 66. Enhancement in the conductivity of LaCrO₃ upon doping with: (a) Sr³⁺, and (b) Ca²⁺. Conductivities were measured at 1000 °C in air. ((a–b) Reprinted with permission from Ref. [952], copyright Elsevier, 2004).

suitable interconnect. These aspects can be further improved either through sandwich structures or via doping.

One of the major issues related to alkaline-earth-doped LaCrO₃ has been their poor sinterability in air. This is attributed to the high vapor pressure of volatile chromium components [935]. In order to meet this challenge sintering is usually performed in reducing atmosphere [936], or by making Cr₂O₃/lanthanum chromite/Cr₂O₃ sandwiches [937], which, as a result, lowers the vapor pressure of chromium species in gaseous phase. Precipitating secondary phases and formation of stable compounds with chromium is also employed as another way to lower the CrO₃ vapor pressure. For example, CaO can be made to react with CrO₃ and improve the densification of (La, Ca)CrO₃ [938,939]. The secondary phase presents as a melt of calcium oxychromate Ca_m(CrO₄)_n above 1050 °C in air, which increases the densification rate via liquid-phase sintering mechanism [940–942]. This approach

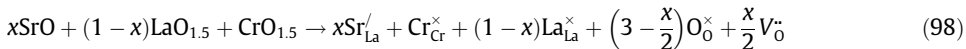
renders good sinterability even at 1300 °C, which allows (La, Ca)CrO₃ to be used as an interconnect material for tubular SOFCs. Liquid phase sintering approach is also successfully utilized for the sintering of other systems such as (La, Ca)(Cr, Co)O₃ [943,944], and (La, Ca)(Cr, Ni)O₃ [945].

In the perovskite structure of LaCrO₃, larger-sized cations, such as, Ca²⁺ and Sr²⁺ can substitute for La³⁺ while smaller cations, such as, Ni²⁺, Cu²⁺ or Al³⁺ can replace Cr³⁺. Fig. 66a and b shows the improvement in conductivity of LaCrO₃ on doping with divalent cations, such as, Ca²⁺ or Sr²⁺. The divalent cations will act as acceptor dopant when residing at the trivalent (La³⁺ or Cr³⁺) sites. Thus, in order to maintain charge neutrality, holes are created as a charge compensating defect, which consequently leads to *p*-type conductivity. Similarly, adding trivalent cations, such as Al³⁺, has also been found to increase the *p*-type conductivity, but it occurs mainly due to an increase in carrier mobility [946]. It may be noted that the solubility of the divalent cations decreases on increasing P_{O₂} [248,947–950]. In the literature, a wide range of conductivity values are reported for these compositions. Examination of the processing conditions suggests that the discrepancy is related to the difference in microstructures like porosity, phase content/size, and phase distribution [248,949–951]. When compared to calcium, strontium doped lanthanum chromite exhibits formation of secondary phase in air during processing (and leads to decreased conductivity), whereas the former one remains in single phase.

It has been observed that doping LaCrO₃ with Ca²⁺ will result in higher conductivity than with Sr²⁺ [952]. However, the flexural strength of Sr²⁺ doped LaCrO₃ is generally better than that of Ca²⁺ doped compositions [953]. Furthermore, Sr²⁺ doping also leads to increase in the CTE value of LaCrO₃ interconnect ($\sim 10.3 \times 10^{-6}/\text{K}$ at dopant concentration of $\sim 18\%$), which is similar to that of YSZ ($\sim 10.3 \times 10^{-6}/\text{K}$) as discussed later [952]. Recently, composites of La_{0.7}Ca_{0.3}Cr_{0.3}O₃ and 20 mol.% M_{0.20}Ce_{0.80}O_{1.9} (where M³⁺ is Sm³⁺, Gd³⁺ and Y³⁺) were tested as interconnect in SOFCs. Addition of doped CeO₂ up to 3–5 wt.% in La_{0.7}Ca_{0.3}Cr_{0.3}O₃ has been reported to increase the conductivity. At 800 °C, the highest conductivity (687.8 S/cm) is shown by 5 wt.% Ce_{0.8}Sm_{0.2}O_{1.9}/La_{0.7}Ca_{0.3}Cr_{0.3}O₃ composite, which is 38.7 times higher than commonly used La_{0.7}Ca_{0.3}Cr_{0.3}O₃. Increase in the oxide ion conductivity is attributed to the enhancement in oxygen permeation rate on addition of doped ceria [954–956].

During operation, the interconnect material is exposed to both air as well as fuel. Therefore, the high conductivity in both conditions is a key to achieve high fuel cell performance. In doped LaCrO₃, Sr²⁺ replaces La³⁺ and creates an effective negative charge, which is compensated by the oxidation of Cr³⁺ to Cr⁴⁺. The presence of Cr³⁺/Cr⁴⁺ redox couple in LaCrO₃ results in electronic conduction via small polaron hopping mechanism [957–961]. In order to enhance the electronic conduction, it is essential to have an understanding of defect chemistry model applicable in these materials. The defect chemistry has been studied in detail for some of the A-site and B-site substituted lanthanum chromites, e.g., La_{0.8}Sr_{0.2}CrO₃, La_{0.9}Ca_{0.1}CrO₃, La_{0.8}Ca_{0.2}CrO₃, La_{0.95}Ca_{0.05}Cr_{0.84}Al_{0.16}O₃, LaCr_{0.79}Al_{0.16}Mg_{0.05}O₃, LaCr_{0.79}Al_{0.16}Co_{0.05}O₃ [958,962,963].

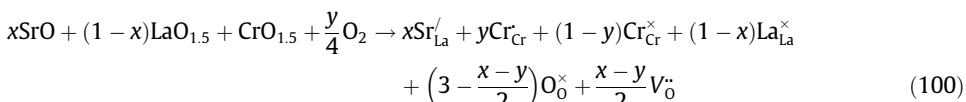
In the case of La_{0.8}Sr_{0.2}CrO₃, Sr²⁺ act as an acceptor dopant substituting A-site cation (i.e., La³⁺), which leads to the formation of oxygen vacancies as compensating defects in air [952,964]. The incorporation reaction can be represented in Kröger–Vink notation as:



Due to the presence of Cr³⁺/Cr⁴⁺ redox couple in LaCrO₃, in highly oxidizing conditions, material will shift from an ionic compensation mechanism to compensation by holes according to:



Writing the extra holes as Cr⁴⁺ (Cr_{Cr}), the complete defect reaction in highly oxidizing conditions can be given as:



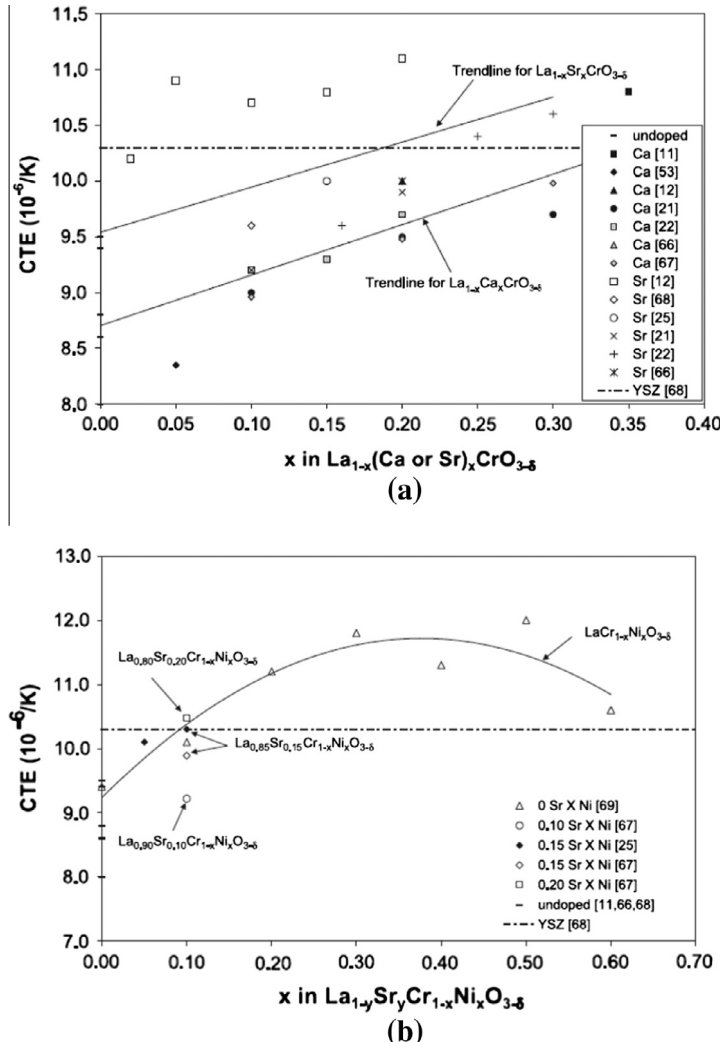


Fig. 67. CTE of (a) calcium- or strontium-doped lanthanum chromite, and (b) nickel doped lanthanum chromite, with and without strontium doping. The numbers in square bracket are comparisons from back-references mentioned in the article. (Reprinted with permission from Ref. [952], copyright Elsevier, 2004).

The above equations illustrate the dependence of concentration of Cr^{4+} or oxygen vacancies on dopant concentration, x , and P_{O_2} . In high P_{O_2} regime, Cr^{4+} defects are predominantly present in the stoichiometric LaCrO_3 (i.e., $x = y$), whereas on decreasing P_{O_2} , the oxygen vacancy concentration increases at the expense of holes.

Doping with isovalent cations such as Co^{3+} or Cu^{3+} can form oxygen vacancies at relatively higher P_{O_2} as they can accommodate electrons formed in the reduction reaction:



where $\text{Co}_{\text{Cr}}^{\times}$ and $\text{Co}_{\text{Cr}}^{\circ}$ represent extrinsic defects. Similarly, Cu^{3+} can also lower its charge valence and form oxygen vacancies according to the reactions at moderate- and low- P_{O_2} . At moderate P_{O_2} , Cu^{3+} reduces to form Cu^{2+} :

Table 11CTE and electrical conductivity of LaCrO_3 -based interconnect materials. (Adapted from Ref. [931], Elsevier, 2003).

Ceramic based Interconnects	CTE ($\times 10^{-6}/\text{K}$)	Electrical conductivity (S/cm)
LaCrO_3	9.5	0.34 at 700 °C, 1 at 1000 °C
$\text{LaCr}_{0.9}\text{Mg}_{0.1}\text{O}_3$	9.5	3 at 1000 °C
$\text{La}_{0.9}\text{Sr}_{0.1}\text{CrO}_3$	10.7	11.2 at 1000 °C
$\text{La}_{0.7}\text{Sr}_{0.3}\text{CrO}_3$	19	15 at 700 °C
$\text{La}_{0.7}\text{Ca}_{0.3}\text{CrO}_3$	14.6	18 at 700 °C
$\text{La}_{0.95}\text{Ca}_{0.05}\text{CrO}_3$	10.8	2.3 at 700 °C
$\text{La}_{0.8}\text{Ca}_{0.2}\text{CrO}_3$		7.1 at 700 °C, 35 at 1000 °C
$\text{LaCr}_{0.9}\text{Co}_{0.1}\text{O}_3$	13.1	–
$\text{LaCr}_{0.8}\text{Co}_{0.2}\text{O}_3$	14.6	–
$\text{LaCr}_{0.6}\text{Co}_{0.4}\text{O}_3$	18.7	–
$\text{LaCr}_{0.2}\text{Co}_{0.8}\text{O}_3$	20.9	–
$\text{La}_{0.7}\text{Ca}_{0.3}\text{Cr}_{0.5}\text{Co}_{0.5}\text{O}_3$	–	85 at 700 °C
$\text{La}_{0.8}\text{Ca}_{0.2}\text{Cr}_{0.5}\text{Co}_{0.1}\text{O}_3$	11.1	–
$\text{La}_{0.8}\text{Ca}_{0.2}\text{Cr}_{0.8}\text{Fe}_{0.2}\text{O}_3$	–	9.2 at 700 °C
$\text{La}_{0.8}\text{Ca}_{0.2}\text{Cr}_{0.8}\text{Ni}_{0.2}\text{O}_3$	–	18 at 700 °C
$\text{La}_{0.7}\text{Sr}_{0.3}\text{Cr}_{0.5}\text{Co}_{0.5}\text{O}_3$	19	58 at 700 °C
$\text{La}_{0.87}\text{Sr}_{0.1}\text{Cr}_{0.95}\text{Cu}_{0.05}\text{O}_3$	9.81	23.9 at 1000 °C
$\text{La}_{0.9}\text{Sr}_{0.1}\text{Cr}_{0.95}\text{V}_{0.05}\text{O}_3$	9.87	9.7 at 1000 °C
$\text{La}_{0.9}\text{Sr}_{0.1}\text{Cr}_{0.9}\text{Mg}_{0.05}\text{V}_{0.05}\text{O}_3$	9.64	15.2 at 1000 °C
$\text{La}_{0.87}\text{Sr}_{0.1}\text{Cr}_{0.935}\text{Cu}_{0.05}\text{Co}_{0.015}\text{O}_3$	10.4	25.6 at 1000 °C
$\text{La}_{0.85}\text{Sr}_{0.15}\text{Cr}_{0.935}\text{V}_{0.05}\text{Co}_{0.015}\text{O}_3$	10.5	22.9 at 1000 °C
$\text{La}_{0.95}\text{Sr}_{0.05}\text{Cr}_{0.85}\text{Mg}_{0.1}\text{V}_{0.05}\text{O}_3$	9.22	12.9 at 1000 °C
$\text{La}_{0.85}\text{Sr}_{0.15}\text{Cr}_{0.95}\text{V}_{0.05}\text{O}_3$	10	19.9 at 1000 °C
$\text{La}_{0.85}\text{Sr}_{0.15}\text{Cr}_{0.98}\text{Cu}_{0.02}$	9.91	32.5 at 1000 °C
$\text{LaCr}_{0.6}\text{Ni}_{0.4}\text{O}_3$	>11.8	26 at 700 °C
$\text{LaCr}_{0.9}\text{Ni}_{0.1}\text{O}_3$	10.1	–
$\text{LaCr}_{0.8}\text{Ni}_{0.2}\text{O}_3$	11.2	–
$\text{LaCr}_{0.7}\text{Ni}_{0.3}\text{O}_3$	11.8	–
$\text{La}_{0.7}\text{Ca}_{0.3}\text{Cr}_{0.8}\text{Co}_{0.2}\text{O}_3$	>11.1	45 at 700 °C
$\text{La}_{0.95}\text{Ca}_{0.05}\text{Cr}_{0.5}\text{Co}_{0.5}\text{O}_3$	–	63 at 700 °C

whereas at low P_{O_2} , Cu^{2+} reduces to form Cu^+ :These reactions of oxygen vacancy formation with extrinsic type defects also occur in the doped lanthanum chromites of type $\text{LaCr}_{0.79}\text{Al}_{0.16}\text{Co}_{0.05}\text{O}_3$ and $\text{LaCr}_{0.79}\text{Al}_{0.16}\text{Cu}_{0.05}\text{O}_3$.As Cr exhibits multiple valance states, viz., III, IV and VI, a change in oxidation number is often accompanied by the change in ionic radii, e.g., 0.550–0.615 Å corresponding to Cr^{4+} reducing to Cr^{3+} [736]. This can also generate a change in volume (expansion) of the solid, thereby inducing significant mechanical stress, approaching (and in some cases surpassing) fracture stress levels [965].According to Hilpert et al., a linear relationship exists between CTE and oxygen stoichiometry [963,966]. The increase in acceptor dopant content makes the material more oxygen deficient, which in turn, enhances the CTE value. Fig. 67 shows the CTE behavior of $\text{La}_{1-x}\text{Ca}_x\text{CrO}_3$, $\text{La}_{1-x}\text{Sr}_x\text{CrO}_3$ and $\text{La}_{1-y}\text{Sr}_y\text{Cr}_x\text{Ni}_{1-x}\text{O}_3$ as a function of dopant content x. Fig. 67a shows that Sr^{2+} is a stronger contributor in affecting CTE, i.e., less Sr^{2+} is required to get a CTE value close to that of YSZ. Other dopants, e.g., Ni^{2+} (Fig. 67b), can be used either separately or as co-dopant to control the CTE. However, doping with Ni^{2+} [965,967,968], Ti^{4+} [967,969] and V^{5+} [970] can also lower the amount of lattice expansion associated with chromium reduction, which results in lower conductivity. For example, yttrium chromite exhibits lower conductivity than lanthanum chromites due to lower lattice expansion during reduction [971].Effect of doping on CTE and electrical conductivity of some of the commonly used LaCrO_3 -based interconnect materials are summarized in Table 11.

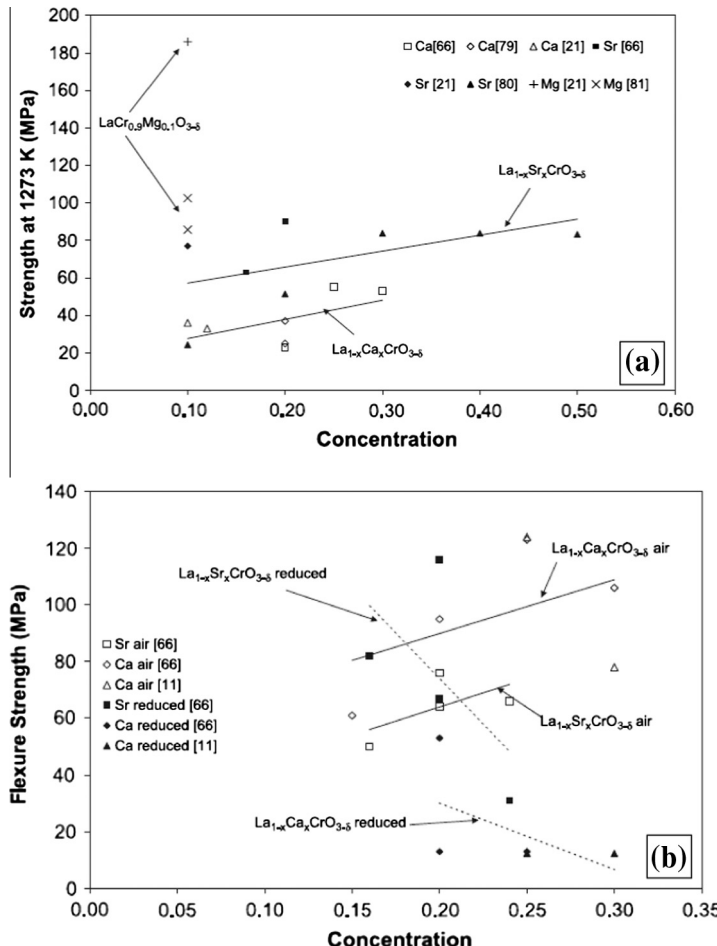


Fig. 68. (a) Strength of Ca- and Sr-doped lanthanum chromite at 1000 °C, (b) measured at room temperature in air and after being reduced. The numbers in square bracket are back-references cited in the article. ((a and b) Reprinted with permission from Ref. [952], copyright Elsevier, 2004).

Although a range of CTE values obtained via doping (Table 11) can be matched with that of anode and cathode, design of the composition is often met with a compromise between optimization of various properties, such as conductivity and mechanical properties (i.e., fracture strength, flexural strength, fracture toughness, etc.) [952]. Requirement of stringent mechanical strength (such as fracture strength, and flexural strength) on the material is demanded by the presence of various kinds of load and thermal stresses during operation. The fracture and flexural strength of Ca-, Mg- and Sr-doped LaCrO₃ at 1000 °C are shown in Fig. 68. The stresses generated during operation is also associated with the changes in temperature and P_{O₂}, and cannot be completely eliminated (see Table 12).

Doping with Mg exhibits highest mechanical fracture strength [977] followed by Sr [973–976] and Ca [976,977] because of solid-state sintering, and liquid-phase sintering mechanisms. The Mg doped specimens LaCr_{0.9}Mg_{0.1}O₃ consisted of a smaller grain size of 3–6 μm processed through solid-state sintering, whereas the grain growth in Ca doped La_{0.9}Ca_{0.1}CrO₃, and Sr doped La_{0.9} Sr_{0.1}CrO₃ specimens through liquid-phase sintering was more pronounced. It should be noted that sintering mechanisms affect the microstructures, which, in turn, influence the mechanical strength of sintered ceramics. Further the Sr²⁺ doping in LaCrO₃ results in better mechanical properties compared to Ca²⁺ doping,

Table 12

Phase content of the oxide scales at different spot areas on the sample shown in Fig. 80 after heat treatment at 800 °C for 400 h. (Reprinted with permission from Ref. [1066], copyright Springer, 2006).

Manifold, figure	Distance from mica (μm)	Assumed phase content	Total thickness of oxide scale (μm)
Air, 5a	0	(Cr, Fe, Mn) ₃ O ₄ , (Fe, Cr)-oxide, (Cr, Mn, Mg, Fe) ₃ O ₄	20–25
Air, 5b	500	Two phases, mixed, Cr _{1.9} (Mn, Mg, Fe) _{1.1} O ₄ , Cr ₂ O ₃	3–5
Air 5c	3800	Single phase oxide with Cr _{0.94} (Mn, Fe) _{0.66}	3–5
Fuel, 5d	0	Duplex Cr ₂ O ₃ , Cr _{2.3} (Mn, Mg, Fe) _{0.7} O ₄	8–10
Fuel, 5e	500	Duplex Cr ₂ O ₃ , (Cr, Mn) ₃ O ₄	1–2

which was attributed to the presence of more grain boundary phases [974] in Sr-doped compositions. Furthermore, Sr-doped LaCrO₃ exhibits a stable rhombohedral phase, while Ca²⁺-doped materials undergo a phase transition which also result in their inferior mechanical properties (fracture strength) [974].

As far as expansion of unit cell during reduction is concerned, the lanthanum chromite-based materials show higher mechanical strength (fracture toughness) when compared to calcium-doped yttrium chromite [983]. The mechanical properties can also be improved by reducing the layer thickness and lowering the porosity level in the component [979]. Fig. 68 shows the room-temperature flexural strength of calcium- and strontium-doped lanthanum chromite measured in air. In contrast to the results shown in Fig. 68a, the flexural strength of the calcium-doped materials is radically decreased (from 90 to 50 MPa) at 1000 °C, whereas strontium-doped materials remain comparatively unaffected after reduction. However, the mechanical strength of the calcium-doped materials is significantly decreased by reduction under low P_{O₂} [952].

5.2. Metallic alloys as interconnect materials

Low cost, availability, and ease of fabrication make metals more attractive than ceramic oxides as interconnect materials. In this category, Ni, Fe and Cr based oxidation resistant alloys and some precious metals like Ag have been employed as interconnect materials. However, due to their low melting point, high volatility, intrinsic instability under air-hydrogen dual exposure conditions and high overall cost, the use of precious metals is restricted to a very limited extent [980]. Among metal alloys, Fe–Cr based alloys, Cr-based alloys, Ni(Fe)–Cr-based heat resistant alloys, austenitic and ferritic stainless steels are being extensively used as interconnect materials (as shown in Fig. 69).

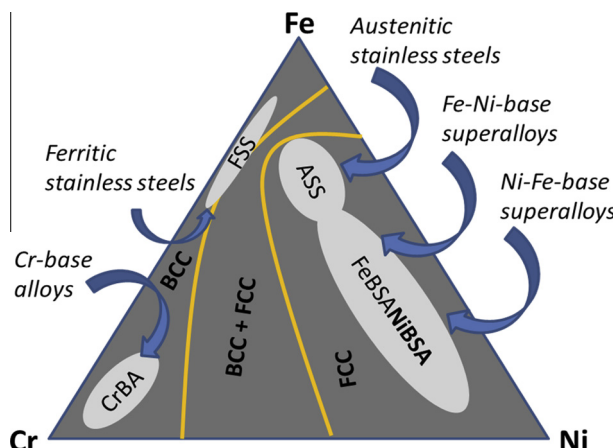


Fig. 69. Schematic showing selection of phases in Fe–Co–Ni based alloys as metallic interconnect materials. (Adapted from Ref. [980]).

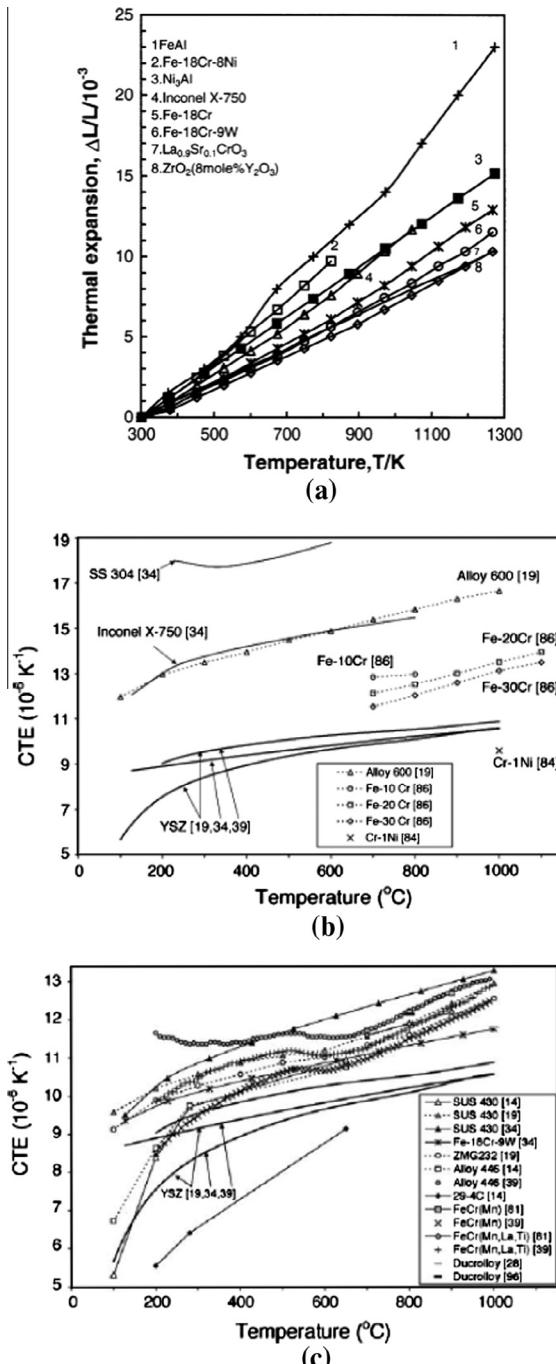


Fig. 70. (a) Thermal expansion behavior of Fe-Cr-based alloys, FeAl, $\text{La}_{0.9}\text{Sr}_{0.1}\text{CrO}_3$ and 8YSZ electrolyte. (Reprinted with permission from Ref. [931], copyright Elsevier, 2003). CTE of (b) chromia-forming alloys and (c) iron- and chromium based alloys as a function of temperature. The numbers in the square brackets are back-references cited in the article. ((b-c) Reprinted with permission from Ref. [986], copyright Elsevier, 2005).

With metallic interconnects, it has been possible to lower the operating temperature of SOFCs to below 800 °C. Among various stainless steels, viz., ferritic, austenitic, martensitic and precipitation hardening steels, ferritic steels are most preferred as interconnect materials due to their bcc structure, which has the CTE values ($11.0\text{--}12.5 \times 10^{-6}/\text{K}$) similar to other SOFC components ($\sim 10.5\text{--}12.5 \times 10^{-6}/\text{K}$) [980]. High ductility, good workability, ease of processing, and comparatively lower cost of fabrication are other advantages related to ferritic steels [981,982].

Most of the metals are unstable in air, so oxidation resistance is a key issue for metallic interconnects. Although metals are excellent electrical conductors, the oxide scales formed during high-temperature exposure in air have much higher resistivity, which, as a result, increases the overall electrical resistance of the metal over time. Therefore, certain additives are used to reduce the electrical resistance of the oxide scale formed on the metallic interconnect material. However, an increase in ions and electrons transport rates will also lead to rapid oxide scale growth, which consequently degrades the oxidation resistance of the material. Thus, the composition of metal for interconnects needs optimization such that adequate electrical conductivity (i.e., 0.1 S/cm at operating temperature) and good oxidation resistance can be achieved.

Fig. 70a shows the thermal expansion characteristics comparison between the Fe-Al-Cr-Ni based alloys and LaCrO₃ ceramics. For comparison, thermal expansion characteristic of 8YSZ electrolyte is

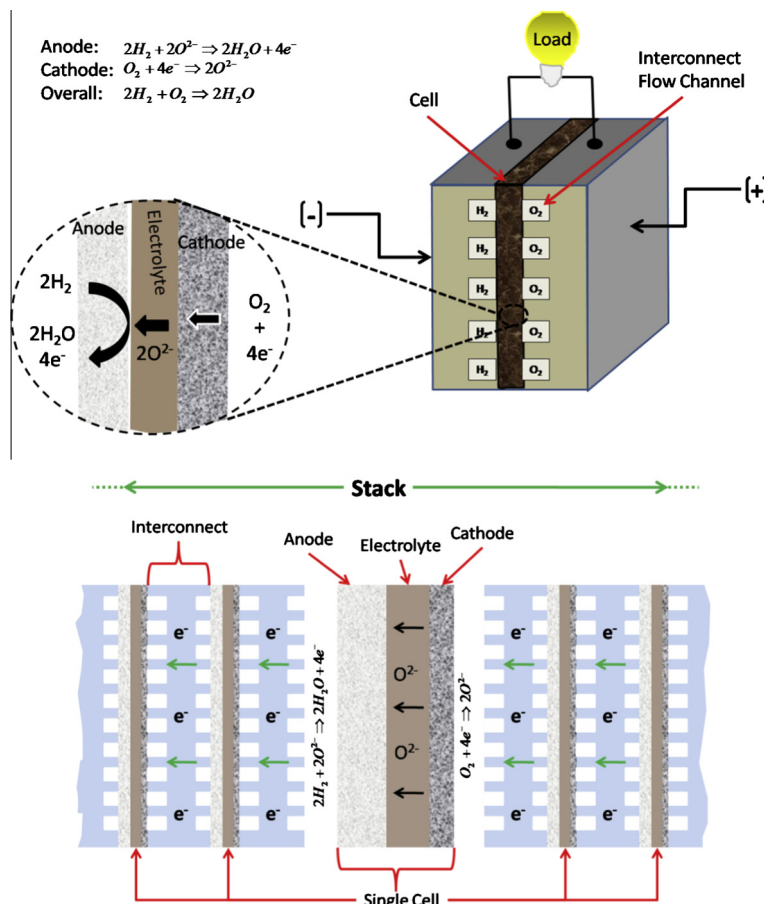


Fig. 71. Schematic showing assembly of cells into stacks with hydrogen as fuel. The interconnect material is exposed to both kinds of atmospheres (i.e., oxidizing and reducing). (Adapted from Ref. [11]).

also shown, where the slope of the curve shown in Fig. 70a is the CTE. Iron aluminide (Fe-Al) exhibits the highest CTE value (with the thermal expansion of $23 \times 10^{-3} /K$ at 1000°C) due to high Al content, whereas Fe-18Cr, Fe-18Cr-9 W, Ni₃Al, inconel X750 (Ni-based alloy), and Fe-18Cr-8Ni alloys show intermediate values (ranging from $10 \times 10^{-3} /K$ to $15 \times 10^{-3} /K$ at 1000°C). Furthermore, the useability of Fe-Cr-W interconnect alloys was evaluated for their high temperature oxidation resistance at 1000°C . Oxidation resistance of Fe-18Cr-9 W is restricted by incorporating trace amounts of La, Ce, Zn or La + Ce (misch metal) which renders a slow growth of protective and conducting oxide scales. Lower than 1 wt.% Zr reinforcement improves oxidation resistance of Fe-18Cr-9 W alloy at 1000°C in air [931]. Ni-25Cr exhibits minor weight loss of ~0.8% at 1000°C when exposed in air for duration of 200 h because of oxide-scale delamination [931]. Fe-20Cr-5Al stands better than Fe-18Cr7W in terms of oxidation resistance due to the formation of insulating Al₂O₃ scale [931]. However, for Fe-18Cr-7 W alloys, a product (containing CrMnO₂ spinel and Cr₂O₃) is formed in the interconnect-LSM interface at 1000°C [983] which follows diffusion controlled kinetics.

The CTE of austenitic stainless steels (e.g., AISI 304), Ni-based alloys, (inconel X750 and 600) are much higher (~66%) than YSZ. The CTE of Ni-based alloys can be lowered by making a metal ceramic composite. However, it will increase both the electrical resistance and fabrication cost [984,985]. On the other hand, both ferritic stainless steels and chromium based alloys have an advantage over Ni-based alloys as their respective CTE ($8.8\text{--}11 \times 10^{-6}/\text{K}$) is close to that of YSZ ($\sim 8.5\text{--}10.5 \times 10^{-6}/\text{K}$), see Fig. 70b and c. Furthermore, it has been observed that CTE value of ferritic steels can be reduced using additive like W, Mo and Nb, e.g., 29-4C (4 wt.% Mo). In addition, Fe-18Cr9W exhibits lower CTE ($5.5 \times 10^{-6}/\text{K}$ for 29-4C and $9.5 \times 10^{-6}/\text{K}$ for Fe-18Cr9W) compared to ferritic steel ($9.5\text{--}13.2 \times 10^{-6}/\text{K}$) [986].

As interconnects, ferritic steels are exposed to dual atmospheres (both reducing and oxidizing), see Fig. 71, and tend to form iron rich spinels or Fe₂O₃ nodules. Active constituents of Cr, Al, etc. present in the alloys get preferentially surface oxidized at high temperature and form passive film which minimizes further damage [987–989]. While Al₂O₃ is insulating (~ 10^{-14} S/cm) in nature, a semiconducting characteristics of Cr₂O₃ (~ 10^{-2} S/cm) at 800°C in air [964,990–993] renders Cr-containing alloys a key advantage. Cr-based alloys not only provide better oxidation resistant than ferritic steel due to formation of chromia layer, which grows during service, but also maintain satisfactory electrical conductivity even at 800°C [991,992]. Trace amounts of Y, Ce, La and Zr added in their native or oxide form were shown to endorse oxidation resistance as well as improve scale adherence in chromia-forming alloys [991].

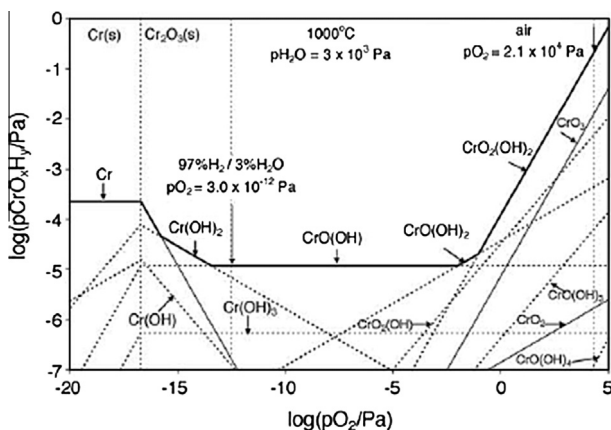


Fig. 72. Equilibrium vapor pressure of chromium-oxygen-hydrogen gas species with a water vapor pressure of 3 kPa at 1000°C using thermodynamic data from Ebbinghaus's work. (Reprinted with permission from Ref. [986], copyright Elsevier, 2005, with data from Ref. [994], copyright Elsevier, 1993).

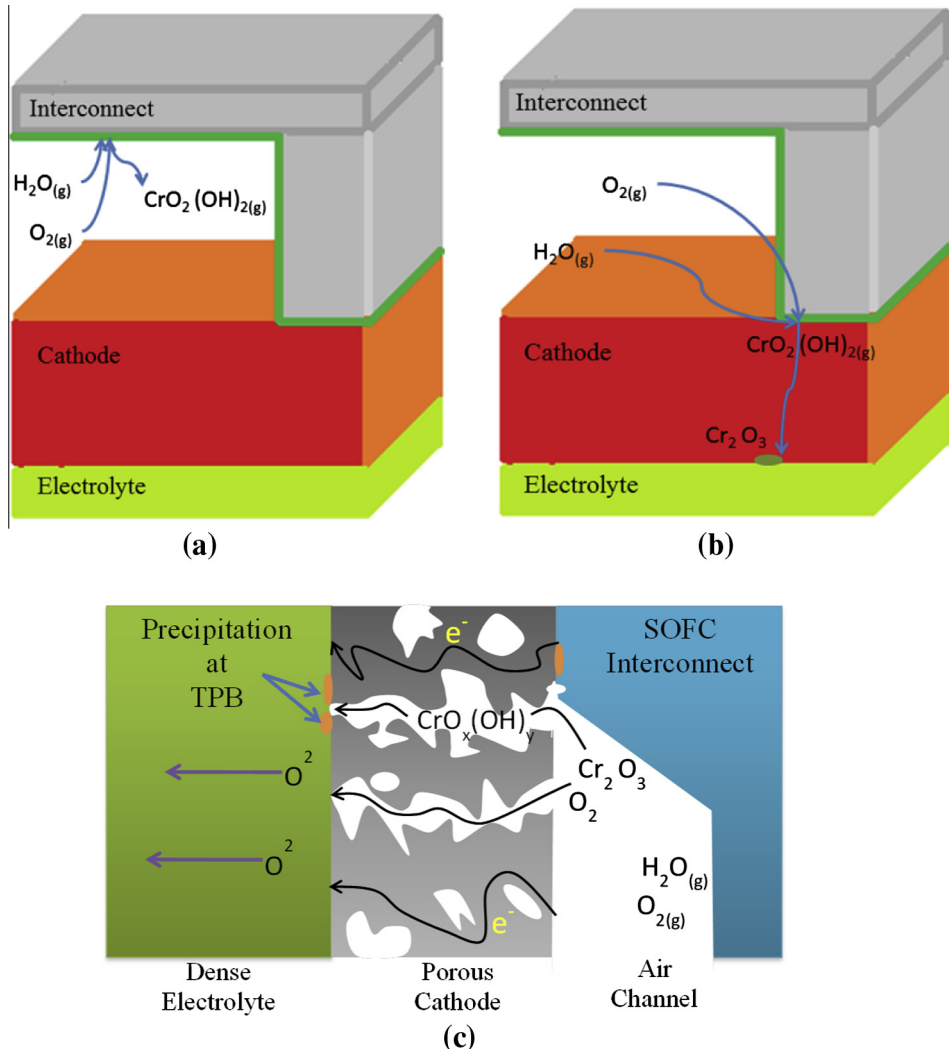
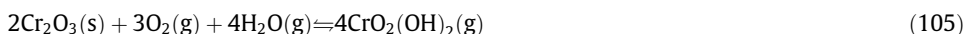
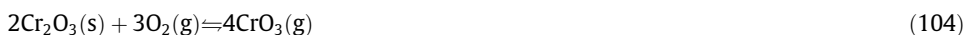


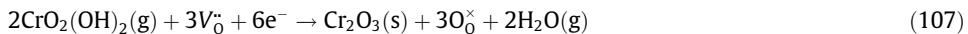
Fig. 73. Schematic representation of formation of (a) $\text{CrO}_2(\text{OH})_2$ at the interconnect and (b) Cr_2O_3 at the cathode and electrolyte interface. ((a and b) adapted from Refs. [953,1006]), and (c) Evaporation of chromium species from interconnect surface and precipitation at triple phase boundary (TPB). (Adapted from Ref. [1012].)

Almost all alloys employed as interconnect materials form chromia scales during oxidation which grow by outward diffusion of Cr ions through the scale. This induces porosity at alloy-scale interface which result into cracking and spallation when growth stresses become significant. Both scale formation and volatilization (generation of volatile Cr (VI) species at temperatures 1000 °C or higher) of chromia forming alloys can take place as:



The equilibrium vapor pressure of chromium–oxygen–hydrogen gas species formation at 1000 °C is shown in Fig. 72. These volatile species diffuse into the porous cathode material, and get reduced in the form of Cr₂O₃ deposits.

The reduction of volatile chromium species may take place chemically or electrochemically at the porous cathode surface. The deposition of Cr₂O₃ product on the TPB sites blocks the active reaction (of reduction) sites and degrades the overall cell performance (Fig. 73) [995–1004]. The degradation is evinced through cell voltage decrease or corresponding increase in electrode overvoltage [1005]. The electrochemical reduction of chromium in vapor phase, and deposition of the reduced species (depending upon the predominant gas species in the vapor phase) can be shown as:



or



Jiang et al. showed that the deposition occurs primarily via chemical reaction rather than electrochemical process [1001–1003]. Electrons would not be available for electrochemical reaction on the zirconia sites since preferentially deposition occurs there. When SDC or Sr²⁺ doped ceria is used in place of YSZ, no evidence of degradation was observed [986]. Jiang et al. also proposed that the manganese ions from the cathode diffuse to electrolyte surface with time and react with Cr-vapor to form (Cr, Mn)₃O₄ phase [1001–1003].

Nickel-based alloys exhibit excellent oxidation resistance in moist hydrogen, and also show better mechanical strength. The oxide scale which grow on its surface consists of (i) Cr₂O₃ and (Mn, Cr, Ni)₃O₄ spinels in Haynes 230 and Hastelloy S or high chromium alloys, and (ii) NiO in Haynes 242 or low chromium alloys. These alloys possess considerable CTE mismatch and, hence, these are often alloyed with W, Mo, Al and Ti to compensate the CTE mismatch with other cell components.

5.3. Material degradation and protection

Addition of titanium was shown to generate ionic defects in the oxide layer and modify the growth kinetics of Cr₂O₃ and MnCr₂O₄. Ti content in a range of 0.05–0.07 wt.% was found to be effective in reducing the rate of oxidation and increasing the electrical conductivity [1008]. Addition of 1 wt.% Ti promotes rapid growth of Cr₂O₃, where oxidation rate constant increased from 2.83 to 20.9 ($\times 10^{-10}$ g²/mm⁴/h). This is because of excess ionic defects present in Cr₂O₃ matrix, and the outermost MnCr₂O₄ layer formation, which is accelerated by Ti segregation near the scale/alloy interface, with effective reduction in Cr evaporation. In comparison to ferritic steel substrate, Seo et al. [1008] reported a well adhered oxide scale interfacing with alloy of 0.98 wt.% Ti in ferritic matrix. In case of 0.05 wt.% Ti, abnormal Fe engulfing was observed in the form of tiny spots of Fe metallic phase, which are dispersed in the oxide scale formed. These metallic phases are connected to Mn–Cr spinel layer and Cr₂O₃ layers, which insinuates formation of abnormal metallic junctions in steel alloyed with 0.05 wt.% Ti. Such a structure is stimulated by fast inward growth of inner Mn–Cr spinel layer, which is assisted by TiO₂ oxide layer with alloying of 0.98 wt.% Ti. Ti segregation without formation of excess ionic defect is enhanced by the addition of a small amount of La along with Ti (0.06 wt.% Ti + 0.04 wt.% La). This also enhanced the electric conductivity and increased resistance toward Cr evaporation. Formation of oxide scale microstructure on ferritic stainless steels can be controlled by co-addition of La with Ti. Although, the total amount of reactive individual elements in (0.06 wt.% Ti + 0.04 wt.% La) is less than 0.1 wt.%, it creates a thick (0.30–0.45 μm) outermost Mn–Cr spinel layer similar to that in 0.98 wt.% Ti [1123]. Moreover, the Cr₂O₃ layer of La and Ti reinforced steel is thinner than that of base steel or ferritic steel with 0.05 wt.% Ti, which suggestss that the electric conduction path is shortened. Therefore, co-addition renders a lower area-specific resistance and reduced Cr evaporation.

In order to protect the interconnect materials from degradation mainly occurring via oxidation (which lowers conductivity), chromium vaporization (or poisoning) and oxide spallation (responsible to cause discontinuous circuit), protective coatings have been developed in the recent years. These coatings have additional requirements of: (i) low electrical resistance, (ii) low diffusion coefficients

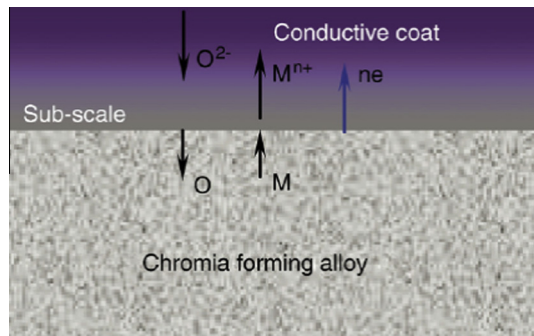


Fig. 74. Schematic diagram showing mass transport in a conductive oxide coating on a chromia forming alloy (Reprinted with permission from Ref. [1030], copyright Elsevier, 2006).

of Cr and O in the coating, (iii) chemical compatibility and stability with respect to the substrate material, electrodes, sealants and contact paste, (iv) thermodynamic stability in both oxidizing and reducing conditions, and most importantly, (v) possessing a matching CTE with the substrate material to resist spalling during thermal cycling [931]. These coatings are classified as:

- (1) *Nitride coatings*: CrN multilayers with CrAlN superlattice [1009], Cr-Al-ON [1010], TiAlN with 30–50% Al and SmCoN [1011,1012]. Introducing oxygen into nitride coatings reduce Fe and Cr migration from substrates. However, nitride coatings have some limitations, such as, high cost and high temperature instability (>600 °C) of coatings.
- (2) *Perovskite coatings*: LaCrO₃, (which itself is an interconnect material), deposited by RF sputtering [1013], and LSM and LSCF coating by aerosol deposition method [1014] are some of the noteworthy perovskite coatings applied to interconnect materials.
- (3) *Spinel*: CoCrO₄ [1015] (MnCo)₃O₄ (Cr free spinel), MnCo₂O₄ [1016,1017] applied by slurry coating [1018], screen printing [1019] and PVD [1020].

Apart from monolithic coatings, electroplating of Mn and Co, either as an individual elements or in alloy form, controlled oxidation and/or reaction to a desired phase have also been reported [1021–1024]. Coating of nanocrystalline Mn–Co–O via anodic deposition was reported by Neifeng et al. [1025,1026]. The coatings typically diminish the area specific resistance by lowering the growth rate of oxide film, and consequently decrease the thickness of the oxide scale [1027–1029].

It is important to note that the protection layers applied onto the chromia forming metallic interconnect materials must serve as barrier to both, inward oxygen transport and outward chromium diffusion (Fig. 74), and at the same time, it must also be electrically insulating (~5–6 m Ω cm²). Chromium-containing conductive oxides, e.g., (La, Sr)CrO₃ often shows low ionic conductivity (10⁻⁵ S/cm) and therefore, might not provide a suitable protection due to the chromium vaporization. Application of non-chromite perovskite coatings, e.g., (La, Sr)FeO₃ exhibits improvement in oxidation resistance (2 times higher growth rate) and electrical conductivity (as resistance decreases 58% at 150 h exposure) when compared to lanthanum chromite coatings. But, applicability of LSF as an effective barrier (in long term working of SOFC stack) against the release of chromium is doubtful, since chromium diffusion may be facilitated through the coating itself. Among the materials studied, the thermally-grown (Mn, Co)₃O₄ spinel on Crofer 22 APU surface showed improved stability and prevented chromium outward migration [1030].

In summary, ceramic interconnects possess poor electrical conductivity although they have high temperature stability, whereas metallic interconnects posses good electrical conductivity, but are prone to oxidation. Ceramic interconnect materials mainly consist of chromites (e.g., Sr- and Cr-doped lanthanum chromite), while metallic interconnect materials include chromia-forming alloys, viz., nickel-based alloys, ferritic stainless steels and chromium- based alloys. The CTE values of nickel-

based alloys are considerably higher than the other cell components, hence, induce compatibility issues. Chromium based alloys, however, can be well dispersed with stable oxides, but, fabrication is rather expensive. In this respect, ferritic stainless steels offer the most desirable choice as metallic interconnect material for SOFC.

During stacking of the individual cells, one of the major challenges still remains, which is to make the system gas tight (or leak-proof), i.e., to separate air and fuel and prevention of leakage. Thus, the following section deals with the progress in the development of suitable sealant materials with necessary adherence, mechanical integrity, and stability.

6. Sealants

In planar design SOFC stacking, the individual cells are connected in series one after the other, separated by interconnect to prevent reactions between the materials of adjoining components. In this aspect, sealant materials play a key role in avoiding any leakages of either fuel or air from their respective chambers, and thereby preventing any direct mixing of fuel and air. Although, with proper engineering design (such as in cylindrical fuel-cell shown in Fig. 64), the necessary requirement of sealants can be completely eliminated, but at the cost of efficiency and ease of manufacturing and stacking. It can be appreciated from Fig. 64 that the sealant materials are always exposed to both oxidizing and reducing atmospheres at high temperatures (700–1000 °C). These stringent conditions demands the following requirements that sealant materials need to fulfill for the proper functioning of SOFC device [1031–1034]:

- **Mechanical**

- Hermeticity, i.e., marginal or no gas leakage.
- The coefficient of thermal expansion of the sealant material should be similar to that of other cell components ($\sim 10\text{--}12 \times 10^{-6}/\text{K}$) in order to reduce thermal stresses and limit cracking and leakages during operation.
- Appreciable bond strength to avoid leakage, and/or compressive loading to bear the stack load, and also render hermeticity as on-service requirement.
- Resistance to damage from thermal cycling and tolerance to thermal shocks.
- Enough resilience and toughness under external static and dynamic forces.

- **Chemical**

- Long-term (>40,000 h) chemical stability under oxidizing/wet fuel.
- Chemical compatibility with the adjoining SOFC components.
- Resistance to hydrogen cracking/embrittlement.

- **Electrical**

- Insulating in nature.

- **Design/fabrication**

- High hermeticity (i.e., conforming to sealing tortuous surfaces).
- Acceptable sealing environment/temperature (i.e., has little effect on the subsequent performance of the stack).
- Design flexibility – for example, that allows use of Ni-based alloys in the interconnect.
- Simplistic application/processing.
- Low cost and economical.

Based on the above-stated requirements, research performed on SOFC's sealant materials can be divided into four important successive steps: (i) investigation and selection of potential seal materials/components (with matching CTE) and approximation of the composition, (ii) processing techniques employed, (iii) investigation of the quantitative impacts of each constituent on the sealing behavior and (iv) optimization of chemical processes and technique, e.g., controlling crystallization kinetics by surface engineering, chemistry and long-term stability, etc. (shown in Fig. 75). Some studies have used finite element analysis method to investigate the effects of scaling and geometry on the material performance during thermal cycling [1035].

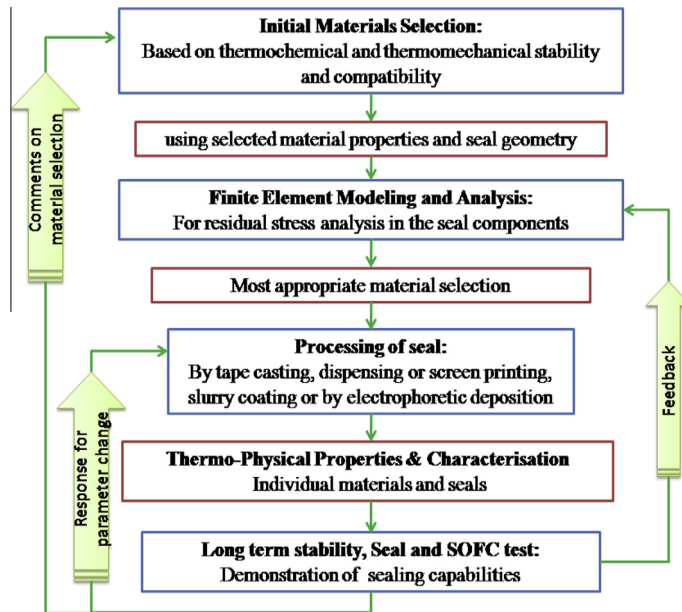


Fig. 75. Important steps in SOFC sealant research. (Adapted from Ref. [1036]).

Schematic shown in Fig. 76a–e illustrates the application of sealant material in a planar SOFC [1037]. Planar design of SOFC facilitates compactness and exhibits better output in terms of efficiency. On the other hand, sealing is generally not a serious problem in tubular SOFCs. Most of the tubular designs are either “seal-less” i.e., the gas seals placed out of high-temperature areas where conventional metals are used as seals, or use some high-temperature seals to join single tubes, or flattened tubes into bundle for attachment to a gas or fuel. The tubular cell with diameter ranging between 1.5 and 15 mm and length up to 15 mm possess much longer life, up to several years and indeed a great advantage over planar counterparts [454,1038–1041]. In the schematic (Fig. 76f and g), the application of a gas sealing of the experimental apparatus for a single micro-tubular SOFC is shown. Such a design ensures that there are no leakages during electrochemical measurements [1042].

The high temperature sealant materials used for SOFC application are made of various type of materials, such as, metal, glass-ceramic, brazes, or mica-based composites. Multiple sealant materials are also used as and when required. There are mainly two standard methods of sealing [818,1043,1044], viz., (i) compressive sealing or glass joining and (ii) rigid sealing, which are detailed in the subsequent sections. A schematic representation of a typical seal type is shown in Fig. 77.

6.1. Compressive seals

In compressive sealing, a material compliant at high temperature is fitted in-between two surfaces of sealing, and compressed (using an external load) in between the components in order to achieve an airtight hermetic sealing.

Although, the sealing surfaces in compressive sealing can slide over one another without disturbing the hermeticity (gas tightness or impervious to gas flow), these sealants suffer from issues relating to oxide scaling and chemical instability in highly reactive environments [1043]. Therefore, there is a huge scope for research on the development of compressive sealing material with good reliability under high-temperature (900–1000 °C) operation, appropriate chemical stability, and with appropriate load frame design.

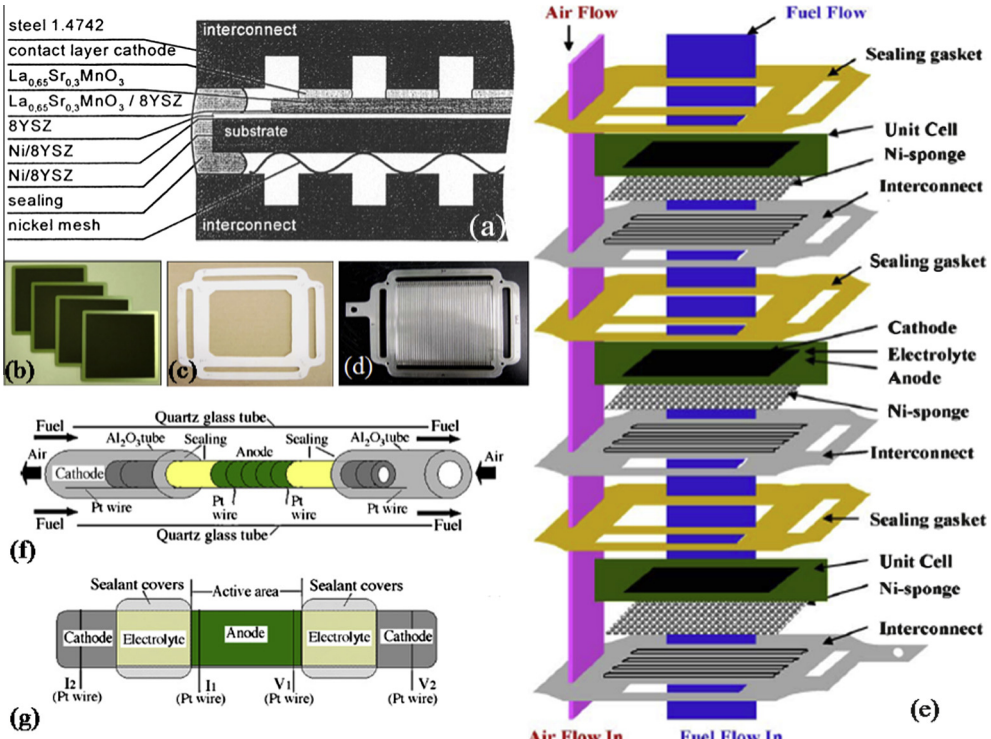


Fig. 76. (a) Schematic diagram of the cross section of a SOFC unit showing positioning of sealant material in a planer stack. Photographs of (b) anode-supported 10×10 cm unit cells (anode electrolyte and cathode), (c) sealing gasket, (d) interconnector. Schematic diagram of (e) an experimental apparatus for the single micro-tubular cathode-supported cell measurement, (f) the enlarged cross sectional view of the sealant cover and current collection through the cell, I_1, I_2 : current collect terminals, and V_1, V_2 : voltage detect terminals, and (g) planar SOFC stack based on anode-supported 10×10 cm unit cells shown in (b-d). (a) Reprinted with permission from Ref. [454], Springer, 1999, (b-e) Reprinted with permission from Ref. [1037], Elsevier, 2006, (f and g) Reprinted with permission from Ref. [1042], Elsevier, 2007.

This category (of compressive seals) is divided into two categories:

- Metallic compressive seals, and
- Mica-based compressive seals.

Since compressive seals are not fixed tightly (or bonded) to the other SOFC components, therefore a requirement of close match of CTE is not essential. In order to maintain gas tightness when attached to the other SOFC components, a constant application of pressure in operation is needed. The compression of the seal during operation allows for adjustment of various components (with different CTE values) and facilitates closure of small gaps to reduce leak rates. Thus, seals are required to possess flexibility to get deformed in response to the applied stress, and render compression in order to serve as an effective sealant. Metals, due to their high ductility, offer a logistic solution to this problem. However, metals are susceptible to oxide scale formation upon exposure to air/ oxygen at high operational temperatures which eventually result in degradation. Therefore, choice of appropriate metals to be used as seals is restricted to noble metals, such as, platinum (m. p. 1774°C), gold (m.p. 1063°C) and silver (m.p. 961°C) [1039,1046–1050]. Platinum and gold are not a cost-effective solution, whereas silver can be used as an economical sealant. In order to be used as potential sealants, the strength of metallic seals must fall in a critical range (i.e., should be lower by a factor of 2–3 of the material to be sealed). If material strength is too high (e.g., yield strength 124 MPa), as in sterling silver containing 7.5% copper, the seal material does not possess sufficient deformability to render its desired function [1049].

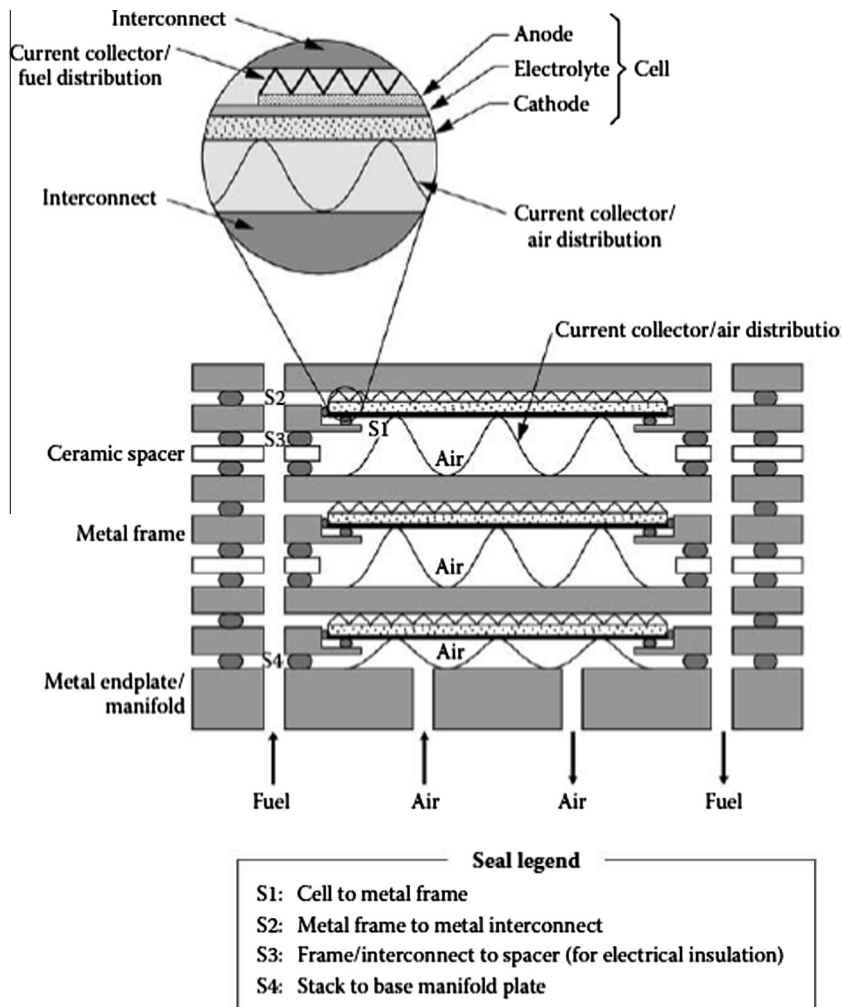


Fig. 77. Schematic representation of typical seal types employed in planer SOFC stacks. Diagram shows metallic interconnect and metallic internal gas manifold channels (cross-flow configuration for the fuel and air gas streams). The upper sketch is a magnified view of unit cell containing anode, electrolyte, cathode, interconnect, and the light-gray colored strips are edge seals. Typical seals, marked as S1–4, function as S1: cell to metal frame, i.e., sealing of the edges of the cells and to a particular cell layer, S2: metal frame to metal interconnect, S3: frame/interconnect pair to electrically insulating spacer, and S4: stack to base manifold plate. (Reprinted with permission from Ref. [1045], copyright Springer, 2007).

whereas on being softer, the leakage rates will be enhanced. Another problematic issue relating with the use of silver as sealant is the significant solubility of both oxygen and hydrogen in silver. Exposure to both oxygen (at cathode side) and hydrogen (at anode side) results in the formation of water, which consequently lead to the failure of silver as sealant. Also, due to high vapor pressure, silver tends to develop high porosity when exposed to the dual atmosphere (H_2 -3% H_2O). Furthermore, Chou and Stevenson have conducted an investigation on the thermal cycling of Ag/mica compressive seals composed of naturally cleaved muscovite mica sheet and two thin silver layers [1050]. The composite material was reported to exhibits good thermal cycling stability for SOFC but with leak rates higher than the seal material composed of mica with glass interlayers at 800 °C [1050].

Other metallic compressive sealants include less-deformable metals, such as, superalloys fabricated into corrugated or C-shaped gaskets [1047,1048]. These were designed to have good oxidation

resistance while maintaining gas tightness on applying pressure (~ 1500 mbar). The gas tightness and deformable shape of these seal materials is further enhanced by coating a more ductile metal (such as Cu, Ag) on sealant surface, and combining with rigid seals. The latter is done by brazing the seal or gasket to the electrolyte and interconnect where the primary sealing is performed by rigid seal, whereas compliant gasket absorbs partial strain, and thus, reduces the entire stress from damaging the rigid sealant [1051].

In silver-ceramic composite based sealant materials, silver forms a three-dimensional network, which as a result, reduces the high CTE value of silver [991] and other metal oxide/silver systems, viz., Ag–CuO “fluxless” seals, Ag– V_2O_5 , etc. [1034,1052–1054]. Ferritic and chromium containing alloys, e.g., Crofer, E-Brite (26% Cr–1% Mo), FeCrAlY (Fe 22% Cr, 5% Al, 0.2% Y) brazed to YSZ, SS 304, SS 430 and Ni, etc. tend to form chromium oxide layers, which provide oxidative stability and conductive scale-forming ability that make them suitable for interconnect application [1055]. An external coating of $LaCrO_3$ on T446 stainless steel has been found to promote oxidation resistance by reducing scale growth rate [1036].

Another type of seal in this category is mica-based materials [1044,1048,1050,1056–1063], which belong to phyllosilicates minerals, a class possessing high resistivity and high dielectric constant. These materials are composed of parallel sheets of silicate tetrahedra, which enable them to accommodate large thermal stresses. As mica does not bind well to SOFC components, mica seals alone shows high leak rates, which is several orders of magnitude higher, when compared to that of glass-based seals (leakage rate of glass composite material is reported to be as low as 2.41×10^{-4} sccm at STP [1064]). Therefore, mica is combined with other materials, such as silver and glass, to make a composite with improved hermeticity up to an acceptable level (described later) [818]. In principle, gas tightness can also be achieved by the application of pressure on the overlapped plate-like mica as shown schematically in Fig. 78a. However, gas leakage can still occur, typically, at the mica and the metal or ceramic interface, which can be restricted by introducing a compliant layer of metal or a glass (Fig. 78b) on the mica surface, to form a hybrid seal. Mica powder can be placed between the gaps of the corrugated metal seal (Fig. 78c) to achieve good hermeticity. Infiltrating a phase (bismuth nitrate) can also allows sealing between the adjacent mica particles (Fig. 78d) and enhancing the gas-tightness. The performance of various mica seals are compared in Fig. 79 [1045,1048,1056–1059].

Stevenson and coworkers have conducted test on hybrid mica seals infiltrated with wetting material ($Bi(NO_3)_3 \cdot 5H_2O$) in a reducing atmosphere ($\sim 2.5\text{--}2.7\%$ H_2 –Ar– $\sim 3\%$ H_2O , at flow rate of 64 sccm) for ~ 1000 h at $800\text{ }^\circ C$. The tests were performed for ~ 30 thermal cycles between 100 and $800\text{ }^\circ C$

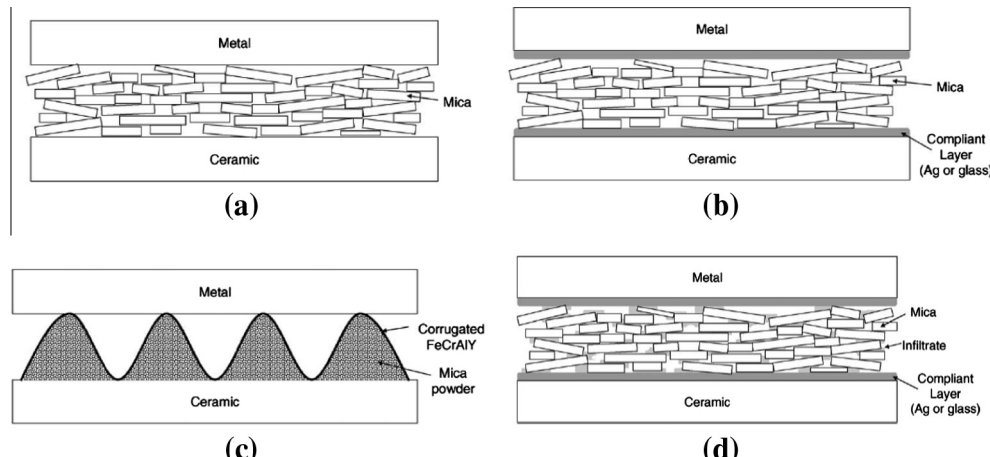


Fig. 78. Mica based SOFC seals: (a) plain mica seal, (b) hybrid mica seal with compliant layer (glass or metal). ((a and b) Reprinted with permission from Ref. [1044,1057], copyright John Wiley and Sons, 2004), (c) mica powder with corrugated alloy. (Reprinted with permission from Ref. [1058], copyright Elsevier, 2004), and (d) hybrid mica seal with compliant layer and infiltrated mica. (Reprinted with permission from Ref. [1059], copyright Elsevier, 2004).

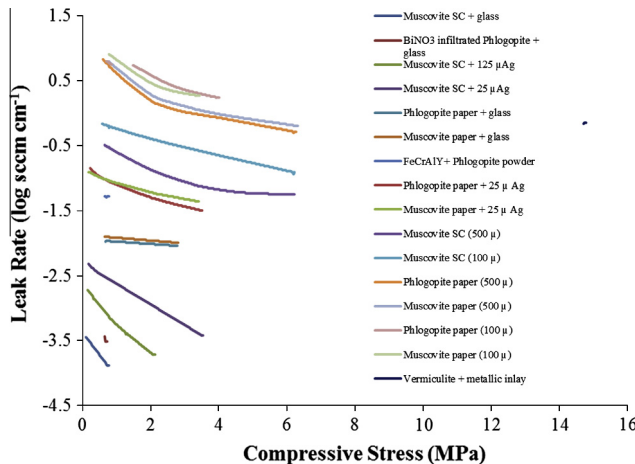


Fig. 79. Leak rates for mica-based seals [1044,1048,1056–1059]. The gas pressure difference across seal is 50 kPa from Bram et al. [1048,1058] and 14 kPa from Chou et al. [1044,1056,1059]. “SC” stands for single crystal. The leak rates are presented as standard cubic centimeters per minute per unit leak length of seal (sccm/min). The tests were conducted at 800 °C.

[1044,1056,1059]. The mica layer was pressed between an IN600 fixture and 8YSZ electrolyte plate (50 mm × 50 mm) at 41.4 kPa. It was shown that the leak rates (of 4×10^{-3} sccm/cm) decreased by ten times than that estimated for conventional mica seals (3×10^{-2} sccm/cm). The initial leak rate was found to be $\sim 2 \times 10^{-2}$ sccm/cm, which gradually decreased to $\sim 2 \times 10^{-3}$ – 3×10^{-3} sccm/cm after ~600 h. On further aging, the leak rate rapidly increased up to ~ 0.05 sccm/cm, which may be because of the decomposition of bismuth nitrate with time. After 1036 h, thermal cycling was initiated between ~ 100 and 800 °C. The leak rate increased to $\sim 8 \times 10^{-2}$ sccm/cm at the 5th cycle, ~ 0.1 sccm/cm at the 15th cycle, and ~ 0.3 sccm/cm at the 21st cycle. Such high leak rates were reported to be equivalent to the leak rate of rigid glass seals measured after fracture caused due to CTE mismatch. Thus, it was concluded that hybrid mica seals may have fractured out of cyclic thermal stresses. In addition, the material elicited constant OCP of 0.934 V with continued operation of over 1000 thermal cycles (at 800 °C) [1065].

Muscovite ($KAl_2(AlSi_3O_{10})(F, OH)_2$) and phlogopite ($KMg_3(AlSi_3O_{10})(OH)_2$) are the two main types of mica used as sealants [1060–1062]. The CTE of phlogopite ($\sim 10 \times 10^{-6}/K$) is higher than that of muscovite ($\sim 7 \times 10^{-6}/K$) [1060]. Of the two forms of mica tested, viz., cleaved crystal and mica paper, cleaved crystal always provide a better seal than mica paper. In all cases, thick layers (0.5 mm) have been found to perform better than the thin layers (0.1–0.2 mm). Thus, a higher thickness of cleaved crystal strongly ensue a good sealing effect. The leak rate can be further reduced by using compliant interlayers, such as, glass and silver. The leak-rate for seal of mica powders with FeCrAlY (Fig. 79) is within the resolution limit of experimentation, and could be well below that of the reported values. Phlogopite paper can be made more effective by infiltrating $Bi(NO_3)_3$ glass compliant layer. The performance of mica-based seals at high-temperature with thermal cycling has not shown to strongly affect the leak-rate of phlogopite paper based seals [1060]. However, the leak rate of cleaved muscovite crystals seals increases ($\sim 1.6 \times 10^{-3}$ sccm/cm per cycle for plane and $\sim 4.4 \times 10^{-4}$ sccm/cm per cycle for hybrid) with thermal cycling [1061]. For infiltrated mica, leak rate (of $1\text{--}4 \times 10^{-3}$ sccm/cm) either remains unaffected (e.g., for $(BiNO_3)_3$) or decreases (leak rate $< 5 \times 10^{-4}$ sccm/cm for H_3BO_3) with cycling [1059]. An insignificant degradation of mica-based seals was observed at 800°C, which indicates that these seals are stable up to 800°C [1060,1062]. With the introduction of glass compliant layer/gas-infiltration into a mica paper, the resulting sealant material resembles a glass-ceramic. Wiener et al. [1066] performed corrosion experiments by simulating SOFC conditions at 800°C for 400 h, and investigated potential interactions between the Crofer 22 APU (interconnect steel) and the mineral phases vermiculite (exfoliated) ($K, Mg, Fe)_3(Si, Al)Al_4O_{10}(OH)_2$) and talc ($Mg_3Si_4O_{10}(OH)_2$).

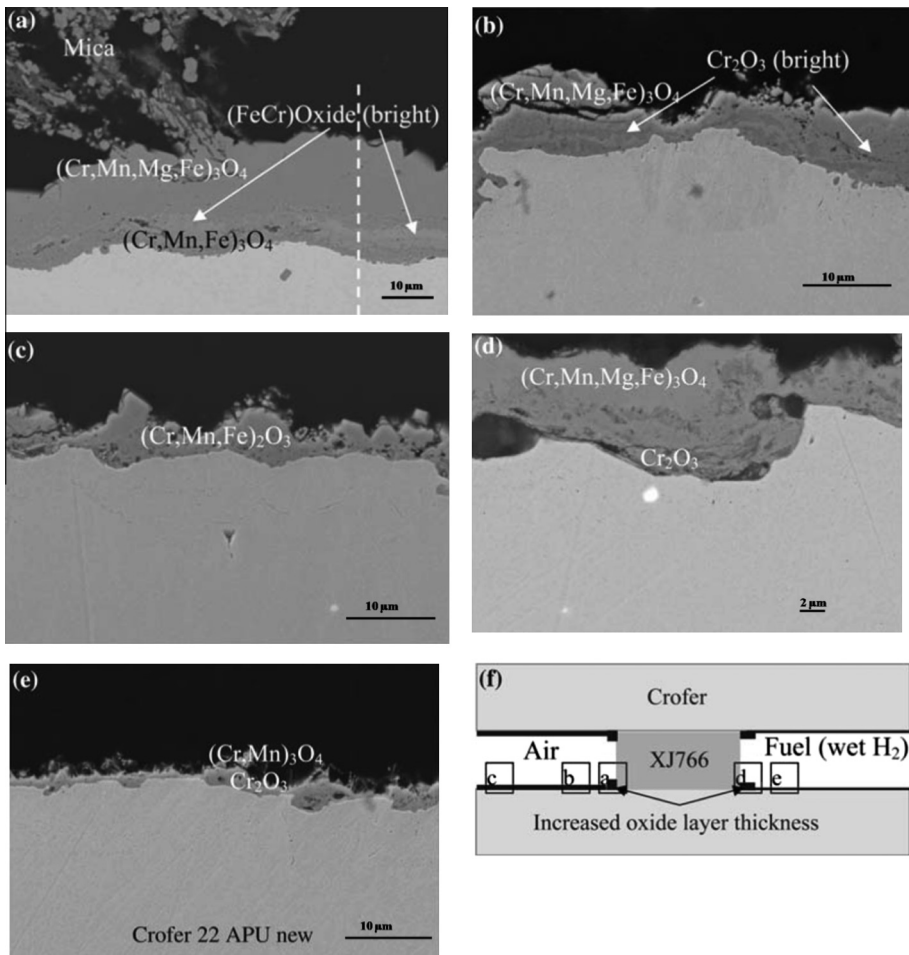


Fig. 80. Overview of findings in terms of formation of different phases during investigation on Thermiculite XJ766 mica paper gasket after corrosion experiments conducted in simulated SOFC conditions at 800 °C for 400 h (a) air manifold, contact area. (b) Air manifold, 500 μm distance from mica; (c) air manifold, 3800 μm distance; (d) fuel manifold, contact area; (e) fuel manifold, 500 μm distance; (f) overview of the spots selected for analysis. ((a–f) Reprinted with permission from Ref. [1066], copyright Springer, 2006).

Like any actual operation, the opposite walls of the sealant gaskets were exposed to oxidant (air) and fuel (wet H₂). Authors observed a substantial oxide layers thickening (from 20–25 μm to 250–300 μm) on the surface of interconnect steel, which was mainly composed of oxides of chromium, magnesium and iron. Cr₂O₃/(Cr, Mn)₃O₄ duplex layer, which is normally formed in Crofer, was observed to get eventually replaced by a 5–10 times thick layer of another oxide layer containing Cr₂O₃, (Cr, Mn, Mg, Fe)₃O₄ and Fe₂O₃ phases (Fig. 80a–f). It was also proposed that magnesium, which is released by talc on decomposition (shown in Eq. (110)), plays a key role in accelerating oxide formation.



Mica-based glass-ceramics are commercially available and have also been utilized as SOFC sealants. MACOR® (Corning, NY), Dicor, Vitronit, and Photoveel are commercial brands of machinable glass ceramics, which are largely composed of mica crystals in their microstructure. They possess high

CTE ($10\text{--}12 \times 10^{-6}/\text{K}$) comparable to most of the metals and sealing glasses with almost no porosity. Furthermore, they possess excellent insulation at high temperature (900°C) [1067]. MACOR® has been used successfully to bond YSZ electrolyte to both metallic (ferritic stainless steel) and ceramic ($\text{La}_0.8\text{Ca}_{0.22}\text{CrO}_3$) [1068,1069] interconnect materials [1070]. However, at above 1000°C in air, MACOR® was shown to react with $\text{La}_0.8\text{Ca}_{0.22}\text{CrO}_3$ material [1068,1069]. In comparison, compressive mica seals do not exhibit these complicated reactions at $700\text{--}800^\circ\text{C}$, which was attributed to the lower working temperature and glass devoid of potassium (which is inherently present in MACOR®) [1068,1069].

6.2. Rigid seals

Rigid seals make an effective bonding with the sealing surfaces. Rigid sealants offer an advantage over compressive seals as these require a relatively simple method of bonding ceramic and metal parts (rather than externally applying the load for sealing) [818]. Besides this, rigid seals are cost effective. In this category, sealants made of glass, glass-ceramic and alloy based braze materials are included. For a promising rigid sealing, there should be minimal mismatch in CTE values of seal material and adjoining cell components. If the mismatch is large, then it may induce high thermal stresses during heating and cooling cycles. Cubic phase stabilized ZrO_2 has a relatively high CTE value ($\sim 10\text{--}11 \times 10^{-6}/\text{K}$) with respect to other ceramic materials, but is lower in comparison to the most metals. Upon melting and cooling, glass seals become brittle and if the sealing glass does not crystallizes, then the cracks that form because of thermal cycling are capable of “self-healing”. In comparison to polycrystalline ceramics, glass possesses relatively low strength. When the glass with amorphous or vitreous structure and high CTE are soaked at high temperature (between T_c (crystallization temperature) and T_{liq} (liquid temperature)) for 2–10 h, crystallization of glass occurs which results in the formation of glass-ceramics possessing much higher strength than the parent glass. Glass-ceramics, derived from “invert” (Fig. 81) [1071] alkaline earth silicate glasses, are commonly used as sealing materials [1072]. The term “invert” glass was introduced by Trapp and Stevles [1071] due to its non continuous molecular/ionic network of SiO_2 , B_2O_3 , and P_2O_5 , which are traditional network forming oxides. In fact, the glasses are structurally inverted due to higher concentration of network modifying oxides, in contrast to soda-lime glasses.

Alkali glasses containing Li^+ , Na^+ , or K^+ are not suitable for sealing application due to alkali ion migration under the electric field causing rapid degradation of the material during operation.

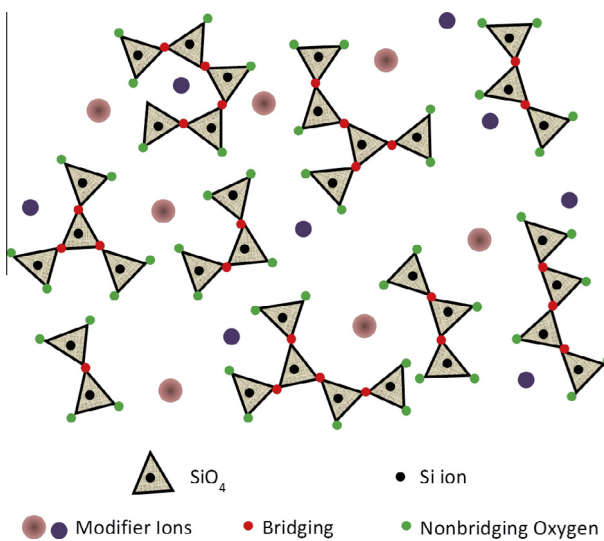


Fig. 81. Structure of “invert” glass. (Adapted from Ref. [1073]).

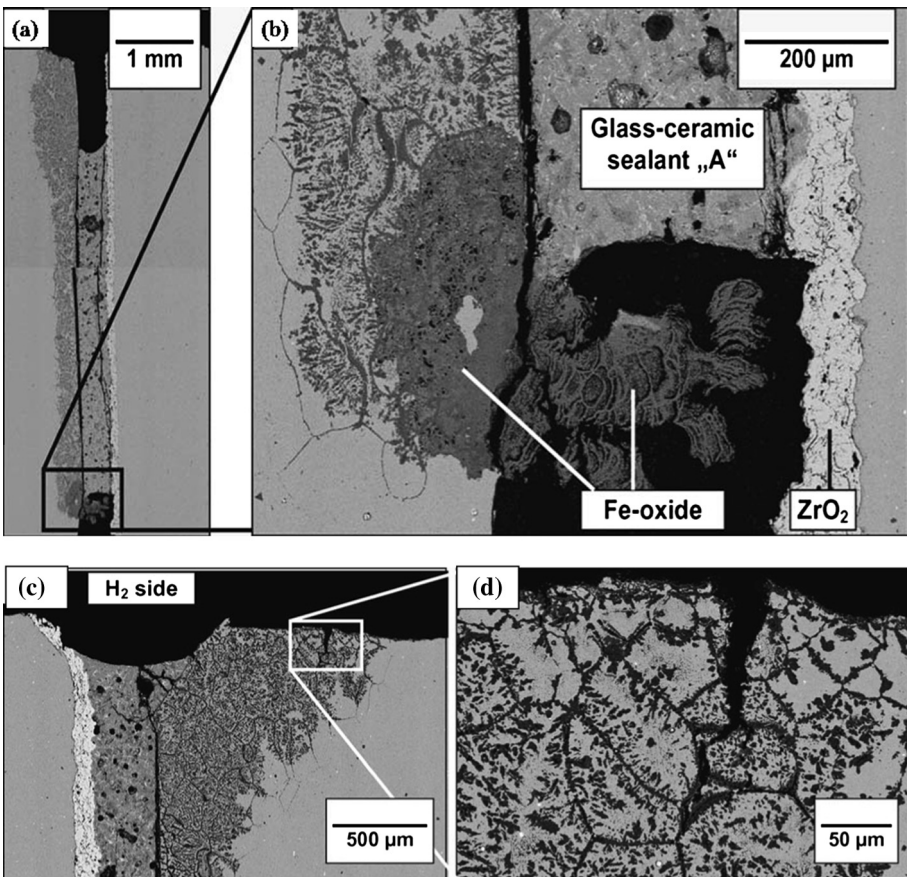


Fig. 82. SEM micrograph of cross section showing BACS seal of gas channel between YSZ-coated cell frame and steel interconnect: (a) complete width of seal from fuel to outer ambient atmosphere. Internal oxidation underneath uncoated steel surface and presence of delamination crack along interface between glass-ceramic and steel, (b) formation of Fe-oxide, (c) asymmetric chemical interaction at inner rim of the seal (fuel gas side), and (d) internal oxidation along grain boundaries of steel and cracking. ((a-d) Reprinted with permission from Ref. [1088], Elsevier, 2006).

Borosilicate glass-ceramics [1072,1074–1081], boron-free alkaline earth silicates [1082], and phospho-silicate glass-ceramics [1083,1084] are commonly used for making SOFC seals. Glass-ceramic compositions based on silica, barium and aluminosilicate-based compositions are prone to react with the oxide scales of chromium or aluminum at metal interconnect or edge rails to form barium chromate or a celsian phase at the interface [1085] with low mechanical strength, which results in delamination. Although, B_2O_3 concentration below 10 mol.% found to impart good chemical stability, a high CTE value ($\sim 12 \times 10^{-6}/\text{K}$), and renders a low sintering and sealing temperature ($\sim 900^\circ\text{C}$). However, boron present in glass can react over time with water/steam to produce $\text{B}_2(\text{OH})_2$ or $\text{B}(\text{OH})_3$ gas. Furthermore, it may also react with other cell components. Due to its higher reactivity, low boron content glass compositions are normally preferred [1045,1073]. Lahl et al. [1086] investigated crystallization kinetics in a series of compositions in $\text{AO}-\text{SiO}_2-\text{Al}_2\text{O}_3-\text{B}_2\text{O}_3$ ($\text{A} = \text{Ba}, \text{Ca}, \text{Mg}$) systems while restricting boron content below 5 wt.%. Reactivity of MgO -containing glasses was found to be significantly lower compared to those containing BaO or CaO . MgO -containing glasses tend to form an $\text{Mg}_2\text{Al}_5\text{Si}_5\text{O}_{13}$ phase which is detrimental and can be suppressed by using low Al_2O_3 concentration and adding other nucleating agents. Eichler et al. [1087] performed the metal-to-metal joining experiments using four different glass ceramic compositions in the $\text{BaO}-\text{MgO}-\text{SrO}-\text{Al}_2\text{O}_3-\text{B}_2\text{O}_3-\text{SiO}_2$

system. It was shown that MgO containing compositions react with the interconnect alloy (here Cr–5Fe–1Y₂O₃) to form MgCr₂O₄ spinel. Also, many joints exhibit an increase in the leak rates upon thermal cycling (annealing at 850 °C for 400 h, followed by cooling to room temperature). Researchers have attributed this effect to the glass delamination (cracking) at the metal interface which is probably caused by the presence of MgCr₂O₄ spinel with low CTE value (6.9×10^{-6} /K). Barium aluminosilicate sealing glass bonded to a chromium oxide-forming alloy metal surface is susceptible to react and deplete the protective chromium oxide layer on the air side as shown in the reactions given below [1079].



Barium chromate that is formed as a product possesses high CTE value, which physically separates the sealing glass and the metal alloy. Along the interfacial regions (where oxygen or air access is blocked), chromium or chromium oxide may also react with barium-calcium-aluminosilicate glass–ceramic to form a porous chromium-rich solid solutions (e.g., Fig. 82a and b) [1088]. In addition, reactions may also generate ~200 μm pores across the metal–glass interface [1080]. In Fig. 82a–d, cross sectional SEM images of the chemical interaction of BACS (BaO–CaO–Al₂O₃–SiO₂) based glass–ceramic sealant (containing minor addition of transition metal oxides, such as ZnO, PbO, and V₂O₅) and interconnect material (Crofer 22 APU) at both the rims of glass–ceramic sealant (air and fuel side) are shown [1088]. Internal oxidation and formation of chromia leads to delamination (due to local volume increase of steel) along its interface (Fig. 82a and b) with glass–ceramic and indicates permeation of fuel gas. The cascading effect of internal oxidation and swelling of the steel leads to further delamination of interface. The high stress intensity experienced at the crack tip directs the crack to move towards the opposite rim of the seal in the air side (Fig. 82c and d), and results in ultimate delamination of seal. Such an effect causes loss of contact between the cathode and interconnect, and/or between the anode and Ni mesh, and severely affects the overall electrochemical performance of the individual cells. Authors suggested that the thin plasma-sprayed 8YSZ layer can be a potential solution to restrict any unwanted chemical interactions between the glass–ceramic and ferritic steel [1088].

Alkali metal cations, typically present in most of the glass and glass ceramic based sealant materials [1089], make them prone to react with other cell components [1090–1092]. This leads to an accelerated volatility of chromium present in interconnects [1086,1093] and cause the poisoning of cathode materials. The two foremost deciding factors for the selection of glass to be used as SOFC sealants are: glass transition temperature (T_g) and CTE. The T_g value gives an idea about the extent of glass fluidity to provide a flexible seal, while retaining required rigidity and mechanical integrity at operational temperature. On the other hand, matching of CTE of the sealant material with other cell components, i.e., YSZ electrolyte and interconnect material, is imperative for minimizing the thermal stresses [1094]. Some important compositions of glass–ceramic materials are listed in Table 13 [818].

Table 13

Glass and glass–ceramic sealants with values of T_g and CTE in the target range for SOFC application. Reprinted with permission from Ref. [816], Elsevier, 2005.

Sealant material	Composition (mol.%)	T_g (°C)	CTE × 10 ⁶ (/K)	Ref.
Boroaluminosilicates	29–38 (SiO ₂), 13–22 (B ₂ O ₃), 10 (Al ₂ O ₃), 35–40 (BaO), 5 (La ₂ O ₃)	652–739	10.6–11.2	[1074,1095]
	29–38 (SiO ₂), 13–22 (B ₂ O ₃), 10 (Al ₂ O ₃), 35–40 (BaO), 2 (ZrO ₂)	614	10.6	
	29–38 (SiO ₂), 13–22 (B ₂ O ₃), 10 (Al ₂ O ₃), 35–40 (BaO), 2 (NiO)	617	11.5	
Borsilicates	31–34 (SiO ₂), 2–8 (B ₂ O ₃), 37–42 (BaO), 8–16 (CaO)	623–662	10.5–11.4	[1094]
	50 (SiO ₂), 45 (BaO)	730	10.7	[1096]
Aluminosilicate Silicates	35 (SiO ₂), 44 (BaO), 11 (CaO)	721	10.6	[1094,1097]
	50 (SiO ₂), 40 (BaO), 10 (MgO)	686	12.0	
	50 (SiO ₂), 40 (BaO), 10 (ZnO)	676	10.7	
Borate	8 (SiO ₂), 40 (B ₂ O ₃), 7 (Al ₂ O ₃), 25 (SrO), 20 (La ₂ O ₃)	760	11.5	[1092]

Table 14

List of phases crystallizing during service in alkaline-earth glass-ceramics, and their CTE. Reprinted with permission from Ref. [817], Elsevier, 2005. The back-references mentioned in the square brackets are also reported to facilitate the reader in referring to the original paper.

System	Phase	CTE × 10 ⁶ (/K)	Reference(s)
Mg–Si–O	Enstatite (MgSiO_3)	7–9	[1098,1099]
Ca–Si–O	Wollastonite (CaSiO_3)	4–9	[1099–1101]
	Calcium orthosilicate (Ca_2SiO_4)	10–14	[1099,1100]
Ba–Si–O	Barium silicate (BaSiO_3)	9–13	[1100]
	Barium orthosilicate (BaSi_2O_5)	14	[1100]
Ba–Ca–Si–O	Barium calcium orthosilicate ($\text{Ba}_3\text{CaSi}_2\text{O}_8$)	12–14	[1100]
Mg–Al–Si–O	Cordierite ($\text{Mg}_2\text{Al}_4\text{Si}_5\text{O}_{18}$)	1	[1098,1099]
Sr–Al–Si–O	Hexacelsian ($\text{SrAl}_2\text{Si}_2\text{O}_8$)	8–11	[1107,1108]
	Monocelsian ($\text{SrAl}_2\text{Si}_2\text{O}_8$)	3	[1102]
	Orthocelsian ($\text{SrAl}_2\text{Si}_2\text{O}_8$)	5–8	[1102,1103]
Ba–Al–Si–O	Hexacelsian ($\text{BaAl}_2\text{Si}_2\text{O}_8$)	7–8	[1099,1100,1102]
	Monocelsian ($\text{BaAl}_2\text{Si}_2\text{O}_8$)	2–3	[1099,1100,1102]
	Orthocelsian ($\text{BaAl}_2\text{Si}_2\text{O}_8$)	5–7	[1102]

Barium containing glass ceramics seem to be one of the most satisfactory sealant materials with advantages attributed to its high CTE (e.g., CTE value of $\text{BaO}-\text{MgO}-\text{SiO}_2$ and $\text{BaO}-\text{ZnO}-\text{SiO}_2$ were reported to increase with rising BaO content while SiO₂ content being constant) [1097]. It has been reported that CTE increase is attributed to the formation of barium silicate (as shown in Table 13), and crystallization of phases in a glass-ceramic sealant material during operation (see Table 14) [818].

The presence of alkaline earth metals is essential as they can control the crystallization kinetics and sealing behavior of the material, e.g., slower crystallization of calcium and magnesium aluminosilicate glasses can be chosen over rapid crystallization of barium aluminosilicate glasses [1104–1106]. Another important aspect of glass-ceramic sealants is that it should wet the surface (to achieve a good bonding) before it crystallizes to full density. This depends a lot on the characteristics of glass flow [1082,1097]. If the glass crystallizes before wetting sealant material, it will be loosely adhered to the surfaces, which results in porosity. The crystallization kinetics of the glass ceramics can be modified by the addition of nucleating agents, e.g., B, Al, TiO₂, Cr₂O₃, Ni, ZrO₂, SiO₂, MgO, B₂O₃, etc. [1074,1078,1081,1086,1091,1092,1094,1096,1104,1106–1108]. An appreciable chemical compatibility was observed between glass-ceramic composites and YSZ electrolyte. Furthermore, the addition of Ba, Ca and/or Mg to the glass-ceramic, imparts good adherence to the surface and stabilizes the interface with YSZ [1074,1076,1081,1109–1112]. The addition of MgO-filler (up to ~12 ppm) to the sodium aluminosilicate (NAS) base glass was observed to increase the CTE value of the resultant composite and provided a sufficient match between the components [1031]. However, chromium containing interconnect materials were found to undergo chemical reactions with glass-ceramics sealants, with silicates containing barium oxide have been reported to be highly reactive [1086,1094,1106]. Smeacetto et al. [1113] designed a pressureless procedure at 900 °C and observed that a barium- and boron-free glass successfully joined YSZ and Crofer 22 APU alloy (Cr-23%, Mn-0.45%, Ti-0.06%, La-0.1%, Al-<0.05%, Si-<0.05%, Balance Fe; commercially available since 2002). The glass-ceramic sealant was based on the SACN system containing SiO₂, Al₂O₃, CaO, and Na₂O (50–55 wt.% SiO₂; 10–12 wt.% Al₂O₃; 20–23 wt.% CaO; and 10–12 wt.% Na₂O). After being deposited on Crofer 22 APU substrate via slurry coating or by electrophoretic deposition, a partial surface induced crystallization of the glass was observed during the heat treatment (below 950 °C) (Fig. 83a and b). As a result, glass-ceramic seal is formed with CTE value close to that of both YSZ and Crofer 22 APU alloy.

Furthermore, a considerable Cr-diffusion from Crofer 22 APU alloy towards the seal for a depth of about 30 μm from the interface was observed after thermal ageing in air (Fig. 83c). In this case, Crofer 22 APU alloy was used in the as-received condition, i.e., as non-preoxidised Crofer 22 APU/SACN/YSZ joined sample. However, under the similar ageing conditions, diffusion of Cr ions was not observed through the seal in the preoxidised Crofer 22 APU/SACN/YSZ joined samples (Fig. 83d). A preoxidised layer formed on the Crofer 22 APU alloy substrate with approximately 1 μm thickness acts as a barrier for Cr diffusion into the SACN glass-ceramic.

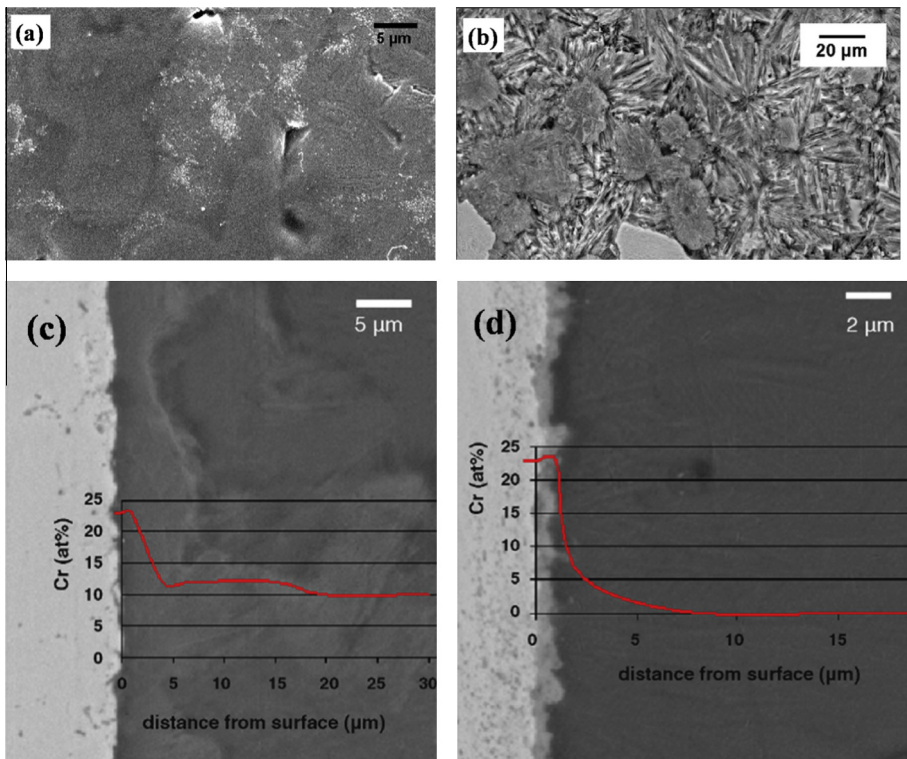


Fig. 83. (a) SEM top view of a sintered layer SACN based glass sealant deposited by EPD and (b) Glass–ceramic microstructure of the sintered sealant ($900\text{ }^{\circ}\text{C}$, $25\text{ }^{\circ}\text{C}/\text{min}$, 30 min) after HF etching. Cr EDS mapping at the interface between SACN glass–ceramic and Crofer 22 APU substrate after 400 h of exposure in air at $800\text{ }^{\circ}\text{C}$: (c) non preoxidised Crofer 22/SACN interface, and (d) preoxidised Crofer 22 APU/SACN interface. ((a-d) Reprinted with permission from Ref. [1113], copyright Elsevier, 2008).

Other glass–ceramic systems investigated for sealant materials include phosphate based systems [1083,1084,1114]. However, phospho-silicates [1083,1084] exhibit comparatively lower CTE values $\sim 5\text{--}6 \times 10^{-6}/\text{K}$ than most commonly used silicates. In addition, P_2O_5 content in the silicate glasses, in most cases, enhances the tendency of the material to crystallize and form excess of meta- or pyrophosphates. Furthermore, phosphate glasses are chemically less stable at high temperatures ($900\text{--}1000\text{ }^{\circ}\text{C}$), and tend to volatilize, and form nickel phosphate and zirconiumoxyphosphate upon reaction with Ni-YSZ anode [1115,1116]. As a result, phosphate glasses do not render appropriate sealing in SOFC applications [1084].

Due to high viscosity ($>10^9$ poise at the working temperature of SOFC), boron-free alkaline earth silicates [1082,1117] are not considered as good sealants for SOFCs. Polymer precursor synthesis of non-oxide systems was also reported by some groups [1118,1119], but stability of these materials in oxidizing environment is still to be thoroughly investigated. Fiber-reinforced glass seals have also been developed to enhance the stress tolerance level in order to sustain the stresses caused by the CTE mismatch of various adjoining components during thermal cycles. These fiber-reinforced glass seals possess certain elasticity at the operating temperature and exhibit a better compliance with the SOFC thermal cycles [1120,1121].

The main advantages of glass and glass–ceramic seals are

- (i) viscous and wetting behavior of glass facilitates hermetic or air tight sealing,
- (ii) ease of fabrication (use economic techniques, such as, tape casting (Fig. 84), and slurry dispensing, thermal and atmospheric plasma spraying [1088,1122–1124]),

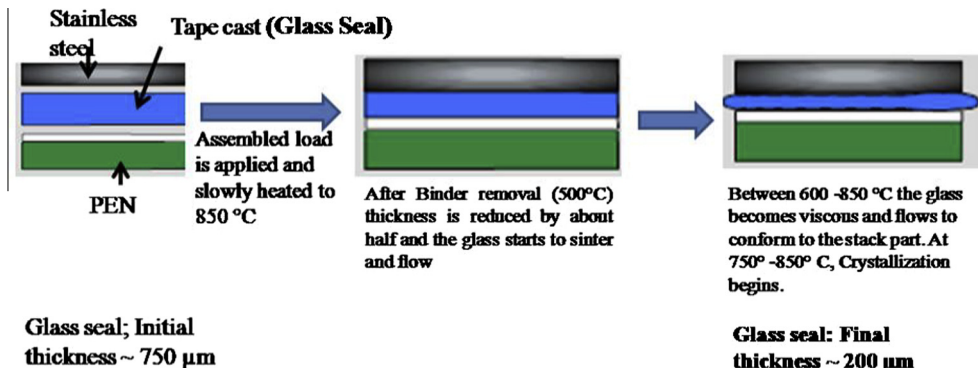


Fig. 84. Glass sealing procedure. Adapted from Ref. [1128].

- (iii) tailorability of thermal properties of the sealant material, such as, CTE, and T_g can be changed by compositional modulation and heat treatment, and
- (iv) enhanced seal rigidity (and restricted viscous flow), and controlled glass–ceramic crystallization during operation.

However, there are some disadvantages, viz.

- (i) brittle behavior of the glasses and glass–ceramics below T_g ,
- (ii) only few systems, such as, Alkaline earth-Al-Si-O exhibit appropriate CTE,
- (iii) tends to react with adjacent cell components, e.g., metal interconnects,
- (iv) have very poor thermal stability; at high temperatures, with the increasing exposure time, there is continuous change in thermal properties of glass based seals,
- (v) glasses are prone to crystallization at SOFC operating temperatures, and result significant change in CTE (>36%) during operation (at 800 °C for 1000 h) [1074], and
- (vi) constituents, such as, SiO_2 , B_2O_3 , alkali metals present in the glass and glass–ceramics, form volatile species at high temperatures.

6.3. Methods of using sealing glass

For proper functioning, the SOFC needs a reliable practice of sealing the gaps between the components. One of the standard methods uses glass sheet, which is comprised of joining agent (i.e., a glass) and organic binder [1125,1126]. Temperature is raised up to 200–1000 °C in order to heat and burn-out the binder and fuse the sealant material between each component and produce a green sheet, Fig. 84. The green-sheet consists of not only glass powder and binder, but also some important processing aids (e.g., nucleating agent TiO_2). Another method uses a bond layer instead of glass sheet, applied as a coating of glass powder slurry to a connection plate followed by the application of a second layer on the top of the bond layer [1127]. After the heat treatment, the glass crystallizes to form a glass–ceramic seal as shown in Fig. 84. It is likely that the formation of duplex structure may reduce the residual stresses induced by CTE mismatch between components.

Since 1984, around 1060 US patents related to SOFC are available, out of which 22 are related to “sealing glass”, “solder glass” or “sealing” [266,1129]. The patenting of sealing glass commenced since 1993, and acquired much attention after 2002. Thirteen patents relating to sealing glass and glass ceramics were issued between the years 2003 and 2008. Composition of some of the important sealing materials, the assignees, and their patent numbers on SOFC sealants are summarized in Table 15.

In the category of rigid seals, metallic brazes have also been developed. As metals can undergo plastic deformation and are relatively more compliant than ceramics, they can accommodate thermal and

Table 15

Assignees and their patents with the claims on sealing glass for SOFC. (Reprinted with permission from Ref. [1129] with minor modification).

Assignee	Patent on sealing glass	CTE × 10 ⁻⁶ / K	Composition of the seals	
			Major	Details
Battelle Memorial Institute, USA	7,258,942	7–15	Mica with B ₂ O ₃ and SiO ₂	B ₂ O ₃ or Bi ₂ O ₃ infiltrated mica seal (gasket) with the layers of G-18 glass (Ca–Ba–Al–B–Si–O glass): Mica ≤ 90 vol.%
	7,222,406			
	6,843,406			
	6,532,769			Glass (M3(SiO ₂ and B ₂ O ₃ (0–50 mol.%)) 40–70 mol.% + M1(BaO, SrO, CaO, MgO, 20–55%) + M2 (Al ₂ O ₃ , 2–15 mol.%) with one component, C1 (ceramic or metal)
	6,430,966			SiO ₂ (15–80 wt.%), B ₂ O ₃ (0–50% replacing SiO ₂), Li ₂ O (0–5%), Na ₂ O (0–5%), K ₂ O (0–10%), MgO (0–5%), CaO (0–32%), Al ₂ O ₃ (0–10%), or SrO (0–25%), All Alkalies (<10%), Glass frit (75–100 wt.%) and ZrO ₂ or leucite 0–30 wt.%): no BaO, Y and Ln- oxide
Corning Incorporated, USA	7,214,441	10–12	SiO ₂	
	7,189,470			
	6,291,092			
	5,273,837			
	EP20080742523 20080403 ¹	10–12		Where the seal includes a sealing material that comprises of: (i) 80–100 wt.% of glass frit, wherein the glass frit includes in mole% MgO (0–10%), CaO (0–30%), BaO (30–50%), B ₂ O ₃ (0–40%), Al ₂ O ₃ (10–30%), SiO ₂ (10–30%); and (ii) a filler, 0 wt.% to 20 wt.%
Hybrid Power Generation Systems, USA	6,541,146	N/A	SiO ₂	Composite sealant; mixture of glass and titanates (1:2 to 30:1 in mass ratio)
	6,677,069			Coring glass (4060 or 3130) Seal-less cell design
AlliedSignal, USA	6,271,158	N/A	SiO ₂	Coring 4060 or 3130: SiO ₂ (50–70 wt.%), ZnO (10–25%), K ₂ O (5–20%), Na ₂ O (1–15%), Li, Ba, Zr, Ca, Mg-oxides (0–8%)
	5,702,837			A mixture of glasses (40–90 wt.%) with metallic filler (Ni, Fe, Cr, W, Co, Al, Mo, Si and Y) alloy particles Reactive ingredient: NiO (5–60 wt.%) ZrO ₂ (5–60%), W, Ta, Nd, Mo, Ti and oxides (Ni, Zr, Si, Al), 1–50 wt.%, at least one of Al ₂ O ₃ (1–20%) and organics
Ford Global Technologies, LLC, USA	7,007,509	N/A	SiO ₂	SiO ₂ (56–75 mol.%), BaO (11–30 mol.%), MgO (2–14 mol.%), or SiO ₂ (56–75 mol.%), BaO (11–30 mol.%), MgO (2–14 mol.%); Glass frit + Mg ₂ SiO ₄ particulates
	6,878,651			
Siemens, Germany University of Chicago, USA	5,942,348	N/A	N/A	Glass solder used for the edges of SOFC
	5,453,331	11–13	B ₂ O ₃	B ₂ O ₃ (15–80 mol.% or 36.6–41.6 %), SrO (5–60 mol.% or 28.8–31.1%), La ₂ O ₃ (1–45% or 3.3–20.2%), Al ₂ O ₃ (0–15% or 10–15.8 %), SiO ₂ (0–40%, 4.6–7.3%)
Murata, Japan	5,585,203	N/A	N/A	Used for glass sheet
Dornier, Germany	5,387,476	N/A	N/A	Conductor layer

(continued on next page)

Table 15 (continued)

Assignee	Patent on sealing glass	CTE × 10 ⁻⁶ / K	Composition of the seals	
			Major	Details
Alstom, UK	6,656,625	8.5–11.5	SiO ₂	SiO ₂ (43–59 wt.%), Al ₂ O ₃ (5–7%), CaO (10–20.8%), MgO (0–30%), BaO (0–36.3%), TiO ₂ (0–4%)
Sarnoff Corporation, USA	6,653,009	N/A	MgO	MgO (45–49 mol.%), BaO (7–50%), B ₂ O ₃ (10–21%), SiO ₂ (7.5–35%), CaC (0 or 10%), ZnO (0.5–8%), Al ₂ O ₃ (0 or 10%)
Delphi Technology Incorporation, USA	7,217,300	N/A	N/A	Gasket withstand vibration
	EP20080157924 20080610 ²	N/A	Alumina-silicate glass ceramic matrix	The seal composition comprises of an alumina-silicate glass ceramic matrix and a ceramic fiber aggregate consisting of zirconium oxide fiber, alumina fiber, and combinations thereof, dispersed in the matrix. The fiber is present at 1–60 wt.% with respect to the weight of glass ceramic, preferably about 30 weight percent. Preferably, the zirconia is stabilized by up to about 10% yttria. Alumina fiber may substitute for a portion of the zirconia fiber

N/A: Not Available.

¹ [1135].

² [1136].

mechanical stresses formed during the operation. Braze alloys are often based on Pt, Au, Ag, Pd, Cu, Ni, Ti, and Cr. These braze, especially those made of Au and Ag, are capable of resisting both reducing and oxidizing atmospheres (even at high temperatures) [1132–1135]. However, the major challenge associated with braze metal is to achieve adequate wetting ability of the ceramic. Wetting behavior can be improved by (i) adding reactive elements, such as, Ti, Hf, and Zr, in order to reduce oxide formation, (ii) bonding to the substrate using thermite reaction (between Al and Ni) and create chemical bond between FeCr alloy and YSZ electrolyte [1136], and (iii) using metal and oxide (such as CuO, Al_2O_3 , Al_3TiO_5) mixture, which exhibits eutectic reaction [1137]. The latter not only improves the wettability, but also lowers the CTE of the braze alloy, which is typically higher (in the range of $16\text{--}21 \times 10^{-6}/\text{K}$) than 8YSZ and other SOFC components. One such braze alloy is Ag–CuO eutectic [1138,1139] used to braze alumina [1140] and perovskites [1141]. Menzler et al. [1142] investigated the interaction of the metallic parts (two compositions of high-chromium steels, viz., Crofer 22 APU and other prepared according to JS-3 formula) and glass-ceramic sealant (of composition $\text{BaO-CaO-Al}_2\text{O}_3-\text{SiO}_2$ or BCAS) under various atmospheric conditions (air, humidified air and humidified hydrogen) at 800 °C for 1–500 h. It was observed that both air and humidified air do not induce negative interaction effects, neither in the metallic (in terms of inner oxidation of metal) nor in the glass-ceramic material (in terms of adhesion or bonding between the glass-ceramic and the metals). However, an internal oxidation in the steel is observed to occur in the humidified hydrogen environment. Furthermore, it was found that corrosion intensity in the steel material was much higher in the presence of minor constituents, such as, Al or Si, when compared to that of Al- and Si-free steel material. It was emphasized that the purity of the metallic material plays a crucial role for the long-term use in SOFCs [1142]. Kobsiriphat and Barnett designed and investigated two Ag–Cu–Ti brazing alloy compositions i.e., Ag–35.25Cu–1.75Ti (Cusil-ABA) and Ag–20.1Cu–1.0Ti (average composition; Ag–Cusil). The YSZ pellets were bonded with the brazed alloys followed by ageing of the brazing joints at 700 °C for up to 100 h in air– H_2 atmosphere in air (separating H_2) and air separately. Both compositions showed metallic Ag and Cu phases, while the filler metal-zirconia interface exhibited a continuous layer of titanium oxide. Cusil-ABA was observed to be perform inferior in air in terms of degradation in microstructure and loss of hermiticity when compared to that of Ag–Cusil [1143].

In H_2 -air atmosphere, performance of Cusil-ABA was better than that of Ag–Cusil with microstructure showing limited degradation. The delamination of Ag–Cusil from YSZ occurs in H_2 -air atmosphere with large interconnected pores present in Ag-rich [1143]. It was proposed that increasing the Ti content along with Ag enhances the interfacial bond quality. Tucker et al. studied the Ag–26.7Cu–4.5Ti filler metal with an enhanced Ti and Ag content, and reported the same to be a good brazing alloy because of good wettability, and lower melting point than that of materials to be joined [1144].

From the available literature, there is an indication that no single material can be taken up as universal sealant material for SOFC application. Besides well studied sealant materials, such as, compressive and rigid seals, a large number of novel sealing concepts in SOFC are also available. For example, Lewinsohn et al. [1145] reported the use of polymers of Si–C–N as a paste to join two adjacent surfaces. However, these materials have low oxidation resistance in air at high temperatures or moist fuel. In order to achieve an appropriate CTE value, use of ceramic and metallic fillers were also suggested [1145]. Loehman [1146] put forth an idea of viscous seals for attaching SOFC components. Viscous seals are a new class of sealing materials that are capable of healing *in situ* leaks that occur during operation. The challenge resides in developing an appropriate glass composition that retains its viscous nature over the entire duration of SOFC operation (for >40,000 h). In addition, it should offer electrical insulation, retain thermo-mechanical stability, and remains chemically compatible with adjacent cell components at 800–1000 °C. Tanaguchi et al. [1125] reported a combination of glass/YSZ and Fiberfaxfiber matte (essentially alumina fiber) to be applied as a potential seal material. The fiber layer was porous and compliant, and therefore assisted in stress reduction on the electrolyte electrode assembly. Review article by Donald [1089] provides an extensive coverage of the glasses and glass-metal seals that can be used as a reference for the selection of required seal material.

7. Conclusions

In summary, the progress in the material selection of the solid oxide fuel cell (SOFC) components elicits extreme complexity, as each of the layer must be designed strictly keeping the adjoining components, and fuel (and its purity) in mind. So, there is no single material that suffices the concerns that are raised in each of the components of SOFC. The design of anode requires enhanced triple phase boundaries (TPB: gas, electrolyte and anode), while minimizing coking or sulfur poisoning in order to enhance the efficiency of charge transfer. This class includes metals (Ni, Cu), cermets (Ni/Cu-YSZ), perovskites, and pyrochlores. It has been observed that dissociative adsorption of reactants and surface diffusion also strongly affects the reaction rate at anode. Fuel composition and over-voltage determines the impedance response at high frequency, whereas, P_{H_2O} , combination of proton and oxide ion, and the migration of electron/oxide ions and protons dictate the impedance response at lower frequency. Also, it has been observed that the finer microstructure and lower sintering temperature result in enhancing the performance of anode. The ceria impregnated Ni-YSZ appears to be one of the high performing anodes as it possesses high melting point (1453 °C), and sustain resistance to enhanced sulfur poisoning (from hydrocarbon fuels). Electrolytes require high ionic diffusion (thus high working operation temperature of SOFC) with minimum electronic conduction. Typically, open lattice structures: such as fluorite, perovskites, brownmillerite-like phases, and pyrochlore, are used as solid electrolytes for SOFC. Since the phase and thermal stability becomes a stringent requirement, when the SOFC has to work at elevated temperatures for durations of 40,000 h or more, the use of ceramic materials becomes the only choice. In addition, processing of dense electrolytes is required to allow only oxide ion (or proton) diffusion, while restricting gas flow or recombination of ions, so that the short circuiting can be minimized and the highest power density can be drawn. Utilization of acceptor dopant cation of similar size as of host cation (such as Sc ion doping in ZrO₂ lattice) has shown enhancement in the ionic conductivity of solid electrolyte. Thinning the electrolyte layer or utilizing composite thin-layer laminates (~ tens of nm each) has also evinced enhanced ionic conduction of the electrolyte. Furthermore, co-doping has shown reduction in the defect association, and grain refinement has also elicited enhanced grain-boundary conduction. The potential of achieving enhanced ionic conduction with low working temperature appears to be in co-doping of ScSZ along with GDC. Cathodes require gas-diffusion type porous electrodes, and their electrochemical kinetics is governed by overpotential, and other factors such as geometry of active surfaces. Both electrochemical kinetics and impedance analysis has contributed in enhancing the understanding on surface adsorption and transport of gases, interfacial electrokinetics of reactions, and performance of cathode. Popular choice among cathode materials are perovskites owing to their high *p*-type electronic conductivity and high oxide ion conductivity under oxidizing atmospheres. Furthermore, the minimal mismatch in the CTE value with electrolyte, high permeability of oxygen molecules to cathode/electrolyte interface, chemical compatibility with interconnects/sealants and ease of processing porous structure make them a perfect choice. LSCF with a thin LSM coating appears to be one of the promising cathode materials. Further, it is also observed that the cathodic polarization can lead to enhancement in the cathodic activity as well. Interconnects are the barrier materials physically isolating reducing and oxidizing regions of the SOFC. Very low area-specific resistance (of <0.1 Ω cm²), dimensional-, chemical-, and microstructural-stability at operating temperatures of 800–1000 °C, leak-proof and impervious to oxygen and hydrogen, matching CTE with adjoining components, chemical inertness, and load bearing strength are the main requirements for a successful interconnect. Thermally grown (Mn, Co)₃O₄ spinel on Crofer22 is claimed to be the best interconnect for SOFC that can sustain both oxidizing and reducing atmospheres without any significant degradation in performance for prolonged operational hours. Sealants are present to prevent the leakage of fuel (at anode) or oxidizer (at cathode), or even mixing of fuels, while being exposed to operating temperatures of 800–1000 °C. The second prime requirement of sealants is to possess a CTE similar to those of other SOFC components to avoid cracking. The tubular SOFC designs can be made seal-less (or away from high-temperature exposure areas), but planar-cell or other designs may have problems relating to oxide scaling or chemical instability especially for metallic seals at high temperatures. Seals also require certain flexibility to deform and hermetically isolate the region in response to compressive

stress. At operational temperature, the thermal exposure can also induce self-healing of seals (in case there are cracks in the seal). Mica-based glass seals (with absence of potassium) have shown good sealing of ferritic steel interconnects. Brazed seals offer hermetic sealing owing to their inherent wetting behavior, but have limited application due to their conductive nature. In addition, certain barium and boron-free glasses have also shown successful joining of YSZ and Crofer 22 APU via pressureless exposure to 900 °C. Metallic alloys have not prospered as potential sealants owing to their poor oxidation resistance, high volatility, and high cost. Also the oxidation layer formed during service induces porosity which leads to cracking/spallation of film. In order to prevent this, the protective coatings of nitride, perovskite and spinel have been utilized. Thus, in summary, achieving high performance SOFCs operating at intermediate temperatures (500–800 °C) for prolonged working hours mandate appropriate selection and designing of third generation materials.

Acknowledgements

KB and SO acknowledge funding from DST, MHRD, Govt. of India, CARE grant, and Dean R&D office, IIT Kanpur. Authors appreciate constructive discussions with Raj G. Pala, Chemical Engineering, and Malay Das, Mechanical Engineering, IIT Kanpur. S. Ariharan, Ambreen Nisar, and Rita Maurya, are acknowledged for assisting with the formatting of this article and obtaining copyrights for few figures.

References

- [1] Lee TS, Chung JN, Chen Y-C. Design and optimization of a combined fuel reforming and solid oxide fuel cell system with anode off-gas recycling. *Energy Convers Manage* 2011;52:3214–26.
- [2] Stambouli AB, Traversa E. Solid oxide fuel cells (SOFCs): a review of an environmentally clean and efficient source of energy. *Renew Sustain Energy Rev* 2002;6:433–55.
- [3] Minh NQ. Solid oxide fuel cell technology-features and applications. *Solid State Ionics* 2004;174:271–7.
- [4] Yamamoto O. Solid oxide fuel cells: fundamental aspects and prospects. *Electrochim Acta* 2000;45:2423–35.
- [5] Steele BCH, Heinzel H. A materials for fuel cell technologies. *Nature* 2001;414:345–52.
- [6] Park S, Vohs JM, Gorte RJ. Direct oxidation of hydrocarbons in a solid oxide fuel cell. *Nature* 2000;404:265–7.
- [7] Hibino T. An intermediate solid oxide fuel cell providing higher performance with hydrocarbons than with hydrogen. *Electrochim Solid-State Lett* 2002;5:A242–4.
- [8] Singhal SC. Solid oxide fuel cells for stationary, mobile and military applications. *Solid State Ionics* 2002;152:405–10.
- [9] Lamp P. Development of auxiliary power unit with solid oxide fuel cells for automotive application. *Fuel Cells* 2003;3:146–52.
- [10] Zongping S, Zhou W, Zhonghua Z. Advanced synthesis of materials for intermediate temperature solid oxide fuel cell. *Prog Mater Sci* 2012;57:804–74.
- [11] Brett DJL et al. Intermediate temperature solid oxide fuel cells. *Chem Soc Rev* 2008;37:1568–78.
- [12] Grove WR. On voltaic series and combination of gases by platinum. *Philos Magaz J Sci* 1839;14:127–30.
- [13] Camaratta M. Microstructural engineering of composite cathode systems for intermediate and low temperature solid oxide fuel cells. Ph.D. Thesis. Gainesville, Florida: University of Florida; 2007.
- [14] Gaugain JM. Note sur les signes électriques attribués au mouvement de la chaleur. *C R Séances Acad Sci* 1853;37:82–4.
- [15] Becquerel AC. Note sur la production des courants pyroélectriques. *C R Séances Acad Sci* 1854;38:905–10.
- [16] Buff H. Über die elektrische Beschaffenheit der Flamme. *Ann Chem Pharm* 1851;80:1–16.
- [17] MGaugain J. Note sur une classe nouvelle de couples gazeux. *C R Séances Acad Sci* 1853;37:584–8.
- [18] Grove WR. On voltaic series and the combination of gases by platinum. *Philos Mag* 1839;14:127–30.
- [19] Möbius HH. On the history of solid electrolyte fuel cells. *J Solid State Electrochem* 1997;1:2–16.
- [20] Gaugain JM. Note sur les signes électriques attribuées au mouvement de la chaleur. *C R Séances Acad Sci* 1853;37:82–4.
- [21] Wiedemann G. Die Lehre von der Electricität, 2nd ed. Vieweg u Sohn, Braunschweig; 1893/98. vol. 1 p. 553–61, 815–9, vol. 2 p. 491–3.
- [22] Souza Sd, Visco SJ, Jonghe LCD. Thin-film solid oxide fuel cell with high performance at low-temperature. *Solid State Ionics* 1997;98:57–61.
- [23] Nernst W. Über die elektrolytische Leitung fester Körper bei sehr hohen Temperaturen. *Z Elektrochem* 1899;6:41–3.
- [24] Haber F. Das Generatorgas- und das Kohlenelement. *Z Elektrochem* 1905;11:593–609.
- [25] Haber F. Verfahren zur Erzeugung von elektrischer Energie aus Kohle und gasförmigen Brennstoffen. Öster Pat. 1907;27:743.
- [26] Schottky W. Über stromliefernde Prozesse im Konzentrationsgefälle fester Elektrolyte. *Wiss Veroff Siemens-Werke* 1935;14:1–19.
- [27] Steele BCH. Interfacial reactions associated with ceramic ion transport membranes. *Solid State Ionics* 1995;75:157–65.
- [28] Wagner C. Über den Mechanismus der elektrischen Stromleitung im Nernststift. *Naturwissenschaften* 1943;31:265–8.
- [29] Baur E. Über das Problem der elektromotorischen Verbrennung der Brennstoffe. *Brennstoff Chemie* 1939;20:385–7.
- [30] Baur E, Preis H. Über Brennstoff-Ketten Mit Festleitern. *Z Elektrochem* 1937;43:727–32.
- [31] Baur E, Preis H. Brennstoff-Ketten mit Festleitern. *Z Elektrochem* 1938;44:695–8.
- [32] Blum L. Worldwide SOFC technology overview and benchmark. *Int J Appl Ceram Technol* 2005;2:1–13.

- [33] Fabbri E, Pergolesi D, Traversa E. Ionic conductivity in oxide heterostructures: the role of interfaces. *Sci Technol Adv Mater* 2010;11:1–9.
- [34] Garcia-Barriocanal J. Colossal ionic conductivity at interfaces of epitaxial $ZrO_2\cdot Y_2O_3/SrTiO_3$. *Heterostruct Sci* 2008;321:676–80.
- [35] Tarancón A. Strategies for lowering solid oxide fuel cells operating temperature. *Energies* 2009;2:1130–50.
- [36] Guo XX. Ion conduction across nanosized CaF_2/BaF_2 multilayer heterostructures. *Appl Phys Lett* 2007;91:103102.
- [37] Zhu B. Next generation fuel cell R&D. *Int J Energy Res* 2006;30:895–903.
- [38] Zhu B. Solid oxide fuel cell (SOFC) technical challenges and solutions from nano-aspects. *Int J Energy Res* 2009;33:1126–37.
- [39] Zhu B. Fuel cells: three in one. *Nature Nanotechnol* 2011.
- [40] Liu Q, Qin H, Raza R, Fan L, Li Y, Zhu B. Advanced electrolyte-free fuel cells based on functional nanocomposites of a single porous component: analysis, modeling and validation. *Roy Soc Chem* 2012;2:8036–40.
- [41] <http://www.netl.doe.gov/technologies/coalpower/fuelcells/seca/primer/cell.html>.
- [42] Wincewicz KC, Cooper JS. Taxonomies of SOFC material and manufacturing alternatives. *J Power Sour* 2005;140:280–96.
- [43] Tietz F, Buchkremer H-P, Stovér D. Components manufacturing for solid oxide fuel cells. *Solid State Ionics* 2002;373–81.
- [44] Baertsch CD. Fabrication and structural characterization of self-supporting electrolyte membranes for a micro solid-oxide fuel cell. *J Mater Res* 2004;19:2604–15.
- [45] Virkar AV. The role of electrode microstructure on activation and concentration polarizations in solid oxide fuel cells. *Solid State Ionics* 2000;131:189–98.
- [46] Xia C. $Sm_{0.5}Sr_{0.5}CoO_3$ cathodes for low-temperature SOFCs. *Solid State Ionics* 2002;149:11–9.
- [47] Horita T. Imaging of oxygen transport at SOFC cathode/electrolyte interfaces by a novel technique. *J Power Sour* 2002;106:224–30.
- [48] Sasaki K. Pt-perovskite cermet cathode for reduced-temperature SOFCs. *Solid State Ionics* 2002;148:551–5.
- [49] Chan SH, Low CF, Ding OL. Energy and exergy analysis of simple solid oxide fuel-cell power systems. *J Power Sour* 2002;103:188–200.
- [50] Ishihara T. Doped $PrMnO_3$ perovskite oxide as a new cathode of solid oxide fuel cells for low temperature operation. *J Electrochem Soc* 1995;142:1519–24.
- [51] Horita T, Yamaji K, Sakai N, Yokokawa H, Weber A, Ivers-Tiffée E. Oxygen reduction mechanism at porous $La_{1-x}Sr_xCoO_{3-d}$ cathodes/ $La_{0.8}Sr_{0.2}Gd_{0.8}Mg_{0.2}O_{2.8}$ electrolyte interface for solid oxide fuel cells. *Electrochim Acta* 2001;46:1837–45.
- [52] Mogensen M, Skaarup S. Kinetic and geometric aspects of solid oxide fuel cell electrodes. *Solid State Ionics* 1996;86:1151–60.
- [53] Jiang SP, Chan SH. A review of anode materials development in solid oxide fuel cells. *J Mater Sci* 2004;39:4405–39.
- [54] Minh NQ. Ceramic fuel cells. *J Am Ceram Soc* 1993;76:563–88.
- [55] Spacil HS. Electrical device including nickel-containing stabilised zirconia electrode. US Patent; 1970.
- [56] Ramirez-Cabrer E, Atkinson A, Chadwick D. Catalytic steam reforming of methane over $Ce_{0.9}Gd_{0.1}O_{2-d}$. *Appl Catal B: Environ* 2004;47:127–31.
- [57] McEvoy A. High temperature solid oxide fuel cells: fundamentals, design, and applications. In: Singhal SC, Kendall K, editors. Oxford (UK): Elsevier; 2003. p. 149–68.
- [58] Cassidy M, Lindsay G, Kendall K. The reduction of nickel-zirconia cermet anodes and the effects on supported thin electrolytes. *J Power Sour* 1996;61:189–92.
- [59] Faes A, Nakajo A, Hessler-Wyser A, Dubois D, Brisse A, Modena S, et al. Redox study of anode-supported solid oxide fuel cell. *J Power Sour* 2009;193:55–64.
- [60] Laurencin J, Delette G, Morel B, Lefebvre-Joud F, Dupeux M. Solid oxide fuel cells damage mechanisms due to Ni-YSZ re-oxidation: case of the anode supported cell. *J Power Sour* 2009;192:344–52.
- [61] Nikooyeh K, Clemmer R, Alzate-Restrepo V, Hill JM. Effect of hydrogen on carbon formation on Ni/YSZ composites exposed to methane. *Appl Catal A: Gen* 2008;347:106–11.
- [62] Rasmussen JFB, Hagen A. The effect of H_2S on the performance of Ni-YSZ anodes in solid oxide fuel cells. *J Power Sour* 2009;191:534–41.
- [63] Iwata T. Characterization of Ni-YSZ anode degradation for substrate-type solid oxide fuel cells. *J Electrochem Soc* 1996;143:1521–5.
- [64] Kim SD, Moon H, Hyun SH, Moon J, Kim J, Lee HW. Performance and durability of Ni-coated YSZ anodes for intermediate temperature solid oxide fuel cells. *Solid State Ionics* 2006;177:931–8.
- [65] Waldbillig D, Wood A, Ivey DG. Thermal analysis of the cyclic reduction and oxidation behaviour of SOFC anodes. *Solid State Ionics* 2005;176:847–59.
- [66] Benyoucef A, Klein D, Coddet C, Benyoucef B. Development and characterisation of (Ni, Cu, Co)-YSZ and Cu-Co-YSZ cermets anode materials for SOFC application. *Surf Coat Technol* 2008;202:2202–7.
- [67] Grgicak CM, Pakulski MM, O'Brien JS, Giorgi JB. Synergistic effects of $Ni_{1-x}Co_x-YSZ$ and $Ni_{1-x}Cu_x-YSZ$ alloyed cermet SOFC anodes for oxidation of hydrogen and methane fuels containing H_2S . *J Power Sour* 2008;183:26–33.
- [68] Zhu WZ, Deevi SC. A review on the status of anode materials for solid oxide fuel cells. *Mater Sci Eng A* 2003;362:228–39.
- [69] Lepe FJ, Fernández-Urbán J, Mestres L, Martínez-Sarrión ML. Synthesis and electrical properties of new rare-earth titanium perovskites for SOFC anode applications. *J Power Sour* 2005;151:74–8.
- [70] Pudmich G, Boukamp BA, Gonzalez-Cuenca M, Jungen W, Zipprich W, Tietz F. Chromite/titanate based perovskites for application as anodes in solid oxide fuel cells. *Solid State Ionics* 2000;135:433–8.
- [71] Primdahl S, Hansen JR, Grahl-Madsen L, Larsen PH. Sr-doped $LaCrO_3$ anode for solid oxide fuel cells. *J Electrochem Soc* 2001;148:A74–81.
- [72] Marina OA, Canfield NL, Stevenson JW. Thermal, electrical, and electrocatalytical properties of lanthanum-doped strontium titanate. *Solid State Ionics* 2002;149:21–8.
- [73] Fergus JW. Oxide anode materials for solid oxide fuel cells. *Solid State Ionics* 2006;177:1529–41.
- [74] Mogensen M, Kammer K. Conversion of hydrocarbons in solid oxide fuel cells. *Ann Rev Mater Res* 2003;33:321–31.

- [75] Atkinson A, Barnett S, Gorte RJ, Irvine JTS, McEvoy AJ, Mogensen M, et al. Advanced anodes for high-temperature fuel cells. *Nat Mater* 2004;3:17–27.
- [76] Gorte RJ, Vohs JM, McIntosh S. Recent developments on anodes for direct fuel utilization in SOFC. *Solid State Ionics* 2004;175:1–6.
- [77] Flot DM, Irvine JTS. Synthesis, electrical properties and thermal analysis of transition metal-doped Mg_2TiO_4 spinels. *Solid State Ionics* 2000;135:513–8.
- [78] Holtappels P, Poulsen FW, Mogensen M. Electrical conductivities and chemical stabilities of mixed conducting pyrochlores for SOFC applications. *Solid State Ionics* 2000;135:675–9.
- [79] Tsipis EV, Kharton VV, Frade JR. Mixed conducting components of solid oxide fuel cell anodes. *J Euro Ceram Soc* 2005;25:2623–6.
- [80] Kaiser A, Bradley JL, Slater PR, Irvine JTS. Tetragonal tungsten bronze type phases ($Sr_{1-x}Ba_x$)_{0.6} $Ti_0.8Nb_{0.8}O_{3-\delta}$: material characterisation and performance as SOFC anodes. *Solid State Ionics* 2000;135:519–24.
- [81] Mori M, Hiei Y, Itoh H, Tompsett GA, Sammes NM. Evaluation of Ni and Ti-doped Y_2O_3 stabilized ZrO_2 cermet as an anode in high-temperature solid oxide fuel cells. *Solid State Ionics* 2003;160:1–14.
- [82] Fang X, Zhu G, Xia C, Liu X, Meng G. Synthesis and properties of Ni-SDC cermets for IT-SOFC anode by co-precipitation. *Solid State Ionics* 2004;168:31–6.
- [83] Mogensen M, Lybye D, Bonanos N, Hendriksen PV, Poulsen FW. Factors controlling the oxide ion conductivity of fluorite and perovskite structured oxides. *Solid State Ionics* 2004;174:279–86.
- [84] Corbel G, Mestiri S, Lacorre P. Physicochemical compatibility of CGO fluorite, LSM and LSCF perovskite electrode materials with $La_2Mo_2O_9$ fast oxide-ion conductor. *Solid State Sci* 2005;7:1216–24.
- [85] Costa-Nunes O, Gorte RJ, Vohs JM. Comparison of the performance of Cu-CeO₂-YSZ and Ni-YSZ composite SOFC anodes with H₂, CO and syngas. *J Power Sour* 2005;141:241–49.
- [86] Fagg DP, Mather GC, Frade JR. Cu-Ce_{0.8}Gd_{0.2}O_{2-δ} materials as SOFC electrolyte and anode. *Ionics* 2003;9:214–9.
- [87] He H, Vohs JM, Gorte RJ. Effect of synthesis conditions on the performance of Cu-CeO₂-YSZ anodes in SOFCs. *J Electrochem Soc* 2003;150:A1470–5.
- [88] Lu C, Worrell WL, Vohs JM, Gorte RJ. A comparison of Cu-Ceria-SDC and Au-Ceria-SDC composites for SOFC anodes. *J Electrochem Soc* 2003;150:A1357–9.
- [89] Mizusaki J, Tagawa H, Saito T, Kamitani K, Yamamura T, Hirano K, et al. Preparation of nickel pattern electrodes on YSZ and their electrochemical properties in H₂-H₂O atmospheres. *J Electrochem Soc* 1994;141:2129–34.
- [90] Mizusaki J, Tagawa H. Kinetics of the electrode reaction at the H₂-H₂O porous Pt/stabilized zirconia interface. *J Electrochem Soc* 1994;141:1674–83.
- [91] Mizusaki J, Tagawa H, Miyaki Y, Yamauchi S, Fueki K, Koshiro I, et al. Kinetics of the electrode reaction at the CO-CO₂, porous Pt/stabilized zirconia interface. *Solid State Ionics* 1992;53–56(Part 1):126–34.
- [92] Mizusaki J, Amano K, Yamauchi S, Fueki K. Electrode reaction at Pt, O₂(g)/stabilized zirconia interfaces. Part II: electrochemical measurements and analysis. *Solid State Ionics* 1987;22:323–30.
- [93] Bieberle A. The electrochemistry of solid oxide fuel cell anodes: experiments, modeling and simulations, Ph.D. Thesis. Zürich: Swiss Federal Institute of Technology Zürich; 2000.
- [94] Kawada T, Sakai N, Yokokawa H, Dokiya M, Mori M, Iwata T. Structure and polarization characteristics of solid oxide fuel cell anodes. *Solid State Ionics* 1990;40/41:402–6.
- [95] Kawada T, Sakai N, Yokokawa H, Dokiya M, Mori M, Iwata T. Characteristics of slurry-coated nickel zirconia cermet anodes for solid oxide fuel cells. *J Electrochem Soc* 1990;137:3042–7.
- [96] Yamamura T, Tagawa H, Saito T, Mizusaki J, Kamitani K, Hirano K, et al. Reaction kinetics at the nickel pattern electrode on YSZ and its dependence on temperature. In: Dokiya M, Yamamoto O, Tagawa H, Singhal SC, editors. 4th International symposium on solid oxide fuel cells. Pennington (NJ), Yokohama (Japan): The Electrochemical Society; 1995. p. 741–9.
- [97] Norby T, Velle OJ, Leth-Olsen H, Tunold R. Reaction resistance in relation to three phase boundary length of Ni/YSZ electrodes. In: Singhal SC, Iwahara H, editors. 3rd International symposium on solid oxide fuel cells. Pennington (NJ), Honolulu (HI, USA): The Electrochemical Society; 1993. p. 473–8.
- [98] Mizusaki J, Tagawa H, Saito T, Yamamura T, Kamitani K, Hirano K, et al. Kinetic studies of the reaction at the nickel pattern electrode on YSZ in H₂-H₂O atmospheres. *Solid State Ionics* 1994;70/71:52–8.
- [99] Mizusaki J, Tagawa H, Saito T, Kamitani K, Yamamura T, Hirano K, et al. Preparation of Nickel pattern electrodes on YSZ and their electrochemical properties in H₂-H₂O atmospheres. In: Singhal SC, Iwahara H, editors. 3rd International symposium on solid oxide fuel cells. Pennington (NJ), Honolulu (HI, USA): The Electrochemical Society; 1993. p. 533–41.
- [100] Bieberle A, Gauckler LJ. Reaction mechanism of Ni pattern anodes for solid oxide fuel cells. *Solid State Ionics* 2000;135:337–45.
- [101] Bieberle A, Meier LP, Gauckler LJ. The electrochemistry of Ni pattern anodes used as solid oxide fuel cell model electrodes. *J Electrochem Soc* 2001;148:A646–56.
- [102] Boer Bd, Gonzalez M, Bouwmeester HJM, Verweij H. The effect of the presence of fine YSZ particles on the performance of porous nickel electrodes. *Solid State Ionics* 2000;127:269–76.
- [103] Aaberg RJ, Tunold R, Mogensen M, Berg RW, Odegard R. Morphological changes at the interface of the nickel-yttria stabilized zirconia point electrode. *J Electrochem Soc* 1998;145:2244–52.
- [104] Pizzini S, Bianchi M, Colombo P, Torchio S. On the influence of the annealing temperature and heavy current treatments on the porous structure of platinum electrodes and on the kinetics of the oxygen reaction at high temperatures. *J Appl Electrochem* 1973;3:153–9.
- [105] Schouler EJL, Kleitz M. Electrocatalysis and inductive effects at the gas, Pt/stabilized zirconia interface. *J Electrochem Soc* 1987;134:1045–50.
- [106] Aaberg RJ, Tunold R, Rørd. On the electrochemistry of metal-YSZ single contact electrodes. *Solid State Ionics* 2000;136–137:707–12.
- [107] Bay L, Jacobsen T. Dynamics of the YSZ-Pt interface. *Solid State Ionics* 1997;93:201–6.
- [108] Guindet J, Roux C, Hammou A. Hydrogen oxidation at the Ni/zirconia electrode. In: Grosz F, editor. 2nd International symposium on solid oxide fuel cells. Pennington (NJ), Athens (Greece): The Electrochemical Society; 1991. p. 553–8.

- [109] Mohamedi-Boulenouar FZ, Guindet J, Hammou A. Influence of water vapour on electrochemical oxidation of hydrogen at the Ni/Zirconia interface. In: Poulsen FW, Bonanos N, Linderoth S, Mogensen M, Christiansen BZ, editors. 17th Risø international symposium on material science: high temperature electrochemistry: ceramics and metals. Roskilde (Denmark): Risø National Laboratory; 1996. p. 441–50.
- [110] Osborg PA, Norby T. Characterisation of a H₂ + H₂O/Ni/YSZ point electrode system by impedance spectroscopy. In: 7th SOFC workshop, theory and measurement of microscale processes in solid oxide fuel cells, 18–20 January. Wadahl, Norway; 1995. p. 47–50.
- [111] de Boer B. SOFC anodes: hydrogen oxidation at porous nickel and nickel/yttria stabilised zirconia cermet electrodes, Ph.D. Thesis. Twente: University of Twente; 1998.
- [112] Habibzadeh B. Understanding Co oxidation in SOFCs using nickel patterned anode, Ph.D. Thesis. College Park, Baltimore: University of Maryland; 2007.
- [113] Bessler WG, Warnatz J, Goodwin DG. The influence of equilibrium potential on the hydrogen oxidation kinetics of SOFC anodes. Solid State Ionics 2007;177:3371–83.
- [114] Bessler WG. A new approach for SOFC impedance from detailed electrochemical reaction–diffusion models. Solid State Ionics 2005;176:997–1011.
- [115] Kek D, Mogensen M, Pejovnik S. A study of metal (Ni, Pt, Au)–yttria-stabilized zirconia interface in hydrogen atmosphere at elevated temperature. J Electrochem Soc 2001;148:A878–86.
- [116] Jensen KV, Primdahl S, Chorkendorff I, Mogensen M. Microstructural and chemical changes at the Ni–YSZ interface. Solid State Ionics 2001;144:197–209.
- [117] Jiang SP, Badwal SPS. Hydrogen oxidation at the nickel and platinum electrodes on yttria-tetragonal zirconia electrolyte. J Electrochem Soc 1997;144:3777–84.
- [118] Beckel D, Bieberle, Hüttner A, Harvey A, Infortuna A, Muecke UP, Prestat M, et al. Thin films for micro solid oxide fuel cells. J Power Sour 2007;2007:325–45.
- [119] Ehn A, Høgh J, Graczyk M, Normann K, Montelius L, Linne M, et al. Electrochemical measurements made in dry CO/CO₂ and H₂/H₂O atmospheres on single crystal YSZ using pattern electrodes. In: Linderoth S, Smith A, Bonanos N, Hagen A, Mikkelsen L, Kammer K, et al., editors. 26th Risø international symposium on materials science: solid state electrochemistry. Roskilde (Denmark): Risø National Laboratory; 2005. p. 177–84.
- [120] Sukeshini AM, Habibzadeh B, Becker BP, Pompert MB, Demircan O, Walker RA, et al. CO and CH₄ electrochemical oxidation on Ni-patterned anodes. In: Singhal SC, Mizusaki J, editors. 9th International symposium on solid oxide fuel cells. Pennington (NJ), Quebec City (Canada): The Electrochemical Society; 2005. p. 1294–303.
- [121] Mogensen M, Lindegaard T. The kinetics of hydrogen oxidation on a Ni/YSZ SOFC electrode at 1000 °C. In: Singhal SC, Iwahara H, editors. 3rd International symposium on solid oxide fuel cells. Pennington (NJ), Honolulu (HI, USA): The Electrochemical Society; 1993. p. 484–93.
- [122] Mogensen M, Sunde S, Primdahl S. SOFC anode kinetics. In: Poulsen FW, Bonanos N, Linderoth S, Mogensen M, Christiansen BZ, editors. 17th Risø international symposium on materials science: solid state electrochemistry. Roskilde (Denmark): Risø National Laboratory; 1996. p. 77–100.
- [123] Aaberg RJ, Turnold R, Ødegård R, Tjelle S. A possible reaction mechanism for the oxidation of H₂ on Ni/YSZ cermet electrodes. In: Stimming U, Singhal SC, Tagawa H, Lehnert W, editors. 5th International symposium on solid oxide fuel cells. Pennington (NJ), Aachen (Germany): The Electrochemical Society, Inc.; 1997. p. 557–64.
- [124] Skaarup S, Zachau-Christiansen B, Jacobsen T. Surface species and surface mobility on Ni/YSZ anodes. In: Poulsen FW, Bonanos N, Linderoth S, Mogensen M, Zachau-Christiansen B, editors. 17th Risø international symposium on materials science: solid state electrochemistry. Roskilde (Denmark): Risø National Laboratory; 1996. p. 423–30.
- [125] Mizusaki J, Yamamura T, Yoshitake H, Tagawa H, Hirano K, Ehara S, et al. Kinetic studies on Ni/YSZ anode reaction of SOFC in H₂-H₂O atmospheres by the use of Nickel pattern electrodes. In: Poulsen FW, Bonanos N, Linderoth S, Mogensen M, Christiansen BZ, editors. 17th Risø international symposium on material science: high temperature electrochemistry: ceramics and metals. Roskilde (Denmark): Risø National Laboratory; 1996. p. 363–8.
- [126] Minh NQ, Takahashi T. Science and technology of ceramic fuel cells. Amsterdam: Elsevier; 1995.
- [127] Primdahl S. Nickel/yttria-stabilised zirconia cermet anodes for solid oxide fuel cells, Ph.D. Thesis. Twente: University of Twente; 1999.
- [128] Mogensen M, Høgh J, Hansen KV, Jacobsen T. A critical review of models of the H₂/H₂O/Ni/SZ electrode kinetics. ECS Trans 2007;7:1329–38.
- [129] Wagner C. The solubility of water vapor in ZrO₂–Y₂O₃ mixed crystals. Berichte der Bunsen-Gesellschaft für Physikalische Chemie 1968;72:778–81.
- [130] Bieberle A, Gauckler LJ. Reaction mechanism of Ni pattern anodes for solid oxide fuel cells. Solid State Ionics 2000;135:337–45.
- [131] Brown M, Primdahl S, Mogensen M. Structure/performance relations for Ni/yttria-stabilized zirconia anodes for solid oxide fuel cells. J Electrochem Soc 2000;147:475–85.
- [132] Störmer H. Ni model anodes. KIT-University of the State of Baden-Württemberg and National Research Center of the Helmholtz Association; Karlsruhe.
- [133] Primdahl S, Mogensen M. Gas diffusion impedance in characterization of solid oxide fuel cell anodes. J Electrochem Soc 1999;146:2827–33.
- [134] Primdahl S, Mogensen MJ. Gas conversion impedance: a test geometry effect in characterization of solid oxide fuel cell anodes. J Electrochem Soc 1998;145:2431–8.
- [135] Murray EP, Tsai T, Barnett SA. A direct-methane fuel cell with a ceria-based anode. Nature 1999;400:649–51.
- [136] Norby T, Velle OJ, Leth-Olsen H, Tunold R. Reaction resistance in relation to three phase boundary length of Ni/YSZ electrodes. In: Singhal SC, Iwahara H, editors. 3rd International symposium on solid oxide fuel cells. Honolulu (HI, USA): The Electrochemical Society; 1993. p. 473–8.
- [137] Mizusaki J, Tagawa H, Saito T, Kamitain K, Yamamura T, Hirano K, et al. Preparation of Nickel pattern electrodes on YSZ and their electrochemical properties in H₂-H₂O atmospheres. J Electrochem Soc 1994;141:2129–34.

- [138] Yamamura T, Yoshitaka H, Tagawa H, Mori N, Hirano K, Mizusaki J, et al. Experimental evidence for three phase boundary as active site on nickel/YSZ system. In: Thorstensen B, editor. Proceedings of 2nd European solid oxide fuel cell forum. Oslo (Norway): The European Fuel Cell Forum; 1996. p. 617–25.
- [139] Primdahl S, Mogensen M. Oxidation of hydrogen on Ni/yttria-stabilized zirconia cermet anodes. *J Electrochim Soc* 1997;144:3409–19.
- [140] Aaberg RJ, Tunold R, Tjelle S, Ødegård R. Oxidation of CO and H₂ on Ni/YSZ cermet electrodes. In: Poulsen FW, Bonanos N, Linderöd S, Mogensen M, Christiansen BZ, editors. 17th Risø international symposium on material science: high temperature electrochemistry: ceramics and metals. Roskilde (Denmark): Risø National Laboratory; 1996. p. 511–6.
- [141] Holtappels P, Haart LGJd, Stimming U. Reaction of hydrogen/water mixtures on nickel-zirconia cermet electrodes: I. DC polarization characteristics. *J Electrochim Soc* 1999;146:1620–5.
- [142] Holtappels P, Vinke IC, Haart LGJd, Stimming U. Reaction of hydrogen/water mixtures on nickel-zirconia cermet electrodes: II AC polarization characteristics. *J Electrochim Soc* 1999;146:2976–82.
- [143] Jiang SP, Badwal SPS. Electrodes on yttria-tetragonal zirconia electrolyte hydrogen oxidation at the nickel and platinum. *J Electrochim Soc* 1997;144:3777–84.
- [144] Holtappels P, Vinke IC, Haart LGJd, Stimming U. Reaction of hydrogen/water mixtures on nickel-zirconia cermet electrodes: II. AC polarization characteristics. *J Electrochim Soc* 1999;146:2976–82.
- [145] Dees DW, Claar TD, Easier TE, Fee DC, Mrazek FC. Conductivity of porous Ni/ZrO₂-Y₂O₃ cermets. *J Electrochim Soc* 1987;134:2141–6.
- [146] Corbin SF, Qiao X. Development of solid oxide fuel cell anodes using metal-coated pore-forming agents. *J Am Ceram Soc* 2003;86:401–6.
- [147] Lee J-H, Moon H, Lee H-W, Kim J, Kim J-D, Yoon K-H. Quantitative analysis of microstructure and its related electrical property of SOFC anode, Ni-YSZ cermet. *Solid State Ionics* 2002;148:15–26.
- [148] Lee J-H, Heo W, Lee D-S, Kim J, Kim G-H, Lee H-W, et al. The impact of anode microstructure on the power generating characteristics of SOFC. *Solid State Ionics* 2003;158:225–32.
- [149] Wen C, Kato R, Fukunaga H, Ishitani H, Yamada K. The overpotential of nickel/yttria-stabilized zirconia cermet anodes used in solid oxide fuel cells. *J Electrochim Soc* 2000;147:2076–80.
- [150] Chan SH, Xia ZT. Anode micro model of solid oxide fuel cell. *J Electrochim Soc* 2001;148:A388–94.
- [151] Matsuzaki Y, Yasuda I. The poisoning effect of sulfur-containing impurity gas on a SOFC anode: part I. Dependence on temperature, time, and impurity concentration. *Solid State Ionics* 2000;132:261–9.
- [152] Primdahl S, Mogensen M. Mixed conductor anodes: Ni as electrocatalyst for hydrogen conversion. *Solid State Ionics* 2002;152–153:597–608.
- [153] Matsui T, Kishida R, Kim J-Y, Muroyama H, Eguchi K. Performance deterioration of Ni-YSZ anode induced by electrochemically generated steam in solid oxide fuel cells. *J Electrochim Soc* 2010;157:B776–81.
- [154] Zhu H, Kee RJ, Janardhanan VM, Deutschmann O, Goodwin DG. Modeling elementary heterogeneous chemistry and electrochemistry in solid-oxide fuel cells. *J Electrochim Soc* 2005;152:A2427–40.
- [155] Zhao F, Virkar AV. Dependence of polarization in anode-supported solid oxide fuel cells on various cell parameters. *J Power Sour* 2005;141:79–95.
- [156] Coutelieris FA, Douvartzides S, Tsakaras P. The importance of the fuel choice on the efficiency of a solid oxide fuel cell system. *J Power Sour* 2003;123:200–5.
- [157] Liese EA, Gemmen RS. Performance comparison of internal reforming against external reforming in a solid oxide fuel cell, gas turbine hybrid system. *J Eng Gas Turb Power* 2005;127:86–90.
- [158] Maiya PS, Anderson TJ, Mieville RL, Dusek JT, Picciolo JJ, Balachandran U. Maximizing H₂ production by combined partial oxidation of CH₄ and water gas shift reaction. *Appl Catal A: Gen* 2000;196:65–72.
- [159] Holtappels P, Haart LGJd, Stimming U, Vinke IC, Mogensen M. Reaction of CO/CO₂ gas mixtures on Ni-YSZ cermet electrodes. *J Appl Electrochim* 1999;29:561–8.
- [160] Lee S-I, Vohs JM, Gorte RJ. A study of SOFC anodes based on Cu-Ni and Cu-Co bimetallics in CeO₂-YSZ. *J Electrochim Soc* 2004;151:A1319–23.
- [161] Sasaki K, Susuki K, Iyoshi A, Uchimura M, Imamura N, Kusaba H, et al. H₂S poisoning of solid oxide fuel cells. *J Electrochim Soc* 2006;153:A2023–9.
- [162] Zha S, Cheng Z, Liu M. Sulfur poisoning and regeneration of Ni-based anodes in solid oxide fuel cells. *J Electrochim Soc* 2007;154:B201–6.
- [163] Rasmussen JFB, Hagen A. The effect of H₂S on the performance of Ni-YSZ anodes in solid oxide fuel cells. *J Power Sour* 2009;191:534–41.
- [164] Cheng Z, Liu M. Characterization of sulfur poisoning of Ni-YSZ anodes for solid oxide fuel cells using in situ Raman microspectroscopy. *Solid State Ionics* 2007;178:925–35.
- [165] Bartholomew CH. Mechanisms of catalyst deactivation. *Appl Catal A: Gen* 2001;212:17–60.
- [166] Cheng Z, Zha S, Liu M. Influence of cell voltage and current on sulfur poisoning behavior of solid oxide fuel cells. *J Power Sour* 2007;172:688–93.
- [167] Rostrup-Nielsen JR, Hansen JB, Helveg S, Christiansen N, Jannasch A-K. Sites for catalysis and electrochemistry in solid oxide fuel cell (SOFC) anode. *Appl Phys A* 2006;85:427–30.
- [168] Schubert SK, Kusnezoff M. Sulphur poisoning of SOFC anodes. In: 2nd International workshop on degradation issues on fuel cells. Thessaloniki (Greece); 2011.
- [169] Wang J-H, Liu M. Surface regeneration of sulfur-poisoned Ni surfaces under SOFC operation conditions predicted by first-principles-based thermodynamic calculations. *J Power Sour* 2008;176:23–30.
- [170] Rasmussen FBj, Hagen A. The effect of H₂S on the performance of Ni-YSZ anodes in solid oxide fuel cells. *J Power Sour* 2009;191:534–41.
- [171] Hagen A, Rasmussen JFB, Thydén K. Durability of solid oxide fuel cells using sulfur containing fuels. *J Power Sour* 2011;196:7271–6.
- [172] Horita T, Kishimoto H, Yamaji K, Xiong Y, Sakai N, Brito ME, et al. Materials and reaction mechanisms at anode/electrolyte interfaces for SOFCs. *Solid State Ionics* 2006;177:1941–8.

- [173] Raz S, Sasaki K, Maier J, Riess I. Characterization of adsorbed water layers on Y_2O_3 -doped ZrO_2 . Solid State Ionics 2001;143:181–204.
- [174] Sumi H, Lee Y-H, Muroyam H, Matsui T, Kamijo M, Mimuro S, et al. Effect of carbon deposition by carbon monoxide disproportionation on electrochemical characteristics at low temperature operation for solid oxide fuel cells. J Power Sour 2011;196:4451–7.
- [175] Singh D, Hernández-Pacheco E, Hutton PN, Patel N, Mann MD. Carbon deposition in an SOFC fueled by tar-laden biomass gas: a thermodynamic analysis. J Power Sour 2005;142:194–9.
- [176] Chen T, Wang WG, Miao H, Li T, Xu C. Evaluation of carbon deposition behavior on the nickel/yttrium-stabilized zirconia anode-supported fuel cell fueled with simulated syngas. J Power Sour 2011;196:2461–8.
- [177] Takeguchi T, Kani Y, Yano T, Kikuchi R, Eguchi K, Tsujimoto K, et al. Study on steam reforming of CH_4 and C_2 hydrocarbons and carbon deposition on Ni-YSZ cermets. J Power Sour 2002;112:588–95.
- [178] Kishimoto H, Horita T, Yamaji K, Xiong Y, Sakai N, Brito ME, et al. Feasibility of *n*-dodecane fuel for solid oxide fuel cell with Ni-ScSZ anode. J Electrochem Soc 2005;152:A532–8.
- [179] McIntosh S, Vohs JM, Gorte RJ. Role of hydrocarbon deposits in the enhanced performance of direct-oxidation SOFCs. J Electrochem Soc 2003;150:A470–6.
- [180] Chun CM, Mumford JD, Ramanarayanan TA. Carbon induced corrosion of nickel anode. J Electrochem Soc 2000;147:3680–6.
- [181] Chun CM, Ramanarayanan TA. Mechanism and control of carbon deposition on high temperature alloys. J Electrochem Soc 2007;154:C465–71.
- [182] Zhao X-Y, Yao Q, Li S-Q, Cai N-S. Studies on the carbon reactions in the anode of deposited carbon fuel cells. J Power Sour 2008;185:104–11.
- [183] Nabae Y, Yamanaka I, Hatano M, Otsuka K. Catalytic behavior of Pd–Ni/composite anode for direct oxidation of methane in SOFCs. J Electrochem Soc 2006;153:A140–5.
- [184] Gorte RJ, Park S, Vohs JM, Wang C. Anodes for direct oxidation of dry hydrocarbons in a solid-oxide fuel cell. Adv Mater 2000;12:1465–9.
- [185] Kim H, Vohs JM, Gorte RJ. Direct oxidation of sulfur-containing fuels in a solid oxide fuel cell. Chem Commun 2001;2334–5.
- [186] Kim H, Lu C, Worrell WL, Vohs JM, Gorte RJ. Cu–Ni cermet anodes for direct oxidation of methane in solid oxide fuel cells. J Electrochem Soc 2002;149:A247–50.
- [187] An S, Lu C, Worrell WL, Gorte RJ, Vohs JM. Characterization of Cu– CeO_2 direct hydrocarbon anodes in a solid oxide fuel cell with lanthanum gallate electrolyte. Solid State Ionics 2004;175:135.
- [188] Gorte RJ, Vohs JM, Wang C. Anodes for direct oxidation of dry hydrocarbons in a solid-oxide fuel cell. Adv Mater 2000;12:1465–9.
- [189] Feduska W, Isenberg AO. High-temperature solid oxide fuel cell-technical status. J Power Sour 1983;10:89–102.
- [190] Iritani J, Kougamii K, Komiya N, Nagata K, Ikeda K, Tomida K. Pressurized 10 kW Class Module SOFC. In: Yokokawa H, Singhal SC, editors. 7th International symposium on solid oxide fuel cells. Pennington (NJ), Tsukuba (Japan): The Electrochemical Society; 2001. p. 63–71.
- [191] Stolten D, Späh R, Schamm R. Status of SOFC development at Daimler-Benz/Dornier. In: Stimming U, Singhal SC, Tagawa H, Lehnert W, editors. 5th International symposium on solid oxide fuel cells. Pennington (NJ), Aachen (Germany): The Electrochemical Society; 1997. p. 88–93.
- [192] Batawi E, Weissen U, Schuler A, Keller M, Voisard C. Cell manufacturing processes at Sulzer Hexis. In: Yokokawa H, Singhal SC, editors. 7th International symposium on solid oxide fuel cells. Pennington (NJ), Tsukuba (Japan): The Electrochemical Society; 2001. p. 140–7.
- [193] Dees DW, Balachandran U, Dorris SE, Heiberger JJ, McPheeters CC, Picciolo JJ. Electrode development in monolithic solid oxide fuel cells. In: White RE, Appleby AI, editors. Proceedings of the symposium on fuel cells. Pennington (NJ), San Francisco (CA, USA): The Electrochemical Society; 1989. p. 130–6.
- [194] Prindahl S, Mogensen M. Limitations in the hydrogen oxidation rate on Ni/YSZ anodes. In: Singhal SC, Dokya M, editors. 6th International symposium on solid oxide fuel cells. Pennington (NJ), Honolulu (HI, USA): The Electrochemical Society; 1999. p. 530–40.
- [195] Matsuzaki Y, Yasuda I. Effect of a sulfur-containing impurity on electrochemical properties of a Ni–YSZ cermet electrode. In: Yokokawa H, Singhal SC, editors. 7th International symposium on solid oxide fuel cells. Pennington (NJ), Tsukuba (Japan): The Electrochemical Society; 2001. p. 769–79.
- [196] Sasaki K, Susuki K, Iyoshi A, Uchimura M, Imamura N, Kusaba H, et al. Sulfur tolerance of solid oxide fuel cells. In: Singhal SC, Mizusaki J, editors. 9th International symposium on solid oxide fuel cells. Pennington (NJ), Quebec City (Canada): The Electrochemical Society; 2005. p. 1267–74.
- [197] Xia SJ, Birss VI. Deactivation and recovery of Ni–YSZ anode in H_2 fuel containing H_2S . In: Singhal SC, Mizusaki J, editors. 9th International symposium on solid oxide fuel cells. Pennington (NJ), Quebec City (Canada): The Electrochemical Society, Inc.; 2005. p. 1275–83.
- [198] Tremblay JP, Marquez AI, Ohrn TR, Bayless DJ. Effects of coal syngas and H_2S on the performance of solid oxide fuel cells: single-cell tests. J Power Sour 2006;158:263–73.
- [199] Zhang L, Jiang SP, He HQ, Chen X, Ma J, Song XC. A comparative study of H_2S poisoning on electrode behavior of Ni/YSZ and Ni/GDC anodes of solid oxide fuel cells. Int J Hydro Energy 2010;35:12359–68.
- [200] Mukerjee S, Haltiner K, Kerr R, Chick L, Sprenkle V, Meinhardt K, et al. Solid oxide fuel cell development: latest results. ECS Trans 2007;7:59–65.
- [201] Sprenkle V, Kim JY, Meinhardt K, Lu C, Chick L, Canfield N, et al. Sulfur poisoning studies on the Delphi-Battelle SECA program. In: 31st International conference and exposition on advanced ceramics and composites. Daytona Beach (FL, USA): The American Ceramic Society; 2007.
- [202] Li TS, Wang WG. Sulfur-poisoned Ni-based solid oxide fuel cell anode characterization by varying water content. J Power Sour 2011;196:2066–9.

- [203] Li TS, Wang WG, Chen T, Miao H, Xu C. Hydrogen sulfide poisoning in solid oxide fuel cells under accelerated testing conditions. *J Power Sour* 2010;195:7025–32.
- [204] Lussier A, Sofie S, Dvorak J, Idzerda YU. Mechanism for SOFC anode degradation from hydrogen sulfide exposure. *Int J Hydro Energy* 2008;33:3945–51.
- [205] Cheng Z, Abernathy H, Liu M. Raman spectroscopy of nickel sulfide Ni_3S_2 . *J Phys Chem C* 2007;111:17997–8000.
- [206] Cheng Z, Liu M. Characterization of sulfur poisoning of Ni-YSZ anodes for solid oxide fuel cells using *in situ* raman microspectroscopy. *Solid State Ionics* 2007;178:925–35.
- [207] Yokokawa H, Horita T, Sakai N, Yamaji K, Brito ME, Xiong YP, et al. Protons in ceria and their roles in SOFC electrode reactions from thermodynamic and SIMS analyses. *Solid State Ionics* 2004;174:205.
- [208] Godickeimer M, Sasaki K, Gauckler LJ. Current–voltage characteristics of fuel cells with ceria-based electrolytes. In: Dokiya M, Yamamoto O, Tagawa H, Singhal SC, editors. 4th International symposium on solid oxide fuel cells. Pennington (NJ), Yokohama (Japan): The Electrochemical Society; 1995. p. 1072–81.
- [209] Steele BCH. Appraisal of $\text{Ce}_{1-y}\text{Gd}_y\text{O}_{2-y/2}$ electrolytes for IT-SOFC operation at 500 °C. *Solid State Ionics* 2000;129:95–110.
- [210] Omar S, Wachsman ED, Jones JL, Nino JC. Crystal structure–ionic conductivity relationships in doped ceria systems. *J Am Ceram Soc* 2009;92:2674–81.
- [211] Omar S, Wachsman ED, Nino JC. A co-doping approach towards enhanced ionic conductivity in fluorite-based electrolytes. *Solid State Ionics* 2006;177:3199–203.
- [212] Omar S, Wachsman ED, Nino JC. Higher ionic conductive ceria based electrolytes for SOFCs. *Appl Phys Lett* 2007;91:144106.
- [213] Steele BCH, Middleton PH, Rudkin RA. Material science aspects of SOFC technology with special reference to anode development. *Solid State Ionics* 1990;40:388.
- [214] Tsai T, Barnett SA. Increased solid-oxide fuel cell power density using interfacial ceria layers. *Solid State Ionics* 1997;98:191–6.
- [215] McIntosh S, Vohs JM, Gorte RJ. An examination of lanthanide additives on the performance of Cu-YSZ cermet anodes. *Electrochim Acta* 2002;47:3815–21.
- [216] Aravind PV, Ouwteljes JP, Woudstra N, Rietveld G. Impact of biomass-derived contaminants on SOFCs with Ni/gadolinia-doped ceria anodes. *Electrochim Solid State Lett* 2008;11:B24–8.
- [217] Ouwteljes JP, Aravind PV, Woudstra N, Rietveld G. Biosyngas utilization in solid oxide fuel cells with Ni/GDC anodes. *J Fuel Cell Sci Technol* 2006;3:495–8.
- [218] He H, Gorte RJ, Vohs JM. Highly sulfur tolerant Cu-ceria anodes for SOFCs. *Electrochim Solid-State Lett* 2005;8:A279–80.
- [219] Liu M, Wei G, Luo J, Sanger AR, Chuang KT. Use of metal sulfides as anode catalysts in H_2 -air SOFCs. *J Electrochem Soc* 2003;150:A1025–9.
- [220] Yates C, Winnick J. Anode materials for a hydrogen sulfide solid oxide fuel cell. *J Electrochim Soc* 1999;146:2841–4.
- [221] Smith M, McEvoy AJ. Sulfur-tolerant cermet anodes. In: Singhal SC, Mizusaki J, editors. 9th International symposium on solid oxide fuel cells. Pennington (NJ), Quebec City (Canada): The Electrochemical Society; 2005. p. 1437–44.
- [222] Mukundan R, Broska EL, Garzon FH. Sulfur tolerant anodes for SOFCs. *Electrochim Solid-State Lett* 2004;7:A5–7.
- [223] Tao S, Irvine JTS. A redox-stable efficient anode for solid-oxide fuel cells. *Nat Mater* 2003;2:320–3.
- [224] Zha S, Tsan P, Cheng Z, Liu M. Electrical properties and sulfur tolerance of $\text{La}_{0.75}\text{Sr}_{0.25}\text{Cr}_{1-x}\text{Mn}_x\text{O}_3$ under anodic conditions. *J Solid State Chem* 2005;178:1844–50.
- [225] Aguilar L, Zha SW, Cheng Z, Winnick J, Liu ML. A solid oxide fuel cell operating on hydrogen sulfide (H_2S) and sulfur-containing fuels. *J Power Sour* 2004;135:17–24.
- [226] Cheng Z, Zha S, Aguilar L, Wang D, Winnick J, Liu M. A solid oxide fuel cell running on $\text{H}_2\text{S}-\text{CH}_4$ fuel mixtures. *Electrochim Solid State Lett* 2006;9:A31–3.
- [227] Smyth DM. Oxidative nonstoichiometry in perovskite oxides, Properties and applications of perovskite-type oxides, CRC Press, Taylor & Francis Group; New York (USA); 1993.
- [228] Kurokawa H, Sholkalapper TZ, Jacobson CP, Jonghe LCD, Visco SJ. Ceria nanocoating for sulfur tolerant Ni-based anodes of solid oxide fuel cells. *Electrochim Solid-State Lett* 2007;10:B135–8.
- [229] Chen XJ, Liu QL, Chan SH, Brandon NP, Khor KA. High performance cathode-supported SOFC with perovskite anode operating in weakly humidified hydrogen and methane. *Electrochim Commun* 2007;9:767–72.
- [230] Jiang SP, Chen XJ, Chan SH, Kwok JT, GDC-impregnated $(\text{La}_{0.75}\text{Sr}_{0.25})(\text{Cr}_{0.5}\text{Mn}_{0.5})\text{O}_3$ anodes for direct utilization of methane in solid oxide fuel cells. *J Electrochim Soc* 2006;153:A850–6.
- [231] Blennow P, Hansen KK, Wallenberg LR, Mogensen M. Electrochemical characterization and redox behavior of Nb-doped SrTiO_3 . *Solid State Ionics* 2009;180:63–70.
- [232] Singhal SC, Ruka RJ, Bauerle JE, Spengler CJ. Final technical report: anode development for solid oxide fuel cells. Pittsburgh (PA); 1986.
- [233] Kurokawa H, Sholkalapper TZ, Jacobson CP, Jonghe LCD, Visco SJ. Ceria nanocoating for sulfur tolerant Ni-based anodes of solid oxide fuel cells. *Electrochim Solid-State Lett* 2007;10:B135–8.
- [234] Yun JW, Yoon SP, Park S, Kim HS, Nam SW. Analysis of the regenerative H_2S poisoning mechanism in $\text{Ce}_{0.8}\text{Sm}_{0.2}\text{O}_2$ -coated Ni/YSZ anodes for intermediate temperature solid oxide fuel cells. *Int J Hydro Energy* 2011;36:787–96.
- [235] McEvoy AJ, Smith MJ. Regeneration of anodes exposed to sulfur. *ECS Trans* 2007;7:373–80.
- [236] Marina OA, Coyle CA, Engelhard MH, Pederson LR. Mitigation of sulfur poisoning of Ni/Zirconia SOFC anodes by antimony and tin. *J Electrochim Soc* 2011;158:B424–9.
- [237] Xie Z, Zhu W, Zhu B, Xia C. $\text{Fe}_x\text{Co}_{0.5-x}\text{Ni}_{0.5}/\text{SDC}$ anodes for low-temperature solid oxide fuel cells. *Electrochim Acta* 2006;51:3052–7.
- [238] Wang S, Ando M, Ishihara T, Takita Y. High performance $\text{Ni}/\text{Sm}_{0.15}\text{Ce}_{0.85}\text{O}_{2-\delta}$ cermet anodes for intermediate temperature solid oxide fuel cells using LaGaO_3 based oxide electrolytes. *Solid State Ionics* 2004;174:49–55.
- [239] Wisniewski M, Boréave A, Gélin P. Catalytic CO_2 reforming of methane over $\text{Ir}/\text{Ce}_{0.9}\text{Gd}_{0.1}\text{O}_{2-x}$. *Catal Commun* 2005;6:596–600.
- [240] Kikuchi R, Koashi N, Matsui T, Eguchi K, Norby T. Novel anode materials for multi-fuel applicable solid oxide fuel cells. *J Alloys Comp* 2006;408–412:622–7.

- [241] Ye X-F, Huang B, Wang SR, Wang ZR, Xiong L, Wen TL. Preparation and performance of a Cu–CeO₂–ScSZ composite anode for SOFCs running on ethanol fuel. *J Power Sour* 2007;164:203–9.
- [242] Naito H, Arashi H. Electrical properties of ZrO₂–TiO₂–Y₂O₃ system. *Solid State Ionics* 1992;53–56:436–41.
- [243] Kobayashi K, Kai Y, Yamaguchi S, Fukatsu N, Kawashima T, Iguchi Y. Electronic conductivity measurements of 5 mol% TiO₂-doped YSZ by a d.c.-polarization technique. *Solid State Ionics* 1997;93:193–9.
- [244] Wang C, Worrell WL, Park S, Vohs JM, Gorte RJ. Fabrication and performance of thin-film YSZ solid oxide fuel cells. *J Electrochem Soc* 2001;148:A864–8.
- [245] Colomer MT, Duran P, Caballero A, Jurado JR. Microstructure, electrical properties and phase equilibria relationships in the ZrO₂–Y₂O₃–TiO₂ system: the subsolidus isothermal section at 1500 °C. *Mater Sci Eng: A* 1997;229:114–22.
- [246] Sauvet AL, Fouletier J, Gaillard F, Primet M. Surface properties and physicochemical characterizations of a new type of anode material, La_{1-x}Sr_xCr_{1-y}Ru_yO_{3-d}, for a solid oxide fuel cell under methane at intermediate temperature. *J Catal* 2002;209:25–34.
- [247] Sauvet AL, Irvine JTS. Catalytic activity for steam methane reforming and physical characterisation of La_{1-x}Sr_xCr_{1-y}Ni_yO_{3-d}. *Solid State Ionics* 2004;167:1–8.
- [248] Seifir J. LaCrO₃-based anodes: stability considerations. *J Power Sour* 2003;118:276–85.
- [249] Weston M, Metcalfe IS. La_{0.6}Sr_{0.4}Co_{0.2}Fe_{0.8}O₃ as an anode for direct methane activation in SOFCs. *Solid State Ionics* 1998;113–115:247–51.
- [250] Vernoux P, Guillodo M, Fouletier J, Hammou A. Alternative anode material for gradual methane reforming in solid oxide fuel cells. *Solid State Ionics* 2000;135:425–31.
- [251] Hui S, Petric A. Evaluation of yttrium-doped SrTiO₃ as an anode for solid oxide fuel cells. *J Euro Ceram Soc* 2002;22:1673–81.
- [252] Fagg DP, Kharton VV, Kovalevsky AV, Viskup AP, Naumovich EN, Frade JR. The stability and mixed conductivity in La and Fe doped SrTiO₃ in the search for potential SOFC anode materials. *J Euro Ceram Soc* 2001;21:1831–5.
- [253] Weston M, Metcalfe IS. La_{0.6}Sr_{0.4}Co_{0.2}Fe_{0.8}O₃ as an anode for direct methane activation in SOFCs. *Solid State Ionics* 1998;247:113–5.
- [254] Skarmoutsos D, Nikolopoulos P, Tietz F, Vinke IC. Physical characterization of Y_{0.25}Zr_{0.60}Ti_{0.15}O_{2-x} and its performance as a Ni/Y_{0.25}Zr_{0.60}Ti_{0.15}O_{2-x} anode cermet in an SOFC. *Solid State Ionics* 2004;170:153–8.
- [255] Tsai T, Barnett SA. Effect of mixed-conducting interfacial layers on solid oxide fuel cell anode performance. *J Electrochem Soc* 1998;145:1696–701.
- [256] Wu Y, Wang W, Wang K, Zeng Y, Dong D, Shao Z, et al. Morphology and catalytic performance of flake-shaped NiO–Yttria-stabilized zirconia (YSZ) particles with nanocrystalline YSZ grains. *Indust Eng Chem Res* 2012;51:6387–94.
- [257] Wu Y, Dong D, Ran R, Zeng Y, Wang K, Shao Z, et al. Synthesis of flake-shaped NiO–YSZ particles for high porosity anode of solid oxide fuel cell. *J Am Ceram Soc* 2011;94:3666–70.
- [258] Aricò AS, Bruce P, Scrosati B, Tarascon JM, Schalkwijk Wv. Nanostructured materials for advanced energy conversion and storage devices. *Nat Mater* 2005;4:366–77.
- [259] Gong M, Liu X, Tremblay J, Johnson C. Sulfur-tolerant anode materials for solid oxide fuel cell application. *J Power Sour* 2007;168:289–98.
- [260] Sun C, Stimming U. Recent anode advances in solid oxide fuel cells. *J Power Sour* 2007;171:247–60.
- [261] Cheng Z, Wang J-H, Liu M. Solid oxide fuel cells: materials properties and performance. Boca Raton (FL, USA): CRC Press; Taylor and Francis Group; 2009.
- [262] Marina OA, Canfield NL, Stevenson JW. Thermal, electrical, and electrocatalytical properties of lanthanum-doped strontium titanate. *Solid State Ionics* 2002;149:21–8.
- [263] Marina OA, Walker MS, Stevenson JW. Development of ceramic composites as SOFC anodes. Fuel Cell Seminar, Miami (FL, USA); 2003. p. 340–3.
- [264] Kurokawa H, Yang L, Jacobson CP, Jonghe LCD, Visco SJ. Y-doped SrTiO₃ based sulfur tolerant anode for solid oxide fuel cells. *J Power Sour* 2007;164:510–8.
- [265] Burke A, Li S, Winnick J, Liu M. Sulfur-tolerant cathode materials in electrochemical membrane system for H₂S removal from hot fuel gas. *J Electrochem Soc* 2004;151:D55–60.
- [266] Aguilar L, Zha SW, Li SW, Winnick J, Liu M. Sulfur-tolerant materials for the hydrogen sulfide SOFC. *Electrochim Solid-State Lett* 2004;7:A324–6.
- [267] Cheng Z, Zha SW, Aguilar L, Liu ML. Chemical, electrical, and thermal properties of strontium doped lanthanum vanadate. *Solid State Ionics* 2005;176:1921–8.
- [268] Cooper M, Channa K, Silva RD, Bayless DJ. Comparison of LSV/YSZ and LSV/GDC SOFC anode performance in coal syngas containing H₂S. *J Electrochem Soc* 2010;157:B1713–8.
- [269] Danilovic N, Luo JL, Chuang KT, Sanger AR. Ce_{0.9}Sr_{0.1}VO_x (x = 3, 4) as anode materials for H₂S-containing CH₄ fueled solid oxide fuel cells. *J Power Sour* 2009;192:247–57.
- [270] Danilovic N, Luo J-L, Chuang KT, Sanger AR. Effect of substitution with Cr³⁺ and addition of Ni on the physical and electrochemical properties of Ce_{0.9}Sr_{0.1}VO₃ as a H₂S-active anode for solid oxide fuel cells. *J Power Sour* 2009;194:252–62.
- [271] Zha SW, Tsang P, Cheng Z, Liu ML. Electrical properties and sulfur tolerance of La_{0.75}Sr_{0.25}Cr_{1-x}Mn_xO₃ under anodic conditions. *J Solid State Chem* 2005;178:1844–50.
- [272] Huang YH, Dass RI, Xing ZL, Goodenough JB. *Science* 2006;312:254–7.
- [273] Huang YH, Dass RI, Denysyn JC, Goodenough JB. Synthesis and characterization of Sr₂MgMoO_{6-δ}: an anode material for the solid oxide fuel cell. *J Electrochem Soc* 2006;153:A1266–72.
- [274] Xiao G, Liu Q, Dong X, Huang K, Chen F. Sr₂Fe_{4/3}Mo_{2/3}O₆ as anodes for solid oxide fuel cells. *J Power Sour* 2010;195:8071–4.
- [275] Zha SW, Cheng Z, Liu ML. A sulfur-tolerant anode material for SOFCs: Gd₂Ti_{1.4}Mo_{0.6}O₇. *Electrochim Solid-State Lett* 2005;8:A406–8.
- [276] Zha S, Cheng Z, Liu M. Gd₂Ti_{2-x}Mo_xO₇-based anode materials for H₂S-air solid oxide fuel cells. *ECS Trans* 2006;1:293–302.

- [277] Wang S, Liu M, Winnick J. Stabilities and electrical conductivities of electrode materials for use in H₂S-containing gases. *J Solid State Electrochem* 2001;5:188–95.
- [278] Cheng Z, Wang J-H, Choi Y, Yang L, Lin MC, Liu M. From Ni–YSZ to sulfur-tolerant anode materials for SOFCs: electrochemical behavior, in situ characterization, modeling, and future perspectives. *Energy Environ Sci* 2011;4:4380.
- [279] Cheng Z. Investigations into the interactions between sulfur and anodes for solid oxide fuel cells. Ph.D. Thesis, Georgia Institute of Technology; Atlanta; 2008.
- [280] Hui S, Petric A. Evaluation of yttrium-doped SrTiO₃ as an anode for solid oxide fuel cells. *J Eur Ceram Soc* 2002;22:1673–81.
- [281] Hui S, Petric A. Electrical properties of yttrium-doped strontium titanate under reducing conditions. *J Electrochem Soc* 2002;149:J1–J10.
- [282] Escudero J, Irvine JTS, Daza L. Development of anode material based on La-substituted SrTiO₃ perovskites doped with manganese and/or gallium for SOFC. *J Power Sour* 2009;192:43–50.
- [283] Ruiz-Morales JC, Canales-Vazquez J, Savaniu C, Marrero-Lopez L, Zhou W, et al. Disruption of extended defects in solid oxide fuel cell anodes for methane oxidation. *Nature* 2006;439:568–71.
- [284] Blennow P, Hagen A, Hansen KK, Wallenberg LR, Mogensen M. Defect and electrical transport properties of Nb-doped SrTiO₃. *Solid State Ionics* 2008;179:12.
- [285] Balachandran U, Eror NG. Electrical conductivity in lanthanum-doped strontium titanate. *J Electrochem Soc* 1982;129:1021.
- [286] Akhtar MJ, Akhtar ZU-N, Jackson RA, Catlow CR. Computer simulation studies of strontium titanate. *J Am Ceram Soc* 1995;78:421–8.
- [287] Putna ES, Stubenrauch J, Vohs JM, Gorte RJ. Ceria-based anodes for the direct oxidation of methane in solid oxide fuel cells. *Langmuir* 1995;11:4832–7.
- [288] Boukamp BA. Fuel cells: the amazing perovskite anode. *Nat Mater* 2003;2:294–6.
- [289] Tao SW, Irvine JTS. Discovery and characterization of novel oxide anodes for solid oxide fuel cells. *Chem Rec* 2004;4:83–95.
- [290] Marina OA, Pederson LR. Novel ceramic anodes for SOFCs tolerant to oxygen, carbon and sulfur. In: Huijsmans J, editor. Proceedings of 5th European solid oxide fuel cell forum. Lucerne (Switzerland): The European Fuel Cell Forum; 2002. p. 481–9.
- [291] Miller DN, Irvine JTS. B-site doping of lanthanum strontium titanate for solid oxide fuel cell anodes. *J Power Sour* 2011;196:7323–7.
- [292] Vincent A, Luo JL, Chuang KT, Sanger AR. Effect of Ba doping on performance of LST as anode in solid oxide fuel cells. *J Power Sour* 2010;195:769–74.
- [293] Slater PR, Fagg DP, Irvine JTS. Synthesis and electrical characterisation of doped perovskite titanates as potential anode materials for solid oxide fuel cells. *J Mater Chem* 1997;7:2495–8.
- [294] Kolodiaznyi T, Petric A. The applicability of Sr-deficient *n*-type SrTiO₃ for SOFC anodes. *J Electroceram* 2005;15:5–11.
- [295] Haag JM, Barnett SA, Richardson JW, Poepelmeier KR. Structural and chemical evolution of the SOFC anode La_{0.30}Sr_{0.70}Fe_{0.70}Cr_{0.30}O_{3-δ} upon reduction and oxidation: an in situ neutron diffraction study. *Chem Mater* 2010;22:3283–9.
- [296] Elena K, Irvine John TS. Thermochemical and structural stability of A- and B-Site-substituted perovskites in hydrogen-containing atmosphere. *Chem Mater* 2009;21:1514–23.
- [297] Nakamura T, Petzow G, Gauckler LJ. Stability of the perovskite phase LaBO₃ (B = V, Cr, Mn, Fe, Co, Ni) in reducing atmosphere: I. Experimental results. *Mater Res Bullet* 1979;14:649–59.
- [298] Yoo J, Vema A, Wang SY, Jacobson AJ. Oxygen transport kinetics in SrFeO_{3-d}, La_{0.5}Sr_{0.5}FeO_{3-d}, and La_{0.2}Sr_{0.8}Cr_{0.2}Fe_{0.8}O_{3-d} measured by electrical conductivity relaxation. *J Electrochem Soc* 2005;152:A497–505.
- [299] Huang YH, Dass RI, Denyszyn JC, Goodenough JB. Synthesis and characterization of Sr₂MgMoO_{6-d} an anode material for the solid oxide fuel cell. *J Electrochem Soc* 2006;153:A1266–72.
- [300] Huang YH, Dass RI, Xing ZL, Goodenough JB. Double perovskites as anode materials for solid-oxide fuel cells. *Science* 2006;312:254–7.
- [301] Ji Y, Huang YH, Ying JR, Goodenough JB. Electrochemical performance of La-doped Sr₂MgMoO_{6-d} in natural gas. *Electrochim Commun* 2007;9:1881–5.
- [302] Kobayashi KI, Kimura T, Sawada H, Terakura K, Tokura Y. Room-temperature magnetoresistance in an oxide material with an ordered double-perovskite structure. *Nature* 1998;395:677–80.
- [303] Serrate D, Teresa JMD, Ibarra MR. Double perovskites with ferromagnetism above room temperature. *J Phys: Cond Matter* 2007;19:023201.
- [304] Garcia-Hernandez M, Martinez JL, Martinez-Lope MJ, Casais MT, Alonso JA. Finding universal correlations between cationic disorder and low field magnetoresistance in FeMo double perovskite series. *Phys Rev Lett* 2001;86:2443.
- [305] Huang YH, Karppinen M, Yamauchi H, Goodenough JB. Systematic studies on effects of cationic ordering on structural and magnetic properties in Sr₂FeMoO₆. *Phys Rev B* 2006;73:104408.
- [306] Bernuy-Lopez C, Alix M, Bridges CA, Claridge JB, Rosseinsky MJ. Sr₂MgMoO_{6-d}: structure, phase stability, and cation site order control of reduction. *Chem Mater* 2007;19:1035–43.
- [307] Marrero-López D, Peña-Martínez J, Ruiz-Morales JC, Pérez-Coll D, Aranda MAG, Núñez P. Synthesis, phase stability and electrical conductivity of Sr₂MgMoO_{6-d} anode. *Mater Res Bull* 2008;43:2441–50.
- [308] Graves C, Sudreddy BR, Mogensen M. Molybdate based ceramic negative-electrode materials for solid oxide cells. *ECS Trans* 2010;28:173–92.
- [309] Huang Y-H, Liang G, Croft M, Lehtimaki M, Karppinen M, Goodenough JB. Double-perovskite anode materials Sr₂MMoO₆ (M = Co, Ni) for Solid Oxide Fuel Cells. *Chem Mater* 2009;21:2319–26.
- [310] Tao SW, Irvine JTS. A redox-stable efficient anode for solid-oxide fuel cells. *Nat Mater* 2003;2:320–3.
- [311] Peña-Martínez J, Marrero-López D, Ruiz-Morales JC, Savaniu C, Núñez P, Irvine JTS. Anodic performance and intermediate temperature fuel cell testing of La_{0.75}Sr_{0.25}Cr_{0.5}Mn_{0.5}O_{3-δ} at lanthanum gallate electrolytes. *Chem Mater* 2006;18:1001–6.

- [312] Lu XC, Zhu JH. Cu(Pd)-impregnated $\text{La}_{0.75}\text{Sr}_{0.25}\text{Cr}_{0.5}\text{Mn}_{0.5}\text{O}_{3-\delta}$ anodes for direct utilization of methane in SOFC. Solid State Ionics 2007;178:1467–75.
- [313] Zhang X, Zhong Q. Preparation and characterization of $\text{La}_{0.7}\text{Sr}_{0.3}\text{Cr}_{1-x}\text{Fe}_x\text{O}_{3-d}$ anode catalyst with sulfur tolerance for SOFC. Huagong Jinzhan 2009;28:788–92.
- [314] Bierschenk DM, Haag JM, Poeppelmeier KR, Barnett SA. Effect of coal syngas fuel composition on the performance and stability of oxide anode. In: Singhal S, Yokokawa H, editors. 216th ECS transactions. Pennington (NJ), Vienna (Austria): The Electrochemical Society; 2009. p. 2107–16.
- [315] Lu XC, Zhu JH, Yang Z, Xia G, Stevenson JW. Pd-impregnated SYT/LDC composite as sulfur-tolerant anode for solid oxide fuel cells. J Power Sour 2009;192:381–4.
- [316] Tao S, Irvine JTS. Synthesis and characterization of $(\text{La}_{0.75}\text{Sr}_{0.25})\text{Cr}_{0.5}\text{Mn}_{0.5}\text{O}_{3-\delta}$, a redox-stable, efficient perovskite anode for SOFCs. J Electrochem Soc 2004;151:A252–9.
- [317] Marina OA. Development of advanced SOFC anodes. SECA Core Technology Program Peer Review. Boston (MA, USA); 2004.
- [318] Matsuzaki Y, Yasuda I. The poisoning effect of sulfur-containing impurity gas on a SOFC anode: Part I. Dependence on temperature, time, and impurity concentration. Solid State Ionics 2000;132:261–9.
- [319] Zhang L, Jiang SP, He HQ, Chen X, Ma J, Song XC. A comparative study of H_2S poisoning on electrode behavior of Ni/YSZ and Ni/GDC anodes of solid oxide fuel cells. nt J Hydro Energy 2010;35:12359–68.
- [320] Marina OA, Pedersen LR, Stevenson JW. Effect of sulfur and hydrocarbon fuels on titanate/ceria SOFC anodes. SECA Core Technology Program Peer Review. Tampa (FL, USA); 2005.
- [321] Kim Y, Son M, Lee I-B. Numerical study of a planar solid oxide fuel cell during heat-up and start-up operation. Indust Eng Chem Res 2011;50:1360–8.
- [322] Deng ZQ, Niu HJ, Kuang XJ, Allix M, Claridge JB, Rosseinsky MJ. Highly conducting redox stable pyrochlore oxides. Chem Mater 2008;20:6911–6.
- [323] Blundred GD, Bridges CA, Rosseinsky MJ. New oxidation states and defect chemistry in the pyrochlore structure. Angew Chem Int Ed 2004;43:3562–5.
- [324] Subramanian MA, Aravamudan G, Rao GVS. Oxide pyrochlores – a review. Prog Solid State Chem 1983;15:55–143.
- [325] Kramer SA, Tuller HL. A novel titanate-based oxygen ion conductor: $\text{Gd}_2\text{Ti}_2\text{O}_7$. Solid State Ionics 1995;82:15–23.
- [326] Haile SM, Wuensch BJ, Prince E. Neutron rietveld analysis of anion and cation disorder in the fast-ion conducting pyrochlore system $\text{Y}_2(\text{Zr}_{1-x})_2\text{O}_7$. Mater Res Soc Symp Proc 1990;166:81–6.
- [327] Shlyakhina AV, Kolbanov IV, Karyagina OK, Shcherbakova LG. Effect of heterovalent substitution on the electrical conductivity of $(\text{Yb}_{1-x}\text{M}_x)_2\text{Ti}_2\text{O}_7$ ($\text{M} = \text{Ca}, \text{Ba}; x = 0, 0.05, 0.1$). Inorg Mater 2006;42:528–31.
- [328] Kuang XJ, Allix M, Ibberson RM, Claridge JB, Niu HJ, Rosseinsky MJ. Oxygen vacancy ordering phenomena in the mixed-conducting hexagonal perovskite $\text{Ba}_7\text{Y}_2\text{Mn}_3\text{Ti}_2\text{O}_{20}$. Chem Mater 2007;19:2884–93.
- [329] Sprague JJ, Tuller HL. Mixed ionic and electronic conduction in Mn/Mo doped gadolinium titanate. J Euro Ceram Soc 1999;19:803–6.
- [330] Porat O, Heremans C, Tuller HL. Phase stability and electrical conductivity in $\text{Gd}_2\text{Ti}_2\text{O}_7$ – $\text{Gd}_2\text{Mo}_2\text{O}_7$ solid solutions. J Am Ceram Soc 1997;80:2278–84.
- [331] Marrero-López D, Peña-Martínez J, Ruiz-Morales JC, Gabás M, Núñez P, Aranda MAG, et al. Redox behaviour, chemical compatibility and electrochemical performance of $\text{Sr}_2\text{MgMoO}_{6-\delta}$ SOFC anode. Solid State Ionics 2010;180:1672–82.
- [332] Ivers-Tiffée E, Welsing W, Schießl M, Greiner H. Ceramic and metallic components for a planar SOFC. Berichte der Bunsen-Gesellschaft für Physikalische Chemie 1990;94:978–81.
- [333] Itoh H, Yamamoto T, Mori M. Configurational and electrical behavior of Ni-YSZ cermet with novel microstructure for solid oxide fuel cell anodes. J Electrochem Soc 1997;144:641–6.
- [334] Pratihar SK, Baus RN, Mazumder S, Maiti HS. Electrical conductivity and microstructure of Ni-YSZ anode prepared by liquid dispersion method. In: Singhal SC, Doktya M, editors. 6th international symposium on solid oxide fuel cells. Pennington (NJ), Honolulu (HI, USA): The Electrochemical Society; 1999. p. 513–21.
- [335] Lee JH, Moon H, Lee H-W, Kim JD, Kim J-D, Yoon K-H. Quantitative analysis of microstructure and its related electrical property of SOFC anode, Ni-YSZ cermet. Solid State Ionics 2002;148:15–26.
- [336] Ma Q, Ma J, Zhou S, Yan R, Gao J, Meng G. A high-performance ammonia-fueled SOFC based on a YSZ thin-film electrolyte. J Power Sour 2007;164:86–9.
- [337] Chen M, Kim BH, Xu Q, Nam OJ, Ko JH. Synthesis and performances of Ni-SDC cermets for IT-SOFC anode. J Euro Ceram Soc 2008;28:2947–53.
- [338] Mantzouris X, Triantafyllou G, Tietz F, Nikolopoulos P. Physical characterization of Y_2O_3 – CeO_2 – TiO_2 (YCT) mixed oxides and Ni/YCT cermets as anodes in solid oxide fuel cells. J Mater Sci 2008;43:7057–65.
- [339] Zhang Y, Huang X, Lu Z, Liu Z, Ge X, Xu J, et al. $\text{Ni-Sm}_{0.2}\text{Ce}_{0.8}\text{O}_{1.9}$ anode-supported YSZ electrolyte film and its application in solid oxide fuel cells. J Alloys Comp 2007;428:302–6.
- [340] Ding D, Li L, Feng K, Liu Z, Xia C. High performance Ni- Sm_2O_3 cermet anodes for intermediate-temperature solid oxide fuel cells. J Power Sour 2009;187:400–2.
- [341] He B, Ding D, Xia C. Ni-Ln_xO_y ($\text{Ln} = \text{La, Ce, Pr, Nd, Sm, Eu, and Gd}$) cermet anodes for intermediate-temperature solid oxide fuel cells. J Power Sour 2010;195:1359–64.
- [342] Zhen YD, Tok AIY, Jiang SP, Boey FYC. Fabrication and performance of gadolinia doped ceria based intermediate-temperature solid oxide fuel cells. J Power Sour 2008;178:69–74.
- [343] Suzuki T, Hasan Z, Funahashi Y, Yamaguchi T, Fujishiro Y, Awano M. Impact of anode microstructure on solid oxide fuel cells. Science 2009;325:852–5.
- [344] Mantzouris X, Triantafyllou G, Tietz F, Nikolopoulos P. Physical characterisation of Y_2O_3 – CeO_2 – TiO_2 (YCT) mixed oxides and Ni/YCT cermets as anodes in solid oxide fuel cells. J Mater Sci 2008;43:7057–65.
- [345] Nabae Y, Yamanaka I. Alloying effects of Pd and Ni on the catalysis of the oxidation of dry CH_4 in solid oxide fuel cells. Appl Catal A: Gen 2009;369:119–24.
- [346] Kim G, Lee S, Shin JY, Corre G, Irvine JTS, Vohs JM, et al. Investigation of the structural and catalytic requirements for high-performance SOFC anodes formed by infiltration of LSCM. Electrochim Solid-State Lett 2009;12:B48–52.

- [347] Cowin PI, Petit CTG, Lan R, Irvine JTS, Tao S. Recent progress in the development of anode materials for solid oxide fuel cells. *Adv Energy Mater* 2011;1:314–32.
- [348] Fu C, Chan SH, Liu Q, Ge X, Pasciak G. Fabrication and evaluation of Ni-GDC composite anode prepared by aqueous-based tape casting method for low-temperature solid oxide fuel cell. *Int J Hydro Energy* 2010;35:301–7.
- [349] Storjohann D, Daggett J, Sullivan NP, Zhu H, Kee RJ, Menzer S, et al. Fabrication and evaluation of solid-oxide fuel cell anodes employing reaction-sintered yttria-stabilized zirconia. *J Power Sour* 2009;193:706–12.
- [350] Bozza F, Polini R, Traversa E. High performance anode-supported intermediate temperature solid oxide fuel cells (IT-SOFCs) with $\text{La}_{0.8}\text{Sr}_{0.2}\text{Ga}_{0.8}\text{Mg}_{0.2}\text{O}_{3-\delta}$ electrolyte films prepared by electrophoretic deposition. *Electrochim Commun* 2009;11:1680–3.
- [351] Wang F-Y, Cheng S, Wan B-Z. Porous Ag-CGO cermets as anode materials for IT-SOFC using CO fuel. *Fuel Cells Bullet* 2008;2008:12–6.
- [352] Wang F-Y, Jung G-B, Su A, Chan S-H, Hao X, Chiang Y-C. Porous Ag- $\text{Ce}_{0.8}\text{Sm}_{0.2}\text{O}_{1.9}$ cermets as anode materials for intermediate temperature solid oxide fuel cells using CO fuel. *J Power Sour* 2008;185:862–6.
- [353] Ding J, Liu J, Guo W. Fabrication and study on $\text{Ni}_{1-x}\text{Fe}_x\text{O}$ -YSZ anodes for intermediate temperature anode-supported solid oxide fuel cells. *J Alloys Comp* 2009;480:286–90.
- [354] Wang K, Ran R, Shao Z. Methane-fueled IT-SOFCs with facile in situ inorganic templating synthesized mesoporous $\text{Sm}_{0.2}\text{Ce}_{0.8}\text{O}_{1.9}$ as catalytic layer. *J Power Sour* 2007;170:251–8.
- [355] Savanju CD, Irvine JTS. La-doped SrTiO_3 as anode material for IT-SOFC. *Solid State Ionics* 2011;192:491–3.
- [356] Ye X-F, Wang SR, Hu Q, Chen JY, Wen TL, Wen ZY. Improvement of Cu-CeO₂ anodes for SOFCs running on ethanol fuels. *Solid State Ionics* 2009;180:276–81.
- [357] Ye X-F, Wang SR, Hu Q, Wang ZR, Wen TL, Wen ZY. Improvement of multi-layer anode for direct ethanol solid oxide fuel cells. *Electrochim Commun* 2009;11:823–6.
- [358] Bozza F, Polini R, Traversa E. High performance anode-supported intermediate temperature solid oxide fuel cells (IT-SOFCs) with $\text{La}_{0.8}\text{Sr}_{0.2}\text{Ga}_{0.8}\text{Mg}_{0.2}\text{O}_{3-\delta}$ electrolyte films prepared by electrophoretic deposition. *Electrochim Commun* 2009;11:1680–3.
- [359] Zhan Z, Lee SI. Thin film solid oxide fuel cells with copper cermet anodes. *J Power Sour* 2010;195:3494–7.
- [360] Wang Z, Weng W, Cheng K, Du P, Shen G, Han G. Catalytic modification of Ni-Sm-doped ceria anodes with copper for direct utilization of dry methane in low-temperature solid oxide fuel cells. *J Power Sour* 2008;179:541–6.
- [361] Sin A, Kopnin E, Dubitsky Y, Zaopo A, Aricò AS, Rosa DL, et al. Performance and life-time behaviour of NiCu-CGO anodes for the direct electro-oxidation of methane in IT-SOFCs. *J Power Sour* 2007;164:1–430.
- [362] Bi ZH, Zhu JH. $\text{Cu}_{1-x}\text{Pd}_x/\text{CeO}_2$ impregnated cermet anodes for direct oxidation of methane in LaGaO_3 -electrolyte solid oxide fuel cells. *J Power Sour* 2010;195:3097–104.
- [363] Choi S, Wang J, Cheng Z, Liu M. Surface modification of Ni-YSZ using niobium oxide for sulfur-tolerant anodes in solid oxide fuel cells. *J Electrochem Soc* 2008;155:B449–54.
- [364] Mukundan R, Broska E, Garzon F. Sulfur tolerant anodes for SOFCs. *Electrochim Solid-State Lett* 2004;7:A5–7.
- [365] Marina O, Stevenson J. SOFC anode materials development at PNNL. Office of fossil energy fuel cell program annual report: office of fossil energy. U.S. Department of Energy; 2004. p. 90–2.
- [366] Li X, Zhao H, Xu N, Zhou X, Zhang C, Chen N. Electrical conduction behavior of La, Co co-doped SrTiO_3 perovskite as anode material for solid oxide fuel cells. *Int J Hydro Energy* 2009;34:6407–14.
- [367] Li X, Zhao H, Zhou X, Xu N, Xie Z, Chen N. Electrical conductivity and structural stability of La-doped SrTiO_3 with A-site deficiency as anode materials for solid oxide fuel cells. *Int J Hydro Energy* 2010;35:7913–8.
- [368] Li X, Zhao H, Gao F, Chen N, Xu N. La and Sc co-doped SrTiO_3 as novel anode materials for solid oxide fuel cells. *Electrochim Commun* 2008;10:1567–70.
- [369] Kurokawa H, Yang L, Jacobson CP, Jonghe LCD, Visco SJ. Y-doped SrTiO_3 based sulfur tolerant anode for solid oxide fuel cells. *J Power Sour* 2007;164:510–8.
- [370] Blennow P, Hagen A, Hansen KK, Wallenberg LR, Mogensen M. Defect and electrical transport properties of Nb-doped SrTiO_3 . *Solid State Ionics* 2008;179:2047–58.
- [371] Smith BH, Holler WC, Gross MD. Electrical properties and redox stability of tantalum-doped strontium titanate for SOFC anodes. *Solid State Ionics* 2011;192:383–6.
- [372] Zhao H, Gao F, Li X, Zhang C, Zhao Y. Electrical properties of yttrium doped strontium titanate with A-site deficiency as potential anode materials for solid oxide fuel cells. *Solid State Ionics* 2009;180:193–7.
- [373] Li X, Zhao H, Shen W, Gao F, Huang X, Li Y, et al. Synthesis and properties of Y-doped SrTiO_3 as an anode material for SOFCs. *J Power Sour* 2007;166:47–52.
- [374] Gao F, Zhao H, Li X, Cheng Y, Zhou X, Cui F. Preparation and electrical properties of yttrium-doped strontium titanate with B-site deficiency. *J Power Sour* 2008;185:26–31.
- [375] Li X, Zhao H, Gao F, Zhu Z, Chen N, Shen W. Synthesis and electrical properties of Co-doped $\text{Y}_{0.08}\text{Sr}_{0.92}\text{TiO}_{3-\delta}$ as a potential SOFC anode. *Solid State Ionics* 2008;179:1588–92.
- [376] Lu X, Pine TS, Mumina DR, Brouwer J. Modified Pechini synthesis and characterization of Y-doped strontium titanate perovskite. *Solid State Ionics* 2007;178:1195–9.
- [377] Kan H, Lee H. Enhanced stability of Ni-Fe/GDC solid oxide fuel cell anodes for dry methane fuel. *Catal Commun* 2010;12:36–9.
- [378] Rossmeisl J, Bessler WG. Trends in catalytic activity for SOFC anode materials. *Solid State Ionics* 2008;178:1694–700.
- [379] Lee S, Kim G, Vohs JM, Gorte RJ. SOFC anodes based on infiltration of $\text{La}_{0.3}\text{Sr}_{0.7}\text{TiO}_3$. *J Electrochim Soc* 2008;155:B1179–83.
- [380] Zha S, Tsang P, Cheng Z, Liu M. Electrical properties and sulfur tolerance of $\text{La}_{0.75}\text{Sr}_{0.25}\text{Cr}_{1-x}\text{Mn}_x\text{O}_3$ under anodic conditions. *J Solid State Chem* 2005;178:1844–50.
- [381] Bao W, Guan H, Cheng J. A new anode material for intermediate solid oxide fuel cells. *J Power Sour* 2008;175:232–7.
- [382] Tao S, Irvine JTS. Synthesis and characterization of $(\text{La}_{0.75}\text{Sr}_{0.25})\text{Cr}_{0.5}\text{Mn}_{0.5}\text{O}_{3-\delta}$, a redox-stable, efficient perovskite anode for SOFCs. *J Electrochim Soc* 2004;151:A252–9.

- [383] Raj ES, Irvine JTS. Synthesis and characterization of $(\text{Pr}_{0.75}\text{Sr}_{0.25})_{1-x}\text{Cr}_{0.5}\text{Mn}_{0.5}\text{O}_{3-\delta}$ as anode for SOFCs. *Solid State Ionics* 2010;180:1683–9.
- [384] Zhu X, Lü Z, Wei Bo, Chen K, Liu M, Huang X, et al. Fabrication and performance of membrane solid oxide fuel cells with $\text{La}_{0.75}\text{Sr}_{0.25}\text{Cr}_{0.5}\text{Mn}_{0.5}\text{O}_{3-d}$ impregnated anodes. *J Power Sour* 2010;195:1793–8.
- [385] Zhu X, Lü Z, Wei Bo, Liua M, Huanga X, Sua W. A comparison of $\text{La}_{0.75}\text{Sr}_{0.25}\text{Cr}_{0.5}\text{Mn}_{0.5}\text{O}_{3-d}$ and Ni impregnated porous YSZ anodes fabricated in two different ways for SOFCs. *Electrochim Acta* 2010;55:3932–8.
- [386] Zhu X, Lü Z, Wei B, Zhang Y, Huang X, Su W. Impregnated $\text{La}_{0.75}\text{Sr}_{0.25}\text{Cr}_{0.5}\text{Fe}_{0.5}\text{O}_{3-d}$ based anodes operating on H_2 , CH_4 and $\text{C}_2\text{H}_5\text{OH}$ fuels. *Electrochem Solid-State Lett* 2010;13:B91–4.
- [387] Zhu X, Lü Z, Wei Bo, Chena K, Liua M, Huanga X, et al. Enhanced performance of solid oxide fuel cells with Ni/CeO_2 modified $\text{La}_{0.75}\text{Sr}_{0.25}\text{Cr}_{0.5}\text{Mn}_{0.5}\text{O}_{3-d}$ anodes. *J Power Sour* 2009;190:326–30.
- [388] Lu XC, Zhu JH. Cu(Pd)-impregnated $\text{La}_{0.75}\text{Sr}_{0.25}\text{Cr}_{0.5}\text{Mn}_{0.5}\text{O}_{3-\delta}$ anodes for direct utilization of methane in SOFC. *Solid State Ionics* 2007;178:1467–75.
- [389] Madsen WKBD, Kobsiriphat W, Wang Y, Marks LD, Barnett SA. SOFC anode performance enhancement through precipitation of nanoscale catalysts. In: Eguchi K, Mizusaki J, Singhal SC, Yokokawa H, editors. 10th International symposium on solid oxide fuel cells. Pennington (NJ), Nara (Japan): The Electrochemical Society; 2007. p. 1339–48.
- [390] Kobsiriphat W, Madsen BD, Wang Y, Marks LD, Barnett SA. $\text{La}_{0.8}\text{Sr}_{0.2}\text{Cr}_{1-x}\text{Ru}_x\text{O}_{3-\delta}-\text{Gd}_{0.1}\text{Ce}_{0.9}\text{O}_{1.95}$ solid oxide fuel cell anodes: Ru precipitation and electrochemical performance. *Solid State Ionics* 2009;180:257–64.
- [391] Zhu X, Lü Z, Wei Bo, Liu M, Huang X, Su W. A comparison of $\text{La}_{0.75}\text{Sr}_{0.25}\text{Cr}_{0.5}\text{Mn}_{0.5}\text{O}_{3-d}$ and Ni impregnated porous YSZ anodes fabricated in two different ways for SOFCs. *Electrochim Acta* 2010;55:3932–8.
- [392] Zha S, Cheng Z, Liu MA. A sulfur-tolerant anode materials for SOFCs: $\text{Gd}_2\text{Ti}_{1.4}\text{Mo}_{0.6}\text{O}_7$. *Electrochem Solid-State Lett* 2005;8:A406–8.
- [393] Huang Y, Dass R, Xing Z, Goodenough J. Double perovskites as anode materials for solid oxide fuel cells. *Science* 2006;312:254–6.
- [394] Huang Y-H, Dass RI, Denyszyn JC, Goodenough JB. Synthesis and characterization of $\text{Sr}_2\text{MgMoO}_{6-d}$ an anode material for the solid oxide fuel cell. *J Electrochem Soc* 2006;153:A1266–72.
- [395] Aguadero A, Calle Cdl, Alonso JA, Pérez-Coll D, Escudero MJ, Daza L. Structure, thermal stability and electrical properties of $\text{Ca}(\text{V}_{0.5}\text{Mo}_{0.5})\text{O}_3$ as solid oxide fuel cell anode. *J Power Sour* 2009;192:78–83.
- [396] Hou S-e, Aguadero A, Alonso JA, Goodenough JB. Fe-based perovskites as electrodes for intermediate-temperature solid oxide fuel cells. *J Power Sour* 2011;196:5478–84.
- [397] Danilovic N, Luo J-L, Chuang KT, Sanger AR. $\text{Ce}_{0.9}\text{Sr}_{0.1}\text{VO}_x$ ($x = 3, 4$) as anode materials for H_2S -containing CH_4 fueled solid oxide fuel cells. *J Power Sour* 2009;192:247–57.
- [398] Wei T, Ji Y, Meng X, Zhang Y. $\text{Sr}_2\text{NiMoO}_{6-d}$ as anode material for LaGaO_3 based solid oxide fuel cell. *Electrochim Commun* 2008;10:1369–72.
- [399] Zheng Y, Zhang C, Ran R, Cai R, Shao Z, Farrusseng D. A new symmetric solid-oxide fuel cell with $\text{La}_{0.8}\text{Sr}_{0.2}\text{Sc}_{0.2}\text{Mn}_{0.8}\text{O}_{3-d}$ perovskite oxide as both the anode and cathode. *Acta Mater* 2009;57:1165–75.
- [400] Zhang P, Huang Y-H, Cheng J-G, Mao Z-Q, Goodenough JB. $\text{Sr}_2\text{CoMoO}_6$ anode for solid oxide fuel cell running on H_2 and CH_4 fuels. *J Power Sour* 2011;196:1738–43.
- [401] Vasala S, Lehtimäki M, Huang YH, Yamauchi H, Goodenough JB, Karppinen M. Degree of order and redox balance in B-site ordered double-perovskite oxides, $\text{Sr}_2\text{MMoO}_{6-d}$ ($\text{M} = \text{Mg}, \text{Mn}, \text{Fe}, \text{Co}, \text{Ni}, \text{Zn}$). *J Solid State Chem* 2010;183:1007–12.
- [402] Marrero-López D, Peña-Martínez J, Ruiz-Morales JC, Pérez-Coll D, Aranda MAG, Núñez P. Synthesis, phase stability and electrical conductivity of $\text{Sr}_2\text{MgMoO}_{6-d}$ anode. *Mater Res Bullet* 2008;43:2441–50.
- [403] Pechini MP. Method of preparing lead and alkaline earth titanates and niobates and coating method using the same to form a capacitor. In: Office USP, editor. USA; 1967.
- [404] Pujare NU, Semkow KW, Sammells AF. A direct $\text{H}_2\text{S}/\text{air}$ solid oxide fuel cell. *J Electrochem Soc* 1987;134:2639–40.
- [405] Pujare NU, Tsai KJ, Sammells AF. An electrochemical claus process for sulfur recovery. *J Electrochim Soc* 1989;136:3662–78.
- [406] Liu M, Wei G, Luo JL, Sanger AR, Chuang KT. Use of metal sulfides as anode catalysts in H_2S -air SOFCs. *J Electrochim Soc* 2003;150:A1025–9.
- [407] Wei G, Luo J, Sanger A, Chuang K. High-performance anode for H_2S -air SOFCs. *J Electrochim Soc* 2004;151:A232–7.
- [408] Xia C. Electrolytes. In: Fergus JW, Hui R, Li X, Wilkinson DP, Zhang J, editors. Solid oxide fuel cells: materials properties and performance. Boca Raton (FL, USA): CRC Press; Taylor & Francis Group; 2009.
- [409] Kharton VV, Marques FMB, Atkinson A. Transport properties of solid oxide electrolyte ceramics: a brief review. *Solid State Ionics* 2004;174:135–49.
- [410] Pérez-Coll D, Mather GC. Electrical transport at low temperatures in dense nanocrystalline Gd-doped ceria. *Solid State Ionics* 2010;181:20–6.
- [411] Malavasi L, Fisher CAJ, Islam MS. Oxide-ion and proton conducting electrolyte materials for clean energy applications: structural and mechanistic features. *Chem Soc Rev* 2010;39:4370–87.
- [412] Punn R, Feteira AM, Sinclair DC, Greaves C. Enhanced oxide ion conductivity in stabilized delta- Bi_2O_3 . *J Am Chem Soc* 2006;128:15386–7.
- [413] Basu RN. Materials for solid oxide fuel cells. New Delhi (India): Anamaya Publishers; 2007.
- [414] Etself TH, Flengas SN. The electrical properties of solid oxide electrolytes. *Chem Rev* 1970;70:339–76.
- [415] Takahashi T. Physics of electrolytes. London: Academic Press; 1972.
- [416] Taylor MA, Kilo M, Borchardt G, Weber S, Scherrer H. $\text{Zr}-96$ diffusion in polycrystalline scandia stabilized zirconia. *J Euro Ceram Soc* 2005;25:1591–5.
- [417] Badwal SPS, Ciacci FT. Oxygen-ion conducting electrolyte materials for solid oxide fuel cells. *Ionics* 2000;6:1–21.
- [418] Omar S, Najib WB, Bonanos N. Conductivity ageing studies on 1M10ScSZ ($\text{M}^{4+} = \text{Ce}, \text{Hf}$). *Solid State Ionics* 2011;189:100–6.
- [419] Jiang N, Wachsman ED. Structural stability and conductivity of phase-stabilized cubic bismuth oxides. *J Am Ceram Soc* 1999;82:3057–64.

- [420] Kilner JA, Waters CD. The effects of dopant cation-oxygen vacancy complexes on the anion transport properties of non-stoichiometric fluoride oxides. *Solid State Ionics* 1982;6:253–9.
- [421] Kilner JA, Steele BCH. Nonstoichiometric oxides. New York (USA): Academic Press; 1981.
- [422] Gelings Pj, Bouwmeester HJM. The CRC handbook of solid state electrochemistry. Boca Raton (FL, USA): CRC Press, Taylor and Francis Group; 1996.
- [423] Yahiro H, Eguchi K, Arai H. Electrical properties and reducibilities of ceria-rare earth oxide systems and their applications to solid oxide fuel cells. *Solid State Ionics* 1989;36:71–5.
- [424] Yahiro H, Eguchi Y, Eguchi K, Arai H. Oxygen ion conductivity of the ceria-samarium oxide system with fluorite structure. *J Appl Electrochem* 1988;18:527–31.
- [425] Eguchi K, Setoguchi T, Inoue T, Arai H. Electrical properties of ceria-based oxides and their application to solid oxide fuel cells. *Solid State Ionics* 1992;52:165–72.
- [426] Arachi Y, Sakai H, Yamamoto O, Takeda Y, Imanishi N. Electrical conductivity of the $ZrO_2-Ln_2O_3$ (Ln 1/4 lanthanides) system. *Solid State Ionics* 1999;12:133–9.
- [427] Molenda J, Swierczek K, Zaj W. Functional materials for the IT-SOFC. *J Power Sour* 2007;173:657–70.
- [428] Kharton VV, Naumovich EN, Vecher AA. Research on the electrochemistry of oxide ion conductors in the former Soviet Union. I. ZrO_2 based ceramic materials. *J Solid State Electrochem* 1999;3:61–81.
- [429] Nakamura A, Wagner JB. Defect structure, ionic conductivity and diffusion in calcia-stabilized zirconia. *J Electrochem Soc* 1980;127:2325–33.
- [430] Fergus JW. Electrolytes for solid oxide fuel cells. *J Power Sour* 2006;162:30–40.
- [431] Yamamoto O, Arachi Y, Sakai H, Takeda Y, Imanishi N, Mizutani Y, et al. Zirconia based oxide ion conductors for solid oxide fuel cells. *Ionics* 1998;4:403–8.
- [432] Inaba H, Tagawa H. Ceria based solid electrolytes. *Solid State Ionics* 1996;83:1–16.
- [433] Mogensen M, Sammes NM, Tompsett GA. Physical, chemical and electrochemical properties of pure and doped ceria. *Solid State Ionics* 2000;129:63–94.
- [434] Butler V. Dopant ion radius and ionic conductivity in cerium dioxide. *Solid State Ionics* 1983;8:109–13.
- [435] Kim D-J. Lattice parameters, ionic conductivities, and solubility limits in fluorite-structure MO_2 oxide [$M = Hf^{4+}, Zr^{4+}, Ce^{4+}, Th^{4+}, U^{4+}$] solid solutions. *J Am Ceram Soc* 1989;72:1415–21.
- [436] Kilner JA, Brook RJ. A study of oxygen ion conductivity in doped non-stoichiometric oxides. *Solid State Ionics* 1982;6:237–52.
- [437] Andersson DA, Simak SI, Skorodumova NV, Abrikosov IA, Johansson B. Optimization of ionic conductivity in doped ceria. *Proc Nat Acad Sci USA* 2006;103:3518–21.
- [438] Omar S, Wachsman ED, Nino JC. Higher conductivity Sm^{3+} and Nd^{3+} co-doped ceria-based electrolyte materials. *Solid State Ionics* 2008;178:1890–7.
- [439] Atkinson A. Chemically-induced stresses in gadolinium-doped ceria solid oxide fuel cell electrolytes. *Solid State Ionics* 1997;95:249–58.
- [440] Omar S, Nino JC. Consistency in the chemical expansion of fluorites: a thermal revision of the doped ceria. *Acta Mater* 2013;61:5406–13.
- [441] Sammes NM, Tompsett GA, Näfe H, Aldinger F. Bismuth based oxide electrolytes structure and ionic conductivity. *J Euro Ceram Soc* 1999;19:1801–26.
- [442] Marquesa FMB, Navarroa LM. Performance of double layer electrolyte cells Part II: GCO/YSZ, a case study. *Solid State Ionics* 1997;100:29–38.
- [443] Tsoga A, Gupta A, Naoumidis A, Skarmoutsos D, Nikolopoulos P. Performance of a double-layer CGO/YSZ electrolyte for solid oxide fuel cells. *Ionics* 1998;4:234–40.
- [444] Hrovat M, Ahmad-Khanlou A, Samardzija Z, Holc J. Interactions between lanthanum gallate based solid electrolyte and ceria. *Mater Res Bullet* 1999;34:2027–34.
- [445] Doshi R, Richards VL, Carter JD, Wang X, Krumpelt M. Development of solid oxide fuel cells that operate at 500 °C. *J Electrochem Soc* 1999;146:1273–8.
- [446] Liu J, Madsen BD, Ji Z, Barnett SA. A fuel-flexible ceramic-based anode for solid oxide fuel cells. *Electrochim Solid-State Lett* 2002;5–6:A122–4.
- [447] Xia C, Liu M. A simple and cost-effective approach to fabrication of dense ceramic membranes on porous substrates. *J Am Ceram Soc* 2001;84:1903–5.
- [448] Prabhakaran K, Beigh MO, Lakra J, Gokhale NM, Sharma SC. Characteristics of 8 mol% yttria stabilized zirconia powder prepared by spray drying process. *J Mater Process Technol* 2007;189:178–81.
- [449] Jiang YZ, Gao JF, Liu MF, Wang YY, Meng GY. Fabrication and characterization of Y_2O_3 stabilized ZrO_2 films deposited with aerosol-assisted MOCVD. *Solid State Ionics* 2007;177:3405–10.
- [450] Brahim C, Ringude A, Cassir M, Putkonen M, Niinisto L. Electrical properties of thin yttria-stabilized zirconia overlayers produced by atomic layer deposition for solid oxide fuel cell applications. *Appl Surf Sci* 2007;253:3962–8.
- [451] Ivanov VV, Lipilin AS, Kotov YA, Khrustov VR, Shkerin SN, Parani SN, et al. Formation of a thin-layer electrolyte for SOFC by magnetic pulse compaction of tapes cast of nanopowders. *J Power Sour* 2006;159:605–12.
- [452] Hirano M, Inagaki M, Mizutani Y, Nomura K, Kawai M, Nakamura Y. Mechanical and electrical properties of Sc_2O_3 -doped zirconia ceramics improved by postsintering with HIP. *Solid State Ionics* 2000;133:1–9.
- [453] Mizutani Y, Tamura M, Kawai M, Yamamoto O. Development of high-performance electrolyte in SOFC. *Solid State Ionics* 1994;72:271–5.
- [454] Tietz F. Thermal expansion of SOFC materials. *Ionics* 1999;5:129–39.
- [455] Badwal SPS, Ciacci FT, Milosevic D. Scandia-zirconia electrolytes for intermediate temperature solid oxide fuel cell operation. *Solid State Ionics* 2000;136–137:91–9.
- [456] Zhang TS, Ma J, Cheng H, Chan SH. Ionic conductivity of high-purity Gd-doped ceria solid solutions. *Mater Res Bullet* 2006;41:563–8.
- [457] Huang W, Shuk P, Greenblatt M. Properties of sol-gel prepared $Ce_{1-x}Sm_xO_2-x/2$ solid electrolytes. *Solid State Ionics* 1997;100:23–7.

- [458] Kharton VV, Figueiredo FM, Navarro L, Naumovich EN, Kovalevsky AV, Yaremchenko AA, et al. Ceria-based materials for solid oxide fuel cell. *J Mater Sci* 2001;36:1105–17.
- [459] Mogensen M, Lindegaard T, Hansen UR, Mogensen G. Physical properties of mixed conductor solid oxide fuel cell anodes of doped CeO_2 . *J Electrochem Soc* 1994;141:2122–34.
- [460] Seo DJ, Ryu KO, Park SB, Kim KY, Song RH. Synthesis and properties of $\text{Ce}_{1-x}\text{Gd}_x\text{O}_{2-x/2}$ solid solution prepared by flame spray pyrolysis. *Mater Res Bullet* 2006;41:359–66.
- [461] Herle JV, Horita T, Kawada T, Sakai N, Yokokawa H, Dokuya M. Low temperature fabrication of (Y, Gd, Sm)-doped ceria electrolyte. *Solid State Ionics* 1996;86–88:1255–8.
- [462] Huang W, Shuk P, Greenblatt M. Hydrothermal synthesis and properties of $\text{Ce}_{1-x}\text{Sm}_x\text{O}_{2-x/2}$ solid solutions. *Chem Mater* 1997;9:2240–5.
- [463] Xu HM, Yan HG, Chen ZH. Sintering and electrical properties of $\text{Ce}_{0.8}\text{Y}_{0.2}\text{O}_{1.9}$ powders prepared by citric acid-nitrate low temperature combustion process. *J Power Sour* 2006;163:409–14.
- [464] Zhu B. Fast ionic conducting film ceramic membranes with advanced applications. *Solid State Ionics* 1999;119:305–10.
- [465] Kimpton J, Randle TH, Drennan J. Investigation of electrical conductivity as a function dopant-ion radius in the systems $\text{Zr}_{0.75}\text{Ce}_{0.08}\text{M}_{0.17}\text{O}_{1.92}$ ($\text{M} = \text{Nd}, \text{Sm}, \text{Gd}, \text{Dy}, \text{Ho}, \text{Y}, \text{Er}, \text{Yb}, \text{Sc}$). *Solid State Ionics* 2002;149:89–98.
- [466] Liu Y, Li B, Wei X, Pan W. Citric-nitrate combustion synthesis and electrical conductivity of the Sm_{31} and Nd_{31} co-doped ceria electrolyte. *J Am Ceram Soc* 2008;91:3926–30.
- [467] Yasuda I, Matsuzaki Y, Yamakawa T, Koyama T. Electrical conductivity and mechanical properties of alumina-dispersed doped lanthanum gallates. *Solid State Ionics* 2000;135:381–8.
- [468] Stevenson JW, Armstrong TR, Pederson LR, Li J, Lewinsohn CA, Baskaran S. Effect of A-site cation nonstoichiometry on the properties of doped lanthanum gallate. *Solid State Ionics* 1998;113–115:571–83.
- [469] Stevenson JW, Hasinska K, Canfield NL, Armstrong TR. Influence of cobalt and iron additions on the electrical and thermal properties of $(\text{La}, \text{Sr})(\text{Ga}, \text{Mg})\text{O}_{3-\delta}$. *J Electrochem Soc* 2000;147:3213–8.
- [470] Nguyen TL, Dokuya M. Electrical conductivity, thermal expansion and reaction of $(\text{La}, \text{Sr})(\text{Ga}, \text{Mg})\text{O}_3$ and $(\text{La}, \text{Sr})\text{AlO}_3$ system. *Solid State Ionics* 2000;132:217–26.
- [471] Lybye D, Poulsen FW, Mogensen M. Conductivity of A- and B-site doped LaAlO_3 , LaGaO_3 , LaScO_3 and LaInO_3 perovskites. *Solid State Ionics* 2000;128:91–103.
- [472] Nomura K, Tanase S. Electrical conduction behavior in $(\text{La}_{0.9}\text{Sr}_{0.1})\text{M}^{\text{III}}\text{O}_{3-\delta}$ ($\text{M}^{\text{III}} = \text{Al}, \text{Ga}, \text{Sc}, \text{In}, \text{and Lu}$) perovskites. *Solid State Ionics* 1997;98:229–36.
- [473] Fujii H, Katayama Y, Shimura T, Iwahara H. Protonic conduction in perovskite-type oxide ceramics based on LnScO_3 ($\text{Ln} = \text{La}, \text{Nd}, \text{Sm}$ or Gd) at high temperature. *J Electroceram* 1998;2:119–25.
- [474] Mori M, Tompsett GM, Sammes NM, Suda E, Takeda Y. Compatibility of $\text{Gd}_x\text{Ti}_2\text{O}_7$ pyrochlores ($1.72 \leq x \leq 2.0$) as electrolytes in high-temperature solid oxide fuel cells. *Solid State Ionics* 2003;158:79–90.
- [475] Kharton VV, Tsipis EV, Yaremchenko AA, Vyshatko NP, Shaula AL, Naumovich EN, et al. Oxygen ionic and electronic transport in $\text{Gd}_{2-x}\text{Ca}_x\text{Ti}_2\text{O}_{7-d}$ pyrochlores. *J Solid State Electrochem* 2003;7:468–76.
- [476] Shaula AL, Kharton VV, Waerenborgh JC, Rojas DP, Tsipis EV, Vyshatko NP, et al. Transport properties and Mössbauer spectra of Fe-substituted $\text{La}_{10-x}(\text{Si}, \text{Al})_6\text{O}_{26}$ apatites. *Mater Res Bullet* 2004;39:763–73.
- [477] Kharton VV, Shaula AL, Patrakeev MV, Waerenborgh JC, Rojas DP, Vyshatko NP, et al. Oxygen ionic and electronic transport in apatite-type solid electrolytes. *J Electrochem Soc* 2004;151:A1236–46.
- [478] Marozau IP, Shaula AL, Kharton VV, Vyshatko NP, Viskup AP, Frade JR, et al. Transport properties and thermal expansion of $\text{La}_2\text{Mo}_2\text{O}_9$ -based solid electrolytes. *Mater Res Bullet* 2005;40:361–71.
- [479] Yaremchenko AA, Kharton VV, Naumovich EN, Marques FMB. Physicochemical and transport properties of BICUVOX-based ceramics. *J Electroceram* 2000;4:233–42.
- [480] Yaremchenko AA, Kharton VV, Naumovich EN, Tonoyan AA, Samokhval VV. Oxygen ionic transport in Bi_2O_3 -based oxides: II. The $\text{Bi}_2\text{O}_3\text{-ZrO}_2\text{-Y}_2\text{O}_3$ and $\text{Bi}_2\text{O}_3\text{-Nb}_2\text{O}_5\text{-Ho}_2\text{O}_3$ solid solutions. *J Solid State Electrochem* 1998;2:308–14.
- [481] Guo X, Waser R. Electrical properties of the grain boundaries of oxygen ion conductors: acceptor-doped zirconia and ceria. *Prog Mater Sci* 2006;51:151–210.
- [482] Aoki M, Chiang Y-M, Kosacki I, Lee LJ-R, Tuller H, Liu Y. Solute segregation and grain boundary impedance in high purity stabilized zirconia. *J Am Ceram Soc* 1996;79:1169–80.
- [483] Tuller HL. Ionic conduction in nanocrystalline materials. *Solid State Ionics* 2000;131:143–57.
- [484] Martin MC, Mecartney ML. Grain boundary ionic conductivity of yttrium stabilized zirconia as a function of silica content and grain size. *Solid State Ionics* 2003;161:67–79.
- [485] Mondal P, Klein A, Jaegermann W, Hahn H. Enhanced specific grain boundary conductivity in nanocrystalline Y_2O_3 -stabilized zirconia. *Solid State Ionics* 1999;118:331–9.
- [486] Tian C, Chan SW. Ionic conductivities, sintering temperatures and microstructures of bulk ceramic CeO_2 -doped with Y_2O_3 . *Solid State Ionics* 2000;134:89–102.
- [487] Guo X, Maier J. Grain boundary blocking effect in zirconia: a Schottky barrier analysis. *J Electrochem Soc* 2001;148:E121–6.
- [488] Badwal SPS, Rajendran S. Effect of micro- and nano-structures on the properties of ionic conductors. *Solid State Ionics* 1994;70–71:83–95.
- [489] Heijmans P, Indris S. Diffusion and ionic conduction in nanocrystalline ceramics. *J Phys: Cond Matter* 2003;15:R1257–89.
- [490] Badwal SPS. Grain boundary resistivity in zirconia-based materials: effect of sintering temperatures and impurities. *Solid State Ionics* 1995;76:67–80.
- [491] Singh V, Babu S, Singh A, Karakoti AS, Agarwal A, Seal S. Effect of submicron grains on ionic conductivity of nanocrystalline doped ceria. *J Nanosci Nanotechnol* 2010;10:1–9.
- [492] Yoshida H, Inagaki T. Effects of additives on the sintering properties of samaria-doped ceria. *J Alloys Comp* 2006;408–412:632–6.
- [493] Zhang TS, Ma J, Kong LB, Zeng ZQ, Hing P, Kilner JA. Final-stage sintering behavior of Fe-doped CeO_2 . *Mater Sci Eng: B*. 2003;103:177–83.

- [494] Jud E, Huwiler CB, Gauckler LJ. Sintering analysis of undoped and cobalt oxide doped ceria solid solutions. *J Am Ceram Soc* 2005;88:3013–9.
- [495] Zhang T, Hing P, Huang H, Kilner J. Sintering and grain growth of CoO-doped CeO₂ceramics. *J Euro Ceram Soc* 2002;22:27–34.
- [496] Kleinlogel C, Gauckler LJ. Sintering of nanocrystalline CeO₂ ceramics. *Adv Mater* 2001;13:1081–5.
- [497] Arunkumar P, Meena M, Babu KS. A review on cerium oxide-based electrolytes for IT-SOFC. *Nanomater Energy* 2012;1:288–305.
- [498] Ralph JM, Kilner JA, Steele BCH. Improving Gd-doped ceria electrolytes for low temperature solid oxide fuel cells. *Mater Res Soc Symp Proc* 2001;575:309.
- [499] Guo X. Effect of Nb₂O₅ on the space-charge conduction of Y₂O₃-stabilized ZrO₂. *Solid State Ionics* 1997;99:137–42.
- [500] Guo X. Space-charge conduction in yttria and alumina codoped-zirconia. *Solid State Ionics* 1997;96:247–54.
- [501] Dijk TV, Burggraaf AJ. Grain boundary effects on ionic conductivity in ceramic Gd_xZr_{1-x}O_{2-(x/2)} solid solutions. *Physica Status Solidi A: Appl Res* 1981;63:229–40.
- [502] Maier J. On the conductivity of polycrystalline materials. *Berichte der Bunsengesellschaft für physikalische Chemie* 1986;90:26–33.
- [503] Maier J. Ionic conduction in space charge regions. *Prog Solid State Chem* 1995;23:171–263.
- [504] Gerhardt R, Nowick AS, Mochel ME, Dumler I. Grain-boundary effect in ceria doped with trivalent cations: II, microstructure and microanalysis. *J Am Ceram Soc* 1986;69:647–51.
- [505] Gerhardt R, Nowick AS. Grain-boundary effect in ceria doped with trivalent cations: I. Electrical measurements. *J Am Ceram Soc* 1986;69:641–6.
- [506] Hong SJ, Mehta K, Virkar AV. Effect of microstructure and composition on ionic conductivity of rare-earth oxide-doped ceria. *J Electrochem Soc* 1998;145:638–47.
- [507] Hui R, Wang Z, Kesler O, Rose L, Jankovic J, Yick S, et al. Thermal plasma spraying for SOFCs: applications, potential advantages, and challenges. *J Power Sour* 2007;170:308–23.
- [508] Butler EP, Drennan J. Microstructural analysis of sintered high-conductivity zirconia with Al₂O₃ additions. *J Am Ceram Soc* 1982;65:474–8.
- [509] Zhang TS, Ma J, Chan SH, Hing P, Kilner JA. Intermediate-temperature ionic conductivity of ceria-based solid solutions as a function of gadolinia and silica contents. *Solid State Sci* 2004;6:565–72.
- [510] Zhang T, Zeng Z, Huang H, Hing P, Kilner J. Effect of alumina addition on the electrical and mechanical properties of Ce_{0.8}Gd_{0.2}O_{2-δ} ceramics. *Mater Lett* 2002;57:124–9.
- [511] Guo X, Tang C-Q, Yuan R-Z. Grain boundary ionic conduction in zirconia-based solid electrolyte with alumina addition. *J Euro Ceram Soc* 1995;15:25–32.
- [512] Ivanova D, Kovalevsk A, Kharton VV, Marques FMB. Silica-scavenging effects in ceria-based solid electrolytes. *Boletín de la Sociedad Española de Cerámica y Vidrio* 2008;47:201–6.
- [513] Cho YH, Cho P-S, Auchterlonie G, Kim DK, Lee J-H, Kim D-Y, et al. Enhancement of grain-boundary conduction in gadolinia-doped ceria by the scavenging of highly resistive siliceous phase. *Acta Mater* 2007;55:4807–15.
- [514] Rajendran S, Drennan J, Badwal SPS. Effect of alumina additions on the grain boundary and volume resistivity of tetragonal zirconia polycrystals. *J Mater Sci Lett* 1987;14:31–4.
- [515] Lee J-H, Mori T, Li J-G, Ikegami T, Komatsu M, Haneda H. Improvement of grain-boundary conductivity of 8 mol% yttria-stabilized zirconia by precursor scavenging of siliceous phase. *J Electrochem Soc* 2000;147:2822–9.
- [516] Lee J-H, Mori T, Li J-G, Ikegami T, Komatsu M, Haneda H. Imaging secondary-ion mass spectroscopy observation of the scavenging of siliceous film from 8-mol%-yttria-stabilized zirconia by the addition of alumina. *J Am Ceram Soc* 2000;83:1273–5.
- [517] Zhang TS, Ma J, Chan SH, Kilner JA. Improvements in sintering behavior and grain-boundary conductivity of ceria-based electrolytes by a small addition of Fe₂O₃. *J Electrochem Soc* 2004;151:J84–90.
- [518] Zhang TS, Ma J, Leng YJ, Chan SH, Hing P, Kilner JA. Effect of transition metal oxides on densification and electrical properties of Si-containing Ce_{0.8}Gd_{0.2}O_{2-d} ceramics. *Solid State Ionics* 2004;168:187–95.
- [519] Jurado JR. Present several items on ceria-based ceramic electrolytes: synthesis, additive effects, reactivity and electrochemical behaviour. *J Mater Sci* 2001;36:1133–9.
- [520] Pérez-Coll D, Núñez P, Abrantes JCC, Fagg DP, Kharton VV, Frade JR. Effects of firing conditions and addition of Co on bulk and grain boundary properties of CGO. *Solid State Ionics* 2005;176:2799–805.
- [521] Pérez-Coll D, Marrero-López D, Núñez P, Piñol S, Frade JR. Grain boundary conductivity of Ce_{0.8}Ln_{0.2}O_{2-δ} ceramics (Ln = Y, La, Gd, Sm) with and without Co-doping. *Electrochim Acta* 2006;51:6463–9.
- [522] Lane JA, Neff JL, Christie GM. Mitigation of the deleterious effect of silicon species on the conductivity of ceria electrolytes. *Solid State Ionics* 2005;177:1911–5.
- [523] Jung Y-S, Lee J-H, Lee J-H, Kim D-Y. Improvement of grain-boundary conduction in 15 mol% calcia-stabilized zirconia by postsintering heat-treatment. *J Electrochem Soc* 2003;150:J49–53.
- [524] Shuk P, Wiemhofer H-D, Guth U, Gijpeld W, Greenblatt M. Oxide ion conducting solid electrolytes based on Bi₂O₃. *Solid State Ionics* 1996;89:179–96.
- [525] Kharton VV, Naumovich EN, Yaremchenko AA, Marques FMB. Research on the electrochemistry of oxygen ion conductors in the former Soviet Union: IV Bismuth oxide based ceramics. *J Solid State Electrochem* 2001;5:160–87.
- [526] Boyapati S, Wachsman ED, Chakoumakos BC. Neutron diffraction study of occupancy and positional order of oxygen ions in phase stabilized cubic bismuth oxides. *Solid State Ionics* 2001;138:293–304.
- [527] Takahashi T, Iwahara H, Nagai Y. High oxide ion conduction in sintered Bi₂O₃ containing SrO, CaO or Sr₂O₃. *J Appl Electrochem* 1972;2:97–104.
- [528] Boyapati S, Wachsman ED, Jiang N. Effect of oxygen sublattice ordering on interstitial transport mechanism and conductivity activation energies in phase-stabilized cubic bismuth oxides. *Solid State Ionics* 2001;140:149–60.
- [529] Battle PD, Catlow CRA, Drennan J, Murray AD. The structural properties of the oxygen conducting δ phase of Bi₂O₃. *J Phys C: Solid State Phys* 1983;16:L561–6.

- [530] Jiang N, I RMB, Stevenson DA, Nix WD, Li J-Z, Yang J-L. Anion ordering in aged stabilized bismuth oxide. *Mater Lett* 1995;22:215–9.
- [531] Takahashi T, Esaka T, Iwahara H. Conduction in Bi_2O_3 -based oxide ion conductor under low oxygen pressure. II. Determination of the partial electronic conductivity. *J Appl Electrochem* 1977;7:303–8.
- [532] Takahashi T, Iwahara H, Esaka T. High oxide ion conduction in sintered oxide of the system Bi_2O_3 – M_2O_5 . *J Electrochem Soc* 1977;124:1563–9.
- [533] Takahashi T, Iwahara H, Arao T. High oxide ion conduction in sintered oxides of the system Bi_2O_3 – Y_2O_3 . *J Appl Electrochem* 1975;5:187–95.
- [534] Takahashi T, Iwahara H. Oxide ion conductors based on bismuth sesquioxide. *Mater Res Bullet* 1978;13:1447–53.
- [535] Takahashi T, Esaka T, Iwahara H. High oxide ion conduction in the sintered oxides of the system Bi_2O_3 – Gd_2O_3 . *J Appl Electrochem* 1975;5:197–202.
- [536] Takahashi T, Yamamoto O. Solid-state ionics-solid electrolyte cells with copper ion conductors. *J Appl Electrochem* 1977;7:37–43.
- [537] Verkerk MJ, Burggraaf AJ. High oxygen ion conduction in sintered oxides of the Bi_2O_3 – Dy_2O_3 System. *J Electrochem Soc* 1981;128:75–82.
- [538] Kharton VV, Marques FMB, Kilner JA, Atkinson A. Oxygen ion-conducting materials. Wiley-VCH Verlag GmbH & Co., KGaA; Berlin (Germany); 2009.
- [539] Jiang N, Wachsman ED, Jung S-H. A higher conductivity Bi_2O_3 -based electrolyte. *Solid State Ionics* 2002;150:347–53.
- [540] Verkerk MJ, Keizer K, Burggraaf AJ. High oxygen ion conduction in sintered oxides of the Bi_2O_3 – Er_2O_3 system. *J Appl Electrochem* 1980;10:81–90.
- [541] Kruidhof H, Bouwmeester HJM, Vries KJd, Gellings PJ, Burggraaf AJ. Thermochemical stability and nonstoichiometry of erbia-stabilized bismuth oxide. *Solid State Ionics* 1992;50:181–6.
- [542] Takahashi T, Esaka T, Iwahara H. Conduction in Bi_2O_3 -based oxide ion conductors under low oxygen pressure. I. Current blackening of the Bi_2O_3 – Y_2O_3 -electrolyte. *J Appl Electrochem* 1977;7:299–302.
- [543] Yaremenko AA, Kharton VV, Naumovich EN, Tonoyan AA. Stability of δ - Bi_2O_3 -based solid electrolytes. *Mater Res Bullet* 2000;35:515–20.
- [544] Park J-Y, Yoon H, Wachsman ED. Fabrication and characterization of high-conductivity bilayer electrolytes for intermediate-temperature solid oxide fuel cells. *J Am Ceram Soc* 2005;88:2402–8.
- [545] Abraham F, Boivin JC, Mairesse G, Nowogrocki G. The BIMEVOX series: a new family of high performances oxide ion conductors. *Solid State Ionics* 1990;40–41:934–7.
- [546] Paszak G, Prociow K, Mielcarek W, Gornicka B, Mazurek B. Solid electrolytes for gas sensors and fuel cells applications. *J Euro Ceram Soc* 2001;21:1867–70.
- [547] Lazure S, Vernochet C, Vannier RN, Nowogrocki G, Mairesse G. Composition dependence of oxide anion conduction in the BIMEVOX family. *Solid State Ionics* 1996;90:117–23.
- [548] Krok F, Abrahams I, Malys M, Bogusz W, Dygas JR, Nelstrop JAG, et al. Structural and electrical consequences of high dopant levels in the BIMEVOX system. *Solid State Ionics* 2000;136–137:119–25.
- [549] Pirovano C, Vannier RN, Capoen E, Nowogrocki G, Boivin JC, Mairesse G, et al. Characterisation of the electrode–electrolyte BIMEVOX system for oxygen separation. Part I. In situ synchrotron study. *Solid State Ionics* 2003;159:167–79.
- [550] Vannier RN, Mairesse G, Abraham F, Nowogrocki G. Double substitutions in $\text{Bi}_4\text{V}_2\text{O}_{11}$. *Solid State Ionics* 1994;70–71:248–52.
- [551] Pernot E, Anne M, Bacmann M, Strobe P, Fouletier J, Vannier RN, et al. Structure and conductivity of Cu and Ni-substituted $\text{Bi}_4\text{V}_2\text{O}_{11}$ compounds. *Solid State Ionics* 1994;70/71:259–63.
- [552] Mairesse G, Boivin JC, Lagrange G, Cocolios P. International patent application PCT WO 94/06544; 1994.
- [553] Wachsman ED, Jayaweera P, Jiang N, Lowe DM, Pound BG. Stable high conductivity ceria/bismuth oxide bilayered electrolytes. *J Electrochem Soc* 1997;144:233–6.
- [554] Williford RE, Weber WJ. Cation vacancy energetics in the gadolinium titanate/zirconate system. *J Am Ceram Soc* 1999;82:3266–8.
- [555] Kramer SA, Tuller HL. A novel titanate-based oxygen ion conductor: $\text{Gd}_2\text{Ti}_2\text{O}_7$. *Solid State Ionics* 1995;82:15–23.
- [556] Dijk MPV, Vries KJd, Burggraaf AJ. Oxygen ion and mixed conductivity in compounds with the fluorite and pyrochlore structure. *Solid State Ionics* 1983;9–10:913–20.
- [557] Yamaguchi S, Kobayashi K, Abe K, Yamazaki S, Iguchi Y. Electrical conductivity and thermoelectric power measurements of $\text{Y}_2\text{Ti}_2\text{O}_7$. *Solid State Ionics* 1998;113–115:393–402.
- [558] Wuensch BJ, Eberman KW. Order-disorder phenomena in $\text{A}_2\text{B}_2\text{O}_7$ pyrochlore oxides. *J Min Metals Mater Soc* 2000;52:19–21.
- [559] Dijk MPV, Vries KJd, Burggraaf AJ. Electrical conductivity and defect chemistry of the system $(\text{Tb}_x\text{Gd}_{1-x})_2\text{Zr}_2\text{O}_{7+y}$ ($0 \leq x \leq 1$; $0 \leq y \leq 0.25$). *Solid State Ionics* 1985;16:211–24.
- [560] Yu T-H, Tuller HL. Electrical conduction and disorder in the pyrochlore system $(\text{Gd}_{1-x}\text{Ca}_x)_2\text{Sn}_2\text{O}_7$. *J Electroceram* 1998;2:49–55.
- [561] Minervini L, Grimes RW, Sickafus KE. Disorder in pyrochlore oxides. *J Am Ceram Soc* 2000;83:1873–8.
- [562] Pirzada M, Grimes RW, Minervini L, Maguire JF, Sickafus KE. Oxygen migration in $\text{A}_2\text{B}_2\text{O}_7$ pyrochlores. *Solid State Ionics* 2001;140:201–8.
- [563] Lian J, Wang L, Chen J, Sun K, Ewing RC, Farmer JM, et al. The order-disorder transition in ion-irradiated pyrochlore. *Acta Mater* 2003;51:1493–502.
- [564] Subramanian MA, Aravamudan G, Rao GVS. Oxide pyrochlores – a review. *Prog Solid State Chem* 1983;15:55–143.
- [565] Wuensch BJ, Eberman KW, Heremans C, Ku EM, Onnerud P, Yeo EME, et al. Connection between oxygen-ion conductivity of pyrochlore fuel-cell materials and structural change with composition and temperature. *Solid State Ionics* 2000;129:111–33.
- [566] Moon PK, Tuller HL. Ionic conduction in the $\text{Gd}_2\text{Ti}_2\text{O}_7$ and $\text{Gd}_2\text{Zr}_2\text{O}_7$ system. *Solid State Ionics* 1988;28–30:470–4.
- [567] Wilde PJ, Catlow CRA. Molecular dynamics study of the effect of doping and disorder on diffusion in gadolinium zirconate. *Solid State Ionics* 1998;112:185–95.

- [568] Wilde PJ, Catlow CRA. Defects and diffusion in pyrochlore structured oxides. *Solid State Ionics* 1998;112:173–83.
- [569] Williford RE, Waber WJ, Devanathan R, Gale JD. Effects of cation disorder on oxygen vacancy migration in $Gd_2Ti_2O_7$. *J Electroceram* 1999;3:409–24.
- [570] Kramer S, Spears M, Tuller HL. Conduction in titanate pyrochlores: role of dopants. *Solid State Ionics* 1994;72:59–66.
- [571] Virkar AV. Theoretical analysis of solid oxide fuel cells with two-layer, composite electrolytes: electrolyte stability. *J Electrochem Soc* 1991;138:1481–7.
- [572] Wachsman ED, Jayaweera P, Jiang N, Lowe DM, Pound BG. Stable high conductivity functionality gradient bilayered solid oxide electrolytes and membranes. *J Electrochem Soc* 1997;95:24–237.
- [573] Suzuki T, Funahashi Y, Yamaguchi T, Fujishiro Y, Awano M. Improvement of micro tubular SOFCs using multilayered electrolyte. *ECS Trans* 2008;16:165–70.
- [574] Zhonghe B, Bao-lian Y, Mo-jie C. Intermediate temperature SOFC with multi-layer electrolyte. *Battery Bimonthly* 2005;01:10–1.
- [575] Han M, Tang X, Yin H, Peng S. Fabrication, microstructure and properties of a YSZ electrolyte for SOFCs. *J Power Sour* 2007;165:757–63.
- [576] Chen Y, Omar S, Keshri AK, Balani K, Babu K, Nino JC, et al. Ionic conductivity of plasma-sprayed nanocrystalline yttria-stabilized zirconia electrolyte for solid oxide fuel cells. *Scripta Mater* 2009;60:1023–6.
- [577] Balani K. Solid electrolytes: emerging global competitors for satisfying energy needs. *Nanomater Energy* 2012;1:243–6.
- [578] Visco SJ, Jacobson C, Jonghe LCD. High performance SOFCs at temperature below 700 °C. In: Singhal SC, Dokiya M, editors. 6th International symposium on solid oxide fuel cells. Pennington (NJ), Honolulu (HI, USA): The Electrochemical Society; 1999. p. 861–8.
- [579] Honegger K, Kruschwitz R, Keller M, Christie GM. Performance of SOFC stacks operated with CH_4 at reduced temperatures. In: Singhal SC, Dokiya M, editors. 6th International symposium on solid oxide fuel cells. Pennington (NJ), Honolulu (HI, USA): The Electrochemical Society; 1999. p. 1019–26.
- [580] Godicke M, Gauckler LJ. Engineering of solid oxide fuel cells with ceria-based electrolytes. *J Electrochem Soc* 1998;145:414–21.
- [581] Kleinlogel C, Godicke M, Honegger K, Gauckler LJ. Solid oxide fuel cells operating with cathode supported thin film electrolyte. In: Ramanarayanan TA, Worrell WL, Tuller HL, Khandkar AC, Mogensen M, Gopel W, editors. 3rd International symposium on ionic and mixed conducting ceramics. Pennington, (NJ), Paris, (France): The Electrochemical Society; 1997. p. 97–105.
- [582] Peredinis D, Gauckler JD. Solid oxide fuel cells with YSZ films prepared using spray pyrolysis. In: Singhal SC, Dokiya M, editors. 8th International symposium on solid oxide fuel cells. Pennington (NJ), Paris (France): The Electrochemical Society; 2003. p. 970–5.
- [583] Peredinis D, Honegger K, Gauckler LJ. Deposition of thin YSZ films by spray pyrolysis. In: McEvoy AJ, editor. Proceedings of 4th European solid oxide fuel cell forum. Lucerne (Switzerland): The European Fuel Cell Forum; 2000. p. 819–24.
- [584] Holtappels P, Graule T, Gut B, Vogt U, Gauckler L, Jörger M, et al. Fabrication and performance of anode supported solid oxide fuel cells. In: Singhal SC, Dokiya M, editors. 8th International symposium on solid oxide fuel cells. Pennington (NJ), Paris (France): The Electrochemical Society; 2003. p. 1003–10.
- [585] Peredinis D, Gauckler LJ. Solid oxide fuel cells with electrolytes prepared via spray pyrolysis. *Solid State Ionics* 2004;166:229–39.
- [586] Yamaguchi T, Shimizu S, Suzuki T, Fujishiro Y, Awano m. Evaluation of micro LSM-supported GDC/ScSZ bilayer electrolyte with LSM–GDC activation for intermediate temperature SOFCs. *J Electrochem Soc* 2008;155:B423–6.
- [587] Matsuda M, Hosomi T, Murata K, Fukui T, Miyake M. Fabrication of bilayered YSZ/SDC electrolyte film by electrophoretic deposition for reduced-temperature operating anode-supported SOFC. *J Power Sour* 2007;165:102–7.
- [588] Chockalingam R, Amarakoon VRW, Giesche H. Alumina/cerium oxide nano-composite electrolyte for solid oxide fuel cell applications. *J Euro Ceram Soc* 2008;28:959–63.
- [589] Mishima Y, Mitsuyasu H, Ohtaki M, Eguchi K. Solid oxide fuel cell with composite electrolyte consisting of samaria-doped ceria and yttria-stabilized zirconia. *J Electrochem Soc* 1998;145:1004–7.
- [590] Liu YH, Yin CQ, Wang LH, Li DB, Lian JS, Hu JD, et al. Properties of a ceria-based ($Ce_6S_2G_2$) solid oxide electrolyte sintered with Al_2O_3 additive. *Sci Sint* 2008;40:13–20.
- [591] Huang J, Yuan J, Mao Z, Sundén B. Analysis and modeling of novel low-temperature SOFC with a co-ionic conducting ceria-based composite electrolyte. *J Fuel Cell Sci Technol* 2010;7:011012–7.
- [592] Kim S-G, Yoon SP, Nam SW, Hyun S-H, Hong S-A. Fabrication and characterization of a YSZ/YDC composite electrolyte by a sol-gel coating method. *J Power Sour* 2002;110:222–8.
- [593] Liu W, Liu Y, Li B, Sparks TD, Wei X, Pan W. Ceria (Sm^{3+} , Nd^{3+})/carbonates composite electrolytes with high electrical conductivity at low temperature. *Compos Sci Technol* 2010;70:181–5.
- [594] Matsuda M, Hosomia T, Murata K, Fukui T, Miyake M. Fabrication of bilayered YSZ/SDC electrolyte film by electrophoretic deposition for reduced-temperature operating anode-supported SOFC. *J Power Sour* 2007;165:102–7.
- [595] Horita T, Sakai N, Yokokawa H, Dokiya M, Kawada T, Herle JV, et al. Ceria-zirconia composite electrolyte for solid oxide fuel cells. *J Electroceram* 1997;2:155–64.
- [596] Wang LS, Barnett SA. Sputter-deposited medium-temperature solid oxide fuel cells with multi-layer electrolytes. *Solid State Ionics* 1993;61:273–6.
- [597] Wang Y, An L, Saraf LV, Wang CM, Shutthanandan V, McCready DE, et al. Microstructure and ionic conductivity of alternating-multilayer structured Gd-doped ceria and zirconia thin films. *J Mater Sci* 2009;44:2021–6.
- [598] Sata N, Eberman K, Eberl K, Maier J. Mesoscopic fast ion conduction in nanometre-scale planar heterostructures. *Nature* 2000;408:21–8.
- [599] Azad S, Marina OA, Wang CM, Saraf L, Shutthanandan V, McCready DE, et al. Nanoscale effects on ion conductance of layer-by-layer structures of gadolinia-doped ceria and zirconia. *Appl Phys Lett* 2005;86:131906.
- [600] Hui SR, Roller J, Yick S, Zhang X, Decès-Petit C, Xie Y, et al. A brief review of the ionic conductivity enhancement for selected oxide electrolytes. *J Power Sour* 2007;172:493–502.

- [601] Ishihara T, Matsuda H, Takita Y. Doped LaGaO_3 perovskite type oxide as a new oxide ionic conductor. *J Am Chem Soc* 1994;116:3801–3.
- [602] Feng M, Goodenough JB. A superior oxide-ion electrolyte. *Euro Solid State Inorg Chem* 1994;T31:663–72.
- [603] Cherry M, Islam MS, Catlow CRA. Oxygen ion migration in perovskite-type oxides. *J Solid State Chem* 1995;118:125–32.
- [604] Khan MS, Islam MS, Bates DR. Dopant substitution and ion migration in the LaGaO_3 -based oxygen ion conductor. *J Phys Chem B* 1998;102:3099–104.
- [605] Lerch M, Boysen H, Hansen T. High-temperature neutron scattering investigation of pure and doped lanthanum gallate. *J Phys Chem Solids* 2001;62:445–55.
- [606] Gunter MM, Boysen H, Corte C, Lerch M, Suard E. In-situ investigation of oxygen diffusion in Sr-, Mg-doped LaGaO_3 superionic conductors with a simultaneously applied electric field. *Zeitschrift für Kristallographie*. 2005;220:218–224.
- [607] Souza RAD, Maier J. A computational study of cation defects in LaGaO_3 . *Phys Chem Chem Phys* 2003;5:740–8.
- [608] Anderson HU. Review of *p*-type doped perovskite materials for SOFC and other applications. *Solid State Ionics* 1992;52:33–41.
- [609] Yamamoto O, Takeda Y, Kanno R, Noda M. Perovskite-type oxides as oxygen electrodes for high temperature oxide fuel cells. *Solid State Ionics* 1987;22:241–6.
- [610] Tejura LG, Fierro JLG, Tascon JMD. Structure and reactivity of perovskite-type oxides. *Adv Catal* 1989;36:237–328.
- [611] Yamazoe N, Teraoka Y. Oxidation catalysis of perovskites—relationships to bulk structure and composition (valancy, defect, etc.). *Catal Today* 1990;8:175–99.
- [612] McCarty JG, Wise H. Perovskite catalysis for methane combustion. *Catal Today* 1990;8:231–48.
- [613] Alcock CB, Carberry JJ, Doshi R, Gunasekaran N. Methane coupling on oxide solid solution catalysis. *J Catal* 1993;143:533–8.
- [614] Salomonsson P, Griffin T, Kasemo B. Oxygen desorption and oxidation-reduction kinetics with methane and carbon monoxide over perovskite type metal oxide catalysts. *Appl Catal A: Gen* 1993;104:175–97.
- [615] Marti PE, Baiker A. Influence of the A-site cation in $\text{AMnO}_{3-\delta}$ and $\text{AFeO}_{3-\delta}$ ($\text{A} = \text{La, Pr, Nd and Gd}$) perovskite-type oxides on the catalytic activity for methane combustion. *Catal Lett* 1994;26:71–84.
- [616] Islam MS, Davies RA. Atomistic study of dopant site-selectivity and defect association in the lanthanum gallate perovskite. *J Mater Chem* 2004;14:86–93.
- [617] Drennan J, Zelizko V, Hay D, Ciacchi FT, Rajendran S, Badwal SPS. Characterisation, conductivity and mechanical properties of the oxygen-ion conductor $\text{La}_{0.8}\text{Sr}_{0.1}\text{Ga}_{0.8}\text{Mg}_{0.2}\text{O}_{3-\delta}$. *J Mater Chem* 1997;7:79–83.
- [618] Haavik C, Ottesen EM, Nomura K, Kilner JA, TN. Temperature dependence of oxygen ion transport in Sr plus Mg-substituted LaGaO_3 (LSGM) with varying grain sizes. *Solid State Ionics* 2004;174:233–43.
- [619] Slater PR, Irvine JTS, Ishihara T, Takita Y. High-temperature powder neutron diffraction study of the oxide ion conductor $\text{La}_{0.9}\text{Sr}_{0.1}\text{Ga}_{0.8}\text{Mg}_{0.2}\text{O}_{2.85}$. *J Solid State Chem* 1998;139:135–43.
- [620] Kajitani M, Matsuda M, Hoshikawa A, Harjo S, Kamiyama T, Ishigaki T, et al. In situ neutron diffraction study on fast oxide ion conductor LaGaO_3 -based perovskite compounds. *Chem Mater* 2005;17:4235–43.
- [621] Hayashi H, Inaba H, Matsuyama M, Lan NG, Dokuya M, Tagawa H. Structural consideration on the ionic conductivity of perovskite-type oxides. *Solid State Ionics* 1999;122:1–15.
- [622] Ishihara T, Akbay T, Furutani H, Takita Y. Improved oxide ion conductivity of Co doped $\text{La}_{0.8}\text{Sr}_{0.2}\text{Ga}_{0.8}\text{Mg}_{0.2}\text{O}_3$ perovskite type oxide. *Solid State Ionics* 1998;113–115:585–91.
- [623] Trofimenko N, Ullmann H. Transition metal doped lanthanum gallates. *Solid State Ionics* 1999;118:215–27.
- [624] Kharton VV, Viskup AP, Yaremchenko AA, Baker RT, Gharbage B, Mather GC, et al. Ionic conductivity of $\text{La}(\text{Sr})\text{Ga}(\text{Mg},\text{M})\text{O}_{3-\delta}$ ($\text{M} = \text{Ti, Cr, Fe, Co, Ni}$): effects of transition metal dopants. *Solid State Ionics* 2000;132:119–30.
- [625] Djurado E, Labeau M. Second phases in doped lanthanum gallate perovskites. *J Euro Ceram Soc* 1998;18:1397–404.
- [626] Yamaji K, Horita T, Ishikawa M, Sakai N, Yokokawa H. Chemical stability of the $\text{La}_{0.9}\text{Sr}_{0.1}\text{Ga}_{0.8}\text{Mg}_{0.2}\text{O}_{2.85}$ electrolyte in a reducing atmosphere. *Solid State Ionics* 1999;121:217–24.
- [627] Nguyen TL, Dokuya M, Wang S, Tagawa H, Hashimoto T. The effect of oxygen vacancy on the oxide ion mobility in LaAlO_3 -based oxides. *Solid State Ionics* 2000;130:229–41.
- [628] Takahashi T, Iwahara H. Ionic conduction in perovskite-type oxide solid solution and its application to the solid electrolyte fuel cell. *Energy Conversion*. 1971;11:105–11.
- [629] Mizusaki J, Yasuda I, Shimoyama J-i, Yamauchi S, Fueki K. Electrical conductivity, defect equilibrium and oxygen vacancy diffusion coefficient of $\text{La}_{1-x}\text{Ca}_x\text{AlO}_{3-d}$ single crystals. *J Electrochem Soc* 1993;140:467–71.
- [630] Ishihara T, Matsuda H, Takita Y. Oxide ion conductivity in doped NdAlO_3 perovskite-type oxides. *J Electrochem Soc* 1994;141:3444–9.
- [631] Anderson PS, Marques FMB, Sinclair DC, West AR. Ionic and electronic conduction in $\text{La}_{0.95}\text{Sr}_{0.05}\text{GaO}_{3-\delta}$, $\text{La}_{0.95}\text{Sr}_{0.05}\text{AlO}_{3-\delta}$ and $\text{Y}_{0.95}\text{Sr}_{0.05}\text{AlO}_{3-\delta}$. *Solid State Ionics* 1999;118:229–39.
- [632] Fagg DP, Kharton VV, Frade JR. P-type electronic transport in $\text{Ce}_{0.8}\text{Gd}_{0.2}\text{O}_{2-\delta}$: the effect of transition metal oxide sintering aids. *J Electroceram* 2002;9:199–207.
- [633] He H, Huang X, Chen L. Sr-doped LaInO_3 and its possible application in a single layer SOFC. *Solid State Ionics* 2000;130:183–93.
- [634] Yamamura H, Yamazaki K, Kakinuma K, Nomura K. The relationship between crystal structure and electrical conductivity in the $\text{LaY}_{1-x}\text{In}_x\text{O}_3$ ($x = 0.0–0.7$) system. *Solid State Ionics* 2002;150:255–61.
- [635] Thangadurai V, Weppner W. Synthesis and electrical properties of K and Pr-substitutes LaGaO_3 and LaInO_3 . *J Electrochem Soc* 2001;148:A1294–301.
- [636] Ruiz-Trejo E, Kilner JA. Oxygen diffusion and proton conduction in $\text{La}_{1-x}\text{Sr}_x\text{YO}_3$. *Solid State Ionics* 1997;97:529–34.
- [637] Ferguson JD, Kim Y, Kourkoutis LF, Vodnick A, Woll AR, Muller DA, et al. Epitaxial oxygen getter for a brownmillerite phase transformation in manganite films. *Adv Mater* 2011;23:1226–30.
- [638] Mancini A, Shin JF, Orresa A, Slater PR, Tealdi C, Ren Y, et al. Insight into the local structure of barium indate oxide-ion conductors: an X-ray total scattering study. *Dalton Trans* 2012;41:50–3.
- [639] Berastegui P, Hull S, Garcia FJG, Eriksson S-G. The crystal structures, microstructure and ionic conductivity of $\text{Ba}_2\text{In}_2\text{O}_5$ and $\text{Ba}(\text{In}_x\text{Zr}_{1-x})\text{O}_{3-x/2}$. *J Solid State Chem* 2002;164:119–30.

- [640] Schober T, Friedrich J, Krug F. Phase transition in the oxygen and proton conductor $\text{Ba}_2\text{In}_2\text{O}_5$ in humid atmospheres below 300 °C. Solid State Ionics 1997;99:9–13.
- [641] Manthiram A, Kuo JF, Goodenough JB. Characterization of oxygen-deficient perovskites as oxide-ion electrolytes. Solid State Ionics 1993;62:225–34.
- [642] Hashimoto T, Inagaki Y, Kishi A, Dokiya M. Absorption and secession of H_2O and CO_2 on $\text{Ba}_2\text{In}_2\text{O}_5$ and their effects on crystal structure. Solid State Ionics 2000;128:227–31.
- [643] Goodenough JB, Ruiz-Diaz JE, Zhen YS. Oxide-ion conduction in $\text{Ba}_2\text{In}_2\text{O}_5$ and $\text{Ba}_3\text{In}_2\text{MO}_8$ ($\text{M} = \text{Ce}, \text{Hf}, \text{or} \text{Zr}$). Solid State Ionics 1990;44:21–31.
- [644] Schober T, Friedrich J. The oxygen and proton conductor $\text{Ba}_2\text{In}_2\text{O}_5$: thermogravimetry of proton uptake. Solid State Ionics 1998;113–115:369–75.
- [645] Yao T, Uchimoto Y, Kinuhata M, Inagaki T, Yoshida H. Crystal structure of Ga-doped $\text{Ba}_2\text{In}_2\text{O}_5$ and its oxide ion conductivity. Solid State Ionics 2000;132:189–98.
- [646] Fisher CAJ, Derby B, Brook RJ. Oxygen ion conductivity in brownmillerite structured oxides $\text{Ba}_2\text{In}_{2-x}\text{M}_x\text{O}_5$, where $\text{M} = \text{Y}, \text{Yb}, \text{Sc}, \text{Ga}, \text{Br}$. Brit Ceram Proc 1996;56:25–33.
- [647] Mori M, Abe T, Itoh H, Yamamoto O, Takeda Y, Kawahara T. Cubic-stabilized zirconia and alumina composites as electrolytes in planar type solid oxide fuel cells. Solid State Ionics 1994;74:157–64.
- [648] Schober T. Protonic conduction in $\text{BaIn}_{0.5}\text{Sn}_{0.5}\text{O}_{2.75}$. Solid State Ionics 1998;109:1–11.
- [649] Goodenough JB. Ceramic solid electrolytes. Solid State Ionics 1997;94:17–25.
- [650] Yamamura H, Hamazaki H, Kakinuma K. Order-disorder transition and electrical conductivity of the brownmillerite solid-solutions system $\text{Ba}_2(\text{In},\text{M})_2\text{O}_5$ ($\text{M} = \text{Ga}, \text{Al}$). J Kor Phys Soc 1999;35:S200–4.
- [651] Kuramochi H, Mori T, Yamamura H, Kobayashi H, Mitamura T. Preparation and conductivity of $\text{Ba}_2\text{In}_2\text{O}_5$ ceramics. J Ceram Soc Jap 1994;102:1159–62.
- [652] Kakinuma K, Yamamura H, Haneda H, Atake T. Oxide-ion conductivity of the perovskite-type solid-solution system, $(\text{Ba}_{1-x-y}\text{Sr}_x\text{La}_y)_2\text{In}_2\text{O}_{5+y}$. Solid State Ionics 2002;154–155:571–6.
- [653] Shaula AL, Pivala YV, Waerenborgh JC, Gaczyński P, Yaremchenko AA, Kharton VV. I conditions. Solid State Ionics 2006;177:2923–30.
- [654] Chiba R, Ishii T, Yoshimura F. Temperature dependence of ionic conductivity in $(1-x)\text{ZrO}_{2-(x-y)}\text{Sc}_2\text{O}_{3-y}\text{Yb}_2\text{O}_3$ electrolyte material. Solid State Ionics 1996;91:249–56.
- [655] Sammells AF, Cook RL, White JH, Osborne JJ, MacDuff RC. Rational selection of advanced solid electrolytes for intermediate temperature fuel cells. Solid State Ionics 1992;52:111–23.
- [656] Cook RL, Sammells AF. On the systematic selection of perovskite solid electrolytes for intermediate temperature fuel cells. Solid State Ionics 1991;45:311–21.
- [657] Lacorre P. The LPS concept, a new way to look at anionic conductors. Solid State Sci 2000;2:755–8.
- [658] Goutenoire F, Isnard O, Retoux R, Lacorre P. Crystal structure of $\text{La}_2\text{Mo}_2\text{O}_9$, a new fast oxide-ion conductor. Chem Mater 2000;12:2575–80.
- [659] Goutenoire F, Isnard O, Suard E, Bohnke O, Laligant Y, Retoux R, et al. Structural and transport characteristics of the LAMOX family of fast oxide-ion conductors, based on lanthanum molybdenum oxide $\text{La}_2\text{Mo}_2\text{O}_9$. J Mater Chem 2001;11:119–24.
- [660] Georges S, Goutenoire F, Altorfer F, Sheptyakov D, Fauth F, Suard E, et al. Thermal, structural and transport properties of the fast oxide-ion conductors $\text{La}_{2-x}\text{R}_x\text{Mo}_2\text{O}_9$ ($\text{R} = \text{Nd}, \text{Gd}, \text{Y}$). Solid State Ionics 2003;161:131–41.
- [661] Lacorre P, Goutenoire F, Bohnke O, Retoux R, Laligant Y. Designing fast oxide-ion conductors based on $\text{La}_2\text{Mo}_2\text{O}_9$. Nature 2000;404:856–8.
- [662] Marrero-López D, Peña-Martínez J, Ruiz-Morales JC, Pérez-Colla D, Martín-Sedeño MC, Núñez P. Applicability of $\text{La}_2\text{Mo}_{2-y}\text{W}_y\text{O}_9$ materials as solid electrolyte for SOFCs. Solid State Ionics 2007;178:1366–78.
- [663] Wells AF. Structural inorganic chemistry. 5th ed. New York (USA): Oxford University Press; 1987. p. 1187.
- [664] Subasri R, Nafe H, Aldinger F. On the electronic and ionic transport properties of $\text{La}_2\text{Mo}_2\text{O}_9$. Mater Res Bullet 2003;38:1965–77.
- [665] Tealdi C, Chiodelli G, Malavasi L, Flor G. Effect of alkaline-doping on the properties of $\text{La}_2\text{Mo}_2\text{O}_9$ fast oxygen ion conductor. J Mater Chem 2004;14:3553–7.
- [666] Kendrick E, Islam MS, Slater PR. Developing apatites for solid oxide fuel cells: insight into structural, transport and doping properties. J Mater Chem 2007;17:3104–11.
- [667] Baikie T, Mercier PHJ, Elcombe MM, Kim JY, Page YL, Mitchell LD, et al. Triclinic apatites. Acta Crystallograph Sect B: Struct Sci 2007;63:251–6.
- [668] Islam MS, Tolchard JR, Slater PR. An apatite for fast oxide-ion conduction. Chem Commun 2003:1486–7.
- [669] Tolchard JR, Islam MS, Slater PR. Defect chemistry and oxygen ion migration in the apatite-type materials $\text{La}_{9.33}\text{Si}_6\text{O}_{26}$ and $\text{La}_8\text{Sr}_2\text{Si}_6\text{O}_{26}$. J Mater Chem 2003;13:1956–61.
- [670] Sansom JEH, Richings D, Slater PR. A powder neutron diffraction study of the oxide-ion-conducting apatite-type phases, $\text{La}_{9.33}\text{Si}_6\text{O}_{26}$ and $\text{La}_8\text{Sr}_2\text{Si}_6\text{O}_{26}$. Solid State Ionics 2001;139:205–10.
- [671] Yoshioka H, Tanase S. Magnesium doped lanthanum silicate with apatite-type structure as an electrolyte for intermediate temperature solid oxide fuel cells. Solid State Ionics 2005;176:2395–8.
- [672] Najib A, Sansom JEH, Tolchard JR, Slater PR, Islam MS. Doping strategies to optimise the oxide ion conductivity in apatite-type ionic conductors. Dalton Trans 2004;3106–9.
- [673] Sansom JEH, Najib A, Slater PR. Oxide ion conductivity in mixed Si/Ge-based apatite-type systems. Solid State Ionics 2004;175:353–5.
- [674] Sansom JEH, Sermon PA, Slater PR. Synthesis and conductivities of the Ti doped apatite-type phases $(\text{La}/\text{Ba})_{10-x}(\text{Si}/\text{Ge})_{6-y}\text{Ti}_y\text{O}_{26-z}$. Solid State Ionics 2005;176:1765–8.
- [675] Sansom JEH, Slater PR. Oxide ion conductivity in the mixed Si/Ge apatite-type phases $\text{La}_{9.33}\text{Si}_{6-x}\text{Ge}_x\text{O}_{26}$. Solid State Ionics 2004;167:23–7.
- [676] Sansom J, Kendrick E, Tolchard J, Islam M, Slater P. A comparison of the effect of rare earth vs Si site doping on the conductivities of apatite-type rare earth silicates. J Solid State Electrochem 2006;10:562–8.

- [677] Shaula AL, Kharton VV, Marques FMB. Oxygen ionic and electronic transport in apatite-type $\text{La}_{10-x}(\text{Si},\text{Al})_6\text{O}_{26\pm\delta}$. *J Solid State Chem* 2005;178:2050–61.
- [678] León-Reina L, Losilla ER, Martínez-Lara M, Martín-Sedeño MC, Bruque S, Nunez P, et al. High oxide ion conductivity in Al-doped germanium oxyapatite. *Chem Mater* 2005;17:596–600.
- [679] Nakayama S, Kageyama T, Aono H, Sadaoka Y. Ionic conductivity of lanthanoid silicates, $\text{Ln}_{10}(\text{SiO}_4)_6\text{O}_3$ ($\text{Ln} = \text{La, Nd, Sm, Gd, Dy, Y, Ho, Er and Yb}$). *J Mater Chem* 1995;11:1801–5.
- [680] Nakayama S, Aono H, Sadaoka Y. Ionic conductivity of $\text{Ln}_{10}(\text{SiO}_4)_6\text{O}_3$ ($\text{Ln} = \text{La, Nd, Sm, Gd and Dy}$). *Chem Lett* 1995:431–42.
- [681] Guillot S, Savignat SB, Lambert S, Vannier R-N, Roussel P, Porcher F. Evidence of local defects in the oxygen excess apatite $\text{La}_{9.67}(\text{SiO}_4)_6\text{O}_{2.5}$ from high resolution neutron powder diffraction. *J Solid State Chem* 2009;182:3358–64.
- [682] McFarlane J, Barth S, Swaffer M, Sansom JEH, Slater DPR. Synthesis and conductivities of the apatite-type systems, $\text{La}_{9.33+x}\text{Si}_{6-y}\text{MyO}_{26+z}$ ($M = \text{Co, Fe, Mn}$) and $\text{La}_8\text{Mn}_2\text{Si}_6\text{O}_{26}$. *Ionics* 2002;8:149–54.
- [683] Kendrick E, Kendrick J, Knight KS, Islami MS, Slater PR. Cooperative mechanisms of fast-ion conduction in gallium-based oxides with tetrahedral moieties. *Nat Mater* 2007;6:871–5.
- [684] León-Reina L, Martín-Sedeño MC, Losilla ER, Cabeza A, Martínez-Lara M, Bruque S, et al. Crystal chemistry and oxide ion conductivity in the lanthanum oxygermanate apatite series. *Chem Mater* 2003;15:2099–108.
- [685] León-Reina L, Porras-Vázquez JM, Losilla ER, Aranda MAG. Phase transition and mixed oxide-proton conductivity in germanium oxy-apatites. *J Solid State Chem* 2007;180:1250–8.
- [686] Li S, Schönberger F, Slater P. $\text{La}_{1-x}\text{Ba}_{1+x}\text{GaO}_{4-x/2}$: a novel high temperature proton conductor. *Chem Commun* 2003;21:2694–9.
- [687] Thomas CI, Kuang X, Deng Z, Niu H, Claridge JB, Rosseinsky MJ. Phase stability control of interstitial oxide ion conductivity in the $\text{La}_{1+x}\text{Sr}_{1-x}\text{Ga}_3\text{O}_{7+x/2}$ melilite family. *Chem Mater* 2010;22:2510.
- [688] Kuang X, Green MA, Niu H, Zajdel P, Dickinson C, Claridge JB, et al. Interstitial oxide ion conductivity in the layered tetrahedral network melilite structure. *Nat Mater* 2008;7:498–504.
- [689] Boysen H, Kaiser-Bischoff I, Lerch M. Anion diffusion processes in O- and N-mayenite investigated by neutron powder diffraction. *Diffus-Fund* 2008;8:2.1–8.
- [690] Hosono H, Hayashi K, Kajihara K, Sushko PV, Shluger AL. Oxygen ion conduction in $12\text{CaO}\cdot7\text{Al}_2\text{O}_3\cdot\text{O}_2$ -conduction mechanism and possibility of O-fast conduction. *Solid State Ionics* 2009;180:550.
- [691] Strandbakke R, Kongshaug C, Haugsrud R, Norby T. High temperature hydration and conductivity of mayenite, $\text{Ca}_{12}\text{Al}_{14}\text{O}_{33}$. *J Phys Chem C* 2009;113:8938–44.
- [692] Lee DK, Kogel L, Ebbinghaus SG, Valov I, Wiemhoefer HD, Lerch M, et al. Defect chemistry of the cage compound, $\text{Ca}_{12}\text{Al}_{14}\text{O}_{33-\delta}$ —understanding the route from a solid electrolyte to a semiconductor and electrode. *Phys Chem Chem Phys* 2009;11:3105.
- [693] Kao W-X, Lee M-C, Chang Y-C, Lin T-N, Wang C-H, Chang J-C. Fabrication and evaluation of the electrochemical performance of the anode-supported solid oxide fuel cell with the composite cathode of $\text{La}_{0.8}\text{Sr}_{0.2}\text{MnO}_3$ -Gadolinia-doped ceria oxide/ $\text{La}_{0.8}\text{Sr}_{0.2}\text{MnO}_3$. *J Power Sour* 2010;195:6468–72.
- [694] Li S, Lü Z, Wei B, Huang X, Miao J, Cao G, et al. A study of $(\text{Ba}_{0.5}\text{Sr}_{0.5})_{1-x}\text{Sm}_x\text{Co}_{0.8}\text{Fe}_{0.2}\text{O}_{3-\delta}$ as a cathode material for IT-SOFCs. *J Alloys Comp* 2006;426:408–14.
- [695] Veen ACv, Rebeilleau M, Farrusseng D, Mirodatos C. Studies on the performance stability of mixed conducting BSCFO membranes in medium temperature oxygen permeation. *Chem Commun* 2003;9:32–3.
- [696] Möbius H-H. On the history of solid electrolyte fuel cells. *J Solid State Electrochem* 1997;1:2–16.
- [697] Newman JS. Electrochemical systems. 2nd ed. New York (USA): Prentice Hall; 1991.
- [698] Wang DY, Nowick AS. Cathodic and anodic polarization phenomena at platinum electrodes with doped CeO_2 as electrolyte: II. Transient overpotential and AC impedance. *J Electrochem Soc* 1979;126:1166–72.
- [699] Wang DY, Nowick AS. Cathodic and anodic polarization phenomena at platinum electrodes with doped CeO_2 as electrolyte: I. Steady-state overpotential. *J Electrochem Soc* 1979;126:1155–65.
- [700] Vetter KJ. Electrochemical kinetics, theoretical and experimental aspects. New York (USA): Academic Press; 1967.
- [701] Hassel BA, Boukamp BA, Burggraaf AJ. Electrode polarization at the Au, $\text{O}_2(\text{g})/\text{yttria stabilized zirconia}$ interface. Part I: theoretical considerations of reaction model. *Solid State Ionics* 1991;48:139–54.
- [702] MacDonald JR. Impedance spectroscopy; emphasizing solid materials and systems. New York (USA): John Wiley and Sons; 1987.
- [703] Bauerle JE. Study of solid electrolyte polarization by a complex admittance method. *J Phys Chem Solids* 1969;30:2657–70.
- [704] Adler SB. Factors governing oxygen reduction in solid oxide fuel cell cathodes. *Chem Rev* 2004;104:4791–843.
- [705] Gödickemeier M, Sasaki K, Gauckler LJ, Riess I. Electrochemical characteristics of cathodes in solid oxide fuel cells based on ceria electrolytes. *J Electrochem Soc* 1997;144:1635–46.
- [706] Okamoto H, Kawamura G, Kudo T. Study of oxygen adsorption on platinum through observation of exchange current in a solid electrolyte concentration cell. *Electrochim Acta* 1983;28:379–82.
- [707] Hu H, Liu M. Interfacial polarization characteristics of $\text{Pt}|\text{BaCe}_{0.8}\text{Gd}_{0.2}\text{O}_3|\text{Pt}$ cells at intermediate temperatures. *J Electrochem Soc* 1997;114:3561–7.
- [708] Schouler E, Giroud G, Kleitz M. Application of complex admittance diagram of Bauerle in electrochemistry of solids. 2. Study of electrical conductivity of yttria-stabilized zirconia. *J Chem Phys Phys-Chim Biol* 1973;70:1309–16.
- [709] Kleitz M, Dessemont L, Kloiddt T, Steil MC. Space expansions of the regular oxygen electrode reaction on YSZ-II Silver electrode. In: Doikya M, Yamamoto O, Tagawa H, Singhal SC, editors. 4th International symposium of solid oxide fuel cells. Yokohoma (Japan): The Electrochemical Society, Pennington (NJ); 1995. p. 527–36.
- [710] Verkerk MJ, Burggraaf AJ. Oxygen transfer on substituted ZrO_2 , Bi_2O_3 , and CeO_2 electrolytes with platinum electrodes II. A-C impedance study. *J Electrochem Soc* 1983;130:78–84.
- [711] Mizusaki J, Amano K, Yamaguchi S, Fueki K. Electrode reaction at Pt, $\text{O}_2(\text{g})/\text{stabilized zirconia}$ interfaces Part I: theoretical consideration of reaction model. *Solid State Ionics* 1987;22:313–22.
- [712] Mizusaki J, Amano K, Yamaguchi S, Fueki K. Electrode reaction at Pt, $\text{O}_2(\text{g})/\text{stabilized zirconia}$ interfaces, part II: Electrochemical measurements and analysis. *Solid State Ionics* 1987;22:323–30.

- [713] Wang DY. Low-temperature diffusion-controlled polarization of Pt electrodes with yttria-stabilized zirconia electrolyte. *J Electrochim Soc* 1990;137:3660–6.
- [714] Robertson NL, Michaels JN. Oxygen exchange on platinum electrodes in zirconia cells: location of electrochemical reaction sites. *J Electrochim Soc* 1990;137:129–35.
- [715] Nowotny J, Bak T, Nowotny MK, Sorrell CC. Charge transfer at oxygen/zirconia interface at elevated temperatures: part 1: basic properties and terms. *Adv Appl Ceram* 2005;104:147–53.
- [716] Mitterdorfer A, Gauckler LJ. Identification of the reaction mechanism of the Pt, O₂(g)/yttria-stabilized zirconia system: part I: general framework, modelling, and structural investigation. *Solid State Ionics* 1999;117:187–202.
- [717] Mitterdorfer A, Gauckler LJ. Reaction kinetics of the Pt, O₂(g)/c-ZrO₂ system: precursor-mediated adsorption. *Solid State Ionics* 1999;120:211–25.
- [718] Mitterdorfer A, Gauckler LJ. Identification of the reaction mechanism of the Pt, O₂(g)/yttria-stabilized zirconia system: part II: model implementation, parameter estimation, and validation. *Solid State Ionics* 1999;117:203–17.
- [719] Berthier F, Diard JP, Gorrec BL, Montella C. Method for determining the faradaic impedance of an electrode reaction: application to metal corrosion rate measurements. *Corrosion* 1995;51:105.
- [720] Janek J, Rohnke M, Luerssen B, Imbihl R. Promotion of catalytic reactions by electrochemical polarisation. *Phys Chem Chem Phys* 2000;2:1935–41.
- [721] Luerßen B, Janek J, Imbihl R. Electrocatalysis on Pt/YSZ electrodes. *Solid State Ionics* 2001;141–142:701–7.
- [722] Yoon SP, Nam SW, Kim S-G, Hong S-A, Hyun S-H. Characteristics of cathodic polarization at Pt/YSZ interface without the effect of electrode microstructure. *J Power Sour* 2003;115:27–34.
- [723] Verker MJ, Hammink MWJ, Burggraaf AJ. Oxygen transfer in substituted ZrO₂, Bi₂O₃ and CeO₂ electrolytes with platinum electrodes. Part I. Electrode resistance by DC polarization. *J Electrochim Soc* 1983;130:70–8.
- [724] Kleitz M, Kloiddt T, Dessemond L. High temperature electrochemical behaviour of fast ion and mixed conductors on material science. In: Poulsen FW, Bentzen JJ, Jacobsen T, Skou E, Østergård MJ, editors. 14th Risø international symposium on materials science. Roskilde, Denmark Risø National Laboratory; 1993. p. 89–116.
- [725] Velho LR, Bartlett RW. Diffusivity and solubility of oxygen in platinum and Pt–Ni alloys. *Metall Trans* 1972;3:65–72.
- [726] Widmer S, Tate TJ, Thampi KR, McEvoy AJ. Transition metal ion implantation for modification of cathode interfaces. In: Stimming U, Singhal SC, Tagawa H, Lehnert W, editors. 5th International symposium on solid oxide fuel cells. Pennington (NJ), Aachen (Germany): The Electrochemical Society; 1997. p. 451–61.
- [727] McEvoy AJ. Thin SOFC electrolytes and their interfaces: a near-term research strategy. *Solid State Ionics* 2000;132:159–65.
- [728] Chao T, Walsh KJ, Fedkiw PS. Cyclic voltammetric study of the electrochemical formation of platinum oxide in a platinum/yttria-stabilized zirconia cell. *Solid State Ionics* 1991;47:277–85.
- [729] Sridhar S, Stancovski V, Pal UB. Transient and permanent effects of direct current on oxygen transfer across YSZ-electrode interfaces. *J Electrochim Soc* 1997;144:2479–85.
- [730] Jacobsen T, Zachau-Christiansen B, Bay L, Jørgensen MJ. Hysteresis in the solid oxide fuel cell cathode reaction. *Electrochim Acta* 2001;46:1019–24.
- [731] Shkerin SN, Perfilev MV. Reaction kinetics at a model electrode in the O₂–Pt–O₂ system low temperature anode polarization. *Soviet Electrochem* 1992;28:1106–11.
- [732] Shkerin SN, Perfilev MV. Elektrokhimiya 1990;26:1468.
- [733] Button DD, Archer D. Development of La_{1-x}Sr_xCoO₃ air electrodes for solid electrolyte fuel cells. In: American Ceramic Society Meeting. Washington; 1966.
- [734] Jiang SP. Development of lanthanum strontium manganite perovskite cathode materials of solid oxide fuel cells: a review. *J Mater Sci* 2008;43:6799–833.
- [735] Sun C, Hui R, Rollier J. Cathode materials for solid oxide fuel cells: a review. *J Solid State Electroch* 2010;14:1125–44.
- [736] Shannon RD. Revised effective ionic radii and systematic studies of interatomic distances in halides and chalcogenides. *Acta Crystall Sect A* 1976;32:751–67.
- [737] Tofield BC, Scott WR. Oxidative nonstoichiometry in perovskites, an experimental survey; the defect structure of an oxidized lanthanum manganite by powder neutron diffraction. *J Solid State Chem* 1974;10:183–94.
- [738] Kuo JH, Anderson HU, Sparlin DM. Oxidation-reduction behavior of undoped and Sr-doped LaMnO₃: defect structure, electrical conductivity, and thermoelectric power. *J Solid State Chem* 1990;87:55–63.
- [739] Hammouche A, Schouler EJL, Henault M. Electrical and thermal properties of Sr-doped lanthanum manganites. *Solid State Ionics* 1988;28–30:1205–7.
- [740] Yokokawa H, Sakai N, Kawada T, Dokiya M. Thermodynamic analysis on interface between perovskite electrode and YSZ electrolyte. *Solid State Ionics* 1990;40–41:398–401.
- [741] Mizusaki J, Yonemura Y, Hiroyuki Kamata, Ohyama K, Mori N, Takai H, et al. Electronic conductivity, Seebeck coefficient, defect and electronic structure of nonstoichiometric La_{1-x}Sr_xMnO₃. *Solid State Ionics* 2000;132:167–80.
- [742] Zhong-tai Z, Lin O, Zi-Long T. Synthesis and characteristics of La_{1-x}Sr_xMnO₃ ceramics for cathode materials of SOFC. In: Dokiya M, Yamamoto O, Tagawa H, Singhal SC, editors. 5th International Symposium on Solid Oxide Fuel Cells. Pennington (NJ), Yokohoma (Japan): The Electrochemical Society; 1995. p. 1018–27.
- [743] Li Z, Behruzi M, Fuerst L, Stover D. In: Singhal SC, Iwahara H, editors. 3rd International Symposium on Solid Oxide Fuel Cells. Pennington (NJ), Honolulu (HI, USA): The Electrochemical Society; 1993. p. 1018–27.
- [744] Nowotny J, Rekas M. Defect chemistry of (La,Sr)MnO₃. *J Am Ceram Soc* 1998;81:67–80.
- [745] Alonso JA, Martinez-Lope MJ, Casais MT, Macmanus-Driscoll JL, Silva PSIPND, Cohen LF, et al. Non-stoichiometry, structural defects and properties of LaMnO_{3+δ} with high δ values (0.11 ≤ δ ≤ 0.29). *J Mater Chem* 1997;7:2139–44.
- [746] Roosmalen JAMV, Cordfunke EHP. The defect chemistry of LaMnO_{3±δ}: 3. The density of (La,A)MnO_{3+δ} (A = Ca, Sr, Ba). *J Solid State Chem* 1994;110:106–8.
- [747] Mitchell JF, Argyriou DN, Potter CD, Hinks DG, Jorgenson JD, Bader SD. Structural phase diagram of La_{1-x}Sr_xMnO_{3+δ}: Relationship to magnetic and transport properties. *Phys Rev B* 1996;54:6172–6183.
- [748] Nakamura K, Xu M, Kläser M, Linker G. Excess oxygen in low Sr doping La_{1-x}Sr_xMnO_{3+δ} epitaxial films. *J Solid State Chem* 2001;156:143–53.

- [749] Nakamura K, Ogawa K. Excess oxygen in $\text{LaMnO}_{3+\delta}$. *J Solid State Chem* 2002;163:65–76.
- [750] Alonso JA, Martínez-Lope MJ, Casais MT. High oxygen pressure synthesis of $\text{LaMnO}_{3+\delta}$ with high δ values. *Euro J Solid State Inorg Chem* 1996;33:331–41.
- [751] Alonso JA, Martínez-Lope MJ, Casais MT, Macmanus-Driscoll JL, Silva PSIPNd, Cohen LF, et al. Non-stoichiometry, structural defects and properties of $\text{LaMnO}_{3+\delta}$ with high δ values ($0.11 = \delta = 0.29$). *J Mater Chem* 1997;7:2139–44.
- [752] Mizusaki J, Mori N, Takai H, Yonemura Y, Minamiue H, Tagawa H, et al. Oxygen nonstoichiometry and defect equilibrium in the perovskite-type oxides $\text{La}_{1-x}\text{Sr}_x\text{MnO}_{3+\delta}$. *Solid State Ionics* 2000;129:163–77.
- [753] Kuo JH, Anderson HU, Sparlin DM. Oxidation-reduction behavior of undoped and Sr-doped LaMnO_3 nonstoichiometry and defect structure. *J Solid State Chem* 1989;83:52–60.
- [754] Endo A, Ihara M, Komiya H, Yamada K. Cathodic reaction mechanism for dense Sr-doped lanthanum manganite electrodes. *Solid State Ionics* 1996;86–88:1191–5.
- [755] Ullmann H, Trofimenko N, Tietz F, Stöver D, Ahmad-Khanlou A. Correlation between thermal expansion and oxide ion transport in mixed conducting perovskite-type oxides for SOFC cathodes. *Solid State Ionics* 2000;138:79–90.
- [756] Godoi GS, Souza DPF. Electrical and microstructural characterization of $\text{La}_{0.7}\text{Sr}_{0.3}\text{MnO}_3$ (LSM), $\text{Ce}_{0.8}\text{Y}_{0.2}\text{O}_2$ (CY) and LSM-CY composites. *Mater Sci Eng: B* 2007;140:90–7.
- [757] Jaya SM, Jagadish R, Rao RS, Asokamani R. Electronic structure and magnetism of SrFeO_3 and SrCoO_3 . *Phys Rev B* 1991;43:13274–9.
- [758] Ishikawa T, Park SK, Katsufuji T, Arima T, Tokura Y. Optical spectroscopy of charge-ordering transition in $\text{La}_{1/3}\text{Sr}_{2/3}\text{FeO}_3$. *Phys Rev B* 1998;58:R13326–9.
- [759] Raccah PM, Goodenough JB. First order localized electron collective electron transition in LaCo_3 . *Phys Rev* 1967;155:932–48.
- [760] Raccah PM, Goodenough JB. A localized electron to collective electron transition in the system $(\text{La}, \text{Sr})\text{CoO}_3$. *J Appl Phys* 1968;39:1209–10.
- [761] Bhide VG, Rajoria DS, Reddy YS, Rao GR, Rao GVS, Rao CNR. Localized-to-itinerant electron transitions in rare earth cobaltates. *Phys Rev Lett* 1972;28:1133–6.
- [762] Bhide VG, Rajoria DS, Rao CNR, Rao GR, Jadho VG. Itinerant-electron ferromagnetism in $\text{La}_{1-x}\text{Sr}_x\text{CoO}_3$: a Mössbauer study. *Phys Rev B* 1975;12:2832–43.
- [763] Ganguly P, Kumar PSA, Santhosh PN, Mulla IS. On the origin of itinerant electron behaviour and long-range ferromagnetic order in $\text{La}_{1-x}\text{Sr}_x\text{CoO}_3$. *J Phys: Cond Matter* 1994;6:533–44.
- [764] Señaris-Rodríguez MA, Goodenough JB. Magnetic and transport properties of the system $\text{La}_{1-x}\text{Sr}_x\text{CoO}_{3-\delta}$ ($0 < x = 0.50$). *J Solid State Chem* 1995;118:323–36.
- [765] Takahashi H, Munakata F, Yamanaka M. Ab initio study of the electronic structures in LaCoO_3 – SrCoO_3 systems. *Phys Rev B* 1998;57:15211–8.
- [766] Caciuffo R, Mira J, Rivas J, Senaris-Rodríguez MA, Radaelli PG, Carsughi F, et al. Transition from itinerant to polaronic conduction in $\text{La}_{1-x}\text{Sr}_x\text{CoO}_3$ perovskites. *Europhys Lett* 1999;45:399–405.
- [767] Mizusaki J, Tabuchi J, Matsuura T, Yamauchi S, Fukui K. Electrical conductivity and seebeck coefficient of nonstoichiometric $\text{La}_{1-x}\text{Sr}_x\text{CoO}_{3-\delta}$. *J Electrochem Soc* 1989;136:2082–8.
- [768] Petrov AN, Kononchuk OF, Andreev AV, Cherenpanov VA, Kofstad P. Crystal structure, electrical and magnetic properties of $\text{La}_{1-x}\text{Sr}_x\text{CoO}_{3-y}$. *Solid State Ionics* 1995;80:189–99.
- [769] Chainani A, Mathew M, Sarma DD. Electronic structure of $\text{La}_{1-x}\text{Sr}_x\text{FeO}_3$. *Phys Rev B* 1993;48:14818–25.
- [770] Torrance JB, Lacorre P, Asavaroengchai C, Metzger RM. Why are some oxides metallic, while most are insulating?. *Physica C* 1991;182:351–64.
- [771] Mizusaki J, Sasamoto T, Cannon WR, Bowen HK. Electronic conductivity, seebeck coefficient, and defect structure of $\text{La}_{1-x}\text{Sr}_x\text{FeO}_3$ ($x = 0.1, 0.25$). *J Am Ceram Soc* 1983;66:247–52.
- [772] Tai L-W, Nasrallah MM, Anderson HU, Sparlin DM, Sehlin SR. Structure and electrical properties of $\text{La}_{1-x}\text{Sr}_x\text{Co}_{1-y}\text{Fe}_y\text{O}_3$. Part 1. The system $\text{La}_{0.8}\text{Sr}_{0.2}\text{Co}_{1-y}\text{Fe}_y\text{O}_3$. *Solid State Ionics* 1995;76:259–71.
- [773] Stevenson JW, Armstrong TR, Carneim RD, Pederson LR, Weber WJ. Electrochemical properties of mixed conducting perovskites $\text{La}_{1-x}\text{M}_x\text{Co}_{1-y}\text{Fe}_y\text{O}_{3-\delta}$ ($\text{M} = \text{Sr}, \text{Ba}, \text{Ca}$). *J Electrochem Soc* 1996;143:2722–9.
- [774] Choi Y, Lynch ME, Lin MC, Liu M. Prediction of O_2 dissociation kinetics on LaMnO_3 -based cathode materials for solid oxide fuel cells. *J Phys Chem* 2009;113:7290–7.
- [775] Co AC, Birss VI. Mechanistic analysis of the oxygen reduction reaction at $(\text{La}, \text{Sr})\text{MnO}_3$ cathodes in solid oxide fuel cells. *J Phys Chem B* 2006;110:11299–309.
- [776] Endo A, Fukunaga H, Wen C, Yamada K. Cathodic reaction mechanism of dense $\text{La}_{0.6}\text{Sr}_{0.4}\text{CoO}_3$ and $\text{La}_{0.81}\text{Sr}_{0.09}\text{MnO}_3$ electrodes for solid oxide fuel cells. *Solid State Ionics* 2000;135:353–8.
- [777] Kawada T, Suzuki J, Sase M, Kaimai A, Yashiro K, Nigara Y, et al. Determination of oxygen vacancy concentration in a thin film of $\text{La}_{0.6}\text{Sr}_{0.4}\text{CoO}_{3-\delta}$ by an electrochemical method. *J Electrochem Soc* 2002;149:E252–9.
- [778] Zhang C, Deng H, Varon J, Abeles B, Yang Y, Pham AQ, et al. Structural, electrical and optical properties of laser deposited thin films of $\text{SrCo}_{0.8}\text{Fe}_{0.2}\text{O}_{3-\delta}$. *Mater Res Soc* 1994:369.
- [779] Gharbage B, Pagnier T, Hamiou A. Oxygen reduction at $\text{La}_{0.5}\text{Sr}_{0.5}\text{MnO}_3$ thin film/yttria-stabilized zirconia interface studied by impedance spectroscopy. *J Electrochem Soc* 1994;141:2118–21.
- [780] Herle JV, McEvoy AJ, Thampi KR. Oxygen reduction at porous and dense cathodes for solid oxide fuel cells. *Electrochim Acta* 1994;39:1675–80.
- [781] Mizusaki J, Saito T, Tagawa H. A chemical diffusion controlled electrode reaction at the compact $\text{La}_{1-x}\text{Sr}_x\text{MnO}_3$ /stabilized zirconia interface in oxygen atmospheres. *J Electrochem Soc* 1996;143:3065–73.
- [782] Masuda K, Kaimai A, Kawamura K, Nigara Y, Kawada T, Mizusaki J, et al. Electrochemical reaction kinetics of mixed conducting electrodes on CeO_2 -based solid electrolytes. In: Stimming U, Singhal SC, Tagawa H, Lehnert W, editors. *5th International symposium on solid oxide fuel cells*. Pennington (NJ), Aachen (Germany): The Electrochemical Society; 1997. p. 473–82.
- [783] Ioroi T, Hara T, Uchimoto Y, Ogumi Z, Takehara Z-i. Preparation of perovskite-type $\text{La}_{1-x}\text{Sr}_x\text{MnO}_3$ films by vapor-phase processes and their electrochemical properties. *ChemInform* 1997;28:1362–70.

- [784] Ioroi T, Tatsunori Hara, Uchimoto Y, Ogumi Z, Takehara Z-i. Preparation of Perovskite-type $\text{La}_{1-x}\text{Sr}_x\text{MnO}_3$ films by vapor-phase processes and their electrochemical properties II. Effects of doping strontium to formula on the electrode properties. *J Electrochem Soc* 1998;145:1999–2004.
- [785] Kawada T, Masuda K, Suzuki J, Kaimai A, Kawamura K, Nigara Y, et al. Oxygen isotope exchange with a dense $\text{La}_{0.6}\text{Sr}_{0.4}\text{CoO}_{3-\delta}$ electrode on a $\text{Ce}_{0.9}\text{Ca}_{0.1}\text{O}_{1.9}$ electrolyte. *Solid State Ionics* 1999;121:271–9.
- [786] Yang YL, Chen CL, Chen SY, Chu CW, Jacobson AJ. Impedance studies of oxygen exchange on dense thin film electrodes of $\text{La}_{0.5}\text{Sr}_{0.5}\text{CoO}_{3-\delta}$. *J Electrochem Soc* 2000;147:4001–7.
- [787] Fukunaga H, Koyama M, Takahashi N, Wen C, Yamada K. Reaction model of dense $\text{Sm}_{0.5}\text{Sr}_{0.5}\text{CoO}_3$ as SOFC cathode. *Solid State Ionics* 2000;132:279–85.
- [788] Mims CA, Joos NI, Heide PAWvd, Jacobson AJ, Chen C, Chu CW, et al. Oxygen transport in oxide thin film structures oriented $\text{La}_{0.6}\text{Sr}_{0.5}\text{CoO}_{3-x}$ on single-crystal yttria-stabilized zirconia. *Electrochim Solid-State Lett* 2000;3:59–61.
- [789] Yang YL, Jacobson AJ, Chen CL, Luo GP, Ross KD, Chu CW. Oxygen exchange kinetics on a highly oriented $\text{La}_{0.5}\text{Sr}_{0.5}\text{CoO}_{3-\delta}$ thin film prepared by pulsed-laser deposition. *Appl Phys Lett* 2001;79:776.
- [790] Ringuedé A, Fouletier J. Oxygen reaction on strontium-doped lanthanum cobaltite dense electrodes at intermediate temperatures. *Solid State Ionics* 2001;139:167–77.
- [791] Kawada T, Masuda K, Suzuki J, Kaimai A, Kawamura K, Nigara Y, et al. Oxygen isotope exchange with a dense $\text{La}_{0.6}\text{Sr}_{0.4}\text{CoO}_{3-\delta}$ electrode on a $\text{Ce}_{0.9}\text{Ca}_{0.1}\text{O}_{1.9}$ electrolyte. *Solid State Ionics* 1999;121:271–9.
- [792] Adler SB. Limitations of charge-transfer models for mixed-conducting oxygen electrodes. *Solid State Ionics* 2000;135:603–12.
- [793] Adler SB. Mechanism and kinetics of oxygen reduction on porous $\text{La}_{1-x}\text{Sr}_x\text{CoO}_{3-\delta}$ electrodes. *Solid State Ionics* 1998;111:125–34.
- [794] Adler SB, Lane JA, Steele BCH. Electrode kinetics of porous mixed-conducting oxygen electrodes. *J Electrochem Soc* 1996;143:3554–64.
- [795] Maguire E, Gharbage B, Marques FMB, Labrincha JA. Cathode materials for intermediate temperature SOFCs. *Solid State Ionics* 2000;127:329–35.
- [796] Steele BCH, Bae JM. Properties of $\text{La}_{0.6}\text{Sr}_{0.4}\text{Co}_{0.2}\text{Fe}_{0.8}\text{O}_{3-x}$ (LSCF) double layer cathodes on gadolinium-doped cerium oxide (CGO) electrolytes – II. Role of oxygen exchange and diffusion. *Solid State Ionics* 1998;106:255–61.
- [797] Endo A, Wada S, Wen CJ, Komiyama H, Yamada K. Low overvoltage mechanism of high ionic conducting cathode for solid oxide fuel cell. *J Electrochem Soc* 1998;145:L35–7.
- [798] Horita T, Yamaji K, Sakai N, Yokokawa H, Weber A, Ivers-Tiffée E. Electrode reaction of $\text{La}_{1-x}\text{Sr}_x\text{CoO}_{3-d}$ cathodes on $\text{La}_{0.8}\text{Sr}_{0.2}\text{Ga}_{0.8}\text{Mg}_{0.2}\text{O}_{3-y}$ electrolyte in solid oxide fuel cells. *J Electrochem Soc* 2001;148:A456–62.
- [799] Jiang SP. A comparison of O_2 reduction reactions on porous ($\text{La}, \text{Sr})\text{MnO}_3$ and ($\text{La}, \text{Sr})(\text{Co}, \text{Fe})\text{O}_3$ electrodes. *Solid State Ionics* 2002;146:1–22.
- [800] Fleig Ju. Solid oxide fuel cell cathode: polarization mechanisms and modeling of the electrochemical performance. *Ann Rev Mater Res* 2003;33:361–82.
- [801] Koyama M, Wen C-j, Masuyama T, Otomo J, Fukunaga H, Yamada K, et al. The mechanism of porous $\text{Sm}_{0.5}\text{Sr}_{0.5}\text{CoO}_3$ cathodes used in solid oxide fuel cells. *J Electrochem Soc* 2001;148:A795–801.
- [802] Mizusaki J, Tagawa H, Tsuneyoshi K, Sawata A. Reaction kinetics and microstructure of the solid oxide fuel cells air electrode $\text{La}_{0.6}\text{Ca}_{0.4}\text{MnO}_3/\text{YSZ}$. *J Electrochem Soc* 1991;138:1867–73.
- [803] Schmid A. Die diffusions-elektrode. Stuttgart: Enke; 1923.
- [804] Skinner SJ. Recent advances in perovskite-type materials for solid oxide fuel cell cathodes. *Int J Inorg Mater* 2001;3:113–21.
- [805] Yamamoto O, Takeda Y, Kanno R, Tomida Y. Electrode reaction of perovskite oxides $\text{La}_{1-x}\text{Sr}_x\text{MnO}_{3-z}$ ($M = \text{Mn, Fe, Co}$) for high-temperature solid electrolyte fuel cells. *Nippon Kagaku Kaishi* 1988;1324–8.
- [806] Gödickemeier M, Sasaki k, Gauckler LJ, Riess I. Perovskite cathodes for solid oxide fuel cells based on ceria electrolytes. *Solid State Ionics* 1996;86–88:691–701.
- [807] Kilner JA. Ceramic electrodes for SOFC's. *Boletín de la Sociedad Española de Cerámica y Vidrio* 1998;37:247–55.
- [808] Steele BCH, Hori KM, Uchino S. Kinetic parameters influencing the performance of IT-SOFC composite electrodes. *Solid State Ionics* 2000;135:445–50.
- [809] Colomer MT, Steele BCH, Kilner JA. Structural and electrochemical properties of the $\text{Sr}_{0.8}\text{Ce}_{0.1}\text{Fe}_{0.7}\text{Co}_{0.3}\text{O}_{3-d}$ perovskite as cathode material for IT-SOFCs. *Solid State Ionics* 2002;147:41–8.
- [810] Steele BCH. Behaviour of porous cathodes in high temperature fuel cells. *Solid State Ionics* 1997;94:239–48.
- [811] Dusastre V, Kilner JA. Optimisation of composite cathodes for intermediate temperature SOFC applications. *Solid State Ionics* 1999;126:163–74.
- [812] Schafer W, Koch A, Heroldschmidt U, Stolten D. Materials, interfaces and production techniques for planer solid oxide fuel cells. *Solid State Ionics* 1996;86:1235–9.
- [813] Liu W, Zhang ZX, Xia CR, Xie JQ, Chen CS. Preparation and characterization of porous $\text{La}_{0.6}\text{Sr}_{0.4}\text{C}_{0.2}\text{Fe}_{0.8}\text{O}_{3-\delta}$ ceramics. *J Inorg Mater* 2000;15:849–54.
- [814] Liu M, Lynch ME, Blinn K, Alamgir FM, Choi Y. Rational SOFC material design: new advances and tools. *Mater Today* 2011;14:534–46.
- [815] Murray EP, Barnett SA. Improved performance in (La, Sr) MnO_3 cathodes by the addition of a Gd-doped ceria second phase. In: Singhal SC, Dokiya M, editors. 6th International symposium on solid oxide fuel cells. Pennington (NJ), Honolulu (HI, USA): The Electrochemical Society; 1999. p. 369–78.
- [816] Murray EP, Sever MJ, Barnett SA. Electrochemical performance of ($\text{La}, \text{Sr})(\text{Co}, \text{Fe})\text{O}_3-(\text{Ce}, \text{Gd})\text{O}_3$ composite cathodes. *Solid State Ionics* 2002;148:27–34.
- [817] Hart NT, Brandon NP, Day MJ, Lapena-Rey N. Functionally graded composite cathodes for solid oxide fuel cells. *J Power Sour* 2002;106:42–50.
- [818] Fergus JW. Sealants for solid oxide fuel cells. *J Power Sour* 2005;147:46–57.
- [819] Świerczek K. Electrolyte-supported IT-SOFC with LSCF-SCFN composite cathode. *Solid State Ionics* 2011;192:486–90.

- [820] Ivers-Tiffée E, Weber A, Herbstritt D. Materials and technologies for SOFC-components. *J Euro Ceram Soc* 2001;21:1805–11.
- [821] Molenda J, Świerczek K, Zająć W. Functional materials for the IT-SOFC. *J Power Sour* 2007;173:657–70.
- [822] Jonghe LCD, Jacobson CP, Visco SJ. Supported electrolyte thin film synthesis of solid oxide fuel cells. *Ann Rev Mater Res* 2003;33:169–82.
- [823] Koyama M, Wena C-j, Yamada K. $\text{La}_{0.6}\text{Ba}_{0.4}\text{CoO}_3$ as a cathode material for solid oxide fuel cells using a BaCeO_3 electrolyte. *J Electrochem Soc* 2000;147:87–91.
- [824] Backhaus-Ricoult M, Adib K, St. Clair T, Luerssen B, Gregoratti L, Barinov A. In-situ study of operating SOFC LSM/YSZ cathodes under polarization by photoelectron microscopy. *Solid State Ionics* 2008;179:891–5.
- [825] Ia' GJ, Savinell RF, Shao-Horn Y. Activity enhancement of dense strontium-doped lanthanum manganite thin films under cathodic polarization: a combined AES and XPS study. *J Electrochem Soc* 2009;156:B771–81.
- [826] Woo LY, Glass RS, Gorte RJ, Orme CA, Nelson AJ. Dynamic changes in LSM nanoparticles on YSZ: a model system for non-stationary SOFC cathode behavior. *J Electrochem Soc* 2009;156:B602–8.
- [827] Jiang SP, Love JG, Zhang JP, Hoang M, Ramprakash Y, Hughes AE, et al. The electrochemical performance of LSM/zirconia-yttria interface as a function of a-site non-stoichiometry and cathodic current treatment. *Solid State Ionics* 1999;121:1–10.
- [828] Wang W, Jiang SP. A mechanistic study on the activation process of $(\text{La}, \text{Sr})\text{MnO}_3$ electrodes of solid oxide fuel cells. *Solid State Ionics* 2006;177:1361–9.
- [829] Jiang SP. Activation, microstructure, and polarization of solid oxide fuel cell cathodes. *J Solid State Electrochem* 2007;11:93–102.
- [830] Vohs JM, Gorte RJ. High-performance SOFC cathodes prepared by infiltration. *Adv Mater* 2009;21:943–56.
- [831] Bebelis S, Kotsionopoulos N, Mai A, Tietz F. Electrochemical characterization of perovskite-based SOFC cathodes. *J Appl Electrochem* 2007;37:15–20.
- [832] Bebelis S, Kotsionopoulos N, Mai A, Rutenbeck D, Tietz F. Electrochemical characterization of mixed conducting and composite SOFC cathodes. *Solid State Ionics* 2006;177:1843–8.
- [833] Simmer SP, Anderson MD, Coleman JE, Stevenson JW. Performance of a novel $\text{La}(\text{Sr})\text{Fe}(\text{Co})\text{O}_3-\text{Ag}$ SOFC cathode. *J Power Sour* 2006;161:115–22.
- [834] Shao Z, Haile SM. A high-performance cathode for the next generation of solid-oxide fuel cells. *Nature* 2004;431:170–3.
- [835] Yoon J, Araújo R, Grunbaum Ns, Baqué L, Serquis A, Caneiro A, et al. Nanostructured cathode thin films with vertically-aligned nanopores for thin film SOFC and their characteristics. *Appl Surf Sci* 2007;254:266–9.
- [836] Kenney BA. An experimental and modelling study of oxygen reduction in porous LSM/YSZ solid oxide fuel cell cathodes. Kingston: Ph.D. Thesis, Queen's University; 2009.
- [837] Badwal SPS, Fogar K. Materials for solid oxide fuel cells. *Mater Forum* 1997;21:187–224.
- [838] Badwal SPS. Zirconia-based solid electrolytes: microstructure, stability and ionic conductivity. *Solid State Ionics* 1992;52:23–32.
- [839] Bidrawn F, Küngas R, Vohs JM, Gorte RJ. Modeling impedance response of SOFC cathodes prepared by infiltration. *J Electrochem Soc* 2011;158:B514–25.
- [840] Mahato N, Gupta A, Balani K. Doped zirconia and ceria-based electrolytes for solid oxide fuel cells: a review. *Nanomater Energy* 2011;1:27–45.
- [841] Manning PS, Sirman JD, Souza RAD, Kilner JA. The kinetics of oxygen transport in 9.5 mol% single crystal yttria stabilised zirconia. *Solid State Ionics* 1997;100:1–10.
- [842] Manning PS, Sirman JD, Kilner JA. Oxygen self-diffusion and surface exchange studies of oxide electrolytes having the fluorite structure. *Solid State Ionics* 1996;93:125–32.
- [843] Kilo M, Argirakis C, Borchardt Gn, Jackson RA. Oxygen diffusion in yttria stabilised zirconia—experimental results and molecular dynamics calculations. *Phys Chem Chem Phys* 2003;5:2219–24.
- [844] Kim JH, Cassidy M, Irvine JTS, Bae J. Electrochemical investigation of composite cathodes with $\text{SmBa}_{0.5}\text{Sr}_{0.5}\text{Co}_{2}\text{O}_{5-\delta}$ cathodes for intermediate temperature-operating solid oxide fuel cell. *Chem Mater* 2010;22:883–92.
- [845] Kostoglouidis GC, Tsiniarakis G, Ftikos C. Chemical reactivity of perovskite oxide SOFC cathodes and yttria stabilized zirconia. *Solid State Ionics* 2000;135:529–35.
- [846] Opitz AK, Fleig J. Investigation of O_2 reduction on Pt/YSZ by means of thin film microelectrodes: the geometry dependence of the electrode impedance. *Solid State Ionics* 2010;181:684–93.
- [847] O'GJL, Yildiz B, McEuen S, Shao-Horn Y. Probing oxygen reduction reaction kinetics of Sr-Doped LaMnO_3 supported on Y_2O_3 -stabilized ZrO_2 EIS of dense, thin-film microelectrodes. *J Electrochem Soc* 2007;154:B427–38.
- [848] Ji Y, Kilner JA, Carolan MF. Electrical properties and oxygen diffusion in yttria-stabilised zirconia (YSZ)- $\text{La}_{0.8}\text{Sr}_{0.2}\text{MnO}_{3+\delta}$ (LSM) composites. *Solid State Ionics* 2005;176:937–43.
- [849] Mori M, Hiei Y, Sammes NM, Tompsett GA. Thermal expansion behavior of Ca- or Sr-doped lanthanum manganites under oxidizing atmospheres. In: Singhal SC, Dokiya M, editors. 6th International symposium on solid oxide fuel cells. Pennington (NJ), Honolulu (HI, USA): The Electrochemical Society; 1999. p. 347–54.
- [850] Jiang SP, Li J. Cathodes. In: Fergus JW, Hui R, Li X, Wilkinson DP, Zhang J, editors. Solid oxide fuel cells: materials properties and performance. Boca Raton (FL, USA): CRC Press, Taylor and Francis; 2009.
- [851] Ishigaki T, Yamaguchi S, Mizusaki J, Fueki K, Tamura H. Diffusion of oxide ions in LaFeO_3 single crystal. *Solid State Chem* 1984;55:50–3.
- [852] Hjalmarsson P, Mogensen M. $\text{La}_{0.99}\text{Co}_{0.4}\text{Ni}_{0.6}\text{O}_{3-\delta}-\text{Ce}_{0.8}\text{Gd}_{0.2}\text{O}_{1.95}$ as composite cathode for solid oxide fuel cells. *J Power Sour* 2011;196:7237–44.
- [853] Kim JH, Cassidy M, Irvine JTS, Bae J. Advanced electrochemical properties of $\text{LnBa}_{0.5}\text{Sr}_{0.5}\text{Co}_{2}\text{O}_{5+\delta}$ ($\text{Ln} = \text{Pr, Sm, and Gd}$) as cathode materials for IT-SOFC. *J Electrochem Soc* 2009;156:B682–9.
- [854] Fergus J, Hui R, Li X, Wilkinson DP, Zhang J. Solid oxide fuel cells: materials properties and performance. Boca Raton (FL, USA): CRC Press, Taylor and Francis; 2009.
- [855] Aruna ST, Muthuraman M, Patil KC. Combustion synthesis and properties of strontium substituted lanthanum manganites $\text{La}_{1-x}\text{Sr}_x\text{MnO}_3$ ($0 = x = 0.3$). *J Mater Chem* 1997;7:2499–503.

- [856] Kharton VV, Viskup AP, Naumovich EN, Lapchuk NM. Mixed electronic and ionic conductivity of $\text{LaCo}(\text{M})\text{O}_3$ ($\text{M} = \text{Ga, Cr, Fe or Ni}$) – I. Oxygen transport in perovskites $\text{LaCoO}_3\text{-LaGaO}_3$. *Solid State Ionics* 1997;104:67–78.
- [857] Hrovat M, Katsarakis N, Reichmann K, Bernik S, Kuscer D, Holc J. Characterisation of $\text{LaNi}_{1-x}\text{Co}_x\text{O}_3$ as a possible SOFC cathode material. *Solid State Ionics* 1996;83:99–105.
- [858] Chiba R, Yoshimura F, Sakurai Y. An investigation of $\text{LaNi}_{1-x}\text{Fe}_x\text{O}_3$ as a cathode material for solid oxide fuel cells. *Solid State Ionics* 1999;124:281–8.
- [859] Zhen YD, Tok AIY, Jiang SP, Boey FYC. $\text{La}(\text{Ni, Fe})\text{O}_3$ as a cathode material with high tolerance to chromium poisoning for solid oxide fuel cells. *J Power Sour* 2007;170:61–6.
- [860] Komatsua T, Araia H, Chiba R, Nozawa K, Arakawa M, Sato K. Cr poisoning suppression in solid oxide fuel cells using $\text{LaNi}(\text{Fe})\text{O}_3$ electrodes. *Electrochem Solid-State Lett* 2006;9:A9–A12.
- [861] Hjalmarsson P, Søgaard M, Hagen A, Mogensen M. Structural properties and electrochemical performance of strontium- and nickel-substituted lanthanum cobaltite. *Solid State Ionics* 2008;179:636–46.
- [862] Huang K, Lee HY, Goodenough JB. Sr- and Ni-doped LaCoO_3 and LaFeO_3 perovskites new cathode materials for solid oxide fuel cells. *J Electrochem Soc* 1998;145:3220–7.
- [863] Aguadero A, Calle Cdl, Alonso JA, Escudero MJ, Fernández-Díaz MT, Daza L. Structural and electrical characterization of the novel $\text{SrCo}_{0.9}\text{Sb}_{0.1}\text{O}_{3-\delta}$ perovskite: evaluation as a solid oxide fuel cell cathode material. *Chem Mater* 2007;19:6437–44.
- [864] Carter S, Selcuk A, Chater RJ, Kajda J, Kilner JA, Steele BCH. Oxygen transport in selected nonstoichiometric perovskite-structure oxides. *Solid State Ionics* 1992;53–56:597–605.
- [865] Tai L-W, Nasrallah MM, Anderson HU, Sparlin DM, Sehlin SR. Structure and electrical properties of $\text{La}_{1-x}\text{Sr}_x\text{Co}_{1-y}\text{Fe}_y\text{O}_3$. Part 2. The system $\text{La}_{1-x}\text{Sr}_x\text{Co}_{0.2}\text{Fe}_{0.8}\text{O}_3$. *Solid State Ionics* 1995;76:273–83.
- [866] Petrica A, Huangb P, Tietzc F. Evaluation of La-Sr-Co-Fe-O perovskites for solid oxide fuel cells and gas separation membranes. *Solid State Ionics* 2000;135:719–25.
- [867] Teraoka Y, Nobunaga T, Okamoto K, Miura N, Yamazoe N. Influence of constituent metal cations in substituted LaCoO_3 on mixed conductivity and oxygen permeability. *Solid State Ionics* 1991;48:207–12.
- [868] Crumlin EJ, Mutoro E, Ahn S-J, O GJ, Leonard D, Borisevich A, et al. Oxygen reduction kinetics enhancement on a heterostructured oxide surface for solid oxide fuel cells. *J Phys Chem Lett* 2010;1:3149–55.
- [869] Wang L, Merkle R, Maier J, Acarturk T, Starke U. Oxygen tracer diffusion in dense $\text{Ba}_{0.5}\text{Sr}_{0.5}\text{Co}_{0.8}\text{Fe}_{0.2}\text{O}_{3-\delta}$ films. *Appl Phys Lett* 2009;94:071908/1–8.
- [870] Atkinson A, Chater RJ, Rudkin R. Oxygen diffusion and surface exchange in $\text{La}_{0.8}\text{Sr}_{0.2}\text{Fe}_{0.8}\text{Cr}_{0.2}\text{O}_{3-\delta}$ under reducing conditions. *Solid State Ionics* 2001;139:233–40.
- [871] Raj ES, Kilner JA, Irvine JTS. Oxygen diffusion and surface exchange studies on $(\text{La}_{0.75}\text{Sr}_{0.25})_{0.95}\text{Cr}_{0.5}\text{Mn}_{0.5}\text{O}_{3-\delta}$. *Solid State Ionics* 2006;177:1747–52.
- [872] Albert Tn, Stephen JS, Richard JC, Hernández-Ramírez F, JohnKilner A. Layered perovskites as promising cathodes for intermediate temperature solid oxide fuel cells. *J Mater Chem* 2007;17:3175–81.
- [873] Tarancón A, Morata A, Dezanneau G, Skinner SJ, Kilner JA, Estrade S, et al. $\text{GdBaCo}_2\text{O}_{5-x}$ layered perovskite as an intermediate temperature solid oxide fuel cell cathode. *J Power Sour* 2007;174:255–63.
- [874] Chengjun Z, Xiaomei L, Cuishan Y, Duanting Y, Wenhui S. Electrochemical performance of $\text{PrBaCo}_2\text{O}_{5-\delta}$ layered perovskite as an intermediate-temperature solid oxide fuel cell cathode. *J Power Sour* 2008;185:193–6.
- [875] Aimin C, Stephen JS, John AK. Electrical properties of $\text{GdBaCo}_2\text{O}_{5-x}$ for IT-SOFC applications. *Solid State Ionics* 2006;177:2009–11.
- [876] Kun Z, Lei G, Ran R, Zongping S, Shaomin L. Synthesis, characterization and evaluation of cation ordered $\text{LnBaCo}_2\text{O}_{5-\delta}$ as materials of oxygen permeation membranes and cathodes of SOFCs. *Acta Mater* 2008;56:4876–89.
- [877] Kim J-H, Manthiram A. $\text{LnBaCo}_2\text{O}_{5-\delta}$ oxides as cathodes for intermediate-temperature solid oxide fuel cells. *J Electrochem Soc* 2008;155:B385–90.
- [878] Li S, Lü Z, Huang X, Su W. Thermal, electrical, and electrochemical properties of Nd-doped $\text{Ba}_{0.5}\text{Sr}_{0.5}\text{Co}_{0.8}\text{Fe}_{0.2}\text{O}_{3-\delta}$ as a cathode material for SOFC. *Solid State Ionics* 2008;178:1853–8.
- [879] Niu Y, Sunarso J, Liang F, Zhou W, Zhu Z, Shao Z. A comparative study of oxygen reduction reaction on Bi- and La-doped $\text{SrFeO}_{3-\delta}$ perovskite cathodes. *J Electrochem Soc* 2011;158:B132–8.
- [880] Jua Y-W, Inagaki T, Ida S, Ishihara T. Sm(Sr) CoO_3 cone cathode on LaGaO_3 thin film electrolyte for IT-SOFC with high power density. *J Electrochem Soc* 2011;158:B825–30.
- [881] Chen D, Huang C, Ran R, Park HJ, Kwak C, Shao Z. New $\text{Ba}_{0.5}\text{Sr}_{0.5}\text{Co}_{0.8}\text{Fe}_{0.2}\text{O}_{3-\delta} + \text{Co}_3\text{O}_4$ composite electrode for IT-SOFCs with improved electrical conductivity and catalytic activity. *Electrochim Commun* 2011;13:197–9.
- [882] Tietz F, Mai A, Stöver D. From powder properties to fuel cell performance: a holistic approach for SOFC cathode development. *Solid State Ionics* 2008;179:1509–15.
- [883] Lynch ME, Yang L, Qin W, Choi J-J, Liu M, Blinn K, et al. Enhancement of $\text{La}_{0.6}\text{Sr}_{0.4}\text{Co}_{0.2}\text{Fe}_{0.8}\text{O}_{3-\delta}$ durability and surface electrocatalytic activity by $\text{La}_{0.85}\text{Sr}_{0.15}\text{MnO}_{3\pm\delta}$ investigated using a new test electrode platform. *Energy Environ Sci* 2011;4:2249–58.
- [884] Nie L, Liu M, Zhang Y, Liu M. $\text{La}_{0.6}\text{Sr}_{0.4}\text{Co}_{0.2}\text{Fe}_{0.8}\text{O}_{3-\delta}$ cathodes infiltrated with samarium-doped cerium oxide for solid oxide fuel cells. *J Power Sour* 2010;195:4704–8.
- [885] Kim J-H, Manthiram A. Low thermal expansion $\text{RBa}(\text{Co, M})_4\text{O}_7$ cathode materials based on tetrahedral-site cobalt ions for Solid Oxide Fuel Cells. *Chem Mater* 2010;22:822–31.
- [886] Badwal S, Föger K. SOFC development at ceramic fuel cells limited. In: Stevens P, editor. Proceedings of 3rd European solid oxide fuel cell forum. Nantes (France): The European Fuel Cell Forum; 1998. p. 95–104.
- [887] Tietz F, Haart LGJd, Laatsch J, Malzbender J, Nabielek H, Steinbrech RW, et al. Component reliability in solid oxide fuel cell systems for commercial operation ('CORE-SOFC'). In: Mogensen M, editor. Proceedings of 6th European solid oxide fuel cell forum. Lucerne (Switzerland): The European Fuel Cell Forum; 2004. p. 289–98.
- [888] Singhal SC. Recent progress in tubular solid oxide fuel cell technology. In: Stimming U, Singhal SC, Tagawa H, Lehnert W, editors. 5th International symposium on solid oxide fuel cells. Pennington (NJ), Aachen (Germany): The Electrochemical Society, Inc.; 1997. p. 37–50.

- [889] Tedmon Jr CS, Spacil HS, Mitoff SP. Cathode materials and performance in high-temperature zirconia electrolyte fuel cells. *J Electrochem Soc* 1969;116:1170–5.
- [890] Lau SK, Singhal SC. Corrosion/85: the national association of corrosion engineers meeting. Houston (TX), Boston (USA): National Association of Corrosion Engineers; 1985. 1–9.
- [891] Takeda Y, Sakai Y, Ichikawa T, Imanishi N, Yamamoto O, Mori M, et al. Stability of $\text{La}_{1-x}\text{A}_x\text{MnO}_{3-z}$ ($\text{A} = \text{Ca}, \text{Sr}$) as cathode materials for solid oxide fuel cells. *Solid State Ionics* 1994;72:257–64.
- [892] Yokokawa H, Sakai N, Kawada T, Dokiya M. Thermodynamic analysis of reaction profiles between LaMO_3 ($\text{M} = \text{Ni}, \text{Co}, \text{Mn}$) and ZrO_2 . *J Electrochem Soc* 1991;138:2719–27.
- [893] Yokokawa H, Horita T, Sakai N, Dokiya M, Kawada T. Thermodynamic representation of nonstoichiometric lanthanum manganite. *Solid State Ionics* 1996;86–88:1161–5.
- [894] Yokokawa H, Sakai N, Kawada T, Dokiya M. Chemical thermodynamic stabilities of the interface. In: Badwal SPS, Bannister MJ, Hannink RHJ, editors. *Science and technology of zirconia V*. Melbourne (Australia): Technomic Publishing Company, Inc.; 1993. p. 752–63.
- [895] Yokokawa H. Understanding materials compatibility. *Ann Rev Mater Res* 2003;33:581–610.
- [896] Waller D, Sirman JD, Kilner JA. Manganese diffusion in single crystal and polycrystalline yttria stabilized zirconia. In: Stimming U, Singhal SC, Tagawa H, Lehnert W, editors. *5th International symposium on solid oxide fuel cells*. Pennington (NJ), Aachen (Germany): The Electrochemical Society; 1997. p. 1140–9.
- [897] Mori M, Abe T, Itoh H, Yamamoto O, Shen GQ, Takeda Y, et al. Reaction mechanism between lanthanum manganite and yttria doped cubic zirconia. *Solid State Ionics* 1999;123:113–9.
- [898] Mitterdorfer A, Gauckler LJ. $\text{La}_2\text{Zr}_2\text{O}_7$ formation and oxygen reduction kinetics of the $\text{La}_{0.85}\text{Sr}_{0.15}\text{MnO}_3, \text{O}_2(\text{g})|\text{YSZ}$ system. *Solid State Ionics* 1998;111:185–218.
- [899] Tricker DM, Stobbs WM. High temperature electrochemical behaviour of fast ion and mixed conductors. In: Poulsen FW, Bentzen JJ, Jacobsen T, Skou E, Østergård MJL, editors. *14th Risø international symposium on materials science*. Roskilde (Denmark): Risø National Laboratory; 1993. p. 453–60.
- [900] Jiang SP, Zhang JP, Ramprakash Y, Milosevic D, Wilshier K. An investigation of shelf-life of strontium doped LaMnO_3 materials. *J Mater Sci* 2000;35:2735–41.
- [901] Roosmalen JAMV, Cordfunke EHP. Chemical reactivity and interdiffusion of $(\text{La}, \text{Sr})\text{MnO}_3$ and $(\text{Zr}, \text{Y})\text{O}_2$, solid oxide fuel cell cathode and electrolyte materials. *Solid State Ionics* 1992;52:303–12.
- [902] Tsai T, Scott A. Effect of LSM-YSZ cathode on thin-electrolyte solid oxide fuel cell performance. *Solid State Ionics* 1997;93:207–17.
- [903] Stochniol G, Syskakis E, Naoumidis A. Chemical compatibility between strontium-doped lanthanum manganite and yttria-stabilized zirconia. *J Am Ceram Soc* 1995;78:929–32.
- [904] Brugnoni C, Ducati U, Scagliotti M. SOFC cathode/electrolyte interface. Part I: reactivity between $\text{La}_{0.85}\text{Sr}_{0.15}\text{MnO}_3$ and $\text{ZrO}_2\text{-Y}_2\text{O}_3$. *Solid State Ionics* 1995;76:177–82.
- [905] Kenjo T, Nishiyama M. LaMnO_3 air cathodes containing ZrO_2 electrolyte for high temperature solid oxide fuel cells. *Solid State Ionics* 1992;57:295–302.
- [906] Yamamoto O, Takeda Y, Kanno R, Kojima T. In: Singhal SC, editor. *1st International symposium on solid oxide fuel cells*. Pennington (NJ), Hollywood (FL, USA): The Electrochemical Society; 1989. p. 242.
- [907] Sakai Y, Takeda Y, Kato A, Imanishi N, Yamamoto O, Hattori M, et al. $\text{Ln}_{1-x}\text{Sr}_x\text{MnO}_3$ ($\text{Ln} = \text{Pr}, \text{Nd}, \text{Sm}$ and Gd) as the cathode material for solid oxide fuel cells. *Solid State Ionics* 1999;118:187–94.
- [908] Yoon HS, Choi SW, Lee D, Kim BH. Synthesis and characterization of $\text{Gd}_{1-x}\text{Sr}_x\text{MnO}_3$ cathode for solid oxide fuel cells. *J Power Sour* 2001;93:1–7.
- [909] Kawada T, Sakai N, Yokokawa H, Dokiya M. Reaction between solid oxide fuel cell materials. *Solid State Ionics* 1992;50:189–96.
- [910] Yamamoto O, Shen GQ, Takeda Y, Imanishi N, Sakai Y. In: Grosz F, editor. *2nd International symposium on solid oxide fuel cells*. Pennington (NJ), Athens (Greece): The Electrochemical Society; 1991. p. 158.
- [911] Labrinch JA, Frade JR, Marques FMB. $\text{La}_2\text{Zr}_2\text{O}_7$ formed at ceramic electrode/YSZ contacts. *J Mater Sci* 1993;28:3809–15.
- [912] Poulsen FW, Puil Nvd. Phase relations and conductivity of Sr- and La-zirconates. *Solid State Ionics* 1992;53–56:777–83.
- [913] Taniguchi S, Kadowaki M, Kawamura H, Yasuo T, Akiyama Y, Miyake Y, et al. Degradation phenomena in the cathode of a solid oxide fuel cell with an alloy separator. *J Power Sour* 1995;55:73–9.
- [914] Badwal SPS, Deller R, Fogar K, Ramprakash Y, Zhang JP. Interaction between chromia forming alloy interconnects and air electrode of solid oxide fuel cells. *Solid State Ionics* 1997;99:297–310.
- [915] Paulson SC, Birss VI. Chromium poisoning of LSM-YSZ SOFC cathodes I. Detailed study of the distribution of chromium species at a porous, single-phase cathode. *J Electrochem Soc* 2004;151:A1961–8.
- [916] Matsuzaki Y, Yasuda I. Electrochemical properties of a SOFC cathode in contact with a chromium-containing alloy separator. *Solid State Ionics* 2000;132:271–8.
- [917] Hilpert K, Das D, Miller M, Peck DH, Weiß R. Chromium vapor species over solid oxide fuel cell interconnect materials and their potential for degradation processes. *J Electrochem Soc* 1996;143:3642–7.
- [918] Konysheva E, Penkalla H, Wessel E, Mertens J, Seeling U, Singheiser L, et al. Chromium poisoning of perovskite cathodes by the ODS alloy $\text{Cr}_x\text{Fe}_1\text{Y}_2\text{O}_3$ and the high chromium ferritic steel crofer22APU. *J Electrochem Soc* 2006;153:A765–73.
- [919] Matsuzaki Y, Yasuda I. Dependence of SOFC cathode degradation by chromium-containing alloy on compositions of electrodes and electrolytes. *J Electrochem Soc* 2001;148:A126–31.
- [920] Jiang SP, Zhang JP, Fogar K. Deposition of chromium species at Sr-doped LaMnO_3 electrodes in solid oxide fuel cells: III. Effect of air flow. *J Electrochem Soc* 2001;148:C447–55.
- [921] Jiang SP, Zhang JP, Apateanu L, Fogar K. Deposition of chromium species on Sr-doped LaMnO_3 cathodes in solid oxide fuel cells. *Electrochim Commun* 1999;1:394–7.
- [922] Jiang SP, Zhang JP, Zheng XG. A comparative investigation of chromium deposition at air electrodes of solid oxide fuel cells. *J Euro Ceram Soc* 2002;22:361–73.

- [924] Jiang SP, Zhang S, Zhen YD. Early interaction between Fe–Cr alloy metallic interconnect and Sr-doped LaMnO₃ cathodes of solid oxide fuel cells. *J Mater Res* 2005;20:747–58.
- [925] Wang S, Cruse TA, Krumpelt M, Ingram BJ, Salvador PA. Microstructural degradation of (La, Sr)MnO₃/YSZ cathodes in solid oxide fuel cells with uncoated E-brrite interconnects. *J Electrochem Soc* 2011;158:B152–8.
- [926] Zachau-Christiansen B, Jacobsen T, Skaarup S. Oxygen stoichiometry in cation deficient (La, Sr)_{1-x}MnO₃ SOFC cathode materials. In: Stimming U, Singh SC, Tagawa H, Lehnert W, editors. 5th International symposium on solid oxide fuel cells. Pennington (NJ), Aachen (Germany): The Electrochemical Society; 1996. p. 795.
- [927] Nielsen J, Mogensen M. SOFC LSM: YSZ cathode degradation induced by moisture: an impedance spectroscopy study. *Solid State Ionics* 2011;189:74–81.
- [928] Zuo C, Liu M, Liu M. Solid oxide fuel cells. New York (USA): Springer Science + Business Media; 2012.
- [929] <http://www.aki.che.tohoku.ac.jp/~koyama/html/research/SOFC.html>.
- [930] Yokokawa H. Overview of intermediate-temperature solid oxide fuel cells, Springer Science-Business Media, LLC; Berlin (Germany); 2009.
- [931] Zhu WZ, Deevi SC. Development of interconnect materials for solid oxide fuel cells. *Mater Sci Eng A* 2003;348:227–43.
- [932] Sakai N, Yokokawa H, Horita T, Yamaji K. Lanthanum chromite-based interconnects as key materials for SOFC stack development. *Int J Appl Ceram Technol* 2004;1:23–30.
- [933] Akashi T, Maruyama T, Goto T. Transport of lanthanum ion and hole in LaCrO₃ determined by electrical conductivity measurements. *Solid State Ionics* 2003;64:177–83.
- [934] Vielstich W, Hubert A, Gasteiger M, Lamm A. Handbook of fuel cells-fundamentals, technology and applications. New York (USA): Wiley; 2003.
- [935] Anderson HU. Fabrication and property control of LaCrO₃ based oxides. *Proces Crystal Ceram Mater Sci Res* 1978;11:469–77.
- [936] Groupy L, Anderson HU. Densification of La_{1-x}Sr_xCrO₃. *J Am Ceram Soc* 1976;59:449–50.
- [937] Tai L-W, Lessing PA. Tape casting and sintering of strontium-doped lanthanum chromite for a planar solid oxide fuel cell bipolar plate. *J Am Ceram Soc* 1991;74:155–60.
- [938] Sakai N, Kawada T, Yokokawa H, Dokiya M, Iwata T. Sinterability and electrical conductivity of calcium-doped lanthanum chromites. *J Mater Sci* 1990;25:4531–4.
- [939] Yokokawa H, Sakai N, Kawada T, Dokiya M. Chemical thermodynamic considerations in sintering of LaCrO₃-based perovskites. *J Electrochem Soc* 1991;138:1018–27.
- [940] Sakai N, Kawada T, Yokokawa H, Dokiya M, Iwata T. Thermal expansion of some chromium deficient lanthanum chromites. *Solid State Ionics* 1990;40/41:394–7.
- [941] Mori M, Sakai N, Kawada T, Yokokawa H, Dokiya M. Low-temperature air-sinterable lanthanum calcium chromites with chromium deficit for SOFC separator. *Denki Kagaku* 1991;59:314–9.
- [942] Sakai N, Kawada T, Yokokawa H, Dokiya M, Kojima I. Liquid-phase-assisted sintering of calcium-doped lanthanum chromites. *J Am Ceram Soc* 1993;76:609–16.
- [943] Koc R, Anderson HU. Low temperature sintering of LaCrO₃ based ceramics. *Ceram Trans* 1990;12:659–66.
- [944] Koc R, Anderson HU. Liquid phase sintering of LaCrO₃. *J Euro Ceram Soc* 1992;9:285–92.
- [945] Christie GM, Middleton PH, Steele BCH. Liquid phase sintering, electrical conductivity, and chemical stability of lanthanum chromite doped with calcium and nickel. *J Euro Ceram Soc* 1994;14:163–75.
- [946] Fergus JW, Hui R, Li X, Wilkinson DP, Zhang J. Solid oxide fuel cells: material properties and performance, Green chemistry and chemical engineering, 2009, CRC Press, Taylor and Francis; Boca Raton (FL, USA).
- [947] Onuma S, Miyoshi S, Yashiro K, Kaimai A, Kawamura K, Nigara Y, et al. Phase stability of La_{1-x}Ca_xCrO_{3-d} in oxidizing atmosphere. *J Solid State Chem* 2003;170:68–74.
- [948] Miyoshi S, Onuma S, Kaimai A, Matsumoto H, Yashiro K, Kawada T, et al. Chemical stability of La_{1-x}Sr_xCrO₃ in oxidizing atmospheres. *J Solid State Chem* 2004;177:4112–8.
- [949] Peck DH, Miller M, Hilpert K. Phase diagram study in the CaO–Cr₂O₃–La₂O₃ system in air and under low oxygen partial pressure. *Solid State Ionics* 1999;123:47–57.
- [950] Peck DH, Miller M, Hilpert K. Phase diagram study in the SrO–Cr₂O₃–La₂O₃ system in air and under low oxygen partial pressure. *Solid State Ionics* 1999;123:59–65.
- [951] Ianculescu A, Braileanu A, Pasuk I, Zaharescu M. Phase formation study of alkaline earth-doped lanthanum chromites. *J Therm Anal Calor* 2001;66:501–7.
- [952] Fergus JW. Lanthanum chromite based materials for solid oxide fuel cell interconnects. *Solid State Ionics* 2004;171:1–15.
- [953] Wu J, Liu X. Recent development of SOFC metallic interconnect. *J Mater Sci Technol* 2010;26:293–305.
- [954] Zhou X, Deng F, Zhu M, Meng G, Liu X. High performance composite interconnect La_{0.7}Ca_{0.3}CrO₃/20 mol% ReO_{1.5} doped CeO₂ (Re = Sm, Gd, Y) for solid oxide fuel cells. *J Power Sour* 2007;164:293–9.
- [955] Zhou X-L, Ma J-J, Deng F-J, Meng G-Y, Liu X-Q. A high performance interconnecting ceramic for solid oxide fuel cells (SOFCs). *Solid State Ionics* 2006;177:3461–6.
- [956] Zhou X, Zhu M, Deng F, Meng G, Liu X. Electrical properties, sintering and thermal expansion behavior of composite ceramic interconnecting materials, La_{0.7}Ca_{0.3}CrO_{3-x}/Y_{0.2}Ce_{0.8}O_{1.9} for SOFCs. *Acta Mater* 2007;55:2113–8.
- [957] Hilpert K, Steinbrech RW, Boroomand F, Wessel E, Meschke F, Zuev A, et al. Defect formation and mechanical stability of perovskites based on LaCrO₃ for solid oxide fuel cells (SOFC). *J Euro Ceram Soc* 2003;23:3009–20.
- [958] Zuev A, Singheiser L, Hilpert K. Defect structure and isothermal expansion of A-site and B-site substituted lanthanum chromites. *Solid State Ionics* 2002;147:1–11.
- [959] Anderson HU, Nasrallah MM, Flandermeyer BK, Agrawal AK. High-temperature redox behavior of doped SrTiO₃ and LaCrO₃. *J Solid State Chem* 1985;56:325–34.
- [960] Anderson HU, Kuo JH, Sparlin DM. Review of defect chemistry of LaMnO₃ and LaCrO₃. *Proc Electrochem Soc* 1989;89:111–28.
- [961] Yasuda I, Hishinuma M. Electrical conductivity and chemical diffusion coefficient of Sr-doped lanthanum chromites. *Solid State Ionics* 1995;80:141–50.

- [962] Boroomand F, Wessel E, Bausinger H, Hilpert K. Correlation between defect chemistry and expansion during reduction of doped LaCrO_3 interconnects for SOFCs. *Solid State Ionics* 2000;129:251–8.
- [963] Hilpert K, Steinbrech RW, Boroomand F, Wessel E, Meschke F, Zuev A, et al. Defect formation and mechanical stability of perovskites based on LaCrO_3 for solid oxide fuel cells (SOFC). *J Euro Ceram Soc* 2003;23:3009–20.
- [964] Kofstad P. Nonstoichiometry, diffusion and electrical conductivity in binary metal oxides. New York (USA): Wiley-Interscience; 1972.
- [965] Armstrong TJ, Stevenson JW, Pederson LR, Raney PE. Dimensional instability of doped lanthanum chromite. *J Electrochem Soc* 1996;143:2919–25.
- [966] Zuev A, Singheiser L, Hilpert K. Defect formation and thermal expansion of perovskites on the basis of LaCrO_3 for Solid Oxide Fuel Cells. In: Singhal SC, Dokya M, editors. 8th International symposium on solid oxide fuel cells. Pennington (NJ), Paris (France): The Electrochemical Society; 2003. p. 817–31.
- [967] Simmer SP, Hardy JS, Stevenson JW. Sintering and properties of mixed lanthanide chromites. *J Electrochem Soc* 2001;148:A351–60.
- [968] Mori K, Miyamoto H, Takenobu K, Matsudaira T. Controlling the chromite expansion in reducing atmosphere at high temperature. In: McEvoy AJ, editor. Proceedings of 4th European solid oxide fuel cell forum. Lucerne (Switzerland): The European Fuel Cell Forum; 2000. p. 875–80.
- [969] Mori M. Enhancing effect on densification and thermal expansion compatibility for $\text{La}_{0.8}\text{Sr}_{0.2}\text{Cr}_{0.9}\text{Ti}_{0.1}\text{O}_3$ -based SOFC interconnect with B-site doping. *J Electrochem Soc* 2002;149:A797–803.
- [970] Larsen PH, Hendriksen PV, Mogensen M. Dimensional stability and defect chemistry of doped lanthanum chromites. *J Therm Anal* 1997;49:1263–75.
- [971] Schäfer W, Schmidberger R. Ca and Sr doped LaCrO_3 : preparation, properties, and high temperature applications. In: Vincenzini P, editor. High tech ceramics. Amsterdam (The Netherlands): Elsevier Science; 1987. p. 1737–42.
- [972] Montross CS, Yokokawa H, Dokiya M, Bekessy L. Mechanical properties of magnesia-doped lanthanum chromite versus temperature. *J Am Ceram Soc* 1995;78:1869–72.
- [973] Mori M, Yamamoto T, Itoh H, Watanabe T. Compatibility of alkaline earth metal (Mg, Ca, Sr)-doped lanthanum chromites as separators in planar-type high-temperature solid oxide fuel cells. *J Mater Sci* 1997;32:2423–31.
- [974] Paulik SW, Baskaran S, Armstrong TR. Mechanical properties of calcium- and strontium-substituted lanthanum chromite. *J Mater Sci* 1997;33:2397–404.
- [975] Sammes NM, Ratnaraj R. High temperature mechanical properties of $\text{La}_{1-x}\text{Sr}_x\text{Cr}_{1-y}\text{Co}_y\text{O}_3$ for SOFC interconnect. *J Mater Sci* 1995;30:4523–6.
- [976] Yasuda I, Ogiwara T, Yakabe H. Accumulation of detailed property data for LaCrO_3 -based interconnector materials. *Proc Electrochem Soc* 2001;16:783–92.
- [977] Montross CS, Yokokawa H, Dokiya M. Toughening in lanthanum chromite due to metastable phase. *Scripta Mater* 1996;34:913–7.
- [978] Paulik SW, Baskaran S, Armstrong TR. Mechanical properties of calcium-substituted yttrium chromite. *J Mater Sci Lett* 1999;18:819–22.
- [979] Majumdar S, Claar T, Flandermeyer B. Stress and fracture behavior of monolithic fuel cell tapes. *J Am Ceram Soc* 1986;69:628–33.
- [980] Yang Z, Weil KS, Paxton DM, Stevenson JW. Selection and evaluation of heat-resistant alloys for SOFC interconnect applications. *J Electrochem Soc* 2003;150:A1188–201.
- [981] Piccardo P, Gannon P, Chevalier S, Viviani M, Barbucci A, Caboche G, et al. ASR evaluation of different kinds of coatings on a ferritic stainless steel as SOFC interconnects. *Surf Coat Technol* 2007;202:1221–5.
- [982] Qu W, Jian L, Ivey DG, Hill JM. Yttrium, cobalt and yttrium/cobalt oxide coatings on ferritic stainless steels for SOFC interconnects. *J Power Sour* 2006;157:335–50.
- [983] Ueda M, Taimatsu H. In: McEvoy AJ, (Ed), Proceedings of 4th European solid oxide fuel cell forum, 2000, The European Fuel Cell Forum, Lucerne (Switzerland), 835–843.
- [984] Li JQ, Zeng XR, Tanga JN, Xiaob P. Fabrication and thermal properties of a YSZ-NiCr joint with an interlayer of YSZ-NiCr functionally graded material. *J Euro Ceram Soc* 2003;18:1847–53.
- [985] Wei X, Atkinson A. Nickel/ceramic composites for current collection terminals. In: Singhal SC, Dokya M, editors. 8th International symposium on solid oxide fuel cells. Pennington (NJ), Paris (France): The Electrochemical Society; 2003 . p. 898–904.
- [986] Fergus JW. Metallic interconnects for solid oxide fuel cells. *Mater Sci Eng*, A 2005;397:271–83.
- [987] Sims CT, Stoloff NS, Hagel WC. Superalloys II. New York (USA): John Wiley & Sons; 1987.
- [988] Davis JR. ASM specialty handbook: stainless steels. Materials Park (OH, USA): ASM International®; 1994.
- [989] Wasielewski GE, Robb RA. High temperature oxidation in the superalloys. New York (USA): John Wiley & Sons, Inc.; 1972.
- [990] Kofstad P. High temperature oxidation of chromium and chromium-forming alloys. In: Thorstensen B, editor. Proceedings of 2nd European solid oxide fuel cell forum. Oslo (Norway): The European Fuel Cell Forum; 1996. p. 479–90.
- [991] Kofstad P, Bredesen R. High temperature corrosion in SOFC environments. *Solid State Ionics* 1992;52:69–75.
- [992] Holt A, Kofstad P. Electrical conductivity and defect structure of Cr_2O_3 . II. Reduced temperatures ($<\sim 1000^\circ\text{C}$). *Solid State Ionics* 1994;69:137–43.
- [993] Holt A, Kofstad P. Electrical conductivity and defect structure of Cr_2O_3 . I. High temperatures ($>\sim 1000^\circ\text{C}$). *Solid State Ionics* 1994;69:127–36.
- [994] Ebbinghaus BB. Thermodynamics of gas phase chromium species: the chromium oxides, the chromium oxyhydroxides, and volatility calculations in waste incineration processes. *Combust Flame* 1993;93:119–37.
- [995] Gindorf C, Singheiser L, Hilpert K, Schroeder M, Martin M, Greiner H, et al. Chromium vaporization from metallic interconnect and retention by perovskite layers. In: Singhal SC, Dokya M, editors. 6th International symposium on solid oxide fuel cells. Pennington (NJ), Honolulu (HI, USA): The Electrochemical Society; 1999. p. 774–82.
- [996] Matsuzakiz Y, Yasuda I. Dependence of SOFC cathode degradation by chromium-containing alloy on compositions of electrodes and electrolytes. *J Electrochem Soc* 2001;148:A126–31.

- [997] Hilpert K, Dos D, Miller M, Peck DH, Wei R. Chromium vapor species over solid oxide fuel cell interconnect materials and their potential for degradation processes. *J Electrochem Soc* 1996;143:3642–7.
- [998] Badwal SPS, Deller R, Fogera K, Ramprakash Y, Zhang JP. Interaction between chromia forming alloy interconnects and air electrode of solid oxide fuel cells. *Solid State Ionics* 1997;99:297–310.
- [999] Li JQ, Xiao P. Fabrication and characterization of $\text{La}_{0.8}\text{Sr}_{0.2}\text{MnO}_3$. *J Euro Ceram Soc* 2001;21:659–68.
- [1000] Jiang SP. Use of gaseous Cr species to diagnose surface and bulk process for O_2 reduction in solid oxide fuel cells. *J Appl Electrochem* 2001;31:181–92.
- [1001] Jiang SP, Zhang JP, Apateanu L, Foger K. Deposition of chromium species at Sr-doped LaMnO_3 electrodes in solid oxide fuel cells I. Mechanism and kinetics. *J Electrochem Soc* 2000;147:4013–22.
- [1002] Jiang SP, Zhang JP, Foger K. Deposition of chromium species at Sr-doped LaMnO_3 electrodes in solid oxide fuel cells: II. Effect on O_2 reduction reaction. *J Electrochem Soc* 2000;147:3195–205.
- [1003] Jiang S-P, Zhang J-P, Apateanu L, Foger K. Deposition of chromium species on Sr-doped LaMnO_3 cathodes in solidoxide fuel cells. *Electrochim Commun* 1999;1:394–7.
- [1004] Quadakkers WJ, Greiner H, Htinseil M, Pattaik A, Khanna AS, Mallener W. Compatibility of perovskite contact layers between cathode and metallic interconnector plates of SOFCs. *Solid State Ionics* 1996;91:55–67.
- [1005] Taniguchi S, Kadowaki M, Kawamura H, Yasuo T, Akiyama Y, Miyake Y, et al. Degradation phenomena in the cathode of a solid oxide fuel cell with an alloy separator. *J Power Sour* 1995;55:73–9.
- [1006] Liu D, Almer J, Cruses T, Krumpelt M. 31st International conference and exposition on advanced ceramics and composites. Daytona Beach (FL, USA): The American Ceramic Society; 2007.
- [1007] http://www.mie.utoronto.ca/labs/sofc/reza_bateni.html.
- [1008] Seo HS, Yun DW, Kim KY. Effect of Ti addition on the electric and ionic property of the oxide scale formed on the ferritic stainless steel for SOFC interconnect. *Int J Hydro Energy* 2012;1–10.
- [1009] Gannon PE. High-temperature oxidation resistance and surface electrical conductivity of stainless steels with filtered arc Cr-Al-N multilayer and/or superlattice coatings. *Surf Coat Technol* 2004;55–61.
- [1010] Kayani A, Smith RJ, Teintze S, Kopczyk M, Gannon PE, Deibert MC, et al. Oxidation studies of CrAlON nanolayered coatings on steel plates. *Surf Coat Technol* 2006;201:1685–94.
- [1011] Wu J, Li C, Johnson C, Liu X. Evaluation of SmCo and SmCoN magnetron sputtering coatings for SOFC interconnect applications. *J Power Sour* 2008;175:833–40.
- [1012] Liu X, Johnson C, Li C, Xu J, Cross C. Developing TiAlN coatings for intermediate temperature solid oxide fuel cell interconnect applications. *Int J Hydro Energy* 2008;33:189–96.
- [1013] Orlovskaya N, Coratolo A, Johnson C, Gemmen R. Structural characterization of lanthanum chromite perovskite coating deposited by magnetron sputtering on an iron-based chromium containing alloy as a promising interconnect material for SOFCs. *J Am Ceram Soc* 2004;87:1981–7.
- [1014] Choi J-J, Lee J-H, Park D-S, Hahn B-D, Yoon W-H, Lin H-T. Oxidation resistance coating of LSM and LSCF on SOFC metallic interconnects by the aerosol deposition process. *J Am Ceram Soc* 2007;90:1926–9.
- [1015] Johnson C, Wu J, Liu X, Gemmen R. Solid oxide fuel cell performance using metallic interconnects coated by electroplating methods. In: The 5th international conference on fuel cell science, engineering and technology. Brooklyn, New York (USA): American Society of Mechanical Engineers; 2007.
- [1016] Larringz, Norby T. Spinel and perovskite functional layers between plansee metallic interconnect (Cr-5 wt%Fe-1 wt% Y_2O_3) and Ceramic ($\text{La}_{0.85}\text{Sr}_{0.15}\text{MnO}_3$) cathode materials for solid oxide fuel cells. *J Electrochem Soc* 2000;147:3251–6.
- [1017] Chen X, Hou PY, Jacobson CP, Visco SJ, Jonghe LCD. Protective coating on stainless steel interconnect for SOFCs: oxidation kinetics and electrical properties. *Solid State Ionics* 2005;176:425–33.
- [1018] Yang Z, Xia G-G, Li X-H, Stevenson JW. (Mn, Co)₃O₄ spinel coatings on ferritic stainless steels for SOFC interconnect applications. *Int J Hydro Energy* 2007;32:3648–54.
- [1019] Yang Z, Xia G, Simmer SP, Stevenson JW. Thermal growth and performance of manganese cobaltite spinel protection layers on ferritic stainless steel SOFC interconnects. *J Electrochem Soc* 2005;152:A1896–901.
- [1020] Gorokhovsky VI, Gannon PE, Deibert MC, Smith RJ, Kayani A, Kopczyk M, et al. Deposition and evaluation of protective PVD coatings on ferritic stainless steel SOFC interconnects. *J Electrochem Soc* 2006;153:A1886–93.
- [1021] Brenner A. Electrodeposition of alloys: principles and practice. University of Michigan; Ann Arbor: Ph.D. Thesis, Academic Press; 1963.
- [1022] Paunovic M, Schlesinger M. Fundamental of electrochemical deposition. Wiley; New York (USA); 1998.
- [1023] Bateni MR, Wei P, Deng X, Petric A. Spinel coatings for UNS 430 stainless steel interconnects. *Surf Coat Technol* 2007;201:4677–84.
- [1024] Gong J, Zangari G. Electrodeposition of sacrificial tin/manganese alloy coatings. *Mater Sci Eng, A* 2003;344:268–78.
- [1025] Wei W, Chen W, Ivey DG. Anodic electrodeposition of nanocrystalline coatings in the Mn-Co-O system. *Chem Mater* 2007;19:2816–22.
- [1026] Mukerjee S, Jaltiner K, Kerr R, Chick L, Sprinkle V, Meinhardt K. Solid oxide fuel cell development: latest results. *ECS Trans* 2007;7:59–65.
- [1027] Yoo Y, Dauga M. In: Yokokawa H, Singhal SC, editors. 7th International symposium on solid oxide fuel cells. Pennington (NJ), Tsukuba (Japan): The Electrochemical Society; 2001. p. 837–46.
- [1028] Nie HW, Wen T-L, Tu HY. Protection coatings for planar solid oxide fuel cell interconnect prepared by plasma spraying. *Mater Res Bullet* 2003;38:1531–6.
- [1029] Linderoth S, Larsen PH. Investigations of Fe-Cr ferritic steels as SOFC interconnect material, In: Doughty DH, Brack HP, Naoi K, Nazar LF, editors. New materials for batteries and fuel cells, 2000, Materials Research Society, Warrendale (PA, USA).
- [1030] Yang Z, Xia G-G, Maupin GD, Stevenson JW. Conductive protection layers on oxidation resistant alloys for SOFC interconnect applications. *Surf Coat Technol* 2006;201:4476–83.
- [1031] Nielsen KA, Solveng M, Nielsen SBL, Dinesen AR, Beeaff D, Larsen PH. Glass composite seals for SOFC application. *J Euro Ceram Soc* 2007;27:1817–22.

- [1032] Smeacetto F, Salvo M, Ferraris M, Chob J, Boccaccini AR. Glass-ceramic seal to join Crofer 22 APU alloy to YSZ ceramic in planar SOFCs. *J Euro Ceram Soc* 2008;28:61–8.
- [1033] Laosiripojana N, Wiyaratn W, Kiatkittipong W, Arpornwichanop A, Soottitantawat A, Assabumrungrat S. Reviews on solid oxide fuel cell technology. *Eng J* 2009;13:65–83.
- [1034] Weil KS, Coyle CA, Hardy JS, Kim JY, Xia GG. Alternative planar SOFC sealing concepts. *Fuel Cells Bullet* 2004;12–6.
- [1035] Koeppl BJ, Weil KS. Finite element analysis of the bonded compliant seal design – a new sealing concept for use in planar solid oxide fuel cells. In: Bansal NP, Zhu D, Kriven WM, editors. 29th International conference on advanced ceramics and composites. OH (USA), Cocoa Beach (FL, USA): The American Ceramic Society; 2005.
- [1036] Singh RN. High-temperature seals for solid oxide fuel cells (SOFC). *J Mater Eng Perform* 2006;15:422–6.
- [1037] Jung HY, Choi S-H, Kim H, Son J-W, Kim J, Lee H-W, et al. Fabrication and performance evaluation of 3-cell SOFC stack based on planar 10 cm × 10 cm anode-supported cells. *J Power Sour* 2006;159:478–83.
- [1038] Liu W, Sun X, Khaleel MA. Predicting Young's modulus of glass/ceramic sealant for solid oxide fuel cell considering the combined effects of aging, micro-voids and self-healing. *J Power Sour* 2008;185:1193–200.
- [1039] Lessing PA, Hartvigsen J, Elangovan S. Sealants in solid oxide fuel cells: materials properties and performance. Boca Raton (FL, USA): CRC Press, Taylor and Francis; 2009.
- [1040] Williams M. Status and market applications for the solid oxide fuel cell in the US-A new direction. In: Yokokawa H, Singhal SC, editors. 7th International symposium on solid oxide fuel cells. Pennington (NJ), Tsukuba (Japan): The Electrochemical Society; 2001.
- [1041] Suzuki T, Yamaguchi T, Fujishiro Y, Awano M. Improvement of SOFC performance using a microtubular, anode-supported SOFC. *J Electrochem Soc* 2006;153:A925–8.
- [1042] Liu Y, Hashimoto S-I, Nishino H, Takei K, Mori M, Suzuki T, et al. Fabrication and characterization of miero-tubular cathode-supported SOFC for intermediate temperature operation. *J Power Sour* 2007;174:95–102.
- [1043] Singh RN. Sealing technology for solid oxide fuel cells (SOFC). *Int J Appl Ceram Technol* 2007;4:134–44.
- [1044] Chou Y-s, Stevenson JW, Chick LA. Novel compressive mica seals with metallic interlayers for solid oxide fuel cell applications. *J Am Ceram Soc* 2003;86:1003–7.
- [1045] Lessing PA. A review of sealing technologies applicable to solid oxide electrolysis cells. *J Mater Sci* 2007;42:3465–76.
- [1046] Weber A, Mueller A, Herbsttritt D, Ivers-Tiffey W. Characterization of SOFC single cells. In: Yokokawa H, Singhal SC, editors. 7th International symposium on solid oxide fuel cells. Pennington (NJ), Tsukuba (Japan): The Electrochemical Society; 2001. p. 952–62.
- [1047] Bram M, Bruenings SE, Meschke F, Meulenberg WA, Buchkremer HP, Steinbrech RW, et al. Applications of metallic gaskets in SOFC stacks. In: Yokokawa H, Singhal SC, editors. 7th International symposium on solid oxide fuel cells. Pennington (NJ), Tsukuba (Japan): The Electrochemical Society; 2001. p. 875–84.
- [1048] Bram M, Reckers S, Drinovac P, Moench J, Steinbrech RW, Buchkremer HP, et al. Characterization and evaluation of compression loaded sealing concepts for SOFC stacks. In: Singhal SC, Dokya M, editors. 8th International symposium on solid oxide fuel cells. Pennington (NJ), Paris (France): The Electrochemical Society; 2003. p. 888–97.
- [1049] Duquette J, Petric A. Silver wire seal design for planar solid oxide fuel cell stack. *J Power Sour* 2004;137:71–5.
- [1050] Chou Y-S, Stevenson JW. Novel silver/mica multilayer compressive seals for solid oxide fuel cells: the effect of thermal cycling and material degradation on leak behavior. *J Mater Res* 2003;18:2243–50.
- [1051] Weil KS, Hardy JS. Developement of a compliant seal for use in planer Solid Oxide Fuel Cells. In: Lara-Curzio E, Readey MJ, editors. 28th International conference on advanced ceramics and composites a: ceramic engineering and science proceedings. Cocoa Beach (FL, USA): The American Ceramic Society; 2004. p. 321–6.
- [1052] Shao ZB, Liu KR, Liu LQ, Liu HK, Dou S-x. Equilibrium phase diagrams in the systems PbO–Ag and CuO–Ag. *J Am Ceram Soc* 1993;76:2663–4.
- [1053] Meier AM, Chidambaram PR, Edwards GR. A comparison of the wettability of copper-copper oxide and silver-copper oxide on polycrystalline alumina. *J Mater Sci* 1995;30:4781–6.
- [1054] Yang ZG, Weil KS, Paxton DM, Stevenson JW. Selection and evaluation of heat-resistant alloys for SOFC interconnect applications. *J Electrochem Soc* 2003;150:A1188–201.
- [1055] Meier G. Fundamental study of the durability of materials for interconnect in solid oxide fuel cells. SECA core technology program review. Albany (NY, USA); 2003.
- [1056] Simmer SP, Stevenson JW. Compressive mica seals for SOFC applications. *J Power Sour* 2001;102:310–6.
- [1057] Chou Y-S, Stevenson JW, Chick LA. Ultra-low leak rate of hybrid compressive seals for solid oxide fuel cells. *J Power Sour* 2002;112:130–6.
- [1058] Bram M, Reckers S, Drinovac P, Mönch J, Steinbrech RW, Buchkremer HP, et al. Deformation behavior and leakage tests of alternate sealing materials for SOFC stacks. *J Power Sour* 2004;138:111–9.
- [1059] Chou Y-S, Stevenson JW. Novel infiltrated phlogopite mica compressive seals for solid oxide fuel cells. *J Power Sour* 2004;135:72–8.
- [1060] Chou Y-S, Stevenson JW. Phlogopite mica-based compressive seals for solid oxide fuel cells: effect of mica thickness. *J Power Sour* 2003;124:473–8.
- [1061] Chou Y-s, Stevenson JW. Thermal cycling and degradation mechanisms of compressive mica-based seals for solid oxide fuel cells. *J Power Sour* 2002;112:376–83.
- [1062] Chou Y-S, Stevenson JW. Mid-term stability of novel mica-based compressive seals for solid oxide fuel cells. *J Power Sour* 2003;115:274–8.
- [1063] Chou Y-S, Stevenson JW. Long-term thermal cycling of Phlogopite mica-based compressive seals for solid oxide fuel cells. *J Power Sour* 2005;140:340–5.
- [1064] Jinnapat A, Jiamsirilert S, Charojrochkul S. Study of ceramic seal for solid oxide fuel cells. *Adv Technol Mater Mater Process* 2007;9:109–14.
- [1065] Chou Y-S, Stevenson JW. Compressive mica seals for Solid Oxide Fuel Cells. *J Mater Eng Perform* 2006;15:414–21.
- [1066] Wiener F, Bram M, Buchkremer H-P, Sebold D. Chemical interaction between Crofer 22 APU and mica-based gaskets under simulated SOFC conditions. *J Mater Sci* 2007;42:2643–51.
- [1067] Zanotto ED. A bright future for glass-ceramics. *Am Ceram Soc Bullet* 2010;89:19–27.

- [1068] Yamamoto T, Itoh H, Mori M, Mori N, Watanabe T. Compatibility of mica glass ceramics as gas-sealing materials for SOFC. Denki Kagaku Oyobi Kogyo Butsuri Kagaku 1996;64:575–81.
- [1069] Yamamoto T, Itoh H, Mori M, Mori N, Abe T. Applications of mica glass-ceramics to gas-sealing material for SOFC. In: Dokiya M, Yamamoto O, Tagawa H, Singhal SC, editors. 4th International symposium on solid oxide fuel cells. Pennington (NJ), Yokohama (Japan): The Electrochemical Society; 1995. p. 245–54.
- [1070] Boersma RJ, Sammes NM, Zhang Y. Measurement of properties of sealant materials for solid oxide fuel cell system. *J Aust Ceram Soc* 1998;34:242–7.
- [1071] Trapp HJL, Stevels JM. Physical properties of invert glasses. *Glastechn Ber*. 1959.
- [1072] Meinhardt KD, Vienna JD, Armstrong TR, Pederson LR. Glass-ceramic joint and method of joining US Pat. 65327692003.
- [1073] www.glassproperties.com/sofc/.
- [1074] Sohn S-B, Choi S-Y, Kim G-H, Song H-S, Kim G-D. Suitable glass-ceramic sealant for planar solid-oxide fuel cells. *J Am Ceram Soc* 2004;87:254–60.
- [1075] Ohara S, Mukai K, Fukui T, Sakaki Y, Hattori M, Esaki Y. A new sealant material for solid oxide fuel cells using glass-ceramic. *J Ceram Soc Jap* 2001;109:186–90.
- [1076] Loehman RE, Dumm HP, Hofer H. Evaluation of sealing glasses for solid oxide fuel cells. *Ceram Eng Sci Proc* 2002;23:699–710.
- [1077] Yang Z, Xia G, Meinhardt KD, Weil KS, Stevenson JW. Chemical stability of glass seal interfaces in intermediate temperature solid oxide fuel cells. *J Mater Eng Perform* 2004;13:327–34.
- [1078] Sohn S-B, Choi S-Y, Kim G-H, Song H-S, Kim G-D. Stable sealing glass for planar solid oxide fuel cell. *J Non-Crystall Solids* 2002;297:103–12.
- [1079] Yang Z, Meinhardt KD, Stevenson JW. Chemical compatibility of barium–calcium–aluminosilicate-based sealing glasses with the ferritic stainless steel interconnect in SOFCs. *J Electrochem Soc* 2003;150:A1095–101.
- [1080] Yang Z, Stevenson JW, Meinhardt KD. Chemical interactions of barium–calcium–aluminosilicate-based sealing glasses with oxidation resistant alloys. *Solid State Ionics* 2003;160:213–25.
- [1081] Zheng R, Wang SR, Nie HW, Wen T-L. $\text{SiO}_2\text{-CaO}\text{-B}_2\text{O}_3\text{-Al}_2\text{O}_3$ ceramic glaze as sealant for planar IT-SOFC. *J Power Sour* 2004;128:165–72.
- [1082] Lara C, Pascual MJ, Prado MO, Durán A. Sintering of glasses in the system $\text{RO}\text{-Al}_2\text{O}_3\text{-BaO}\text{-SiO}_2$ ($\text{R} = \text{Ca}, \text{Mg}, \text{Zn}$) studied by hot-stage microscopy. *Solid State Ionics* 2004;170:201–8.
- [1083] Larsen PH, James PF. Chemical stability of $\text{MgO}/\text{CaO}/\text{Cr}_2\text{O}_3\text{-Al}_2\text{O}_3\text{-B}_2\text{O}_3$ -phosphate glasses in solid oxide fuel cell environment. *J Mater Sci* 1998;33:2499–507.
- [1084] Larsen PH, Poulsen FW, Berg RW. The influence of SiO_2 addition to $2\text{MgO}\text{-Al}_2\text{O}_3\text{-3.3P}_2\text{O}_5$ glass. *J Non-Crystall Solids* 1999;244:16–24.
- [1085] Singh RN. High temperature seals for solid oxide fuel cells. In: Lara-Curzio E, Readey MJ, editors. 28th International conference on advanced ceramics and composites a: ceramic engineering and science proceedings. Cocoa Beach (FL, USA): The American Ceramic Society; 2004. p. 299–307.
- [1086] Lahl N, Singheiser L, Hilpert K, Singh K, Bahadur D. Aluminosilicate glass-ceramics as sealant in SOFC stacks. In: Singhal SC, Dokiya M, editors. 6th International symposium on solid oxide fuel cells. Pennington (NJ), Honolulu (HI, USA): The Electrochemical Society; 1999. p. 1057–65.
- [1087] Eichler K, Solow G, Otschik P, Schaffrath W. Degradation effects at sealing glasses for the SOFC. In: McEvoy AJ, editor. Proceedings of 4th European solid oxide fuel cell forum. Lucerne (Switzerland): The European Fuel Cell Forum; 2000 . p. 899–906.
- [1088] Battafsky P, Haanappel VAC, Malzbender J, Menzler NH, Shemet V, Vinke IC, et al. Chemical interaction between glass-ceramic sealants and interconnect steels in SOFC stacks. *J Power Sour* 2006;155:128–37.
- [1089] Donald IW. Preparation, properties and chemistry of glass and glass-ceramic-to-metal seals and coatings. *J Mater Sci* 1993;28:2841–86.
- [1090] Nielsen KA, Solväng M, Poulsen FW, Larsen PH. Evaluation of sodium aluminosilicate glass composite seal with magnesia filler. In: Lara-Curzio E, Readey MJ, editors. 28th International conference on advanced ceramics and composites a: ceramic engineering and science proceedings. Cocoa Beach (FL, USA): American Ceramic Society; 2004. p. 309–14.
- [1091] Bieberle A, Gauckler LJ. Glass Seals, proceedings of the NATO advanced study institute. In: Tuller HL, Schoonman J, Riess I, editors. Oxygen ion and mixed conductors and their technological applications. Erice (Italy): Springer; 2000. p. 389–97.
- [1092] Ley KL, Krumpelt M, Kumar R, Meiser JH, Bloom I. Glass-ceramic sealants for solid oxide fuel cells: part I. Physical properties. *J Mater Res* 1996;11:1489–93.
- [1093] Jiang SP, Christiansen L, Hughan B, Fogar K. Effect of glass sealant materials on microstructure and performance of Sr-doped LaMnO_3 cathodes. *J Mater Sci Lett* 2001;20:695–7.
- [1094] Geasee P, Schwickert T, Diekmann U, Conradt R. Ceramic materials and components for engines. Weinheim (Germany): Wiley-VCH Verlag GmbH; 2001.
- [1095] Sohn S-B, Choi S-Y, Kim G-H, Song H-S, Kim G-D. Stable sealing glass for planar solid oxide fuel cell. *J Non-Crystall Solids* 2002;297:103–12.
- [1096] Sung YM. The effect of additives on the crystallization and sintering of $2\text{MgO}\text{-2Al}_2\text{O}_3\text{-5SiO}_2$ glass-ceramics. *J Mater Sci* 1996;31:5421–7.
- [1097] Lara C, Pascual MJ, Dura'n A. Glass-forming ability, sinterability and thermal properties in the systems $\text{RO}\text{-BaO}\text{-SiO}_2$ ($\text{R} = \text{Mg}, \text{Zn}$). *J Non-Crystall Solids* 2004;348:149–55.
- [1098] Höland W, Beall G. Glass-ceramic technology. Westerville (OH, USA): The American Ceramic Society; 2002.
- [1099] Touloukian YS. Thermophysical properties of high temperature solid materials. New York (NY, USA): The MacMillan Co.; 1967.
- [1100] Weil KS, Deibler JE, Hardy JS, Kim DS, Xia G-G, Chick LA, et al. Rupture testing as a tool for developing planar solid oxide fuel cell seals. *J Mater Eng Perform* 2004;13:316–26.

- [1101] Menzler NH, Bram M, Buchkremer HP, ver DS. Development of a gastight sealing material for ceramic components. *J Eur Ceram Soc* 2003;23:445–54.
- [1102] Bansal NP, Hyatt MJ, Drummond III CH. Crystallization and properties of Sr–Ba aluminosilicate glass-ceramic matrices. *Ceram Eng Sci Proc* 1991;12:1222–34.
- [1103] Bahat D. Several metastable alkaline earth feldspar modifications. *J Mater Sci* 1972;7:198–201.
- [1104] Lahl N, Singh K, Singheiser L, Hilpert K, Bahadur D. Crystallisation kinetics in AO–Al₂O₃–SiO₂–B₂O₃ glasses (A = Ba, Ca, Mg). *J Mater Sci* 2000;35:3089–96.
- [1105] Lahl N, Singheiser L, Hilpert K, Singh K, Bahadur D. Aluminosilicate glass ceramics as sealant in SOFC stacks. In: Singhal SC, Dokiya M, editors. 6th International symposium on solid oxide fuel cells. Pennington (NJ), Honolulu (HI, USA): The Electrochemical Society; 2005. p. 1057–65.
- [1106] Lahl N, Bahadur D, Singh K, Singheiser L, Hilpert K. Chemical interactions between aluminosilicate base sealants and the components on the anode side of solid oxide fuel cells. *J Electrochem Soc* 2002;149:A607–14.
- [1107] Bahadur D, Lahl N, Singh K, Singheiser L, Hilpert K. Influence of nucleating agents on the chemical interaction of MgO–Al₂O₃–SiO₂–B₂O₃ glass sealants with components of SOFCs. *J Electrochem Soc* 2004;151:A558–62.
- [1108] McMillan PW. Glass-ceramics. London (UK): Academic Press; 1979.
- [1109] Sakaki Y, Hattori M, Esaki Y, Ohara Y, Fukui T, Kodera K, et al. Glass-ceramic sealants based on CaO–Al₂O₃–SiO₂ system. In: Stimming U, Singhal SC, Tagawa H, Lehnert W, editors. 5th International symposium on solid oxide fuel cells. Pennington (NJ), Aachen (Germany): The Electrochemical Society, Inc; 1997. p. 652–60.
- [1110] Wen T-L, Wang D, Chen M, Tu H, Lu Z, Zhang Z, et al. Material research for planar SOFC stack. *Solid State Ionics* 2002;148:513–9.
- [1111] Schwickert T, Reisgen U, Geasee P, Conradt R. Electrically insulating high-temperature joints for ferritic chromium steel. *J Adv Mater* 2003;35:44–7.
- [1112] Esposito L, Bellosi A. Interfacial characteristics in ceramic joining with glass interlayers. In: Lin H-T, Singh M, editors. 26th Annual conference on composites, advanced ceramics, materials, and structures a: ceramic engineering and science proceedings. Cocoa Beach (FL, USA): The American Ceramic Society; 2002. p. 793–800.
- [1113] Smeacetto F, Salvo M, Ferraris M, Chob J, Boccaccini AR. Glass–ceramic seal to join Crofer 22 APU alloy to YSZ ceramic in planar SOFCs. *J Euro Ceram Soc* 2008;28:61–8.
- [1114] Brow RK, Tallant DR. Structural design of sealing glasses. *J Non-Crystall Solids* 1997;222:396–406.
- [1115] Meinhardt KD, Vienna JD, Armstrong TR, Pederson LR. Glass-ceramic material and method of making. US: Battelle Memorial Institute (Richland, WA, USA); 2003.
- [1116] Larsen PH, Bagger C, Mogensen M, Larsen JG. Stacking of planar SOFCs. In: Dokiya M, Yamamoto O, Tagawa H, Singhal SC, editors. 4th International symposium on solid oxide fuel cells. Pennington (NJ), Yokohama (Japan): The Electrochemical Society, Inc.; 1995. p. 69–78.
- [1117] Cleek GW, Babcock CL. Properties of glasses in some ternary systems containing BaO and SiO₂. National bureau of standards monograph, vol. 135. Library of Congress, Catalog No. 73-600135; 1973.
- [1118] Lewinsohn CA, Elangovan S, Quist SM. Durable seal materials for planar solid oxide fuel cells. In: Lara-Curcio E, Readey MJ, editors. 28th Annual conference on composites, advanced ceramics, materials, and structures a: ceramic engineering and science proceedings. Cocoa Beach (FL, USA): The American Ceramic Society; 2004. p. 315–20.
- [1119] Lewinsohn CA, Elangovan S. Development of amorphous, non-oxide seals for solid oxide fuel cells. In: Kriven WM, Lin H-T, editors. 27th Annual conference on composites, advanced ceramics, materials, and structures a: ceramic engineering and science proceedings. Cocoa Beach (FL, USA): The American Ceramic Society; 2003. p. 317–22.
- [1120] Taniguchi S, Kadokami M, Yasuo T, Akiyama Y, Miyake Y, Nishio K. Improvement of thermal cycle characteristics of a planar-type solid oxide fuel cell by using ceramic fiber as sealing material. *J Power Sour* 2000;90:163–9.
- [1121] Xue LA, Piascik J, Yamanis J, Lear G, Powers J, Dalfonzo D. Composite sealant material for solid oxide fuel cells, US Patent 627115 B1, US7 August 2001.
- [1122] Huang X, Ridgeway K, Narasimhan S, Reifsnider K, Ma X. Application of plasma sprayed coatings in a novel integrated composite seal for SOFCs, Building on 100 years of success. Seattle (WA, USA): ASM International; 2006.
- [1123] Bianchi L, Toulchoat J, Bories C. Solid seal which is obtained by means of thermal spraying, 2007, WO/2007/042505.
- [1124] Fauchais P, Vardelle A, Dussoubs B. *Quo vadis thermal spraying?* *J Therm Spray Technol* 2001;10:44–66.
- [1125] Chikagawa O, Takagi H, Iha M. US5585203; 1996.
- [1126] Jansing T, Martens T. US5942348; 1999.
- [1127] Tompson C, Wood A, Pyke S. US20036656625B1; 2003.
- [1128] <http://www.netl.doe.gov/publications/proceedings/03/seca-seal/OverviewStevenson.pdf>.
- [1129] Wei W-CJ. Sealing glass-ceramics for solid oxide fuel cell. Recent Patents Mater Sci 2008;1:217–22.
- [1130] http://www.inpi.gov.br/images/stories/downloads/pdf/Alerta_82_CC6_Cel_Comb_2012_1_semestre.pdf.
- [1131] http://worldwide.espacenet.com/publicationDetails/biblio?CC=EP&NR=2028707&KC=&FT=E&locale=en_EP.
- [1132] Tucker MC, Jacobson CP, Jonghe LCD, Visco SJ. A braze system for sealing metal-supported solid oxide fuel cells. *J Power Sour* 2006;160:1049–57.
- [1133] Weil KS, Rice JP. Substrate effects on the high temperature oxidation behavior of a gold-based braze filler metal. *Scripta Mater* 2005;52:1081–5.
- [1134] Rice JP, Paxton D, Weil K. Oxidation behavior of a commercial gold-based braze alloy for ceramic-to-metal joining. Westerville (OH, USA): American Ceramic Society; 2002.
- [1135] Khan TI, Al-Badri A. Reactive brazing of ceria to an ODS ferritic stainless steel. *J Mater Sci* 2003;38:2483–8.
- [1136] Mei J, Xiao P. Joining metals to zirconia for high temperature applications. *Scripta Mater* 1999;40:587–94.
- [1137] Weil KS, Coyle CA, Darsell JT, Xia GG, Hardy JS. Effects of thermal cycling and thermal aging on the hermeticity and strength of silver–copper oxide air-brazed seals. *J Power Sour* 2005;152:97–104.
- [1138] Nishiura H, Suzuki RO, Ono K, Gauckler LJ. Experimental phase diagram in the Ag–Cu₂O–CuO system. *J Am Ceram Soc* 1998;81:2181–7.
- [1139] Roth RS. ACerS-NIST phase equilibria diagrams, vol. 13. Westerville (OH, USA): The American Ceramic Society; 2001.

- [1140] Schuler CC, Stuck A, Beck N, Keser H, Taek U. Direct silver bonding- an alternative for substrates in power semiconductor packaging. *J Mater Sci: Mater Electron* 2000;11:389–96.
- [1141] Erskine KM, Meier AM, Pilgrim SM. Brazing perovskite ceramics with silver/copper oxide braze alloys. *J Mater Sci* 2002;37:1705–9.
- [1142] Menzler NH, Sebold D, Zahid M, Gross SM, Koppitz T. Interaction of metallic SOFC interconnect materials with glass-ceramic sealant in various atmospheres. *J Power Sour* 2005;152:156–67.
- [1143] Kobsiriphat W, Barnett S. Ag–Cu–Ti braze materials for sealing SOFCs. *J Fuel Cell Sci Technol* 2008;5:011002–9.
- [1144] Tucker MC, Jacobson CP, DeJonghe LC, Visco SJ. A braze system for sealing metal-supported SOFCs. In: Singhal SC, Mizusaki J, editors. *9th International symposium on solid oxide fuel cells*. Pennington (NJ), Quebec City (Canada): The Electrochemical Society; 2005. p. 1967–75.
- [1145] Lewinsohn C, Quist S, Elangovan S. Novel materials for obtaining compliant, high temperature seals for solid oxide fuel cells, SECA core technology program review. Albany (NY, USA); 2003.
- [1146] Loehman R. Development of high performance seals for solid oxide fuel cells. SECA core technology program review. Albany (NY, USA); 2003.